IRE Transactions

on Microwave Theory and Techniques

Volume MTT-7 **JANUARY, 1959** Number 1

In This Issue

Message From The Chairman	page 2
Frontispiece	page 3
Editorial	page 4
Foreword	page 5
Contributions	page 6
Correspondence	page 174
PGMTT News	page 178
Call for Papers 1959 National Symposium	page 180
Contributors	page 181

PUBLISHED BY THE
essional Group on Microwave Theory and Techniques

IRE PROFESSIONAL GROUP ON MICROWAVE THEORY AND TECHNIQUES

The Professional Group on Microwave Theory and Techniques is an association of IRE members with professional interest in the field of Microwave Theory and Techniques. All IRE members are eligible for membership and will receive all Group publications upon payment of the prescribed annual fee of $3.00. Members of the American Physical Society and the Institution of Electrical Engineers of Great Britain may become affiliated with PGMTT and receive all Group publications upon payment of the Affiliate fee of $7.50 per year.

IRE TRANSACTIONS®

on Microwave Theory and Techniques

Published by the Institute of Radio Engineers, Inc., for the Professional Group on Microwave Theory and Techniques, at 1 East 79th Street, New York 21, New York. Responsibility for the contents rests upon the authors, and not upon the IRE, the Group, or its members. Price per copy: IRE PGMTT members, $3.75; IRE members, $5.60, nonmembers, $11.25. Annual subscription price: IRE members, $8.50; colleges and public libraries, $12.75; nonmembers, $17.00.

Address all manuscripts to Donald D. King, PGMTT Editor, Electronic Communications, Inc., 1830 York Road, Timonium, Md. Submission of three copies of manuscripts, including figures, will expedite the review.

IRE Transactions on Microwave Theory and Techniques

Volume MTT-7 JANUARY, 1959 Number 1

TABLE OF CONTENTS

Message from The Chairman ..... *T. S. Saad* 2
Frontispiece ..... *Wilbur L. Pritchard* 3
Education and Science in a Mature Society ..... *Wilbur L. Pritchard* 4
Foreword ..... *A. L. Aden* 5

CONTRIBUTIONS

Microwave Radiation from Ferrimagnetically Coupled Electrons in Transient Magnetic Fields ..... *Frederic R. Morgenthaler* 6
Ferrite High-Power Effects in Waveguides ..... *E. Stern and R. S. Mangiaracina* 11
Temperature Effects in Microwave Ferrite Devices ..... *J. L. Melchor and P. H. Vartanian* 15
Characteristics of Ferrite Microwave Limiters ..... *G. S. Uebele* 18
Nonreciprocity in Dielectric Loaded TEM Mode Transmission Lines ..... *D. Fleri and G. Hanley* 23
Ferrite Phase Shifter for the UHF Region ..... *C. M. Johnson* 27
A Ferrite Serrodyne for Microwave Frequency Translation ..... *F. J. O'Hara and H. Scharfman* 32
Broad-Band Ferrite Rotators Using Quadruply-Ridged Circular Waveguide ..... *H. N. Chait and N. G. Sakiotis* 38
Present State of the Millimeter Wave Generation and Technique Art—1958 ..... *P. D. Coleman and R. C. Becker* 42
Millimeter-Wave Generation Experiment Utilizing Ferrites ..... *Wesley P. Ayres* 62
Some Characteristics of Dielectric Image Lines at Millimeter Wavelengths ..... *James C. Wiltse* 65
The Interaction of Microwaves with Gas-Discharge Plasmas ..... *Sanborn C. Brown* 69
High Power, Magnetic Field Controlled Microwave Gas Discharge Switches ..... *S. J. Tetenbaum and R. M. Hill* 73
Solid-State Microwave Amplifiers ..... *Hubert Heffner* 83
A UHF Solid-State Maser ..... *R. H. Kingston* 92
A Microwave Frequency Standard Employing Optically Pumped Sodium Vapor ..... *W. E. Bell, A. Bloom, and R. Williams* 95
Microwave Filter Design Using an Electronic Digital Computer ..... *Leo Young* 99
Measurement of Two-Mode Discontinuities in a Multimode Waveguide by a Resonance Technique ..... *L. B. Felsen, W. K. Kahn, and L. Levey* 102
Mode Couplers and Multimode Measurement Techniques ..... *D. J. Lewis* 110
Measurement of Harmonic Power Generated by Microwave Transmitters ..... *Vernon G. Price* 116
Tunable Passive Multicouplers Employing Minimum-Loss Filters ..... *J. F. Cline and B. M. Schiffman* 121
A Wide-Band Strip-Line Balun ..... *E. M. T. Jones and J. K. Shimizu* 128
Periodic Structures in Trough Waveguide ..... *A. A. Oliner and W. Rotman* 134
A Study of a Serrated Ridge Waveguide ..... *H. S. Kirschbaum and R. Tsu* 142
Design Considerations for High-Power Microwave Filters ..... *Seymour B. Cohn* 149
Evacuated Waveguide Filter for Suppressing Spurious Transmission from High-Power *S*-Band Radar ..... *H. A. Wheeler and H. L. Bachman* 154
Hybrid Junction—Cutoff Waveguide Filters ..... *Eugene N. Torgow* 163
Practical Design of Strip-Transmission-Line Half-Wavelength Resonator Directional Filters ..... *R. D. Wanselow and L. P. Tuttle, Jr.* 168

CORRESPONDENCE

A High Average Power Broad-Band Ferrite Load Isolator for *S* Band ..... *E. N. Skomal* 174
Reflection Coefficient of *E*-Plane Tapered Waveguides ..... *R. F. H. Yang and K. Matsumaru* 175
The Permeability Matrix for a Ferrite Medium Magnetized at an Arbitrary Direction and Its Eigenvalues ..... *George Tyras* 176
Resistive-Film Calorimeters for Microwave Power Measurement ..... *J. A. Lane* 177
PGMTT News 178
Call for Papers for 1959 PGMTT National Symposium 180
Contributors 181

Message from the Chairman

A major portion of the operation of the PGMTT rests each year upon several editors, committee chairmen and other individuals. While it has not been customary to honor them with any special recognition, we wish to take this opportunity to identify them to express appreciation for their generous contribution of time and effort.

Editors

Editor of the TRANSACTIONS	Donald D. King (Effective January 1, 1959)
Advertising Editor	Tore N. Anderson
Newsletter Editor	Gustave Shapiro

Committees

Annual Review Committee	(Chairman unannounced)
Awards Committee	William W. Mumford
Meetings Committee	Arthur A. Oliner
Membership Committee	Richard F. Schwartz
Nomination Committee	Alfred C. Beck
Sectional Activities Committee	Tore N. Anderson

Tasks

Constitution and By-Laws	Herbert F. Engelmann
Foreign Distribution of TRANSACTIONS	Arthur A. Oliner
National Convention Record	Gustave Shapiro
WESCON	Seymour B. Cohn

THEODORE S. SAAD, *Chairman*
PGMTT Administrative Committee

Wilbur L. Pritchard

Wilbur L. Pritchard (A'45–M'48–SM'52) was born in New York, N. Y., on May 31, 1923. He received the B.E.E. degree in 1943 from the College of the City of New York. From 1948 to 1951 he was gaged in part-time graduate study at the Massachusetts Institute of Technology.

He was a junior engineer with Philco Radio and Television Corporation from 1943 to 1946 and worked on the development of airborne radar equipment, home radios, and phonographs. In 1946 he joined Raytheon Manufacturing Company as a senior engineer. He was promoted to section manager of the Microwave Section in 1949, and in 1954 became manager of the Microwave-Transmitter Branch. Since 1958 he has been manager of the Surface Radar Department, which is responsible for the design, development, and release to production of ground-based and marine radar equipment.

Mr. Pritchard has published several articles covering such topics as filters, echo boxes, microwave receivers, and magnetron operation. He is a past chairman of the EIA Waveguide Committee, and a member and past chairman of the Administrative Committee of PGMTT.

Education and Science in a Mature Society

WILBUR L. PRITCHARD†

DURING recent years self-examination by many thinking Americans has evolved extensive criticism of our educational system.

On the one hand, just after the war the criticism was engendered largely by the apparent political naivete of some engineers and scientists. This unawareness on their part contributed to several unfortunate incidents and made the public sensitive to the need for political and cultural sophistication on the part of scientists. Our professional schools were criticized freely for providing curricula so narrowly technical that they did not produce wholly educated people. This criticism was just. No one disputes the need for broad education in scientific and engineering schools.

On the other hand, the onset of the space age and its implications have pointed up the need for ever-increasing numbers of scientists and engineers; now the criticism of our schooling system is driving us towards increasing the number and quality of technically trained people. But the full realization of new technological standards in education cannot come about without some infusion of science into the political influences that determine our standards of education.

Recent criticism has been along the lines that our modern educators have gone too far in the direction of permissive schooling, that we have departed from rigorous discipline and have been victimized by "progressive" educators. Unquestionably some of this is true now, as it has always been. However, if we revert to the criticism of ten years ago, centering about the lack of political education among scientists, we find that it was not at all accompanied by a criticism of the lack of scientific education among politicians, although it must be fairly obvious that such a lack would undermine the basis of improvement of the scientific status of the community.

It seems to be a fact that most of our political leaders, both domestic and international, have educational backgrounds in liberal arts, economics, law, and the social sciences. A cursory look at the curricula for these courses, even in the best schools, for both undergraduate and graduate work, shows an appalling lack of science. Remember that technology is a dominant key in modern society. And yet, we educate people ultimately to become leaders of this society with no more scientific knowledge than is included in a one or two-semester "survey" course. As a result, they never develop the slightest understanding of either the aims of scientific research or the methods of engineering development.

Consider the plight of an administrator, a business executive or legislator, making decisions or voting on policy questions of dramatic consequence to the whole nation, although not equipped to understand even the simplest scientific or engineering problem. How much postwar major international policy was predicated on the assumption that nuclear weapon development was based on "secret" processes. This happened despite the frequent assertions of scientists that there was no "secret," and that one nation could duplicate the performance of another in a short time. They were ignored under the popular assumption that since scientists were uneducated politically, politicians were, perforce, well educated technically.

There is no intent to apply this criticism solely to people concerned with public affairs. As a matter of fact, legislators, administrators, and businessmen reflect the prevalent opinions of the public more often than not, and this is as it should be in a democratic country. Unfortunately this public opinion is often uninformed, or worse, misinformed. Lay concepts of science are too frequently based on the Hollywood picture.

All this means that the situation must be corrected at its source. A sharp increase is called for in the amount of scientific education in a general curriculum. A high-school physics course or one year of college chemistry and no mathematics do not provide sufficient educational breadth to prepare a man for intelligent political or business management.

Worse, an alarming number of our present educators, by virtue of their own inadequate elementary scientific training, are perpetuating these standards for our next era of educators! This degenerative chain must be broken.

The civilization and maturity of a future society will depend not on having a swarm of trained robot scientists at the disposal of a nontechnical directorate, but on a blending of the goals of technology and political and social science. This will be achieved only as a result of a mutual appreciation, stemming from a common educational background, that provides a sound scientific understanding in addition to an awareness of political and social responsibility.

† Raytheon Mfg. Co., Wayland, Mass.

Foreword

PLANS for the 1958 PGMTT National Symposium started during August, 1957 with a decision by the San Francisco Chapter of the PGMTT to try to hold the Symposium on the West Coast. Preliminary inquiry indicated that Stanford University would be willing to provide the facilities. Subsequent endorsement of the plan was given by the San Francisco Section of the IRE, the PGMTT Administrative Committee, and IRE Headquarters. The PGMTT Administrative Committee assumed financial responsibility and approved A. L. Aden as Symposium Chairman. It also approved a list of names submitted as candidates for the Symposium Steering Committee. As a policy guideline it was suggested that the scope of the Symposium be expanded to include all fields of interest to the PGMTT.

The Steering Committee was formed comprising the eleven members listed with representation from the PGMTT Administrative Committee, the San Francisco Section of the IRE, the San Francisco Chapter of the PGMTT, the two major universities in the area, the previous year's Symposium Chairman, and local industry.

Steering Committee

A. L. Aden, Sylvania Microwave Physics Laboratory, Mountain View, Calif.
T. N. Anderson, Airtron, Inc., Linden, N. J. Ex-officio member, Chairman, 1957 Annual PGMTT Meeting.
S. B. Cohn, Stanford Research Institute, Menlo Park, Calif.
W. A. Edson, General Electric Microwave Laboratory, Palo Alto, Calif.
H. Heffner, Stanford University, Stanford, Calif.
P. D. Lacy, Hewlett-Packard Company, Palo Alto, Calif.
J. L. Melchor, Microwave Engineering Laboratories, Palo Alto, Calif.
T. Moreno, Varian Associates, Palo Alto, Calif.
W. H. Thon, Sylvania Microwave Tube Laboratory, Mountain View, Calif.
K. Tomiyasu, General Electric Microwave Laboratory, Palo Alto, Calif.
J. R. Whinnery, University of California, Berkeley, Calif.

The Steering Committee formulated the general plans and appointed a five-man Symposium Committee consisting of the following chairmen:

A. L. Aden—*Symposium*
K. Tomiyasu—*Technical Program*
T. Moreno—*Finance*
G. H. Keitel—*Publicity*
H. W. Schroeder—*Local Arrangements.*

This committee was responsible for the detailed planning and organization of the Symposium.

The Symposium was held at Stanford University on May 5–7. The technical program was conducted in 6 single sessions, with 2 sessions on ferrites, 2 sessions on microwave physics, 1 session on microwave techniques, and 1 session on microwave filters. There were 6 invited papers which were chosen to be tutorial to the topic of the session in which they were given. Thirty-three contributed papers were selected out of 79 submitted. Total registered attendance at the Symposium was 437. A banquet was held at Rickey's Studio Inn, Palo Alto, on the evening of May 6, with 183 in attendance. Dr. F. E. Terman, Dean of Engineering and Provost, Stanford University, presented the keynote address, "Basic Research in Industry and Education." The Microwave Prize for the best paper published in these TRANSACTIONS was awarded at the banquet to H. Seidel.

The large attendance and enthusiastic response to the 1958 PGMTT National Symposium was most gratifying to the Symposium Committee. Thanks are extended to many people who helped make this possible. Particular acknowledgment is made to Stanford University for providing the facilities and for the endorsement by the Electrical Engineering Department; to the Steering Committee for their guidance and assistance in planning the Symposium; and to the PGMTT Administrative Committee for their cooperation and support

A. L. ADEN
Chairman, 1958 PGMTT National Symposium

Microwave Radiation from Ferrimagnetically Coupled Electrons in Transient Magnetic Fields*

FREDERIC R. MORGENTHALER†

Summary—Under certain restrictive conditions it appears that ferrimagnetically coupled electron spins are capable of coupling energy from a transient magnetic field and giving it up in the form of microwave radiation.

This paper analyzes the behavior of the uniform precession of motion in ferrimagnetic insulators under the influence of transient magnetic fields of changing amplitude and direction.

The expected radiation power and efficiency are calculated for such an oscillator employing yttrium iron garnet.

Introduction

THE transient behavior of ferrimagnetically coupled electrons in pulsed magnetic fields is of considerable interest since it has been found that under certain conditions such electrons appear capable of coupling energy from the field and converting it into electromagnetic radiation. R. V. Pound of Harvard University has proposed a solid-state ferrimagnetic microwave oscillator that would operate as follows.

A small ferrimagnetic crystal is placed in the minimum constant magnetic field required for saturation. At right angles to this constant field, a large pulsed magnetic field is applied. The electrons previously aligned to the constant biasing field will now align themselves with the resultant. If the rise time of the pulsed field is sufficiently rapid, this realignment will consist of the electrons precessing about the larger field, gradually spiraling in at a rate dependent upon the damping. This damping is due to radiation from the precession and heat losses. To be practical, the pulse magnetic rise time must be fast compared with the relaxation time constant of the ferrimagnetic crystal and the latter large enough for an appreciable pulse of radiation to result. The frequency of the radiated energy depends upon the precession frequency of the electrons which is a function of the magnitude of the magnetic pulse as given by the Larmor relation $\omega = -\gamma\mu_0 H$ where γ is the gyromagnetic ratio (including g factor) for ferromagnetic electrons.

In a private conversation with the author, C. L. Hogan postulated that the rise time of the pulsed magnetic field would be critical in another sense as illustrated in Fig. 1.

Here the magnetic field is assumed to jump in discrete steps (as from H_1 to H_2) during the rise. Originally, the electron magnetic moment vector precesses about H_1, generating a cone of small angle. If the jump of the magnetic field to H_2 occurs when the tip of the vector is at x, the small circle is the new precession path; if the tip of the vector is at y, the large circle is the precession path. It is extremely critical in this example when the magnetic field jump occurs, for in the first case the electron will have coupled energy *to* the magnetic field whereas in the second case it will have coupled energy *from* the field. The behavior is not quite so obvious when the discrete jumps are made continuous and so a theoretical analysis was undertaken. The formulation is for an electron interacting with a transient magnetic field of changing amplitude and direction but always lying in the same plane.

The problem can be generalized for the field moving in three dimensions but this is a needless complexity for this application.

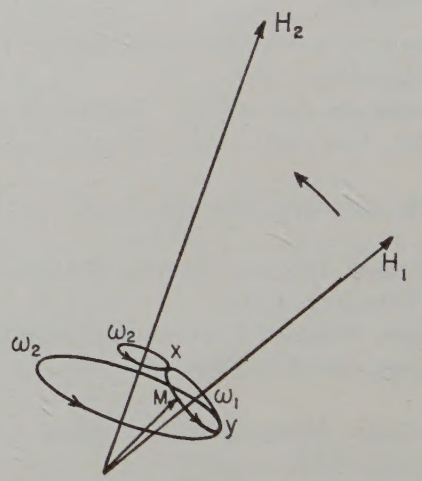

Fig. 1—Magnetization under transient field conditions.

Differential Equations

A Lagrangian formulation is used to derive the differential equations of motion of the magnetization. Fig. 2 gives the coordinate systems to be used. A spherical sample shape is assumed, so that the Kittel frequency will be independent of θ. Since demagnetizing effects cancel, only a single classical electron spin needs to be considered. The electron is considered to be a sphere of mass M, containing a charge e, located at the origin. It is spinning about a diameter with some radian frequency ω_0, with an angular momentum J_0, and magnetic moment $m = \gamma J_0$ (where $\gamma \simeq -e/M$). The mks system of units will be used throughout.

Reference to the figure shows that $x'y'z'$ is a moving

* Manuscript received by the PGMTT, June 16, 1958; revised manuscript received, September 5, 1958.

† Air Force Cambridge Res. Center, Air Res. and Dev. Command, Bedford, Mass.

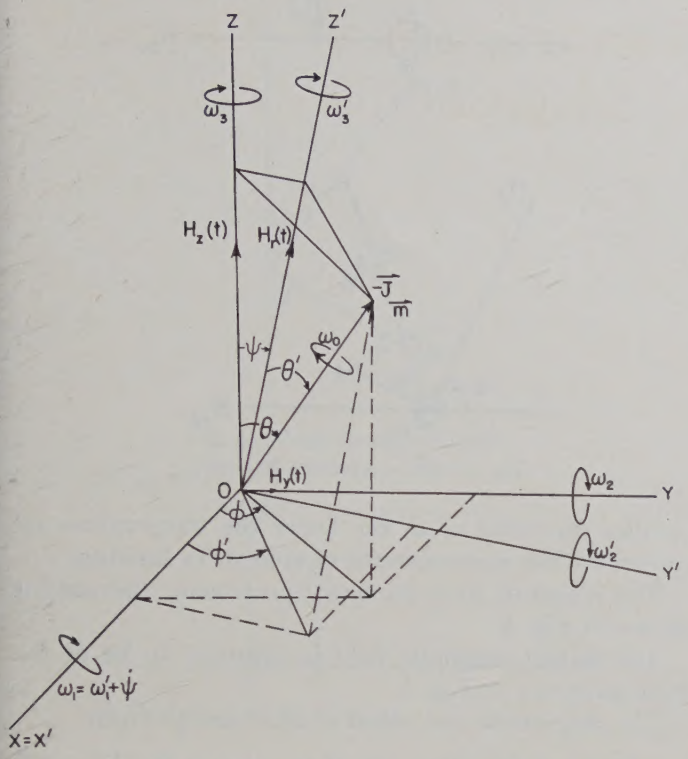

Fig. 2—Rotating coordinate system.

coordinate system which rotates so as to have its z' axis aligned with the instantaneous resultant internal magnetic field $H_r(t)$. This resultant is assumed always to stay in the yz plane of the fixed coordinate system xyz so that the angle $\psi(t)$ between z and z' is also in this plane.

The total kinetic energy of the electron written in terms of the moving coordinate system is

$$T = \frac{I_0}{2}\left[(\dot{\theta}')^2 + (\dot{\phi}')^2 + \omega_0^2 + (\dot{\psi})^2 - 2\omega_0\dot{\phi}'\cos\theta' + 2\dot{\psi}(\dot{\theta}'\sin\phi' + \omega_0\cos\phi'\sin\theta')\right] \quad (1)$$

where I_0 is the moment of inertia. The potential energy $(\boldsymbol{m}\cdot\mu_0\boldsymbol{H})$ is given by

$$V = \mu_0 m H_r(t)(1 - \cos\theta'). \quad (2)$$

The Langrangian function is $L = T - V$. The differential equations are given by

$$\frac{d}{dt}\left(\frac{\partial L}{\partial \dot{q}_i}\right) - \frac{\partial L}{\partial q_i} = Q_i \qquad i = 1, 2$$

$$q_1 = \theta' \qquad q_2 = \phi$$

where Q_i is a dissipation term.

It is convenient to break the pulsed magnetic field transient into two sections; first a buildup and second a constant plateau and decay. The pulses would in practice be periodic but are assumed to be separated far enough in time so that only one need be considered. The rise time of the pulse, T, will be assumed short compared with the relaxation times involved and so during the pulse buildup when ψ is changing the system will be assumed conservative and $Q_i = 0$.

The differential equations then become (since $\gamma = -m/I_0\omega_0$)

$$\frac{\ddot{\theta}'}{\omega_0} - \dot{\phi}'\sin\theta' + \frac{\ddot{\psi}}{\omega_0}\sin\phi' + \dot{\psi}\cos\phi'\left(\frac{\dot{\phi}'}{\omega_0} - \cos\theta'\right) - \mu_0\gamma H_r(t)\sin\theta' = 0 \quad (3)$$

$$\frac{\ddot{\phi}'}{\omega_0} - \dot{\theta}'\sin\theta' - \dot{\psi}\left(\frac{\dot{\theta}}{\omega_0}\cos\phi' - \sin\theta'\sin\phi'\right) = 0. \quad (4)$$

Since ω_0 is very large compared with the various derivatives it is permissible to approximate the equations as

$$\dot{\phi}' + \dot{\psi}\cos\phi'\cot\theta + \mu_0\gamma H_r(t) = 0 \quad (5)$$

$$\dot{\theta}' + \dot{\psi}\sin\phi' = 0 \qquad (\sin\theta' \neq 0). \quad (6)$$

It is assumed that $\boldsymbol{m}$ is initially aligned with the y axis by a constant field ($\psi = \pi/2$). The initial phase of ϕ' is therefore unimportant since $\boldsymbol{m}$ is precessing about the y axis with very small cone angle ($\theta' \simeq 0$). The phase of ϕ' can be taken as that value which leads to the easiest solution of the differential equations, therefore the initial phase is chosen so that $\cos\phi'$ is exactly zero when $\dot{\psi}$ has its maximum value. Since $\dot{\psi}$ normally drops rapidly from its maximum value or else never attains a large value [compared with $\mu_0\gamma H_r(t)$] at all, it is permissible to neglect the ψ term in (5). For very small values of t the cot θ' is quite large but the oscillatory nature of $\cos\phi'$ prevents any important contribution to ϕ' from being made. The approximation is valid if $\dot{\psi}$ is never comparable to the precession frequency or if $\dot{\psi}$ approaches an impulse. Certain intermediate cases may require further consideration.

If the approximation is accepted it follows that

$$\dot{\phi}' \simeq -\gamma\mu_0 H_r(t) \quad (7)$$

$$\dot{\theta} \simeq -\dot{\psi}\sin\phi \quad (8)$$

and $\cos\phi' = 0$ when $\dot{\psi} = \dot{\psi}_{\max}$. If this maximum occurs when $t = u_0$ then

$$\phi' \simeq -\int_{u_0}^{t} \mu_0\gamma H_r(x)dx + \frac{\pi}{2}$$

and

$$\theta' \simeq -\int_0^t \dot{\psi}\cos\left[-\int_{cc_0}^{t}\mu_0\gamma H_r(x)dx\right]dt \quad (0 \leq t \leq T). \quad (9)$$

The value of θ' at the end of the transient ($t = T$) is given by

$$\theta_T \simeq \int_0^T \dot{\psi}\cos\left[-\int_{u_0}^{t}\mu_0\gamma H_r(x)dx\right]dt. \quad (10)$$

Example

Consider a transient such that the magnitude of the pulsed field (H_0) is always constant and the angle ψ changes from ψ_0 to 0 at a constant rate in time T. Since $-\dot{\psi} = \psi_0/T$ and $H(x) = H_0$ it follows that

$$\theta_T \simeq \frac{\psi_0}{T}\int_0^T \cos\left[\int_{u0}^{t}(-\gamma\mu_0 H_0)dx\right]dt. \tag{11}$$

Since ψ has its maximum over the whole range of time $0 \leq t \leq T$ it appears that u_0 is ambiguous. However $\dot{\psi}\cot\theta'$ is a maximum when t is zero. Using this value and defining $\omega_0 = -\gamma\mu_0 H_0$

$$\theta_T \simeq \psi_0\left|\frac{\sin\omega_0 T}{\omega_0 T}\right|. \tag{12}$$

It is apparent in this case that for θ_T to be a large fraction of ψ_0, T should be short compared with the period of precession $(2\pi/\omega_0)$, and not just the relaxation time.

Actually, because of the approximation involved this result is only strictly valid when $T \gg 0$ or when $\psi_0 \ll \omega_0 T$. Nevertheless, the rise time dependence is quite evident.

The example chosen is instructive but in practice T will never be short compared with the period of precession. The problem is not as hopeless as it seems, however, because it is possible to change ψ substantially in a small fraction of the rise time, if the pulsing geometry is properly chosen.

180 Degrees $-\alpha$ Pulse Field Geometry

Previous considerations have indicated that it is necessary to have $\psi(t)$ change very rapidly if θ_T is to be an appreciable angle. It is apparent that if the pulse field is applied at 180 degrees to the saturation field, $\psi(t)$ must be a step function independent of T. This implies that θ_T would be π radians and that the spins would be given the maximum amount of potential energy, independent of T (so long as T is short compared with the damping time constant). Unhappily this may not be the solution because of the following consideration. Consider layers of aligned spins which have suddenly been placed in an anti-parallel magnetic field. The equilibrium is unstable because of thermal agitation, and it is equally likely that the net moment vector from a given spin layer will want to move in any direction, so that on the average two layers or groups of spins want to precess 180 degrees out of phase, spiraling out and then in until both are aligned with the resultant field. Exchange forces prevent this, but spin wave modes are likely to build up quickly. The radiation fields from such spin waves cancel and all the potential energy initially given these spins must go into heating the lattice.

To overcome this difficulty the pulsed field may be oriented at 180 degrees $-\alpha$, where α is some small angle (see Fig. 3). The spins now have a preferred direction and want to precess in phase. However, as soon as α is nonzero, $\psi(t)$ departs from a true step function and θ_T again becomes a function of the rise time T, as well as the other parameters. If α is made very small the amount of this departure is not large but the spin wave buildup appears again nearly as pronounced as before since thermal agitation always spreads the spins randomly over some small cone angle. It appears that the smaller the value of α, the lower the temperature required for the same amount of spin wave buildup.

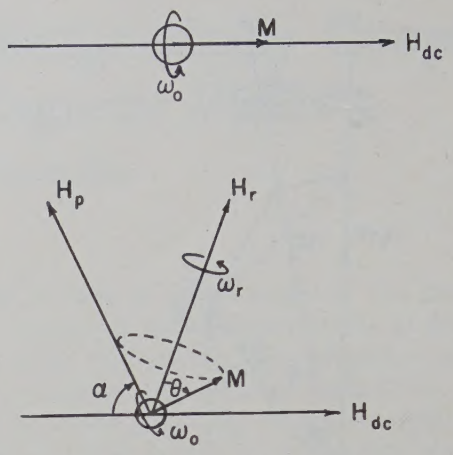

Fig. 3—180°$-\alpha$ pulsing geometry.

The magnetic field geometry previously discussed is shown in Fig. 4.

The pulsed magnetic field is assumed to be of the form as shown in Fig. 5.

The magnitude and phase of $H_r(t)$ are given by

$$|H_r(t)| = [H_p(t)^2 - 2H_{dc}H_p(t)\cos\alpha + H_{dc}^2]^{1/2} \tag{13}$$

and

$$\tan\psi = \frac{H_{dc}\sin\alpha}{H_p(t) - H_{dc}\cos\alpha}. \tag{14}$$

The latter expression leads to

$$-\dot{\psi} = \frac{H_{dc}\dot{H}_p(t)\sin\alpha}{H_p(t)^2 - 2H_p(t)H_{dc}\cos\alpha + H_{dc}^2} \tag{15}$$

over the region of interest $(0 < t < T)$, for which $H_p(t) = (H_0/T)t$.

The Larmor precession frequencies corresponding to H_0, H_{dc}, and H_r are $\omega_p = -\gamma\mu_0 H_0$, $\omega_{dc} = -\gamma\mu_0 H_{dc}$, and $\omega_r = -\gamma\mu_0 H_r$, respectively.

If two parameters, u_0 and v_0, are defined so that

$$u_0 = \frac{\omega_{dc}}{\omega_p} T\cos\alpha \tag{16}$$

and

$$v_0 = \frac{\omega_{dc}}{\omega_p} T\sin\alpha \tag{17}$$

then the integral (10), giving θ_T may be written as

$$\theta_T = \int_0^T \frac{V_0}{t^2 - 2u_0 t + u_0^2 + v_0^2} \cdot\cos\left[\frac{\omega_p}{T}\int_{u_0}^{t}[x^2 - 2u_0 x + u_0^2 + v_0^2]^{1/2}dx\right]dt. \tag{18}$$

Since $-\dot{\psi}$ consists of an impulse at $t = u_0$ when $\alpha \to 0$, the constant u_0 is evaluated so that $\cos\phi(u_0) = 0$, in accordance with previous remarks. The angle α has been assumed small, therefore a permissible approximation is to

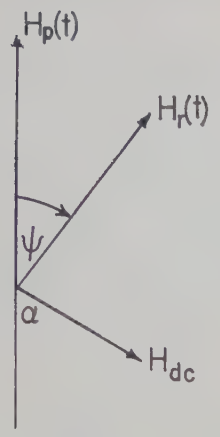

Fig. 4—Magnetic field geometry.

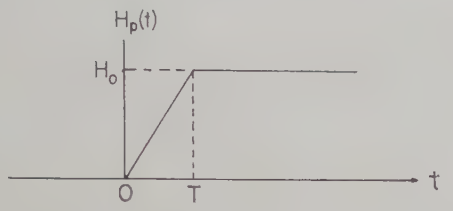

Fig. 5—Pulsed magnetic field as a function of time.

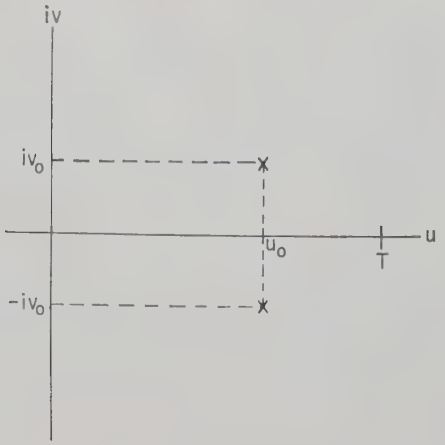

Fig. 6—Complex $(u+iv)$ plane.

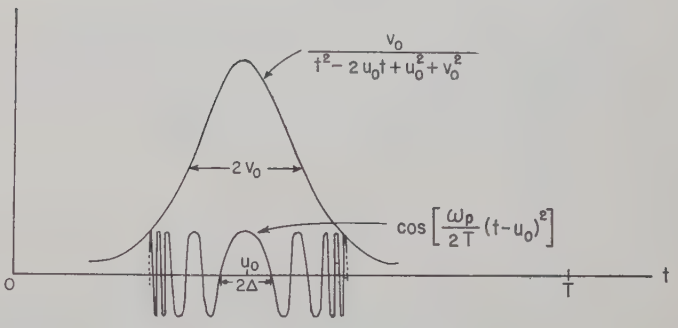

Fig. 7—Integrand functions.

neglect the v_0^2 term in the $\int_{u_0}^{t}\omega(x)dx$ factor. The integral then reduces to

$$\theta_T \simeq \int_0^T \frac{v_0}{(t-u_0)^2+v_0^2}\cos\left[\frac{\omega_p}{2T}(t-u_0)^2\right]dt. \quad (19)$$

The first factor $(-\dot{\psi})$ in the integrand may be represented in the complex t plane $(t=u+iv)$ by a pair of poles as shown in Fig. 6.

In the limit as $\alpha\rightarrow 0$, v_0 vanishes and a double order pole exists at $t=u_0$. Since the integration proceeds along the real axis, it is clear that the major contribution to the integral occurs near $t=u_0$. The second factor in the integrand is unity at the same point and oscillates very rapidly for smaller or larger values of t. Fig. 7 represents the functions whose integrated product yields θ_T.

The cos $[\omega_p/2T(t-u_0)^2]$ factor varies so rapidly from plus to minus one that contributions to the integral are essentially zero except near $t=u_0$. If θ_T is to be large (it is $\pi-\alpha$ for $\alpha=0$ or $T=0$) it is clear that the resonant peak must have a width $(2v_0)$ comparable to the width (2Δ) of the positive half cycle of cos $[\omega_p/2T(t-u_0)^2]$, centered about $t=u_0$.

The evaluation of the integral (19) has been carried out numerically for two values of T (10^{-7} and 10^{-8} sec) for a range of values of α and ω_r. H_{dc} was assumed constant throughout and equal to approximately 500 gauss so that $\omega_{dc}=10^{10}$ rad/sec. The results are shown in Figs. 8 and 9.

Radiation Transient

When the pulse rise is completed there will exist a cone angle θ_T between the magnetization $\boldsymbol{m}$ and the resultant field $\boldsymbol{H}$ (which is now constant in magnitude and direction) $\boldsymbol{m}$ spirals into $\boldsymbol{H}$ at a precession frequency ω_r due to radiation and heat losses. If N_0 is the total number of spins available in the sample there is some fraction N_{eff}/N_0 capable of radiating (the remainder are assumed to be in the form of spin waves as discussed previously).

The radiation field is simply that due to a rotating magnetic moment[1] (or amperian loopcurrent) of magnitude m sin $\theta(t)$.

If α is large enough to ensure N_{eff}/N_0 being near unity, the initial cone angle, θ_T, will probably be relatively small (an engineering compromise is needed—as usual). Assuming a small angle for θ_T, it may be shown that the average radiated power per pulse transient of magnetic field is

$$P_{\substack{\text{ave. rad.}\\ \text{power per pulse}}} = K\frac{\mu_0 m^2}{12\pi c^3}N_{eff}^2\omega_r^4\theta_T^2 \quad (20)$$

where K is a coupling coefficient ($K=1$ if dipoles radiate to free space). The radiation time constant is given by

$$\tau_r = \frac{12\pi c^3}{KN_{eff}\mu_0 m|\gamma|\omega_r^3}. \quad (21)$$

The total time constant of the magnetization decay is

$$\tau_t = \frac{\tau_r\tau_l}{\tau_r+\tau_l} \quad (22)$$

[1] J. A. Stratton, "Electromagnetic Theory," McGraw-Hill Book Co., Inc., New York, N. Y., pp. 437–438; 1941.

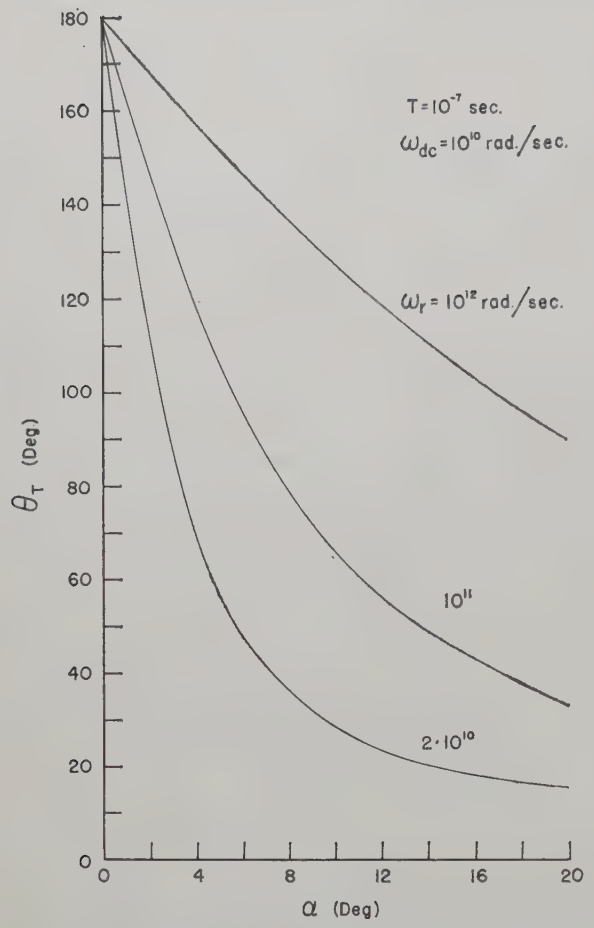

Fig. 8—θ_T vs α.

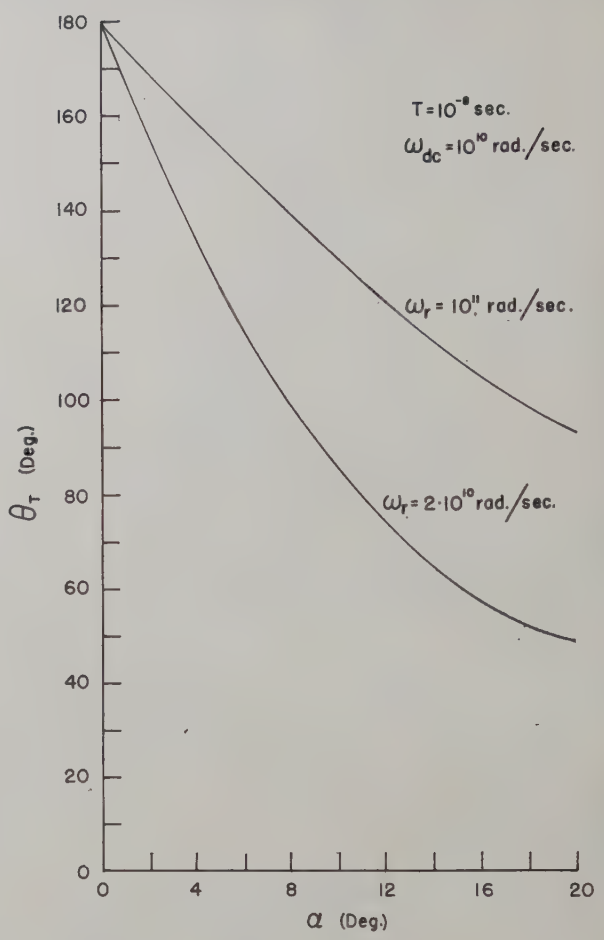

Fig. 9—θ_T vs α.

where τ_l is the lattice relaxation time assuming Bloch-Bloembergen damping.

The radiation efficiency is defined by and is equal to

$$\eta = \frac{\text{energy radiated}}{\text{energy coupled}} \simeq \frac{\dfrac{N_{\text{eff}}}{N_0}}{1 + \dfrac{\tau_r}{\tau_l}}. \qquad (23)$$

It should be noted that a type of unfavorable instability appears possible. Assume that a small angle α is chosen and the initial operating temperature made low enough so that the spins are highly aligned to provide efficient operation. Now if in operation the crystal heats up a little, the spins spread out somewhat. This decreases the effective number of spins and increases the radiation time constant, thereby causing more power to be dissipated leading to a still further increase in temperature and decrease in efficiency. If the closed "loop gain" of the feedback system is greater than unity, the crystal eventually stops radiating and may even be destroyed.

Quantitative Considerations

The normal ferrites are impractical for such oscillators because the Bloch lattice relaxation time (τ_l) is very short ($10^{-8}-10^{-7}$ seconds) and it would be nearly impossible to provide large magnetic pulses with rise times (T) small compared with τ_l. The newly discovered yttrium iron garnet single crystals are reported to have intrinsic resonant line widths of the order of one oersted. This corresponds to a τ_l of $10^{-7}-10^{-6}$ seconds and a required T in the range $10^{-8}-10^{-7}$ seconds (possible to obtain for reasonable magnetic field strengths). The minimum saturation field (H_{do}) required for these materials may be assumed to be $5/4\pi\times10^5$ amperes per meter (500 gauss) which corresponds to an ω_{do} of about 10^{10} rad/sec. The saturation magnetization, M_s, is approximately $17/4\pi\times10^5$ amperes/meter ($4\pi M_s=1700$ gauss) and there are 10^{19} spins/mm^3. It is instructive to compute the power and radiation efficiency.

For a one mm^3 crystal with a pulsed field of magnitude such that $\omega_r=10^{11}$ rad/sec and $T=10^{-7}$ seconds and assuming that $K\simeq\frac{1}{2}$, $\alpha\simeq20$ degrees, $N_{\text{eff}}\simeq3N_0/4$ and $\tau_l\approx0.15$ μsec it follows that $\theta_T\simeq\pi/10$ radians. (The value of 36 degrees from the Fig. 8 curves is halved to take into account the fact that the pulse rise is not conservative.)

The average power per pulse is approximately 30 watts and the radiation efficiency 40 per cent. The pulse of radiation lasts about 0.05 μsec.

Conclusions

The preceding analysis has shown that under certain restrictive conditions the electron spins appear able to couple energy from a pulsed magnetic field and radiate it efficiently at some microwave frequency. The analysis has been done for a vastly simplified system where such factors as anisotropy have been neglected. Nevertheless, certain basic limitations such as the geometrical dependence of the initial precession cone angle (θ_T) have become apparent as well as the need to consider carefully the operating temperature.

Several alternate methods of coupling the magnetic energy from the pulsed field have been proposed by the author,[2] and depend on a pulsed RF field coupling energy to the spins before the spin wave spectrum can build up. This RF field would be of lower frequency than the radiation which is desired and so a pulsed magnetic field would raise the system to the desired energy level.

A great deal of fundamental knowledge must be obtained, and many engineering problems solved, before a practical oscillator can be built. With this goal in mind, experiments are being carried out at the Air Force Cambridge Research Center.

A last point worth mentioning is that the possibility of studying the relaxation behavior of the precessional cone angle of the magnetization by means of the observed radiation is an exciting idea which may lead to a more conclusive theory of ferrimagnetic resonance damping.

Acknowledgment

The author is deeply indebted to Prof. C. L. Hogan of Harvard University for bringing the subject to his attention, and for continued encouragement and criticism. Mrs. M. R. Hoes of Air Force Cambridge Research Center performed the numerical integrations.

[2] Presented orally at the International Conference on Solid State Physics as Applied to Electronics and Telecommunications, Brussels, Belgium; June, 1958.

Ferrite High-Power Effects in Waveguides*

E. STERN† and R. S. MANGIARACINA‡

Summary—**Deterioration of ferrite devices caused by both high power thermal and nonlinear effects are discussed. It is shown that thermal effects can be described, at least qualitatively, by a simple exponential equation. A theoretical maximum power capacity is derived in terms of ferrite configuration parameters. The results of experiments with high peak powers at both *S*-band and *X*-band frequencies are compared with predictions of Suhl's theory on nonlinear, high power effects in ferrites. Steady-state and transient effects are considered. It is shown that high power effects may be eliminated in ferrite devices by properly choosing ferrite properties and geometry.**

LOW POWER ferrite components generally deteriorate when subjected to high power.[1] This paper includes a discussion of the thermal and nonlinear[2] ferrite effects commonly found at high power, and a description of an anamolous transient effect.

Fig. 1 shows the drastic decrease with power in a ferrite resonance attenuation characteristic that, at low power levels, is effectively utilized to build isolators. Methods are indicated to eliminate these undesirable effects.

* Manuscript received by the PGMTT, July 21, 1958; revised manuscript received, August 28, 1958.

† Sperry Gyroscope Co., Great Neck, N. Y.

‡ Dept. of Phys., University of Buffalo, Buffalo, N. Y. Formerly at Sperry Gyroscope Co., Great Neck, N. Y.

[1] N. Sakiotis, H. N. Chait, and M. L. Kales, "Nonlinearity of propagation in ferrite media," Proc. IRE, vol. 43, p. 1011; August, 1955.

[2] H. Suhl, "The nonlinear behavior of ferrites at high microwave signal levels," Proc. IRE, vol. 44, pp. 1270–1284; October, 1956.

Thermal Effects

Assuming that the microwave power is absorbed at the top surface of the ferrite, and that the generated heat flows directly through the ferrite and into the waveguide wall, then a simple calculation can be made of the steady-state temperature distribution on the ferrite. As shown in Part A of the Appendix

$$T(X) - T_0 = \frac{0.24\alpha T}{WK} P_{\text{in}} e^{-\alpha X}$$

where

α = attenuation constant
$T(X)$ = temperature of the top surface of the ferrite (Fig. 2) at the longitudinal position x
K = thermal conductivity of the ferrite
W = width of the ferrite slab
t = thickness of the ferrite slab
T_0 = wall temperature.

In applying this equation, special care must be taken in establishing T_0; at high powers a large thermal gradient may exist through the cement between the ferrite and waveguide wall. Fig. 2 shows the theoretical temperature gradient in a specific ferrite. This gradient was qualitatively observed with a temperature indicator.

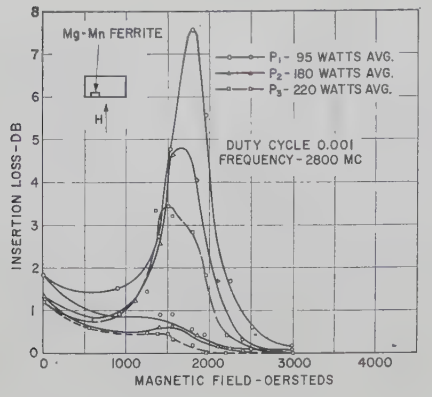

Fig. 1—Insertion loss vs magnetic field for several power levels.

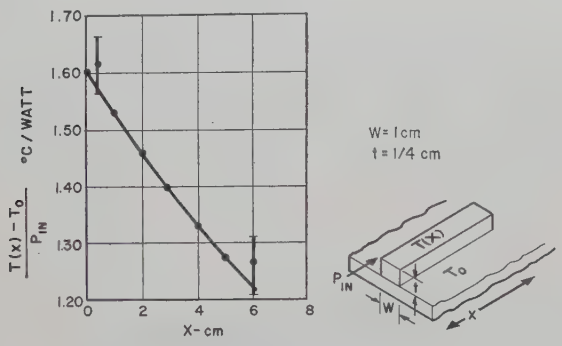

Fig. 2—Calculated thermal gradient for top surface of ferrite slab in waveguide.

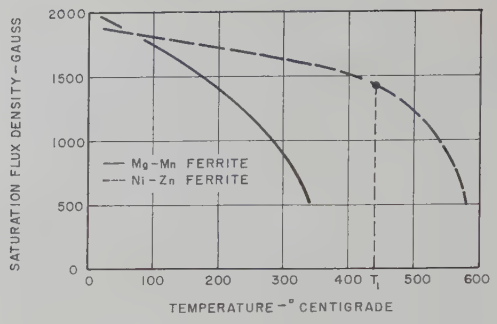

Fig. 3—Saturation magnetization vs temperature for two ferrites.

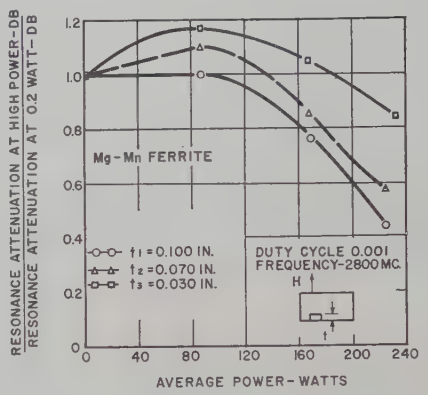

Fig. 4—Resonance deterioration for several ferrite slab thicknesses.

If the applied power is very large, then a thermal instability may occur. The mechanism is as follows. The temperature of the first inch of ferrite increases with time until it approaches the Curie temperature. When this happens the saturation magnetization decreases markedly. This causes a proportional decrease of the attenuation constant which in turn increases the power absorbed in the cooler second inch of ferrite. The process continues and an unstable condition is produced. The end result may be a serious deterioration of attenuation of the type shown in Fig. 1.

Using the temperature indicator, an experiment was performed to verify this phenomenon. The attenuation was found to decrease with time in relation to this thermal gradient.

Fig. 3 indicates the variation of saturation magnetization ($4\pi M_s$) with temperature for two different ferrites. Note that the nickel zinc ferrite $4\pi M_s$ and therefore the attenuation remains relatively constant up to temperature T_1. At temperatures greater than T_1, the saturation magnetization drops rapidly. Therefore, it is possible to define the theoretical maximum power capacity for a given ferrite configuration.

$$P_{\max} = \frac{4.17WK}{\alpha t}\,[T_1 - T_0].$$

This expression holds true if the waveguide wall temperature is maintained at T_0 and the product αt is kept less than 0.01. On the other hand, severe deterioration can be expected from the magnesium manganese ferrite at relatively low power.

Fig. 4 shows the relative resonant attenuation as a function of average power for several Mg-Mn ferrite thicknesses. It is anticipated that $P_{\max}$ should vary inversely with ferrite thicknesses. This was corroborated by the measurements shown in this figure. Note that a marked deterioration occurs at a specific power level for each ferrite thickness. Furthermore, at medium power levels, the attenuation ratio exceeds unity. This is a typical thermal effect[3] that is caused in some ferrites by the decrease of anisotropy with increasing temperature.

Nonlinear Effects

The detailed Suhl theory[2] was derived for small ferrite samples immersed in a uniform microwave magnetic field. Ordinary ferrite components use large ferrites in nonuniform microwave magnetic fields. Therefore, a comparison between theory and observations is restricted to estimates of orders of magnitude.

Fig. 5 illustrates the reverse insertion loss vs magnetic field at two peak powers. The average power was held constant to minimize thermal effects. Note that the attenuation decreases somewhat with peak power. The ferrite has a saturation magnetization of 2050 gauss and a full linewidth of 120 oersteds. Suhl's criteria for the coincidence of subsidiary and main resonance for this

[3] B. J. Duncan and L. Swern, "Temperature behavior of ferrimagnetic resonance in ferrites located in waveguide," *J. Appl. Phys.*, vol. 27, pp. 209–215; March, 1956.

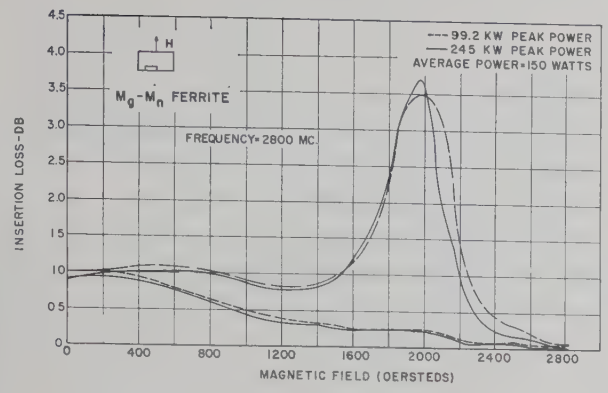

Fig. 5—The decline of the main resonance with peak power at a fixed average power level.

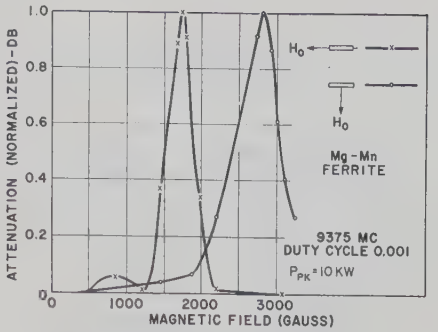

Fig. 6—The dependence of subsidiary resonance on ferrite geometry in waveguide.

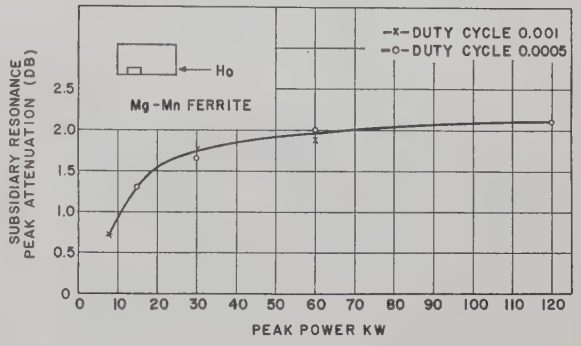

Fig. 7—The variation of subsidiary resonance with peak power.

ferrite geometry predicts that coincidence does not occur. Therefore, h_{crit}^2 is equal to

$$h_{crit} = \Delta H \sqrt{\frac{2\Delta H}{(4\pi M_s)}}$$

where ΔH is the half width of the main resonance line.

This defines the threshold for the deterioration of the main resonance. If this equation is solved for the given frequency and waveguide size (see Part B of the Appendix), it is found that the critical power is equal to 150 kw. This agrees approximately with the data shown in this figure. Note that for the slab configuration magnetized as shown, subsidiary resonance is not evident.

The normalized resonance attenuation as a function of dc field for two orientations of the field is shown in Fig. 6. Note that a subsidiary resonance peak is observed if the magnetic field lies in the plane of the slab. However, if the field is transverse to the slab, the subsidiary resonance is partially suppressed. This agrees qualitatively with Suhl's theory since it is expected that a very thin slab will not exhibit subsidiary resonance. These measurements were made at 9375 mc with a peak power of 10 kw. The main resonance did not deteriorate with peak power since it lies below the calculated instability threshold of 15 kw.

The maximum amplitude of the subsidiary resonance for the field lying in the plane of the ferrite slab as a function of peak power is shown in Fig. 7. Note that the data was taken at two duty cycles. Since the two sets of data fall on the same curve, it is clear that heating and other extraneous effects are negligible. Note also that the subsidiary resonance tends to saturate. This agrees qualitatively with the observations made by Scovil of Bell Telephone Laboratories with small single crystal samples. The calculated critical power for the onset of subsidiary resonance is equal to 30 kw. In this calculation N_x equals 1 in order to arrive at a minimum critical power level. This prediction is completely out of line with the experimental data. If h_{crit} is calculated for subsidiary and main resonance coincidence,

$$h_{crit} = \frac{(\Delta H)^2}{4\pi M_s}$$

where ΔH is the half width of the resonance line, and the critical power equals 250 watts. This calculation provides a much better approximation of the critical power for subsidiary resonance.

On the basis of the studies described above, a material and dimensions were chosen to minimize the Suhl and thermal effects in an *S*-band isolator.

The attenuation as a function of magnetic field for two power levels is seen in Fig. 8. Note that the attenuation is virtually unaffected by the power in the region lying slightly above resonance. The resonance shift with power can be attributed to a slight decrease of $4\pi M_s$ with temperature. The slight decrease of attenuation below resonance may be due to subsidiary main resonance coincidence. A field should be chosen that places the operating point in this region of minimum deterioration.

Fig. 9 gives the effect produced on the resonance line of ferrite at low power by the introduction of dielectric. Note that the apparent resonance for the ferrite-dielectric combination is shifted to a somewhat higher field and the attenuation is increased. If this principle is incorporated into a high power isolator and the ferrite and dielectric dimensions are chosen so that nonlinear effects and thermal instabilities are minimized, a high power isolator can be obtained that has minimum size and weight.

A picture of high power *S*-band isolator that requires only forced air cooling is shown in Fig. 10. With a peak power of 5 megawatts and an average power of 5 kw looking into a mismatch of 1.8 at 2900 mc, the measured

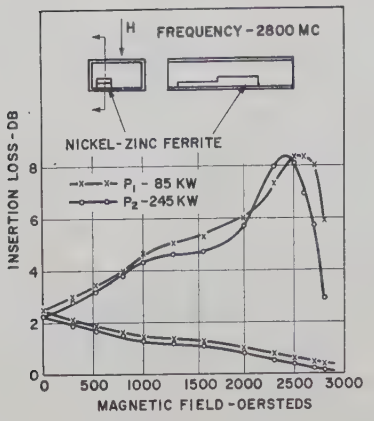

Fig. 8—Attenuation vs magnetic field for special ferrite configuration.

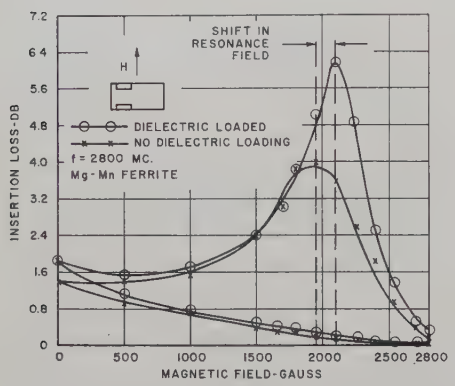

Fig. 9—The effect of dielectric loading on the main resonance.

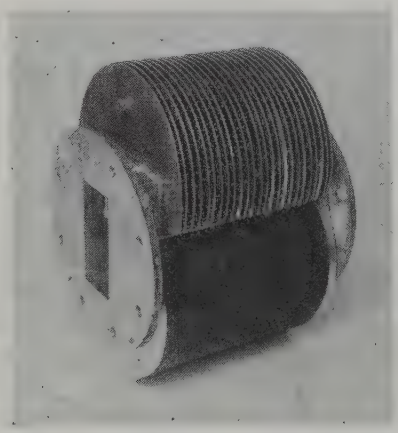

Fig. 10—Air-cooled, 5-mw peak, 5-kw average power, *S*-band isolator.

forward loss was less than 0.2 db and the reverse loss was greater than 10 db. The isolator is six inches long. Its bandwidth extends from 2700 mc to 2900 mc.

During these high power investigations an anomalous effect was observed at *X* band, especially with oversize ferrites. Fig. 11 shows the magnetizing field and the attenuation of the ferrite as a function of time. Now the expected behavior is a slight increase of attenuation, and later on a decrease. However, when the field is increased, the attenuation drops sharply within 70 milliseconds

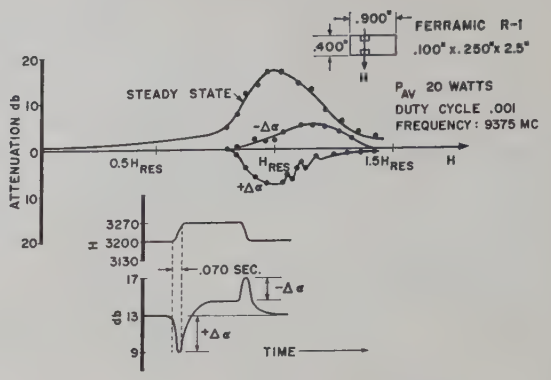

Fig. 11—The transient effect produced at high power with oversize ferrite slabs.

and then drifts slowly to the expected steady-state value above the initial attenuation. When the field is switched back to its initial value, a sharp increase in attenuation is first observed and then a slow decrease of attenuation occurs back to the expected initial level. The amplitude of the sharp increase in attenuation produced by a decrease in field is $-\Delta\alpha$ and the resultant decrease in attenuation with an increase of magnetic field is $+\Delta\alpha$. The graph in the upper portion of Fig. 11 shows the steady-state attenuation as a function of field and a plot of $+\Delta\alpha$ and $-\Delta\alpha$ that is produced at the indicated field by switching the field by a small increment.

The measurements were taken at 9375 mc with 20 watts average power and a duty cycle of 0.001. Note that the attenuation transient is sensitive to the sense of the magnetic field transient and to magnetic bias. In addition, the transients are ferrite size dependent. If the ferrite thickness is made less than 0.050 inch, the transients are suppressed. The intrinsic rise time of the effect is known now.

In conclusion, high power effects can be eliminated by choosing the appropriate ferrite geometry. A ferrite with a broad linewidth, a high Curie temperature, a slow decline of the saturation magnetization with temperature, a low $4\pi M_s$ and a transversely magnetized slab configuration should enable the engineer to build a very high power component. If a large amount of power is to be dissipated in the ferrite, it is recommended that the ferrite be soldered directly to the waveguide wall and that the coolant be applied in a fashion such that the thermal gradient between coolant and ferrite is minimized. The ferrite dimensions should be adjusted so that neither thermal nor nonlinear critical powers are reached. The judicious use of dielectric should help to overcome some of the effects produced by high power.

The anomalous effect can be prevented from occurring in high power switches, variable attenuators, and modulators if the switching speed is made long or if the ferrite dimensions are reasonably small.

Special care must be taken in all high power devices where the transverse demagnetizing coefficients are greater than zero because the subsidiary resonance peak is then likely to occur.

Appendix

Part A

The microwave power that is absorbed per differential ferrite segment is

$$dP_x = -\alpha P_{in} e^{-\alpha x} dx. \tag{1}$$

If it is assumed that all the microwave energy is absorbed in the top surface of the ferrite and that all the heat flows directly into the waveguide wall at temperature T_0, then the following expression holds true:

$$d\dot{Q}_x = 0.24 dP_x = \frac{WK}{t}[T_x - T_0]dx \tag{2}$$

where

K = thermal conductivity of ferrite
W = width of the ferrite slab
t = thickness of the ferrite slab
T_0 = wall temperature.

Substituting (1) in (2),

$$[T_x - T_0] = 0.24 \frac{\alpha t}{WK} P_{in} e^{-\alpha x}.$$

The assumption has been made that the heat flows directly to the waveguide wall. The assumption is justified if

$$\frac{\dfrac{d[T_x - T_0]}{dx}}{\dfrac{d[T_x - T_0]}{dy}} = \alpha t \ll 1.$$

Part B

Microwave magnetic fields in waveguide may be expressed as

$$H_x = 0.0719 \sqrt{\frac{P_t}{ab}} \sqrt{1 - \left(\frac{\lambda}{\lambda_0}\right)^2} \sin\left(\frac{\pi}{a} x\right) \sin \omega t \text{ oersteds}$$

$$H_z = 0.0719 \sqrt{\frac{P_t}{ab}} \frac{1}{\sqrt{1 - (\lambda/\lambda_0)^2}} \cdot \frac{\lambda}{\lambda_0} \cos\left[\frac{\pi}{a} x\right] \cos \omega t \text{ oersteds}$$

where

P_t = transmitted power in watts
a, b = waveguide dimensions in inches
λ = free space wavelength
λ_0 = cutoff wavelength for the TE_{10} waveguide mode.

Part C

The coincidence of main and subsidiary resonance is achieved provided that

$$(N_x + N_y + \sqrt{N_x^2 + N_y^2 + 14 N_x N_y}) \frac{4\pi M_s}{3} > \frac{\omega}{\gamma}$$

where

the demagnetizing factors $N_x + N_y + N_z = 1$
$4\pi M_s$ = saturation magnetization in gauss
ω = applied angular frequency
$\gamma = 2\pi \times 2.82 \times 10^6$ radians/oersted.

Temperature Effects in Microwave Ferrite Devices*

J. L. MELCHOR† and P. H. VARTANIAN†

Summary—**With proper choice of shape, it is possible to minimize the frequency shift of ferromagnetic resonance in microwave ferrite components operating over a wide range of ambient temperatures. Calculations have been made for minimum resonance frequency shift with change in saturation moment. Curves relating the resonance frequency shift as a function of saturation magnetization are plotted for several ferrite geometries. Design curves are presented for reducing dependence of resonance frequency on temperature.**

* Manuscript received by the PGMTT, July 3, 1958; revised manuscript received, September 5, 1958.
† Microwave Engineering Labs., Inc., Palo Alto, Calif.

Introduction

IN THE DESIGN of microwave devices containing ferrites, the choice of ferrite shape can have an important effect on the characteristics achieved. The ferrite dimensions should be chosen to give optimum performance. Fig. 1, derived from Kittel's equation,[1]

$$\omega^2 = \gamma^2[H + (N_y - N_z)4\pi M][H + (N_x - N_z)4\pi M]$$

[1] C. Kittel, "On the theory of ferromagnetic resonance absorption," *Phys. Rev.*, vol. 73, pp. 155–161; January, 1948.

shows the relation between the applied magnetic field and the ferromagnetic resonance frequency for several commonly used ferrite shapes. The X's in Fig. 1 denote abscissa values for which the applied field is sufficiently large to overcome internal demagnetizing fields for each shape, so that saturation may be produced. The range over which low field magnetic losses occur in a demagnetized sample of any shape is shown. Fig. 1 is useful in comparing the various shapes commonly used in devices. Choice of a shape is easily made on the basis of requirements for low frequency operation, low applied magnetic field, or a particular ferrite. Points above the lines correspond to operation below ferromagnetic resonance field (or above ferromagnetic resonance frequency) and include most low field devices such as Faraday rotators and differential phase shifters.

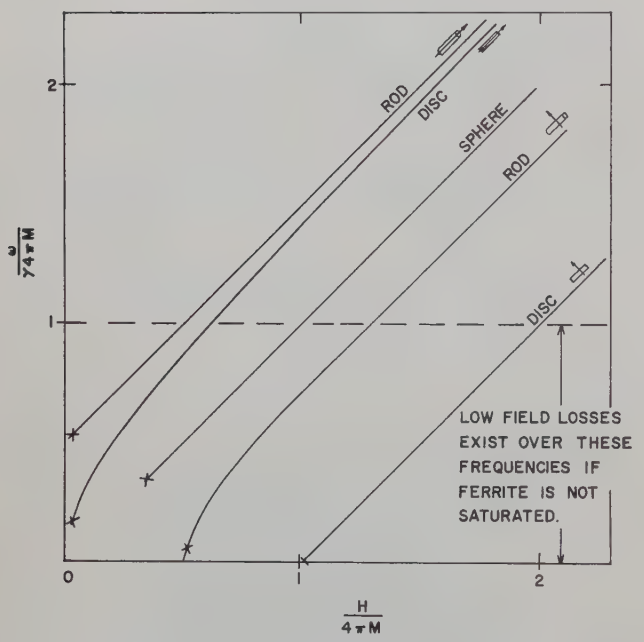

Fig. 1—Resonance frequency as a function of applied field and saturation magnetization for different ferrite shapes.

As the temperature increases, due to ambient conditions or power absorption, a typical ferrite's saturation magnetization is found to decrease as shown in Fig. 2. Measurements made on a Mg-Mn-Al ferrite show the magnetization dropping from 900 gauss at room temperature to zero at a Curie temperature of 92°C. Two effects will be noted on microwave device characteristics as the saturation magnetization decreases. First, the nonreciprocal property, absorption or phase shift, for example, decreases in magnitude because of the reduction in saturation magnetization. Second, a change in magnetization causes the ferromagnetic resonance frequency to shift in a manner which can be predicted from Kittel's equation. By proper choice of ferrite shape it is possible to minimize this shift in resonance frequency. Figs. 3(a) and (b) show the shift in resonance frequency as a function of saturation magnetization for two com-

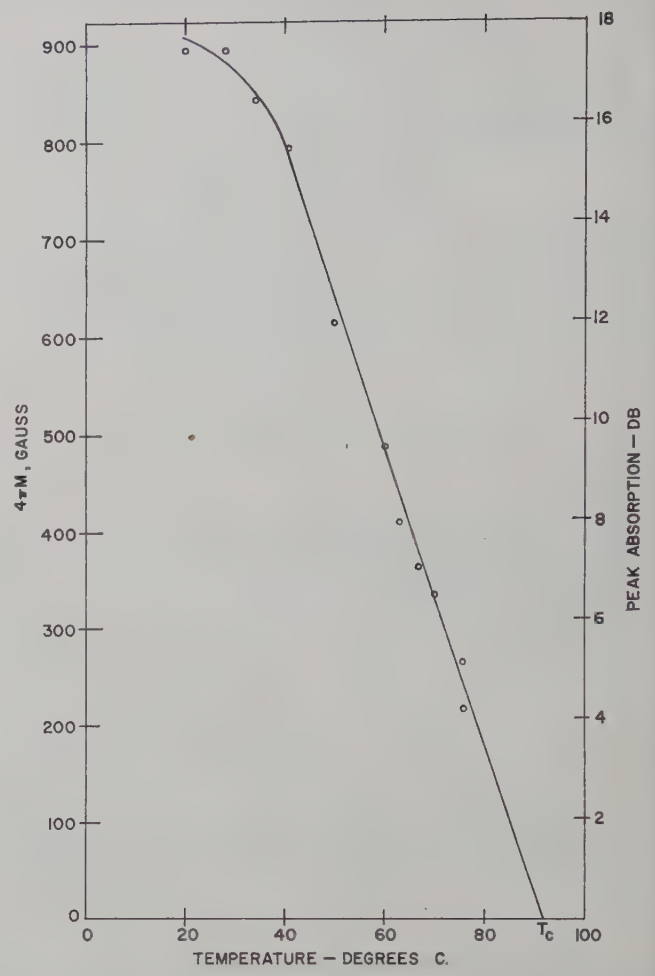

Fig. 2—Absorption vs temperature for thin slab of Mn-Mg-Al ferrite with saturation magnetization of 900 gauss and Curie temperature, T_c, of 92°C.

monly used ferrite-loaded waveguide geometries. Fig. 3(c) shows the possible results which can be obtained with a more suitable choice of ferrite shape. It is seen in this case that the resonance frequency remains almost independent of saturation magnetization.

Discussion

As shown by the ferromagnetic resonance absorption characteristics of Fig. 3, the operating frequency range of an isolator depends on the applied magnetic field, the saturation magnetization of the material used, and the demagnetizing factors associated with the choice of geometry. These quantities are related through Kittel's equation.

Since most ferrite devices use geometries which are long compared to a wavelength and vary only in transverse shape, the demagnetizing factor N_y, where y is along the waveguide axis, has been assumed to be zero. For this geometry Kittel's equation normalized to the applied field becomes

$$\left(\frac{\omega}{\gamma H}\right)^2 = \left[1 - N_z \frac{4\pi M}{H}\right]\left[1 + (1 - 2N_z)\frac{4\pi M}{H}\right] \quad (1)$$

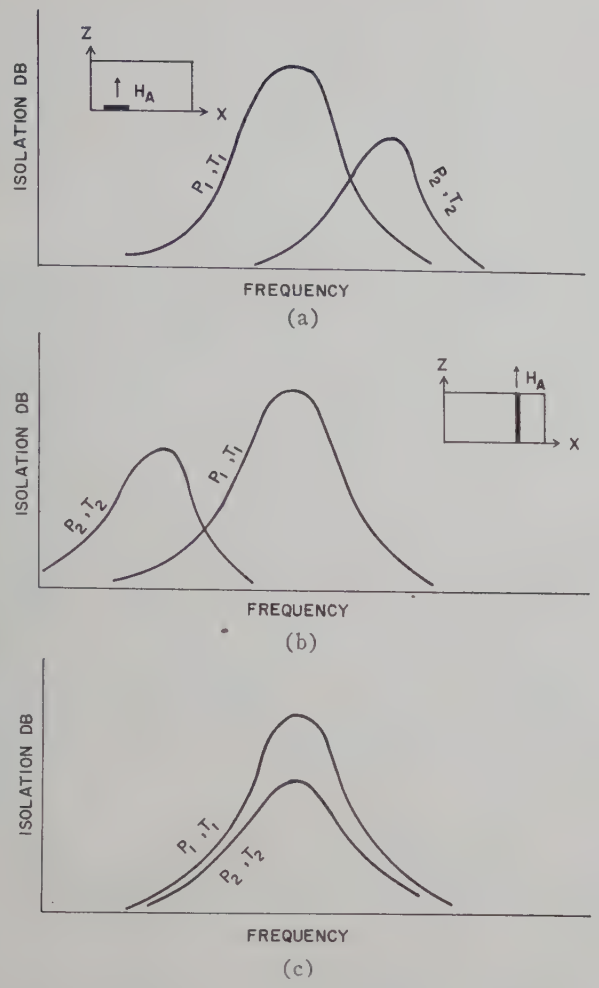

Fig. 3—Isolator characteristics for ferrite slabs magnetized (a) normal to plane, (b) parallel to plane, and for (c) ferrite shape chosen for minimum dependence of resonance frequency on magnetic moment. P_2 and T_2 are greater than P_1 and T_1.

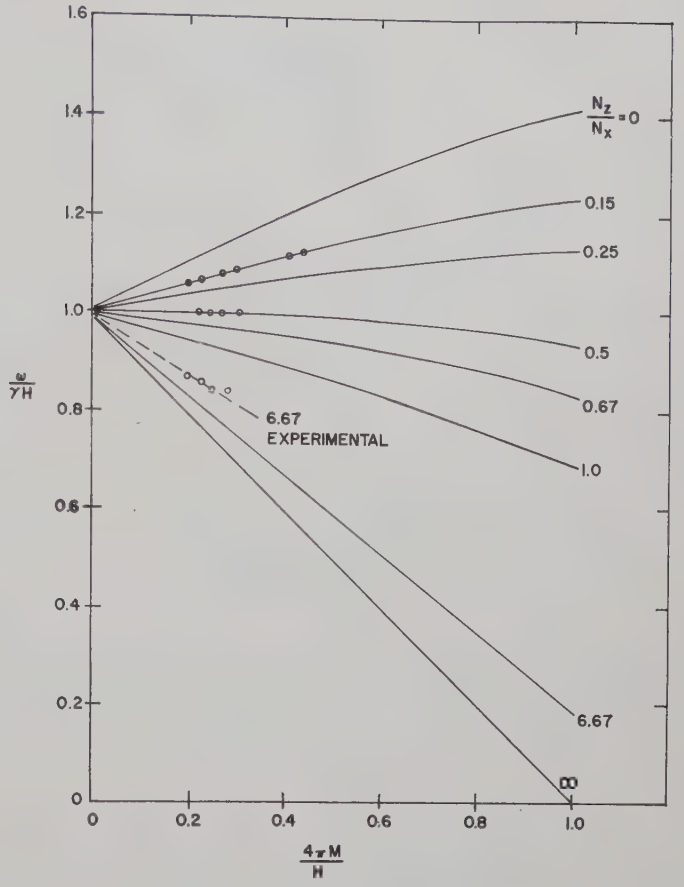

Fig. 4—Resonance frequency vs saturation magnetization for different demagnetizing factors.

where

ω = ferromagnetic resonance frequency

γ = gyromagnetic ratio

$N_z = 1 - N_x$ = demagnetizing factor along direction of field

$4\pi M$ = saturation magnetization of the ferrite.

Calculated curves based on (1) for different values of N_z/N_x are shown in Fig. 4. Here it can be seen that for a ferrite shape chosen such that $N_z/N_x = 0.5$, the saturation magnetization can decrease from half the applied resonance field value to zero without an appreciable change in resonance frequency. For any value of N_z/N_x less than 0.5 the curves of Fig. 4 will have maxima; and in the neighborhood of these maxima the moment can change over wide ranges with little effect on resonance frequency. Experimental points are plotted for ferrite samples chosen with $N_z/N_x = 0.15$, 0.5 and 6.67. Correlation between calculated and experimental data for the first two shapes is found to be quite good. However, for the latter shape there is a discrepancy between calculation and measurement. The values for N_z/N_x were determined from Osborn,[2] assuming the slabs to be ellipsoids. For the dimensions used, it is found that N_z/N_x is approximately equal to the ratio of the x dimension to the z dimension. However, since the ferrite was mounted flat on a waveguide wall, one should use double the z dimension because of the RF image dipole required by the metal surface boundary conditions.[3] Consequently, the points labeled "6.67 experimental" should be for an effective N_z/N_x of 3.33, and again, agreement between theory and experiment would be good.

For each operating microwave frequency there is a corresponding combination of geometry, applied magnetic field, and saturation magnetization to give minimum temperature dependence. Fig. 5 shows the locus of points derived from Kittel's equation when $d\omega/dM$ is zero. These curves provide the necessary information to design a microwave ferrite device with minimum dependence of resonance frequency on temperature. As an example, assume we have need for an isolator at 5600 mc which is subjected to a variable ambient temperature. Now, if we choose a low loss ferrite with a saturation magnetization of 2000 gauss, $\omega/4\pi M\gamma$ is 2.0. The optimum choice of N_z/N_x is seen to be 0.415 and $4\pi M/H$ is

[2] J. A. Osborn, "Demagnetizing factors," *Phys. Rev.*, vol. 67, pp. 351–357; March, 1945.

[3] Private communication, M. Sirvetz and H. Sharfman, Raytheon Manufacturing Co.

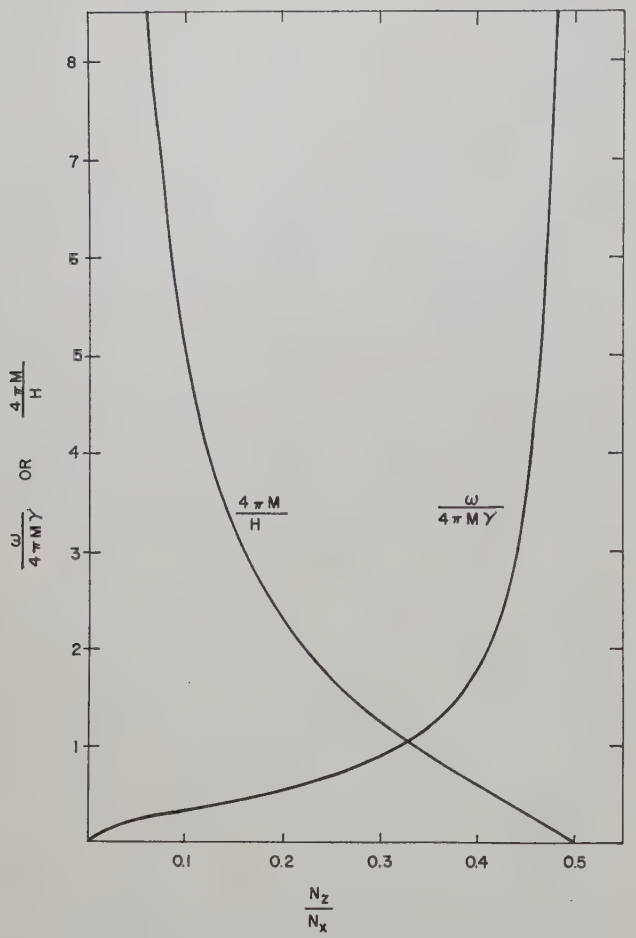

Fig. 5—Resonance frequency or magnetic field value vs N_z/N_x for $d\omega/dM=0$.

0.50, or the field to be applied is 4000 gauss. Suppose, however, we choose to use a high Curie temperature ferrite with a saturation magnetization of 3500 gauss. Then, $\omega/4\pi M\gamma$ is 0.57, N_z/N_x is 0.20 and $4\pi M/H$ is 2.25. Here the field required for resonance is 1555 gauss.

Conclusions

Ferrite shapes can be chosen to minimize change in microwave resonance frequency whenever saturation moment decreases due to ambient temperature changes. However, if the temperature rise is due to power absorption within the ferrite, several additional factors must be considered in designing a device for minimum shift of resonance frequency. First is the cooling effect of the metallic wall on the ferrite. This sets up a thermal gradient across the ferrite and consequently the optimum N_z/N_x varies, since $4\pi M$ varies throughout the material. Second, presence of the metallic wall tends to stabilize the ferrite temperature, and it will probably be found that the optimum shape for the extremely high average power device is a compromise between maximizing the area between the ferrite and waveguide wall for heat transfer reasons, and choosing an optimum shape for minimizing the thermally caused shift in resonance frequency. For applications where environmental temperature of the device is to vary over wide ranges, choice of N_z/N_x, as shown in Fig. 5, is optimum.

Discrepancies between the resonance frequency predicted by Kittel's equation and that measured for the configuration of Fig. 3(a) can be attributed to an RF image at the waveguide wall.

Characteristics of Ferrite Microwave Limiters*

G. S. UEBELE†

Summary—**Microwave ferrites that exhibit a nonlinear RF absorption as a function of RF power level can be utilized in the construction of a passive microwave device which will allow small RF signals to be transmitted with very little attenuation but which will attenuate large RF signals considerably. Such a device tends to "limit" the amplitude of the microwave energy passing through the device and is therefore called a ferrite microwave limiter.**

One application of the ferrite limiter is in the protection of crystal detectors in pulsed radar sets. However, when a rectangular pulse of *X*-band RF energy is transmitted through the limiter, the output waveform is no longer rectangular but consists of a leading edge spike of 0.1-μsec duration followed by a plateau of highly attenuated RF energy. At the present time the leading edge spike is the major obstacle in the successful use of the ferrite microwave limiter as a TR cell in the protection of crystal detectors.

Experimental techniques used to improve the performance of the limiter are presented, and the performance characteristics of an *X*-band ferrite microwave limiter are shown.

Principle of Operation

THE nonlinear properties of ferrites were first observed in cavity experiments conducted by Damon[1] and by Blombergen and Wang[2] in 1950 and 1951. Similar observations in ferrite-loaded waveguide

* Manuscript received by the PGMTT, July 1, 1958; revised manuscript received, September 2, 1958.

† Systems Dev. Labs., Hughes Aircraft Co., Culver City, Calif.

[1] R. W. Damon, "Relaxation effects in ferromagnetic resonance," *Rev. Mod. Phys.*, vol. 25, pp. 239–245; January, 1953.

[2] N. Blombergen and S. Wang, "Relaxation effects in para- and ferromagnetic resonance," *Phys. Rev.*, vol. 93, pp. 72–83; January, 1954.

experiments at other laboratories[3–5] influenced the choice of ferrite material for use in high-power ferrite devices.

In Fig. 1[6] the attenuation of a ferrite-loaded waveguide is plotted as a function of the magnitude of the magnetic bias field. An attenuation curve is plotted both for a small RF signal (about 100 mw at 9000 mc) and for a large RF signal of 60 kw. The attenuation curve for 60 kw of RF power clearly shows a subsidiary resonance at about 1250 gauss which did not occur at the lower power level. If the amplitude of the magnetic bias is fixed at 1250 gauss, a 100-mw RF signal is essentially unattenuated, but a 60-kw signal is attenuated by 1 db. The ferrite microwave limiter is based upon this effect.

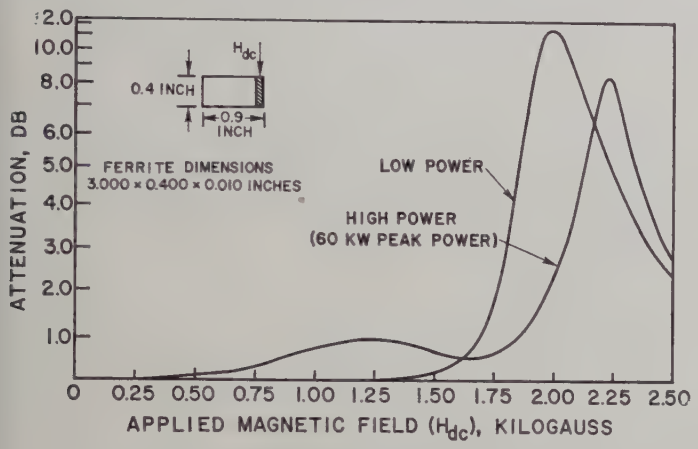

Fig. 1—Low-power and high-power attenuation curves for General Ceramics Ferramic R-1 ferrite.

A theory which qualitatively accounts for the subsidiary resonance at high RF power levels has recently been advanced by Suhl[7] of Bell Telephone Laboratories. In brief, the ferrite's nonlinear absorption and the existence of the subsidiary resonance are contributed to the generation of lossy spin modes within the ferrite's crystal lattice when the strength of the RF magnetic field reaches a critical threshold value. The threshold of RF energy is related to the saturation magnetization and ferromagnetic resonance linewidth of the ferrite for the case of single crystals of ferrite of spheroidal geometry and circularly polarized RF excitation. Suhl's theory indicates that a ferrite with a narrow ferromagnetic resonance linewidth and a high saturation magnetization is required for the greatest limiting effect.

[3] M. T. Weiss, "High Microwave Power Effects on Ferromagnetic Resonance in Ferrites; I. Main Resonance," Bell Telephone Labs., Holmdel, N. J., Tech. Memo. No. 56-123-43; October 22, 1956.

[4] N. G. Sakiotis, H. N. Chait, and M. L. Kales, "Nonlinearity of microwave ferrite media," IRE Trans. on Antennas and Propagation, vol. AP-4, pp. 111–115; April, 1956.

[5] E. T. Wierman, unpublished data, Hughes Aircraft Co., Culver City, Calif.; September, 1956.

[6] In Fig. 1 the increased magnetic bias field required for ferromagnetic resonance at high RF power levels is due to the lowering of M_s when the ferrite temperature is raised by RF losses.

[7] H. Suhl, "The nonlinear behavior of ferrites at high microwave signal levels," Proc. IRE, vol. 44, pp. 1270–1284; October, 1956.

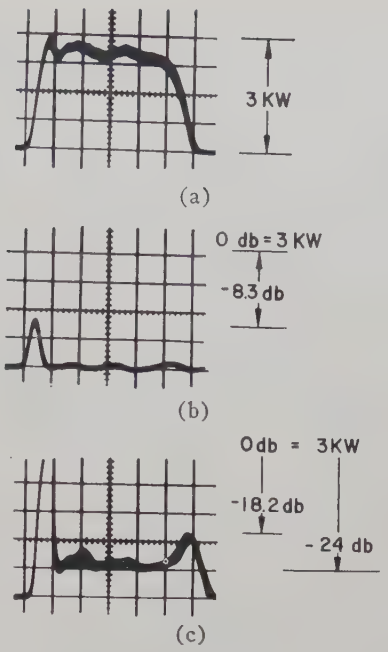

Fig. 2—Input and output RF pulse shapes for an experimental ferrite limiter (Fig. 3 configuration). (a) Input pulse, 0.1 μsec per division. (b) Output pulse. (c) Output pulse magnified 20 times.

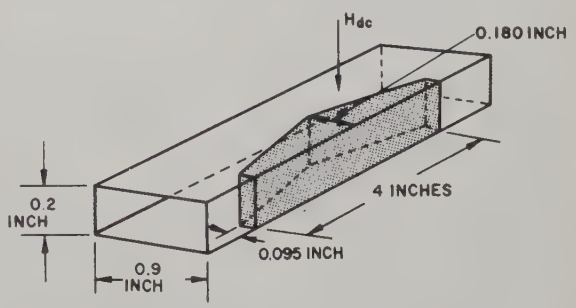

Fig. 3—An experimental ferrite microwave limiter using Ferramic R-1 ferrite.

Design Objectives

One application of the ferrite limiter is in the protection of crystal detectors in pulsed radar sets. The effect of the ferrite microwave limiter on the waveshape of pulses of high-power RF energy is therefore of considerable interest. Fig. 2 shows oscilloscope traces of an RF pulse before and after limiting for the specific ferrite waveguide configuration shown in Fig. 3, in which General Ceramic's Ferramic R-1 ferrite was used. In general, the shape of the limited RF pulse is a flat plateau with spikes of energy, approximately 0.1 μsec in duration, at the leading and trailing edges. Because of this RF waveshape distortion, it is advisable to review the theory of crystal detector "burnout" before design objectives for the limiter can be established.

It is generally accepted that crystal burnout is due primarily to excess heating in the proximity of the whisker silicon contact area.[8] The temperature in this

[8] H. C. Torrey and C. A. Whitmer, "Crystals Rectifiers," M.I.T. Rad. Lab. Ser., McGraw-Hill Book Co., Inc., New York, N. Y., vol. 15, pp. 236–263; 1948.

area is a function of the energy vs time distribution of the RF input pulse and the thermal capacity of the crystal. If the RF spike energy impinging on the crystal has a time duration less than the thermal time constant (τ) of the crystal, then the energy content of the spike is the important burnout factor. However, if the width of the spike is greater than the thermal relaxation constant of the crystal, the temperature attained depends upon the rate at which energy is applied to the crystal, *i.e.*, the power amplitude of the spike.

For crystals in the 1N23 series, the burnout temperature of the whisker-silicon contact is about 500°C and the thermal time constant is of the order of 0.02 μsec. The thermal capacity of the 1N23E[9] crystal is such that, for RF pulses of about 0.02 μsec or less, the crystal burnout is 2 ergs. Since the duration of the leading edge spike of the output from a gas *TR* cell is about 0.002 μsec, gas *TR* cells are rated in ergs of energy output. By extrapolating these data (Fig. 4), one arrives at a maximum allowable peak-power level of 10 watts for spikes of long-time duration. Since the duration of the leading edge spike of a "limited" pulse of RF energy is 0.1 μsec, this spike amplitude must not exceed 10 watts if crystal burnout is to be prevented.

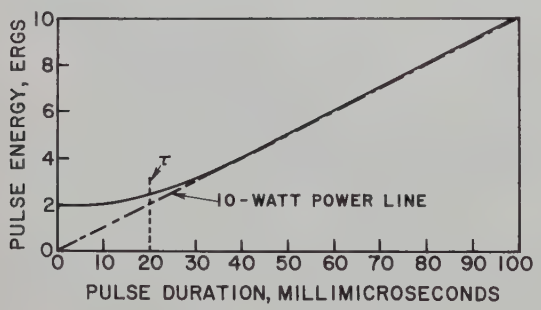

Fig. 4—Probable energy for burnout of 1N23E crystal as a function of RF pulse width.

However, crystal burnout is not the only parameter to be considered in designing a *TR* cell for crystal protection in a radar system. Equally important is the amount of service a crystal detector will give before it has to be replaced. This is determined by loss of conversion efficiency of the crystal and by the increase of noise level as a function of time. Both of these deleterious "aging" factors of a crystal are directly related to the amplitude of the input RF pulses to the crystal. Therefore, the *TR* cell requirements established by the radar designer will be a compromise between crystal life and *TR* protection required, and no rigorous specification can be made on the limiter for this purpose. However, since it appears that manufacturers design gas *TR* cells with a spike leakage value of 10 per cent of that required for crystal burnout, it seems reasonable to require that the output RF waveform from a ferrite limiter exhibit no amplitude greater than one watt.

[9] Microwave Associates, Inc., Boston, Mass., Short Form Catalog 57-BG.

Parameters Affecting Limiting

A number of commercially available ferrites as well as ferrites synthesized at Hughes Aircraft Company were tested for their nonlinear properties. Of the ferrites tested, General Ceramic's Ferramic R-1 ferrite was chosen to demonstrate limiter characteristics because it exhibits considerable nonlinearity and is readily available in quantity. Ferramic R-1 ferrite has a saturation magnetization of 2500 gauss and a ferromagnetic resonance linewidth of 320 oersteds at 9000 mc.

One of the first parameters investigated was the direction of the applied magnetic bias field in relation to the ferrite sample and the direction of RF propagation. For a slab of Ferramic R-1 ferrite, 1.5 inches by 0.195 inch by 0.120 inch, placed adjacent to the narrow wall of a 0.2-inch by 0.9-inch waveguide, there appeared to be no preferred direction of H_{dc} for greatest limiting effect. Therefore, the practical aspects of achieving the large magnetic bias fields required were considered, and the magnetic bias field transverse to the wide wall of the waveguide was chosen for further tests.

With the direction of the applied magnetic bias field established, the next parameter varied was the distance of the ferrite slab from the side wall of a 0.2-inch by 0.9-inch waveguide. For this test the ferrite was 0.030 inch thick, 0.195 inch high, and 4 inches long. Suhl's theory[7] and work done by Sakiotis, Chait, and Kales[4] would seem to indicate that optimum results will occur at that distance where a circular polarized RF magnetic field is encountered. When the ferrite is placed at this location, there is a decided difference in RF attenuation for opposite polarities of the magnetic bias field. However, there is not enough improvement in the limiting which is observed when the ferrite is in direct contact with the side wall to warrant removing the ferrite from the side wall, which acts as a good heat sink.

With the direction of the magnetic bias field and the placement of the ferrite in the waveguide established, techniques for increasing limiting action by intensification of the RF magnetic field in the ferrite can now be considered. Fig. 5 illustrates two techniques for intensifying the field: reduction of the waveguide height, and the use of dielectric loading. Since the majority of measurements on ferrite limiters were done in 0.2-inch by 0.9-inch waveguide, this size waveguide is used as a standard for comparison [Fig. 5(a)]. The ferrite used was a slab of Ferramic R-1, 0.030 inch thick and 6 inches long. The height of the ferrite was 0.195 inch for the 0.2-inch by 0.9-inch waveguide and 0.095 inch for the 0.1-inch by 0.9-inch waveguide.

Since the RF magnetic field intensity is inversely proportional to the height of the waveguide, reduction of the waveguide height by one half to 0.1 inch [Fig. 5(b)] increased the limiting by 3 db.

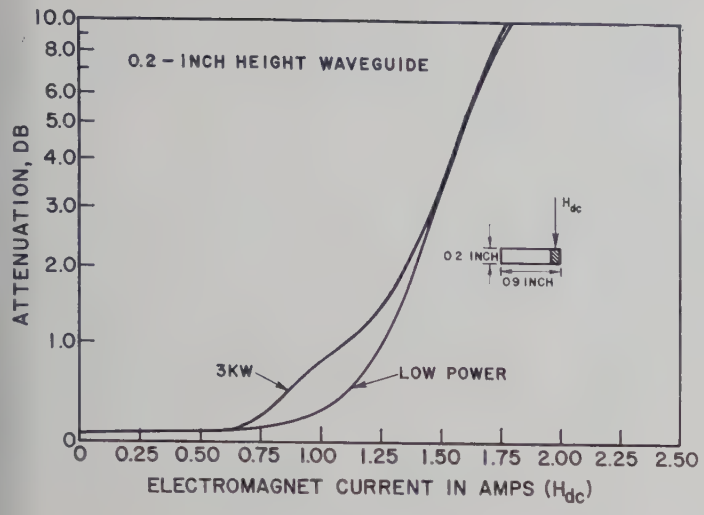

(a)

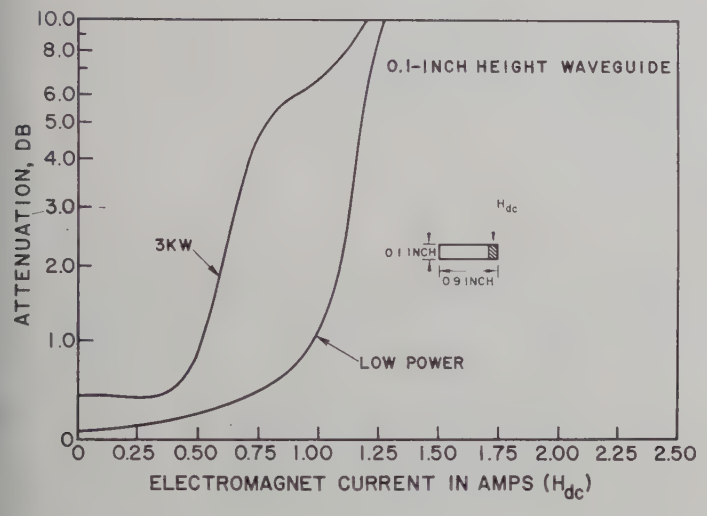

(b)

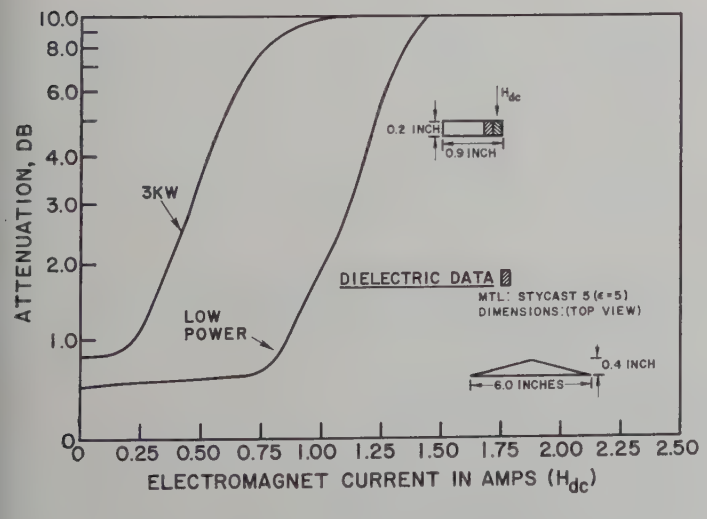

(c)

Fig. 5—Effect on limiting by enhancing the RF field intensity in the ferrite. (a) "Standard" waveguide. (b) Effect of reducing height of waveguide. (c) Effect of dielectric loading.

If a dielectric material is placed adjacent to the ferrite, as shown in Fig. 5(c), the RF energy in the waveguide is "pulled over" into the ferrite. The resultant intensification of RF magnetic field increases the limiting effect considerably. In this case a 7-db increase was achieved.

Very large RF magnetic field intensities can be achieved by resonant cavity techniques.[10] The main disadvantage to this method of enhancing limiting is the narrow bandwidth of the device. However, for a narrow-bandwidth microwave system, the cavity technique should give superior results.

The effect of ferrite length on the leading edge spike and the plateau of a limited RF pulse is shown in Fig. 6.

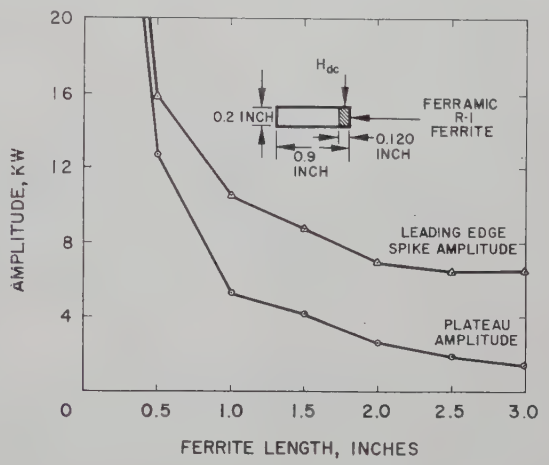

Fig. 6—Output pulse shape vs ferrite length (48-kw peak power input).

It is apparent that there must be sufficient ferrite in the waveguide to utilize the nonlinearity to its utmost, but a compromise must be made if the low power loss is to be kept at a minimum. An input power of 48 kw was chosen so that an effect could be clearly demonstrated for the shorter lengths of ferrite.

Effect on RF Waveshape

An experimental limiter using Ferramic R-1 ferrite (see configuration in Fig. 3) was constructed for the purpose of observing the operating characteristics of a limiter at high RF power levels.

The waveform of a 3-kw pulse of RF energy at 9000 mc, limited by this limiter, is shown in Fig. 2. The resultant waveform consists of a spike of energy of 650 watts amplitude and 0.1 μsec duration, then a plateau of

[10] If the RF phase shift exhibited by a ferrite, magnetically biased for optimum limiting, were different at low and high RF power levels, then a transmission cavity (containing the ferrite) adjusted for minimum loss at low power levels would be "detuned" at high RF power levels and would achieve very large *TR* attenuation ratios. A similar technique is used in most gas *TR* cells. However, phase shift measurements made on a limiter (Fig. 3) and a number of ferrite phase shifters at RF power levels up to 10 kw showed no change in phase that could not be accounted for by the change of M_s of the ferrite due to RF heating.

highly attenuated RF energy of 11.0 watts amplitude and 0.4 μsec duration, followed by a trailing edge spike of 45.5 watts amplitude and 0.1 μsec duration. The energy distribution for the leading edge spike, the plateau, and the trailing edge spike is 210 ergs, 70 ergs, and 25 ergs, respectively. At the present time it is believed that the 0.1 μsec duration of the leading edge spike is due to the conversion time from the uniform mode to the spin modes, and that the 0.1 μsec duration of the trailing edge spike is due to the relaxation time of the spin modes.

It was felt that if the build-up time of the input RF pulse was prolonged, perhaps the leading edge spike could be eliminated. Therefore, the limiter (Fig. 3 configuration) was subjected to high-power RF pulses of 0.05-μsec rise time and then to RF pulses of 0.3-μsec rise time. It was found that while the rise time of the leading edge spike was longer for the latter case, the amplitude of the spike and its decay time were unchanged.

If the limiter is to be used as a *TR* cell for a crystal detector, it is important to know how the limiter performs for various values of input power level. Therefore, an examination of the "limited" RF waveform as a function of input power level was made. A magnetron with the RF pulse shape shown in Fig. 2(a) was used as the signal source.

The results, presented in graph form in Fig. 7, show that no limiting effect takes place until the input power level reaches 110 watts. Above 110 watts a plateau is formed rapidly until, at 3 kw, the plateau reaches its lowest magnitude. During the same range of input power levels, a leading edge spike is formed. Between 3 and 9 kw input power, the plateau and leading edge spike remain unchanged. In practice it would be desirable to operate the limiter so that this stabilized region in ferrite characteristics coincides with the range of input power levels expected. Above 9 kw the plateau amplitude rises rapidly.

A possible explanation for this power level dependence is as follows. Consider the spin modes being coupled with the uniform mode through a nonlinear coupling coefficient. In this case, below 110 watts, the RF threshold of nonlinearity, the coupling coefficient is zero. Between 110 watts and 3 kw the coupling coefficient increases from zero to some finite value, energy is coupled into a lossy spin mode, and the plateau is formed. But since the coupling coefficient increases as the input power is increased, energy is coupled into the spin mode at a greater rate than if the coupling coefficient were a constant. As the result, the plateau power level is a decreasing function in this range of power levels. Because the spin modes require a certain time to build up, 0.1 μsec, the leading edge spike is formed.

Above 3 kw the coupling coefficient is constant, but as one spin mode is saturated, higher order spin modes are excited until at 9 kw all possible spin modes are excited. This would explain the stabilized region from 3 to 9 kw.

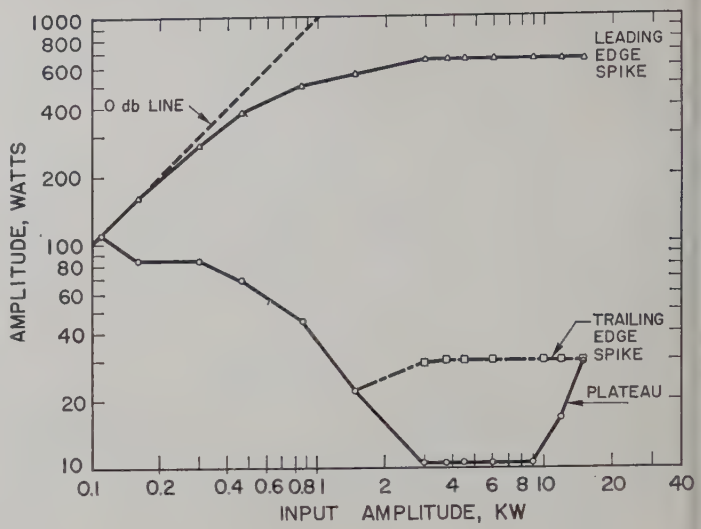

Fig. 7—Output pulse shape vs input power for a ferrite limiter (Fig. 3 configuration).

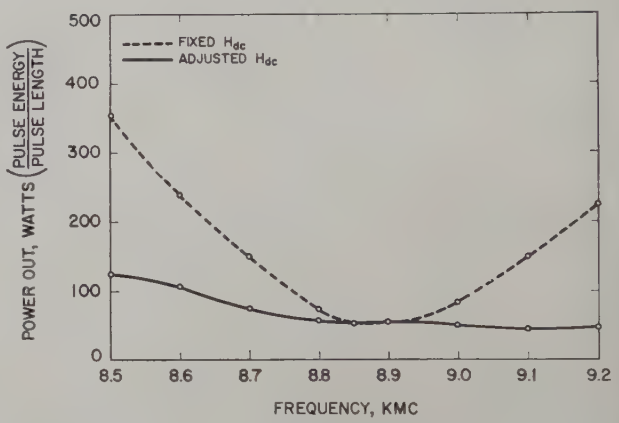

Fig. 8—Limiting vs frequency for a ferrite limiter (Fig. 3 configuration).

Above 9 kw, since all possible spin modes are saturated, the plateau power level rises.

The trailing edge spike appears to be reactive energy stored in the spin modes which is recoupled from the spin modes to the uniform mode when the input RF power level is removed; *i.e.*, similar to the ringing of an inductance or capacitance after it is de-energized. The trailing edge spike is usually hidden by the plateau until the plateau amplitude is reduced to a sufficiently small value.

In these tests, it was also observed that while the nonlinear behavior of the ferrite reached a maximum for one value of magnetic bias field, the effect existed, to a lesser degree, at all magnetic bias fields below ferromagnetic resonance but never above.

Bandwidth characteristics of the limiter (Fig. 3 configuration) are shown in Fig. 8. As can be seen, the magnetic bias field must be programmed as a function of frequency if optimum limiting is to be expected over the desired bandwidth. This programming of the magnetic bias field can be reduced or perhaps even eliminated by the use of a nonuniform magnetic bias field or a different

ferrite geometry. At low RF power levels the limiter exhibits a maximum insertion loss of 0.9 db and a maximum VSWR of 1.13 over the band.

Conclusion

In this paper several techniques for increasing the insertion loss of ferrite-loaded waveguide structures at high RF power levels have been presented, and the operating characteristics of a ferrite microwave limiter have been described. The most important problem appears to be the distortion of the RF pulse waveform by the ferrite limiter. While the plateau of the limited RF pulse has been reduced to 11 watts and further improvement can reasonably be expected, the leading edge spike, because of its large amplitude and long duration, is a more severe problem. Perhaps as we learn more about the mechanism of the ferrite's nonlinear behavior, engineering techniques can be found which will solve the spike problem by an appropriate waveguide-ferrite configuration or through the use of new ferromagnetic materials.

Acknowledgment

The author wishes to thank the various laboratory personnel who contributed suggestions in a number of the experiments. The assistance of W. Asp in the laboratory measurements is especially appreciated.

Nonreciprocity in Dielectric Loaded TEM Mode Transmission Lines*

D. FLERI† and G. HANLEY†

Summary—**An analysis is presented of partially dielectric loaded strip transmission line from the point of view of ferrite applications. It is shown that the microwave magnetic field is elliptically polarized both at the dielectric surface and within the dielectric. The degree of elliptical polarization is expressed analytically as a function of the dielectric constant, the degree of dielectric loading, and the frequency. For specific values of dielectric constant and loading, a high degree of circularity may be made to exist at the dielectric surface over extremely broad frequency bands. Experimental data are presented which are in accord with the theoretical predictions.**

Introduction

A GREAT variety of nonreciprocal propagation characteristics has been achieved at microwave frequencies through the use of ferrites. A necessary requirement for nonreciprocity is that the microwave magnetic field in the region of the ferrite be circularly polarized.[1] This requirement is easily met in rectangular waveguide propagating the dominant mode[2–4] and in circular waveguide propagating the circularly polarized TE_{11} mode.[3–4] In coaxial line and strip transmission line propagating the TEM mode, however, the microwave magnetic field is linearly polarized at all points, and therefore any ferrite effects will be completely reciprocal. It has been reported previously[5–6] that partially filling the cross section of coaxial line with a dielectric serves to distort the mode pattern and create an almost true sense of circular polarization at the air-dielectric interface. This mode distortion technique thereby renders coaxial line suitable for nonreciprocal applications. In a similar manner, polarization conversion may be effected in strip transmission line by appropriate dielectric loading.[7] Analysis of this latter transmission line structure forms the substance of this paper.

The dielectric loaded strip transmission line configuration is shown in Fig. 1. The co-ordinate axes are chosen so that Z represents the direction of propagation, and Y represents what will be referred to subsequently as the transverse direction. It will be shown that the polarization is elliptical both at the dielectric surface and within the dielectric. The degree of elliptical polarization at the dielectric surface is a function of the dielec-

* Manuscript received by the PGMTT, July 7, 1958; revised manuscript received, September 2, 1958. This work was supported by the U. S. Air Force Cambridge Res. Center, Contract No. AF19(604)-2248.

† Sperry Gyroscope Co., Div. of Sperry Rand Corp., Great Neck, N. Y.

[1] C. L. Hogan, "The ferromagnetic Faraday effect at microwave frequencies and its applications: The microwave gyrator," *Bell Sys. Tech. J.*, vol. 31, pp. 1–31; January, 1952.

[2] M. L. Kales, N. H. Chait, and N. G. Sakiotis, "A nonreciprocal microwave component," *J. Appl. Phys.*, vol. 23, pp. 816–817; June, 1953.

[3] J. H. Rowen, "Ferrites in microwave applications," *Bell Sys. Tech. J.*, vol. 32, pp. 1333–1369; November, 1953.

[4] A. G. Fox, S. E. Miller, and M. T. Weiss, "Behavior and applications of ferrites in the microwave region," *Bell Sys. Tech. J.*, vol. 34, pp. 5–103; January, 1955.

[5] B. J. Duncan, L. Swern, K. Tomiyasu, and J. Hannwacker, "Design considerations for broadband ferrite coaxial line isolators," Proc. IRE, vol. 45, pp. 483–490; April, 1957.

[6] H. Seidel, "Ferrite slabs in transverse electric mode waveguide," *J. Appl. Phys.*, vol. 28, pp. 218–226; February, 1957.

[7] R. S. Mangiaracina and B. J. Duncan, "Nonreciprocal ferrite devices in TEM mode transmission line," presented at Natl. PGMTT Symp., New York, N. Y.; May, 1957.

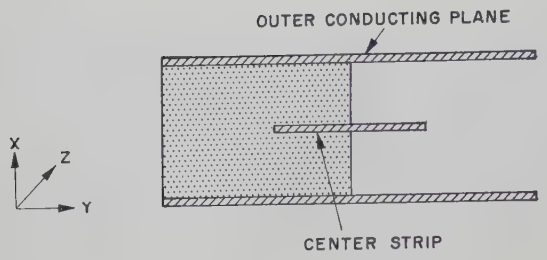

Fig. 1—Cross-sectional view of dielectric loaded strip transmission line structure.

tric constant, the degree of dielectric loading, and the frequency. It is the purpose of this paper to derive analytically the equation which relates these quantities and to discuss, on the basis of the derived result, the choice of parameters which renders the structure suitable for broad-band applications.

Although the analysis is presented in terms of strip transmission line, it is valid within engineering accuracy for dielectric loaded coaxial line as well.

Discussion

The microwave electric and magnetic fields in balanced strip transmission line propagating the TEM mode are purely transverse. However, if the structure is partially loaded with dielectric, a longitudinal component of the microwave magnetic field is required in order to satisfy the boundary conditions. This Z-directed H field interacts with the X component of the microwave E field to generate a Poynting vector in the transverse direction. Since a propagating mode exists in the transverse direction, the transverse resonance formulation may be used to determine the propagation constants of the transmission line system.[8]

For ease of analysis, the dielectric loaded strip transmission line structure is replaced by a simpler equivalent circuit. This circuit and the relationship it bears to the original structure is shown in Fig. 2(a) and 2(b). Symmetry allows the equivalent representation to be further simplified as shown in Fig. 2(c). A discussion of the various steps involved in formulating this equivalent representation is contained in the reference previously cited.[8]

The equivalent width of the transmission line structure, D, and of the dielectric, d, may be determined from the dimensions of the original structure as shown in Fig. 2. The ground plane separation, b, strip width, w, and the quantity, t, are directly measurable. S is the distance of the open circuit plane from the edge of the center strip. In general, S is a function of frequency, but if the operating conditions are such that $b/\lambda g$ never exceeds approximately 0.2, S may be represented by a constant independent of frequency. Under these conditions S is equal to (b/π) ln 2. Thus,

[8] G. Hanley, "The determination of propagation constants for partially filled strip line," unpublished thesis, Polytechnic Inst. of Brooklyn, Brooklyn, N. Y.; June, 1957.

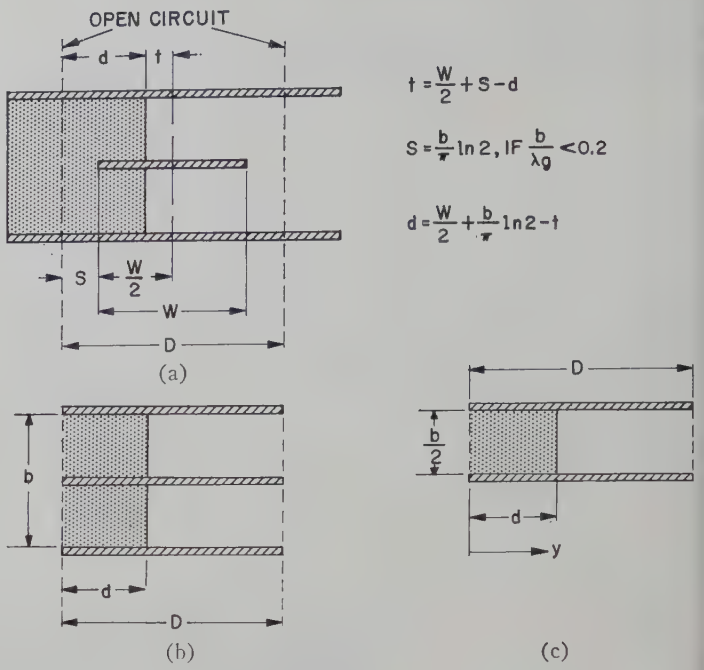

Fig. 2—Equivalent representation of the dielectric loaded strip transmission line structure.

$$D = w + \frac{2b}{\pi} \ln 2 \tag{1}$$

$$d = \frac{w}{2} + \frac{b}{\pi} \ln 2 - t. \tag{2}$$

The ratio, D/d, is referred to as the degree of loading.

By the method of transverse resonance the field equations for the dominant mode may be derived. These are obtained from a knowledge of the resonance voltage and current distribution and the mode functions of the uniform waveguides in the transverse direction.

There are two sets of field equations, one valid in the dielectric region, and the other valid in the air region.[8]

In the dielectric region:

$$H_X = 0 \tag{3a}$$

$$H_Y = I(Z)NV(0) \cos [k_{\epsilon Y} Y] \tag{3b}$$

$$H_Z = j \frac{k_{\epsilon Y}}{k_Z} I(Z)NV(0) \sin [k_{\epsilon Y} Y]. \tag{3c}$$

In the air region:

$$H_X = 0 \tag{4a}$$

$$H_Y = \frac{I(Z)NV(0) \cos [k_{\epsilon Y} d] \cosh [|k_Y| (D - Y)]}{\cosh [|k_Y| (D - d)]} \tag{4b}$$

$$H_Z = j \frac{|k_Y| I(Z)NV(0) \cos [k_{\epsilon Y} d] \sinh [|k_Y| (D - Y)]}{k_Z \cosh [|k_Y| (D - d)]} \tag{4c}$$

where

$I(Z)$ = current distribution in direction of propagation,

N = normalization factor,

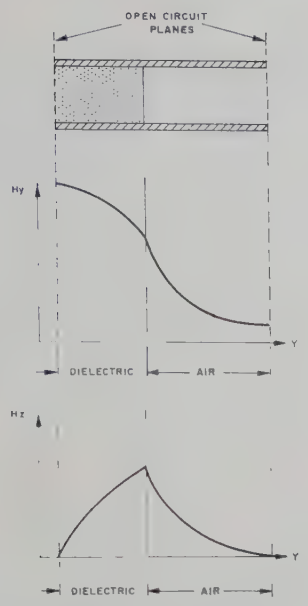

Fig. 3—The microwave magnetic field configuration in the dielectric loaded strip transmission line.

$V(0)$ = amplitude factor,
k_Z = guide wave number $= 2\pi/\lambda_g$,
k_Y = transverse wave number in air,
$= \sqrt{(2\pi/\lambda_0)^2 - (2\pi/\lambda_g)^2}$,
$k\epsilon_Y$ = transverse wave number in dielectric,
$= \sqrt{(2\pi/\lambda_0)^2\epsilon - (2\pi/\lambda_g)^2}$,
D = equivalent width of transmission line structure,
d = equivalent width of dielectric,
Y = as defined in Fig. 2.

In the dielectric region, the magnetic field variation is sinusoidal whereas in the air region the variation exhibits a hyperbolic dependence on transverse position. The field components are shown graphically in Fig. 3. The dominant mode is characterized by a guide wavelength smaller than that of free space.

The degree of elliptical polarization may be represented by the ratio of H_Y to H_Z. This ratio is termed the polarization factor. The polarization factor depends on the dielectric constant, the degree of loading, and the frequency. The functional dependence of the polarization on these parameters is easily found by forming the ratio H_Y to H_Z in both regions of the structure.

In the dielectric region:

$$\alpha_\epsilon = \left|\frac{H_Y}{H_Z}\right| = \frac{k_Z}{k_{\epsilon Y}} \cot [k_{\epsilon Y} Y]. \tag{5}$$

In the air region:

$$\alpha_a = \left|\frac{H_Y}{H_Z}\right| = \frac{k_Z}{|k_Y|} \coth [|k_Y| (D - Y)]. \tag{6}$$

α_a is the polarization factor in the air region and α_ϵ is the polarization factor in the dielectric region. Circular polarization corresponds to a factor of unity. It is clear from (6) that the polarization factor may never be equal to unity in the air region since the quantity, $k_Z/|k_Y|$, is always greater than unity (since $\lambda_g < \lambda_0$) and the hyperbolic cotangent is never less than unity. Therefore, circular polarization does not exist in this region.

Since the Y and Z components of the magnetic field are continuous at the dielectric boundary, H_Y must be greater than H_Z in the dielectric as well as in the air region. Hence, circular polarization does not exist at any point in this structure. It is obvious from the field configuration (Fig. 3) that the best sense of circularity exists at the air-dielectric interface.

Eq. (5) provides the functional dependence of the degree of elliptical polarization on the dielectric constant, the degree of loading, and the frequency. The nature of this dependence is more easily illustrated graphically.

Fig. 4 depicts the variation of the polarization factor at the dielectric surface as a function of wavelength (normalized with respect to the parameter, d) for several degrees of loading. At higher frequencies, *i.e.*, for $\lambda/2d$ less than approximately 3, the polarization factor is independent of the degree of loading.

As the wavelength increases, the curves diverge. For a loading factor of one third, *i.e.*, for a D/d ratio of 3, the polarization factor remains less than 1.2 for $\lambda/2d$ between 1 and 8.5. This represents more than an 8 to 1 frequency band.[9] A polarization factor of 1.2 corresponds to a resonance attenuation ratio of about 20 to 1 db if it is assumed that the only loss mechanism is the absorption by the ferrite of negative circularly polarized energy. A D/d ratio of 2 yields a polarization of 1.2 or less over approximately 5 to 1 frequency band. The band becomes increasingly narrow as the degree of loading is increased.

Fig. 5 shows the variation of the polarization factor with normalized wavelength for various values of dielectric constant. The degree of loading for this case corresponds to a D/d ratio of 3. It is seen that the polarization factor increases without limit in the large wavelength region of the curve. This may be expected for at zero frequency, *i.e.*, in the static case, H_Z is equal to zero, and therefore, the ratio of H_Y to H_Z is infinite. The dual condition exists at short wavelengths and the ellipticity tends to infinity in this region as well. Between these two extremes the polarization factor remains close to unity over a wide range of wavelengths. The higher the dielectric constant the lower and broader the characteristic becomes. This trend is offset, however, by the inception of higher order modes. The higher the dielectric constant, the lower is the frequency at which these modes may propagate. In many applications a dielectric constant of 10 represents a good compromise between a well-defined sense of circularity over a wide band and suitable mode purity.

[9] Mode pure operation exists only for $\lambda/2d$ greater than approximately 4.5. When operation corresponds to $\lambda/2d$ less than 4.5 special effort must be made not to excite higher order modes.

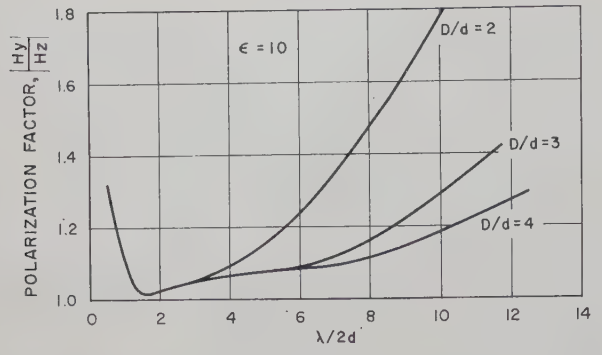

Fig. 4—The polarization factor as a function of normalized wavelength for various degrees of dielectric loading.

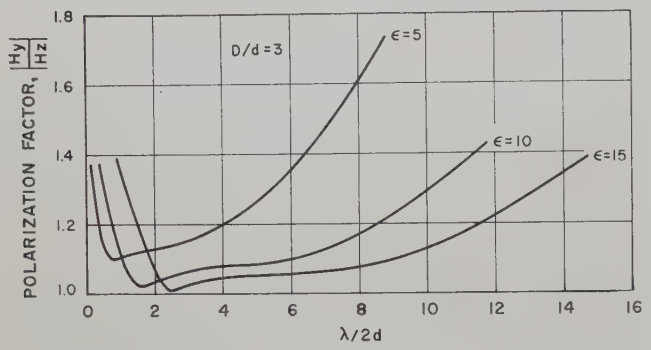

Fig. 5—The polarization factor as a function of normalized wavelength for various values of dielectric constant.

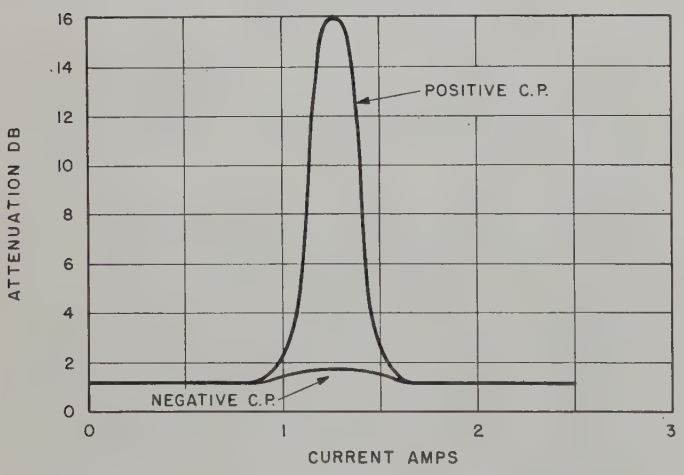

Fig. 6—Typical attenuation characteristic of ferrite dielectric loaded strip transmission line structure.

The foregoing analysis was conducted in an effort to determine the parameters which render dielectric loaded strip transmission line suitable for broad-band nonreciprocal ferrite applications. It was seen that for a dielectric constant of 10 and a D/d ratio of 3, the polarization factor at the air-dielectric interface remained less than 1.2 over an extremely broad frequency band. As was pointed out, a polarization factor of 1.2 corresponded to a resonance attenuation ratio in db of 20 to 1 db.

Experimental data are now presented which tend to confirm the results of this analysis.

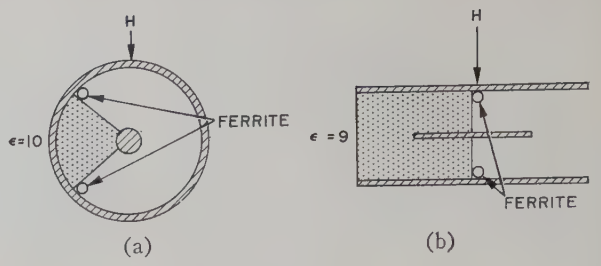

V (mc)	Resonance Attenuation Ratio (db)	
	A	B
1000	12:1	9:1
1500	50:1	20:1
2000	40:1	50:1
3000	30:1	—
4000	25:1	50:1
4500	35:1	—

Fig. 7—Representation of ferrite dielectric loaded coaxial and strip transmission line test structure and tabulation of experimental results.

Ferrite was positioned at the air-dielectric interface and forward and reverse wave attenuation was measured as a function of applied magnetic field. Of course, these measurements cannot be used to test the theoretical results quantitatively as ferrite loading causes considerable perturbation of the microwave field configuration.

Fig. 6 is representative of the data taken. The ferrite was a low $4\pi M_s$ aluminate characterized by a narrow linewidth and extremely low loss away from resonance. The loss away from resonance was primarily that of the mode distorting dielectric. If this is subtracted from the forward and reverse loss at resonance, the resulting attenuation ratio is a measure of the degree of elliptical polarization of the microwave magnetic field within the ferrite. Measurements were made at several frequencies extending from 1000 to 4500 mc. Similar data were taken in coaxial line since the analysis of strip transmission line was approximately valid for this type of line as well.

The resonance attenuation ratios are tabulated in Fig. 7 below the corresponding structures.

It is apparent from the data of Fig. 7 that a well-defined sense of circularity existed at the air-dielectric interface in both coaxial and strip transmission lines. In the coaxial structure the D/d ratio was approximately 3 and the dielectric constant was 10. A high degree of circularity existed from 1500 to 4500 mc—a 3 to 1 frequency band. The dielectric loading of the strip transmission line structure corresponded to a D/d ratio of 2. The dielectric constant of the mode distorting medium was 9. The measurements indicated that a well-defined sense of circularity existed from 1500 mc to at least 4000 mc. It was not feasible to make measurements at higher frequencies, but it is fairly safe to predict that this structure is suitable for applications extending over at least a 3 to 1 frequency band.

Conclusions

It has been shown that in partially dielectric loaded strip transmission line the microwave magnetic field was elliptically polarized at the air-dielectric interface. The degree of elliptical polarization was a function of the dielectric constant, the degree of loading, and the frequency. An expression relating these quantities has been derived. For specific values of dielectric constant and loading, the polarization factor at the dielectric surface was shown to be 1.2 or less over very broad frequency bands. Measurements in ferrite loaded strip transmission line and coaxial structures indicated the existence of a high sense of circularity at the dielectric interface over at least a 3 to 1 band. It is clear from the foregoing analysis and measurements that dielectric loaded strip transmission line and coaxial line are very well suited for broad-band nonreciprocal ferrite applications.

Acknowledgment

The authors are indebted to B. J. Duncan for suggesting the analysis presented in this paper and to L. Swern for his advice during the course of this work.

Ferrite Phase Shifter for the UHF Region*

C. M. JOHNSON†

Summary—**An extremely compact, low-loss, ferrite phase shifter has been developed for the 200 to 800-mc region. It consists of a folded stripline structure approximately 6½ inches long and less than 1 inch square in cross section. The device requires a longitudinal magnetic field of sufficient intensity to place the operating region above resonance. For field swings of about 900 oersteds (from 430 to 1250 oersteds at 400 mc), 360° change in phase shift can be obtained with about 1 db of loss. The phase shifter is reciprocal and shows identical low-power and high-power characteristics up to at least 10-kw peak. Some additional data are included on the operation of the phase shifter down to 10 mc and up to 2000 mc.**

Introduction

SEVERAL different types of electronically controllable ferrite phase shifters have been successfully developed for the microwave region. In the UHF region, however, ferrite devices capable of 360° phase shift have usually proven too lossy and bulky to be practical.

In an attempt to overcome these difficulties in the UHF region, a compact, folded stripline, ferrite phase shifter has been developed which produces 360° change in phase shift with very low loss over an extremely wide frequency region.

This phase shifter is operated on the high-field side of resonance, requiring a relatively large magnetic field. In compensation, however, operation in this region eliminates the nonlinear effects usually observed at high RF power levels. This characteristic, along with the fact that the phase shifter is reciprocal, permits its use in both transmitting and receiving systems.

* Manuscript received by the PGMTT, June 2, 1958; revised manuscript received, August 20, 1958. This research was supported by the AF Cambridge Res. Center under Contract No. AF 19(604)-2407.

† Electronic Communications, Inc., Timonium, Md.

Description

Construction

Fig. 1 shows the phase shifter construction. The device is about 6½ inches long and consists of 5 layers of stripline. Each layer is loaded with two 0.40-inch × 0.05-inch × 6-inch strips of ferrite, one on each side of the center conductor. The center conductor is folded as shown to provide continuity between layers. Thus, the total length of ferrite through which the wave must travel is 32.2 inches, or 82 cm.

Fig. 2 shows a photograph of the complete phase shifter. Input and output lines are standard RG-8/U cables. The transition to stripline is made simply by slotting the center conductor of the coax to receive the rectangular center conductor of the stripline and connecting the coax shield to the stripline ground plates.

In the model shown here the layers of stripline are fastened together by bolts spaced along the sides. These bolts also serve as electrical shorts between the ground plates.

The dimensions of the stripline shown in Fig. 1 are such that

$$\sqrt{\frac{\epsilon_1}{\mu_1}} \qquad Z_0 = 115 \text{ ohms},$$

where Z_0 is the characteristic impedance, ϵ_1 the relative dielectric constant, and μ_1 the relative permeability. For $\epsilon_1 = 11.5$ and $\mu_1 \approx 2$, typical of the ferrite material used, Z_0 is approximately 50 ohms. The permeability, of course, is a variable here, and therefore it is not possible to attain an exact 50-ohm impedance over the full range of phase shift.

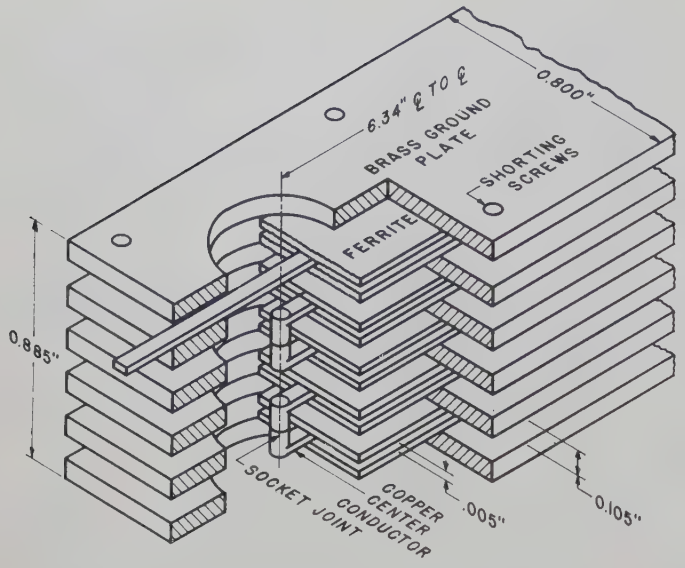

Fig. 1—Cross section of folded stripline phase shifter.

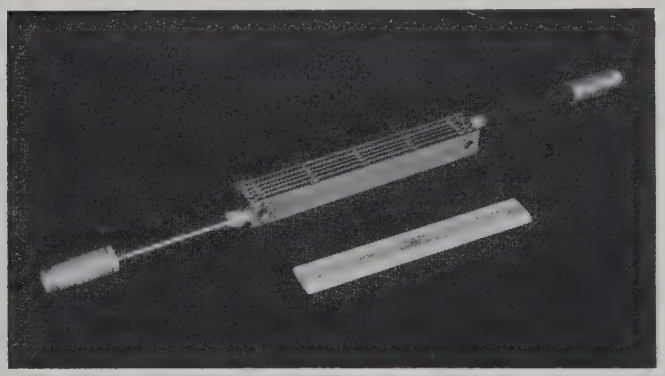

Fig. 2—Photograph of stripline phase shifter.

The phase shifter has generally been operated in a longitudinal magnetic field supplied by a 12-inch long solenoid. The structure fits easily into the $1\frac{1}{4}$-inch inner diameter of the coil, and a reasonably uniform magnetic field is attained (± 5 per cent), since the device extends only over the middle half of the solenoid.

Ferrite Material

Previous to our work, Chu Associates[1] made a series of measurements in the 225 to 400-mc region on $\frac{1}{4}$-inch long samples of ferrite materials shaped to fit a coaxial line. They found that phase shifts of 183° per db of loss could be attained at 400 mc and 169° per db at 225 mc. Their best results were attained with nickel-cobalt-aluminum ferrites.

In the phase shifter described here, type TT-414 ferrite, manufactured by Trans-Tech, Inc., was used. This is a magnesium-manganese-aluminum ferrite with a saturation magnetization of 600 oersteds and a Curie temperature of about 100°C. With this material in the stripline structure, we have measured phase shifts of 400° per db of loss at 400 mc and 300° per db of loss at 225 mc. These measurements, in contrast to Chu's, were made on long samples of the ferrite (6-inch), and the attenuation includes conductor loss.

Measurements

Fig. 3 shows schematic diagrams of the measuring systems used to determine the characteristics of the phase shifter. At low-power levels (milliwatts) a simple reflection scheme with one end of the phase shifter shorted was used to measure phase shift as a function of applied field. A phase shift of 180° is indicated by a half wavelength change on the slotted line. Input VSWR was measured with one end of the phase shifter terminated in a 50-ohm load. Insertion loss was measured by first setting a reference level with the phase shifter removed from the circuit and then inserting the device and recording the attenuation for various values of magnetic field.

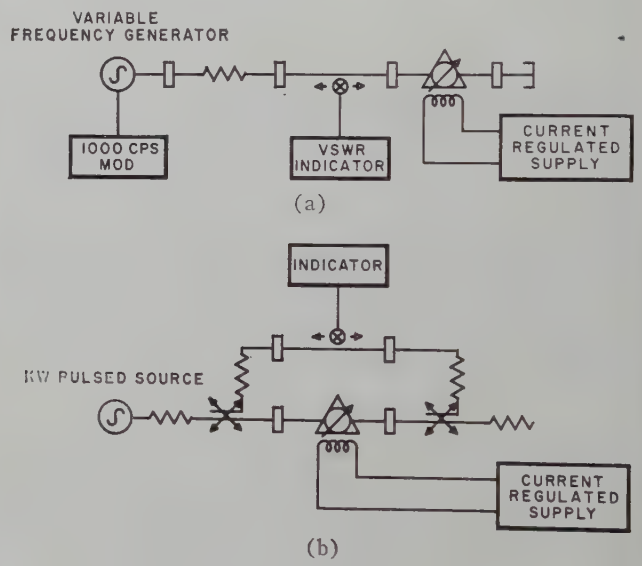

Fig. 3—(a) Low-power measuring system.
(b) High-power measuring system.

At high-power levels (kilowatts) the phase shifter was located in the high-power line and terminated in a 50-ohm load. A directional coupler was inserted in the line on each end of the phase shifter, and the low-level energy coupled from each of these points was sent in opposite directions through the slotted line. In this case, a phase shift of 360° produces a half wavelength change in the probe position. Input VSWR was measured by inserting two identical directional couplers back-to-back at the input to the phase shifter and again sending the coupled signals through the standing wave machine in opposite directions. Insertion loss was measured in the same manner as for the low-power case, except that the crystal detector was isolated from the high-power line by a directional coupler.

[1] Chu Associates, "Ferrite Feasibility Study," Interim Dev. Rep. No. 3, Contract No. NObsr-72586; December 1, 1956–March 31, 1957.

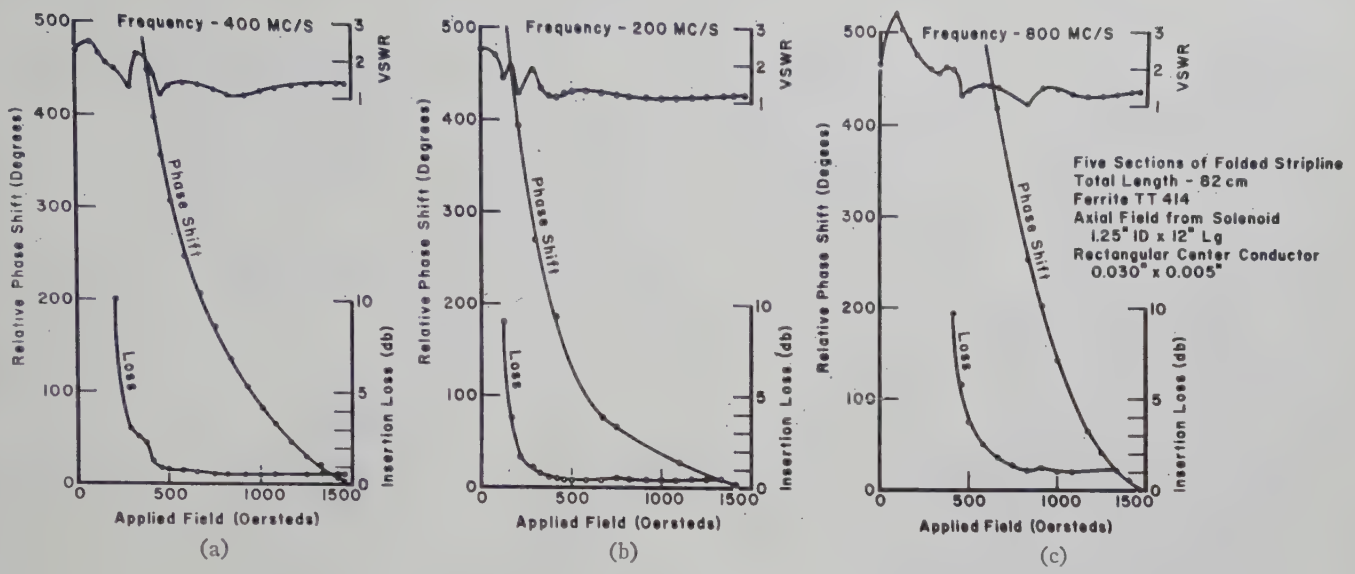

Fig. 4—Phase shifter characteristics at (a) 400 mc, (b) 200 mc, and (c) 800 mc.

Results

Although the range of interest was originally 200 to 600 mc, the characteristics of the phase shifter have been investigated over the frequency range from 2 mc to 2000 mc. The optimum region for the particular length and configuration chosen, however, appears to be 300 to 600 mc.

Typical characteristics of the phase shifter are shown in Fig. 4. At 400 mc, Fig. 4(a) indicates that for an insertion loss of 1 db, 360° change in phase shift (hereafter denoted as relative phase shift) is obtained when the magnetic field is changed from 430 to 1250 oersteds; $\Delta H = 820$ oersteds. The maximum VSWR over this range is 1.45. It can be seen from the graph that the insertion loss has its maximum value of 1 db at the low-field limit of 430 oersteds, and decreases to approximately $\frac{1}{2}$ db by the time the field reaches 700 oersteds. A phase shift of 360° can be obtained for $\frac{3}{4}$-db loss, if the field swing is increased to cover the range from 460 to 1600 oersteds.

Fig. 4(b) shows a similar set of phase shifter characteristics taken at 200 mc. Here 360° phase shift is obtained with a 1.6-db insertion loss when the field is changed from 220 to 1500 oersteds; $\Delta H = 1280$ oersteds. The maximum VSWR in this case is 1.8, again occurring at the low-field end of the range where the ferrite loss is beginning to increase. A better match in this region would result in a sizeable reduction in insertion loss. Even so, for optimum performance at 200 mc, the length of the phase shifter should be increased by about 25 per cent. In this case, the loss would be reduced to 1 db for 360° phase shift, and the required field change would only be from 280 to 1180 oersteds ($\Delta H = 900$ oersteds).

The 800-mc characteristics of the phase shifter are shown in Fig. 4(c). In this case, 360° phase shift is obtained for an insertion loss of 1.4 db and a field change from 730 to 1630; $\Delta H = 900$ oersteds. If the field limits were shifted to higher values, the insertion loss could be reduced to approximately 1 db.

The loss values given in Fig. 4 are actual insertion losses uncorrected for VSWR. If a better match were attained at lower field values, then 360° phase shift with 1-db loss could be attained for an appreciably smaller field change.

From these four sets of data it can be seen that the insertion loss in the low-loss region is increasing with frequency, being less than $\frac{1}{2}$ db at 200 mc and 1 db at 800 mc. The rate of increase appears to be $> \sqrt{\nu}$ but $< \nu$, where ν is the frequency. This indicates that the ferrite losses and the conductor losses are comparable. A calculation of the conductor loss for the stripline, as used here with copper conductors, gives 0.23-db loss at 200 mc and 0.46-db loss at 800 mc, which indeed verifies that the two losses are comparable.

From the data it can also be seen that the low-loss region is moving to higher values of magnetic field as the frequency increases, which, of course, it should, since the resonance region at higher frequencies occurs at larger fields. Eventually, the resonance reaches such a high field value that it is no longer practical to operate on the high side.

As mentioned previously, measurements on the phase shifter were extended over a much wider frequency range than was at first anticipated. Fig. 5 gives a summary of the data obtained from 10 mc to 2000 mc with the folded stripline of 82-cm total length. For convenience, the phase shift curves from 100 mc to 2000 mc are approximately normalized to an origin between 1500 and 1600 oersteds. The lower frequency curves are beginning to approach saturation in this region. The loss curves shown here are corrected for the small reflection loss in order to make them more universally applicable.

At 10 mc these curves show that approximately 90° phase shift can be obtained for a loss of 1 db. The opti-

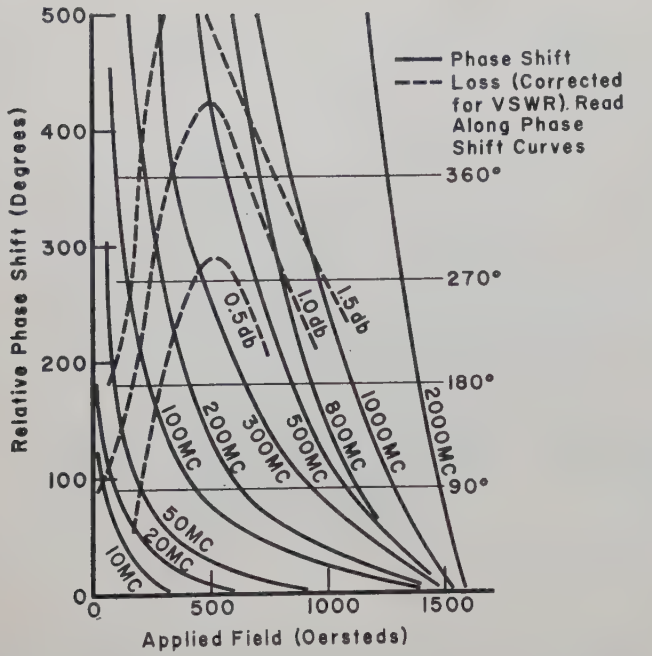

Fig. 5—Summary of phase shift and loss characteristics of folded stripline phase shifter over the region from 10 mc to 2000 mc.

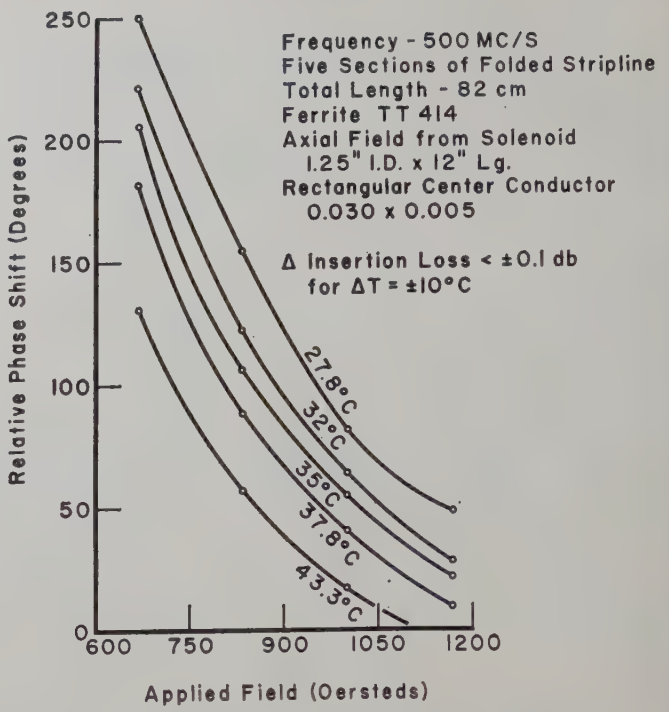

Fig. 6—Temperature characteristics of phase shifter.

mum region for this length shifter is indicated quite clearly as the 300 to 600-mc region. At 2000 mc the loss has reached 2 db, but the phase shift function has not approached saturation at our highest field value. At this frequency a much lower loss could be attained by making the device shorter and operating at higher fields.

Temperature effects in the phase shifter were measured by attaching a thermocouple to the ferrite and heating the device by driving the solenoid at high current with the ventilating fan off. Fig. 6 shows the effects obtained at 500 mc. Here the temperature is changed from 27.8°C to 43.3°C ($\Delta T = 15.5$°C) for various field values from 665 to 1165 oersteds. When relative phase is plotted as a function of applied field with temperature as a parameter, the parametric curves are approximately parallel over the region examined. In the low-field region the phase shift change per degree temperature change is greater than in the high-field region. At any particular field value, however, the phase shift change per degree temperature change is approximately linear.

Fig. 7 gives a comparison of the phase shifter characteristics at high, low, and intermediate powers. Three sets of measurements were taken at 715 mc. One set was taken with approximately 10 kw of peak pulsed power. The pulse length was 1 microsecond and the repetition rate was 500 cps. A second set was taken with this same source attenuated 25 db giving a peak output of 30 watts, and a third set was taken with milliwatts of power modulated at 1000 cps. In the low-loss region no measurable difference exists in the phase shift or loss characteristics. As the side of the resonance is approached the loss curves begin to deviate. The loss curve for the lowest power begins to increase at the fastest rate, and

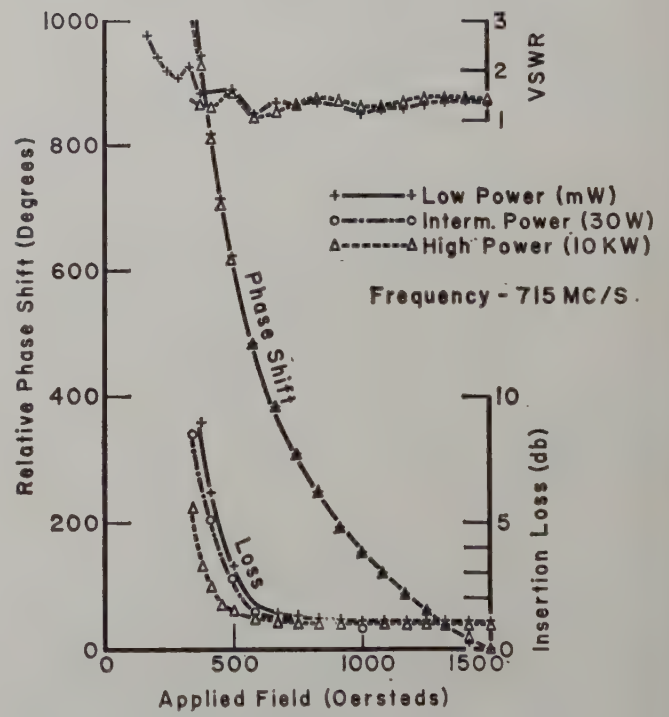

Fig. 7—Comparison of phase shifter characteristics at various power levels.

that for the highest power at the slowest rate. The phase shift curves begin to show a measurable deviation only at low fields after the loss has reached a high value. These characteristics indicate the onset of a saturation effect.

Besides the foregoing major results, a few miscellaneous observations should also be mentioned.

First, the phase shifts obtained when a transverse

magnetic field was applied to the device were considerably less than those obtained with a longitudinal field. The losses were also slightly greater. It should be emphasized, however, that these results are only qualitative, since the field was not uniform.

Second, at 1100 cps the ac modulation current through the solenoid gave about 40 per cent as much phase swing as a dc current equal to the peak-to-peak ac current. Thus, the stripline structure with shorting screws making dc contact with the ground plates shields the ferrite at high modulation frequencies. To overcome this difficulty the shorting screws should be designed to look like RF short circuits but dc open circuits.

Third, resettability of phase shift through the device is limited by the accuracy with which the current can be read (0.1 per cent or better).

Fourth, a few measurements were made using different types of center conductors. A phosphor bronze conductor is more rugged than pure copper and was used at first, but since conductor loss is a major contributor to the total it had to be discarded in favor of the pure copper. A round copper center conductor (0.017 inch) was also tried, but less phase shift was obtained than with the rectangular type. This decrease was attributed to the proportionally greater effect of the air space between the ferrite strips when a round conductor is used.

Fifth, an attempt was made to measure μ_1 and ϵ_1 for the long ferrite samples in the stripline by means of a sliding short technique. The results indicated that $\epsilon_1 \approx 11$ and $\mu_1 \approx 2$, but for accurate results the conductors will have to be plated to the ferrite strips.

Discussion and Conclusions

The above results show that large differential phase shifts can be obtained with low loss over the entire VHF and UHF bands. In this frequency region the stripline structure as used for the foregoing phase shifter will ordinarily allow only the TEM mode to propagate, *i.e.*, when loaded with the usual nongyromagnetic dielectric. However, it has been shown theoretically that a TEM mode cannot exist in a bounded gyromagnetic medium.[2] The exact mode configuration that does exist in this structure when loaded with a gyromagnetic medium is not clear at present, but the Faraday rotation in the ferrite is certainly restrained. A similar type of restraint of the Faraday rotation has been found by Reggia and Spencer[3] in a rectangular waveguide structure loaded with a long cylinder of ferrite magnetized longitudinally.

The low losses, low VSWR's, and wide range of operation are strong indications that the phase shifter is operating in essentially a TEM mode.

The TT-414 ferrite used in the phase shifter is a magnesium-manganese-aluminum ferrite with a line width at *S*-band of about 120 oersteds. It was suggested by C. L. Hogan that at field values several line widths removed from resonance, polycrystalline magnesium ferrites have been found to have effectively much narrower line widths than the 3-db width indicates. This follows, since the line shape is not Lorentzian; it decays much more rapidly in the wings. Low-loss operation down to a few megacycles at fields of about 50 oersteds indicates a very narrow line width.

Other ferrites have been tried in coaxial structures and were found to have very promising characteristics along with higher Curie temperatures. Extensive tests of these materials in the stripline device have not yet been carried out.

The advantages of operation on the high-field side of resonance is pointed out quite clearly in Fig. 7, where the loss is constant from milliwatt power levels to 10-kw levels. Subsidiary resonances of the type that occur on the low-field side of the main resonance are not present.

In summary, it appears that a ferrite-loaded folded-stripline structure magnetized longitudinally has a range of application as a phase shifter from a few megacycles to a few thousand mega-cycles. The structure is extremely compact and the solenoid size is relatively modest below frequencies of a thousand megacycles. (The actual design of the solenoid will depend on the switching time desired.) The length of the structure should be tailored somewhat to the operating frequency for minimum loss and minimum field swing. Actually, the last two parameters are mutually opposed. The field swings can be reduced considerably if a higher loss is permitted.

Acknowledgment

The author wishes to acknowledge the help of G. Buehler of this laboratory in making the foregoing measurements.

[2] P. S. Epstein, "Theory of wave propagation in a gyromagnetic medium," *Rev. Mod. Phys.*, vol. 28, pp. 3–17; January, 1956.

[3] F. Reggia and E. G. Spencer, "A new technique in ferrite phase shifting of beam scanning of microwave antennas," Proc. IRE, vol. 45, pp. 1510–1517; November, 1957.

A Ferrite Serrodyne for Microwave Frequency Translation*

F. J. O'HARA† AND H. SCHARFMAN†

Summary—A ferrite serrodyne has been developed to produce a frequency translation of *X*-band microwave signals over ranges from zero to 50 kc. The device consists of an effiicent longitudinal field ferrite phase shifter and an associated electronic driver for generating the modulating sawtooth. Transmission or reflection operation is possible. A conversion loss of 1 to 2 db is obtained. Suppression of spurious output spectral components is 33 db or more for a 10-kc translation and 21 db for a 50-kc translation.

Introduction

THIS PAPER discusses the theory, design, development, construction, and performance of a ferrite serrodyne for translations of *X*-band microwave signals from 0 to 50 kc. It consists of an efficient longitudinal field ferrite phase shifter and associated electronic drive circuitry necessary to produce a periodic sawtooth of phase shift. These components are described in detail.

Theory

The term, serrodyne, was coined to describe a class of modulators which can cause frequency translation by sawtooth transit time modulation of a signal. When used a bit more generally, this term also includes frequency translators using a sawtooth of phase modulation. A comprehensive analysis of serrodyne operation employing transit time modulation (TTM) has already been accomplished by Cumming,[1] and various successful serrodyne devices employing klystrons, TWT and microwave crystal modulators[2] have been described. The performance of the ferrite serrodyne discussed here is in terms of the criteria established by Cumming. A brief comparison is made between the TTM and phase modulation points of view. The phase modulation approach appears to be the more appropriate formulation for the particular device discussed in this paper although TTM formulations are adequate to describe the small frequency translations encountered here.

Consider a wave disturbance propagating along a transmission line of length, l, with the usual spatial and time variation, expressible as

$$E = E_1 \sin (\omega t - \beta z). \tag{1}$$

A frequency translation may occur at the output of this line in either of two ways; first, by a phase modulation. Consider a change in βz such that

$$\frac{d}{dt}(\beta l) = \text{constant} = \omega_m. \tag{2}$$

If βl is considered here as supplying a particular phase angle relative to the ωt variation for a signal emerging from the given length l of the transmission line, and $d(\beta l) = \omega_m dt$ as postulated, then it is evident that frequency translation has taken place under this phase modulation. A constantly increasing phase angle added to a sinusoid displaces its frequency.

$$E_{\text{out}} = E_1 \sin (\omega t - \omega_m t), \tag{3}$$

$$E_{\text{out}} = E_1 \sin (\omega - \omega_m) t. \tag{4}$$

A displacement to a higher frequency may be had simply by changing the sign of $d/dt(\beta l)$. For the ferrite serrodyne discussed here, β is varied as a sawtooth function under the influence of an external applied magnetic field. Linear increase (or decrease) of β with time by 360 degrees followed by rapid flyback is used to achieve results similar to a continuously increasing β.

A second way to secure frequency translation is by the TTM of individual successive wave periods. Following the theory developed by Cumming, let a wave incident upon the input of the transmission line section be broken into periodic intervals and represented as follows.

$$E_{\text{in}} = \sum_{k=1}^{\infty} E_1 \sin \omega \left(t - \frac{2\pi k}{\omega} \right)$$

when

$$(2k-1)\frac{\pi}{\omega} \leq t \leq (2k+1)\frac{\pi}{\omega} \tag{5a}$$

$$E_{\text{in}} = 0$$

when

$$t < (2k-1)\pi/\omega$$

$$t > (2k+1)\pi/\omega. \tag{5b}$$

[See Fig. 1(a) and 1(b).]

* Manuscript received by the PGMTT, May 19, 1958; revised manuscript received, September 8, 1958.

† Raytheon Manufacturing Co., Waltham, Mass.

[1] A general theory of serrodyne operation has been developed by R. C. Cumming and presented in two reports. "Frequency Translation by Modulation of Transit Time Devices," Applied Electronics Lab., Stanford Univ., Stanford, Calif., Tech. Rep. No. 39, ONR Contract N6 onr 25132, NR 373 762; August 1, 1955. "The serrodyne frequency translator," PROC. IRE, vol. 45, pp. 175–186; February, 1957.

[2] E. M. Rutz and J. E. Dye, "Frequency translation by phase modulation," 1957 IRE WESCON CONVENTION RECORD, pt. 1, pp. 201–207.

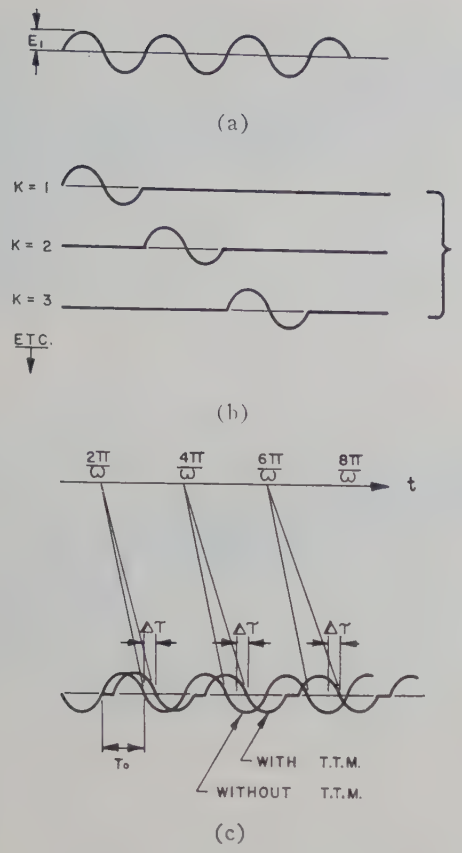

Fig. 1—Transit time modulation.

In the absence of any TTM, the wave emerging at the output of the transmission line section may be represented as

$$E_{out} = \sum_{k=1}^{\infty} E_1 \sin \omega(t - t_k)$$

when

$$t_k - T_0/2 \leq t \leq t_k + T_0/2 \tag{6a}$$

$$E_{out} = 0$$

when

$$t < t_k - T_0/2$$

$$t > t_k + T_0/2 \tag{6b}$$

where T_0 is the output wave period, $t_k = 2\pi k/\omega + T_k$, and T_k is the transit time of the kth wave period. Here, $T_k = T_0 = l/v = \beta l/\omega$; for t as in (5a):

$$E_{out} = \sum_{k=1}^{\infty} E_1 \sin\left[\omega\left(t - \frac{2\pi k}{\omega}\right) - \beta l\right] \tag{7}$$

has the form to be expected.

Now introduce an ideal TTM in which a constant interval ΔT_k is added to the transit time of each successive disturbance, so that

$$t_k = \frac{2\pi k}{\omega} + T_0 + \sum_{k=1}^{\infty} \Delta T_k. \tag{8}$$

In this way the period of the output signal disturbance becomes longer than the input signal periods:

$$T_{out} = T_{in} + \Delta T_k = \frac{2\pi}{\omega} + \Delta T_k, \tag{9}$$

$$\omega_{out} = \frac{2\pi}{\frac{2\pi}{\omega} + \Delta T_k} = \frac{\omega}{1 + \frac{\Delta T_k}{T_{in}}}. \tag{10}$$

[See Fig. 1(c).] This frequency translation has been accomplished by maintaining the pure sinusoidal form of the output disturbances, but there is now a short, blank interval between them. This distortion limits the validity of the TTM analysis, but a Fourier analysis of the output wave train shows that if $\Delta T_k/T_{in} \ll 1$ the TTM formulation is sufficiently accurate.[3]

Physical limitations of most modulating devices preclude infinite changes in transit time or phase shift as have been described. However, a sawtooth of transit time variation or of phase shift may be used as an approximation to infinite continuous change. A spectrum of frequencies periodically spaced about the carrier at the sawtooth modulation frequency may be generated. The amplitude of the sawtooth is carefully chosen so that the periodic signal disturbances from one interval coincide with an extension of those disturbances from the preceding modulation interval and also into the following intervals. The resulting phase coherence insures that most of the output signal energy appears in one sideband adjacent to the carrier. The flyback discontinuity produces a perturbation in the output wave train. For the ideal case of zero flyback interval and for relatively small frequency displacements, this perturbation has negligible effect on the output spectrum since signal energy associated with it is negligible. Carrier and translated frequencies are related as follows.

$$f_o = f_i + nf_m \tag{11}$$

where f_o is the output frequency; f_i, the input frequency; f_m, the modulation frequency; and n, an integer and modulation index, usually is taken equal to one.

Structure of the Ferrite Serrodyne

The type of device presented here consists of an efficient longitudinal field ferrite phase shifter driven by a

[3] For ΔT_k negative, the output signal function as constructed would be double valued where the signal intervals overlap. However the analysis is still valid since the amplitude and relative phase of an element in the output signal spectrum is the product of two separate frequency functions; one is a function only of the TTM employed and the other, a function only of the input waveform. Cf. Cumming, *op. cit.*, p. 13.

If the signal disturbances considered do not have waveforms filling the entire signal periods, but instead have a pulse character with a short duty cycle, the TTM analysis again becomes more accurate. This is the case treated by Cumming in his extended analysis of the serrodyne, where he developed the theory for particular application to klystrons and TWT. From the foregoing considerations it can be seen that a ferrite serrodyne is more accurately considered as phase modulated in the sense described above (in contrast to the definition of phase modulation employed by Cumming) rather than transit time modulated, but that for small time displacements per signal period, *i.e.*, relatively slight frequency translations, the TTM analysis is sufficiently accurate to be useful.

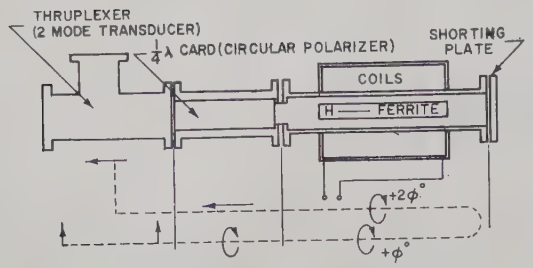

Fig. 2—Cross-polarized phase shifter (transmission-type thruplexer serrodyne).

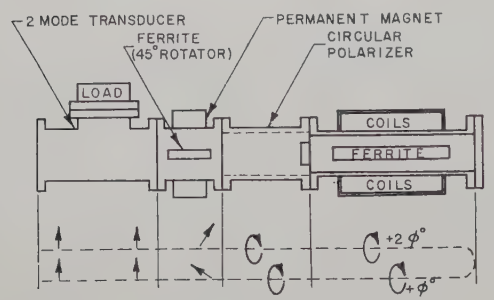

Fig. 3—Electrically controllable short circuit (reflection-type thruplexer serrodyne).

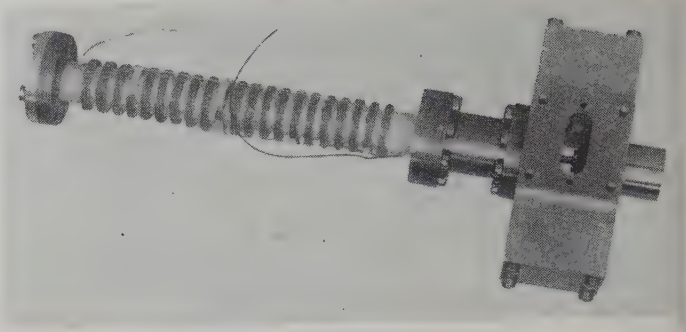

Fig. 4—Turnstile serrodyne.

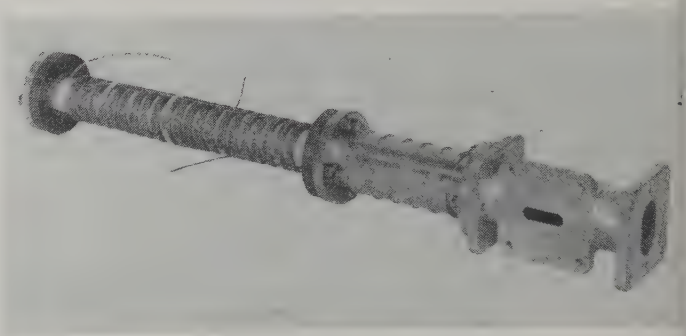

Fig. 5—Transmission-type thruplexer serrodyne.

current sawtooth generator to produce the required sawtooth of phase shift in a microwave transmission line. The phase shift is accomplished by varying the phase propagation constant of a ferrite loaded waveguide under the influence of the changing magnetic field. Several microwave configurations are possible, permitting the translated signal to be either transmitted through the device or reflected back along the line supplying the incident carrier. One such transmission device consists of a thruplexer,[4] quarter-wave plate, ferrite line section, and a shorting plate.[5] (See Fig. 2 and Fig. 5.) A linearly polarized carrier signal enters the thruplexer and in passing through the quarter-wave plate is converted to a circularly polarized wave. It then travels down and back through the ferrite phase shifter where it experiences the sawtooth phase modulation. After traversing the circular polarizer again, the emerging microwave signal is converted back to linear polarization in a plane perpendicular to the incident carrier and, therefore, leaves the thruplexer by its side port. This constitutes a transmission serrodyne. The magnetic modulating field is applied to the ferrite so that the sense of the circularly polarized wave in the ferrite and that of the current producing it is always the same, *i.e.*, the wave propagates with the same β ($\beta+$ as defined by Hogan[6]) during the round trip through the phase shifter. This insures maximum phase sensitivity for a given applied magnetic field permitting a minimum amplitude for the driving current sawtooth.

A reflection serrodyne is easily obtained from this transmission unit by inserting a 45-degree ferrite rotator between the thruplexer and the quarter-wave plate. (See Fig. 3.) The carrier is rotated 45 degrees before reaching the quarter-wave plate. After emerging from the quarter-wave plate in the return direction polarized perpendicular to the incident carrier, the translated signal is again rotated 45 degrees in the same direction as before and leaves coplanar with the carrier, thus producing a reflection serrodyne.

A different microwave configuration also is suitable for service as a serrodyne. It consists of a turnstile junction that has the ferrite line section attached to the round arm and two short circuits set in the side arms.[7] (See Fig. 4.) If the differential path length of the two shorted arms is $\lambda g/4$, and the length of one arm is an odd number of eighth wavelengths, then a signal entering at the input of the turnstile is transmitted up the round arm circularly polarized. After traversing the ferrite line section and experiencing the sawtooth modulation, the translated signal is converted back to linear polarization and passes to the output of the turnstile. Here again, we have a transmission-type serrodyne. This unit may be more compact than the thruplexer quarter-wave plate design, but it is inherently a more narrow band circular polarizer than an inductive-capacitive iris-type quarter-wave plate. (See Fig. 5.)

[4] Orthogonal mode transducer.

[5] H. Scharfman, "Three new ferrite phase shifters," PROC. IRE, vol. 44, pp. 1456–1459; October, 1956.

[6] C. L. Hogan, "The ferromagnetic Faraday effect at microwave frequencies and its applications," *Bell Sys. Tech. J.*, vol. 31, pp. 1–31; January, 1952.

[7] M. A. Meyer and H. B. Goldberg, "Application of turnstile junctions," IRE TRANS. ON MICROWAVE THEORY AND TECHNIQUES, vol. MTT-3, pp. 40–44; December, 1955.

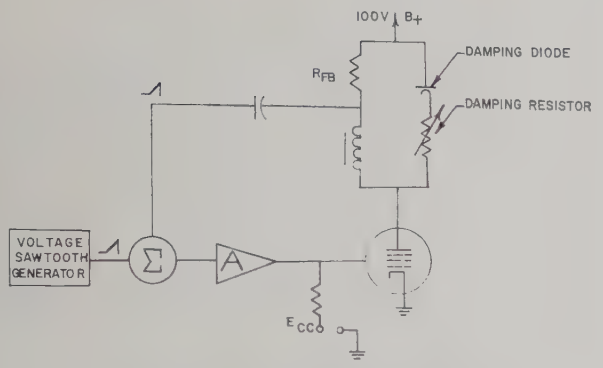

Fig. 6—Schematic diagram of modulator.

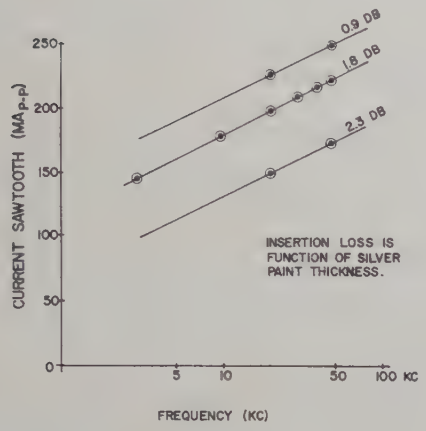

Fig. 7—Driving current vs frequency for various silver paint thicknesses (measured by insertion loss of serrodyne).

Construction Details

The ferrite phase shift section used here consists of six inches of *R*-1 ferrite 0.240 inch in diameter inserted concentrically in a 0.625-inch-diameter rexolite rod with brass flanges attached to its ends. The rexolite is lightly silver painted to form a thin walled waveguide with negligible shorted turn effect to the modulating coil outside.

This modulating coil, multiple-pie wound for low distributed capacity, has 1050 turns over 5 inches and is so connected as to have an inductance of 2.5 mh. Low inductance and stray capacity for a given number of ampere turns are important in securing rapid flyback, a crucial parameter for good serrodyne performance, since the flyback interval is one half the self-resonant period of the coil. A dc coil to compensate a direct current component in the modulating signal is used to set the magnetic operating level in a region of linear phase shift; it is wound on a $1\frac{3}{4}$-inch phenolic tube and slipped over the rest of the phase shifter. A rexolite button matches the ferrite line to 0.875-inch round waveguide with a VSWR under 1.2 across a $2\frac{1}{2}$ per cent band at *X* band.

The sawtooth current generator used here is variable in both frequency and amplitude from 500 cps to 50 kc and from zero to 400 milliamperes peak to peak. It consists of a high perveance driver driving the diode damped modulator coil. The current sawtooth is generated through a current feedback loop controlled by a variable voltage sawtooth generator. (See Fig. 6.) Sawtooth drive current required increases linearly from 145 ma pp at 3000 cps to 225 ma pp at 50 kc. (See Fig. 7.) Total modulator power consumption is 60 watts plus tube heater power.

A useful drive power index is the driver tube plate dissipation, here about 25 watts. However, acceptance of some performance degradation permits circuit simplification requiring less than 5 watts of drive power. A current sawtooth may be generated by merely impressing a large voltage spike across the coil and allowing it to integrate its own current sawtooth.

Performance

For measuring the serrodyne performance, two quantities have been examined. The first is a video waveform obtained from a crystal detector by mixing some of the translated output signal with some of the incoming carrier. (See Fig. 8.) The second is the output spectrum of the translated signal. The video waveform provides an indication of the fractional flyback time and of any distortions that may be present in the sawtooth of phase shift. Correlation of this waveform with the driving current sawtooth indicates that the phase shifter is a very linear device, and that whatever distortion may be present is due primarily to a nonlinear current sawtooth. [See Fig. 9(a) for a sketch of a typical trace.] An adjustable phase shifter is included in the detector circuit so that the flyback perturbation may be moved along the video waveform and the entire wave shape examined for distortion.

The output spectrum contains the following components. First, the translated output signal that is displaced by the modulation frequency either above or below the carrier depending on the sign of the phase shift sawtooth. This signal, designated as the desired sideband (or merely as the sideband), is used as the reference power level for measuring the relative power levels of the other spectral components. Some carrier is present also. The first spectral element on the other side of the carrier has been designated the image sideband, and additional sidebands on this same side of the carrier are called higher order sidebands. The amplitude of these depends primarily on the fractional flyback time. The maximum amplitude of this group of sidebands is displaced considerably from the carrier. [See Fig. 9(b).] Higher sidebands on the same side of the carrier as the desired sideband are called higher harmonic sidebands, *e.g.*, second harmonic and third harmonic sidebands. These are influenced principally by sawtooth waveform distortion, by incorrect sawtooth amplitude, *i.e.*, phase shift per sweep $\neq 360$ degrees, and by an amplitude modulation of the residual carrier or of the sideband it-

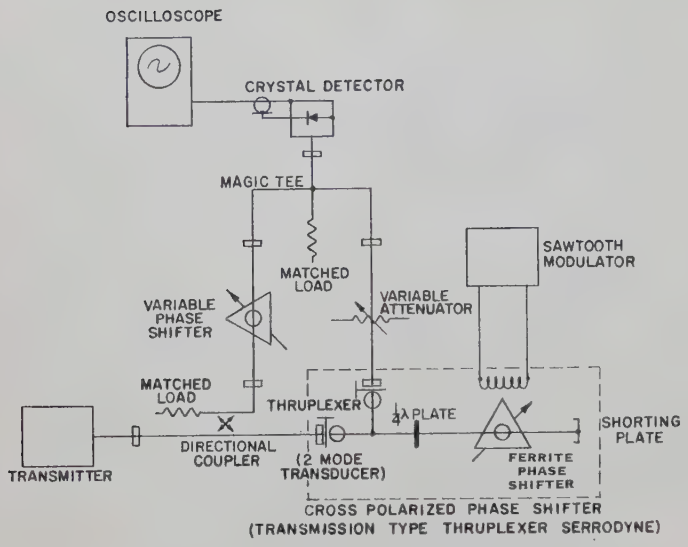

Fig. 8—Ferrite serrodyne measurement diagram.

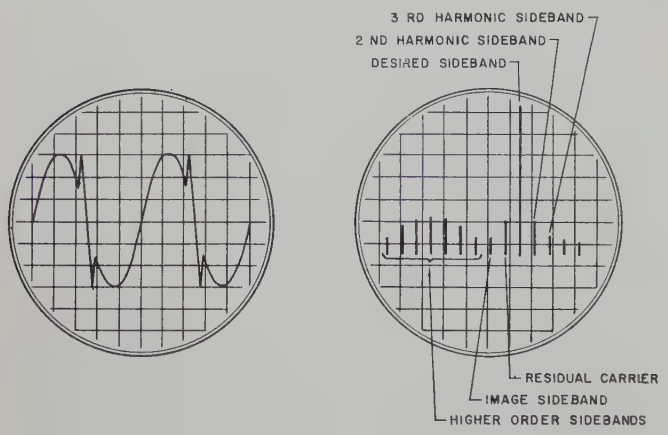

Fig. 9—(a) Oscillogram of typical detected video waveform. (b) Oscillogram of typical microwave spectrum.

self present due to imperfection in the circular polarizer. The sawtooth amplitude is a critical operating parameter. It may be set by optimizing the output spectrum, or in the case where the available spectrum analyzer has insufficient resolution, by adjusting the video wave form to have equally spaced maxima and minima. The preceding designations for the various spectral components are quite arbitrary, but necessary since the spectrum is reversible about the carrier depending upon the sense of the sawtooth drive.

Performance criteria are conversion loss and suppression of undesired spectral elements relative to the desired translated frequency component. Conversion loss is due primarily to the phase shifter insertion loss—between 1 and 2 db for different units (see Fig. 7). Translation loss, due to the energy content of the rest of the spectrum consequent upon the serrodyne modulation, never exceeded 0.5 db; this agrees with theoretical prediction. Conversion loss $= 20 \log (1 - F)$ where F is the fractional flyback time. Suppression of spurious sidebands depends strongly on the optimum amplitude of the modulation sawtooth for given modulation and microwave frequencies, and also on the sawtooth retrace interval. For typical results obtained with a transmission-type serrodyne using a thruplexer and quarter-wave plate see Table I. In spite of low carrier rejection resulting from a circular polarizer with 1 db of ellipticity, the unwanted sideband suppression achieved agrees very well with the comparable theoretical values given by Cumming.

Somewhat better performance was obtained using a turnstile junction to replace the thruplexer and circular polarizer as shown in Table II. Although the ellipticity was 0.3 db, the carrier suppression was limited by the input to output isolation of the turnstile which was only 24 db.

Performance Limitations

The ferrite serrodyne limitations arise from the minimum attainable flyback time consistent with allowable driver plate dissipation from the modulation standpoint. On the microwave side, maximum thruplexer isolation, minimum circular polarizer ellipticity, and maximum phase shift sensitivity must be kept consistent with allowable size. A 2-microsecond flyback was attainable with 25 watts of driver plate dissipation with the structure described. A flyback time of the order of 0.5 μsec with 100 watts of driver plate dissipation appears possible. This would make operation up to 100-kc frequency translation feasible with a 5 per cent flyback and, correspondingly, about 25 db suppression of unwanted sidebands. Thruplexers are readily made with isolation greater than 50 db but ellipticity of the circular polarizer and the match looking from the polarizer into the ferrite phase shift section limits the carrier rejection. Taking 30 db as an acceptable carrier rejection, the polarizer must have less than 0.4-db ellipticity and the VSWR from polarizer into ferrite section must be less than 1.05. At X band the resulting thruplexer, polarizer, and ferrite phase shifter would be about 15 inches long.

The microwave bandwidth of such a device is largely limited by match and ellipticity considerations of the circular polarizer. The 15-inch structure indicated above could probably give greater than 20-db carrier rejection over about a 10 per cent band at X band. Adjustments of dc bias and ac drive would be required to get greater than 20-db carrier and sideband rejections at 100-watt drive at 100-kc translation frequency across the 10 per cent band. Conversion efficiency including microwave losses should be about 2 db.

Comparison with Other Methods of Single-Sideband Generation

Other types of single-sideband generators use transit

TABLE I

PERFORMANCE FOR THRUPLEXER SERRODYNE

Modulation Frequency kc	Current Sawtooth ma pp	Second Harmonic Suppression db	Carrier Suppression db	Image Sideband Suppression db	High-Order Sideband Suppression db	Flyback Time μsec	Fractional Flyback Time F	Cummings' Theoretical Suppression
3	140							
10	180	33	33	>35	33	2.0	0.02	34
20	195	28	28	33	26	2.2	0.044	27
30	216	24	20	>30	23	2.0	0.06	24.5
40	220	—	25	25	22	2.0	0.08	22
50	225	21.5	21.5	28	20.6	2.0	0.1	20

TABLE II

PERFORMANCE FOR TURNSTILE SERRODYNE

Modulation Frequency kc	Current Sawtooth ma pp	Second Harmonic Suppression db	Carrier Suppression db	Image Sideband Suppression db	High-Order Sideband Suppression db	Flyback Time μsec	Fractional Flyback Time F	Cummings' Theoretical Suppression
20	200	21	20	31	31	2.2	0.044	27
30	216	27	21	33	27	2.0	0.06	24.5

time modulation of TWT and klystron characteristics as well as pairs of balanced modulators (ferrite and/or crystal) in complex microwave bridge circuits. In general, their operation and performance characteristics are not readily comparable with the ferrite serrodyne. The ferrite serrodyne is most directly comparable with the continuously rotating half-wave plate using ferrite first described by Cacheris.[8] Performance characteristics in terms of conversion loss, carrier rejections, and sideband rejection are similar. The ferrite serrodyne does appear to be somewhat smaller, lighter, less complex, and requires less driving power.

[8] J. C. Cacheris, "Microwave single-sideband modulator using ferrites," PROC. IRE, vol. 42, pp. 1242–1247; August, 1954.

CONCLUSIONS

A ferrite single-sideband generator or frequency translator has been discussed. Its theory of operation, construction details, design parameters, and performance characteristics have been reviewed. Satisfactory operation up to 50 kc of frequency translation has been reported with good correlation to theoretical treatment. Operation up to 100 kc of translation over 10 per cent of X band with 20 db of carrier and sideband rejection and conversion loss under 2 db seems feasible.

ACKNOWLEDGMENT

It is a pleasure to acknowledge the assistance of Dr. Peter Rizzi, who contributed many ideas and suggestions during the course of this work.

Broad-Band Ferrite Rotators Using Quadruply-Ridged Circular Waveguide*

H. N. CHAIT† AND N. G. SAKIOTIS†

Summary—It has been shown that the rotation of the plane of polarization of a wave propagating in a magnetized unbounded ferrite medium should be independent of frequency. However this is not the case when a ferrite rod of small diameter is placed within a waveguide. For example, if a ferrite rod one-quarter inch in diameter in a fifteen-sixteenth inch diameter circular waveguide is used, the rotation will change by a factor of four to one over the frequency band from 8000 to 10,000 mc. This variation in rotation is substantially due to the waveguide characteristics, and can be minimized by lowering the cutoff frequency of the waveguide.

Various methods of lowering the cutoff of circular waveguide are compared. Data on the broadbanding of the rotation by dielectric loading and also by the use of quadruply-ridged circular waveguide is shown. An experimental study showing the effect of the ridge width and height on the cutoff of the circular waveguide and the frequency dependence of the rotation is discussed.

FERRITE rotators have found wide application in a number of microwave devices. They are used as isolators, phase shifters, switches, modulators, duplexers, etc. In most of these applications it is highly desirable that the rotation be constant over the operating bandwidth of the device. This paper describes some of the propagation studies carried on to determine the dependence of the rotation on various parameters of the waveguide configuration.

The infinite medium theory predicted that the rotation of the plane of polarization of an electromagnetic wave passing through a magnetized ferromagnetic medium should depend on the path length through the medium, the dielectric constant, the permeability, and the magnetization of the medium. It is also predicted that the rotation would be independent of the frequency.[1]

During the early phases of ferrite research it was thought that this infinite medium theory would apply in the case of guided wave propagation. In the center of a circular waveguide there are only transverse components of E and H, and the wave is similar to that of the infinite medium. However, it was found experimentally that rotation increased with frequency.[2]

A number of methods have been used to obtain a rotation constant with frequency. For example, two oppositely magnetized rods of different diameters or different ferrite materials can be selected so that the difference in rotation (*i.e.*, the net rotation) remains more nearly constant with frequency. It is also possible to use a rod whose rotation increases with frequency in combination with a rod whose rotation decreases (negatively) with frequency. Both these methods have the disadvantage of higher loss, since an extra ferrite rod is required and both use larger magnets.

A theoretical analysis of the propagation characteristics of the partially filled circular waveguide is very difficult and no exact numerical solution of the problem is available. However a perturbation theory for rods of small diameter has been derived by a number of workers.[3] The rotation per unit length,

$$\frac{\theta}{L} = 0.22\gamma 4\pi M \left(\frac{r_1}{r_0}\right)^2 \sqrt{1-\left(\frac{f_c}{f}\right)^2} \cdot \left[\frac{1}{1-\gamma^2\left(\frac{H+2\pi M}{b}\right)^2}\right]. \quad (1)$$

γ = gyromagnetic ratio (2.8 megacycles per orested)
M = Magnetization
r_1 = radius of ferrite rod
r_0 = radius of waveguide
f_c = cutoff frequency of the waveguide
f = operating frequency
H = applied magnetic field.

This equation shows that the rotation does indeed depend on the frequency, since the frequency appears in two terms of the equation. The frequency dependence of the rotation is determined, first, by how close the operating frequency is to the cutoff frequency of the waveguide, and, second, by how the ferrite characteristics change with frequency. It is evident that the rotation can be made more constant by lowering the cutoff frequency of the waveguide in relation to the operating frequency. This equation was used to calculate the change in rotation with frequency for waveguides which cut off at 6000 and 7500 mc. Fig. 1 shows the results of this calculation. If, for example, one needed a rotator which could be used from 8000 to 10,000 mc and the waveguide cut off at 7500 mc, the rotation would change from 0.48 to 0.805 or 1.68 to 1. On the other hand, if a waveguide that cut off at 6000 mc was used, the rotation would change from 0.91 to 0.97 or 1.065 to 1, a rather substantial improvement. In addition, the rota-

* Manuscript received by the PGMTT, June 9, 1958; revised manuscript received, August 11, 1958.

† Microwave Antennas and Components Branch, Electronics Div., U. S. Naval Res. Lab., Washington 25, D. C.

[1] C. L. Hogan, "The ferromagnetic Faraday effect at microwave frequencies and its applications—the microwave gyrator," *Bell Sys. Tech. J.*, vol. 31, pp. 22–26; January, 1952.

[2] N. G. Sakiotis and H. N. Chait, "Ferrites at microwaves," PROC. IRE, vol. 41, pp. 87–93; January, 1953.

[3] A. A. Th. M. Van Trier, "Guided electromagnetic waves in anisotropic media," *Appl. Sci. Res. Bulletin*, vol. 3, pp. 305–371; 1953.

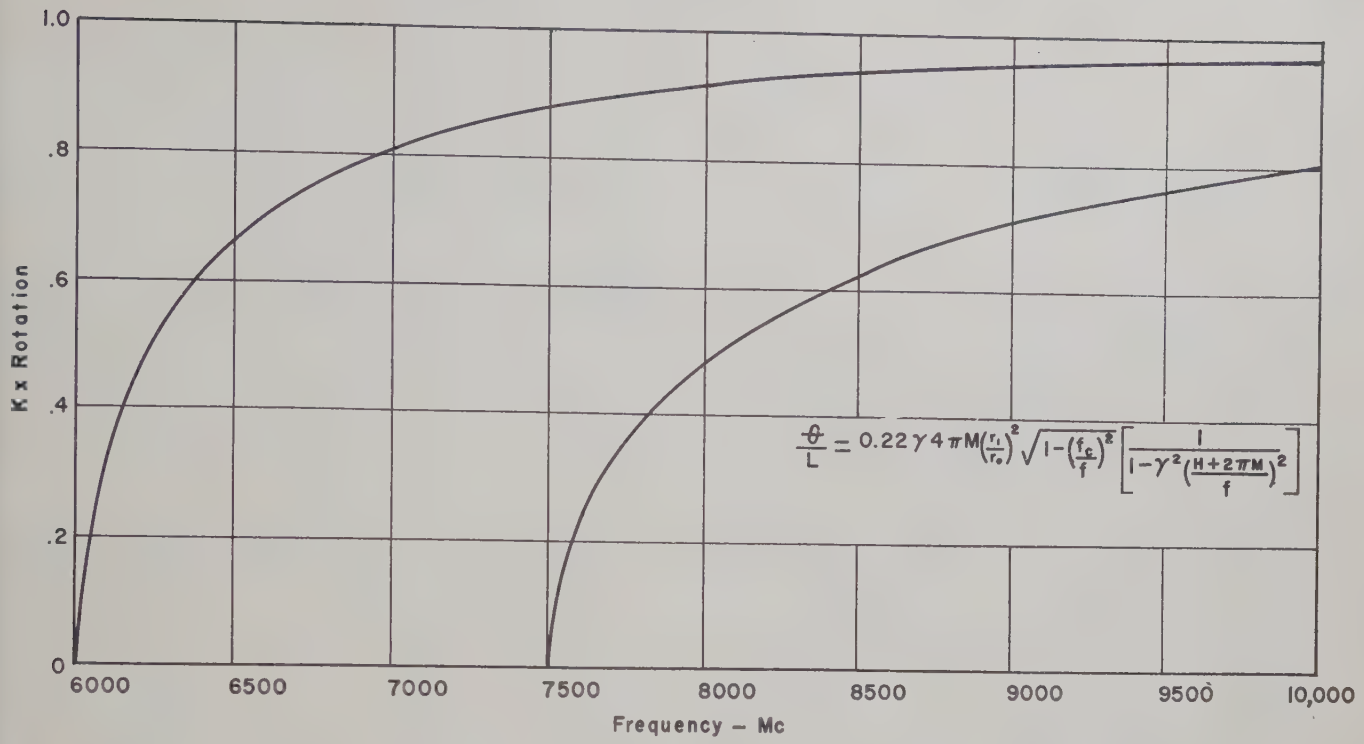

Fig. 1—Rotation vs frequency curves for cutoff frequencies of 6000 and 7500 megacycles.

TABLE I

WAVEGUIDE 15/16 INCH DIAMETER ($\lambda_c' = \sqrt{\epsilon}\,\lambda_c$)

ϵ	1	2.1	5	10
λ_c	4.06 cm	5.89 cm	9.07 cm	12.86 cm
f_c	7400 mc	5100 mc	3310 mc	2340 mc
$R = \frac{\text{ROT.@9800 mc}}{\text{ROT.@7400 mc}}$	$\frac{95}{20} = 4.75$	$\frac{165}{60} = 2.75$	$\frac{140}{75} = 1.87$	$\frac{110}{50} = 2.2$

tion per unit length would be increased from 0.48 to 0.91 at 8000 mc, and from 0.805 to 0.97 at 10,000 mc.

The first method of lowering the cutoff was to fill the waveguide with dielectric material. Although the rotation became more nearly constant, by about 2.5 to 1, the magnitude of the rotation did not seem to increase as predicted by the perturbation formula. Row R of Table I shows a summary of some of the data, the best being $\epsilon = 5$. However it is possible that better results could be obtained by using a dielectric constant between $\epsilon = 2.1$ and $\epsilon = 5$. Ripples on the curves for $\epsilon = 5$ and 10 indicated trouble from higher modes which could propagate in the dielectric loaded waveguide. Therefore, it was thought that this performance could be improved still further by utilizing a waveguide which had a lower cutoff for the dominant mode but did not substantially reduce the cutoff for the next higher mode. This can be accomplished by the use of ridged guide.[4] On the other hand, in the case of the dielectric-filled guide, all of the cutoffs have been lowered by the same percentage.

Even though the perturbation formula for the rotation was not derived for the case of the ridged guide, it was hoped that qualitatively the results might still apply. This turned out to be the case.

In order for the waveguide to support a circularly polarized mode, the waveguide configuration should present the same appearance to two orthogonal linearly polarized modes. For this reason, a structure utilizing two sets of orthogonal ridges was chosen. Data on ridges in circular waveguide was available only for the case of a pair of ridges. It was therefore necessary that a program of measurement of the cutoff of quadruply-ridged circular waveguide be undertaken. A number of sections of ridged waveguide were built having the dimensions shown in Table II.

The guide wavelength of these sections was measured at a few frequencies and then the cutoff was calculated from the formula

$$\lambda_g = \frac{\lambda}{\sqrt{1 - \left(\frac{\lambda}{\lambda_c}\right)^2}}. \qquad (2)$$

λ = operating wavelength
λ_g = guide wavelength
λ_c = cutoff wavelength.

[4] M. L. Kales and H. N. Chait, "Ridged Waveguide Rotator," Naval Res. Lab. Progress Rep.; August, 1954.

TABLE II

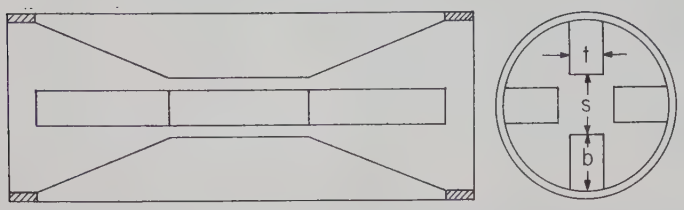

t	b	s	b	s	b	s	b	s
1/16	7/32	1/2	9/32	3/8	5/16	5/16	11/32	1/4
1/8	7/32	1/2	9/32	3/8	5/16	5/16	11/32	1/4
3/16	7/32	1/2	9/32	3/8	5/16	5/16	11/32	1/4

Waveguide diameter = 15/16.

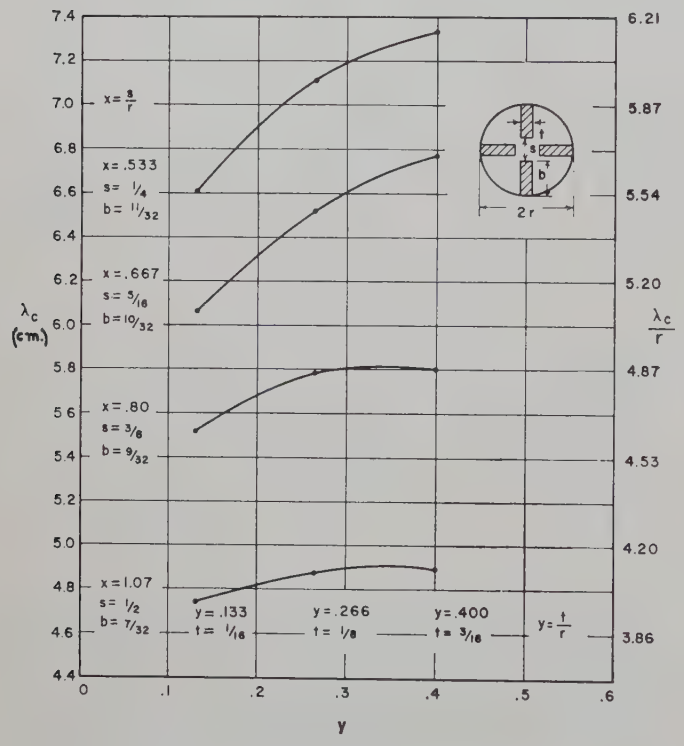

Fig. 2—The dependence of the cutoff wavelength on the dimensions of the ridged waveguide.

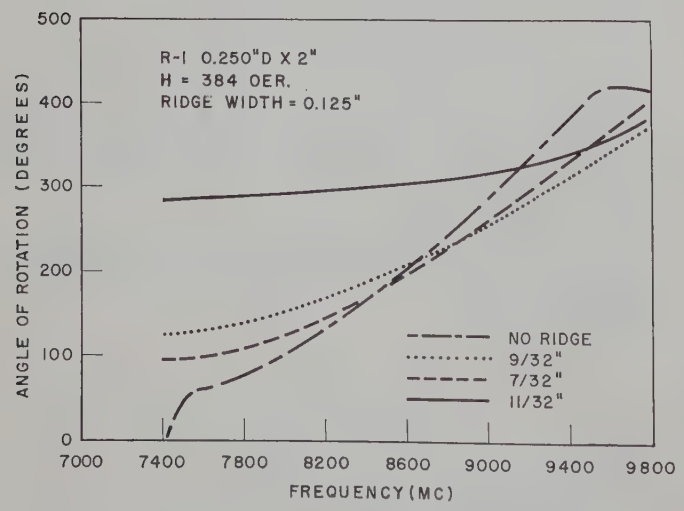

Fig. 3—Rotation vs frequency for quadruply-ridged waveguide containing a ferrite rod.

The results are plotted on Fig. 2. As shown, the cutoff wavelength of the guide can be lowered from 4.06 cm (7390 mc) to 7.3 cm (4110 mc) by the choice of the proper ridges.

The rotation vs frequency at different applied fields was measured for each of the ridged sections containing ferrite rods. Fig. 3 shows a typical set of curves.

Data was taken on samples of R-1, 0.250, 0.225, and 0.200 inch in diameter as well as Trans Tech 390, 0.253 OD by 0.125 ID in each of the ridged sections. Table III shows some of the results of ridges $\frac{1}{8}$ inch thick.

TABLE III

$H = 384$ oer

	Ridge width	Ridge depth	$R = \frac{\text{Rotation at 9800 mc}}{\text{Rotation at 7400 mc}}$
R-1 0.250 D×2 inch	0	0	$\frac{425}{50} = 8.5$
	1/8	7/32	$\frac{400}{100} = 4.0$
	1/8	9/32	$\frac{365}{130} = 2.81$
	1/8	11/32	$\frac{385}{280} = 1.38$
R-1 0.225 D×2 inch	0	0	$\frac{270}{25} = 10.8$
	1/8	7/32	$\frac{245}{75} = 3.3$
	1/8	9/32	$\frac{240}{95} = 2.5$
	1/8	11/32	$\frac{275}{215} = 1.28$
R-1 0.200 D×2 inch	0	0	$\frac{95}{20} = 4.75$
	1/8	7/32	$\frac{105}{35} = 3.0$
	1/8	9/32	$\frac{120}{55} = 2.18$
	1/8	11/32	$\frac{165}{115} = 1.44$
TT 390 0.253 OD×0.125 ID×2 inch	0	0	$\frac{125}{5} = 25$
	1/8	7/32	$\frac{100}{50} = 2$
	1/8	9/32	$\frac{100}{70} = 1.43$
	1/8	10/32	$\frac{105}{85} = 1.24$
	1/8	11/32	$\frac{100}{90} = 1.11$

It is evident from this data that lowering the cutoff of the waveguide by the use of ridges does indeed produce the two changes predicted by the perturbation equation, even though the ferrite rods used were not small. Substantial improvement in the constancy of the rotation and the rotation per unit length are obtained.

A logical conclusion would be to combine the ridges and the dielectric loading. A section of guide was built using the $\frac{1}{8}$ inch $\times\frac{7}{32}$ inch ridges surrounded with poly ($\epsilon = 2.56$). Whereas the ridges alone gave a 2 to 1 variation in rotation, the combination was 1.6 to 1, with, however, a reduction in the rotation per unit length.

The losses of the various combinations studied were so low that they could not be measured with sufficient accuracy to determine a merit figure.

Fig. 4 shows the results obtained on the broadbanding of a 90 degree rotator from 8000 to 9600 mc. A cylinder of TT-390, 0.253 OD $\times$ 0.125 ID $\times$ 2 inch long was used in the $\frac{1}{8}$ inch $\times\frac{11}{32}$ inch ridged waveguide. The rotation is constant within 2 per cent over the entire frequency range.

The propagation studies have shown that the perturbation theory is qualitatively applicable even in cases where the perturbation may be quite large. The results indicate that the quadruply loaded ridged circular waveguide with or without dielectric loading offers a very good transmission path for broadband rotation devices used in low peak power or in CW applications.

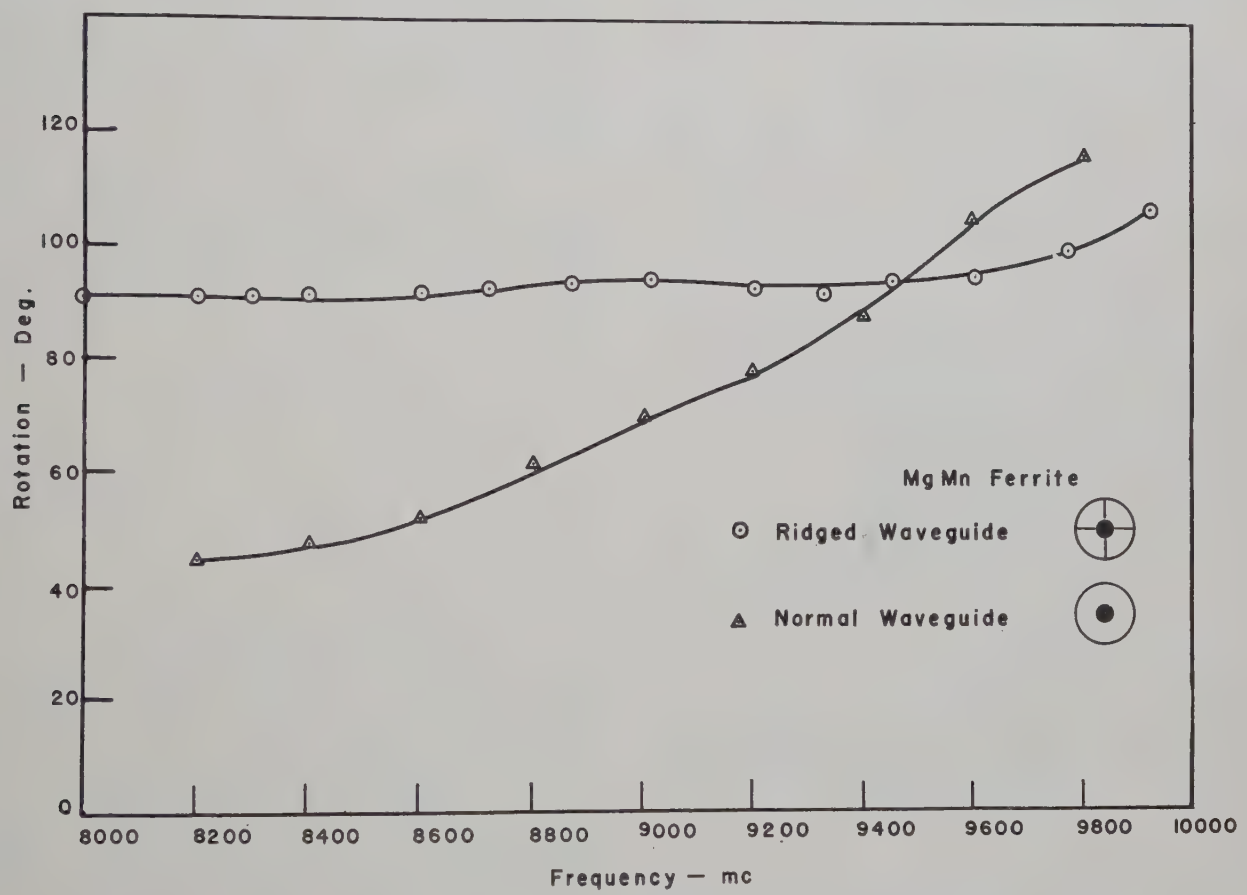

Fig. 4—Rotation vs frequency of a 90-degree rotator with and without ridges.

Present State of the Millimeter Wave Generation and Technique Art—1958*

P. D. COLEMAN† AND R. C. BECKER†

Summary—**Two of the few fruitful approaches to the low millimeter and submillimeter wave generation problem appear to be frequency multiplication by means of nonlinear phenomena and frequency conversion by parametric systems. Current work on frequency multiplication using relativistic megavolt beams, crystal diodes, field emitters, ferrites, etc., is reviewed. A brief account of present efforts to extend conventional tubes below wavelengths of 3 mm is presented. Waveguide components used at 1 to 2 mm are described.**

Introduction

IN SPITE of the fact that Nichols and Tear[1] succeeded in closing the gap between infrared and electric waves in 1923 using the radiation from high-pressure quartz mercury lamps, the generation of electromagnetic radiation in the wavelength range from roughly 0.1 to 3 mm remains today an unsolved practical problem. Moreover, even an idea that might lead to a prime, self-excited source of radiation has yet to be suggested as far as the authors are aware. It is somewhat annoying that of the enormous range (greater than 18 orders of magnitude) of the electromagnetic spectrum, only a small range of frequencies in the submillimeter range cannot be generated.

Most of the effort to push into this frontier region has come from the microwave side of the spectrum since microwave electronic sources are coherent generators of smooth sinusoidal signals as opposed to incoherent, continuous spectrum infrared sources. However, this progress, frequency-wise, has been rather slow.[2–7]

In 1936, Cleeton and Williams[8] achieved a wavelength of 6 mm using a magnetron. In the last 22 years, magnetrons have only been extended by a factor of two to a wavelength of 2.6 mm by a group at Columbia University.[9] The lowest wavelength commercial magnetron operates around 4.3 mm.

By 1946, Lafferty[10] had achieved a wavelength of 4.15 mm with a reflex klystron tube. Twelve years later, the highest frequency klystron available is the DX151 which operates between 4.0 and 4.5 mm wavelength.

In 1951, Millman[11] was able to build a traveling-wave tube amplifier for 6-mm wavelength. More recently, in 1957, Karp[12] produced a wavelength of 1.5 mm by means of a ladder structure backward-wave oscillator.

The preceding historical facts indicate that, frequency-wise, microwave tubes have been extended by a factor of less than five in the last two decades.

All electron tubes utilize the same basic interaction between an electron and an electromagnetic field, namely, the force equation

$$\frac{dm\bar{v}}{dt} = q\bar{E} + q(\bar{v} \times \bar{B}). \tag{1}$$

If the dot product of the velocity $\bar{v}$ on both sides of (1) is performed, then

$$\frac{dmc^2}{dt} = \frac{d\xi}{dt} = q(\bar{v} \cdot \bar{E}) = \mathcal{P} \tag{2}$$

which states that the power $\mathcal{P}$ flowing into the electromagnetic field is equal to the time rate of change of the kinetic energy ξ of the charge q, where v is the electron velocity, c is the speed of light, and $\bar{E}$ is the electric field intensity. To achieve coherence, the electron beam must be bunched or converted into an ac beam.

The problem of producing a bunched beam to interact with an RF field has been achieved in many different ways in such tubes as magnetrons, klystrons, TWT, BWO, retarding field tubes, crossed field tubes, carcinotrons, etc. However, no matter how the interaction is achieved, all these tubes encounter essentially the same fundamental problems[2] as they are pushed into the low millimeter wave region. It is always possible, but highly improbable, that a radically new method of realizing the interaction will be discovered that would permit

* Manuscript received by the PGMTT, May 6, 1958; revised manuscript received, June 26, 1958. This paper has been prepared with the support of the AEC under contract AT(11-1)-392 and AFOSR under contract AF18(603)-62.

† Elec. Eng. Res. Lab., University of Illinois, Urbana, Ill.

[1] E. J. Nichols and J. D. Tear, "Joining the infrared and electric wave spectra," *Astrophys. J.*, vol. 61, pp. 17–37; 1925.

[2] J. R. Pierce, "Millimeter waves," *Phys. Today*, vol. 3, pp. 24–29; November, 1950.

[3] W. E. Willshaw, *et al.*, "Experimental equipment and techniques for the study of millimeter wave propagation," *Proc. IEE*, vol. 102, pt. B, pp. 99–111; January, 1955.

[4] R. Q. Twiss, "On the generation of millimeter radiation," *Services Electronics Res. Lab. J.*, vol. 2, p. 10, 1952.

[5] D. D. King, "Report of advances in microwave theory and techniques—1956," IRE TRANS. ON MICROWAVE THEORY AND TECHNIQUES, vol. MTT-4, pp. 68–74; April, 1956.

[6] S. W. Rubin, "Millimeter waves," *Polytechnic Research and Development Co. Reps.*, vol. 4; October, 1955.

[7] R. S. Ohl, "Millimeter Wave Research," Bell Telephone Labs., Inc., New York, N. Y., Rep. No. 24261–15; October, 1955.

[8] E. E. Cleeton and N. H. Williams, "The shortest continuous radio waves," *Phys. Rev.*, vol. 50, p. 1091; 1936.

[9] Quarterly Reps., Rad. Lab., Physics Dept., Columbia University, New York, N. Y.; Contract DA-36-039 SC-64630, September, 1957.

[10] J. M. Lafferty, "Millimeter-wave reflex oscillator," *J. Appl. Phys.*, vol. 17, pp. 1061–1066; December, 1946.

[11] S. Millman, "A spatial harmonic traveling-wave amplifier for six millimeter wavelength," PROC. IRE, vol. 39, pp. 1035–1043; September, 1951.

[12] A. Karp, "Backward-wave oscillator experiments at 100 to 200 kilomegacycles," PROC. IRE, vol. 45, pp. 496–503; April, 1957.

circumventing existing tube problems.

For reasons such as those just indicated, many people now feel that conventional electron tubes have reached their practical limit somewhere around 2 to 3-mm wavelength and that in order to push on further into the submillimeter range an entirely new set of techniques will be required.

In the past several years many of the workers who have been in millimeter wave research, and especially the newer workers, are turning their attention to solid-state electronics. While the recent work on masers, ferrite multipliers, parametric oscillators, etc., has not as yet produced electromagnetic radiation of wavelengths which are not already obtainable by electron tubes, there seems to be a note of optimism that a breakthrough will come. It should be pointed out that electron tubes are an important part of the work on these solid-state devices since these devices, at present, convert energy at one RF frequency into energy at another RF frequency, thereby requiring an RF source of energy.

In this paper, an effort will be made to present, by a limited number of specific examples, some of the representative work currently in progress in the millimeter region, to point out the problems these endeavors are encountering, and to indicate the directions that research is taking either to solve the present problems or to discover new principles to circumvent the old problems.

Limitations of Conventional Electron Tubes

In a survey article in 1950, Pierce[2] discussed four fundamental problems that plague conventional tubes operating in the low millimeter range: 1) physical size and tolerance, 2) heat dissipation, 3) circuit losses, and 4) cathode and starting current densities.

The resonant element or tube structure has its cross-sectional area comparable to a half wavelength in physical size if it operates in the dominant mode. Hence, constructability in the small dimensions becomes the sole practical criterion in choosing circuit structures. In slow-wave structures, tolerance problems in maintaining periodicity are important. Reflections on the slow-wave structure result in constructive and destructive interference between the wave components, thereby causing the output power to have appreciable "fine structure" as the frequency is swept.

Circuit losses increase with frequency, thus lowering the efficiency of the tube. In order to maintain the output power constant, greater input power is necessary to compensate for the losses, with the result that more heat is dissipated in the structure. However, with the tube structure shrinking in size as the design frequency is increased, dissipation of the heat by conduction and radiation is a major problem.

In reflex klystrons, the starting current density is proportional to the five-halves power of the frequency. In backward-wave oscillators, such as those described by Karp,[12] the longitudinal electric field component E_z falls off exponentially away from the circuit, decaying to a negligible value in a distance small compared to the thickness of the beam. Thus the beam current has physical significance only when expressed as density and when considered as having a "skin effect." These current density problems place difficult requirements on cathode emission.

Fig. 1(a) shows a drawing of a reflex klystron made by Lafferty[10] in 1946. One of his tubes achieved a wavelength of 4.15 mm, a value exceeded today only by the Amperex DX151 klystron which operates in the range of 70 to 75 kmc. Lafferty comments in his paper that it is doubtful if oscillations of wavelengths appreciably shorter than 4 mm can be obtained by the velocity modulation reflex principle until new cathodes are developed with considerably higher emission current density, or some radically new gun design is invented for producing electron beams of extremely high current densities.

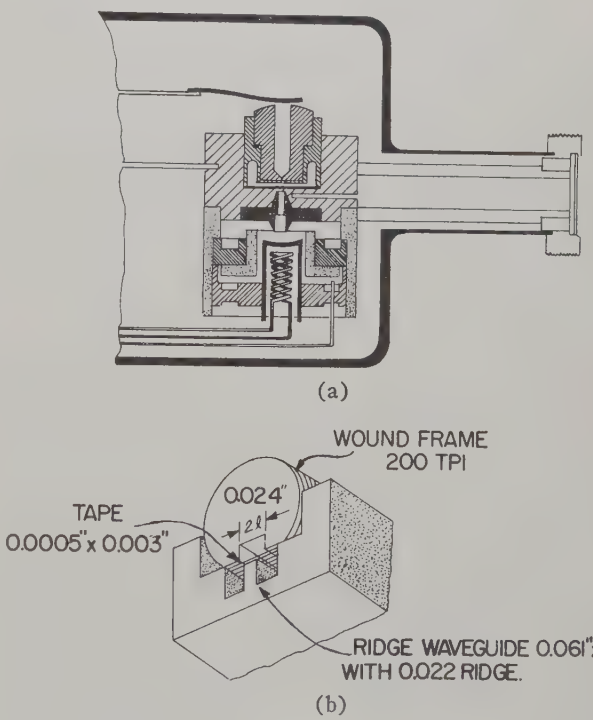

Fig. 1—Millimeter wave tubes. (a) Lafferty (1946) reflex klystron 4.15–5.80 mm. (b) Karp (1957) ladder structure 1.5–1.7 mm.

Fig. 1(b) is a schematic drawing of the "ladder structure" BWO as described by Karp.[12] This tube has produced oscillations as low as 1.5 mm, the shortest wavelength produced thus far with an electronic self-excited oscillator. Karp comments that the circuit parameter of almost overwhelming importance is the circuit "cold" loss and that recognition of the dominating influence of the loss should govern future work. Reduction of the loss is a very urgent need in trying to reach still shorter wavelengths.

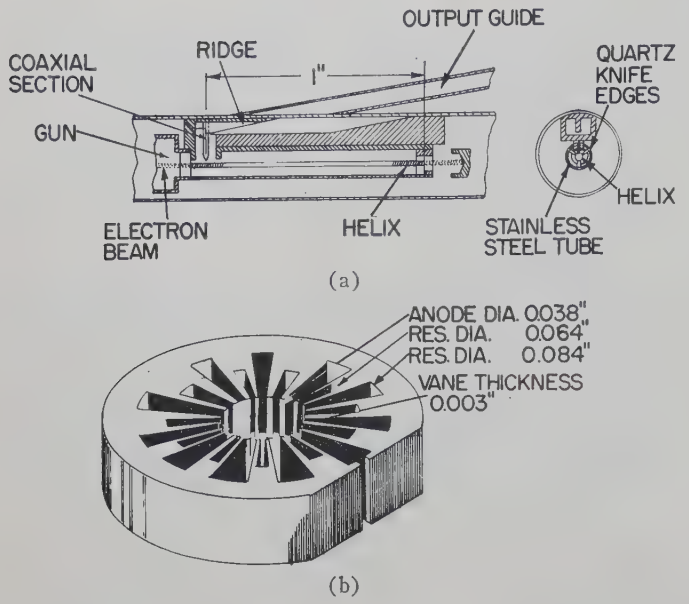

Fig. 2—Millimeter wave tubes. (a) Christensen-Watkins helix BWO tube (1955) 4.5–6.0 mm. (b) Bernstein-Kroll Columbia magnetron (1954) 2.6 mm.

Fig. 2(a) illustrates a helix millimeter-wave tube described by Christensen and Watkins.[13] This tube operates in the range 4.5 to 6.0-mm wavelength. They comment that the CW power output of their present design is limited by helix dissipation (the helix temperature is 1300°C). They calculate that increased circuit loss plus reduction in beam current due to the decrease in cross section would place a lower limit on the wavelength of 2.4 mm using the current density and beam voltage employed in their tube.

Fig. 2(b) shows a rising-sun type magnetron structure which Bernstein and Kroll[14] have pushed to a wavelength of 2.6 mm. These tubes have been designed for "low field" operation. They report a peak power output of 1 and 2 kw with an efficiency of 1 per cent and a lifetime of several hours.

The above examples clearly illustrate the four fundamental problems encountered by conventional tubes as their wavelength is pushed into the low millimeter range.[15] Improvement in the art will undoubtedly permit the wavelengths of present tubes to be reduced still further, but what is really needed is a new generation principle or science to reach 1 mm and lower wavelengths.

Examples of Commercially Available Millimeter Wave Tubes

In Figs. 3–5, a representative list of unclassified tubes in the 20 to 90-kmc range is presented for the benefit

[13] W. V. Christensen and D. A. Watkins, "Helix millimeter-wave tube," Proc. IRE, vol. 43, pp. 93–96; Janury, 1955.
[14] M. J. Bernstein and N. M. Kroll, "Magnetron research at Columbia Radiation Laboratory," IRE Trans. on Microwave Theory and Techniques, vol. MTT-2, pp. 33–37; September, 1954.
[15] R. L. Bell and M. Hillier, "An 8-mm klystron power oscillator," Proc. IRE, vol. 44, pp. 1155–1159; September, 1956.

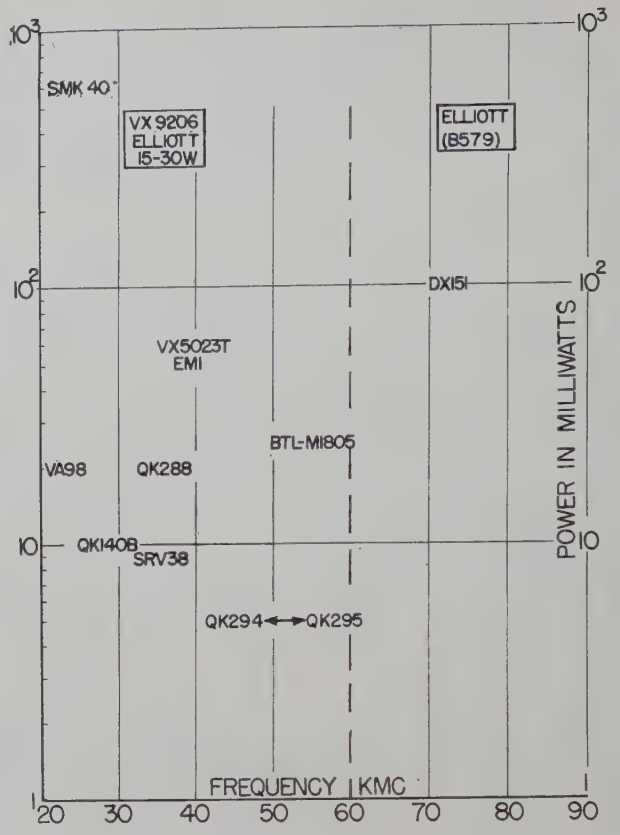

Fig. 3—Klystrons (representative list).

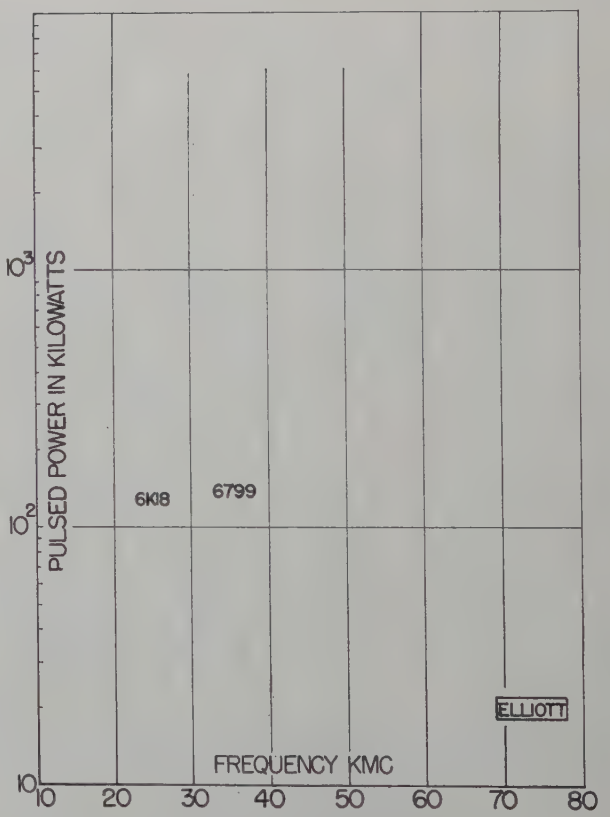

Fig. 4—Magnetrons (representative list).

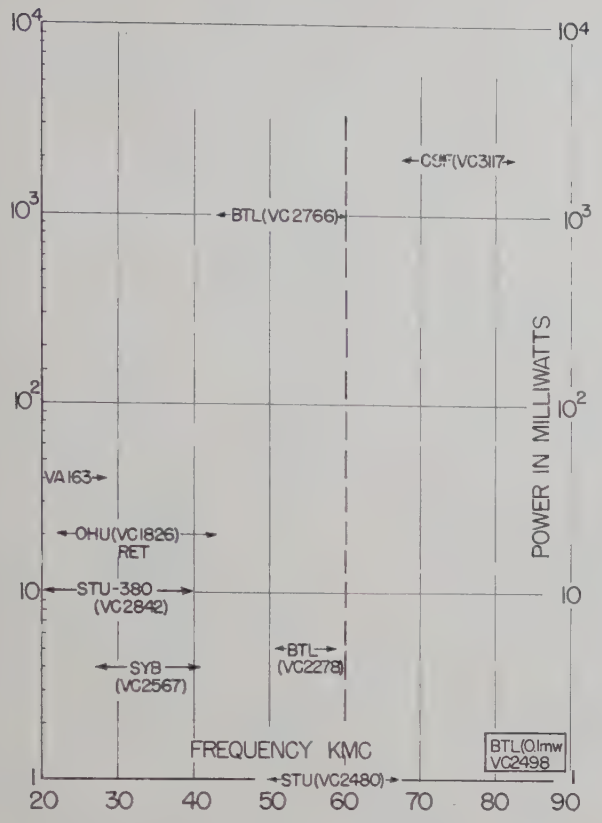

Fig. 5—Backward-wave tubes (representative list).

of those persons who may be considering work in the millimeter range for the first time. These tubes were taken from a special list of microwave tubes supplied by the Advisory Group on Electron Tubes.[16] This Group follows the progress of electron tubes both under development or in production in the U.S.A. By establishing a "need-to-know," the Advisory Group will supply a list of both classified and nonclassified tubes to all interested persons. The VC number indicated for the tube is the Advisory Group's index number for that particular item.

It will be observed that above 60 kmc (5-mm wavelength) about the only available commercial tube is the Amperex DX151. Elliott Brothers, England, plans to bring out a 20-watt magnetron in the range 70 to 75 kmc, perhaps within the next year. The status of the CSF French tube, listed as Advisory Group No. VC3117, is not known.

Waveguides—Connectors

Attempts to extend microwave components and techniques into the low millimeter or submillimeter range is almost as difficult as extending microwave tubes into the same range. It may well be that around 1-mm wavelength both microwave tubes and techniques will be abandoned and replaced by hybrid microwave-physical optics methods. However, there is considerable advantage in extending techniques as far as practical.

JAN rectangular waveguides for the 30 to 300-kmc range are given in the Armed Services Index of RF Transmission Lines and Fittings. Table I lists the RG-96, 97, 98, and 99/U sizes that have been in use for many years. They can be obtained from a number of manufacturers. Unfortunately, the RG-135, 136, 137, 138, and 139/U guides are not commercially available at the present time. These smaller guides are planned to have a circular exterior geometry and are envisioned to be made by electroforming as opposed to being extruded or drawn.

Most workers in the millimeter field are presently using the nonstandard G, F, and E rectangular guides[17] made by Horton-Angell Company of Attleboro, Mass.

Essentially two problems are encountered in millimeter waveguides: 1) small physical size, and 2) excessive attenuation. The modes used on the common waveguides are shown in Fig. 6 and attenuation characteristics are compared in Fig. 7, where all dimentions are given in inches.

It is seen that F-band guide operating in the TE_{10} mode has a theoretical attenuation of the order of 8 to 9 db per meter, a value so large as to severely limit its uses in many practical situations. The use of a TE_{11} mode in a cylindrical guide has a similar attenuation. However the TE_{01} mode in cylindrical guide has an attenuation which decreases indefinitely with increasing frequency since the currents in the guide walls approach zero. For this reason, the TE_{01} mode has been studied rather intently by workers seeking to propagate millimeter waves over long distances.[7] One of the difficulties with this mode is that any asymmetry or bending of the guide produces currents in the walls with a corresponding attenuation. However, a reduction of the TE_{01} transmission loss in a bend can be realized by adding suppressors for the unwanted TM_{11} mode generated in the bend region.[18]

Hybrid modes on dielectric rods and tubes have been under study for some time.[19–21] These modes have longitudinal components of both $\overline{E}$ and $\overline{H}$ and are designated as HEM modes. In addition, these modes are sometimes called HE_{mn} or EH_{mn}, depending upon whether they resemble more strongly an H(TE) mode or an E(TM) mode, respectively. The attenuation of the hybrid

[16] Advisory Group on Electron Tubes, 346 Broadway, New York 13, N. Y.

[17] W. Gordy, *et al.*, "Microwave Spectroscopy," John Wiley and Sons, Inc., New York, N. Y., ch. 1; 1953.

[18] S. E. Miller, "Notes on methods of transmitting circular electric waves around bends," Proc. IRE, vol. 40, pp. 1104–1113; September, 1952.

[19] W. M. Elsasser, "Attenuation in a dielectric rod as wave guide," *J. Appl. Phys.*, vol. 20, pp. 1193–1196; December, 1949.

[20] C. Chandler, "An investigation of dielectric circular rod as wave guide," *J. Appl. Phys.*, vol. 20, pp. 1188–1193; 1949.

[21] R. E. Beam *et al.*, "Investigation of Multi-Mode Propagation in Waveguides and Microwave Optics," Northwestern University, Evanston, Ill., performed under U. S. Army Signal Corps Contract No. W36-039, sc-38240; May 1, 1949 to November, 1950.

TABLE I

MILLIMETER WAVEGUIDES

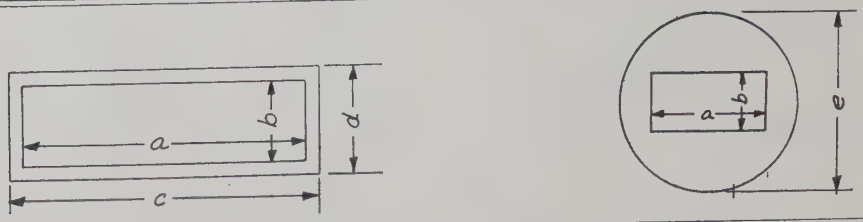

Type	Operating Range		Inside Dimensions		Outside Dimensions			Material	Distributor
	Frequency (kmc)	Wavelength (mm)	a (inch)	b (inch)	c (inch)	d (inch)	e (inch)		
RG-96/U	26.50– 40.00	11.30–7.50	0.280	0.140	0.360	0.220		Silver Copper	Demornay Bonardi Carl Schutter
RG-97/U	33.00– 50.00	9.09–6.00	0.224	0.112	0.304	0.192		Silver	Demornay Bonardi Carl Schutter
RG-98/U	50.00– 75.00	6.00–4.00	0.148	0.074	0.228	0.154		Silver	Demornay Bonardi Carl Schutter
RG-99/U	60.00– 90.00	5.00–3.30	0.122	0.061	0.202	0.141		Silver Copper	Demornay Bonardi Carl Schutter
RG-138/U	90.00–140.00	3.30–2.14	0.080	0.040			0.156		
G	100.00–150.00	3.00–2.00	0.075	0.034	0.135	0.094		Silver Copper	Horton Angell
RG-136/U	110.00–170.00	2.73–1.77	0.0650	0.0325			0.156		
RG-135/U	140.00–220.00	2.14–1.36	0.0510	0.0255			0.156		
F	150.00–230.00	2.00–1.30	0.049	0.022	0.107	0.080		Silver Copper	Horton Angell
RG-137/U	170.00–260.00	1.77–1.15	0.0430	0.0215			0.156		
RG-139/U	220.00–325.00	1.36–0.92	0.0340	0.0170			0.156		
E	230.00–350.00	1.30–0.85	0.033	0.016	0.097	0.080		Silver Copper	Horton Angell

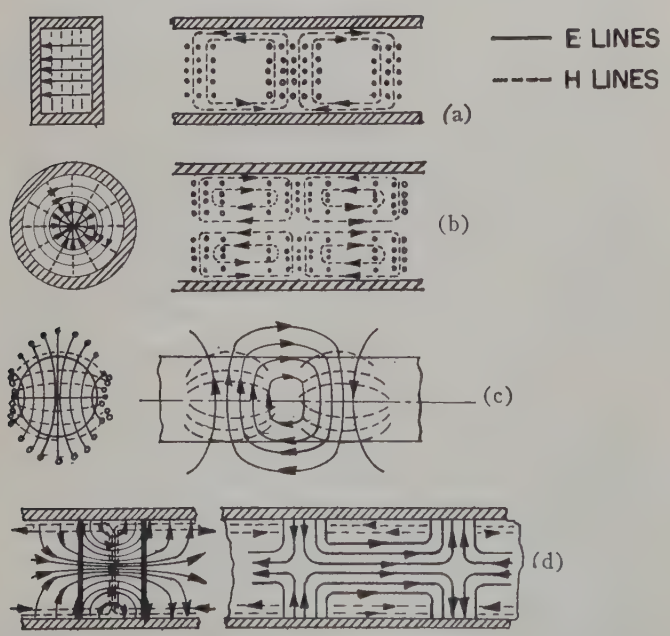

Fig. 6—Field patterns for waveguide modes. (a) Rectangular waveguide—TE_{10} mode. (b) Circular waveguide—TE_{01} mode. (c) Dielectric rod waveguide—HEM_{11} mode. (d) *H*-type waveguide—HEM_{11} mode.

HEM_{11} "dipole" mode of the dielectric rod is plotted in Fig. 7. This mode has no cutoff frequency and is preferred from the mode conversion point of view.

As is seen from the figure, a dielectric rod can provide a much smaller attenuation than metal guides, except for the TE_{01} mode in cylindrical guide. However, the problems of supports, bends, and shielding are not easily solved. Moreover, the lower the loss, the more difficult these problems become. Dielectric image lines[22,23] show promise of convenient application in bends and straight sections in the millimeter range but their cross-sectional area decreases rapidly with decreasing wavelength. Single-conductor, surface-wave transmission lines,[24–26] which have an attenuation which is less than

[22] D. D. King, "Properties of dielectric image lines," IRE TRANS. ON MICROWAVE THEORY AND TECHNIQUES, vol. MTT-3, pp. 75–81; March, 1955.

[23] J. C. Wiltse, "Some characteristics of dielectric image lines at millimeter wavelengths," presented at MTT Symp., Stanford, Calif.; May, 1958.

[24] G. Goubau, "Single-conductor surface-wave transmission lines," PROC. IRE, vol. 39, pp. 619–624; June, 1951.

[25] G. Goubau, "Surface waves and their application to transmission lines," *J. Appl. Phys.*, vol. 21, pp. 1119–1128; November, 1950.

[26] W. Rotman, "A study of single-surface corrugated guides," PROC. IRE, vol. 39, pp. 952–959; August, 1951.

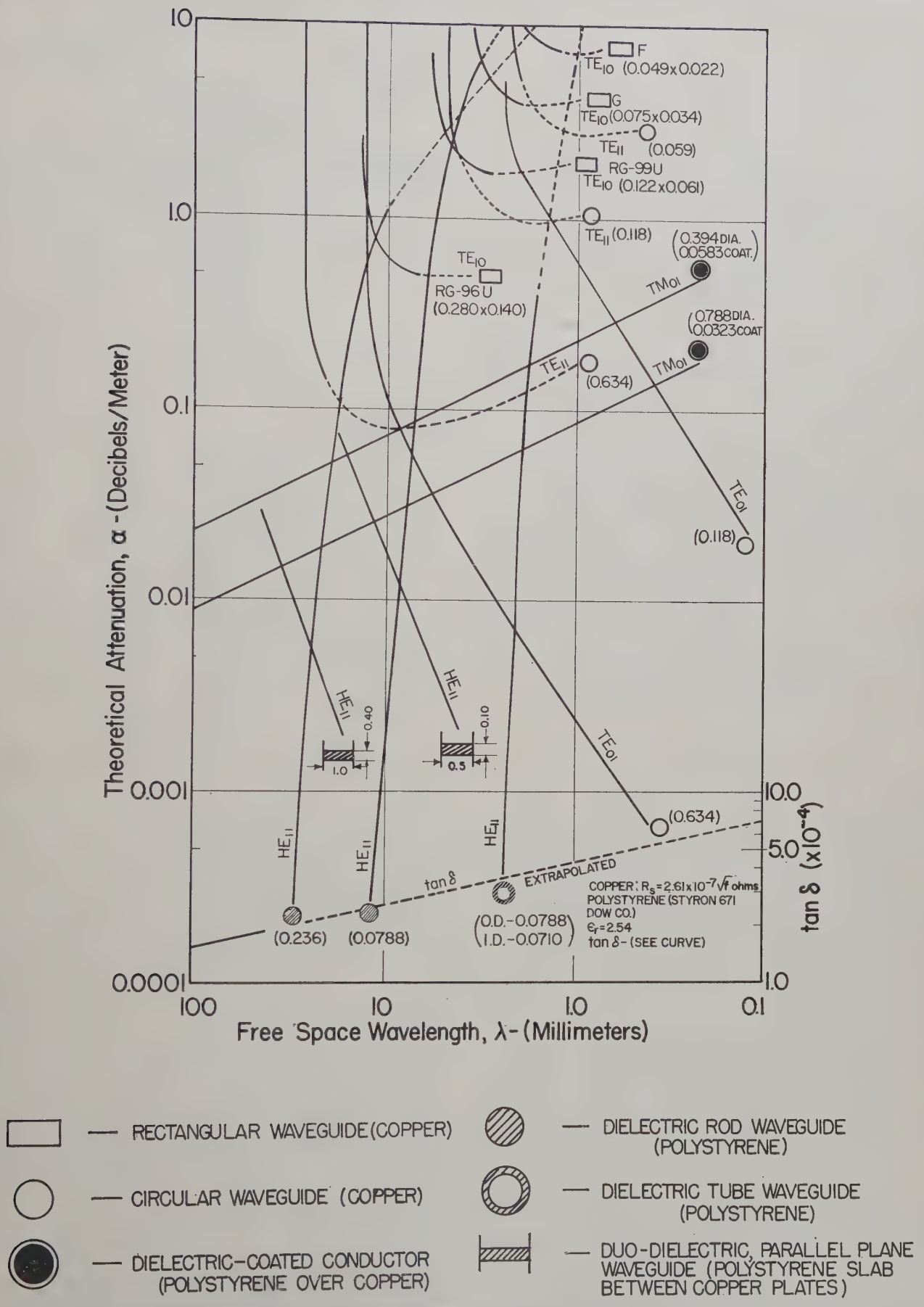

Fig. 7—Comparison of the theoretical attenuation characteristics of waveguides suitable for millimeter wavelength applications.

metal waveguides, have found applications in connection with antennas.

The H guide[27] and duo-dielectric parallel-plane waveguide,[28] consisting of two parallel conducting planes with one or two dielectric slabs between them, have valuable properties for millimeter wave propagation. Tischer reports that one of the hybrid modes, the HEM_{11} which is plotted in Fig. 7, has an attenuation which decreases with increasing frequency similar to the TE_{01} in cylindrical metal guides. The special features claimed for this guide are 1) the nonexistence of longitudinal currents which permits two sections of the guide to be readily joined without special connectors, 2) cross-sectional dimensions greater than those of rectangular guide, and 3) easily fabricated circuits can be made using the guide. However, as far as the authors are aware, there have been no experimental data presented to verify the decreasing attenuation of this mode in the H guide with increasing frequency.

The Armed Services Index does not list any connectors for guides beyond RG-99/U but it is assumed that they might be similar to the UG-387/U cover flanges used with RG-99/U guide. A design of the connector used with the G, F, and E guides by the Ultramicrowave Group at Illinois is shown in Fig. 8. This connector consists essentially of two basic parts, a knurled screw ring and a punched disk. Alignment does not depend on dowel pins but on waveguide tolerances both on the outside and inside dimensions. The connectors are readily joined together and provide a very sturdy joint which is not easily bent out of shape.

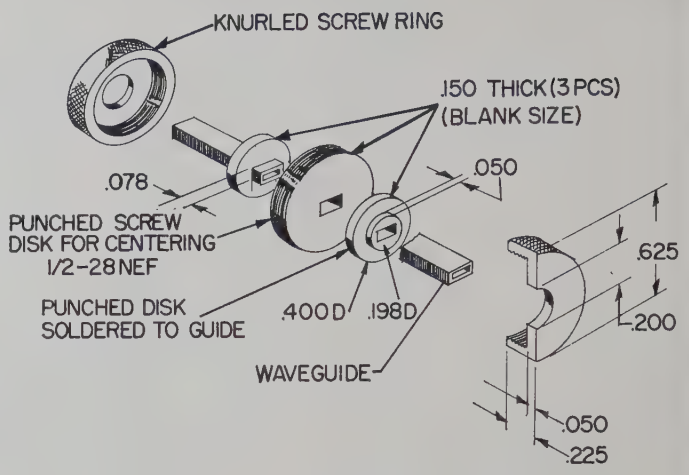

Fig. 8—*G*- and *F*-band waveguide connector (butt type).

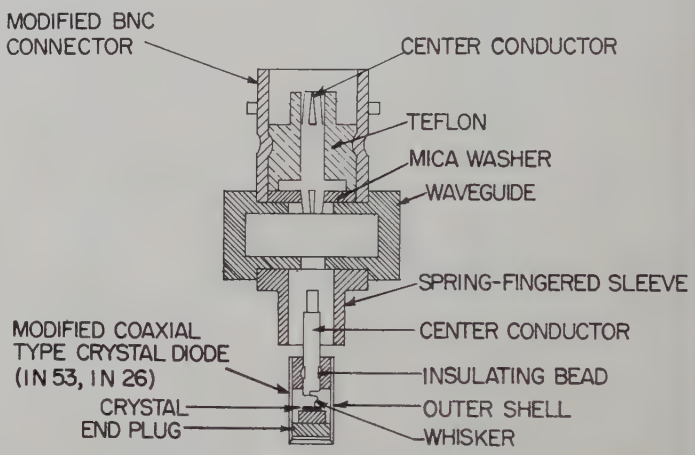

Fig. 9—Crystal cartridge type detector.

Detectors

The three types of detectors most commonly used in the low millimeter range are: 1) the silicon crystal, 2) the Wollaston wire bolometer, and 3) the Golay cell.[29]

A variety of crystal mounts have been designed by workers in the field, but they are essentially only of two basic types: the type where the crystal dicing is mounted directly in the guide, and the type that employs a cartridge crystal such as the 1N26 and 1N53.

Fig. 9 illustrates a typical design[30] using a cut-down 1N26 or 1N53 cartridge. Here, the outer conductor of the cartridge has been machined down to the dielectric bead so as to expose the center conductor. This cut-down cartridge plugs into a fingered sleeve soldered onto one wall of the waveguide. The center conductor of the crystal mates with the center conductor of a BNC connector which has been modified to include either a choke or bypass condenser. A movable short is included in the waveguide for tuning. Also the crystal can be moved up and down or rotated in the fingered sleeve for maximum output signal.

Fig. 10 shows a typical design of the in-guide crystal dicing mount.[31,32] In this unit the pressure of the tungsten cat-whisker against the crystal can be adjusted by advancing or retracting the crystal chip which is mounted on a differential screw. Sharpness of the whisker point is critical in this device. The radius of curvature of the tip is usually made to be of the order 10^{-4} inches or less.

Fig. 11 illustrates an in-guide mount with fixed tuning.[33] Here a tapered ridge from the rectangular guide is used to broadband the device and achieve an RF impedance match. The crystal chip is mounted on a flat spring built into the ridge to provide the contact whisker pressure.

[27] F. J. Tischer, "H-guide—A new microwave concept," *Electronic Ind. Tele-Tech*, vol. 16, pp. 50–51, 130, 134, 136; November, 1956. Also, "The H-guide, a waveguide for microwaves," 1956 IRE Convention Record, pt. 5, pp. 44–47.

[28] R. A. Moore and R. E. Beam, "A duo-dielectric parallel-plane waveguide," *Proc. NEC*, vol. 12, pp. 689–705; 1956.

[29] M. J. E. Golay, "A Pneumatic Infra-Red Detector," *Rev. Sci. Instr.*, vol. 18, pp. 357–362; May, 1947.

[30] H. C. Torrey and C. A. Whitmer, "Crystal Rectifiers," M.I.T. Rad. Lab. Ser., McGraw-Hill Book Co., Inc., New York, N. Y., vol. 15; 1948.

[31] W. C. King, "Millimeter wave spectroscopic components," IRE Trans. on Microwave Theory and Techniques, vol. MTT-2, pp. 13–16; September, 1954.

[32] C. H. Townes and A. L. Schawlow, "Microwave Spectroscopy," McGraw-Hill Book Co., Inc., New York, N. Y., ch. 16; 1955.

[33] Microwave Associates, Burlington, Mass., Catalog 58 S; 1958.

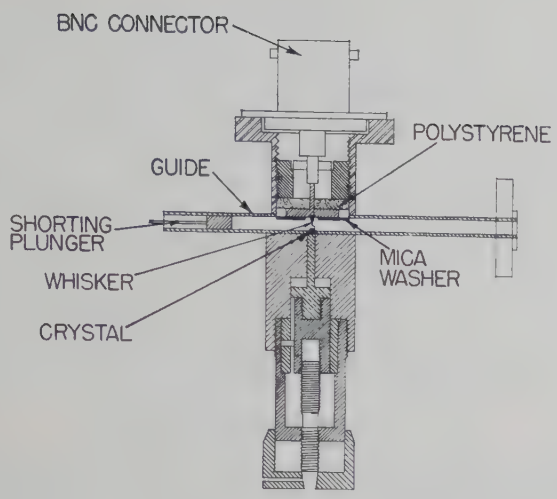

Fig. 10—Crystal-in-guide type detector.

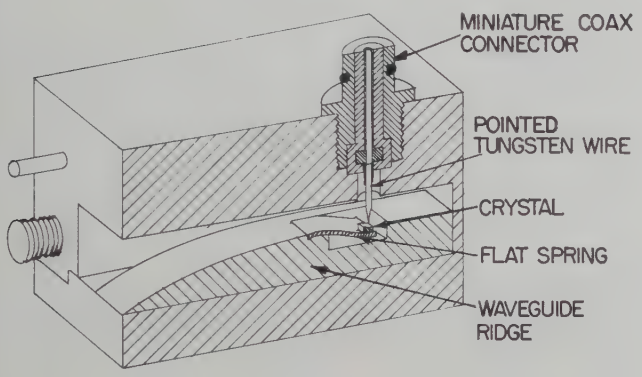

Fig. 11—Ridge waveguide crystal mount.

A mount which combines the features of an in-guide crystal and those of a cartridge is the Sharpless[34] unit shown in Fig. 12. A wafer contains a short section of waveguide across which the point contact rectifier is mounted. The basic idea is that the wafer containing the rectifier can be inserted and moved in a slot at right angles to the waveguide to obtain a resistive match to the waveguide, while the reactive component of the rectifier impedance is tuned out with an adjustable plunger located in the converter block to the rear of the wafer location.

Using the same crystal material, the in-guide mount is in general the most sensitive unit in the low millimeter range. However, it is time-consuming to construct and adjust and less rugged than the other types. At 4 mm, using a mount constructed in RG-99/U guide, the in-guide devices are from 5 to 10 db better than the 1N53 cartridge type units. A cartridge unit has the advantages of being rugged and cheap to make.

While crystal detectors have been used by Gordy[35] and others to detect signals below 1-mm wavelength, there are still many problems associated with their use

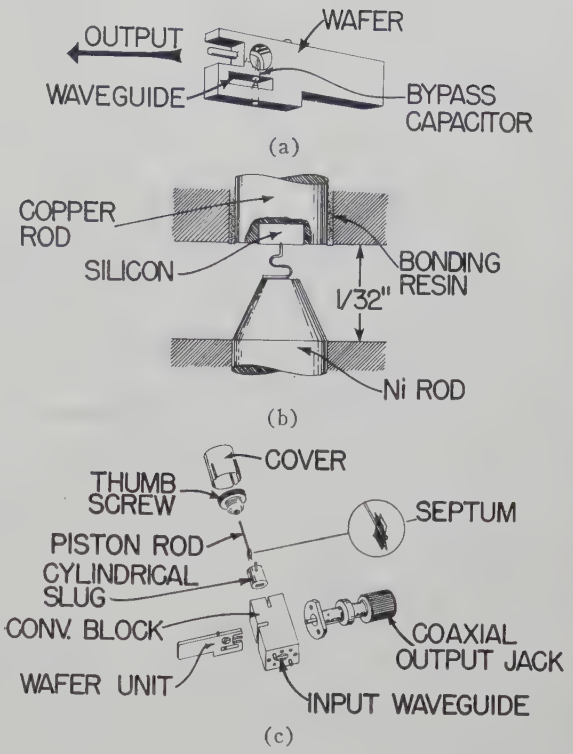

Fig. 12—Wafer type detector.

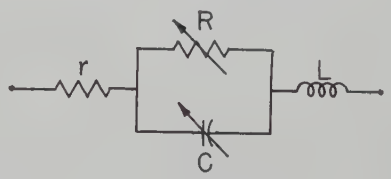

Fig. 13—Equivalent circuit of a crystal rectifier.

in the low millimeter range. The design of good mounts is largely one of art and crystal materials. In the equivalent circuit of the crystal rectifier shown in Fig. 13, the conversion loss is a function of ωCr where C is the barrier capacity and r the ohmic spreading resistance. In terms of the properties of the semiconductor,[30,36,37]

$$\omega Cr = \frac{\pi}{240}\left(\frac{\epsilon}{\epsilon_0}\right)\frac{a}{\sigma D\lambda}\,\alpha\,\frac{a}{\lambda}\left[\frac{\epsilon}{b^2N}\right]^{1/2} \qquad (3)$$

where a is whisker radius of contact; D, the barrier thickness; λ, the wavelength; σ, the conductivity; N, the carrier concentration; b, the mobility; and ϵ, the permittivity of the crystal material.

For silicon doped with 0.02 per cent boron, typical values of the parameters are

$$\frac{\epsilon}{\epsilon_0} = 13 \qquad a = 1.25 \times 10^{-6} \text{ meter}$$

$$\sigma = 1.11 \times 10^{4} \text{ mho/meter}$$

[34] W. M. Sharpless, "Wafer-Type Millimeter-Wave Converters," Bell Telephone Labs., New York, N. Y., Final Rep. on Contract Nonr-687(00); June, 1951 to May, 1955.

[35] C. A. Burrus and W. Gordy, "Submillimeter wave spectroscopy," *Phys. Rev.*, vol. 93, pp. 897–898; February, 1954.

[36] H. K. Henisch, "Rectifying Semi-Conductor Contacts," Oxford University Press, New York, N. Y.,; 1957.

[37] C. T. McCoy, "Present and future capabilities of microwave crystal receivers," Proc. IRE, vol. 46, pp. 61–66; January, 1958.

so that

$$r = \frac{1}{4\sigma a} = 18 \text{ ohms} \qquad D = 10^{-8} \text{ meter}$$

$$C = 5.7 \times 10^{-14} \text{ farad} \qquad \omega Cr = \frac{1.9}{\lambda(\text{mm})} < 1. \tag{4}$$

On the basis of this criterion, a detector using this crystal material would not be suitable for wavelengths below 1.9 mm. An increase in the impurity content or doping increases the value of σ but decreases D. The value of the bracket term in (3) represents fundamental physical constants with a calculable minimum theoretical value[37] for any semiconductor. Germanium has a theoretical value 2.5 times lower than silicon while indium antimonide is much lower than germanium. Thus there is hope in the near future of reducing the value of Cr by an order of magnitude from its best present value.

The surface treatment of the semiconductor also has a marked effect on the rectification characteristics. Bombardment by helium ions[36] is used by some workers to activate the surface, especially for crystals used in crystal multipliers.

While crystal detectors are more sensitive than other detectors at wavelengths longer than those in the millimeter range, at wavelengths below about 3 mm, bolometers show considerable promise. In fact for wavelengths approaching 1 mm, platinum wire bolometers will exceed crystals in sensitivity. Moreover, the response law[38] of a bolometer is accurately known, and the bolometers can probably be made more reproducible.

In commercial bolometers such as the PRD 634,[6] the Wollaston wire is mounted on a mica card. This technique does not appear to be feasible as one goes to smaller wires and guides. Rohrbaugh's[39] group at N.Y.U. has been mounting 10-microinch wire directly in the guide (0.022×0.045 inch) for detection at $K/8$ band. These resistance elements were obtained from Sigmund Cohn Corporation which manufactures Wollaston wires with cores as small as 6 microinches with resistances of the order of 200,000 ohms per inch. Rohrbaugh reports the sensitivity of his bolometers as $\sim 10^{-10}$ watts. A PRD 617 bolometer which contains a 35-microinch wire has a time constant[40,41] of approximately 150 μsec. The N.Y.U. bolometer mounts show a small but definite decrease in rise time and a much greater decrease in the decay time as the wire diameter decreases. Thus there is promise that these small wire bolometers could respond to signal frequencies as high as 10,000 cycles per second or greater.

The Golay detector,[29] a device originally intended as an infrared detector, has been used successfully from the ultraviolet region through the infrared and out to a wavelength of 7.5 mm in the microwave portion of the spectrum. The device consists essentially of a pneumatic chamber which responds to changes in thermal radiation. Typical rise times are about 15 msec in duration, and available sensitivities are of the order of 10^{-8} watts.

Power Measurements

Accurate power measurements in the low millimeter range are difficult to make, especially since the power available for measurement is usually very small. A survey article by Weill[42] gives various methods of measuring the power output of millimeter wave tubes; power ranges from 100 watts to 100 μw are considered. Fig. 14(b) shows one example of a platinum film bolometer described by Weill for the range 100 mw to 100 μw. These enthrakometers avoid the problems of mounting small Wollaston wires but they are still rather delicate.

Commercial bolometer mounts can be obtained from a number of companies. PRD makes a mount, type 632, in RG-98/U guide which uses bolometer wire mounted on a mica card (type 634). F-R Machine Works mounts their Wollaston wires in a cartridge unit identical to the 1N53 crystal so that they can be used interchangeably in the same detector unit.

Sharpless[43] has described a calorimeter for power measurements of the order of 1 mw in the wavelength range 5 to 7 mm. However, there is no reason to believe that this device could not be extended to still shorter wavelengths. Fig. 14(a) illustrates the design of the calorimeter. It consists of a short section of thin-walled round silver waveguide containing a cast conical taper of absorbing material. DC power can be fed through the termination from the outer shell through a small deposited silver band, located at the front end of the termination. The temperature rise is measured by three Western Electric 23A thermistor beads in intimate contact with the exterior of the thin-walled silver tube. Two identical terminations are used in the bridge network shown, where a pulsed signal is used to detect the balance condition.

Frequency Measurements

Most of the frequency meters in the low millimeter range are scaled down versions of TE_{0mn} mode, high-Q cavity wavemeters used at K band which are described, for example, in detail in the M.I.T. Radiation Labo-

[38] G. D. Montgomery, "Techniques of Microwave Measurements," M.I.T. Rad. Lab. Ser., McGraw-Hill Book Co., Inc., New York, N. Y., vol. 11; 1947.

[39] J. H. Rohrbaugh, "A Study of the Generation and Detection of Electromagnetic Waves in the Millimeter Wave Region," New York University, New York, N. Y., Quart. Reps. on AF19(604)-1115; 1956–58.

[40] G. U. Sorgen, "The thermal time constants of a bolometer," IRE Trans. on Instrumentation, no. PGI-4, pp. 165–170; October, 1955.

[41] M. Sucher and H. J. Carlin, "The operation of bolometers under pulsed power conditions," IRE Trans. on Microwave Theory and Techniques, vol. MTT-3, pp. 45–52; October, 1955.

[42] H. Weill, "Mésures de puissance sur tubes millimétriques," *Le Vide*, vol. 12, pp. 122–127; January–February, 1957.

[43] W. M. Sharpless, "A calorimeter for power measurements at millimeter wavelengths," IRE Trans. on Microwave Theory and Techniques, vol. MTT-2, pp. 45–54; September, 1954.

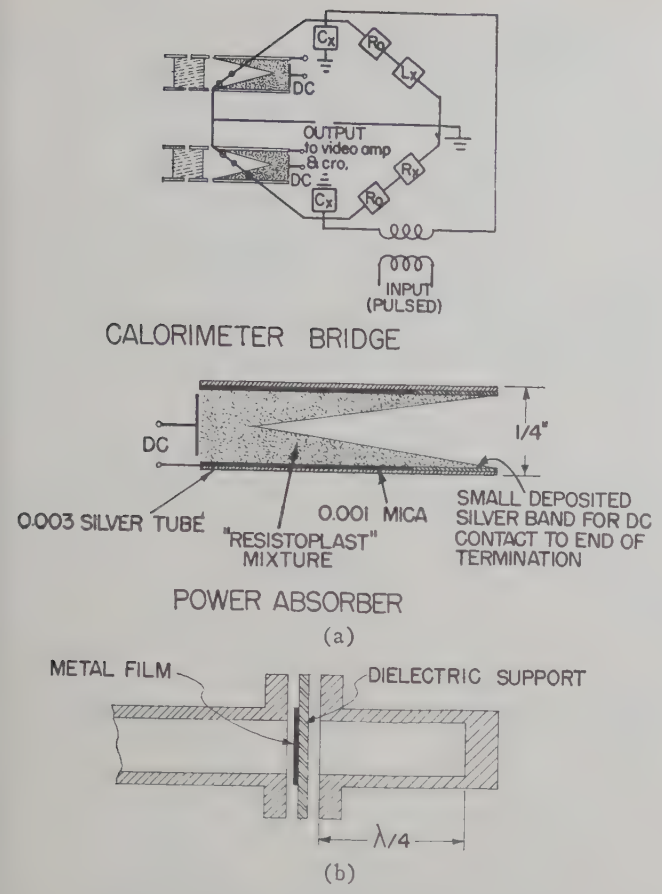

Fig. 14—Power measuring devices. (a) Calorimeter for the 5 to 7-mm range (Sharpless). (b) Platinum film bolometer.

ratory Series.[38] About the only new design change is to replace the micrometer drive with a finer mechanism such as a differential screw which can easily give a travel of 0.001 inch per turn.

As one would expect, microwave analogs of the Michelson and Fabry-Perot interferometers were investigated by a number of workers some years ago.[44,9] Two microwave forms of this device are shown in Fig. 15. The arrangement shown in Fig. 15(b) has obvious disadvantages from the low millimeter viewpoint since it uses a directional coupler and magic tee, both of which are difficult to construct. The Fabry-Perot arrangement, shown in Fig. 15(a), avoids these difficulties by requiring just a horn radiator.

In addition to wavelength measurements, interferometers have uses in the measurement of dielectric constant and attenuation in dielectric materials available in the form of uniform sheets.

Frequency Multiplication with Nonlinear Elements

Circuit Synthesis Problem

Until an idea for a prime, or self-excited, source for the submillimeter wavelength range is discovered, the only

[44] B. A. Lengyel, "A Michelson-type interferometer for microwave measurements," Proc. IRE, vol. 37, pp. 1242–1244; November, 1949.

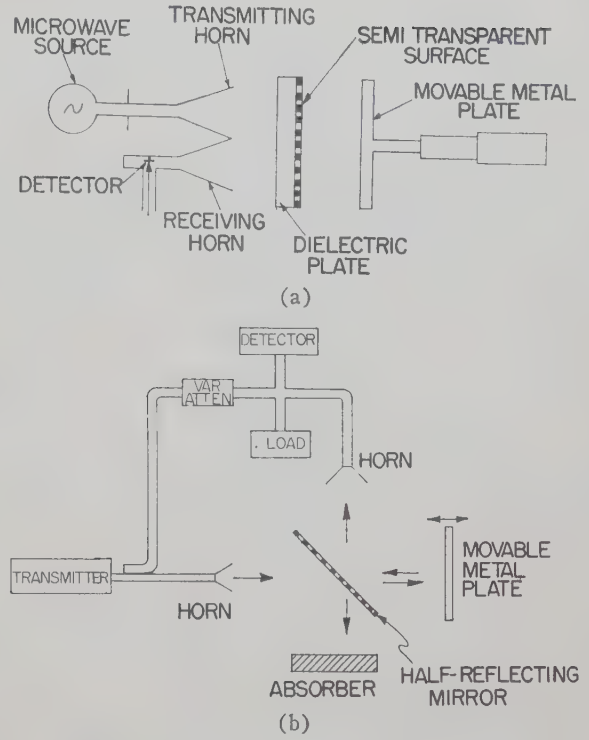

Fig. 15—Frequency measuring devices. (a) Microwave analog of a modified Fabry-Perot interferometer. (b) Microwave analog of Michelson interferometer.

Problems:
1) Impedance at unwanted harmonics to be zero, infinite, or reactive.
2) Input and output coupling.
3) Circuits components.

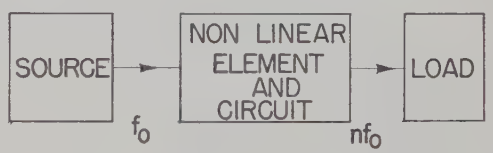

Fig. 16—Frequency multiplication with a nonlinear element.

feasible approach to the problem would appear to be a frequency multiplication by means of some nonlinear effect or element. In principle, this frequency multiplication could be up or down in frequency, since sources exist both above and below the submillimeter range.

Fig. 16 schematically illustrates the frequency multiplication process. A suitable source at frequency f_0 feeds into a circuit containing a nonlinear element. The output coupling is such that only a given harmonic frequency, nf_0, emerges, in turn, to be fed into a load. Ideally, if the nonlinear element used in the circuit were a lossless reactive device and the circuit could be so synthesized that it had dissipation only at a given harmonic frequency nf_0, then it follows that a power gain of one at the desired harmonic could be realized.

The general problems in synthesizing such circuits would be: 1) to find an arrangement where the impedances at the unwanted harmonics are either zero, infinite, or reactive; 2) to find a circuit which could be realized with practical millimeter wave components;

and 3) coupling in and out of the circuit structure.

Nonlinear elements are seldom either purely resistive or reactive. However, two recent papers by Page[45] and Manley and Rowe[46] have appeared which give limits to the power gain for a desired harmonic.

Page considers positive nonlinear resistors through which the current, I, is a real, finite, single-valued, nondecreasing function of the voltage, V, across the terminals. He also assumes the current, I, is zero for V equal to zero.

Let

$$V(t) = \sum_{1}^{\infty} a_n \cos(n\omega t + \theta_n), \tag{5}$$

then the current will be Stepanoff almost periodic (S^2 ap)[45]

$$I(t) = \lim \sum_{1}^{\infty} b_n \cos(n\omega t + \phi_n). \tag{6}$$

From the nondecreasing behavior of I, it follows that

$$\theta(x) \equiv \langle \{V(t) - V(t-x)\} \cdot \{I[V(t) - I[V(t-x)]]\} \rangle_t \geq 0 \tag{7}$$

or

$$\theta(x) = 2 \sum_{1}^{\infty} P_n(1 - \cos n\omega x) \geq 0 \tag{8}$$

where $P_n = a_n b_n/2 \cos(\phi_n - \theta_n)$ is the power absorbed by the resistor at frequency ω^2. Applying (8) to a circuit containing a positive nonlinear resistor wherein there is dissipation only for frequencies ω and $n\omega$, it follows that

$$P_1(1 - \cos \omega x) - |P_n|(1 - \cos n\omega x) \geqq 0 \tag{9}$$

or

$$\frac{|P_n|}{P_1} = \left\{\frac{\sin(\omega x/2)}{\sin(n\omega x/2)}\right\}^2_{x \to 0} \to \frac{1}{n^2}. \tag{10}$$

Thus the efficiency of generating an nth harmonic cannot exceed n^{-2}. If a circuit could be synthesized that would approximate the condition given by (8), one solution to the submillimeter wave generation problem would be immediately achieved since appreciable amounts of power are available at K band and higher frequencies.

Manley and Rowe consider nonlinear inductors and capacitors which may contain hysteresis. For conceptual purposes, they suggest the circuit shown in Fig. 17. Let

$$v = \sum_{m=-\infty}^{\infty} \sum_{n=-\infty}^{\infty} V_{m,n} e^{j(m\omega_1 t + n\omega_0 t)} \tag{11}$$

$$i = \sum_{m=-\infty}^{\infty} \sum_{n=-\infty}^{\infty} I_{m,n} e^{j(m\omega_1 t + n\omega_0 t)}. \tag{12}$$

[45] C. H. Page, "Frequency conversion with positive nonlinear resistors," *J. Natl. Bur. Standards*, vol. 56, pp. 179–182; April, 1956.

[46] J. M. Manley and H. E. Rowe, "Some general properties of nonlinear elements. Part I. General energy relations," PROC. IRE, vol. 44, pp. 904–913; July, 1956.

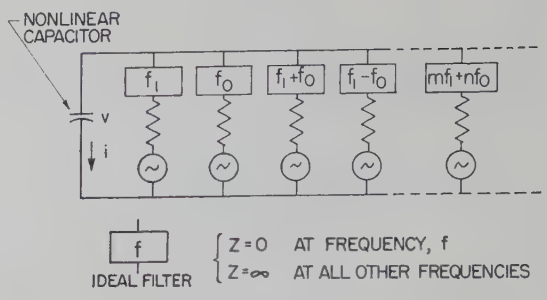

Fig. 17—Circuit with a nonlinear capacitor (Manley-Rowe). Filters—*SC* to desired frequency, *OC* to all other frequencies.

Assume

$$v = f(q) = \sum_{n=0}^{\infty} V_{0,n} e^{jn\omega_0 t}.$$

Let $W_{0,n}$ be the average power flowing into nonlinear element at frequency nf_0. Then

$$\sum_{n=0}^{\infty} \frac{W_{0,n}}{f_0} = 0.$$

Hence

$$W_{0,1} = -\sum_{n=2}^{\infty} W_{0,n}.$$

Special case: $W_{01} = -W_{0,s}$. ($n = s$, conversion to single harmonic frequency.)

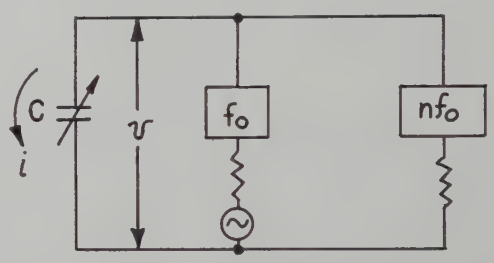

Fig. 18—Frequency conversion with a nonlinear reactive element.

Define

$$2V_{m,n}I_{m,n}^* = W_{m,n} + jX_{m,n} \tag{13}$$

where $W_{m,n}$ is the real or average power flowing into the nonlinear element at this frequency for either choice of indexes.

Manley and Rowe derive the following relationships

$$\sum_{m=0}^{\infty} \sum_{n=-\infty}^{\infty} \frac{mW_{m,n}}{mf_1 + nf_0} = \frac{H}{f_1} \tag{14}$$

and

$$\sum_{m=-\infty}^{\infty} \sum_{n=0}^{\infty} \frac{nW_{m,n}}{mf_1 + nf_0} = 0 \tag{15}$$

where H is the average power dissipated in hysteresis.

In applying this analysis to frequency multiplication the circuit of Fig. 17 reduces to that in Fig. 18 and, when $n = 0$, (14) and (15) become

$$-W_{m,0} = W_{1,0} - H. \tag{16}$$

As the hysteresis power loss, H, approaches zero, the power gain to the desired harmonic can approach 1 independent of the shape of the nonlinear characteristic

of the capacitor C and of the power level. A similar analysis would apply to a nonlinear inductor.

The problem is to find a nonlinear effect in the low millimeter range which can be represented as a high-Q nonlinear capacitor or inductor and then to synthesize a circuit such as that suggested in Fig. 18.

Nonlinear Resistive-Type Elements

Two resistive-type nonlinear elements are currently being used for frequency multiplication in the low millimeter range: the crystal diode and the field emitter diode.

A crystal rectifier is not a positive nonlinear resistor (see the circuit of Fig. 13) so that Page's analysis is not applicable. However, it has been the element used, mainly by spectroscopists, for work in the low millimeter range. The earliest work on crystal multipliers was done by Beringer[47] at M.I.T. in 1944. Most of the recent work has been done by Gordy[35] at Duke University, Johnson *et al.*[48] at Johns Hopkins, Nethercot,[49,50] at Columbia, Ohl[7] at Bell Labs., and Richardson[51] at the National Bureau of Standards. The reports of these groups on crystal multipliers have been mainly on performance characteristics rather than analysis. Hwang[52] has recently attempted an analysis to compute the conversion efficiency of such a device. He obtained values for the second and third harmonics which were fairly close to the experimental results.

Fig. 19 illustrates a typical design of a crossed guide crystal multiplier as given by Johnson *et al.*[48] Energy coming down the larger guide is picked up by the tungsten whisker probe and fed to the silicon crystal. The resulting harmonic currents on the probe are in turn fed into the smaller guide, which is a high-pass filter, filtering out all harmonic frequencies below a certain value.

Hwang gives the equivalent circuit of the multiplier as that shown in Fig. 20 from which he calculates the second and third harmonic powers to be

$$P_2 = 0.011P_{\text{in}} \qquad P_3 = 0.0006P_{\text{in}} \qquad (17)$$

or 20 db and 32 db down from the input power, which is in fair agreement with experimental data.

The over-all loss of a good generator and detector for the low harmonics is about 15 db from one harmonic to

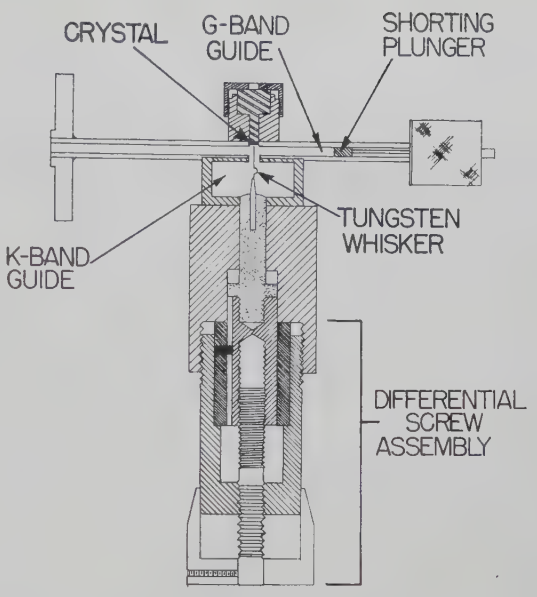

Fig. 19—Cross-guide crystal multiplier.

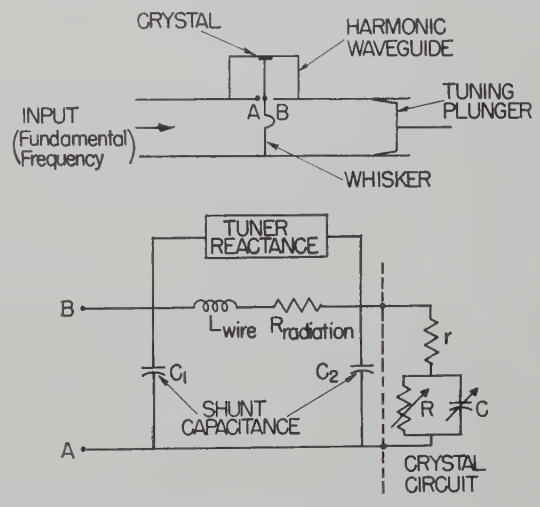

Fig. 20—Equivalent circuit for crystal multiplier (Hwang). The upper diagram shows a crossed-guide crystal multiplier.

the next while from the sixth harmonic on, the loss is probably 3 to 4 db per harmonic. No precise data seem to exist because of the difficulty in making low-level power measurements in the low millimeter and submillimeter range.

Fig. 21 illustrates the data of Richardson and Nethercot on their K-band multipliers. Nethercot does not give actual power output values so that it is difficult to compare their multipliers on this basis. However, it will be noticed that Nethercot's multiplier gives a harmonic power P_n vs fundamental power P_0 relationship, $P_n \propto P_0^n$, which may or may not be significant. Richardson's fourth harmonic power varies as $(P_0)^{1.5}$.

Most of the recent work on crystal multipliers has been done with silicon crystals. Yet North[53] in 1946 showed that welded contact germanium crystal multi-

[47] R. Beringer, *Phys. Rev.*, vol. 70, p. 53; 1946.

[48] C. M. Johnson, D. M. Slager, and D. D. King, "Millimeter waves from harmonic generators," *Rev. Sci. Instr.*, vol. 25, pp. 213–217; March, 1954.

[49] J. A. Klein and A. H. Nethercot, Jr., "Microwave spectrum of DI at 1.5 mm wavelength," *Phys. Rev.*, vol. 91, p. 1018; August 15, 1953.

[50] A. H. Nethercot, Jr., "Harmonics at millimeter wavelengths," IRE Trans. on Microwave Theory and Techniques, vol. MTT-2, pp. 17–20: September, 1954.

[51] J. M. Richardson and R. B. Riley, "Performance of three-millimeter harmonic generators and crystal detectors," IRE Trans. on Microwave Theory and Techniques, vol. MTT-5, pp. 131–135; April, 1957.

[52] Y. C. Hwang, "Harmonic Generation by Crystals at Microwave and Millimeter Wave Frequencies," Elec. Eng. Dept., University of Maryland, College Park, Md., Final Rep. AF18(600)-1246; January, 1956.

[53] H. Q. North, "Properties of welded contact germanium rectifiers," *J. Appl. Phys.*, vol. 17, pp. 912–923; November, 1946.

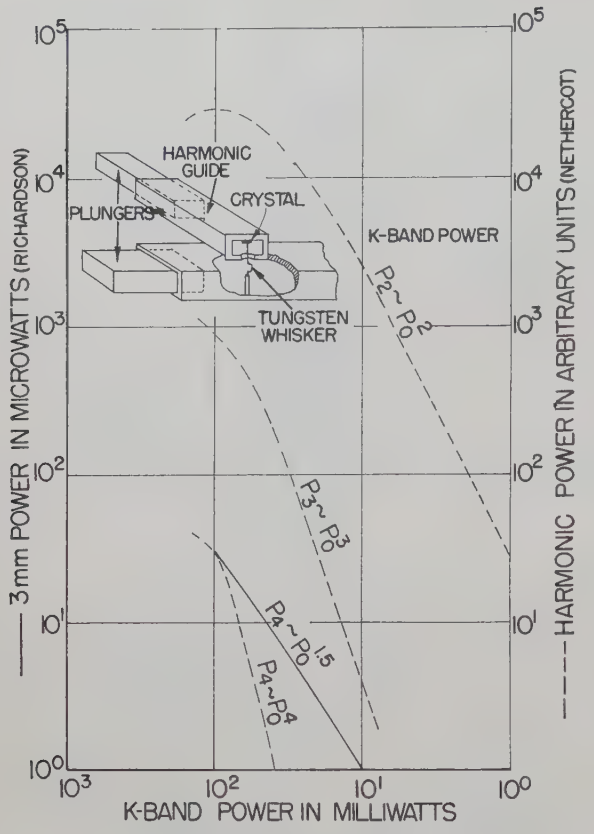

Fig. 21—Power characteristics of the crossed-guide crystal multiplier.

pliers yielded more than twenty times the 4-mm harmonic power output of standard silicon crystals. It would appear that more work on crystal materials and circuit synthesis remains to be done on this type of multiplier.

The crystal multiplier driven by a tube such as a 2K33 klystron is at present the least expensive method of producing low millimeter wave power. In experiments where very low-level signals can be tolerated, the crystal multiplier will probably find use for many years to come, barring the invention of a new self-excited source.

Recent advances in the practical application of field emission[54] have prompted several groups[55–57] to consider field-emission cathodes for harmonic generation. It is well known that electrons are emitted from a cold metal under the action of a strong field, the current-voltage relationship for a given geometry being given by

$$I = Ce^{-D/V} \tag{18}$$

where C and D are constants.

Two characteristics of the field emitter make it attractive for frequency multiplication: its highly nonlinear exponential I vs V relationship, and its high pulsed power capabilities. Characteristics which make its application difficult are 1) high vacuum requirements, 2) stability problems, 3) high impedance, 4) current limitations for a single emitter, 5) multiple emitter fabrication problems, 6) anode heating, and 7) beam focusing.

Fig. 22 illustrates a typical emitter current waveform resulting from the application of a dc bias voltage, V_0, plus an ac voltage, $V_1 \cos \omega_0 t$. Increasing the negative bias causes the current to flow during a shorter phase interval, thereby increasing the harmonic content. The harmonic current amplitudes, under the condition of negative bias, can be computed as follows. From (18)

$$\begin{aligned} I(t) &= Ce^{-D/(V_0+V_1 \cos \omega_0 t)} \\ &\simeq Ce^{-D/(V_0+V_1)} e^{-(DV_1/2)[(\omega_0 t)/(V_0+V_1)])^2} \end{aligned} \tag{19}$$

where V_0 is the dc bias voltage, and $V_1 \cos \omega_0 t$ is the ac voltage.

Only two terms in the cos $\omega_0 t$ expansion about zero have been retained.

Using the approximation that the current flows for only a small fraction of the total RF phase, the current harmonic amplitude is given by

$$I_n \simeq [Ce^{-D/(V_0+V_1)}] \left[\frac{\sqrt{\pi}(V_0+V_1)}{\sqrt{DV_1}} e^{-n^2(V_0+V_1)^2/(2DV_1)} \right]. \tag{20}$$

The first term in the bracket gives the peak value of the current pulse which is limited by the maximum tolerable heating of the emitter. The second term in brackets has its maximum value for $DV_1/(V_0+V_1)^2 = n^2$; hence

$$(I_n)_{\max} \simeq \frac{Ce^{-D/(V_0+V_1)}}{n} = \frac{I_p}{n}. \tag{21}$$

Field emitter current begins to flow when

$$V_0 + V_1 \cos (\theta_0/2) \geqq 0 \tag{22}$$

or

$$\theta_0 \simeq \left[\frac{8(V_0+V_1)}{V_1} \right]^{1/2}. \tag{23}$$

Fig. 23 illustrates the results of a calculation made by Houston[58] on the current obtainable from a field emitter under rectangular pulse conditions. Assuming the current waveforms from the emitter under the conditions given by (19) are rectangular to a first approximation, then

$$(I_p)_{\max} = [Ce^{-D/(V_0+V_1)}]_{\max} \simeq I_{dc} \left[\frac{\pi^2 V_1}{2(V_0+V_1)} \right]^{1/4}_{\max}. \tag{24}$$

[54] W. P. Dyke and W. W. Dolan, "Field emission," in "Advances in Electronics and Electron Physics," Academic Press, New York, N. Y., vol. 8; 1956.

[55] Letter Reports on APL/JHU Subcontract No. 77711, "Field Emission Applications to Microwave Amplifier Tubes," Linfield Res. Inst., McMinnville, Ore.; 1956–58.

[56] Consolidated Quart. Status Reps., Basic Electronics Res., Stanford Electronics and Microwave Lab., Stanford, Calif., 1957.

[57] P. D. Coleman, Ultramicrowave Group Tech. Status Reps. on Contract AF18(603)-62, University of Illinois, Urbana, Ill.; 1957–58.

[58] J. M. Houston, "Calculation of the Tip Temperature of a Field Emitting Point as a Function of Point Geometry and Material," The Knolls Res. Labs., G.E. Co., Schenectady, N. Y.; 1955.

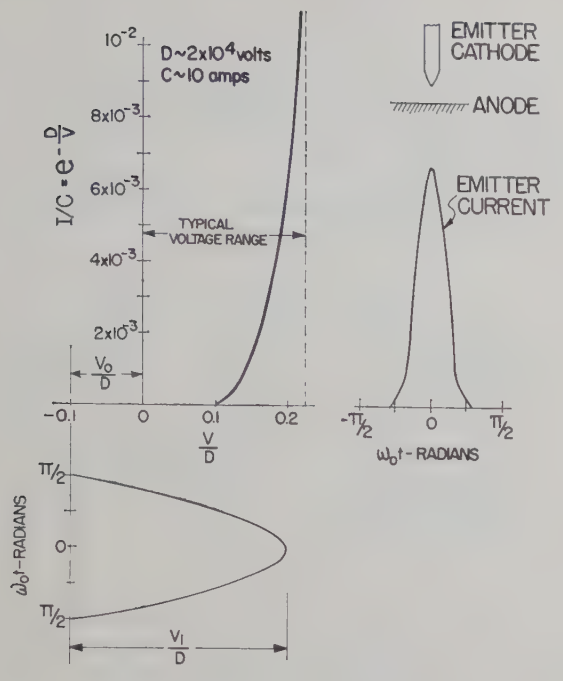

Fig. 22—Field emitter current waveforms.

$$I_P = I_{DC}\left\{\left[\frac{2\tau_0}{1+2.63\sqrt{\tau_0}+2\tau_0}\right]\left[1+\frac{0.74}{\tau_1\sqrt{2.2+\tau_1}}\right]\right\}^{-1/2}$$

(SINGLE PULSE) (REPETITIVE PULSE)

$$I_P \cong I_{DC}\sqrt{\frac{\tau_1}{\tau_0}} = I_{DC}\sqrt{\frac{2\pi}{\theta_0}}$$

WHERE, $\theta_0 = \omega t_0 = 2\pi f t_0$ $\quad t_c = \frac{C_V}{K}\left(\frac{r}{\theta}\right)^2$ $\quad f = \frac{1}{t_1}$

C_V—HEAT CAPACITY
K—HEAT CONDUCTIVITY
T—TEMPERATURE

$\tau_0 = t_0/t_c$
$\tau_1 = t_1/t_c$

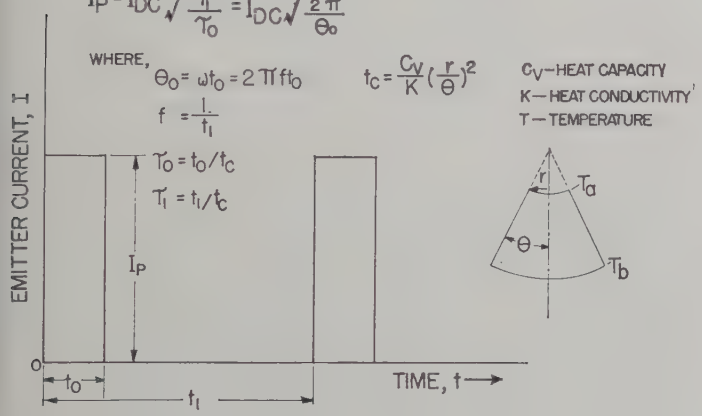

Fig. 23—Pulsed operation of emitter.

The maximum dc current, I_{do}, is determined by the emitter material and geometry. For a typical tungsten emitter having a tip radius of 0.5×10^{-4} cm and a cone half-angle of 0.1 radian, the maximum dc current is computed to be 0.15 amp. The voltages V_0 and V_1 are chosen in such a manner that short current pulses which are rich in harmonics are produced; however, their values, when combined, must not exceed the breakdown voltage in the reverse direction.

In a two-cavity klystron frequency multiplier, the velocity modulated beam must drift to obtain a bunched, harmonic beam. Using a field emitter, the emitted current immediately has a high harmonic content. This fact, along with the high current densities that can be obtained with a field emitter, are the features that workers in this area are trying to exploit for the production of low millimeter wavelengths. However, the technical problems associated with the field emitter are difficult and the devices in which they are being used are encountering essentially the same fundamental problems that plague the extension of conventional tubes to higher frequencies. Sufficient facts are not yet known to make a final evaluation of the field emitter as a frequency multiplier, but the road ahead looks very rough.

Megavolt Electronics

Frequency-multiplier klystrons[59] such as the one illustrated in Fig. 24 have been used for many years to provide precisely known frequencies in the microwave range. The basic idea being used in these devices is that an electron beam is a highly nonlinear element in the sense that, by velocity modulating a dc beam by a signal at frequency f_0, and then allowing it to drift, a high harmonic content beam is produced. But, this scheme, as used in the klystron multiplier, has the same four fundamental problems that plague all conventional tubes as they are extended into the low millimeter wavelength range. Moreover, space charge limits the bunching action and restricts the harmonic content. Also, since the original velocity modulation of the beam is never removed, the high harmonic content of the beam exists only over a small distance because beyond a certain point the velocity modulation destroys the bunch.

In the klystron multiplier shown in Fig. 24(a) there is no real problem in constructing an output cavity either at *S*, *X*, or *K* band, but in the low millimeter range physical size becomes a problem, especially since the cavities normally used are reentrant to reduce the electron transit time. However, with a drive power of the order of watts, harmonics ranging from the 10th to the 20th, with an efficiency of the order of 0.5 per cent, can be achieved.

From the standpoint of a nonlinear element, a frequency multiplication by a factor of 20 with an efficiency of 0.5 per cent, is generally difficult to accomplish. In this respect, an electron beam represents about as nonlinear an element as one can imagine. Hence, if a method could be found to use an electron beam for multiplication and still circumvent the conventional electron tube problems, one would have an excellent tool for an assault on the submillimeter wave problem. The megavolt electronics system shown in Fig. 24(b) is just such a method.

In principle, the megavolt electronics system is closely related to the klystron multiplier, but with a few critical exceptions. A suitable oscillator at frequency f_0, drives a relativistic electron bunching accelerator[60,61] (called a

[59] H. J. Reich, *et al.*, "Microwave Theory and Techniques," D. Van Nostrand Co., Inc., New York, N. Y., p. 630; 1953.

[60] I. Kaufman and P. D. Coleman, "Design and evaluation of an *S*-band rebatron," *J. Appl. Phys.*, vol. 28, pp. 936–944; September, 1957.

[61] P. D. Coleman, "Theory of the rebatron—a relativistic electron bunching accelerator for use in megavolt electronics," *J. Appl. Phys.*, vol. 28, pp. 927–935; September, 1957.

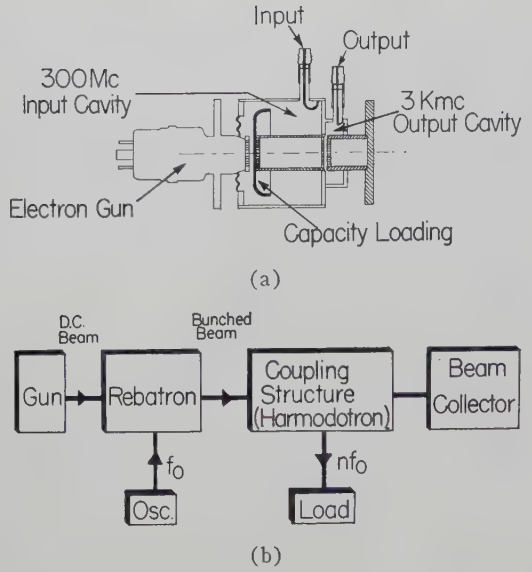

Fig. 24—Frequency multiplication by means of an electron beam. (a) Schematic diagram of a frequency-multiplier klystron. (b) Megavolt electronics system.

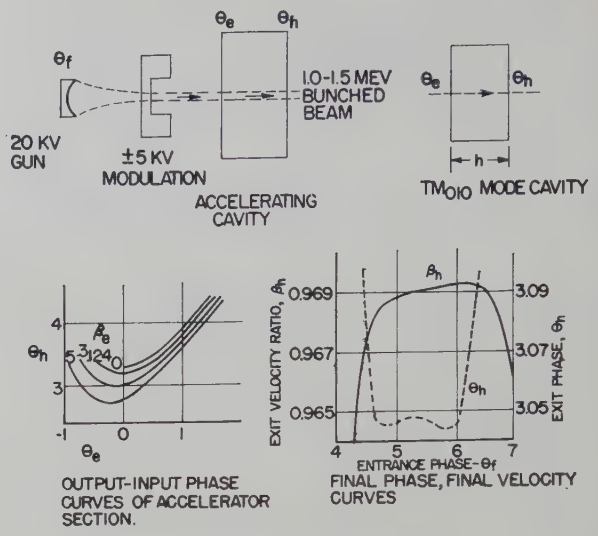

Fig. 25—*S*-band rebatron.

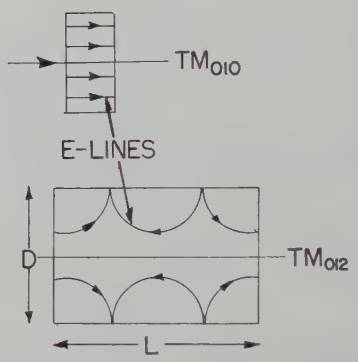

Fig. 26—TM_{0mn} modes for metal cylindrical cavity.

rebatron) as shown in Fig. 25. However, since the electron dynamic equations are nonlinear at relativistic velocities, the velocity-modulation and acceleration process is drastically altered so that it is possible to produce a more tightly bunched beam having very little resultant velocity modulation. This will lead to a traveling current-wave of the form where, ideally

$$i(t, z) = \sum_{n=0}^{\infty} I_n \cos 2\pi f_0 n(t - z/v) \qquad (25)$$

with $I_n \neq I_n(z)$, $v \simeq c$ (the velocity of light), and for perfect bunching

$$i = N\delta(t - t'). \qquad (26)$$

$I_n = 2I_0$ for all n. δ is the Dirac delta function and N, the number of electrons in the bunch.

The output-input phase curves of Fig. 25 give a quantitative indication of the bunching capability of the TM_{010} mode accelerating cavity as a function of the input velocity. These curves are computed for constant entrance velocity ratio, β_e, a condition which is easily realized in practice but which will not yield the desired delta function current and delta function velocity distribution. These characteristics require that β_e be a specified function of the input phase, θ_e, and hence the need for a suitable prebunching system arises. The final phase, final velocity curves which appear in Fig. 25 describe the performance of the over-all rebatron system for a typical set of parametric values.

Megavolt electronics techniques lead to a much higher harmonic content beam than in the klystron multiplier because of better bunching methods and because the bunching forces can be made large compared to the debunching forces. Also, the magnetic force at relativistic velocities "pinches" the beam in the transverse direction to aid in keeping it from spreading.

Assuming that an electron beam of the form given by (25) could be produced, how does this circumvent the problems of conventional electron tubes? First, the cathode and starting current density problem is eliminated since the systems to be considered are not self-excited. Furthermore, by using large gun voltages ($>10^4$ volts), it is not too difficult to produce convergent beams having large current densities.

Second, a beam velocity approaching the velocity of light, c, makes it feasible to couple to higher order modes of a resonant structure,[62,63] thereby greatly increasing the dimensions for the same resonant frequency. For example, take a metal cylindrical cavity operating in the TM_{0mn} modes as shown in Fig. 26. The diameter D, the length L, and the resonant wavelength λ_0 are related by

$$\left(\frac{D}{\lambda_0}\right)^2 = \left(\frac{r_{0m}}{\pi}\right)^2 + \left(\frac{nD}{2L}\right)^2 \qquad (27)$$

[62] P. D. Coleman and M. D. Sirkis, "The Harmodotron—a beam harmonic, higher order mode device for producing millimeter and submillimeter waves," *J. Appl. Phys.*, vol. 26, pp. 1385–1386; November, 1955.

[63] M. D. Sirkis and P. D. Coleman, "The Harmodotron—a megavolt electronics millimeter wave generator," *J. Appl. Phys.*, vol. 28, pp. 944–950; September, 1957.

where r_{0m} is the mth root of the Bessel function of the first kind, and n is an integer. Obviously as r_{0m} and/or n become arbitrarily large, so do D and L. The phase velocity v_p associated with the structure is given by

$$(v_p/c)^2 = 1 + (2Lr_{0m}/n\pi D)^2 \tag{28}$$

and the beam coupling coefficient k_+ by

$$k_+ = \frac{1}{2}\frac{\sin\frac{\omega L}{2}\left(\frac{1}{v}-\frac{1}{v_p}\right)}{\frac{\omega L}{2}\left(\frac{1}{v}-\frac{1}{v_p}\right)} = \frac{1}{2}\left[\frac{\sin\frac{n\pi}{2}\left(\frac{v_p}{v}-1\right)}{\frac{n\pi}{2}\left(\frac{v_p}{v}-1\right)}\right]. \tag{29}$$

An efficient exchange of energy will be possible when $v \rightarrow c$. For example, consider a silver TM_{018} mode cavity driven by a beam whose velocity v is $0.95c$. It can be shown for $D/L=0.6$ that the power generated for a harmonic beam current I_n is given by

$$P(\text{watts}) \simeq 3000[I_n(\text{amps})]^2[\lambda_0(\text{mm})]^{1/2}. \tag{30}$$

For $\lambda_0=1$ mm and $I_n=0.1$ amp, then $P\simeq 30$ watts.

Heat dissipation problems are eliminated since the beam passes directly through the higher order mode cavity with little interception of current. Circuit losses have not been eliminated but the Q of the structure has been greatly increased by going to higher order modes.

Megavolt electronics[64,65] provides other approaches to the millimeter wave generation problem based on the use of the Doppler effect[66–68] and Cerenkov effect.[69] In each of these cases, the tightly bunched, relativistic beam can be used to excite coupling structures which are large compared to the wavelength.

It would appear that bunched, megavolt beams represent the most high-power and most nonlinear element yet suggested for frequency multiplication. A frequency multiplication of the order of 50 to 100 should be practical using megavolt electronics techniques. With the development of good, practical X-band (or possibly K-band) bunching accelerators, wavelengths well below 1 mm are feasible. This technique, however, does lead to a pulsed rather than a CW source of radiation.

[64] P. D. Coleman, Quart. Reps. on Contract AT(11-1)-392, Elec. Eng. Res. Lab., University of Illinois, Urbana, Ill.; 1956–58.
[65] K. B. Mallory, Quart. Reps. on Contract DA-36-039 sc-72785, W. W. Hanson Lab. of Physics, Microwave Lab., Stanford, Calif., 1958.
[66] P. D. Coleman, "Generation of millimeter waves," Ph.D. dissertation, Dept. of Physics, M.I.T., Cambridge, Mass.; 1951.
[67] H. Motz, "Application of the radiation from fast electron beams," *J. Appl. Phys.*, vol. 22, pp. 527–535; May, 1951.
[68] H. Motz, W. Thon, and R. N. Whitehurst, "Radiation by fast electron beams," *J. Appl. Phys.*, vol. 24, pp. 826–833; July, 1953.
[69] M. Danos and H. Lashinsky, "Millimeter wave generation by Cerenkov radiation," IRE Trans. on Microwave Theory and Techniques, vol. MTT-3, pp. 21–22; September, 1954.

Ferrites

The application of an RF magnetic field to a magnetized ferrite results in the precession of the magnetic moments of the unbalanced electron spins. For the lossless infinite medium, the equation of motion of a system with angular moment $\overline{J}$ and magnetic moment $\overline{M}$ in a magnetic field $\overline{H}$ is[70]

$$\frac{d\overline{J}}{dt} = \overline{M} \times \overline{H}. \tag{31}$$

But since $\overline{M}$ and $-\overline{J}$ are proportional to each other

$$\overline{M} = \gamma\overline{J} = -\frac{ge}{amc}\overline{J} \tag{32}$$

where γ is the magnetomechanical ratio of the unpaired electrons, (31) can be written as

$$\frac{d\overline{M}}{dt} = \gamma\overline{M} \times \overline{H}. \tag{33}$$

Let

$$\overline{M} = \bar{k}M_s + \bar{m} \quad \text{with} \quad |\overline{M}| = M_s \tag{34}$$

and

$$\overline{H} = \bar{k}H_0 + \bar{h} \tag{35}$$

where M_s is the saturation magnetization, $\bar{m}$ and $\bar{h}$ are the time varying components, and H_0 is the static magnetic field (see Fig. 27). If the expressions for $\overline{M}$ and $\overline{H}$ from (34) and (35) are substituted into (33) the solution, neglecting cross product terms, is

$$m_x = \left[\frac{\gamma^2 H_0 M_s}{\gamma^2 H_0^2 - \omega^2}\right] h_x - \left[\frac{\gamma M_s}{\gamma^2 H_0^2 - \omega^2}\right]\frac{dh_y}{dt} \tag{36}$$

$$m_y = \left[\frac{\gamma^2 H_0^2 M_s}{\gamma^2 H_0^2 - \omega^2}\right] h_y + \left[\frac{\gamma M_s}{\gamma^2 H_0^2 - \omega^2}\right]\frac{dh_x}{dt} \tag{37}$$

or

$$m_x = \alpha h_x - \beta\frac{dh_y}{dt} \tag{38}$$

and

$$m_y = \beta\frac{dh_x}{dt} + \alpha h_y \tag{39}$$

with

$$\frac{dm_z}{dt} = 0. \tag{40}$$

If second-order terms are retained, the solution for m_z gives

$$\frac{dm_z}{dt} = \gamma(m_x h_y - m_y h_x) \tag{41}$$

[70] D. Polder, "On the theory of ferromagnetic resonance," *Phil. Mag.*, vol. 40, p. 99; 1949.

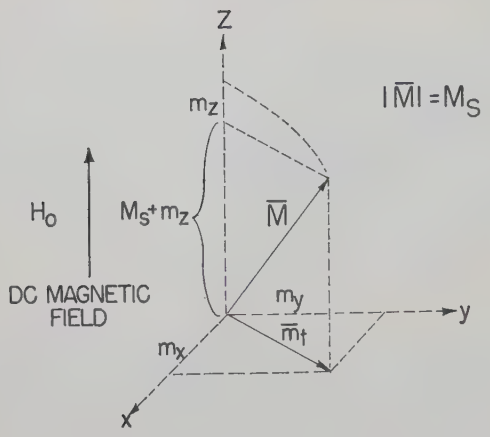

Fig. 27—Frequency doubling in ferrites.

or, using (38) and (39) and then integrating, the value of m_z is given by

$$m_z = -\frac{\gamma\beta}{2}(h_x^2 + h_y^2) + C. \tag{42}$$

The constant of integration C can be obtained from the condition $|\overline{M}| = M_s$, which for the case $m_x^2 + m_y^2 \ll m_s^2$ gives

$$m_z \simeq -\frac{m_x^2 + m_y^2}{\equiv 2M_s}. \tag{43}$$

If

$$h_x = A_1 \sin \omega t \tag{44}$$

$$h_y = A_2 \sin (\omega t + \Delta), \tag{45}$$

then the time varying part of m_z becomes,

$$m_z(\mathrm{RF}) = -\frac{\gamma^2 M_s}{4(\gamma^2 H_0^2 - \omega^2)} D \sin (2\omega t - \delta) \tag{46}$$

where

$$D \sin \delta = A_1^2 + A_2^2 \cos 2\Delta \tag{47}$$

$$D \cos \delta = A_2^2 \sin \Delta 2. \tag{48}$$

Eq. (46) shows that the z component of magnetization has a component oscillating at frequency $2w$ hence the ferrite will radiate an electromagnetic wave of frequency $2w$. Actually the magnetization has still higher-order terms since only the second-order terms have been retained to obtain (46).

Ayres, Melchor, and Vartanian[71,72] have investigated frequency doubling[73] in ferrites from X to K band using the experimental arrangement shown in Fig. 28(a). The peak power output vs. the peak power input is given in Fig. 28(b) which indicates the ferrite is operating according to a 1.8 power law. From (42) one would expect a square-law device. The deviation from square law suggests some of the energy is being converted to a higher-order harmonic.

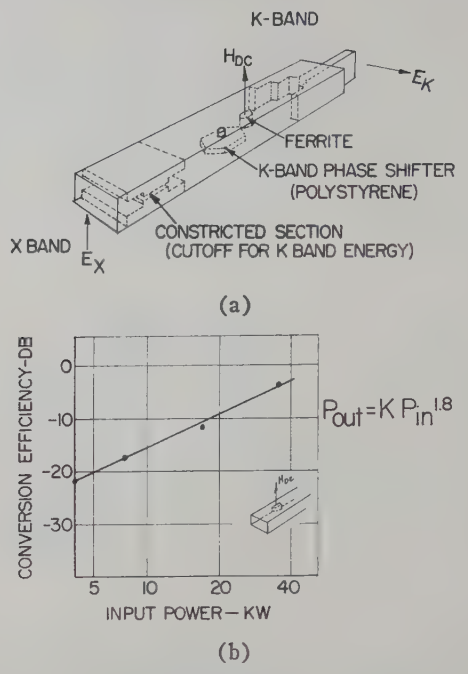

Fig. 28—Frequency doubling in ferrites. (a) Ferrite frequency doubler from X to K band (Melchor, Ayres, and Vartanian). (b) Conversion efficiency (half disk of ferrite against side wall).

An important feature of the ferrite doubler is its high peak power handling capacity and conversion efficiency (the order of -7 db) at these high pulsed power levels.

Parametric Amplifiers

It is well known that one can obtain gain with a modulator as illustrated in Fig. 29(a). Here the signals from the pumping oscillator at frequency f_p and the signal source at frequency f_s are mixed in a variable reactance to generate sidebands at frequencies $f_p \pm f_s$. It is possible for the sidebands to have more power than the signal source. Hence, if a demodulator is used, one could get out an amplified signal at f_s.

In the parametric amplifier,[74,75] the power supplied by the local oscillator is directly converted to signal power at the signal frequency as illustrated in Fig. 29(b). The energy required for amplification in both amplifiers is derived from the pumping oscillator.

The principle of operation of the ferrite parametric amplifier is as follows. First the pump frequency, f_p, and the signal frequency, f_s, are mixed in the ferrite to produce a magnetization varying at the idling frequency $f_i = f_p - f_s$. This magnetization excites the idler circuit into oscillation. Next the idler frequency, f_i, and the pump frequency, f_p, mix in the ferrite to produce a second magnetization varying at the signal frequency. If the signal derived from this magnetization is in phase with the initial signal, amplification can result.

[71] W. P. Ayres, P. H. Vartanian, and J. L. Melchor, "Frequency doubling in ferrites," *J. Appl. Phys.*, vol. 27, pp. 188–189; February, 1956.

[72] J. L. Melchor, W. P. Ayres, and P. H. Vartanian, "Microwave frequency doubling from 9 to 18 kmc in ferrites," Proc. IRE, vol. 45, pp. 643–646; May, 1957.

[73] J. E. Pippin, "Frequency doubling and mixing in ferrites," Proc. IRE, vol. 44, pp. 1054–1055; August, 1956.

[74] H. Suhl, "Theory of the ferromagnetic microwave amplifier," *J. Appl. Phys.*, vol. 28, p. 1225; November, 1957.

[75] M. T. Weiss, "A solid-state microwave amplifier and oscillator using ferrites," *Phys. Rev.*, vol. 107, p. 317; July, 1957.

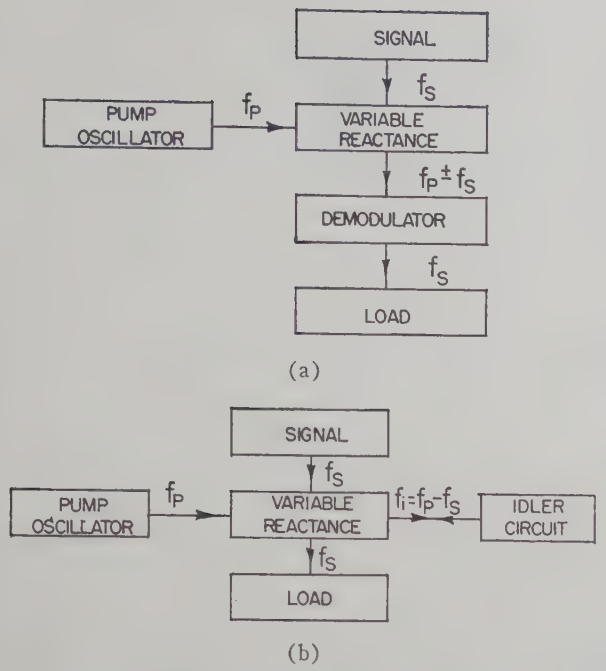

Fig. 29—Block diagrams of amplifiers. (a) Magnetic or dielectric amplifier. (b) Parametric amplifier.

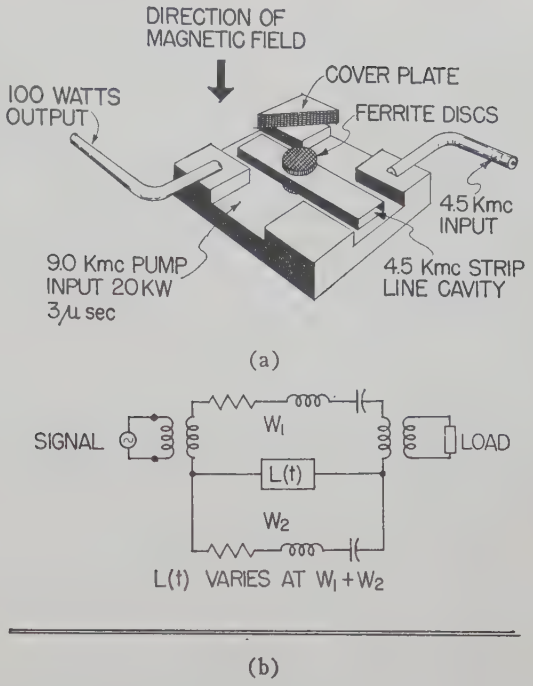

Fig. 30—Solid-state oscillator. (a) M. T. Weiss, "Solid-state microwave amplifier and oscillator using ferrites," *Phys. Rev.*, vol. 107, p. 317; July, 1957. (b) H. Suhl, "Proposal for a ferromagnetic amplifier in the microwave range," *Phys. Rev.*, vol. 107, p. 384; April, 1957.

Three types of operation of the parametric ferrite amplifier may be considered: the magnetostatic, the semistatic, and the electromagnetic. To describe these ways to use a ferrite, one must consider the magnetostatic modes.[76] When the ferrite sample is small compared to an electromagnetic wavelength in the material, propagation effects may be neglected, so that Maxwell's equations become

$$\nabla \times \bar{h} = \nabla \cdot (\bar{h} + 4\pi\bar{m}) = 0. \tag{49}$$

Using

$$\overline{M} = \bar{k}M_0 + \bar{m}\epsilon^{j\omega t} \qquad \overline{H} = \bar{k}H_i + \bar{h}\epsilon^{j\omega t} \tag{50}$$

in the torque equation

$$\frac{d\overline{M}}{dt} = \gamma\overline{M} \times \overline{H} \tag{51}$$

the linear approximation becomes

$$j\omega\bar{m} = \gamma[\bar{k} \times (M_0\bar{h} + H_i\bar{m})]. \tag{52}$$

The solution of (49) and (52), together with boundary conditions, determine the modes of $\bar{m}$ and $\bar{h}$ along with their characteristic frequencies. These modes are called magnetostatic modes. Moreover, their frequencies occupy a limited range on a frequency scale. For a spheroid, for example,

$$\gamma(H_0 - N_z M_0) \leq \omega \leq \gamma(H_0 + 2\pi M_0). \tag{53}$$

In the magnetostatic mode of operation, the pump frequency ω_p is chosen equal to the uniform precession mode γH_0. Since there is coupling between the uniform precession mode and the other magnetostatic modes, any two pairs whose frequencies add up to ω_p will be excited. However, a load can only couple to a small number of these modes so that the power supplied at the pumping frequency would be dissipated as heat in the many unloaded modes, making this type of operation impractical.

In the semistatic type of operation, H_0 is adjusted so that no two magnetostatic mode frequencies add up to the precession frequency. Here the ferrite could be placed in a resonant cavity tuned to resonate at either ω_s or $\omega_p - \omega_s$. One magnetostatic mode is used to supply the other needed circuit at frequency $\omega_p - \omega_s$ or ω_s.

In the electromagnetic type of operation, a doubly resonant cavity is made to supply both low-frequency circuits. The pump frequency is at the uniform precession frequency.

Fig. 30 shows a parametric amplifier made by Weiss.[75] A strip line resonator was used, with coupling by means of coaxial line probes. Both the idler and signal frequencies were made equal at 4.5 kmc. With a peak pumping power of 20 kw, the device oscillated at a peak output of 100 watts, *i.e.*, 23 db down.

A recent investigation[77] has shown that microwave amplification using ferromagnetic materials does not necessarily require the local oscillator or pump frequency to be greater than the signal frequency. New devices requiring four frequencies for signal mixing rather than the usual three, make it possible to obtain

[76] L. R. Walker, "Magnetostatic modes in ferromagnetic resonance," *Phys. Rev.*, vol. 105, pp. 390–399; January, 1957.

[77] C. L. Hogan, R. L. Jepsen, and P. H. Vartanian, "New type of ferromagnetic amplifier," *J. Appl. Phys.*, vol. 29, pp. 422–423; March, 1958.

amplification at a frequency higher than the pump frequency. In addition, such a device can be made to act as a microwave oscillator capable of generating a frequency up to twice the frequency of the local oscillator.

It is seen that the parametric amplifier or oscillator is also a high pulsed power device. However, the structure shown in Fig. 30(a) is not easily made, especially in the low millimeter range. Hence, it may be desirable to try the semistatic type of operation if much higher frequencies are desired.

Other Types of Nonlinear Elements

Nonlinear Capacity--Reverse Biased Semiconductor Junction: A semiconductor *p-n* junction[78] is known to have a nonlinear capacity C shunting the barrier resistance. Its value is given by

$$C = \epsilon A \left[-(V_0 + V) \frac{2\epsilon\mu_n}{\sigma_n} \right]^{-1/2} f. \tag{54}$$

where

ϵ = permittivity of semiconductor,
A = area,
V_0 = contact voltage,
V = applied bias voltage,
μ_n = mobility of electrons in semiconductor,
σ_n = conductivity of semiconductor.

All units are in the rationalized MKS system.

It is seen from (54) that a semiconductor junction, when biased in the reverse (nonconducting) direction, is a capacitance which can be varied by the bias voltage. The Q of this condenser is given by $1/\omega Cr$ where r is the series resistance of the junction.

Giacoletto and O'Connell[78] have recently described a diode having a nominal Q of 17 at 500 mc. In one of their better units a Q of 36 was obtained. Over the bias range 0 to -16 volts, the capacity varied from about 140 to 25 μfd.

It would appear that biased diodes may have applications in parametric amplifiers and possibly frequency multipliers.

Ferroelectrics: If low-loss ferroelectric materials could be found, one has reason to believe that electric analogs of the ferrite multipliers and parametric amplifiers could be made. Higa[79] has suggested the circuit shown in Fig. 31 as a ferroelectric frequency multiplier using barium titanate. He assumes a relation between $\overline{E}$ and $\overline{D}$ of the form

$$E_x = [a + b(D_x^2 + D_y^2)]D_x \tag{55}$$

$$E_y = [a + b(D_x^2 + D_y^2)]D_y. \tag{56}$$

Using these relations in the circuit equation, he derives the following nonlinear Mathieu equation for D_y

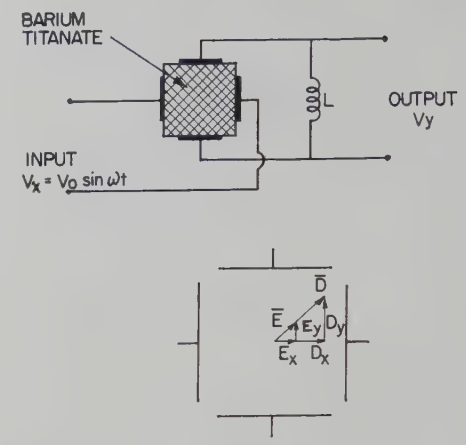

Fig. 31—Ferroelectric frequency multiplier circuit.

$$\frac{d^2 D_y}{dt^2} + (\alpha + \beta \cos 2\omega t) D_y = 0 \tag{57}$$

where, if the constants α and β satisfy certain conditions, the solution for D_y is given by

$$D_y = C_1 \cos \omega t + C_3 \cos 3\omega t + \cdots. \tag{58}$$

Under other conditions, Higa further shows that by tuning the inductor L to resonate with the capacity at a harmonic of the driving frequency, both odd and even harmonics can be produced. In its present form, the device is limited by the "mild" nonlinearities of available ferroelectrics.

Harmonic Generation in Microwave Tubes

In attempting to overcome the physical size limitations on resonators, one possible solution for conventional tubes is to try to generate harmonics of the highest fundamental frequency for which a tube can be constructed. Bernier and Leboutet[80] have reported on harmonics from klystrons and Gourary[81] and others at Columbia University have been working on harmonic generation in magnetrons.

Bernier and Laboutet indicated that it was possible to construct a reentrant klystron cavity wherein one or more of the higher-order mode frequencies, f_n, could be made an exact multiple of the fundamental frequency f_1. Using a 4.08-cm klystron, they reported that they obtained harmonics as large as the 24th at 1.7 mm with the power output the order of a few microwatts.

The group at Columbia[9] has been working on harmonic generation in magnetrons since 1949. Their original idea was as follows. In a magnetron operating in its fundamental π mode, the space charge rotating on the interaction space resembles a rimless wheel with spokes.

[78] L. J. Giacoletto and J. H. O'Connell, "A variable-capacitance germanium junction diode for UHF," *RCA Rev.*, vol. 17, pp. 68–85; March, 1956.

[79] W. H. Higa, "Theory of nonlinear coupling in a novel ferroelectric device," *J. Appl. Phys.*, vol. 27, pp. 775–777; July, 1956.

[80] J. Bernier and H. Leboutet, "Sur la possibilité d'obtenir des ondes entretenues très courtes en utilisant un klystron reflex donnant de l'energie sur des fréquences harmoniques d'ordre elève de l'oscillation fondamentale," *Comp. Rend.*, no. 4, pp. 797–798; October, 1954.

[81] B. S. Gourary, "The Theory of Harmonic Generation in Magnetrons," Rad. Lab., Columbia University, New York, N. Y., Quart. Reps.; June 30, 1949 to December, 1957.

A spacial Fourier analysis of such a charge cloud shows that it contains components of various angular symmetries, all traveling at the same angular velocity. If one of the modes of the cavity contains a similar Fourier component, it will be driven by the space charge. Specifically, if a π mode of a higher frequency is made to have a Fourier component of the proper symmetry traveling at the same angular velocity as the space charge, then that harmonic π mode will be excited.

Bernstein and Kroll at Columbia Radiation Laboratory have been studying harmonic generation in magnetrons using their X-band XHI anodes. In their recent 1957 quarterly reports, these tubes have given a second harmonic power output ranging from 9 to 46 kw with efficiencies of the order of 4 to 12 per cent. Some work has also been carried out on third harmonic generation.

The Ultramicrowave Group at the University of Illinois has tried feeding klystron tubes into waveguides tapered down so that only harmonics of the fundamental can propagate. In particular, it was found that the Amperex DX151 tube gave sufficient 2-mm signals for most low-level test purposes.

Conclusion

The representative, but limited number, of specific examples of conventional microwave tubes, briefly discussed in this paper, has indicated that the present frequency frontier is in the neighborhood of wavelengths of 2 to 3 mm. The fact that all of the tube types are plagued with essentially the same fundamental problems and limitations strongly suggests that one has indeed reached a practical limit in the low millimeter range.

Elliott[82] has indicated that for tubes employing resonant cavities, the frequency limit depends chiefly on the ac beam current density and the noise level in the resonant structure. To put pessimistic numbers in Elliott's current inequality criterion also suggests that experimenters have just about reached the frequency limit with present techniques.

However, with the fabulous tube art and techniques that have been built up, one can expect conventional tubes to make a last-ditch stand by such methods as harmonic generation and subminiature, watchmaker approaches. Whether these techniques can extend the frequency by more than a factor of two to three remains to be seen. It is certain that the present difficulties are taxing the enormous resourcefulness of the people in the electron tube field.

The present status of low millimeter and submillimeter wave generation would appear to be that no ideas for a prime, self-excited, coherent source exist. While it has not been proven that coherent sources in this frequency range are theoretically possible, workers in the field have an optimistic, intuitive feeling that such sources can be made. However, until a "brilliant hunch" bears fruit, most efforts at the present time are directed toward frequency multiplication and conversion using conventional microwave tube sources as driver elements. It may be that the final sources for the submillimeter range will be based on some frequency conversion principle, rather than the dc input rf output energy conversion method used in conventional tubes. It is the author's opinion that for microwave engineers to make progress on this problem they will have to have a good understanding of solid-state electronics.

Megavolt electronics, while not classified here as a conventional electron tube technique, appears to offer the most proven promise of any electronic frequency multiplying method for invading the submillimeter range with a pulsed, coherent source of radiation. Multiplication of the fundamental frequency by a factor of 50 or more is a practical possibility. Hence the development of practical X-band or K-band bunching accelerators would place megavolt electronics techniques in a very competitive position with regard to frequency multiplying devices. This is particularly true with respect to theoretical peak power capabilities at high harmonic frequencies. The words megavolt electronics and bunching accelerators might, off-hand, cause one to imagine large machines and bulky devices limited only to laboratory experimental uses. In rebatrons, fed by a magnetron-ferrite isolator system, the apparatus is only two to three times the size of the magnetron being used, the bulk of the equipment being simply that of the magnetron power supply.

The solid-state electronics approaches, such as ferrite multipliers and oscillators, have not as yet produced frequencies which are unobtainable by electron tubes. Also, at the present time, the ferrite is usually placed in a more or less complicated microwave circuit which is fed by a high pulsed power tube. Hence, from a practical point of view, one might say that one has neither escaped nor circumvented present difficulties facing microwave tubes and/or techniques. This present aspect of the problem may not be important in the long run since the work in this area is relatively new. Triode tubes existed for a long time before klystrons, backward-wave oscillators, etc., were discovered. One is very optimistic, however, that as more is learned about masers, ferrites, ferroelectrics, parametric oscillators, spin resonances, etc., an idea for a self-excited source will eventually emerge.

Work on low millimeter wave components, detectors, etc., is handicapped at the moment by the lack of suitable signal sources to make tests. Therefore, most of the techniques being used are largely scaled-down versions of the tried and proven microwave methods. However, while it is believed that microwave methods may be extended to higher frequencies than microwave tubes, new techniques must also be forthcoming to handle these new ranges of frequencies.

[82] R. S. Elliott, "Some limitations on the maximum frequency of coherent oscillations," *J. Appl. Phys.*, vol. 23, pp. 812–818; August, 1952.

Millimeter-Wave Generation Experiment Utilizing Ferrites*

WESLEY P. AYRES†

Summary—It is estimated that at least 50 watts of peak power at 2-mm wavelength has been generated from 4-mm excitation by harmonic generation in ferrites. This experiment is similar to the frequency doubling previously reported from 9 to 18 kmc, except for some differences in optimum geometry and material. A wide range of ferrites has been used, as well as garnets and permanent magnet type materials. In carrying out this experiment it has been necessary to develop components such as a 4-mm high-power isolator, a calorimeter for measurement of the 4-mm and 2-mm power, and numerous 2-mm waveguide components.

Second Harmonic Generation

In previous work[1,2] it was shown that the equation of motion for uniform precession of the spin system in a magnetized ferromagnetic material, yields the second harmonic component

$$4\pi \dot{m}_{z,2\omega} \doteq -\tfrac{1}{2}j\kappa\gamma(h_x^2 + h_y^2) \qquad (1)$$

where the dc magnetic field is in the z direction, κ is the off diagonal element of the susceptibility tensor, γ is the gyromagnetic ratio, and h_x, h_y are the applied RF fields at the fundamental frequency. The solution of (1) is obtained simply as

$$4\pi m_{z,2\omega} = -\frac{\kappa\gamma}{4\omega}(h_x^2 + h_y^2) \qquad (2)$$

where ω is angular frequency. If one analyzes (2), disregarding geometry factors, one sees that the maximum value of the second harmonic magnetization as a function of dc magnetic field occurs where the magnitude of κ is a maximum, and this maximum is

$$|\kappa|_{\max} = \frac{4\pi M_s}{\Delta H} \qquad (3)$$

where $4\pi M_s$ is the saturation magnetization of the material and ΔH is the ferromagnetic resonance linewidth.

Eq. (3) indicates the dependence of doubling efficiency upon material properties. In a practical experiment one is concerned with other parameters, such as geometry and size. These will tend to obscure the details of the dependence indicated in (3), since the geometries are not simple and the sizes are large compared with a wavelength in the sample. However, one would expect the experimental results to agree generally with the prediction of (3). This is discussed later with the experimental results.

Experimental Work

In past experiments harmonic generation has been observed from S band to C band, using a cavity geometry.[1] This experiment was characterized by a great deal of tuning difficulty and a very low conversion efficiency. In a second experiment, observations were made from X band to K band in a waveguide geometry.[2] This experiment was characterized by relative freedom from tuning difficulties and by a very high conversion efficiency. Also, in this experiment there is the possibility, in fact the probability, that a considerable amount of power was generated in harmonics higher than the second. The objective of the present experiment is to generate 2-mm wavelength energy from 4-mm energy and to study further the factors affecting the conversion efficiency. The experimental arrangement is very nearly the same as the previous waveguide experiment, and is shown in Fig. 1. Due to practical considerations there is

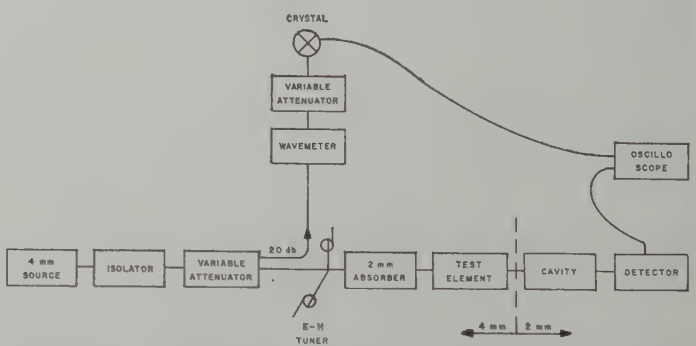

Fig. 1—Measurement block diagram for harmonic generator.

no constricted section to reflect 2-mm energy generated in the test section and propagating toward the 4-mm source back toward the 2-mm output. Instead, resistance material is placed in the H plane of the 4-mm waveguide to absorb the 2-mm energy which is propagating toward the 4-mm source. If this were not done, part of this 2-mm energy, in some unknown phase, would be reflected back toward the 2-mm output and might be adding to or subtracting from the output. Presumably one-half of the generated 2-mm energy is lost in this way.

A large number of different materials and geometries have been tested in the harmonic generator. Materials

* Manuscript received by the PGMTT, July 3, 1958; revised manuscript received, August 27, 1958. Work supported by the U. S. Army Signal Corps under Contract No. DA 36-039 SC-73278.

† Microwave Engineering Labs., Inc., Palo Alto, Calif.

[1] W. P. Ayres, P. H. Vartanian and J. L. Melchor, "Frequency doubling in ferrites," *J. Appl. Phys.*, vol. 27, pp. 188–189; February, 1956.

[2] J. L. Melchor, W. P. Ayres and P. H. Vartanian, "Microwave frequency doubling from 9 to 18 kmc in ferrites," Proc. IRE, vol. 45, pp. 643–646; May, 1957.

with high magnetizations, narrow linewidths, and high anisotropy fields were particularly sought for these experiments. In Table I the materials tested are shown in the order of their $4\pi M_s/\Delta H$ values. The output as shown in Table I is the output in millivolts from the 2-mm crystal detector. The $4\pi M_s/\Delta H$ values are estimated using values of each reported in the literature.

TABLE I
2-MM OUTPUT FROM VARIOUS MATERIALS

No.	Material	Output Millivolts	$4\pi M_s/\Delta H$
1)	Yttrium iron garnet single crystal	130	180
2)	Yttrium iron garnet polycrystalline	108	27
3)	General Ceramics Ferramic G	180	17
4)	General Ceramics Ferramic R-1	80	10
5)	Ferroxcube 104	80	10
6)	Ferroxcube 106	68	6
7)	Oriented Ferroxdure	7	2

Because of variations in these quantities from sample to sample, these values are not assumed to be accurate in detail for the samples used but only indicate the trend. All of the above measurements were made using the half-disk geometry shown in Fig. 2, except for the garnet single crystal, which was not shaped at all. The garnet's general shape resembled the half disk, but it was slightly smaller than the other samples and any shaping, it was felt, would only reduce the output. The table indicates a trend in agreement with that predicted by (3), with the exception of the large output given by Ferramic G. Considering only the true ferrites, numbers 3 through 6, about which more is known than for other materials, the agreement is good in detail; that is, the measured outputs vary in almost the same proportions as the $4\pi M_s/\Delta H$ values. The oriented high anisotropy materials are quite interesting to this study from the standpoint of the reduction in applied magnetic field necessary to reach resonance. However, the outputs from all of these materials tested are disappointingly low. This is probably because the material is not highly enough oriented, so that the linewidth is extremely large.

For one material a different geometry has given greater output than the half disk gave. This is the centered post shown in Fig. 3. Ferramic G in this geometry gave an output of 270 mv, the largest output observed up to this time. This same geometry has been tried for some of the other materials, but it has not given as large an output as has the half disk. Many other geometries have been tried, such as slabs in various places in the waveguide, rods and half-rods, and others, but they have not given nearly as good results as the two geometries discussed here. The reason for this is not understood. However, the fact that the output power is extremely sensitive to very small variations in dimensions of these geometries suggests the possibility that the ferrite may be acting as a resonant cavity at the

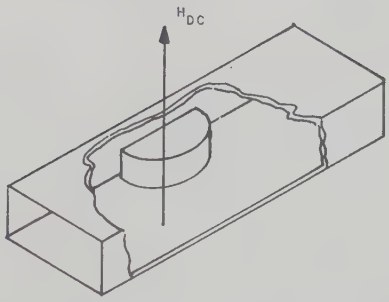

Fig. 2—Half-disk geometry. The disk height is about 60 per cent of the waveguide height, and the disk diameter is about two-thirds the waveguide width.

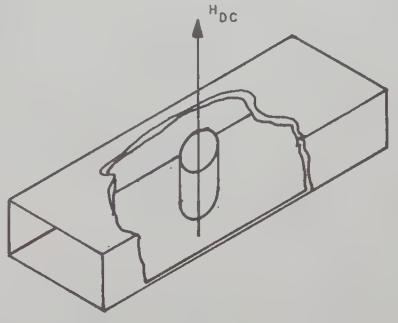

Fig. 3—Centered post geometry. The post diameter is about one-third the waveguide width, and the post height is about 90 per cent of the waveguide height.

4-mm wavelength. If so, it is possible that these geometries provide efficient coupling to the incident waveguide mode.

At the pulse repetition frequency (PRF) producing the maximum average power output, the measured 2-mm power was 0.5 mw average and 7 watts peak for the centered post of Ferramic G, which produces the largest 2-mm output. However, as shown in Fig. 4, the maximum peak power does not occur at the same PRF as the maximum average power. This is because the ferrite heats up as the average power is increased, and in this case reduces $4\pi M_s$ faster than it reduces ΔH so that the important ratio in (3) is reduced. This is not always the result one obtains.[2] From Fig. 4 we see that at a PRF of 30 cps the peak power is 13 watts. Actually, the data of Fig. 4 were taken using a crystal detector and the power scale determined by an average power measurement at the peak of the average power curve with the 2-mm calorimeter. Consequently, except at this point (the point of maximum average power output) the power scale may be inaccurate because the crystal was deviating from true square law response. If this is the case, it will have the effect of increasing the true power output at lower PRF's where the peak power is greater than at the PRF where the power was actually measured. This is because the deviation of the crystal from a square law response will be towards a linear response at higher peak power levels. One must bear in mind that there are a number of losses of 2-mm power before the energy reaches the calorimeter, and these losses have not been taken into account in the results shown in

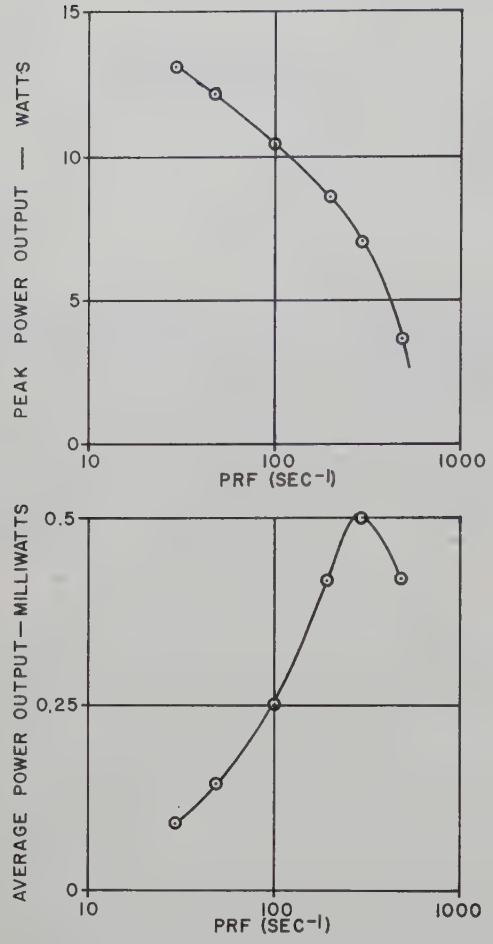

Fig. 4—Average power and peak power output as a function of the pulse repetition frequency.

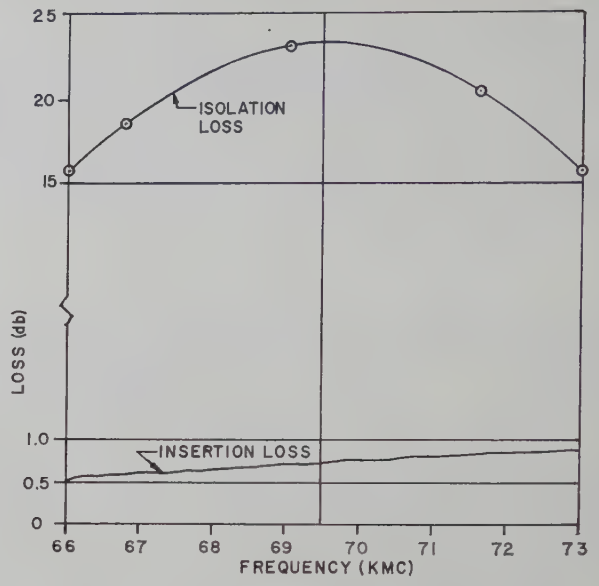

Fig. 5—Characteristics of 4-mm isolator. The input VSWR is below 1.20.

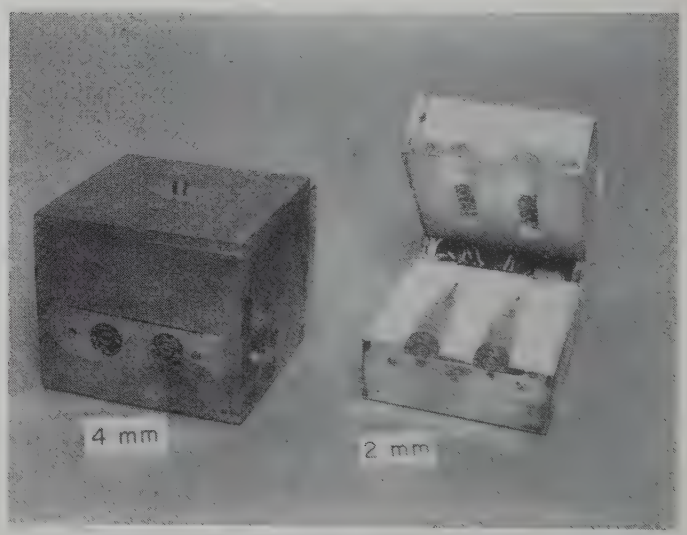

Fig. 6—Photograph of calorimeters for 4-mm and 2-mm wavelengths with 2-mm model opened to show internal construction.

Fig. 4. Half of the 2-mm energy is lost by propagation toward the 4-mm generator. Approximately half of the remainder is lost in the 2-mm transmission system and calorimeter input section. This indicates that the 2-mm energy generated is approximately four times that shown in Fig. 4 or a maximum peak power of 50 watts.

Millimeter Wave Components

During the course of this study a number of components had to be developed for the experiment. Among them is a high-power 4-mm isolator whose characteristics are shown in Fig. 5. The geometry of this isolator is of conventional high-power broad-band design[3,4] using a thin slab of ferrite against the broad wall of the waveguide, and next to it a slab of dielectric twice as thick as the ferrite. The major difference between this isolator and lower frequency models is the gyromagnetic material, which is polycrystalline oriented $BaFe_{12}O_{19}$. This material has an anisotropy field of 17 kilogauss, so that in the oriented form the applied field necessary for resonance is reduced by 17 kilogauss. Thus the magnet used for this isolator needs a field strength of only 12 kilogauss in the air gap.

A variable high-power attenuator was built by making an isolator with a moveable magnet whose position determines the insertion loss.

A 4-mm and a 2-mm calorimeter, shown in Fig. 6, were designed and constructed. In the 2-mm calorimeter the outer box is of aluminum and is filled with polyfoam for heat isolation. The waveguide input on the front is connected to a thin-walled waveguide made by milling down the walls of standard waveguide to 0.010-inch thickness. For about one inch behind the flange the waveguide is potted in an epoxy resin. In this length a $3\lambda_g/4$ slice of waveguide and resin is removed, a sheet of 0.001-inch teflon is placed over each end, and the slice is replaced in its original position separating the waveguide input from the calorimeter loads, so that heat transfer along the waveguide is minimized. The loads

[3] M. T. Weiss, "Improved rectangular waveguide resonance isolators," IRE Trans. on Microwave Theory and Techniques, vol. MTT-4, pp. 240–243; October, 1956.

[4] G. S. Heller and G. W. Catuna, "Measurement of ferrite isolation at 1300 mc," IRE Trans. on Microwave Theory and Techniques, vol. MTT-6, pp. 97–100; January, 1958.

are tapered graphite from a carpenter's marking pencil and they have copper electrodes electrodeposited onto the tip of the taper and the back of the load. These contacts enable dc connections to be made to the load so that dc power dissipated in the load can be used for calibration of the calorimeter. The two waveguide and load units in each calorimeter are identical, so that either one can be used as the active load and the other as the reference load. To measure the temperature of the active load and compare it with the reference load, there is a string of three small bead thermistors connected in series and cemented to each waveguide. The two thermistor strings are incorporated into a 1000 cps bridge in order to measure small temperature changes easily. The remaining bridge components are installed in the small compartment on the back of the outer box. The bridge is operated as a deflection instrument, calibration curves being made of bridge unbalance as a function of time for various dc power inputs to the graphite loads. Then millimeter wave power is measured by graphing the same function with a millimeter wave input. The calorimeters will accurately measure power levels as low as 4 mw for the 4-mm model, and 0.3 mw for the 2-mm model, without taking extreme precautions regarding temperature isolations.

A number of other more conventional waveguide components were designed and constructed for 2-mm operation, and it is of interest to note that despite the short wavelength no particular difficulty was experienced in obtaining reasonable operation. Of course, some mechanical modifications had to be made due to the small size of the waveguide; however, none of these was of major significance.

Conclusion

High-power 2-mm energy has been generated by a ferrite harmonic generator excited by a 4-mm source. However, more 2-mm energy could be generated by further refinements in the experimental system and by the use of better ferrite materials when they become available. The material property of most importance to harmonic generation is the ratio $4\pi M_s/\Delta H$. Millimeter wave isolators, calorimeters, and other components have been designed and constructed without encountering unexpected problems due to the short wavelengths.

Acknowledgment

The author wishes to acknowledge the continuing assistance of Drs. J. L. Melchor and P. H. Vartanian. He also wishes to thank R. Hosking for his excellent laboratory work, including the construction of most of the delicate components.

Some Characteristics of Dielectric Image Lines at Millimeter Wavelengths*

JAMES C. WILTSE†

Summary—**The attenuation characteristics of several dielectric image lines have been calculated for the frequency range extending from 24 to 100 kmc and have been checked experimentally at 35 and 70 kmc. To obtain low attenuation at these high frequencies, dielectric materials with little loss and small size of cross section are required, while low values of the dielectric constant are also desirable. The effects of the size and shape of the dielectric cross section and of low dielectric constant are treated separately. To find proper materials with low dielectric constants several new foam plastics were investigated. Three types were found suitable for image line use, and in fact, these plastics have such good electrical and physical properties that they should be useful in many microwave applications.**

A qualitative measure of field extent is given for several image lines at 35 or 70 kmc, and various image lines and associated components are discussed. A new type of image line, called the tape line, is described.

* Manuscript received by the PGMTT, June 10, 1958.
† Radiation Lab., The Johns Hopkins Univ., Baltimore, Md.

Introduction

IN THE frequency region above K band, dominant-mode rectangular waveguide has the important disadvantage of high attenuation. Fig. 1 shows the theoretical attenuation for several standard waveguides. Further disadvantages are small physical size and relatively low power handling ability. These undesirable properties have stimulated the study of other types of waveguides which might have improved characteristics. One type which appears to be satisfactory is circular metal waveguide propagating the TE_{01} mode. This type has low attenuation, but since it is not a dominant-mode waveguide, mode suppressors are required. This feature adds considerable complexity to the design and construction of components and sections of guide.

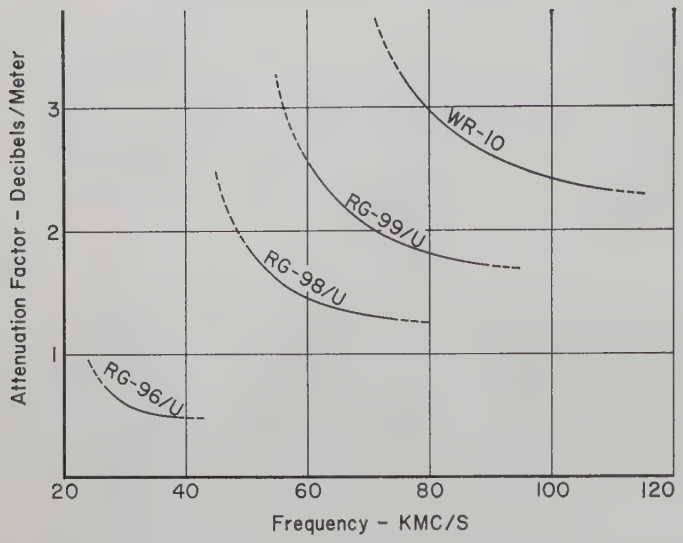

Fig. 1—Attenuation of several types of rectangular waveguide as a function of frequency.

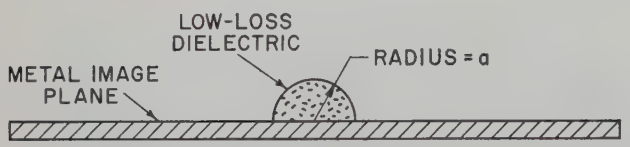

Fig. 2—Cross-sectional view of a dielectric image line.

Another waveguide which has such advantages as low attenuation, dominant-mode operation, and moderate physical size is the dielectric image line. This structure has the further advantages of being simple in design and easy to construct. Fig. 2 shows a sectional view of the dielectric image line. The cross section of the dielectric material need not be semicircular, but this is the only shape which has been mathematically analyzed and for which the field equations and propagation characteristics are fully known.

Prior to the present investigation many properties of image lines had been studied at K band[1] and at X band.[2] These studies included the construction of a variety of image line components and the measurement of losses in straight sections and bends. The present paper deals with the properties of image lines in the frequency region from 24 to 100 kmc.

Losses in a straight uniform section of image line are of two types: conduction loss on the image plane and dielectric loss. Explicit relations have been developed for the contributions to attenuation due to the dielectric and conduction losses when the dielectric has a semicircular cross section (see Appendix). From the information contained in these relationships it is possible to determine which parameters of an image line system should be changed in order to reduce the attenuation. For example, by the use of metals of high conductivity, such as copper or aluminum, the conduction loss may be made relatively small in most cases. Dielectric loss is a function of dielectric constant, loss tangent, and size and shape of the dielectric cross section. Customarily, low-loss plastics such as polystyrene or polyethylene have been used in image lines, and the sizes of the dielectrics have been adjusted to give either a desired attenuatuon or a specified binding of the wave (loose binding results in low loss and vice-versa). In the present study the effects of reduced size, low dielectric constant, and a shape of the cross section other than semicircular were considered separately and in that order.

Small Diameter Polystyrene Image Lines

As a first step in the design of low-loss image lines for use at millimeter wavelengths, values of attenuation were calculated for the case of a copper image plane and a semicircular polystyrene dielectric with a diameter of $\frac{1}{8}$ inch. This diameter was chosen because it appeared to be the smallest size polystyrene rod which could be obtained commercially at that time. The attenuation characteristics of the image line as a function of frequency are given in Fig. 3 where the contributions due to conduction loss (α_c) and dielectric loss (α_d) are shown separately. (In making these and other calculations, a conductivity of 5.8×10^7 mhos per meter was used for copper, while a dielectric constant of 2.56 and a loss tangent of 10^{-3} were assumed for polystyrene.) It is immediately obvious that this particular design is unsatisfactory, because of high attenuation, above 30 kmc.

The next step was to reduce the diameter of the polystyrene rod by turning it down in a lathe to $\frac{3}{64}$ inch, which is about as small as a size as is practicable. Calculated attenuation values for this size semicircular dielectric on a copper image plane are plotted as a function of frequency in Fig. 4. This image line has better attenuation characteristics than RG-98/U rectangular waveguide over most of the latter's normal operating range (50 to 75 kmc). Since this image line showed promise for use at millimeter wavelengths, a section of the line and some associated components (see Fig. 5) were built, tested, and found to give satisfactory performance at frequencies in the vicinity of 70 kmc. The semiparaboloid shown at the right in Fig. 5 is used to focus the guided wave onto a detector mounted in a small gap in the image line dielectric. A micrometer screw drive is provided to permit fine movement of the paraboloid in a direction parallel to the dielectric rod. This makes possible the adjustment of the focus position to give maximum signal from the detector. Further details of the detector are shown in Fig. 6. Much of the diagram is occupied by a drive screw mechanism which has the

[1] D. D. King, "Properties of dielectric image lines," IRE Trans. on Microwave Theory and Techniques, vol. MTT-3, pp. 75–81; March, 1955.

[2] D. D. King and S. P. Schlesinger, "Losses in dielectric image lines," IRE Trans. on Microwave Theory and Techniques, vol. MTT-5, pp. 31–35; January, 1957.

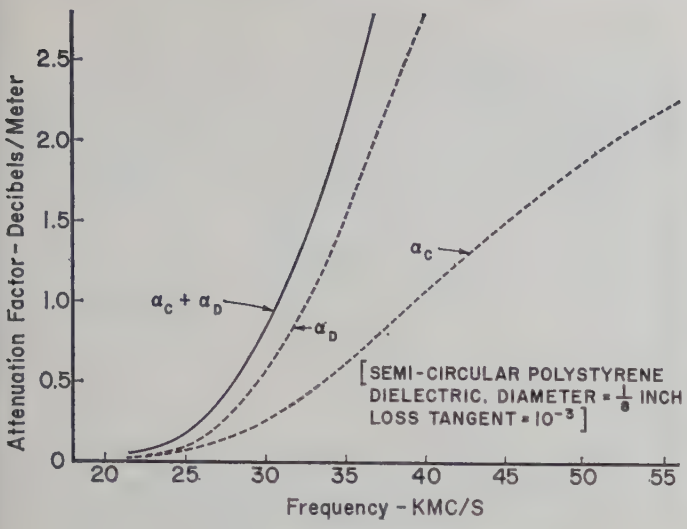

Fig. 3—Image line attenuation due to dielectric loss (α_d) and copper image plane loss (α_c).

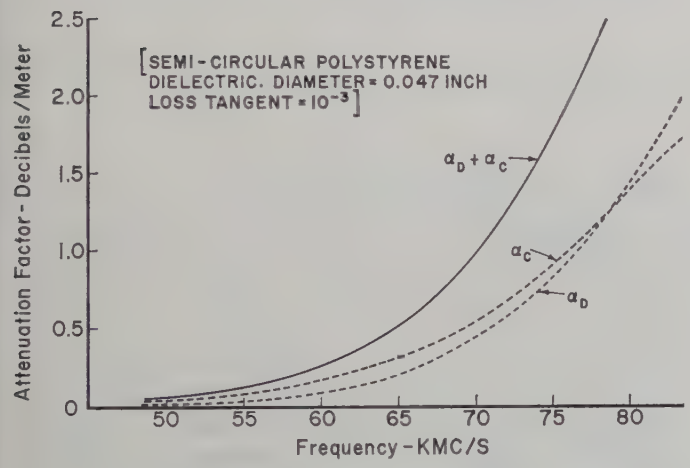

Fig. 4—Image line attenuation due to dielectric loss (α_d) and copper image plane loss (α_c).

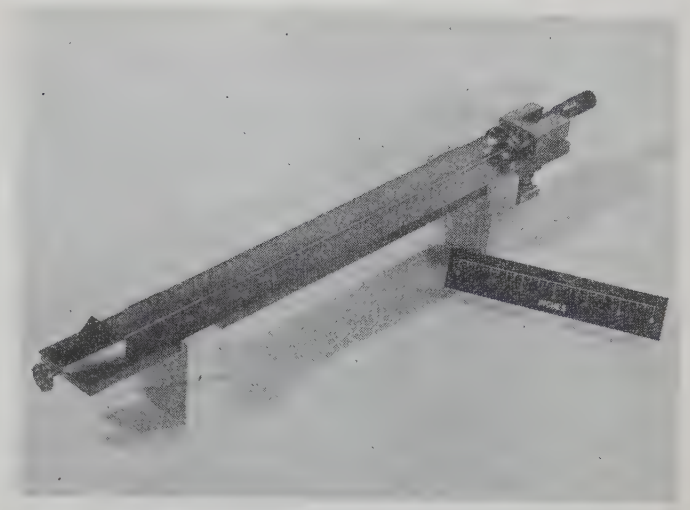

Fig. 5—Dielectric image line with launching horn and detector.

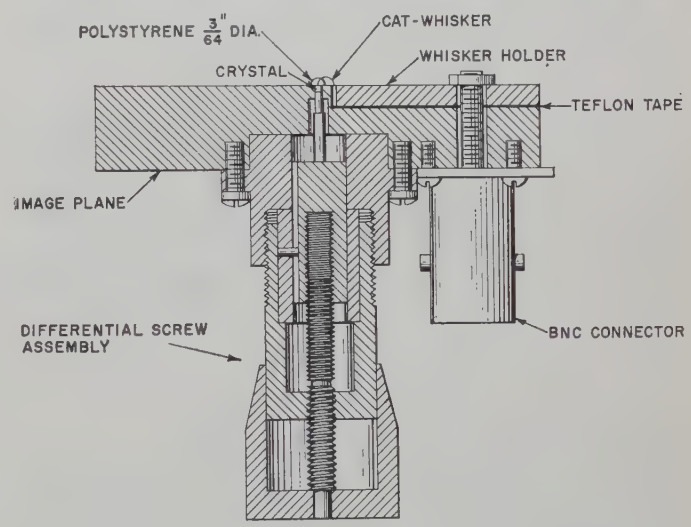

Fig. 6—Crystal detector mount for dielectric image line.

function of raising or lowering the silicon crystal at a very slow rate in order to make a proper contact with the tungsten cat-whisker. The whisker holder is a rectangular piece of metal cut from the image plane and insulated for dc purposes by means of the Teflon tape. The detected signal is taken out through the BNC connector. This detector operated satisfactorily at various frequencies in the range from 40 to 97 kmc.

Foam Polystyrene Image Lines

Above 70 kmc the $\frac{3}{64}$ inch diameter polystyrene image line has undesirably high attenuation. Since it is not practicable to reduce the dielectric size much further in order to obtain lower attenuation, the next step was to obtain low-loss plastics which have dielectric constants considerably lower than polystyrene.

Ordinary polyfoam has the requisite low loss and low dielectric constant, but it has a structure which is extremely nonuniform; cell sizes are appreciable fractions of a wavelength. However, some new foamed polystyrene products now are available which do have very small cell sizes (diameters on the order of 0.1 millimeter for one type), are easily machinable, and still retain the desired low loss, low dielectric constant properties.

Three such materials were selected for image line use. Because their properties had not been studied previously, it was necessary to determine the dielectric constant and loss tangent of each. Samples of the materials were placed in rectangular waveguide and a conventional shorted-line technique previously described by Montgomery[3] was used to measure the values necessary for calculation of the dielectric constant and loss tangent. Table I gives the results obtained for the frequency region from 30 to 40 kmc. In addition, a sample of Dow Q103.21 was measured at 72 kmc and found to have a dielectric constant of 1.09 and a loss tangent slightly less than 10^{-3}.

[3] C. G. Montgomery, "Technique of Microwave Measurements," McGraw-Hill Book Co., Inc., New York, N. Y., p. 621; 1947.

TABLE I

CHARACTERISTICS OF POLYSTYRENE FOAM MATERIALS IN THE FREQUENCY RANGE FROM 30 TO 40 KMC

Type	Manufacturer	Dielectric Constant	Loss Tangent
Q103.21	Dow Chemical Company	1.1	$\leq 7\times10^{-4}$
Q865.2	Dow Chemical Company	1.02	$\leq 5\times10^{-4}$
Extruded Dylite	Koppers Company, Inc.	1.05	$\leq 5\times10^{-4}$

With the availability of the desired materials established, the attenuation characteristics as a function of frequency were calculated for several image lines. The calculated values were checked experimentally at 35 and/or 70 kmc by means of a transmission-type image line resonator. Since the resonator technique has been described by King and Schlesinger,[2] it will not be discussed in detail here. In the present case the aluminum resonator was 24 inches wide, had semicircular end-plates with a 24-inch diameter and could be varied in length from zero to 36 inches. One end-plate was fixed in position, while the other was movable on the image plane and contained a choke joint along the full 24-inch width of contact with the image plane. (Actually, two different movable end-walls were available, each with a different choke joint, designed for operation at 35 kmc in one case and 70 kmc in the second.) Appropriate input and output waveguide coupling holes were made in the fixed and movable end-walls, respectively, with different adapters available for use with either RG-96/U or RG-98/U rectangular waveguide systems.

Calculated attenuation data for two foam image lines are given in Fig. 7. The ordinate scale has been expanded by a factor of ten compared with the previous attenuation figures. The measured attenuations at 35 kmc for line number one and at 70 kmc for line number two were approximately twice the calculated values. The larger measured value is attributed partly to the additional loss introduced by the cement used to fasten the dielectric rod to the image plane. Several different cement materials were used in the experiments, but all were known to have considerably more loss than the polystyrenes used for the image lines. A further small loss term may have been caused by radiation from surface irregularities on the image plane or plastic material; in particular, the dielectric rods were cut in relatively short sections, about two feet in length, which meant that butt joints (which never mated exactly) were present in all of the image lines.

A qualitative measurement of significant "field extent" was determined for the image lines of Fig. 7 by moving the end of a $\frac{3}{8}$ inch square aluminum bar toward the dielectric rod (from directly over the rod and also from the side of the rod) and observing the largest radius at which the bar caused an observable effect on the signal detected at the output of the image line resonator. The radius of field extent is three inches for line number one at 35 kmc and less than $\frac{3}{4}$ of an inch for line number two at 70 kmc.

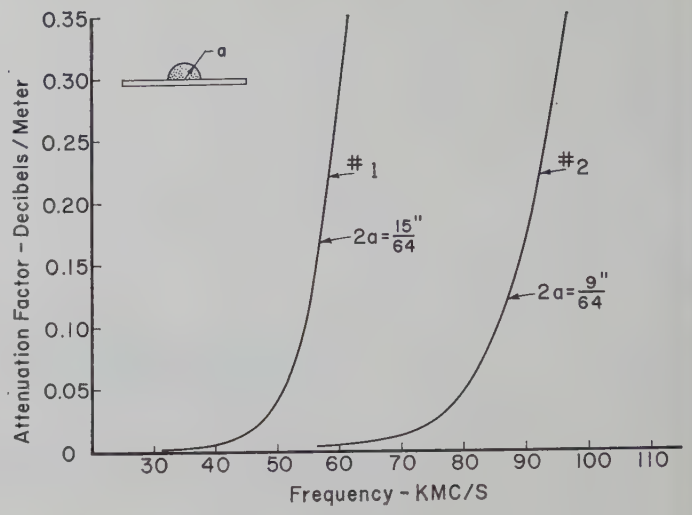

Fig. 7—Characteristics of two different image lines, each with copper image plane and foam polystyrene dielectric ($\epsilon=1.05$, loss tangent $=10^{-3}$).

TAPE OR RIBBON LINES

It is now possible to obtain polyethylene and Teflon in the form of thin, narrow tapes, some of which even have adhesive backing. The cross section of the tapes is rectangular, but the thickness to width ratio of such a rectangle is so small that the shape may be considered to be a degenerate ellipse (*i.e.*, with an eccentricity of unity). The attenuation for a polyethylene tape $\frac{3}{16}$ inch wide and 0.005 inch thick was measured, using the resonator technique, to be 0.02 decibel per meter at 69.4 kmc. A Teflon tape $\frac{1}{4}$ inch wide and 0.002 inch thick, with an adhesive backing 0.0045 inch thick, had a measured attenuation of 0.09 decibel per meter at 69.5 kmc. The radius of field extent for each tape was approximately one inch. Since thinner and/or narrower tapes than these are available, it should be possible to obtain attenuation factors for the 70 to 100 kmc frequency range which would be considerably lower than those shown in Fig. 7 for a $\frac{9}{64}$ inch diameter foam polystyrene image line.

DISCUSSION

This study has shown that it is possible to construct dielectric image lines which have low attenuation and small field extent in the frequency region from 30 to 100 kmc. Operating bandwidths are comparable to those of dominant-mode rectangular waveguides. The three new foam plastic materials discussed earlier have such good electrical and physical properties that they should be very useful for many purposes at millimeter wavelengths. The ease of construction and basic simplicity of the image lines, especially the tape line, have not been emphasized earlier in the text, but certainly should be noted as an advantage of this type of waveguide.

Appendix

The computation of attenuation factors is lengthy and complicated. For image lines which have dielectrics with semicircular cross sections, the contributions to attenuation due to dielectric loss (α_d) and conduction loss (α_c) may be found from the following expressions:

$$\alpha_d = 27.3\left(\frac{\Phi\epsilon}{\lambda}\right)R \quad \text{decibels/meter} \tag{1}$$

$$\alpha_c = 69.5\left(\frac{R_s R'}{\eta\lambda}\right) \quad \text{decibels/meter} \tag{2}$$

where

Φ = loss tangent of the dielectric rod
ϵ = relative dielectric constant of the rod
λ = free-space wavelength (meters)
η = intrinsic impedance of free space
R_s = surface resistivity of the image plane.

The factors R and R' are complicated functions of the dielectric constant and diameter (in free-space wavelengths) of the rod. Explicit expressions for R and R' may be found in the paper by King and Schlesinger.[2]

Acknowledgment

The author wishes to acknowledge the advice of Dr. Donald D. King in early phases of the project. Dr. King also collaborated in the design of the detector shown in Fig. 6.

Dr. S. P. Schlesinger supplied certain calculated data, including values of R and R' (identified in the Appendix), which greatly simplified computation of some of the attenuation factors.

Nearly all of the experimental measurements were carried out by James D. Rodgers, whose care and patience are much appreciated.

The Interaction of Microwaves with Gas-Discharge Plasmas*

SANBORN C. BROWN†

Summary—**The interaction of microwaves with gas-discharge plasmas provides a valuable tool for studying the fundamentals of gas-discharge phenomena and methods of controlling and switching microwave power. A summary of our present state of knowledge in this field is presented by using as particular examples the interaction of high density and low density gas-discharge plasmas in *S*-band resonant cavities, both in the presence and absence of dc magnetic fields.**

Introduction

THE effective dielectric coefficient of a plasma[1] in the absence of a magnetic field is given by

$$K = 1 - \left[\frac{\omega_p^2}{\omega^2}\,\frac{1 + j\dfrac{\nu_c}{\omega}}{1 + \left(\dfrac{\nu_c}{\omega}\right)^2}\right]. \tag{1}$$

Here ω_p is the plasma frequency given by the relation $\omega_p^2 = ne^2/m\epsilon_0$; ω is the applied radian frequency, and ν_c is the collision frequency of electrons in the gas given by ν_c = (constant) p, where p is the pressure. The square root of the dielectric coefficient (1) is related to the attenuation and phase shift of a plane wave, as represented in Fig. 1. This figure is calculated for the specific case of hydrogen gas at a microwave frequency of 4500 mc. In the low density region the attenuation and the phase shift are linear functions of the density, but at higher densities this linearity disappears and the functional relation becomes more complicated. In the usual use of microwave techniques for the diagnostic studies of plasmas, a restriction is placed on the method by the complexities of the solution in high density regions where the linear dependence does not hold. Usually, the microwave technique is restricted to the low density region well below the plasma frequency at which $\omega_p/\omega = 1$.

The solution shown in Fig. 1 is valid in the absence of a magnetic field. If a magnetic field is applied, the dielectric coefficient depends not only upon the density and magnitude of the magnetic field, but also on the geometrical configuration that is under consideration and the direction of propagation of the electromagnetic wave with respect to the magnetic field. Four cases can be distinguished for the purpose of simplifying the discussion; they are given in the following equations.[2]

* Manuscript received by the PGMTT, June 11, 1958; revised manuscript received, July 30, 1958. This work was supported in part by the U. S. Army (Signal Corps), Air Force (Off. of Sci. Res., Air Res. and Dev. Comm.), and Navy (Off. of Naval Res.), and in part by the Atomic Energy Commission.

† Res. Lab. of Electronics, Mass. Inst. Tech., Cambridge, Mass.

[1] H. Margenau, "Conduction and dispersion of ionized gases at high frequencies," *Phys. Rev.*, vol. 69, pp. 508–513; May, 1946.

[2] W. P. Allis, "Motions of Ions and Electrons" in "Handbuch der Physik," Springer Verlag, Berlin, Ger., vol. 21, pp. 383–444; 1956.

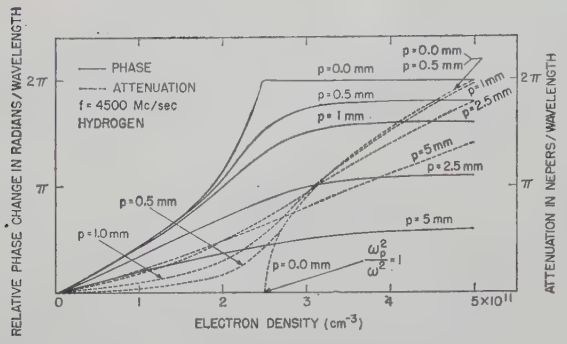

Fig. 1—Phase shift and attenuation of a plane wave as a function of electron density.

Propagation along B Field

Right-handed circularly polarized plane wave:

$$K_r = 1 - \frac{\omega_p^2}{\omega^2} \frac{1}{\left(1 - \frac{\omega_b}{\omega}\right) - j\frac{\nu_c}{\omega}}. \quad (2a)$$

Left-handed circularly polarized plane wave:

$$K_l = 1 - \frac{\omega_p^2}{\omega^2} \frac{1}{\left(1 + \frac{\omega_b}{\omega}\right) - j\frac{\nu_c}{\omega}}. \quad (2b)$$

Propagation Perpendicular to B Field

E field parallel to B:

$$K_\parallel = 1 - \frac{\omega_p^2}{\omega^2} \frac{1}{1 - j\frac{\nu_c}{\omega}}. \quad (2c)$$

E field perpendicular to B:

$$K_\perp = \frac{2K_rK_l}{K_r + K_l} = 1 - \frac{\omega_p^2}{\omega^2} \frac{\omega_p^2 - \omega^2}{\omega_p^2 + \omega_b^2 - \omega^2}. \quad (2d)$$

Here the symbol ω_b refers to the cyclotron frequency eB/m. In (2d) there is a component of E field along the B field so that the E field is not divergenceless. In this equation, also, the approximation is written in the absence of collision $\nu_e = 0$.

In a guiding structure such as a microwave cavity the dielectric coefficient must be represented by one or more of the coefficients mentioned above. As a result, it is not possible, even at low electron densities, to obtain a general theory in a form that is suitable for experimental verification and use in the microwave diagnostics of a magnetized plasma which is valid for all possible configurations of the microwaves. Consequently, only a few special configurations of the microwave field are analyzed. The discussion is restricted to a narrow cylindrical plasma column placed coaxially in a cylindrical microwave cavity. The behavior of the modes TM_{111}, TE_{011}, and TM_{010} or TM_{020} is considered. The static magnetic field, in all cases, is applied along the axis of the cavity.

TM_{111} Mode (Degenerate Modes)

Low Electron Densities

When the measuring mode is degenerate in frequency, the nonisotropic plasma removes the degeneracy. The physical reason for this can be seen when the TM_{111} mode is considered. When the radius of the plasma column is small compared with the cavity radius, the E field of the TM_{111} mode can be considered as linearly polarized in the plasma region. A linearly polarized field can, in turn, be considered as composed of two circularly polarized fields rotating in opposite directions. As mentioned earlier, the refractive index of the plasma is different for the two fields. As a result, the resonant frequency of the cavity splits into two frequencies, and the frequency shifts are given by[3]

$$\left(\frac{\Delta f}{f}\right)_{\circlearrowright} \approx \frac{\omega_p^2}{\omega^2}\left[\frac{\left(1 - \frac{\omega_b}{\omega}\right)}{\left(1 - \frac{\omega_b}{\omega}\right)^2 + \frac{\nu_c^2}{\omega^2}}\right]$$

$$\left(\frac{\Delta f}{f}\right)_{\circlearrowleft} \approx \frac{\omega_p^2}{\omega^2}\left[\frac{\left(1 + \frac{\omega_b}{\omega}\right)}{\left(1 + \frac{\omega_b}{\omega}\right)^2 + \frac{\nu_c^2}{\omega^2}}\right]. \quad (3)$$

The subscript arrows denote the rotation of the E field and the rotation of the electrons in the magnetic field. Thus in the first equation the E field is rotating in the same direction as the electrons; and in the second equation, the E field is considered as rotating in the opposite direction from the electrons. The solution for this set of equations is given graphically in Fig. 2. Also shown in this figure is a diagram of the TM_{111} mode, in which the electric field is represented by solid lines, and the plasma on the axis of the cylindrical cavity is represented by a shaded circle. The magnetic field is perpendicular to the plane of the figure. Fig. 2 gives the solution of (3) for the resonant-frequency shift as a function of electron density with ω_b/ω kept constant. If the equations for the resonant frequency are solved as a function of the ratio ω_b to ω for a constant density, the result is as shown in Fig. 3. It is obvious from this figure that for the case of the electric field rotating in the same direction as the electrons, the frequency shift is a complicated function of the magnetic field applied to the plasma.

High Electron Densities

When the electron densities are high, $\omega_p > \omega$, the relations for the frequency shift are invalid, mainly because the field in the plasma cannot be approximated at high electron density by the field in the absence of a plasma, the approximation which was made in the for-

[3] J. C. Slater, "Microwave electronics," *Revs. Mod. Phys.*, vol. 18, pp. 441–512; October, 1946.

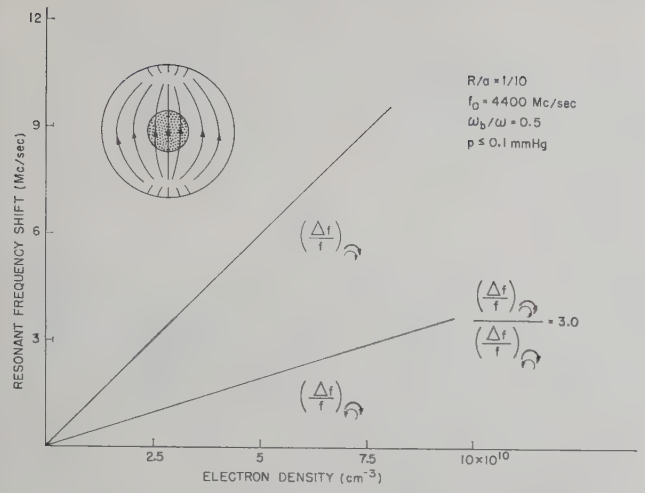

Fig. 2—Resonant frequency shift as a function of electron density for the TM_{111} mode. The magnetic field is perpendicular to the plane of the figure.

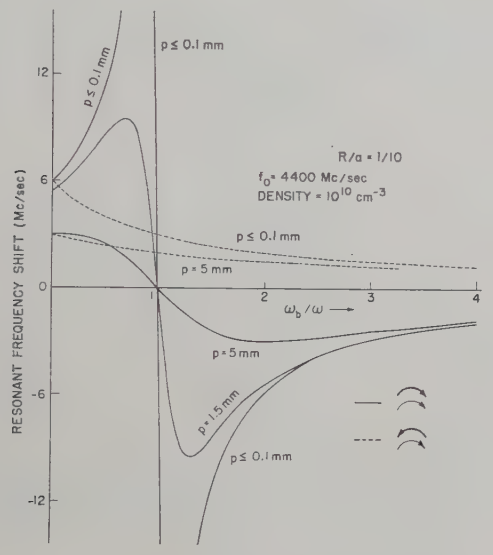

Fig. 3—Frequency shift as a function of magnetic field for the TM_{111} mode.

mer case. By far the most difficult problem is that of the TM_{111} mode. Here the field in the plasma is no longer linearly polarized but, because the skin depths for the left and right-handed rotating waves are different, the field is elliptically polarized. The degree of ellipticity is a function of the radius and of the density distribution. The exact solutions to this problem therefore, have not been attempted.

TE_{011} Mode (Nondegenerate Modes)

Low Electron Densities

In this case the perturbation theory can be extended in a straightforward manner for taking into account the presence of the static magnetic field. The dielectric coefficient becomes a tensor. At low electron densities, the field in the plasma can be approximated by the field in the absence of the plasma, so that only one diagonal component of the tensor needs to be considered. For very low pressures, the frequency shift becomes

$$\frac{\Delta f}{f} \sim \frac{\omega_p^2}{\omega^2} \frac{\omega^2[\nu_c^2 + \omega^2 - \omega_b^2]}{[\nu_c^2 + (\omega + \omega_b)^2][\nu_c^2 + (\omega - \omega_b)^2]}. \quad (4)$$

Eq. (4) exhibits an interesting property of the TE_{011} mode, namely, that the frequency shift is zero when $\omega_b^2 = \omega^2 + \nu_c^2$ independent of the electron density. This has been used as a direct measure of ν_c.

High Electron Densities

The TE_{011} mode is the mode that is ideally suited for measurement of high electron densities in the absence of static magnetic fields,[4] because its azimuthal field does not excite an ac space charge in an axially symmetric plasma. In the presence of a static magnetic field, this is no longer true. The nonisotropic nature of the plasma causes radial currents and radial fields, which contribute to the frequency shift. A first-order correction to the perturbation formula can be obtained by using a pseudostatic approximation, in order to compute the radial microwave field in the plasma. Plots of the frequency shift obtained are shown in Fig. 4, and they are compared with the plot obtained from the simple perturbation formula which neglects the radial fields. A striking feature is the oscillation in $\Delta f/f$. The magnitude of the resonance becomes larger as the ν_c becomes smaller.

The behavior of the Q value of the cavity also can be calculated as a function of the electron density. A calculation of this sort leads to the results shown in Fig. 5, where we see a resonance minimum in $\Delta(1/Q)$. In the vicinity of the resonance, the Q value of the cavity is so low that accurate measurements of $\Delta f/f$ are difficult to obtain. A quantitative experimental verification has not yet been made, although a resonance in the Q value of the cavity has been observed. Although we can predict qualitatively the behavior of $\Delta f/f$ and $\Delta(1/Q)$ with the electron density, we know that quantitatively our solutions are not correct. This is so because the assumptions about the field in the cavity, which were made in order to derive the basic equations, are not compatible with the nonisotropic nature of the plasma when the plasma radius is not negligible compared with the wavelength. It is well known that in a nonisotropic medium, a pure TE mode is not possible. This is also true for the region of the cavity outside the plasma. In the present case the field in the cavity and in the plasma is some superposition of the fields of the TE_{011} and the TM_{011} modes. An exact solution of this problem is possible. It results in a transcendental equation for the complex resonant frequencies of the cavity which is in the form of a 6×6 determinant, and it must be computed by numerical means.

TM_{0m0} (E Parallel to B)

Low Densities

When the microwave mode is such that the E field is parallel to the B field, the effective dielectric coefficient

[4] S. J. Buchsbaum and S. C. Brown, "Microwave measurements of high electron densities," *Phys. Rev.*, vol. 106, pp. 196–199; April 15, 1957.

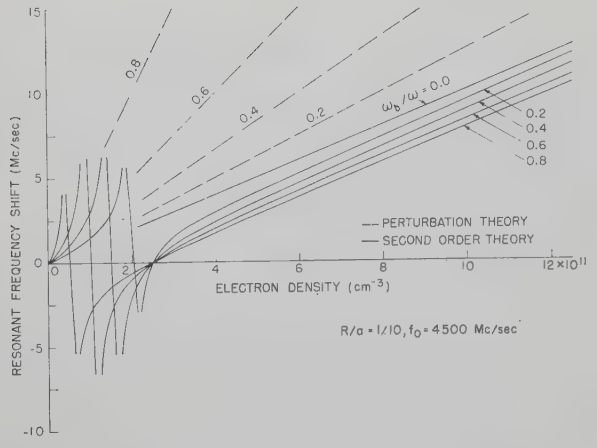

Fig. 4—Frequency shift as a function of electron density for the TE_{011} mode.

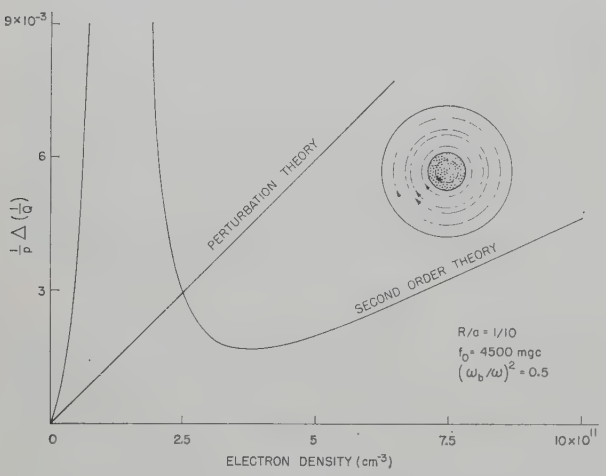

Fig. 5—The Q value as a function of electron density for the TE_{011} mode.

is given by (2c). The frequency shift is independent of the magnetic field in the limit of zero electron temperature, and it is given by

$$\frac{\Delta f}{f} \sim \frac{\omega_p^2}{\omega^2}\left[\frac{1}{1+\frac{\nu_c^2}{\omega^2}}\right]. \qquad (5)$$

The solution of (5) for the frequency shift is given in Fig. 6; the curve is marked "Perturbation Theory."

High Electron Densities

Since the E field of these modes can be made to coincide with the direction of the static magnetic field, the TM_{0m0} modes do not suffer from the disadvantages that the nonisotropic nature of the plasma imposes on all other modes that have a component of the E field at right angles to the B field. Although the TM_{0m0} are not as ideal as the TE_{011} mode, they are well suited for measuring high electron densities in those plasmas that do not possess density gradients in the axial direction. The disadvantage of the TM_{0m0} modes lies in the fact that the shift in the resonant frequency of the cavity is large when the plasma density is high. Consequently, the

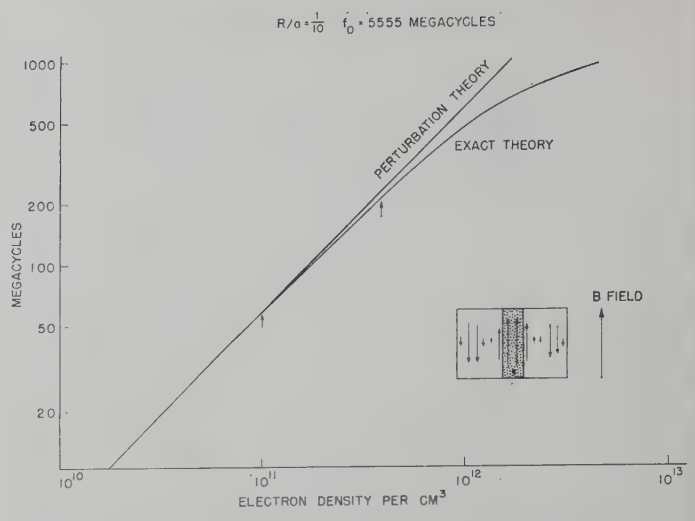

Fig. 6—Frequency shift as a function of electron density for the TM_{020} mode.

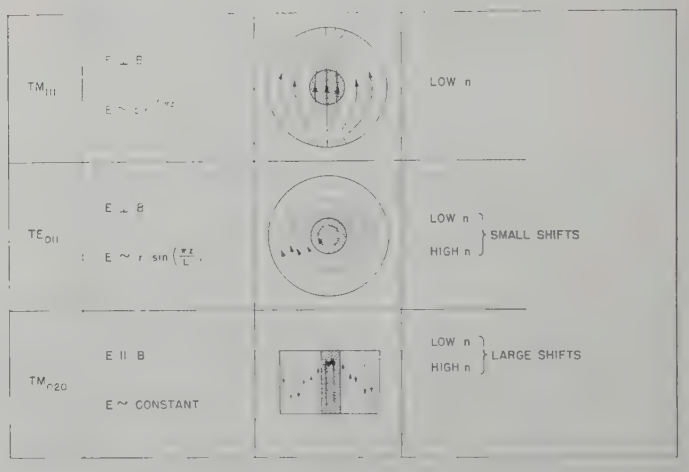

Fig. 7—Summary of field distributions for the TM_{111}, TE_{011}, TM_{020} modes.

perturbation formula is again inadequate and exact analysis must be resorted to. In this case, however, the analysis is fairly straightforward. Fig. 6 shows the frequency shift of a TM_{020} mode cavity as a function of plasma density, which is assumed to be uniform, whose radius is $\frac{1}{10}$ of the cavity radius.

Measurement of Electron Density Distribution

Since the E fields of the three modes that have been discussed have different radial and axial functional dependences, the simultaneous use of two of the three modes yields information about the electron density distribution along the appropriate directions. The use of the TM_{111} mode, with E approximately constant with R, and of the TE_{011} mode, with E varying as R, yields information about the density distribution along the radius. The use of the TM_{111} mode, with E varying as $\sin(\pi z/L)$, and of the TM_{010} mode, with E approximately constant with z, gives the distribution along the axis of the plasma. These results are summarized in Fig. 7.

High Power, Magnetic Field Controlled Microwave Gas Discharge Switches*

S. J. TETENBAUM† AND R. M. HILL†

Summary—A new type of gas discharge switch is described. It is electronically controllable, broadband, and capable of rapidly switching high power pulsed microwaves from either of two waveguide input ports to a single waveguide output port, or from one waveguide input port to either of two waveguide output ports. The electronic control is achieved by turning on or off a magnetic field set for cyclotron resonance. An approximate analysis is given of the operation of the active element of the switch and the results are compared with experiment. An analysis of the effects of frequency scaling indicates that, with the exception of the magnetic flux density which increases with increasing frequency, the switch parameters either improve or remain unchanged in going to higher frequencies. Two different switch configurations are investigated, one a *Y*-junction switch for operation at *S* band and the other a balanced top-wall hybrid coupler switch for operation at K_u band. Their electrical characteristics are described.

Introduction

THERE are many applications in which it is desirable to be able to switch microwave power from one or more waveguide input ports to one or more waveguide output ports in a controlled manner. This investigation has been specifically concerned with switching the output from either of two transmitters to a common antenna.

The controlled switching of pulsed microwave power can be accomplished in a number of different ways. Mechanical waveguide switches are commonly used, but are relatively slow acting, requiring of the order of 100 milliseconds to operate. A voltage pulsed germanium crystal diode can provide microwave switching[1] but is limited to very low powers. The nonreciprocal properties of ferrites in magnetic fields can also be used for switching applications.[2] The temperature dependence of ferrites limits their high power capabilities. The isolation of ferrite switches is also considerably less than that of mechanical switches and gas switches.

Gas discharges are particularly suitable for the rapid switching of high powers. In a TR tube a microwave gas discharge acts as the switching element. The incident high power transmitted signal causes the gas in the tube to break down, thus effectively isolating a receiver. The low power received signal cannot break down the gas and proceeds with low loss to the receiver. Such a power-actuated device has little possibility of providing electronically controlled switching.

Direct current or low-frequency gas discharges can be used to switch microwave power by controlling either the attenuation or phase shift of a switch tube.[3,4] Switching is accomplished by voltage pulsing of the gas tube. Such devices have power limits of a few hundred watts. At higher microwave inputs, the discharge is captured by the microwave power so that the tube fires whether or not the voltage pulse is applied to it, and switching action is lost.

The gas discharge devices mentioned above operate with no applied magnetic field. The presence of a dc magnetic field profoundly changes the characteristics of the discharge,[5,6] and offers the possibility of obtaining controlled high power switching by varying the magnetic field applied to the gas.

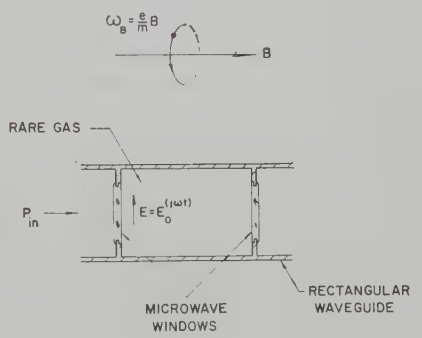

Fig. 1—Schematic of switch tube.

General Description of Switching Element

The active element of the switches to be described below is a tube shown schematically in Fig. 1. It consists of a section of rectangular waveguide sealed off at both ends with vacuum windows and containing a rare gas or mixture of rare gases at a pressure of the order of tenths

* Manuscript received by the PGMTT, July 25, 1958; revised manuscript received, September 5, 1958. A summary of this work has been reported by the authors in "High power, broadband, microwave gas discharge switch tubes," 1958 IRE National Convention Record, vol. 6, pt. 1, p. 83. Part of the work was performed under U. S. Army Signal Corps Contract DA 36-039-SC-73188, and part under Contract DA 30-069-ORD-1082.

† Sylvania Microwave Phys. Lab., Mountain View, Calif.

[1] M. A. Armistead, E. G. Spencer, and R. D. Hatcher, "Microwave semiconductor switch," Proc. IRE, vol. 44, p. 1875; December, 1956.

[2] G. S. Uebele, "High-speed ferrite microwave switch," 1957 IRE National Convention Record, vol. 5, pt. 1, pp. 227–234.

[3] L. Goldstein and N. L. Cohen, "Radio frequency conductivity of gas discharge plasmas in the microwave region," *Phys. Rev.*, vol. 73, p. 83; January, 1948.

[4] E. M. Bradley and D. H. Pringle, "Some new microwave control valves employing the negative glow discharge," *J. Electronics*, vol. 1, pp. 389–404; January, 1956.

[5] B. Lax, W. P. Allis, and S. C. Brown, "The effect of magnetic field on the breakdown of gases at microwave frequencies," *J. Appl. Phys.*, vol. 21, pp. 1297–1304; December, 1950.

[6] L. Goldstein, "Nonreciprocal electromagnetic wave propagation in ionized gaseous media," IRE Trans. on Microwave Theory and Techniques, vol. MTT-6, pp. 19–29; January, 1958.

of millimeters of Hg. A dc magnetic field is applied perpendicular to the microwave electric field in the tube. Either a longitudinal magnetic field as shown or a transverse field parallel to the broad face of the waveguide may be used.

The tube is fired by the incident high level microwave power, in a time of the order of one hundredth of a microsecond, when the applied magnetic field is near electron cyclotron resonance. A cyclotron resonant magnetic field is one for which ω_B, the angular frequency of an electron's spiral motion about the flux lines, is equal to ω, the angular frequency of the microwaves. Denoting the charge and mass of the electron by e and m, respectively, $\omega_B = eB/m$ in mks units. The cyclotron resonant magnetic field is denoted by B_c and has a value of around 1200 gauss at S band. Near cyclotron resonance, there is a large transfer of energy from the microwave electric field to the electrons and a strong discharge occurs. The resultant high electron density of the plasma acts like a short circuit at the inside surface of the input window. When the applied magnetic field is zero or sufficiently far from cyclotron resonance, the tube is unfired in the presence of the incident microwaves, and acts like a low-loss section of waveguide. Thus, the on-off action of the switching element can be controlled by varying the magnitude of the applied magnetic field.

Theory

The high level characteristics of the switch tube depend upon certain fundamental microwave gas discharge parameters such as breakdown field, arc loss, and recovery time. The breakdown field is determined by the properties of the plasma during its breakdown period, the arc loss depends upon the plasma's steady state properties, and the recovery time is a function of the properties of the plasma's afterglow period. A complete theoretical analysis of the behavior of the plasma would be very difficult, but one can obtain qualitative information on the switch tube parameters from an approximate analysis. The principal assumptions are as follow.

1) An average electron interacts with a low pressure rare gas.
2) The magnetic field, electric field, collision frequency, diffusion coefficient, etc., are uniform over the gas volume.
3) The only collision processes are elastic collisions and inelastic ionizing collisions between electrons and atoms.
4) The only electron production mechanism is ionization and the only electron loss mechanism is diffusion (free diffusion in breakdown period and ambipolar diffusion during steady state and afterglow periods).

Additional assumptions are mentioned when pertinent.

The continuity equation for electrons can be written as

$$\frac{dn}{dt} = n(\nu_i - \nu_d) \tag{1}$$

where n is the electron number density, ν_i is the ionization rate per electron, or the number of electrons per electron produced per second by ionization, and ν_d is the number of electrons per electron lost per second by diffusion to the walls of the tube.

During the high power pulse, an electron gains energy from the microwave field until it ionizes a gas atom or diffuses out to the walls. Gas breakdown is initiated and the electron density builds up when the number of electrons produced by ionization just exceeds the number lost by diffusion. The electron density increases exponentially from its initial value of around 10^3/cc to approximately 10^8/cc, at which time the much slower process of ambipolar diffusion sets in and the electron density increases at a much faster rate than before. This electron density buildup continues until a condition of "magneto-plasma resonance"[6] is attained, at which time the plasma acts like a short circuit reflecting most of the incident power except for the small amount absorbed to maintain the discharge. Between pulses the discharge decays. If the incident power is much greater than the power required for breakdown, as is usually true in these tubes, $\nu_i \gg \nu_d$ and the diffusion losses can be neglected in determining the breakdown parameters. Breakdown then is determined solely by the power transfer from the microwave field to the electrons, maximum power transfer and hence maximum rate of ionization, corresponding to minimum breakdown power. For sufficiently low pressures and magnetic fields, however, diffusion losses must be taken into account. Now

$$\nu_i = \frac{\nu}{n_i} = \frac{\nu u_e}{u_i} = \frac{P}{e u_i} \tag{2}$$

where ν is the momentum transfer collision frequency or the number of elastic collisions per second between an electron and a neutral atom, n_i is the average number of collisions for an electron starting from rest to reach ionization potential, u_i is the ionization potential in electron volts, u_e is the average energy gain by an electron between collisions in ev, and P is the power transfer per electron or the power absorbed by an electron. P has been derived by Lax *et al.*[5] and is given by

$$P = \frac{e^2 E_0^2}{4m}\left[\frac{\nu}{(\omega + \omega_B)^2 + \nu^2} + \frac{\nu}{(\omega - \omega_B)^2 + \nu^2}\right]. \tag{3}$$

E_0 is the amplitude of an average electric field over the switch tube during the breakdown period and is assumed uniform. The collision frequency ν is directly proportional to the pressure and can be expressed as

$$\nu = 5.9 \times 10^7 u^{1/2} p P_m \tag{4}$$

where $u = mv^2/2e$ is the electron energy in ev, P_m is the so-called "probability of collision" and is a function of the type of gas and the electron's energy, and p is the

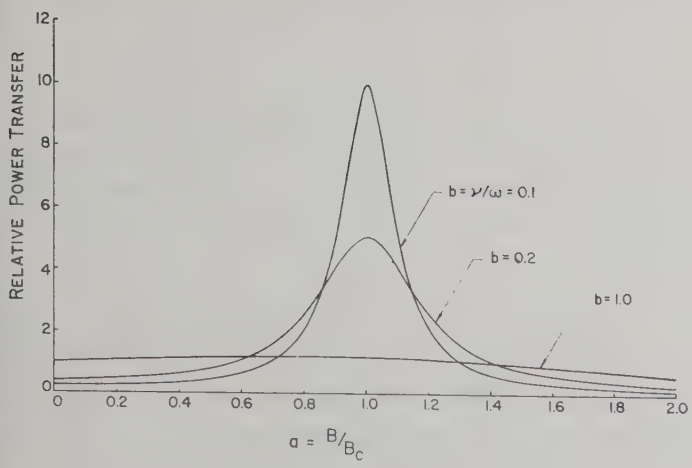

Fig. 2—Power transfer vs magnetic field.

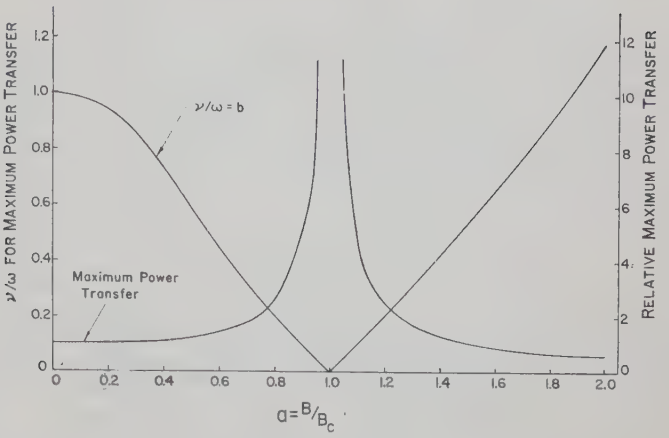

Fig. 3—Maximum power transfer and corresponding ν/ω vs magnetic field.

pressure in mm of Hg. The electronic mean free path is the reciprocal of the quantity pP_m.

The second term of (3) is the resonance term and predominates at low pressures and in the vicinity of cyclotron resonance. Setting $P'=(4m\omega/e^2E_0^2)P$, $a=\omega_B/\omega = B/B_c$ and $b=\nu/\omega$, Eq. (3) is normalized to

$$P' = \frac{b}{(1+a)^2+b^2} + \frac{b}{(1-a)^2+b^2}. \qquad (5)$$

P' is the relative power transfer, a is proportional to the applied magnetic field and is called the relative magnetic field parameter, and b is the relative pressure parameter.

Eq. (5) is plotted in Fig. 2, which shows the relative power transfer vs magnetic field for a number of different pressures. The curve has a maximum close to $a=1$ or cyclotron resonance. The lower the pressure, the nearer the maximum is to $a=1$, occurring within 1 per cent of this point for $b<0.4$. The half width of the resonance (between half-power points) decreases with decreasing pressure, and for low pressures it is equal to b. The power transfer at cyclotron resonance increases with decreasing pressure and the power transfer outside the half-power points increases with increasing pressure.

The condition for maximum power transfer and hence the approximate minimum breakdown power is obtained from (5) by setting $dP'/db=0$. The maximum value of P' and the corresponding value of b as functions of magnetic field are plotted in Fig. 3. The maximum power transfer goes through a resonance at $a=1$ while the value of b for which maximum transfer occurs first decreases and then increases as the magnetic field increases through cyclotron resonance. At zero magnetic field, the maximum value of P' occurs at $b=1$. Conventional TR tubes usually operate near this condition. At cyclotron resonance, the maximum power transfer is infinite and occurs at $b=0$. It is apparent that in order to take advantage of the large increase in power transfer and hence the large decrease in breakdown power near cyclotron resonance, it is necessary to operate at as low a pressure as possible. In actual practice, as b approaches zero, (3) ceases to be valid so that experimentally there is a low pressure limit below which the breakdown power begins to increase due to the decreased ionization rate and increased diffusion losses. For helium in S-band waveguide in a transverse magnetic field, this limit, called the mean free path limit, occurs at a value of b approximately equal to 0.06. The operating pressure which gives optimum breakdown is not necessarily the best pressure as far as the other electrical characteristics of the switch are concerned and it is necessary to compromise on its value. In all cases, however, operation will be in the low pressure region in which $\nu^2 \ll \omega^2$. It therefore is assumed that $b^2 \ll 1$, which is equivalent to the assumption that there are many oscillations per collision. Eq. (5) then reduces to

$$(P')_{a=1} = \frac{1}{b} \quad \text{or} \quad (P_{bk})_{a=1} \sim b. \qquad (6a)$$

$$(P')_{a\neq 1} = \frac{2b(1+a^2)}{(1-a^2)^2} \quad \text{or} \quad (P_{bk})_{a\neq 1} \sim \frac{g(a)}{b}, \qquad (6b)$$

where $g(a)=(1-a^2)^2/1+a^2$.

Eq. (6a) states that the power transfer at cyclotron resonance is inversely proportional to the pressure or that the breakdown power at cyclotron resonance is directly proportional to the pressure. Eq. (6b) implies that beyond the half-power points of the resonance curve, the breakdown power is inversely proportional to the pressure and directly proportional to the magnetic field dependent quantity $g(a)$. The breakdown power dependence given in (6b) would not be valid for pressures and magnetic fields for which the diffusion losses could not be neglected during the breakdown period.

A convenient way to define the breakdown or firing time is to let it represent the time interval between the beginning of the magnetron pulse and the point at which the attenuation of the plasma begins to increase rapidly. This is near the point at which ambipolar diffusion sets in ($n \simeq 10^8$/cc). This point may be identified with the peak of the spike of the transmitted pulse and can be

thought of as corresponding to the end of the breakdown period. The small additional time interval required for n to reach magneto-plasma resonance is neglected. Thus, solving (1) for $\nu_d=0$ and using (2) along with the auxiliary conditions, $n=10^2$/cc at $t=0$ and $n=10^8$/cc at $t=t_{bk}$, one obtains

$$t_{bk} = \frac{12u_i m\omega}{eE_0^2 P'} . \tag{7}$$

Using (6a), (6b), and (4), and assuming that the average energy of the electrons is proportional to the ionization potential and denoting the input power by P_{in},

$$(t_{bk})_{a=1} \sim \frac{u_i^{3/2} p P_m}{P_{\text{in}}} . \tag{8a}$$

$$(t_{bk})_{a\neq 1} \sim \frac{u_i^{1/2} g(a)}{P_{\text{in}} p P_m} . \tag{8b}$$

One difficulty in attempting to verify (8) experimentally is that t_{bk} is of the same order of magnitude as the rise time of the incident high power pulse and hence, P_{in}, instead of being constant, is itself a function of the breakdown time.

The actual breakdown power, P_{bk}, depends upon the shape of the pulse. However, its qualitative dependence upon the magnetic field, gas, and pressure can be obtained by assuming CW conditions and defining P_{bk} as that input power which breaks down the gas in a given time. Hence, using (8a) and (8b),

$$(P_{bk})_{a=1} \sim u_i^{3/2} p P_m . \tag{9a}$$

$$(P_{bk})_{a\neq 1} \sim \frac{u_i^{1/2} g(a)}{p P_m} . \tag{9b}$$

As expected, (9) is consistent with (6), but also gives the explicit dependence on the fundamental constants of the gas.

The important afterglow parameter is the recovery time, t_r, which may be defined as that time after the end of the high power pulse at which the attenuation of a probing signal transmitted through the switch tube has decreased to 3 db more than its attenuation in the absence of the discharge. It is assumed that the electrons and positive ions are in thermal equilibrium with the gas, that $\nu_i=0$, and that the only decay mechanism is ambipolar diffusion. The loss rate per electron is readily obtainable from the diffusion equation and is given by

$$\nu_d = \frac{D_a}{\Lambda_B^2} \tag{10}$$

where D_a is the ambipolar diffusion coefficient and Λ_B is the effective diffusion length of the gas container. For a rectangular parallelopiped switch tube of dimensions L_x, L_y and L_z, the characteristic diffusion length Λ in the absence of a magnetic field is given by

$$\frac{1}{\Lambda^2} = \frac{1}{\Lambda_x^2} + \frac{1}{\Lambda_y^2} + \frac{1}{\Lambda_z^2} \tag{11}$$

where $\Lambda_x = L_x/\pi$, etc. The effect of the magnetic field is to increase the effective size of the tube in directions perpendicular to the field.[5] Thus, for a magnetic field along the z axis, the effective diffusion length Λ_B is given by

$$\frac{1}{\Lambda_B^2} = \frac{\nu^2}{(\nu^2+\omega_B^2)}\left[\frac{1}{\Lambda_x^2} + \frac{1}{\Lambda_y^2}\right] + \frac{1}{\Lambda_z^2} \simeq \frac{1}{\Lambda_z^2} . \tag{12}$$

The approximation in this equation holds except for sufficiently small applied magnetic fields, or for Λ_x or Λ_y very much less than Λ_z.

Substituting (10) into (1) and solving for n under the assumption that the magnetic field is constant during the afterglow period gives

$$n = n_0 \exp\left(-D_a t/\Lambda_B^2\right) \tag{13}$$

where n_0 is the electron density at the beginning of the afterglow. Let n_r be the electron density of the plasma when the 3-db attenuation point is reached. Then $n=n_r$ when $t=t_r$ and

$$t_r = \frac{2.3\Lambda_B^2}{D_a} \log\left(n_0/n_r\right). \tag{14}$$

The quantity $(D_a)p$ is a constant for a given gas. The quantity n_0 varies approximately as $(P_{\text{in}})^\alpha$ where α is a positive constant. Hence a plot of t_r vs log P_{in} is linear.

In the steady-state discharge condition of the high power switch tubes, the density of the plasma is beyond magneto-plasma resonance and thus shields the interior from the fields outside. This means that the incident power is reflected except for the portion required to maintain the plasma in equilibrium. The power not reflected is absorbed by the discharge, since the power transmitted through the discharge is negligible. The absorbed power is dissipated primarily in the form of heat.

The per cent arc loss of a switch tube can be defined as $P_{\text{abs}}/P_{\text{in}}$, where P_{abs} is the power absorbed in the steady-state plasma. P_{abs} may be expressed in terms of σ, the conductivity of the discharge. The presence of the magnetic field gives rise to a tensor conductivity, which can be obtained from the relation $\overleftrightarrow{\sigma} = ne\overleftrightarrow{\mu}$ where the mobility tensor $\overleftrightarrow{\mu}$ is given by Allis.[7] The conductivity tensor, for the magnetic field along the z axis, is

$$\overleftrightarrow{\sigma} = \begin{Vmatrix} \sigma_{11} & \sigma_{12} & 0 \\ -\sigma_{12} & \sigma_{11} & 0 \\ 0 & 0 & \sigma_{33} \end{Vmatrix},$$

$$\sigma_{11} = \frac{e^2 n}{2m}\left[\frac{1}{\nu + j(\omega+\omega_B)} + \frac{1}{\nu + j(\omega-\omega_B)}\right]. \tag{15}$$

[7] W. P. Allis, "Motions of Ions and Electrons" in "Handbuch Der Physik," Springer-Verlag, Berlin, Ger., vol. 21, p. 394; 1956.

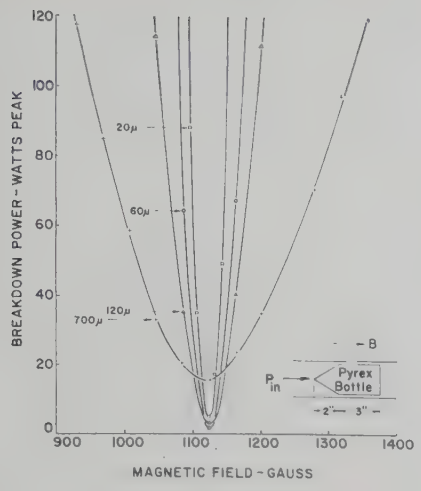

Fig. 4—Breakdown power vs magnetic field in vicinity of cyclotron resonance.

For an incident electric field along the x axis, the electric field E in the plasma will have components essentially along the x and y axes due to the action of the magnetic field. The current density is $\vec{J}=\overleftrightarrow{\sigma}\cdot\vec{E}$ and the absorbed power per unit volume is given by $Re\{\vec{E}\cdot\overleftrightarrow{\sigma}\cdot\vec{E}\}$. Hence using $\vec{E}=i\vec{E}_x+j\vec{E}_y$ and denoting the volume by V,

$$P_{\text{abs}} = VE^2 \text{ Re } \{\sigma_{11}\}. \tag{16}$$

Assuming $\nu^2 \ll \omega^2$, (15) and (16) reduce to

$$(P_{\text{abs}})_{a=1} = \frac{e^2 V n E^2}{2m\nu} \cdot \tag{17a}$$

$$(P_{\text{abs}})_{a\neq 1} = \frac{e^2 V n E^2 \nu}{m\omega^2 g(a)} \cdot \tag{17b}$$

It is not known how E and n in the switch tube vary with the pressure, magnetic field, input power, and type of gas. Experimentally, for peak input powers of around 100 kw, the absorbed power is appreciable, being 10 per cent or more of the incident power. Hence the electric field inside the discharge is determined primarily by the incident electric field rather than the space charge field. Assuming that $E \sim E_{bk}$, or $E^2 \sim P_{bk}$ in so far as their variation with the type of gas, pressure, and magnetic field is concerned, (17), (9), and (4) give for all magnetic fields

$$P_{\text{abs}} \sim n u_i. \tag{18}$$

On discharge, the high power switch tube operates beyond magneto-plasma resonance and it is expected that n will not vary much with changes in pressure or magnetic field. If all the input power went into ionization and there were no losses, $n \sim P_{\text{in}}$. Considering losses, one can say very approximately that $n \sim (P_{\text{in}})^{\alpha}$ where $0<\alpha<1$. Hence, dividing both sides of (18) by P_{in},

$$\text{arc loss} \sim \frac{u_i}{(P_{\text{in}})^{\beta}}, \qquad 0<\beta<1. \tag{19}$$

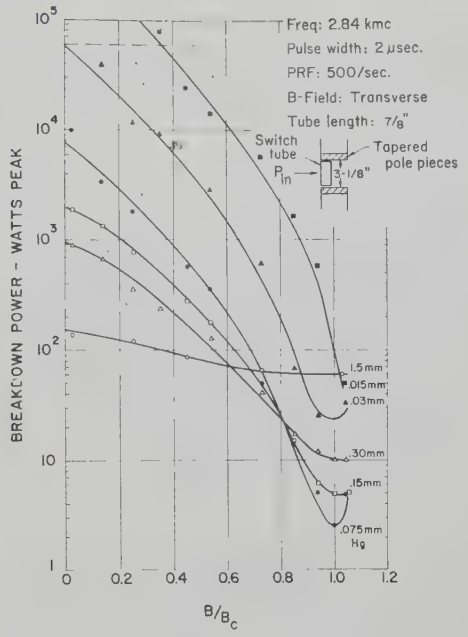

Fig. 5—Breakdown power vs magnetic field in argon.

Comparison of Theory and Experiment

The theoretical curves of Fig. 2 imply that at low pressures, the breakdown power vs magnetic field characteristic should exhibit a minimum at cyclotron resonance, the width of the resonance should decrease with decreasing pressure, the cyclotron resonance breakdown power should decrease with decreasing pressure, and the breakdown power off cyclotron resonance should increase with decreasing pressure.

Fig. 4 is a plot of the experimental breakdown power in helium plus 1 per cent neon in the vicinity of cyclotron resonance. The data were taken under relatively low input power conditions. The frequency was 3.15 kmc, the PRF was 100 per second and the pulse width was 4.7 μsec. The tube was a tapered pyrex bottle fitting snugly into the S-band rectangular waveguide. A solenoid provided a uniform longitudinal magnetic field. The curves are in qualitative agreement with the theory. One interesting feature is the effect of the mean free path limit. As the pressure decreases, the breakdown power at cyclotron resonance decreases until this limit, which occurs at a pressure near 50 microns of Hg, is reached. Below this limit the breakdown power increases with decreasing pressure.

Fig. 5 shows some experimental data in argon taken over a wide range of input powers. Again, the data are in qualitative agreement with the theory. It can be seen that for sufficiently low pressures, the input power required for breakdown at cyclotron resonance is almost four orders of magnitude less than the breakdown power at zero magnetic field. The dashed line in the figure meets the 30 microns breakdown curve at a point corresponding to 60 kw and zero magnetic field. This means that for the controlled switching of a source power of 60-kw peak, it is necessary to operate at a pressure below 30

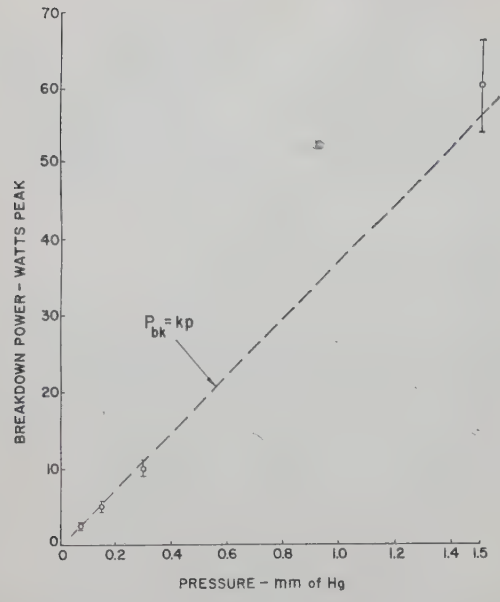

Fig. 6—Breakdown power at cyclotron resonance vs pressure in argon.

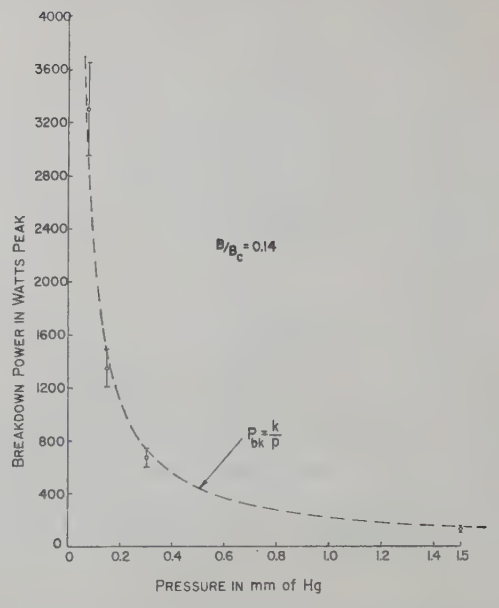

Fig. 7—Breakdown power off cyclotron resonance vs pressure in argon.

microns of Hg. Otherwise, the tube would fire even at zero applied magnetic field and control would be lost. At 30 microns of Hg, less than 25 watts is required for breakdown at cyclotron resonance. At still lower pressures, the breakdown curves are shifted toward higher powers. The power required for cyclotron resonant breakdown also increases, but much more slowly than at zero magnetic field where diffusion losses become important. For example, at pressures below 15 microns, it is possible to hold off approximately 500 kw of pulsed power without breakdown (extrapolated), while at cyclotron resonance the power required for breakdown is still only of the order of 100 watts. The mean free path limit is seen to occur somewhere around 50 microns of Hg and hence, in the particular geometry used, to achieve the wide range of magnetic field control mentioned requires operation below this limit.

The data of Fig. 5 have been replotted for comparison with (6a) and (6b). Fig. 6 shows the breakdown power at cyclotron resonance vs pressure. Only pressures above the mean free path limit were used. The dashed line is the theoretical prediction of (6a), and is in reasonable agreement with the data. Fig. 7 shows the corresponding breakdown characteristic off cyclotron resonance vs pressure. The value of applied field used is sufficient to provide operation beyond the half-power points of the resonance at the highest pressure investigated. The dashed curve is the theoretical prediction of (6b). Fig. 8 shows the breakdown power vs magnetic field in helium in the magnetic field range in which (6b) is applicable. The dashed line is the theoretical prediction of this equation. Breakdown measurements on tubes filled with a number of different gases have given results in qualitative agreement with (9).

The recovery time has been measured in a number of different switch tubes. The results are in qualitative agreement with the predictions of (14).

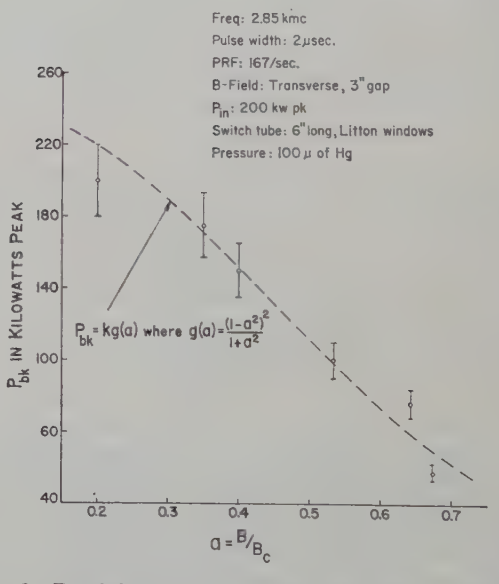

Fig. 8—Breakdown power vs magnetic field in helium.

Experimental arc loss data are in qualitative agreement with (19). In the range of input powers above about 10 kw, the arc loss decreased only slightly with increasing input power; the best experimental fit is for a $\beta \simeq 0.2$. The arc loss is essentially independent of pressure except below the mean free path limit where the excessive diffusion losses cause the arc loss to increase rapidly with decreasing pressure.

Frequency Scaling

An approximate analysis was made of the way in which the switch parameters change in scaling from one frequency band to another. The principal assumptions were that the input power doesn't change in scaling, that the electric field in the steady-state discharge varies with ω in the same way as the breakdown field, and that

the switch operates at the maximum pressure which still allows magnetic field control.

The results of the analysis follow.

1) $p \sim \omega$.
2) $t_{bk} \sim 1/\omega$.
3) P_{bk} is independent of ω.
4) $t_r \sim 1/\omega$.
5) Arc loss is independent of ω.
6) (ΔB) for switching $\sim \omega$.

Although the cyclotron resonant magnetic field varies as ω, the gap spacing of the electromagnet varies approximately as $1/\omega$. Hence, the power rating of the supply for switching the magnetic field remains approximately the same in scaling.

Bandwidth of Switch Tube

The bandwidth of a switch tube depends upon its geometry and upon how the high level switch parameters vary with the frequency for a fixed value of magnetic field. In general, the large energy transfer near cyclotron resonance allows one to use a broadband structure and still achieve a strong discharge.

The low-level bandwidth of a number of S-band tubes was investigated. Two common types of windows used were Sylvania's 1B58 TR tube window and their ATR 345 window (JAN 5792). Fig. 9 illustrates the VSWR of some S-band tubes whose lengths were chosen to optimize the bandwidth. The bandwidth between 1.25:1 VSWR points for the ATR 345 window tube with a window spacing of $\frac{25}{32}$ inch was 37 per cent. The other two ATR 345 window tubes were approximately one halfguide wavelength and one guide wavelength longer than this tube. Although their bandwidth is reduced, the increased length and volume improves both the isolation and tube life.

The cold bandwidth of a number of switch tubes for operation at the upper end of K_u band was also investigated. Bandwidths in excess of 20 per cent were obtained both for tubes using Microwave Associates MA 1341 windows and tubes with ceramic windows in conjunction with a matching section at each end of the tube.

The over-all bandwidth of the switch tubes when in a fired condition could not be measured directly because of the limited frequency range of the high power sources available. However, since the cyclotron resonant magnetic field is directly proportional to the frequency, the frequency variation of the tube parameters at constant magnetic field is approximately equivalent to their magnetic field variation at constant frequency. Experiments were performed to determine how the high level switch tube parameters varied with magnetic field. It was found that the parameters were approximately symmetrical about cyclotron resonance and that they varied only a small amount for variations in the applied magnetic field around cyclotron resonance of ± 20 per cent. For example, for typical operating pressures, the arc loss varied by less than 0.1 db and the isolation decreased by only a few db from its maximum value at cyclotron resonance.

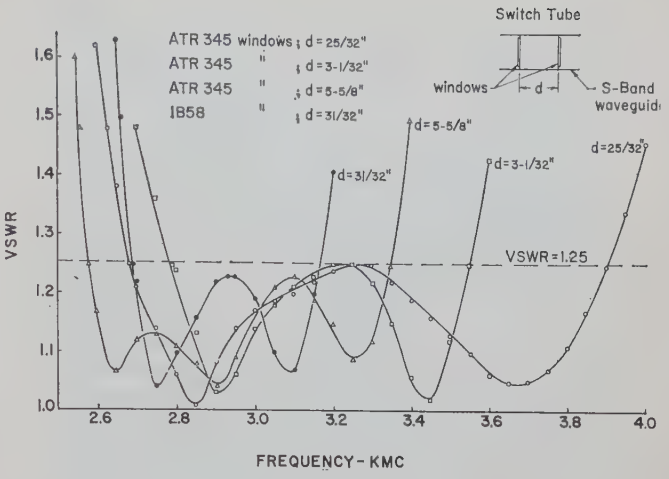

Fig. 9—VSWR of switch tubes.

Design Considerations

The theoretical and experimental switch tube studies have shown that the best over-all operation is obtained by switching between $B=0$ and $B=B_c$ and using the maximum pressure which still allows adequate magnetic field control, *i.e.*, that pressure above which the given incident power would produce breakdown even in the absence of a magnetic field.

The major problem encountered in this investigation was to achieve a satisfactory life. The tubes fail primarily due to excessive gas cleanup. The use of encapsulated windows[8] offers promise of providing increased tube life by eliminating sputtering, which is the major cause of the gas cleanup. Sputtering also reduces life by causing excessive insertion loss. Encapsulated window tubes show a reduced isolation over that of tubes using conventional windows.

The principal gases used in this investigation were argon, helium plus 1 per cent argon, and helium; satisfactory switching was obtained for all three. The lower ionization potential rare gases gave a smaller arc loss and a somewhat larger isolation, but because of the lower pressure required for adequate magnetic field control, the effect of gas cleanup was more pronounced and the life reduced.

The switching time is the time required to go from the condition where the incident power fires the switch tube to the condition where the incident power does not fire the switch tube, or vice versa. It depends upon the recovery time and how fast the magnetic field can be switched; in most cases, the latter is the limiting factor. In this investigation, the tubes were controlled by a manually operated magnetic field but, in principle,

[8] L. Gould, E. V. Edwards, and I. Reingold, "A novel approach to microwave duplexer tube design," IRE Trans. on Electron Devices, vol. ED-4, pp. 300–303; October, 1957.

the tubes can be controlled electronically. Switching times of less than 1 millisecond should be possible. The eddy current losses during the magnetic field switching period are kept small by using a thin-walled tube body.

Switch Applications

Switch tubes can be incorporated into many different kinds of switches depending upon the particular application. Two types of switch configurations were investigated for transferring the output from either of two transmitters to a common antenna and are shown in Fig. 10. The first type is a 120 degree E-plane Y switch and is shown in Fig. 10(a). It consists of two switch tubes located at the junction of a waveguide Y. There are two input ports for connections to the separate transmitters and one output port for connection to the antenna. In one switch state a magnetic field near cyclotron resonance is applied to tube SW1 while a zero or very small magnetic field is applied to SW2. In the other switch state the magnetic fields are interchanged. This type of switch can be used when only one transmitter is active at a time. When transmitter T1 is in operation, the cyclotron resonant field is applied to SW2. The incident power from T1 leaves SW1 unfired but fires SW2, producing an effective short at its input window and thereby connecting T1 to the antenna by means of a 120-degree waveguide bend. When T2 is active, the cyclotron resonant field is applied to SW1 and the antenna is effectively connected to T2.

If it is required that both transmitters be in operation at the same time, the output of the transmitter not connected to the antenna must be dissipated in a high power load. This Y-junction switch could not be used unless high power isolators were inserted in the input ports. It is possible, however, to use a configuration consisting of three Y junctions and four switch tubes to meet this switch requirement.

The second type is a balanced top-wall hybrid coupler switch and is shown in Fig. 10(b). It consists of two 3-db top-wall couplers with a dual switch tube between them. Top-wall couplers are used rather than side-wall couplers because the gap spacing of the electromagnet supplying the magnetic field in the former case is approximately one half that in the latter case. There are two input ports for connections to the separate transmitters and two output ports for connections to the antenna and a matched termination. In one switch state a magnetic field near cyclotron resonance is applied to both tubes. In the other switch state a zero or very small magnetic field is applied to the tubes. The balanced switch can be used whether one or both of the transmitters are in operation at a time. For the case where both transmitters are active, when a cyclotron resonant magnetic field is applied, the incident microwave power fires both tubes simultaneously. The effective shorts at the ends of the tubes cause the output of T2 to go to the antenna and the output of T1 to go to the high power load. When the applied magnetic field

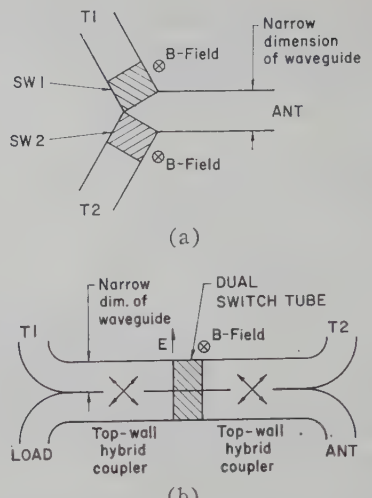

Fig. 10—Switch configurations. (a) 120-degree E-plane Y-junction switch; (b) balanced top-wall hybrid switch.

is zero or sufficiently reduced, the tubes are unfired by the incident power and the output of T1 goes to the antenna, while the output of T2 goes to the load. For the case where only one transmitter is active at a time, a cyclotron resonant magnetic field is applied when T2 is active so that its output is reflected out the antenna port, and the magnetic field is reduced to a low value when T1 is active so that its output goes to the antenna. The termination absorbs the small amount of power due to leakage from the couplers.

Each type of switch has certain advantages over the other. The relative advantages of the balanced switch are, first, that only one electromagnet is required instead of two. Second, no flux leakage problems exist in the balanced switch because both tubes are fired or unfired simultaneously. In the Y switch only one switch tube is to be fired at a time, and flux leakage from one electromagnet to the opposite switch tube can result in decreased magnetic field control. Third, matching sections external to the switch tubes can be used to increase the bandwidth of the balanced switch while this cannot readily be done in the Y switch. Fourth, the magnetrons always see a good match in the balanced switch, while in the Y switch, during the approximately 10^{-8} seconds required to fire the proper tube after the initiation of the transmitter pulse, the magnetron sees a mismatch of approximately 2 to 1.

The relative advantages of the Y switch are, first, that the bandwidth of a 120-degree E-plane bend covers the whole waveguide band while the bandwidth of the balanced switch is limited by that of the top-wall couplers. Second, the isolation between transmitters is large in both switch states of the Y switch, while in the balanced switch, in the switch state in which both tubes are unfired, the isolation is only that of the two couplers in series. Third, the peak power handling capacity of the Y switch is greater than that for the balanced switch. Fourth, the insertion losses are less in the Y switch than in the balanced switch.

Experimental Y-Junction Switch

A Y-junction switch for operation at S band was built and tested. Fig. 11 is a photograph of this switch. An individual switch tube is shown on the side. Each switch tube was approximately 1 inch long and had 1B58 TR tube windows at its ends. Measurements were made with a high power microwave source connected to port T1 of Fig. 10(a) and matched loads connected to ports T2 and ANT. A cyclotron resonant field was manually applied to Switch Tube 2 while the magnetic field applied to Switch Tube 1 was essentially zero. The required magnetic field was approximately 1200 gauss across a 3-inch gap.

Typical experimental results achieved for an argon filling at a pressure of 30 microns of Hg were as follows.

Power switched ($f=2.85$ kmc; $PW=2$ μsec)	250-kw peak, 250-watt average.
High level VSWR	1.20:1.
High level insertion loss	0.5 db.
Isolation	50 db.
High level firing time	$<2\times10^{-8}$ seconds.
Recovery time (3 db)	2 milliseconds.

The power switched was the maximum power obtainable from the available test equipment. The high power limit of the switch is determined by gas cleanup and the heat dissipation capabilities of the input window. This window dissipates an appreciable portion of the power absorbed by the discharge. At the 250-watt average power level this dissipation limit had not been reached. The measured recovery time was quite long, although it is sufficient to allow switching times of a few milliseconds provided the magnetic field switching power supply can switch the electromagnet current in this time. Subsequent investigation has indicated that recovery times smaller by at least a factor of ten can be achieved without adversely affecting the other switch parameters.

Only limited attention has been given thus far to the life of the switch. Due to the relatively low operating pressures, gas cleanup can seriously affect the life. Cleanup due to sputtering was observed over a period of only a few hours of operation. Markedly improved life was obtained by using encapsulated windows.

The bandwidth of the Y-junction switch is limited primarily by the bandwidth of the switch tube since the effect of the 120-degree E-plane bend is small.

Experimental Balanced Hybrid Switch

A balanced switch for operation at the high end of K_u band was built and tested. A photograph of this switch is seen in Fig. 12. The separate components of the switch shown assembled at the top are from left to right, a top-wall coupler, a dual matching section, the dual switch tube, a second dual matching section and a second top-wall coupler. The tapered pole pieces of the electromagnet are positioned at the top and bottom of the dual switch tube. The required magnetic field is approximately 5800 gauss across a $\frac{21}{32}$-inch gap. Each switch tube consists of a 0.020-inch wall low-loss ceramic body with 0.020-inch-thick ceramic windows at each end. A $\frac{3}{16}$-inch ID OFHC copper tube is used for evacuation and gas filling. The outside surface of the body of the tube is metallized to provide the conducting sides of the waveguide and to minimize eddy current losses. The matching sections are required to match out the discontinuities due to the ceramic windows.

Fig. 11—120-degree E-plane Y-junction switch for S band.

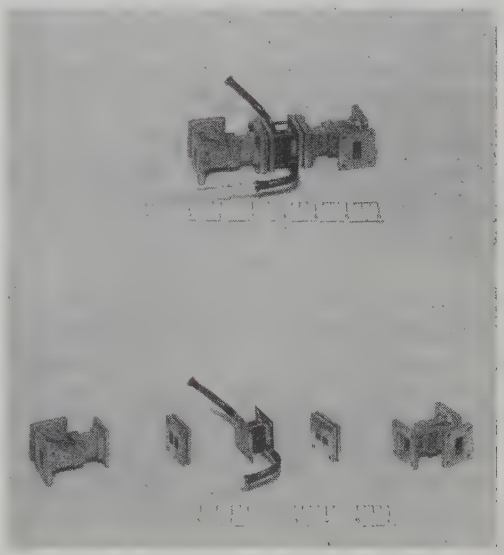

Fig. 12—Balanced top-wall hybrid switch for K_u band.

Fig. 13 shows the VSWR and insertion loss of this switch in its unfired state. The cold bandwidth between 1.25:1 VSWR points is more than 20 per cent. The insertion loss is less than 0.5 db from 15.5 to 17.5 kmc. The increase in insertion loss at each end is due to the fact that the top-wall couplers used were designed for operation only in the 15.5 to 17.5 kmc region. The unfired isolations exceed 20 db over the band.

High power measurements on the balanced switch were made with a microwave source connected to port

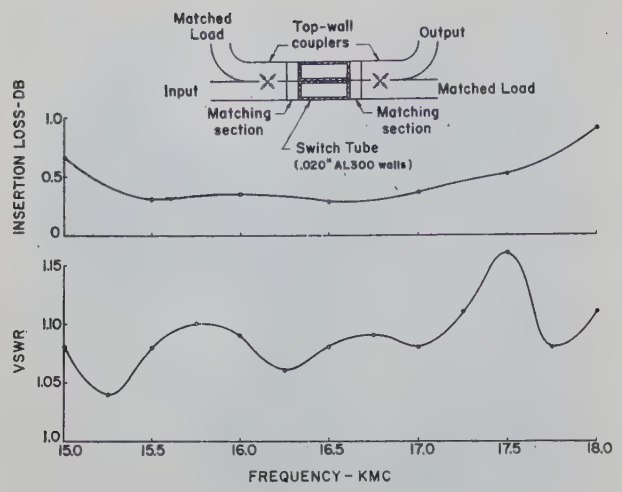

Fig. 13—VSWR and insertion loss of balanced switch in unfired state.

T1 of Fig. 10(b) and matched loads connected to the other three ports. A cyclotron resonant magnetic field was manually applied to the switch tube pair. Typical experimental results achieved for an argon filling at a pressure of 100 microns of Hg were as follows.

Power switched	60-kw peak,
($f=16.0$ kmc; $PW=1$ μsec)	60-watt average.
High level VSWR	1.12:1.
High level insertion loss	1.0 db.
Isolation	50 db.
High level firing time	$<2\times10^{-8}$ seconds.
Recovery time (3 db)	0.60 milliseconds.
Recovery time (0.1 db)	1.0 millisecond.

The power switched was close to the limit of the available sources. The insertion loss measured with a shorting plate simulating the fired tubes was 0.2 db so that the actual arc loss was 0.8 db. In an application in which both transmitters are active simultaneously, the output of the transmitter whose power is to be dissipated in the high power load also contributes to the discharge. Hence less power of the other transmitter is needed to maintain the discharge and the high level insertion loss would be reduced considerably.

The variation in the switch parameters for a ± 20 per cent variation in the magnetic field around cyclotron resonance was relatively small. The principal limitation on the bandwidth of the switch is the limited operating frequency range of the top-wall couplers.

Only preliminary life studies have been performed on this switch so no definite conclusions can be reached.

Conclusion

A new type of waveguide switching element employing a gas-filled tube immersed in a magnetic field was investigated both theoretically and experimentally. The operation of the switching element is based on the phenomenon of cyclotron resonance. The results were sufficiently promising that two different types of switches were constructed for transferring high power pulsed microwaves from either of two transmitters to a common antenna. The switches were broad-band, had high isolation, and can provide switching times considerably less than that of mechanical waveguide switches.

Acknowledgment

The authors gratefully acknowledge the assistance of S. Ichiki and D. Jeong, who performed many of the experiments in this investigation.

Solid-State Microwave Amplifiers*

HUBERT HEFFNER†

Summary—The maser and the parametric amplifier form a new class of microwave amplifiers which can exploit the properties of bound electrons in a solid. These amplifiers have several common characteristics, among them being their very low-noise performance. This paper reviews the method of operation of these amplifiers, discusses the performance achieved and achievable by the various versions, and points up some of the difficulties involved in effectively utilizing the extremely low-noise figures obtainable. A bibliography is included in which an attempt has been made to include all published papers on masers and parametric amplifiers.

TODAY technology is pressing close on the heels of new fundamental scientific discoveries and in turn, advances in understanding nature rely heavily on the technological exploitation of yesterday's new understanding. This intertwining of physics and engineering is perhaps nowhere so vividly illustrated as in the field of microwave solid state amplifiers. Right now certain forms of the maser must be held in abeyance until we obtain a more thorough understanding of the fundamentals of paramagnetic relaxation. At the same time, the successful operation of low-noise solid-state amplifiers has influenced other fields of physics. The astronomer, Gold, has said that the maser which will soon be attached to Harvard's radio telescope should yield measurements which will prove or disprove the cosmological theory of continuous creation of hydrogen. Here the familiar process of fundamental discovery to technology to new discovery has been telescoped from the usual time interval of decades to, at most, a few years.

There are at present—and I emphasize the words "at present"—two types of solid-state amplifiers at microwave frequencies, the maser and the variable parameter or parametric amplifier. The maser is an acronym coined by Townes [35] to stand for "microwave amplification by stimulated emission of radiation." The parametric amplifier draws its name from the fact that the differential equation which governs its operation has one or more parameters which vary with time. These two amplifiers operate on entirely different principles but they do have certain features in common.

1) They draw their energy from an RF source rather than dc
2) They behave as bilateral negative resistances at the amplifying frequency.
3) They are capable of very low-noise amplification.

Before we investigate each amplifier in more detail, let us examine briefly some of the implications of their common characteristics. First consider their behavior as bilateral negative resistances. In lumped circuit terms they appear as a negative resistance across a resonant *LC* tank with input and output coupled in. This is shown in Fig. 1. Because this is a negative resistance amplifier, the product of the square root of the power gain and bandwidth is a constant. The magnitude of this constant depends upon the type of amplifier and the material used.

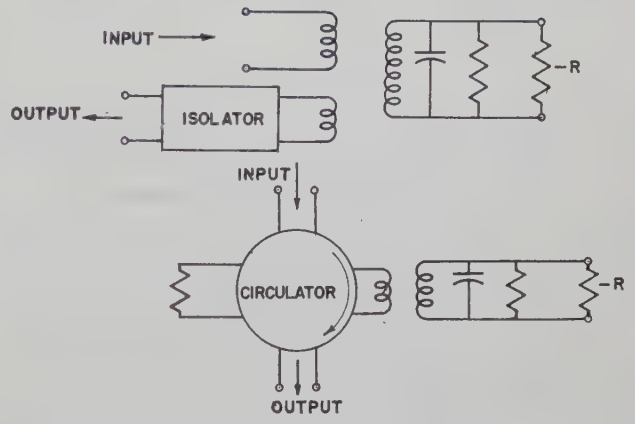

Fig. 1—Schematic representation of a solid-state amplifier as an effective negative resistance, showing its use with an isolator or circulator.

Because the negative resistance is bilateral, the magnitude of both load and source impedance will affect the gain. Thus, for stable amplification independent of the output match, some nonreciprocal element, either a circulator or isolator must be used. These elements serve another purpose also. They prevent thermal noise from a relatively hot load from entering the amplifier, there to be amplified and possibly to destroy the low noise behavior [45].

These new amplifiers, and in particular the maser, offer possibilities of low-noise amplification to a degree heretofore unattainable. The effective noise temperature of the maser can be as low as a few degrees Kelvin [52]. This low a noise temperature can be accomplished only at the expense of complicated external circuitry and use of liquid helium so that it is wise to ask whether such a low temperature is really needed.

To answer that question, let us consider the applications for which one might use a maser. Among these certainly are radio astronomy [46], radar, and scatter communications. Each of these would use a maser to amplify a signal received from an antenna. If now, the effective noise temperature of the antenna and its lead in are many tens of degrees, then an amplifier having an effective noise temperature of a few degrees is obviously of marginal utility in comparison to one ten times as noisy. Fig. 2 shows some measurements taken by J. E.

* Manuscript received by the PGMTT, July 25, 1958; revised manuscript received, September 2, 1958.
† Stanford University, Stanford, Calif.

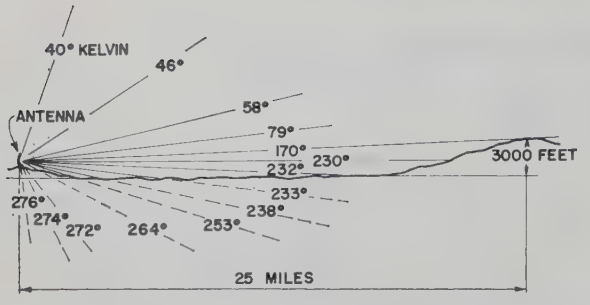

Fig. 2—Antenna temperature at 9270 mc as a function of elevation. The antenna used was an 18-inch parabola. The more-or-less horizontal line indicates the ground contour.

Sterrett of Stanford on antenna temperatures at X band as a function of the angle of elevation. The antenna used was an 18-inch parabola. The solid, more or less horizontal, line represents the ground surface showing a low range of hills some 25 miles away. Notice the minimum temperature measured was 40 degrees Kelvin. Most of this noise was due to side lobes seeing the earth as was shown when two large screens of chicken wire were placed beneath the antenna. With these in place the minimum noise temperature was reduced from 40 to 10 degrees. The same effect might well be achieved by placing the antenna in the center of a lake.

The antenna temperature is not the only limiting factor. If losses are present in the transmission system between antenna and amplifier, another noise source is added. If, for example, the transmission system is at room temperature and has 0.1 db loss, it is an effective noise source at about 7 degrees Kelvin, and if it has 1 db of loss its effective noise temperature is 78 degrees Kelvin.

These figures point up the very stringent requirements on any isolator or circulator which is used in conjunction with the amplifier. Perhaps, in order to make full use of the amplifier capabilities, these elements will have to be cooled also.

For many radio astronomy applications, low amplifier noise figure is not the only consideration. When using the Dicke radiometer system, what is important is the ratio of the amplifier noise temperature to the square root of the amplifier bandwidth. Table I shows a comparison of several forms of solid-state amplifiers with a particular (admittedly the best) low-noise traveling-wave tube. The column on the right gives the figure of merit, which one wants to be as high as possible. The author has marked several numbers in the chart with a question mark to indicate that these are reasonable, although as yet unobtained values. The chart shows several things: first, the relative superiority of the maser over the parametric amplifier; second, the great superiority of the traveling-wave versions of each; and third, just how good the traveling-wave tube is.

This chart does not tell the whole story, however, because, first of all, the noise introduced by antenna sidelobes and lossy lead in, as indicated, sets a lower limit

TABLE I*

$$M = \frac{\sqrt{B}}{F-1} \sim \frac{\sqrt{B}}{T_{amp}}$$

Type of Amplifier	T_{amp} °Kelvin	Bandwidth Mc	M
TWT	360° ($F=3.5$ db)	1000	25.4
Cavity maser	2°	0.4	91.6
Cavity parametric amp	25° (?)	1.0	11.6
TW maser	2°	20 (?)	648
TW parametric amp	25° (?)	300 (?)	201

* Amplifier figure of merit when used in a radiometer at 3000 mc. The question marks indicate reasonable but unobtained performance values.

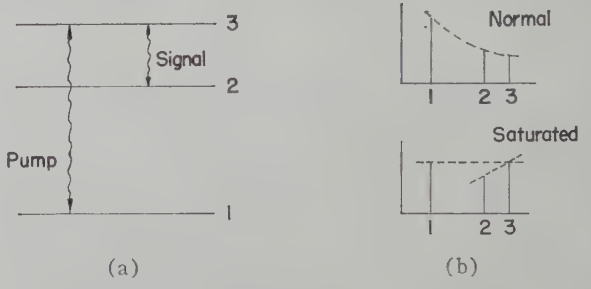

Fig. 3—Mechanism of operation of the three-level maser. (a) Energy levels. (b) Populations.

on useful amplifier temperature; and, second, for many radio astronomy applications a narrow bandwidth is required to pick out a particular spectral line. For this last reason, the apparent advantage in favor of the traveling-wave tube and the traveling-wave versions of the maser and parametric amplifier which result because of their increased bandwidth can often not be used.

Let us turn now to a brief discussion of the three-level maser [39]–[44]. The general way the maser operates is illustrated in Fig. 3, where three paramagnetic energy levels are shown with their normal populations given by Boltzmann distribution shown in the upper right hand corner. A strong microwave signal at the pump frequency corresponding to the energy difference between levels one and three saturates the resonance by bringing the populations of these two levels into equality. Under these conditions the population diagram can look somewhat as shown in the lower right hand corner. The population of the highest energy level, three, is greater than that of a lower energy level, two. This situation could be described by a Boltzmann distribution only if the temperature were taken to be a negative quantity. This negative temperature population distribution is now capable of emitting rather than absorbing energy. The magnitude of the negative temperature is also the effective noise temperature of the maser material [27–32].

Cavity-type masers using this principle have been built by the Bell Telephone Laboratories, Lincoln Laboratory, Harvard University, Columbia University, Hughes Aircraft Company, M.I.T., Ewen-Knight Com-

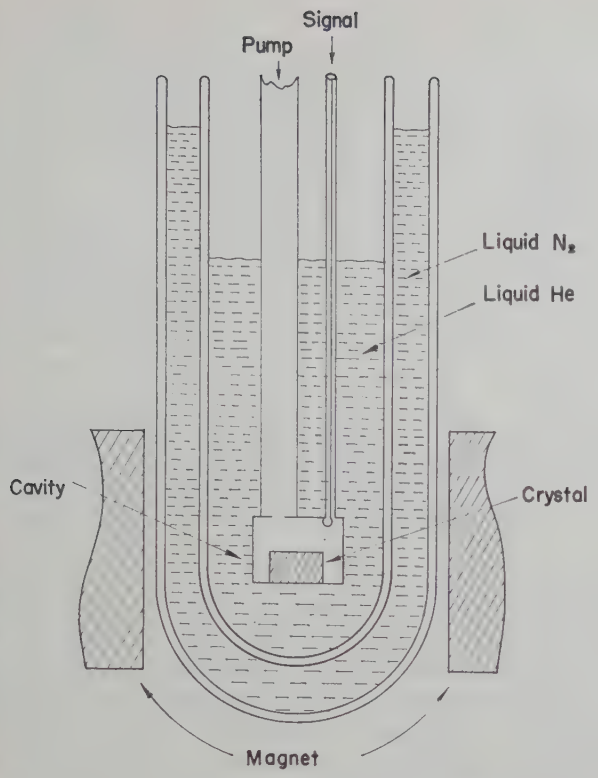

Fig. 4—Diagram of a three-level solid-state maser

pany, Michigan University, A.F.C.R.C., and Stanford University. They have operated at 300, 1400, 3000, 7000, and 10,000 mc, all at liquid helium temperatures. A schematic drawing of a cavity maser is shown in Fig. 4. Here between the pole-pieces which supply the dc magnetic field is an outer Dewar or vacuum flask which contains liquid nitrogen to aid in keeping heat away from the inner Dewar containing liquid helium. Immersed in the liquid helium is a cavity resonant to both the pump and amplifying frequencies containing the paramagnetic crystal. A waveguide supplies the pump power which saturates the upper and lower energy level resonance, and in this drawing a coax serves to feed the incoming signal and return the amplified reflected signal. A circulator (not shown) would be necessary of course to make a practical amplifier.

Typical cavity maser performance has been obtained using a pump power of 1 to 10 mw supplied at 9000 mc. Thirty-db gain at a signal frequency of 3000 mc results with a bandwidth of about 200 kc and a maximum power output of 1 to 10 μw. The noise figure is 0.04 db corresponding to a noise temperature of 3 degrees Kelvin.

Three paramagnetic materials which have been successfully used in three-level masers are single crystals of lanthanum ethyl sulphate $[La(C_2H_5SO_4)_3]$ doped with gadolinium [57], potassium cobalticyanide $[K_3Co(CN)_6]$ [10],[50] and sapphire $[Al_2O_3]$, both doped with chromium [55]. Fig. 5 illustrates the typical variation of the magnetic energy levels of chromium in $K_3Co(CN)_6$.

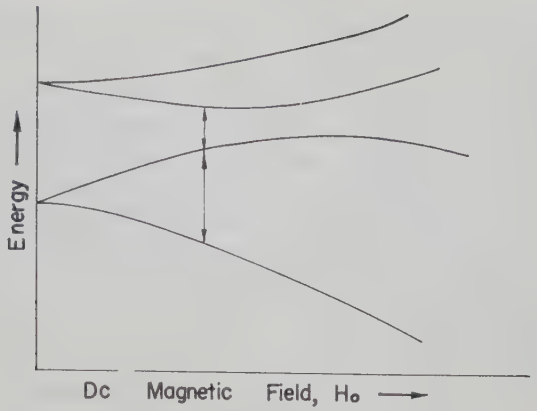

Fig. 5—Typical variation of energy levels of Cr^{+++} in $K_3Co(CN)_6$ with varying dc magnetic field.

These materials are by no means the only ones capable of being used. The double nitrates appear attractive as host crystals and other dopants in sapphire may have advantages. Of the three materials which have been used, the chromium doped sapphire (ruby) seems to be the best. It has favorable relaxation times and has the largest zero field splitting, which is a measure of how high in frequency the maser can operate.

As can be seen, there are three big disadvantages of this amplifier; first, it must be operated at liquid helium temperatures; second, it has an exceedingly small bandwidth; third, energy must be supplied at a higher frequency than that which is amplified. Can we reasonably expect that future developments will overcome these drawbacks?

The answer to whether we can eliminate the liquid helium is still unclear. We can not operate at much higher temperatures with the materials we now know, but the ultimate answer must await better understanding of the spin-lattice relaxation process—the way that microwave energy ultimately is transferred to heat. Possibly, if our paramagnetic crystals achieve the same degree of purity as transistor materials, we might be able to operate at higher temperatures.

The answer to the question of whether we can increase the bandwidth is an unqualified, "yes." The method is simple and involves merely the use of a traveling-wave circuit rather than a cavity. To see why this improves bandwidth, consider the cavity as simply a circuit which allows a wave to bounce back and forth between the walls many times before it dies out. Each time the wave passes through the crystal it is amplified very slightly; but if the cavity Q is high, it makes a sufficient number of passages through the crystal that the small amplitude increments of each passage add up to large gain. The price one pays is, of course, a very small frequency range over which the waves can bounce back and forth without phase interference effects destroying them.

In a wave guide filled with crystal, the wave passes through the crystal only once so the gain is low but the bandwidth can be the full bandwidth of the paramagnetic resonance line, typically 20 to 50 mc. We can increase the gain per unit length by decreasing the group velocity, which can be looked upon as providing the wave with a certain amount of bouncing back and forth as it achieves its net forward progress. The noise figure of the traveling wave version should be the same as that of the cavity maser.

The gain in db of such a traveling wave maser can be written as

$$G = \frac{27N}{Q_m(v_g/c)}$$

where N is the length of the structure in free space wavelengths, Q_m is the magnetic Q, and v_g/c is the ratio of group velocity to velocity of light. The magnetic Q is a function of the properties of the paramagnetic material and the filling factor, *i.e.* how effectively the RF magnetic field fills the crystal. The value of Q_m is typically 500–2000.

Recently Scovil[1] reported a traveling-wave maser using gadolinum doped ethyl sulphate in a filter structure composed of an array of wires shorted along one edge and placed between the two broad faces of a waveguide. The amplifier operated at 6.3 kmc with pumping power supplied at 9 kmc and had a gain of 30 db in about 7-cm length. The bandwidth was 10 mc with the center frequency capable of being tuned over a 350-mc band. The addition of garnet allowed nonreciprocal propagation so that the amplifier had 40-db loss in the reverse direction. One of the most interesting properties of this amplifier was its large signal behavior. The amplifier did not saturate until the output power was 30 milliwatts!

What about the final disadvantage, that of requiring pump power at a frequency higher than the signal? Can this restriction be eliminated? The answer is, "yes." For certain special materials with many energy levels it appears possible to pump up stairstep-wise and then fall back many levels to amplify at a higher frequency.

Let us turn now to the parametric amplifier. Unlike the maser, this amplifier operates on purely classical principles. As a matter of fact, the device which we would now call a parametric oscillator was studied by Lord Rayleigh in the last century. We can illustrate how it works quite simply by Fig. 6. Here is a simple LC resonant circuit in which we imagine we can physically grasp the condenser plates and pull them apart. At the upper right is shown the voltage across the condenser as a function of time. Imagine that when the voltage is a maximum, we suddenly pull the plates apart. We work to separate the charge and to increase the voltage. Now,

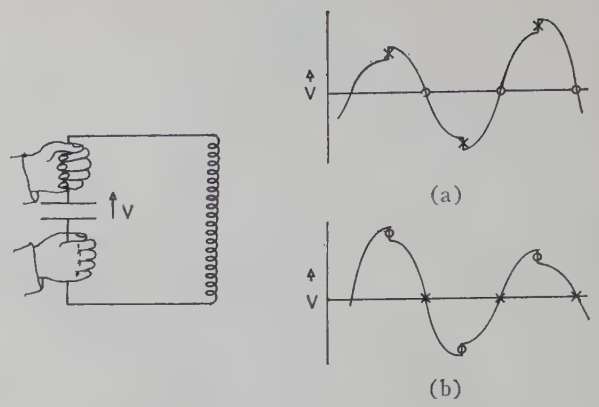

Fig. 6—Illustration of a parametric amplifier. The crosses indicate the sudden pulling apart of the capacitor plates, and the circles, the sudden pushing together. (a) Illustration of the phase relations suitable for growth of the voltage across the capacitor. (b) The attenuating effect of the opposite phase relations.

just as the voltage goes through zero and there is no charge on the plates, we push them back to their original position. No work is done and the voltage is unchanged. When the voltage is a negative maximum, we again pull the plates apart, and so on. In this way a signal at the resonant frequency is amplified by the changing capacitance. By coupling in an input circuit and a load, we have a parametric amplifier. Note the following three points, however.

First, our pushing or pulling, that is the capacitance variation, must be at a frequency which is twice that of the resonant frequency of the LC circuit.

Second, in order to amplify, we must be careful to pull apart when the voltage is maximum and push together when it is zero. If we do the opposite, the signal is attenuated. Another way of saying this is that this amplifier is phase sensitive. The phase of the capacitance variation frequency (we shall call this the pumping frequency) must be adjusted relative to the phase of the signal in order to amplify.

Third, we might just as well have varied the inductance, rather than the capacitance, and achieved the same result.

This circuit is often called a two-frequency parametric amplifier. Its phase sensitivity is usually a drawback, but for certain applications it can be turned into an advantage.

As an example, consider what happens when we introduce a signal whose frequency is slightly different from ω, the value which is just half the pumping frequency. We can treat this signal as though it were at the exact half frequency ω but had a time varying phase at the difference frequency. Thus, as the phase changes, the amplifier, as we have seen, alternately amplifies and attenuates. The output then is an amplified signal, amplitude modulated at the difference frequency. Another way of describing this is that if the incoming signal is treated as a single sideband, the amplifier inserts the other sideband. This behavior, coupled with low-noise characteristics, makes this form of the amplifier attractive for use in doppler radar receivers and in recep-

[1] H. E. D. Scovil, "Some performance characteristics of a solid state maser," presented at the Congres Internationale sur la Physique de l'Etat Solide et ses Applications à l'Electronique et aux Telecommunications, Brussels, Belgium; June, 1958.

tion of single sideband transmission, as employed in scatter communications.

Since the device either amplifies or attenuates, depending upon the phase relations between pump and signal, it can be looked upon as a two-state element, making it suitable for computer use. Indeed, Japanese workers have recently used a low-frequency version in an experimental computer [98].

For most applications, however, this phase sensitivity is a disadvantage. We can overcome this sensitivity by adding another resonant circuit, termed the idling circuit. This is shown in Fig. 7. Here we have a circuit resonant at the signal frequency ω_1 and a circuit resonant at the idling frequency ω_2. The two circuits are coupled together by a capacitance which is varied at a frequency ω_3, which is the sum of the two resonant frequencies ω_1 plus ω_2. The presence of the idling circuit introduces another degree of freedom, and the voltage developed across it will adjust itself in phase so that work is done by the capacitance variation causing both the signal and idling voltages to grow. Again, by coupling an input circuit and load into the signal circuit, we can make an amplifier. Also, by coupling a load into the idling circuit we can make an amplifying frequency converter.

So far, nothing has been said about how one obtains the variable capacitance or, what is equivalent, a variable inductance at microwave frequencies. The original microwave parametric amplifier proposed by Suhl [90] used ferrite as the variable element. Since then, others have proposed and successfully built parametric amplifiers using electron beams [93], [94], [108], [109] and back-biased semiconductor diodes [98], [99]–[102]. Other proposals for the variable element have been the use of ferroelectric materials and cyclotron resonance in semiconductors. Independent of the particular embodiment, however, one can write a general noise figure and gain-bandwidth expression for the amplifier [83], [84].

The sources of noise are threefold: thermal noise, shot noise, and random capacitance or inductance fluctuations in the variable element. Of these three, only the thermal noise appears to be of any importance in the solid-state versions of the parametric amplifier.

With only thermal noise, the noise figure for a parametric amplifier with circulator may be written

$$F = \frac{\omega_p}{\omega_i} \frac{Q_{\text{ext}}}{Q_l},$$

where

ω_p = pump frequency
ω_i = idling frequency
Q_{ext} = the external Q
Q_l = the loaded Q.

Thus, for a low-noise figure, one wants a low ratio of pumping-to-idling frequency, a high ratio of pumping-to-signal frequency, and close coupling of load to cavity. In the limit of negligible cavity and variable element losses, this Q ratio goes to unity and the minimum noise figure is then

$$F_{\min} = \frac{\omega_p}{\omega_i}.$$

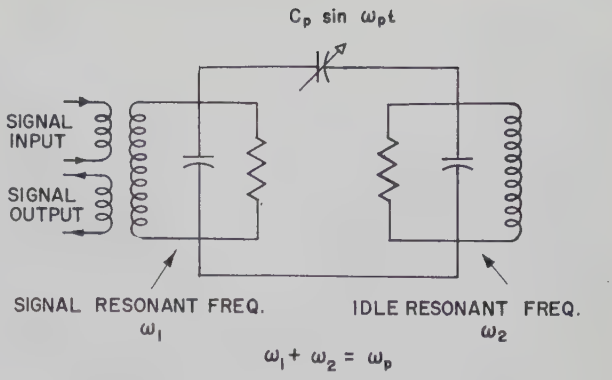

Fig. 7—A two-tank parametric amplifier.

Both of these expressions assume all elements are at the same standard temperature. If the cavity is cooled the appropriate temperature ratios must be employed.

The power-gain, fractional bandwidth product of the cavity version can in most cases be written as

$$G^{1/2} \frac{\Delta f}{f} \cong \frac{\omega_i}{\omega_s} \frac{1}{Q_i},$$

where

ω_i = idling frequency
ω_s = signal frequency
Q_i = idling circuit Q.

(If a circulator is employed, the gain-bandwidth is improved by a factor of two.)

This expression points up the desirability of having a large ratio of idling-to-signal frequency not only for low noise behavior, but also for large gain bandwidth.

As an example of the performance to be expected, this last expression would indicate that for a gain of 20 db, a parametric amplifier having an idling circuit Q of 100 would have a bandwidth of the order of a few tenths of a per cent.

Let us now turn to a discussion of the characteristics of the ferrite and semiconductor diode versions of the parametric amplifier. Hogan has already discussed in detail the characteristics of ferrites which make them suitable for use in these amplifiers, and so the author shall attempt only to assess their advantages and drawbacks relative to the semiconductor diode.

First, we can say that the usual ferrites are not attractive in this application. Their large line widths necessitate the use of unreasonably large amounts of pumping power, of the order of kilowatts. It is the newer garnets, with their narrow line widths, to which we must turn for practical amplifier materials. Even here, it is only the single crystal form which allows the pumping power to be reduced below several tens of watts.

The single crystal garnet, when used in the electromagnetic version, that is when both amplifying and idling modes are cavity resonances, still requires several watts of pumping power. It is only the semi-static or magnetostatic forms, in which one or both resonances are internal spin-wave resonances [115], [116], which allow the pumping power to be reduced below the watt level. It is still probably too early to assess the noise and gain-bandwidth capabilities of these versions. The nature of the loss mechanism of the spin-wave resonances is only imperfectly understood. It is fair to say, however, that the single-crystal garnet amplifier using spin-wave resonances is the only attractive form of the ferrimagnetic version, and that in the present state of the art it offers no advantages over the semiconductor diode. It is possible that as our knowledge improves, we shall find ways of making ferrimagnetic amplifiers with lower noise figures than those of the diode versions. To date, this is not the case.

Let us now consider the diode amplifier. A point contact or junction diode when back-biased has an equivalent circuit shown in Fig. 8. It is composed of a barrier capacitance C_D, which is voltage sensitive in series with a constant spreading resistance R_s. The voltage sensitive barrier resistance, which shunts the barrier capacitance, is so large in the back-biased condition that it can be neglected. Typically the barrier capacitance varies as the square root or cube root of the voltage across it, as is shown in the figure.

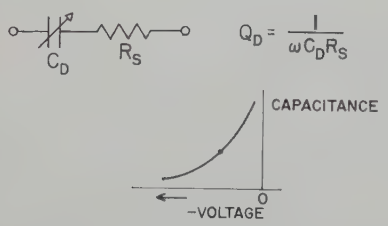

Fig. 8—The equivalent circuit and capacitance variation for a back-biased semiconductor diode.

The Q of the diode, the measure of energy stored to power dissipated, is $1/\omega CR$. It is this quantity which determines the noise performance of the amplifier. If the diode Q is low, the ratio of external Q to loaded Q can not be made small and, as we saw, the noise figure is directly proportional to this quantity.

To give an idea of the sort of performance which has been obtained, the characteristics of a diode parametric amplifier which was constructed a few months ago is mentioned [99]. This amplifier used a rectangular brass box as a cavity whose cross section is shown in Fig. 9. A photograph of this amplifier appears in Fig. 10. A germanium junction diode was supported between two posts in the center of the cavity, and by means of tuning screws, the cavity was made resonant at 1200, 2300, and at the sum frequency 3500 mc. A loop shown on the right of Fig. 10 served to couple in pumping power at 3500 mc causing the diode capacitance to vary at this frequency. With about 70 mw of pumping power, the device would oscillate at 1200 and 2300 mc with an output power of about 2 mw. With slightly reduced pumping power, we were able to amplify at either of the two frequencies. Using it as an amplifier at the lower frequency, we obtained a bandwidth of about 1 mc for 20-db net gain. At 16-db gain, the measured noise figure was less than 4.8 db.

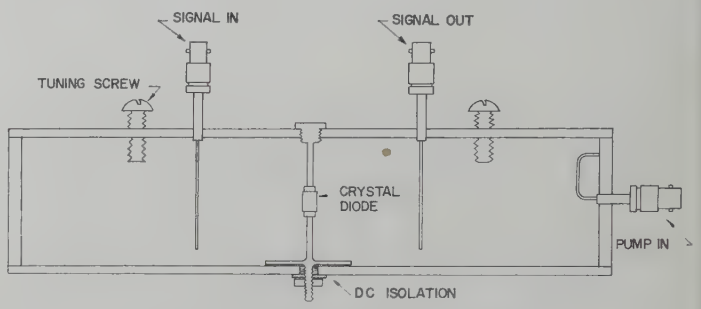

Fig. 9—Cross section of an experimental parametric amplifier.

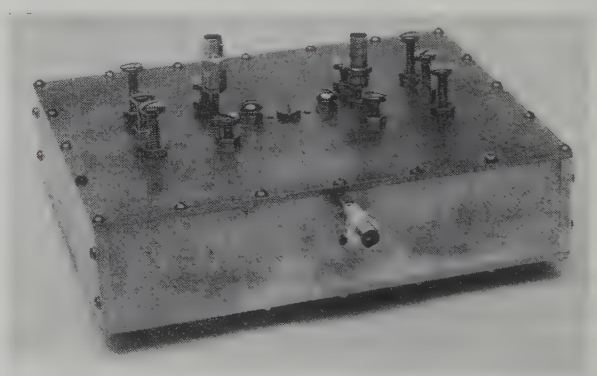

Fig. 10—Photograph of the parametric amplifier shown in Fig. 9.

This noise figure by no means represents the best that one can do. The diode which we employed has a Q of only 30 at the amplifying frequency. Using known techniques to produce better diodes, a better cavity design, and a higher pumping frequency, a noise figure at 1000 mc of about four tenths of a db can be achieved corresponding to an effective noise temperature of 30 degrees Kelvin, and all this without cooling.

It is obvious that the parametric amplifier is a strong adversary to the maser for low-noise amplification. Its one large advantage is that it can be operated at room temperature. Like the cavity maser, the cavity parametric amplifier has the disadvantages of narrow bandwidth and the necessity of pumping at a higher frequency than that to be amplified. As in the maser, these disadvantages can be overcome.

Hogan [85], at Harvard, Bloom and Chang [97], at R.C.A., and the author seem to have all simultaneously hit upon the fact that if one introduces still another resonant circuit to make a four-frequency parametric amplifier, the pump frequency can be made less than the signal frequency. This indicates that its minimum noise

figure is likely to be considerably higher than that of the three frequency scheme.

The disadvantage of narrow bandwidth can be overcome, as it was in the maser, by going to a traveling-wave circuit rather than a cavity [95], [96]. A schematic representation is shown in Fig. 11. Here we consider a transmission line with constant series inductance per unit length and time varying shunt capacitance per unit length. Tien [96] has analyzed such a configuration in detail and has shown that exponential gain can be obtained if the sum of the signal and idling frequencies is equal to the pumping frequency of the capacitance variation and also if the phase constants of the waves are related in the same fashion. One of the outstanding advantages of the traveling-wave parametric amplifier over its maser counterpart is that it is inherently nonreciprocal due to the relations which the phase constants must obey.

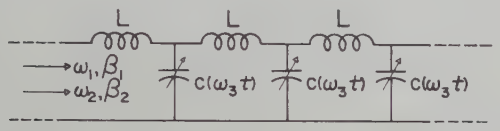

Amplification IF:

$\omega_1 + \omega_2 = \omega_3$

$\beta_1 + \beta_2 = \beta_3$.

Fig. 11—Schematic diagram of a traveling-wave parametric amplifier.

Recently, R. S. Englebrect reported an experimental traveling-wave parametric amplifier using four diodes, which amplified at 400 mc with 10 db gain and had a 25 per cent bandwidth. The amplifier was pumped at 900 mc and had an effective noise temperature in the vicinity of 50 degrees Kelvin.

And now, let us sum up the main points. The first is, that of the solid-state microwave amplifiers we now know, the maser has by far the lowest noise figure, which it achieves at the expense of requiring liquid helium. It is so low in fact, that it may not be effectively utilized in many systems where antenna and lead-in noise may be ten to thirty times that introduced by the maser. In these cases, the parametric amplifiers operating at room temperature with noise figures of one db or less, may be completely satisfactory.

The second point to emphasize is the great advantage of the traveling-wave versions of both the maser and parametric amplifier. To date these forms have not been fully exploited and there is a great deal of room for ingenuity in both their design and in their application.

Finally, it should be made clear that this whole field of microwaves and the solid state is in its infancy but it is a rapidly growing infant. Every month some new idea or technique or measurement comes along. New devices are invented before old ones are tested. The author suspects that a few years from now the forms of the amplifiers mentioned here and the performances will be as obsolete as the Stutz-Bearcat.

Bibliography

Maser Theory

General

[1] P. W. Anderson, "The reaction field and its use in some solid state amplifiers," *J. Appl. Phys.*, vol. 28, pp. 1049–1053; September, 1957.

[2] N. G. Basov and A. M. Prokhorov, "Possible methods of obtaining active molecules for a molecular oscillator," *J. Exp. Theor. Phys., USSR*, vol. 28, pp. 249–250; February, 1955.

[3] N. Bloembergen, "Electron spin and phonon equilibrium in masers," *Phys. Rev.*, vol. 109, p. 2209; March 15, 1958.

[4] N. Bloembergen, "Proposal for a new type solid state maser," *Phys. Rev.*, vol. 104, pp. 324–327; October 1, 1956.

[5] S. Bloom, "Effects of radiation damping on spin dynamics," *J. Appl. Phys.*, vol. 28, pp. 800–805; July, 1957.

[6] S. Bloom, "Molecular ringing," *J. Appl. Phys.*, vol. 27, pp. 785–788; July, 1956.

[7] D. I. Bolef and P. F. Chester, "Two-level solid state masers," Sci. Paper #6-94466-5-P11, Westinghouse Res. Lab.; May, 1957.

[8] D. I. Bolef and P. F. Chester, "Some techniques of microwave generation and amplification using electron spin states in solids," IRE Trans. on Microwave Theory and Techniques, vol. MTT-6, pp. 47–52; January, 1958.

[9] R. Braunstein, "Proposal for a nuclear quadrupole maser," *Phys. Rev.*, vol. 107, p. 1195; August 15, 1957.

[10] P. N. Butcher, "Theory of C. W. Solid State Masers," Stanford Electronics Labs., Stanford Univ., Stanford, Calif.; Tech. Rep. No. 155-1; December, 1957.

[11] P. F. Chester and D. I. Bolef, "Super regenerative masers," Proc. IRE, vol. 45, pp. 1287–1289; September, 1957.

[12] A. M. Clogston, "Susceptibility of the three-level maser," *J. Phys. Chem. Solids*, vol. 4, pp. 271–278; 1958.

[13] J. Combrisson and C. H. Townes, "Production and amplification of microwaves by atomic processes," *Onde élect.*, vol. 36, pp. 989–991; November, 1956.

[14] G. Feher, J. P. Gordon, E. Buehler, E. A. Gere, and C. D. Thurmond, "Spontaneous emission of radiation from electron spin system," *Phys. Rev.*, vol. 109, p. 221; April 1, 1958.

[15] R. P. Feynman, F. L. Vernon, Jr., and R. W. Hellwarth, "Geometrical representation of the Schrodinger equation for solving maser problems," *J. Appl. Phys.*, vol. 28, pp. 49–52; January, 1957.

[16] A. Gamba, "Cooperative phenomena in quantum theory of radiation," *Phys. Rev.*, vol. 110, pp. 601–603; May 1, 1958.

[17] A. Javan, "Theory of a three-level maser," *Phys. Rev.*, vol. 107, pp. 1579–1589; September 15, 1957.

[18] A. Kastler, "Quelques suggestions concernent la production optique et la detection optique d'une inegalite de population des niveaux de quantification spatiale des atoms," *J. Phys. Rad.*, vol. 11, pp. 255–265; June, 1950.

[19] V. M. Kontorovich and A. M. Prokhorov, "Nonlinear effects of the interaction of resonant fields in the molecular generator and amplifier," *J. Exp. Theor. Phys., USSR*, vol. 6, pp. 1100–1102; June, 1958.

[20] H. Motz, "Negative temperature reservoir amplifiers," *J. Electronics*, vol. 2, pp. 568–578; May, 1957.

[21] H. Heffner, "Maximum efficiency of the solid-state maser," Proc. IRE, vol. 45, p. 1289; September, 1957.

[22] A. E. Siegman, "Gain-bandwidth and noise in maser amplifiers," Proc. IRE, vol. 45, p. 1737; December, 1957.

[23] M. L. Stitch, "Maser amplifier characteristics for transmission and reflection cavities," *J. Appl. Phys.*, vol. 29, pp. 782–789; May, 1958.

[24] M. W. P. Strandberg, "Quantum mechanical amplifiers," Proc. IRE, vol. 45, p. 92; January, 1957.

[25] J. Weber, "Amplification of microwave radiation by substances not in thermal equilibrium," IRE Trans. on Electron Devices, ED-3, pp. 1–4; June, 1953.

[26] J. P. Wittke, "New approaches to the amplification of microwaves," *RCA Rev.*, vol. 18, pp. 441–457; December, 1957.

Noise

[27] M. W. Muller, "Noise in a molecular amplifier," *Phys. Rev.*, vol. 106, pp. 8–12; April, 1957.

[28] R. V. Pound, "Spontaneous emission and the noise figure of maser amplifiers," *Annals of Physics*, vol. 1, pp. 24–32; April, 1957.

[29] K. Shimoda, H. Takahasi, and C. H. Townes, "Fluctuations in amplification of quanta," *J. Phys. Soc. Japan*, vol. 12, p. 686; 1957.

[30] M. W. P. Strandberg, "Computation of noise-figure for quantum mechanical amplifiers," *Phys. Rev.*, vol. 107, p. 1483; September 15, 1957.

[31] M. W. P. Strandberg, "Inherent noise of quantum-mechanical amplifiers," *Phys. Rev.*, vol. 106, pp. 617–620; May 15, 1957.
[32] J. Weber, "Maser noise considerations," *Phys. Rev.*, vol. 108, pp. 537–541; November 1, 1957.

Negative Temperature

[33] A. Abragam and N. G. Proctor, "Spin temperature," *Phys. Rev.*, vol. 109, pp. 1441–1458; March 1, 1958.
[34] N. F. Ramsey, "Thermodynamics and statistical mechanics at negative absolute temperatures," *Phys. Rev.*, vol. 103, pp. 20–28; July 1, 1956.

Gas Masers

[35] J. P. Gordon, H. J. Zeiger and C. H. Townes, "The maser—new type of microwave amplifier, frequency standard, and spectrometer," *Phys. Rev.*, vol. 99, pp. 1264–1274; August, 1955.
[36] J. C. Helmer, "Theory of a molecular oscillator," Stanford Univ., Stanford, Calif., Microwave Lab. Rep. No. 311; June, 1956.
[37] K. Shimoda, T. C. Wang, and C. H. Townes, "Further aspects of the theory of the maser," *Phys. Rev.*, vol. 102, pp. 1308–3121; June, 1956.
[38] C. H. Townes, "Comments on frequency-pulling of maser oscillators," *J. Appl. Phys.*, vol. 28, pp. 920–921; August, 1957.

Review Articles

[39] R. W. Damon, "Maser shows promise, some drawbacks" (Pt. I), and "Maser's potential rests on further work" (Pt. II), *Aviation Week*, pp. 76–89; August 19, 1957 and pp. 91–104; August 26, 1957.
[40] J. W. Meyer, "The solid-state maser—a supercooled amplifier," *Electronics*, vol. 31, pp. 66–71; April 25, 1958.
[41] W. V. Smith, "Microwave amplification by maser techniques," *IBM J. Res. Dev.*, vol. 1, pp. 232–238; July, 1957.
[42] M. W. P. Strandberg, "Quantum mechanical amplifiers," PROC. IRE, vol. 45, pp. 92–93; January, 1957.
[43] G. E. Weibel, "Masers and related quantum-mechanical devices," *The Sylvania Technologist*, vol. 10, pp. 90–97; October, 1957 and vol. 11, pp. 26–43; January, 1958.
[44] J. P. Wittke, "Molecular amplification and generation of microwaves," PROC. IRE, vol. 45, pp. 291–316; March, 1957.

Maser Experiments

Solid-State Cavity-Masers

[45] F. R. Arams and G. Krayer, "Design considerations for circulator maser systems," PROC. IRE, vol. 46, pp. 912–913; May, 1958.
[46] J. O. Artman, N. Bloembergen, and S. Shapiro, "Operation of three-level solid-state maser at 21 C.M.," *Phys. Rev.*, vol. 109, p. 1392; February 15, 1958.
[47] S. H. Autler and N. McAvoy, "21 C.M. solid-state maser," *Phys. Rev.*, vol. 110, p. 280; April 1, 1958.
[48] J. Brossel, A. Kastler, and J. Winter, "Creation optique d'une inegalite de population entre les sous-niveaux zeeman de l'etat fondamental des atoms," *J. Phys. Rad.*, vol. 13, pp. 668–000; December, 1952.
[49] P. F. Chester, P. E. Wagner, and J. G. Castle, Jr., "Two-level solid-state maser," *Phys. Rev.*, vol. 110, p. 281; April 1, 1958.
[50] J. Combrisson, A. Honig, and C. H. Townes, "Utilisation de la resonance de spins electroniques pour realiser un oscillateur ou un amplificateur en hyperfrequences," *Compt. Rend.*, vol. 242, pp. 2451–2453; May, 1956.
[51] R. H. Kingston, "A UHF solid-state maser," PROC. IRE, vol. 46, p. 916; May, 1958.
[52] A. L. McWhorter and F. R. Arams, "System noise measurement of a solid state maser," PROC. IRE, vol. 46, pp. 913–914; May, 1958.
[53] A. L. McWhorter and J. W. Meyer, "Solid-state maser amplifier," *Phys. Rev.*, vol. 109, pp. 312–318; January 15, 1958.
[54] A. L. McWhorter, J. W. Meyer, and P. D. Strum, "Noise temperature measurement on solid state maser," *Phys. Rev.*, vol. 108, p. 1642; December 15, 1957.
[55] G. Makov, C. Kikuchi, J. Lambe, and R. W. Terhune, "Maser action in ruby," *Phys. Rev.*, vol. 109, p. 1399; February 15, 1958.
[56] H. E. D. Scovil, "The three-level solid-state maser," IRE TRANS. ON MICROWAVE THEORY AND TECHNIQUES, vol. MTT-6, pp. 29–38; January, 1958.
[57] H. E. D. Scovil, G. Feher, and H. Seidel, "Operation of a solid state maser," *Phys. Rev.*, vol. 105, pp. 762–763; January 1, 1957.
[58] M. W. P. Strandberg, C. F. Davis, B. W. Faughnan, R. W. Kyhl, and G. J. Wolga, "Operation of solid-state quantum mechanical amplifier," *Phys. Rev.*, vol. 109, pp. 1988–1989; March 15, 1958.

Gas Masers

[59] J. P. Gordon, "Hyperfine structure in the inversion spectrum of $N^{14}H_3$ by a new high-resolution microwave spectrometer," *Phys. Rev.*, vol. 99, pp. 1253–1263; August 1, 1955.
[60] J. C. Helmer, "Maser oscillators," *J. Appl. Phys.*, vol. 28, pp. 212–215; February, 1957.
[61] J. C. Helmer and M. W. Muller, "Calculation and measurement of the noise figure of a maser amplifier," IRE TRANS. ON MICROWAVE THEORY AND TECHNIQUES, vol. MTT-6, pp. 210–214; April, 1958.
[62] W. H. Wells, "Maser oscillator with one beam through two cavities," *J. Appl. Phys.*, vol. 29, pp. 714–717; April, 1958.

Miscellaneous

[63] N. G. Basov, V. G. Veselago, and M. E. Zhabatinski, "Improvement of the quality of a cavity resonator by means of regeneration," *J. Exp. Theor. Phys., USSR*, vol. 28, p. 242; February, 1955.
[64] E. M. Purcell and R. V. Pound, "A nuclear spin system at negative temperature," *Phys. Rev.*, vol. 81, p. 279; January 15, 1951.

Parametric Amplifier Theory

Nonlinear Circuit Theory

[65] W. R. Bennett, "A general review of linear varying parameter and nonlinear circuit analysis," PROC. IRE, vol. 38, pp. 259–263; March, 1950.
[66] R. J. Duffin, "Impossible behavior of nonlinear networks," *J. Appl. Phys.*, vol. 26, pp. 603–605; April, 1955.
[67] S. Duinker, "General properties of frequency-converting networks," dissertation, Tech. University of Delft, Netherlands; June, 1957.
[68] C. F. Edwards, "Frequency conversion by a nonlinear admittance," *Bell Sys. Tech. J.*, vol. 35, pp. 1403–1416; November, 1956.
[69] R. V. L. Hartley, "Oscillations in systems with nonlinear reactance," *Bell Sys. Tech. J.*, vol. 15, pp. 424–440; July, 1936.
[70] W. H. Higa, "Theory of nonlinear coupling in a novel ferroelectric device," *J. Appl. Phys.*, vol. 27, pp. 775–777; July, 1956.
[71] L. W. Hussey and L. R. Wrathall, "Oscillations in electromechanical systems," *Bell Sys. Tech. J.*, vol. 15, pp. 441–445; July, 1936.
[72] J. M. Manley and H. E. Rowe, "Some general properties of nonlinear elements—Part I. General energy relations," PROC. IRE, vol. 44, pp. 904–913; July, 1956.
[73] C. H. Page, "Frequency conversion with nonlinear reactance," *J. Res. Natl. Bur. Standards*, vol. 58, pp. 227–236; May, 1957.
[74] L. C. Peterson and F. B. Llewellyn, "The performance and measurement of mixers in terms of linear-network theory," PROC. IRE, vol. 33, pp. 458–476; July, 1945.
[75] H. E. Rowe, "Some general properties of nonlinear elements—Part II. Small signal theory," PROC. IRE, vol. 46, pp. 850–860; May, 1958.
[76] B. Salzberg, "Masers and reactance amplifiers—basic power relations," PROC. IRE, vol. 45, pp. 1544–1545; November, 1957.
[77] A. van der Ziel, "On the mixing properties of nonlinear condensers," *J. Appl. Phys.*, vol. 19, pp. 999–1006; November, 1948.
[78] J. von Neumann, "Nonlinear capacitance or inductance switching," U. S. Pat. No. 2,815,488; issued December 3, 1957.
[79] M. T. Weiss, "Quantum derivation of energy relations analogous to those for nonlinear reactances," PROC. IRE, vol. 45, pp. 1012–1013; July, 1957.

Cavity Amplifiers

[80] S. Bloom and K. K. N. Chang, "Parametric amplification using low frequency pumping," *J. Appl. Phys.*, vol. 29, p. 594; March, 1958.
[81] S. Bloom and K. N. Chang, "Theory of parametric amplification using nonlinear reactances," *RCA Rev.*, vol. 18, pp. 578–593; December, 1957.
[82] C. F. Edwards, "Frequency conversion by means of a nonlinear admittance," *Bell Sys. Tech. J.*, vol. 35, pp. 1403–1416; November, 1956.
[83] H. Heffner and G. Wade, "Gain, bandwidth and noise characteristics of the variable parameter amplifier," *J. Appl. Phys.*, vol. 29, pp. 1321–1331; September, 1958.
[84] H. Heffner and G. Wade, "Minimum noise figure of a parametric amplifier," *J. Appl. Phys.*, vol. 29, p. 1262; August, 1958.
[85] C. J. Hogan, R. L. Jepsen and P. H. Vartanian, "New type of ferromagnetic amplifier," *J. Appl. Phys.*, vol. 29, pp. 422–423; March, 1958.
[86] D. Lennov, "Gain and noise figure of a variable capacitance upconverter," *Bell Sys. Tech. J.*, vol. 37, pp. 989–1008; July, 1958.

Diode Versions

[87] D. Lennov, Bell Telephone Labs. Interim reports on Task 8, Signal Corps Contract No. DA-36-039-s65589; 1954 to present.

[88] A. Uhlir, Jr., "The potential of semiconductor diodes in high frequency communications," Proc. IRE, vol. 46, pp. 1099–1116; June, 1958.

Ferrite Versions

[89] J. M. Manley and E. Peterson, "Negative resistance effects in saturable reactor circuits," *Trans. AIEE*, vol. 65, pp. 870–881; December, 1946.

[90] H. Suhl, "Proposal for a ferromagnetic amplifier in the microwave range," *Phys. Rev.*, vol. 106, pp. 384–385; April 15, 1958.

[91] H. Suhl, "Theory of the ferromagnetic microwave amplifier," *J. Appl. Phys.*, vol. 28, pp. 1225–1236; November, 1957.

[92] H. Suhl, "Quantum analog of the ferromagnetic microwave amplifier," *J. Phys. Chem. Solids*, vol. 4, pp. 278–282; 1958.

Beam Versions

[93] W. H. Louisell and C. F. Quate, "Parametric amplification of space-charge waves," Proc. IRE, vol. 46, pp. 707–716; April, 1958.

[94] G. Wade and H. Heffner, "Gain, bandwidth and noise in a cavity-type parametric amplifier using an electron beam" (To be published.)

Traveling-Wave Versions

[95] A. L. Cullen, "A travelling-wave parametric amplifier," *Nature*, vol. 181, p. 332; February 1, 1958.

[96] P. K. Tien and H. Suhl, "A traveling-wave ferromagnetic amplifier," Proc. IRE, vol. 46, pp. 700–706; April, 1958.

Parametric Amplifier Experiments

Diode Versions

[97] K. K. N. Chang and S. Bloom, "A parametric amplifier using lower-frequency pumping," Proc. IRE, vol. 46, pp. 1383–1387; July, 1958.

[98] E. Goto, "On the application of parametrically excited nonlinear resonators," *J. Elec. Commun. Engs., Japan*, vol. 38, pp. 770–775; October, 1955.

[99] H. Heffner and K. Kotzebue, "Experimental characteristics of a microwave parametric amplifier using a semiconductor diode," Proc. IRE, vol. 46, p. 1301; June, 1958.

[100] G. F. Herrmann, M. Uenohara, and A. Uhlir, Jr., "Noise figure measurements on two types of variable reactance amplifiers using semiconductor diodes," Proc. IRE, vol. 46, pp. 1301–1303; June, 1958.

[101] S. Kita, "A harmonic generator by use of the nonlinear capacitance of germanium diode," Proc. IRE, vol. 46, p. 1307; June, 1958.

[102] B. Salzberg and E. W. Sard, "A low-noise wide-band reactance amplifier," Proc. IRE, vol. 46, p. 1303; June, 1958.

[103] H. C. Torrey and C. A. Whitmer, "Crystal Rectifiers," McGraw-Hill Book Co., Inc., New York, N. Y.; 1948.

Ferrite Versions

[104] V. D. Landon, "The use of ferrite-cored coils as converters, amplifiers and oscillators," *RCA Rev.*, vol. 10, pp. 387–396; September, 1949.

[105] K. M. Poole and P. K. Tien, "A ferromagnetic resonance frequency converter," Proc. IRE, vol. 46, pp. 1387–1396; July, 1958.

[106] M. T. Weiss, "Solid-state microwave amplifier and oscillator using ferrite," *J. Appl. Phys.*, vol. 29, p. 421; March, 1958.

[107] M. T. Weiss, "A solid-state microwave amplifier and oscillator using ferrites," *Phys. Rev.*, vol. 107, p. 317; July 1, 1957.

Beam Versions

[108] R. Adler, "Parametric amplification of the fast electron wave," Proc. IRE, vol. 46, p. 1300; June, 1958.

[109] T. J. Bridges, "A parametric electon beam amplifier," Proc. IRE, vol. 46, pp. 494–495; February, 1958.

[110] L. D. Buchmiller and G. Wade, "Pumping to extend traveling-wave-tube frequency range," Proc. IRE, vol. 46, pp. 1420–1421; July, 1958.

[111] R. W. DeGrasse and G. Wade, "Microwave mixing and frequency dividing," Proc. IRE, vol. 45, pp. 1013–1015; July, 1957.

Parametric Amplifier Materials

Ferrite Microwave Characteristics

[112] H. Suhl, "The nonlinear behavior of ferrites at high microwave frequencies," Proc. IRE, vol. 44, pp. 1270–1284; October, 1956.

[113] H. Suhl, "The theory of ferromagnetic resonance at high signal powers," *J. Phys. Chem. Solids*, vol. 1, pp. 209–227; September/October, 1956.

[114] H. Suhl, "Origin and use of instabilities in ferromagnetic resonance," *J. Appl. Phys.*, vol. 29, pp. 416–421; March, 1958.

[115] L. R. Walker, "Magnetostatic modes in ferromagnetic resonance," *Phys. Rev.*, vol. 105, pp. 390–399; January 15, 1957.

[116] L. R. Walker, "Resonant modes of ferromagnetic spheroids," *J. Appl. Phys.*, vol. 29, pp. 318–323; March, 1958.

Diode Characteristics

[117] L. J. Giacoletto and J. O'Connell, "A variable-capacitance germanium junction diode for U.H.F.," *RCA Rev.*, vol. 17, pp. 68–85; March, 1956.

[118] G. C. Messenger, "New concepts in microwave mixer diodes," Proc. IRE, vol. 46, pp. 1116–1121; June, 1958.

[119] G. C. Messenger and C. T. McCoy, "Theory and operation of crystal diodes as mixers," Proc. IRE, vol. 45, pp. 1269–1283; September, 1956.

[120] A. Uhlir, Jr., "Two-terminal *p-n* junction devices for frequency conversion and computation," Proc. IRE, vol. 44, pp. 1183–1191; September, 1956.

[121] A. Uhlir, Jr., "Shot noise in *p-n* junction frequency converters," *Bell Sys. Tech. J.*, vol. 37, pp. 951–988; July, 1958.

A UHF Solid-State Maser*

R. H. KINGSTON†

Summary—Chromium doped potassium cobalticyanide has been utilized in the design and construction of a solid-state maser operating in the frequency range of 300 to 500 mc. The pumping frequency is fixed at 5400 mc and the magnetic field required is in the vicinity of 80 gauss. The design utilizes a cavity mode at the pumping frequency and a tuned loop at the operating frequency, thus avoiding the design complications associated with the large size of UHF cavities. System measurements using a directional coupler for isolation yield noise temperatures of approximately 70 degrees Kelvin at bandwidths in the 50 kc range.

Introduction

THE operation of a maser using potassium chromicyanide was first described by McWhorter and Meyer.[1] Their device amplified at 2800 mc and used a pumping frequency of approximately 9000 mc. With the success of this mode of operation, it seemed possible to extend the operating range down to frequencies in the UHF region on the basis of extrapolation of the parameters of the initial maser design. The new design involves two major considerations. One is the choice of a suitable region in the paramagnetic energy level scheme of the crystal, while the other is the choice of a doubly resonant structure to support both the pumping and amplifying frequency resonances.

Crystal Operating Region

With 300 to 500 mc as the desired range of amplifying frequencies, the most apparent operating point is near the zero magnetic field range of the energy levels. Although appropriate transitions might be found in the 1000 to 2000 gauss region,[1] the variation of the spacings with field and angular orientation is extremely complicated. In addition the operation of a maser with fields of the order of a hundred gauss was attractive from the instrumentation point of view. (Another advantage connected with the use of superconductivity will become apparent below.) In Fig. 1 is the energy level diagram for two orthogonal orientations of the crystal in the zero-field region. By variation of the angle of the magnetic field with respect to the principal magnetic axis, it is possible to obtain the lower transition anywhere from 300 up to 1000 mc, while maintaining the pump frequency constant in the vicinity of 5400 mc. The theoretical gain-bandwidth to be obtained in this mode of operation may be calculated most directly by comparison with the results of McWhorter and Meyer's experiments. For the same crystal, the magnetic Q, or $|Q_M|$ is inversely proportional to $(f_{\text{pump}} - 2f_{\text{ampl}})$, while the gain-bandwidth product is given by[1]

$$G^{1/2}B = 2f_{\text{ampl}}/|Q_m| .$$

Since McWhorter and Meyer obtained a value of approximately 2×10^6 sec^{-1} for this figure, the expected value at 300 mc would be

$$\frac{5400 - 2(300)}{9400 - 2(2800)} \times \frac{300}{2800} \times 2 \times 10^6 = 0.27 \times 10^6 \text{ sec}^{-1}$$

assuming the same filling factor and equal values for the spin-lattice relaxation times.

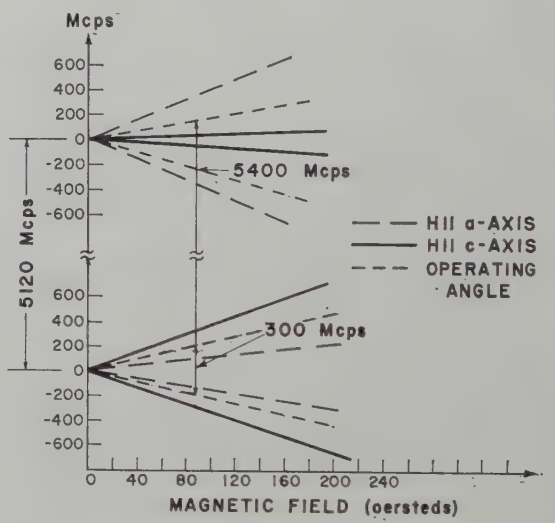

Fig. 1—Energy levels at low field in potassium chromicyanide.

Double Resonant Structure

Previous maser designs have utilized a microwave cavity which resonates both at the pumping and amplifying frequencies. It would be possible to build such a cavity for this design; however, the 18 to 1 ratio of frequencies places severe restrictions on the type of cavity which can be used. In particular, a straightforward coaxial $\lambda/4$ cavity at 300 mc is not only inconveniently large, but the 5400 mc mode would have so many nulls in the RF magnetic field that only a small part of the cavity volume could be used, thus lowering the filling factor. It is possible to foreshorten the low-frequency mode by heavy capacitative loading at the open circuited end as was done by Autler and McAvoy;[2] how-

* Manuscript received by the PGMTT, June 16, 1958; revised manuscript received, August 11, 1958. The research reported here was supported jointly by the U. S. Army, Navy and Air Force under contract with the Mass. Inst. Tech., Cambridge, Mass.

† Lincoln Lab., Mass. Inst. Tech., Lexington, Mass.

[1] A. L. McWhorter and J. W. Meyer, "Solid-state maser amplifiers," *Phys. Rev.*, vol. 109, pp. 312–318; January, 1958.

[2] S. H. Autler and N. McAvoy, "21-centimeter solid-state maser," *Phys. Rev.*, vol. 110, pp. 280–281; April, 1958.

ever, the much higher frequency ratio here required presented much more serious design problems. As an alternative, it was decided to forego a cavity mode at the lower frequency and use a single-turn loop terminated in a lumped capacitance. The dimensions and configuration of this resonant circuit, shown in Fig. 2 were chosen such that the RF magnetic field of the loop could be completely immersed in the RF magnetic field of a 5400 mc cavity mode. By placing the crystal, a cylinder 1.5 cm in diameter and about 2 cm long, such that the ac plane lies in the plane of the loop, most of the RF magnetic field will be perpendicular to the applied dc magnetic field, thus assuring close to the optimum transition probabilities. The dc field may also be rotated in the plane of the loop for tuning of the two resonances. This configuration when placed in a TE_{112} mode cavity, as shown in Fig. 3, was found to have only a small effect upon the unloaded Q of the 5400 mc mode. This mode was chosen since the resultant RF magnetic field at the center of the cavity lies in the plane of the loop and thus does not couple energy out of the mode.

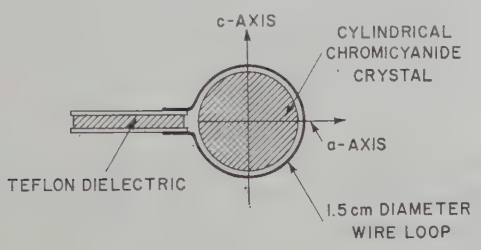

Fig. 2—300 mc resonant circuit.

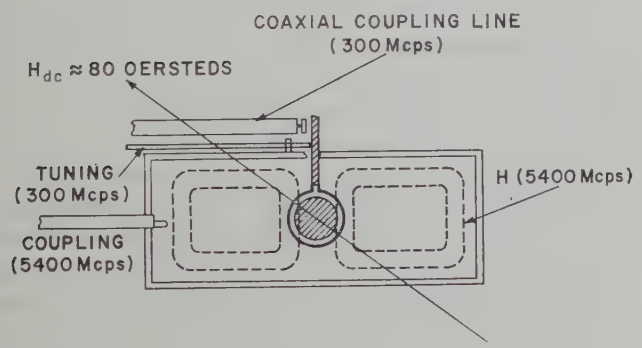

Fig. 3—Final maser assembly, cylindrical cavity (TE_{112} mode). The capacitor plate opposite the two probes is grounded to the cavity wall.

Although the resultant Q of the pumping mode was sufficiently high, that of the wire loop circuit was only about 200 even at liquid helium temperatures. Since the negative Q of the maser material was expected to be of the order of 1000, it was essential that the loop losses be diminished so that the unloaded Q would be much greater than $|Q_M|$. This improvement was obtained by the simple expedient of plating the loop and capacitor plates with lead, which is a superconductor at helium temperature. The resultant unloaded Q was of the order of 10,000. This technique is, of course, dependent upon the low magnetic fields used in the design, since lead ceases to be a superconductor in fields from 600 to 800 gauss in the 4.2 to 0 degrees Kelvin range. Another phenomenon of superconductivity can present difficulties. This is the Meissner effect, the shielding of the magnetic field by a superconducting material. Since the loop is a thin wire and the magnetic field lies in the plane of the loop, this effect is not of a serious nature.

Experimental Results

The instrumentation and mechanical equipment associated with the maser are similar to those used by McWhorter and Meyer with the exception of the actual frequencies. As shown in Fig. 3, both frequencies were coupled to the cavity by means of coaxial lines of silver plated stainless steel inner and outer conductor. In addition, fine tuning of the 300 mc mode was accomplished by external adjustment of the grounded capacitative probe between the coupling line and the cavity. The magnetic field was supplied by a six inch inner diameter wire-wound coil which could be tilted so that the field always lay in the plane of the 300 mc loop. The dc power requirement was 10 volts at 2.5 amperes. Provisions were also made to pump on the liquid helium so that the temperature of the bath could be lowered to 1.25 degrees Kelvin.

The maser was operated initially at 1.6 degrees Kelvin and 300 mc and yielded an oscillator output of approximately 0.1 microwatt. The gain at 100 kc bandwidth was approximately 10 db, giving a gain-bandwidth product of 0.32×10^6 sec^{-1}. Later measurements at 450 mc and 1.25 degrees Kelvin yielded gains as high as 25 db, in this case with a bandwidth of the order of 30 kc. This corresponds to a gain-bandwidth product of about 0.5×10^6, consistent with the higher frequency and the lower operating temperature. These numbers are in quite good agreement with McWhorter and Meyer's data which was taken at 1.25 degrees Kelvin with the same crystal material (0.5 per cent chromium concentration). The slightly higher values are consistent with the higher filling factor obtainable with the cylinder-loop configuration, although marked changes in the $|Q_M|$ could have occurred as a result of small differences in the three relaxation times involved.

System Performance

The theoretical noise contribution of such a maser in a system is of the order of 0.1 degree Kelvin. It should be noted that temperatures below the bath temperature are quite feasible since the high pumping ratio produces a "negative temperature" much smaller than the true positive temperature of the equilibrium electron distribution. With such a low theoretical value it was quite apparent that any serious noise sources in an amplifier system would arise in the associated circuitry and not in the maser crystal itself. As a test of the low-noise performance the maser was connected to a 450 mc antenna

system and low-noise receiver, as shown in Fig. 4. In this method of operation the maser is isolated from the receiver input noise by a directional coupler. The ideal method utilizing a circulator is not possible since such devices are not available at these frequencies. Here 10 db of gain is sacrificed with the advantage of 10 db attenuation of the receiver noise before it enters the maser. A disadvantage is the large reflected signal returned to the antenna terminals; however, the double stub tuner provided an adequate enough match to prevent serious gain fluctuations even when the antenna was moved through its total azimuth and elevation range. Independent radiometer measurements of the antenna system had established that the effective noise at the antenna terminals was 100 degrees Kelvin, when the antenna was pointed at quiet sky. (Sky temperatures off the galactic plane at this frequency are approximately 20 degrees Kelvin.) The remaining 80 degrees Kelvin may be attributed to antenna side and back-lobe pickup and loss in the transmission line between the feed horn

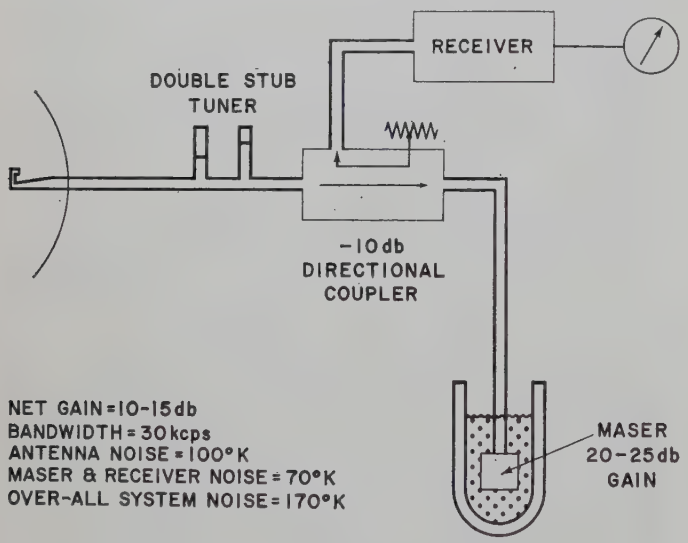

Fig. 4—Maser system measurement.

and the receiver installation. The receiver had a noise figure of 4.8 db, corresponding to 600 degrees Kelvin excess noise. By injecting a measured amount of noise signal from a gas tube into the antenna line by means of a directional coupler, the noise temperature of the over-all maser system was found to be 170 degrees Kelvin. This corresponds to a noise figure of $(1+170/300)=1.57$ or 2 db. When working with cold antennas, it should be remembered that the conventional noise figure definition is misleading, since in this case, the improvement from 4.8 db down to 2.0 db corresponds to an improvement in sensitivity of $(600+100)/(170)$ or 6.1 db. The experimental value checked quite well with the theory, using a maser gain of 25 db, as estimated from independent measurements. The noise sources referred back to the antenna terminals are:

Antenna and transmission line	=100°K
Receiver output noise—600°K down 15 db	= 20°K
Receiver noise into maser—400°K down 10 db	= 40°K
Termination in directional coupler—300°K down 15 db	= 10°K
Total excess noise referred to antenna terminals	=170°K

The receiver noise generated at the input terminals was measured independently with a radiometer and found to be 400 degrees Kelvin as used in the above calculations. This figure applies only to the particular input circuit used, a grounded-grid 416B. It is quite probable that a crystal mixer input, for example, might have an entirely different effect upon the performance, even though the over-all noise figure of the receiver were the same.

Conclusion

The experiments established the fact that a maser could be operated successfully in the UHF range in a reception system, with much lower noise than hitherto obtainable with standard receiver systems. There are, however, serious shortcomings to the system as presently operated. These are:

1) Lack of circulators or isolators in the UHF range. The ultimate in low noise could be obtained with these devices, as well as the elimination of instabilities arising from the high VSWR on the antenna line.
2) Narrow bandwidth. Although suitable for some applications, the critical tuning and lack of flexibility associated with the narrow bandwidth present serious system design problems.
3) Saturation sensitivity. Since the oscillator power output is only 0.1 microwatt it follows that the maser will saturate on incoming signals equal to this level divided by the maser gain. This means that radar use would require duplexer protection down to approximately 10^{-9} watts. Otherwise, the maser would not recover from the leakage pulse for approximately 0.1 second, the lattice relaxation time.
4) Antenna noise. Previously unimportant, the noise generated by the antenna and associated transmission system is now the main limiting factor and will require serious studies to assure optimum design for use with masers.

Acknowledgment

The experimental models and final maser design were constructed and tested by J. H. R. Ward, III, and many original suggestions on the design are due to A. L. McWhorter. The noise measurements were carried out with the cooperation of L. G. Kraft and A. Parsons.

A Microwave Frequency Standard Employing Optically Pumped Sodium Vapor*

W. E. BELL†, A. BLOOM†, AND R. WILLIAMS‡

Summary—An instrument in which a simple microwave triode oscillator is stabilized by reference to a natural atomic resonance—the field-independent hyperfine resonance of sodium—is described. Light from a sodium lamp is transmitted through an absorption cell containing sodium vapor and argon, which is placed in a resonant cavity. This light produces population differences between the two quantum levels which are involved in the desired atomic resonance and provides a means of detecting resonance. The cavity is excited by an external microwave triode oscillator which is frequency modulated to a small degree at 60 cycles. When the exciting oscillator frequency coincides with the center of the atomic resonance line, the signal observed by a photocell will be a modulation of the transmitted light at 120 cycles and higher even-order harmonics. Any deviation from line center will introduce a 60-cycle component whose phase and magnitude may be detected to produce an error signal to retune the oscillator in the usual servo loop manner. Theory predicts that an accuracy of possibly one part in 10^{10} can be achieved by systems using sodium and suitable local oscillators. It is evident also that such systems can be engineered into quite small packages, making possible many new applications of microwave oscillators stabilized to high order.

AN instrument is described in which a simple microwave triode oscillator is stabilized by reference to a natural atomic resonance—the field-independent hyperfine resonance of sodium. Although atomic resonances of this type have been used to produce primary frequency standards of hitherto unobtainable stability, it is not our intent to demonstrate such an instrument here. What we have built is a compact and simple microwave oscillator which has a short-time stability of about 1 part in 10^7 and a long-time stability of 1 part in 10^8 or better. As such, it represents an improvement by at least a factor of ten over previous simple microwave oscillators in this frequency range. The limiting factors determining the stability of this system have been shown to reside in the oscillator, rather than in the stabilization effected by the atomic resonance. It is clear that greater stability could be achieved by use of a microwave source with greater inherent stability, for example, a quartz crystal with multipliers. Such a system would not have the simplicity and compactness of the system presented here.

The over-all system is portrayed in the block schematic diagram of Fig. 1. Light from a sodium lamp is transmitted through an absorption cell containing sodium vapor and argon which is placed in a resonant cavity. The light produces population differences between the two quantum levels which are involved in the desired atomic resonance, and also provides a means of indication of the existence of resonance.[1] The cavity is excited by an external microwave triode oscillator which is frequency modulated to a small degree at 60 cycles. When the exciting oscillator frequency coincides with the center of the atomic resonance line, the signal observed by the photocell will be a modulation of the transmitted light at 120 cycles and higher even-order harmonics. Any deviation from line center will introduce a 60-cycle component whose phase and magnitude may be detected to produce an error signal to retune the oscillator in the usual servo loop manner.

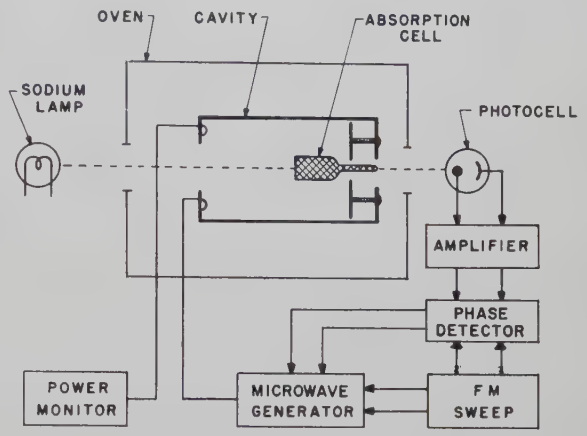

Fig. 1—Sodium vapor stable oscillator, block diagram.

General

A number of methods by which irradiation of a vapor by light can be used to provide population differences (optical pumping) has been described in the literature.[2–4] The one employed here is probably one of the simplest and depends on the fact that the presence of a relatively high pressure of buffer gas tends to disorient the spins of the atoms when they are in the optically excited states (but not in the ground states which are used in the radio-frequency resonance). This may be taken to imply that, although the various sublevels of the ground

* Manuscript received by the PGMTT, May 19, 1958; revised manuscript received, August 15, 1958.
† Varian Associates, Palo Alto, Calif.
‡ U. S. Naval Postgraduate School, Monterey, Calif.

[1] W. Bell and A. Bloom, "Optically detected field-independent transition in sodium vapor," *Phys. Rev.*, vol. 109, pp. 219–220; 1958.
[2] A Kastler, "Optical methods of atomic orientation and of magnetic resonance," *J. Opt. Soc. Amer.*, vol. 47, pp. 460–465; 1957.
[3] H. G. Dehmelt, "Slow spin relaxation of optically polarized sodium atoms," *Phys. Rev.*, vol. 105, pp. 1487–1489; March, 1957.
[4] J. P. Wittke, "Molecular amplification and generation of microwaves," PROC. IRE, vol. 45, pp. 291–316; March, 1957.

state may have different probabilities for absorbing light, they all have the same probability for receiving atoms which are reradiating light and returning from the excited states.[5] Steady-state conditions obviously require that the number of atoms leaving a given ground state sublevel must equal the number returning per unit time, so that one can make the following statement. If a_i is the number of atoms in the ith sublevel and P_i is the number of times per second each atom in the ith sublevel absorbs light, then the steady state condition is $a_i \propto 1/P_i$. In addition, we have the requirement that the total population is a constant. It is convenient to select this constant equal to one. This condition, plus the one given above, determines uniquely the populations of the various sublevels of the ground state provided only that we also know the rate, P_i, at which atoms absorb light in the various sublevels.

Most of the light which is emitted by a sodium lamp and which is absorbed by cold sodium atoms lies within the so-called D lines of sodium, the familiar yellow light of a sodium lamp. The difference between the D_1 and D_2 lines is of no importance here. However, what is important is the fact that each of these lines is in turn split into two closely spaced but completely separate hyperfine components. Fig. 2 shows part of the energy level diagram for the sodium atom, not drawn to scale. The difference between the two lines in a pair of hyperfine components is that one of them is capable of exciting atoms out of the $F=1$ state while the other is capable of exciting them out of the $F=2$ state. These frequencies are quite well separated as to function, since the naturally occurring width of an optical spectrum line of these wavelengths is of the order of several hundred megacycles due to Doppler broadening. This is considerably less than the 1772-mc separation of the energy levels. If the populations of all eight magnetic sublevels shown in Fig. 2 were equal, then it is clear that light capable of exciting atoms out of the $F=2$ level would be attenuated 5/3 as fast as the light exciting atoms out of the $F=1$ level, since there are 5 atoms in $F=2$ for every three atoms in $F=1$.

We are now in a position to describe the light absorption on a quantitative basis. Let us choose x as a normalized distance through the absorption cell; in practice, x is a function of sodium vapor density. Let us assume that we can neglect other effects besides the optical pumping which might contribute to the final population distribution. Then the intensity of the light as a function of distance through the absorption cell can be described by the following system of equations:

$$\begin{aligned} 3a_1 + 5a_2 &= 1 \\ dI_1/dx &= -3a_1I_1 \\ dI_2/dx &= -5a_2I_2 \\ a_1I_1 &= a_2I_2 \end{aligned}$$

[5] W. Bell and A. Bloom, "Optical detection of magnetic resonance in alkali metal vapor," *Phys. Rev.*, vol. 107, pp. 1559–1565; 1957.

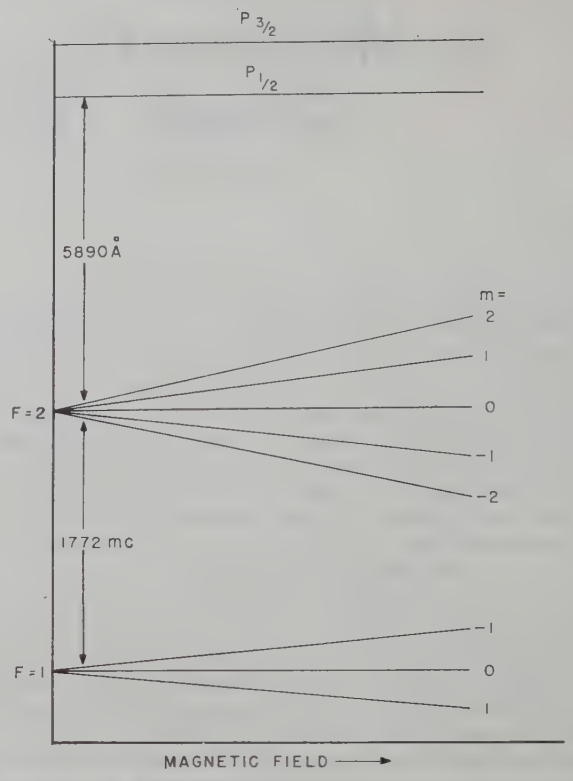

Fig. 2—Sodium atom energy levels diagram.

where we have implicitly substituted I_i for P_i. This is permissible because of their proportionality, which in turn holds because the transition probability per unit time for atoms in all sublevels are equal (assuming unpolarized light). This system of equations has an exact solution as follows, assuming $I_1=I_2=1$ at $x=0$,

$$I_1 = \frac{1}{5}(1 + \sqrt{1 + 15e^{-x}})$$

$$I_2 = \frac{1}{3}(-1 + \sqrt{1 + 15e^{-x}}).$$

These curves have been plotted in Fig. 3 together with the sum I_1+I_2, which is the light intensity as seen by the photocell when the light path through the absorption cell is x. On the other hand, if by some external agent we constrain the populations of all of the eight magnetic sublevels to be equal, then the light intensity would be given by $e^{-3x/8}+e^{-5x/8}$, which is indicated by the dashed line in Fig. 3. The actual reduction in light intensity by equalizing a particular pair of levels, such as the two $M=0$ levels, is probably about one fourth of that indicated. Thus, for example, at $x=3$ one might expect the change in light intensity due to the zero-zero resonance to be something of the order of 4 per cent of the total remaining light intensity. With known light sources, a reduction of intensity equal to that reached at $x=3$ is probably the greatest that can be expected before other effects such as thermal relaxation become important in determining population differences.

In the actual system, the radio frequency was swept

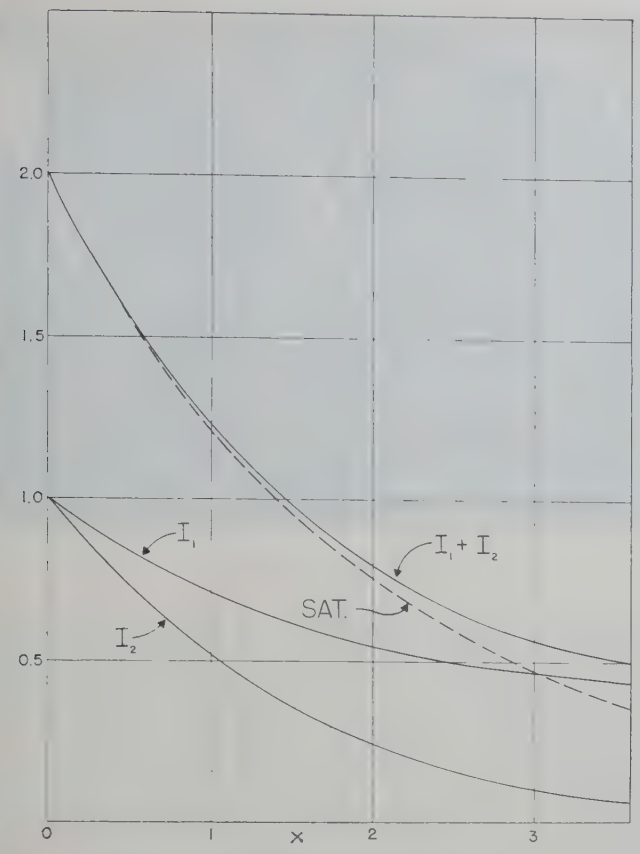

Fig. 3—Light intensity vs total absorption through the gas cell.

back and forth through the resonance at 60 cycles. The type of signal observed in this apparatus, which observes population differences rather than oscillating components of magnetization, is somewhat different from the resonance signals normally encountered. The process of producing a signal may be outlined as follows. As the frequency is swept exactly through resonance, the transient RF coupling to the spins rapidly inverts them,[6] *i.e.*, shifts the population difference. During the remaining half cycle or so when the RF is not exactly at resonance, the spins slowly return to population equilibrium with the pumping light, resulting in a relatively slow recovery of light intensity as observed by the photocell. At the end of the half cycle, the spins are back to equilibrium and ready for another inversion. The important thing which must be understood is that the "width" of the signal as observed in this system is not really a function of natural line width but is merely a function of the manner in which the sweep field operates. For this reason, in order to take full advantage of the relatively narrow line widths of these systems, it is necessary to operate with a quite narrow sweep and weak RF. However, quite satisfactory results also can be obtained with a wider sweep and more RF. The result is effectively a line with somewhat better signal-to-noise ratio and greater line width, and the system as a whole has a lower stabilization.

[6] F. Bloch, "Nuclear induction," *Phys. Rev.*, vol. 70, pp. 460–471; 1946.

Electronics

The oscillator is a conventional microwave triode of the lighthouse type, with cavities tunable about the desired frequency of resonance, 1772 mc. A fine frequency control is provided by a small variation of the plate supply voltage applied to the tube, which simultaneously yields a convenient method for frequency modulating the oscillator. Since the index of modulation needed is so small, no more than 1 part in 10^5, it was merely necessary to superimpose a small 60-cycle ripple on the output of the regulated power supply to sweep the oscillator through the sodium resonance.

The oscillator is loosely coupled to the cavity containing the absorption cell and provides the radiation necessary to excite the sodium hyperfine transition. The cavity is a right circular cylinder resonating in the TE_{011} mode with coaxial holes at each end to allow the light to pass in and out. The absorption cell is inside the cavity and is arranged to intercept the light beam. For a cavity in the TE_{011} mode, the magnetic lines of force of the RF field are parallel to the axis except near the ends where there are some components perpendicular to the axis. To excite the field independent transition, it is necessary that the RF field be parallel to any existing dc field such as the earth's magnetic field. By placing the absorption cell near one end of the cavity where components of the magnetic field in all directions are present, it was possible to achieve a reasonable amount of directional independence, so that the apparatus as a whole did not have to be oriented in one particular direction to give good signals.

The Q of the cavity used in optical detection does not have to be particularly high, since it is light absorption rather than electromagnetic radiation which is being detected. However, a high Q is useful in that it reduces the amount of power which is required from the oscillator to excite the cavity. The configuration employed allows a reasonably high Q (over 10,000) even though the holes at the ends are large enough to allow a beam of light about two inches in diameter to pass through. The absorption cell is a fused quartz cylinder two inches in diameter and three inches long. Quartz is used because of the reduced losses at these frequencies and thereby it does not appreciably perturb the field configuration of the cavity. The cell contains pure metallic sodium deposited at one end in a manner permitting a sufficient area to be transparent to the sodium light. The buffer gas is spectral grade argon at a pressure of about 10 centimeters of Hg, and the cell is operated at a temperature of about 135°C, which provides a vapor pressure for the sodium of about 10^{-5} millimeters of Hg.

The sodium lamp supplying the pumping light is of the electrodeless discharge type. A small glass tube containing the sodium metal with argon at about 1-mm pressure is placed in the tank coil of a self-excited power oscillator running at about 50 mc. This field supplies power to heat the sodium metal to produce vapor and

at the same time excites the vapor and causes the characteristic sodium light to be emitted. It was found that if the light from the lamp was very bright, the gas cell polarization would be quite poor. This could be explained by a broadening of the sodium light spectral line because of too high a vapor pressure. Time did not permit a complete examination of phenomena connected with the lamp, so that for purposes of our experiments we determined a particular set of lamp operating conditions (power dissipation in the oscillator) for which lamp operation was satisfactory. As long as these conditions were not varied drastically, stable operation of the lamp resulted for long periods of time.

The type 6570 photocell used to monitor the light intensity passing through the absorption cell has a surface of S1 material, which has a relative efficiency of about 50 per cent for sodium light. The signal resulting from optical detection of the resonance has a signal-to-noise ratio of 10 or more, with a photocell amplifier bandpass of the order of 10^3 cycles. A photograph (1 or 2 sweep cycles) of the scope presentation is shown in Fig. 4. The vertical signal is the photocell output plotted against the 60-cycle horizontal sweep also used as the phase detector reference.

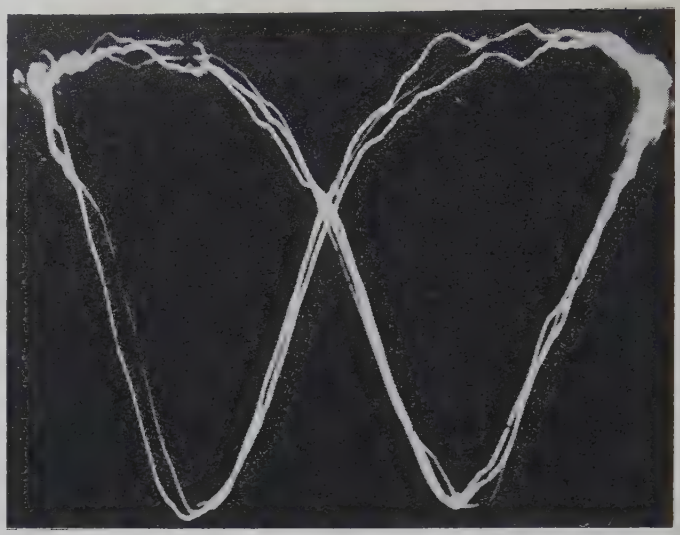

Fig. 4—Optically detected signals from sodium resonance.

Results

Time did not permit a complete examination of the parameters of this particular system; however, one particular set of operating conditions will be described. To evaluate the accuracy to which the frequency of the microwave oscillator triode is being controlled, it is necessary to measure the sweep width so that excursions of resonance within the sweep can be determined. It is fortuitous that the hyperfine structure of the sodium atom itself provides a convenient sweep calibration for these purposes, so that no additional apparatus is needed to make the calibration. If one shifts the frequency of the oscillator by about 350 kc, one can find two other resonances from the hyperfine structure, in particular, those from $F=2$, $m=0$ to $F=1$, $m=-1$ and from $F=2$, $m=-1$ to $F=1$, $m=0$. These resonances are almost coincident, and, as a matter of fact, it can be shown by theory that the separation of the resonances is almost exactly 1155 cycles in the laboratory magnetic field. Thus if the frequency modulation of the oscillator is of the order of several thousand cycles, these two resonances will appear as two separate and distinct peaks on the oscilloscope trace. Their separation relative to the total sweep can then be used to calibrate the sweep.

We operated the system with a sweep width of about 3000 cycles. Under this condition the system was quite stable, and we were able to operate for a total of about 100 hours without any major adjustments to the system. During this time, the crossover point of the oscilloscope signal remained within a factor of 10 per cent at the center of the trace. On this basis, it is clear that the oscillator had a short time stability of the order of 2 parts in 10^7 for periods corresponding to a few tenths of a second. The long-time stability, of course, was much greater than this, since at no time during a period of about 100 hours did the signal wander out of the dynamic range of the servoloop. When we attempted to narrow the sweep, the long-time stability was as good as or better than that given above. But on a short-time basis, it was observed that there were oscillations of the order of 1 cycle per second which could not be controlled by the existing time constants of the feedback loop. These oscillations are believed to be due to a hysteresis effect in the microwave triode, resulting in second derivative terms which cannot be controlled by a feedback loop consisting of simple RC time constants. Time did not permit a complete analysis of this problem. However, it is clear that a more sophisticated servomechanism controlling the feedback would enable us to control this oscillation, thus allowing one to go to much narrower sweeps and consequently much higher degrees of stability.

Theory predicts that an accuracy of possibly 1 part in 10^{10} can be achieved by systems using sodium and suitable local oscillators. It is also evident that such systems can be engineered into quite small packages, making possible many new applications of microwave oscillators stabilized to high order.

Microwave Filter Design Using an Electronic Digital Computer*

LEO YOUNG†

Summary—It is shown how a transmission-line circuit can be analyzed by a digital computer. Transformation matrices are used and broken down into equations which are applicable to a computer.

"Synthesis by computer" involves feeding in an approximate design and programming the computer to search for better parameters until the performance matches the specification. Examples are given to indicate time and cost of both analysis and synthesis procedures on an IBM Type 650 digital computer.

The synthesis of a stagger-tuned three-cavity filter is described.

Introduction

APPROXIMATE design formulas are available for various microwave circuits, such as direct-coupled resonator filters,[1] where the performance in the pass band is specified. To investigate the performance outside the pass band (such as the rejection at higher and lower frequencies, and the location of higher order pass bands), to determine the effect of tolerances, and to test the accuracy of the design formulas, several microwave circuits have been analyzed over wide frequency bands by programming a digital computer. The circuits analyzed in this paper are all direct-coupled multicavity resonator filters exhibiting band-pass behavior.

The synthesis of distributed parameter circuits is more difficult than their analysis. There appears to be one exact method,[2] but it holds only for resistor-transmission-line circuits. Another method of synthesis is described in this paper. Its main usefulness is likely to be in those cases where it is desired to improve an already existing approximate design. This method does not develop algebraic formulas, but arithmetical procedures which are programmed for a digital computer. The design procedure may be broken down into the following steps.

1) The designer estimates his circuit parameters by approximate design formulas, or by means of a Smith chart.
2) He analyzes the resulting rough design on a computer.
3) He varies his parameters until the new performance is acceptable.

Step 3 is usually accomplished by a series of approximations, in which the design adjustments become smaller and smaller as the performance converges on the specification.

The computer is able to reach decisions that make "synthesis by computer" possible. Essentially, this "synthesis" consists in letting the computer not only perform the arithmetical tasks in step 2 above, but also take over the decision making listed in step 3. It is in this narrow sense only that "synthesis by computer" is spoken of in this paper.

Three questions now present themselves.

1) Is the specification realizable with the given circuit configuration?
2) Can the prescribed process of cut and try (adjustment and selection) converge to give the specified performance?
3) Can initial approximate parameter values be found so that the process not only can, but *does* converge?

Only if all three answers are positive, will the search for a better design be successful. No universal test can be applied, and it may be a matter of trial and error until a convergent combination is found.

Time and Cost Considerations

When should a digital computer be used? Briefly, whenever lengthy repetitive calculations are involved, as in the computation of the VSWR of a filter at many frequencies. To gain some idea of the time and cost involved, the following example is given. The machine was an IBM Type 650, a medium fast computer. A basic language program was used, and the computer had a floating decimal device and three index registers. It also had a 60-word magnetic core storage, and bands of data and instructions were transferred from the drum to core storage for execution.

It was required to design a three-cavity direct-coupled transmission line band-pass filter. An optimum (equal ripple) design was specified. To program the computer for the analysis of this circuit took about two days. To run one analysis on the machine takes just three seconds per frequency point, plus one minute loading time. Thus, 40 spot frequencies take three minutes. To synthesize the circuit by trial and error, for example, might involve five adjustments by the operator. Each time, the computed data has to be examined before the next trial solution is loaded into the computer. This particular problem was then programmed for computer synthesis. The computer completed the synthesis in five to six minutes, including the final analy-

* Manuscript received by the PGMTT, June 9, 1958; revised manuscript received, July 16, 1958.

† Westinghouse Electric Corp., Baltimore 3, Md.

[1] S. B. Cohn, "Direct-coupled resonator filters." PROC. IRE, vol. 45, pp. 187–196; February, 1957.

[2] P. I. Richards, "Resistor-transmission-line circuits," PROC. IRE, vol. 36, pp. 217–220; February, 1948.

sis. Computer time is a dollar a minute in round figures, and there was actually a net saving over the repeated analysis method. However, to program the computer for synthesis took about two weeks, as against two days for the analysis alone.

Transformation Matrices

When using a computer, advantage has to be taken of its great facility to perform repetitive calculations. It is best, therefore, to break the problem down into a number of operations of similar form, letting the machine substitute new numbers as it works its way through the problem. This can be understood by visualizing a transmission line containing lumped discontinuities (such as irises or sudden changes in cross section). The transmission line in Fig. 1 is loaded at intervals by obstacles

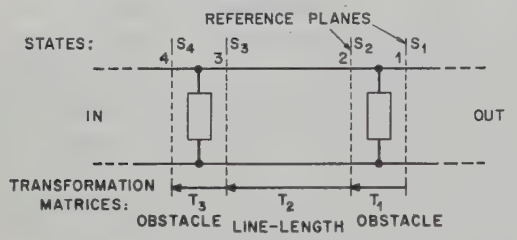

Fig. 1—Transmission line loaded at intervals.

(represented by rectangular boxes). For reasons which are explained presently, we shall always work from output (on the right) to input (on the left). The several vertical broken lines in the figure are the reference planes in the waveguide. The "state" of the waveguide in the various reference planes is denoted by S_1, S_2, S_3, · · · . "State" means any two complex numbers forming a two-dimensional complex column vector, which completely describes the electromagnetic condition or state of the waveguide, assuming only one mode of propagation. The two elements of the vector representing a state are usually the voltage and current,[3] respectively, or the incident and reflected wave amplitudes.[3,4] The state S_2 in reference plane 2 can be calculated from the state S_1 in reference plane 1 by operating on S_1 with the matrix operator T_1:

$$S_2 = T_1 S_1. \tag{1}$$

If, for instance, S is composed of voltage E and current I, so that

$$S = \begin{pmatrix} E \\ I \end{pmatrix} \tag{2}$$

then T is the $ABCD$ matrix[3]

$$T = \begin{pmatrix} A & B \\ C & D \end{pmatrix}. \tag{3}$$

The computer then solves for S_{n+1} by an iterative procedure from

$$S_{n+1} = T_n T_{n-1} \cdot \cdot \cdot T_3 T_2 T_1 S_1. \tag{4}$$

It is more convenient to work back from the output to the input because the state S_1 is always known. Usually, the termination is a matched load, and (after normalization)

$$S_1 = \begin{pmatrix} 1 \\ 1 \end{pmatrix} \tag{5}$$

for the $ABCD$ matrix.

Synthesis by Computer—Advantages and Limitations

At first, to save time and constant reloading, several trial circuits were loaded together, and the machine analyzed one after another. From the computed results a new and, if possible, better set of circuit parameters was estimated, and so on. In many cases, it was found that data accumulated at a greater rate than the human operator's limited capacity to absorb and select. It was then that the idea of letting the computer not only calculate but also select from the data, finally printing only the best design, seemed most attractive.

Certain limitations of the search or synthesis procedure by computer later became apparent. To write the specification exactly as desired into the computer is not always practical. For instance, to specify a certain maximum VSWR inside a given frequency band would require more time programming and computing than to specify the n frequencies at which the reflection coefficient of a lossless n-cavity filter is to be zero, plus one other parameter to fix the scale. For instance, one can let the n frequencies of zero reflection coefficient be determined by a comparison with the corresponding Tchebycheff polynomial having the desired bandwidth. Thus the formulation of the problem will usually involve some compromise; the specification should be written so that it can be programmed readily into the computer, while yet retaining the intentions of the designer.

Synthesis of a Three-Cavity Stagger-Tuned Filter

The circuit to be optimized is a symmetrical lossless three-cavity direct-coupled band-pass filter, as shown in Fig. 2, consisting of a transmission line with four shunt inductive posts. Thus, there are four independent parameters, the values at some fixed frequency of the susceptances $-jb_1$, $-jb_2$ and their spacings ϕ_1, ϕ_2. Since it would be difficult to adjust and optimize four independent parameters, they will be reduced to two. To begin

[3] G. L. Ragan, "Microwave Transmission Circuits," M.I.T. Rad. Lab. Ser., McGraw-Hill Book Co., Inc., New York, N. Y., vol. 9, pp. 544–554; 1948.

[4] L. Young, "Branch guide directional couplers," *Proc. Natl. Electronics Conf.*, vol. 12, pp. 723–732; 1956. (See also *Proc. IEE*, pt. B, vol. 104, p. 586; November, 1957.)

with, they are reduced to three by keeping b_1 fixed. (If necessary, more values of b_1 can be tried later.)

The synthesis of the circuit now is explained briefly with the aid of Fig. 2(b), in which

$$\phi_1 = \tfrac{1}{2}(\beta_1 + \theta_1) \tag{6}$$

where at the plane separating β_1 and θ_1 the admittance is taken real at all frequencies. This defines β_1; θ_1 is made variable and later optimized by the computer.

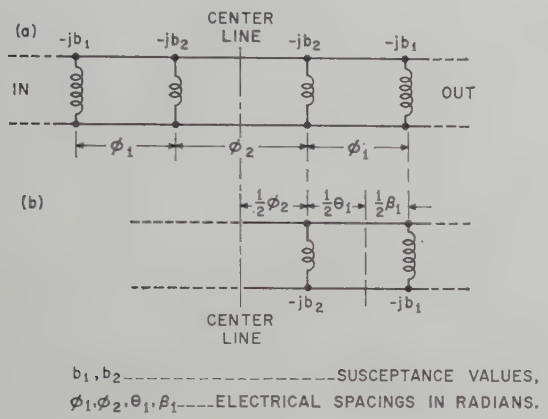

Fig. 2—Symmetrical three-cavity filter.

The susceptance value b_2 is the other variable to be optimized by the computer. If the filter is to be matched at this frequency, then the susceptance value seen from the center plane must be zero, which then determines ϕ_2.

So far, only one frequency has been considered, and θ_1 and b_2 are still arbitrary. Let it be required that the filter also be matched at two other frequencies, one on each side of the fixed frequency. It is required that b_2 and θ_1 be adjusted until a perfect match is obtained at the three given frequencies.

The design procedure, or synthesis by computer, is now as follows. A value of θ_1 and b_2 is estimated from an approximate design formula.[1,5–7] With this as a starting point, the computer keeps θ_1 fixed and solves for b_2 twice, once for $b_2 = b_2'$ which gives a perfect match at the lower specified frequency, and once for $b_2 = b_2''$ which gives a perfect match at the upper specified frequency. This is repeated for several values of θ_1. The design is complete when

$$b_2' - b_2'' = D(\theta_1) = 0. \tag{7}$$

Any frequency dependence can be assumed for the shunt susceptances. The problem of interest concerned a coaxial line with posts between the inner and outer conductors which behave as shunt inductances. Their reactance therefore is made proportional to frequency.

It is important to make the first estimate as accurate as possible; otherwise, the procedure may not converge. This occurs when the initial value is on the wrong side of a local maximum or minimum of the quantity which it is tried to zero (point A in Fig. 3). The increment values should be chosen carefully. In this problem, it was considered better to use two sets of increments. First, the steps are larger until the appropriate zero line is crossed (points 1, 2, 3, 4 in Fig. 3). Then this is repeated in smaller steps, starting from the hitherto best value (points 4, 5, 6, 7, 8 in Fig. 3). Finally, the machine interpolates between the two nearest points (7 and 8 in the figure) on opposite sides of the zero line.

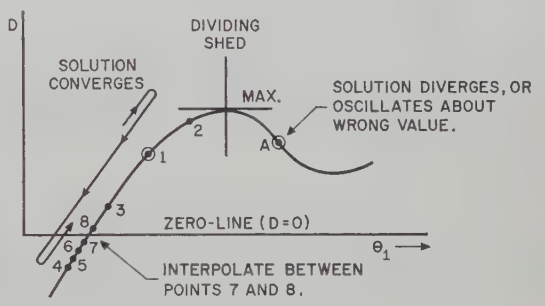

Fig. 3—Illustrating "synthesis by computer."

Conclusion

Most of the numerical and experimental work has been undertaken in connection with the design of three and four-cavity coaxial-line filters. The cavities are defined by posts between the inner and outer conductors, which behave as shunt inductances. The programs also could be applied to dispersive lines in which the shunt susceptances are proportional to the guide wavelength (this holds quite closely for waveguide inductive irises). In this case, frequency is replaced by reciprocal guide wavelength. Programs are now available which analyze direct-coupled resonator filters with up to nine cavities, computing the VSWR, attenuation, and other quantities of interest at all specified frequencies. Small ohmic losses, both distributed in the line and lumped with the inductances, also may be included with these programs.

Acknowledgment

The author thanks Coleman J. Miller, advisory engineer, for many helpful discussions; Tom ap Rhys, project engineer, for working out most of the approximate designs for the computer, and Wade Etchison, section manager, for guidance of the computer programming.

[5] G. C. Southworth, "Principles and Applications of Waveguide Transmission," D. Van Nostrand Co., Inc., New York, N. Y., ch. 9; 1950.

[6] R. Levy, "An improved design procedure for the multi-section generalized microwave filter," *Proc. IEE*, pt. C, vol. 104, pp. 423–432; September, 1957.

[7] H. Seidel, "Synthesis of a class of microwave filters," IRE Trans. on Microwave Theory and Techniques, vol. MTT-5, pp. 107–114; April, 1957.

Measurement of Two-Mode Discontinuities in a Multimode Waveguide by a Resonance Technique*

L. B. FELSEN†, W. K. KAHN†, AND L. LEVEY†

Summary—The deliberate use of two or more propagating modes in a multimode waveguide, and a knowledge of associated control elements, has assumed renewed importance, particularly for millimeter wavelength applications. This paper presents a resonance measurement technique for the precise evaluation of the equivalent network for a lossless shunt discontinuity coupling two nondegenerate modes in a multimode waveguide. The discontinuity structure is placed into a cavity closed by adjustable plungers, and the data consists of those plunger positions which render the cavity resonant in the two modes of interest. This multipoint data is then transformed to permit an analysis of the two-port network in the discontinuity plane by conventional techniques.

Computations and experimental results obtained at *S* band illustrative of the procedure are presented for shunt discontinuities coupling the E_{01} and H_{01} modes in circular waveguide. The accuracy achieved is comparable to that obtained in single mode precision measurements.

I. Introduction

TECHNIQUES for the measurement of the equivalent network parameters of discontinuities coupling two or more modes in a multimode waveguide are of interest for a variety of guided wave systems admitting the propagation of more than one mode. Included among these are coupled closed or open (surface or leaky) waveguides supporting several "normal" modes, and oversized conventional waveguide configurations,[1–6] with renewed interest in the latter provided by millimeter wavelength applications. We may distinguish two broad categories of multimode waveguide operation: those which seek to restrict propagation to a single preferred mode, and those which exploit deliberately the presence of, and interaction between, several modes. The associated multimode measurement techniques reflect the needs of these waveguide systems. For single-mode operation, every effort is made to maintain mode purity, and the aim is to detect and minimize the presence of unwanted propagating modes. Thus, a measurement of the (small) relative power coupled into the spurious modes is usually sufficient.[2–5] For true multimode operation, on the other hand, one is often concerned with discontinuities which cause appreciable interchange of energy between various modes, as utilized, for example, in the design of mode transducers, directional couplers, filters,[6] etc. In this instance, a complete and accurate knowledge of the network properties of a discontinuity is essential.

This paper describes a resonance technique for measuring the complete equivalent circuit for a discontinuity. Although the method can be adapted, in principle, to measure lossless discontinuities coupling an arbitrary number of modes, its experimental utility is demonstrated herein only for shunt discontinuities coupling two modes of a multimode waveguide. In this procedure a cavity is formed by closing a section of uniform waveguide at both ends with adjustable short-circuiting plungers. The two mode coupling or discontinuity structure to be measured is inserted into this simple cavity; the coupling structure may be thought of as a perturbation of the original cavity. The data required for the evaluation of the equivalent network parameters for the discontinuity element are various plunger positions which render the perturbed cavity resonant in the two coupled modes. The method employed for abstracting the circuit parameters from the basic data, reduces this data to that conventionally obtained in the single-mode measurement of a lossless two-port by the method of sliding short circuits. Familiarity with the measurement of lossless two-ports by a movable short circuit technique is assumed.[7–9]

The present scheme appears to offer a number of advantages over other techniques which would rely on the measurement of the amplitudes and phases of the re-

* Manuscript received by the PGMTT, June 16, 1958; revised manuscript received, September 5, 1958. The research described in this paper was performed under contract DA-36-039-sc-71235 with the Signal Corps Eng. Lab., Fort Monmouth, N. J.

† Microwave Research Institute, Polytechnic Inst. of Brooklyn, N. Y.

[1] D. J. Angelakos, "Measurements and components for rectangular multimode waveguides," IRE Trans. on Instrumentation, PGI-4, pp. 1–5; October, 1955.

[2] P. Schiffres, Final Report—Research and Development of Extremely Broad-band Waveguide Components, Polytechnic Res. and Dev. Co., Inc., Brooklyn, N. Y.; December, 1957.

[3] A. C. Beck, "Measurement techniques for multimode waveguides," IRE Trans. on Microwave Theory and Techniques, PGMTT-3, pp. 35–41; April, 1955.

[4] D. A. Lanciani, "H_{01} mode circular waveguide components," IRE Trans. on Microwave Theory and Techniques, PGMTT-2, pp. 45–51; July, 1954.

[5] H. P. Raabe, "A rotary joint for two microwave transmission channels of the same frequency band," IRE Trans. on Microwave Theory and Techniques, PGMTT-3, pp. 30–41; July, 1955.

[6] J. R. Whinnery, "Design of microwave filters," Proc. Symposium on Modern Network Synthesis, Polytechnic Institute of Brooklyn, N. Y., vol. 1, pp. 292–311; 1952.

[7] H. M. Altschuler and L. B. Felsen, "Network methods in microwave measurements," Proc. Symposium on Modern Advances in Microwave Techniques, Polytechnic Institute of Brooklyn, N. Y., vol. 4, pp. 271–307; 1954.

[8] N. Marcuvitz, "Waveguide Handbook," Radiation Lab. Ser. McGraw-Hill Book Co., Inc., New York, N. Y., vol. 10, sec. 3.3, 3.4, pp. 117–138; 1951.

[9] A. Weissfloch, "Schaltungstheorie und Messtechnik des Dezimeter—und Zentimeter—Wellengebietes," Birkhauser Verlag, Basel und Stuttgart, pp. 195–200; 1954.

flected and transmitted waves in each mode.[1-3] First, since only a coupled mode resonance need be detected, it is not necessary to discriminate between the two modes concerned. This feature represents a considerable simplification in instrumentation and procedure. Second, the data required for the complete analysis of lossless discontinuities are merely the resonant plunger positions which can be measured simply and accurately. Third, multipoint data for shunt structures can be analyzed by averaging methods of the semiprecision or precision type familiar from the theory of single mode measurements,[7] thus leading to accurate results for the equivalent network parameters. This feature is particularly important if the discontinuity couples two modes out of a complex of other possible propagating modes, in which case, the measurement procedure must distinguish between resonances in the desired and the spurious modes. A precision analysis will highlight any inconsistencies in the experimental data.

The measurement technique proposed herein has been verified experimentally at the S band of frequencies in a circular waveguide cavity containing a shunt discontinuity coupling the E_{01} and H_{01} modes.

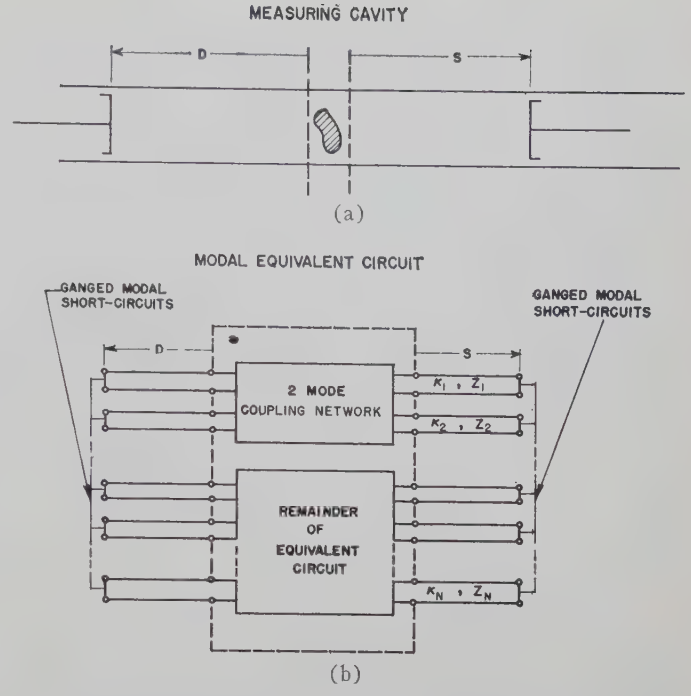

Fig. 1—Measuring cavity and equivalent circuit.

II. Network Description of Multimode Cavity

A. Remarks Concerning N-Mode Discontinuities.

1) The Resonance Relation: The structures considered in this paper comprise lossless discontinuities situated in a multimode uniform waveguide [Fig. 1(a)]. As is well known, the fields in regions far from the discontinuity structure may be expressed as a superposition of the propagating modes of the waveguide, and the modal coefficients may be interpreted as voltages and currents on equivalent uniform transmission lines, one for each mode, coupled only in the discontinuity region. The relationship between several or all of the propagating mode voltages and currents imposed by the presence of the discontinuity can be inferred from the network coupling the transmission lines, as shown in Fig. 1(b).

The measurement procedure for the evaluation of the parameters describing the coupling network is based on an analysis of the cavity formed when the multimode waveguide containing the discontinuity structure is closed by movable conducting plungers located "far" from the discontinuity [Fig. 1(a)]. The quantities D and S are physical lengths, measured from arbitrarily chosen reference planes to the plunger short circuits in the sense indicated by the arrow. In the equivalent circuit of Fig. 1(b), the plungers are represented by ganged modal short circuits, and the discontinuity region (included between the reference planes) by the dashed rectangle. The various modal transmission lines are characterized by propagation constants κ_i and characteristic impedances Z_i, $i=1, 2, \cdots, N$. The internal structure of the discontinuity network, shown by solid lines, is specialized for a two mode discontinuity as will be discussed further below.

The cavity formed by the plungers and waveguide is resonant if a finite field may be sustained in it without excitation. The condition at resonance is expressed by

$$\overleftarrow{B} + \overrightarrow{B} = 0, \tag{1}$$

where $\overleftarrow{B}$ and $\overrightarrow{B}$ designate the susceptance seen looking to the left and to the right, respectively, from a terminal pair chosen anywhere in the equivalent network.

2) The Resonance Diagram: When the positions of the cavity plungers D and S are plotted along cartesian axes, the contours which represent those particular plunger positions that render the cavity resonant constitute the "resonance diagram" of the cavity. In the absence of any discontinuity structure, the contours of the resonance diagram evidently consist of straight lines [see dashed lines in Fig. 2 for the case of only two propagating modes with guide wavelengths $\lambda_{g1,2}$, where the two reference planes in Fig. 1(a) have been chosen to coincide]. The introduction of a discontinuity into the cavity results in the perturbation of some of these lines. The simplest perturbation occurs when the discontinuity disturbs only one of the propagating modes so that only the lines corresponding to that mode are altered. The pertinent contours then assume the form characteristic of a two-port tangent relation curve familiar from the theory of measurement of a lossless two-port by a sliding short circuit technique.[8] The modification of the contours due to the introduction of a multimode discontinuity is much more complicated. Certain special features of these contours will be discussed in subsequent sections.

In the proposed measurement technique, the available data are those positions of the two plungers for

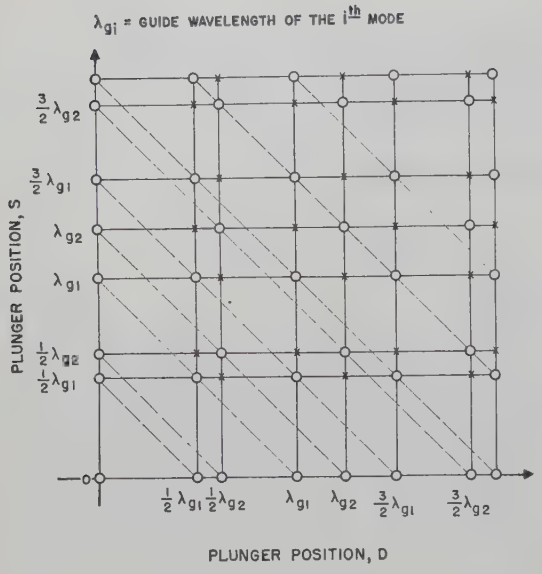

Fig. 2—Resonance diagram of empty measuring cavity.

which the cavity is resonant. Since the equivalent modal short circuits in Fig. 1(b) are not individually adjustable, the question arises as to whether this information suffices to determine the parameters for an arbitrary discontinuity structure. When the various propagating modes have incommensurable wavelengths, it can be shown that the resonant plunger positions provide as complete a set of data[10] as could be obtained if the positions of the modal short circuits on the individual transmission lines were controllable independently. When the guide wavelengths are commensurable, but not in the ratio of small whole numbers, one usually obtains sufficiently general data for the determination of the equivalent circuit.

3) Shunt Discontinuities: A thin transverse structure in a multimode waveguide is characterized by the continuity of the transverse electric field (*i.e.*, the mode voltages) across the discontinuity plane. The corresponding equivalent network is therefore of the type shown in Fig. 3(a), that is, pure shunt with respect to the various modal transmission lines. (Although the present remarks apply to N-mode structures, the figures are drawn for the special case, $N=2$, discussed in detail later.) For such transverse structures, it is convenient to measure the plunger positions relative to the discontinuity plane.

The resonance data for a $2N$-port, namely, the resonant plunger positions D and S of Fig. 3(a), may be reduced to equivalent short circuit data for the N-port network in the discontinuity plane by a procedure schematized in Fig. 3(b) (for $N=2$). The susceptances of the two sections of modal transmission line connected to the ith port of the coupling network may be added

[10] L. B. Felsen, Analysis of Circular Waveguide Modes, Second Quarterly Rep., Signal Corps Eng. Labs., R-503.6-56, PIB-433.6, Contract DA-36-039-sc-71235, sec. III A-2, pp. 2–15; November 27, 1956.

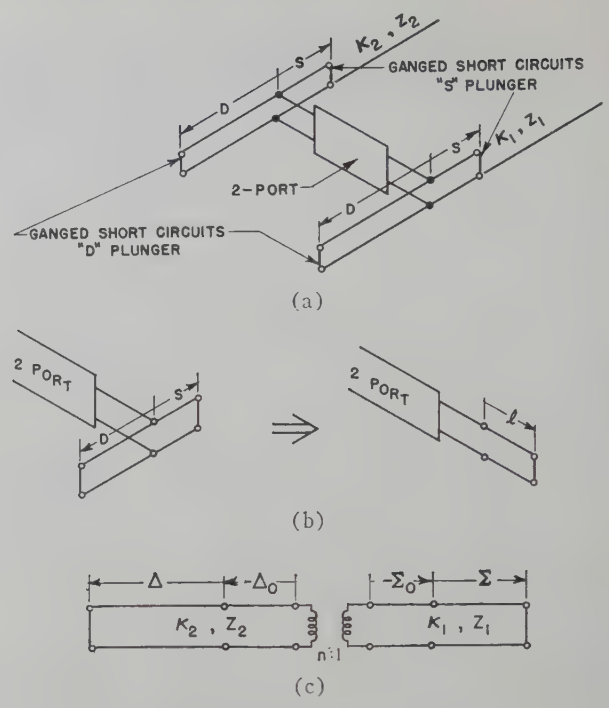

Fig. 3—Analysis of shunt two-mode discontinuities. (a) Equivalent circuit for pure shunt 2-mode discontinuity in measuring cavity. (b) Equivalent length cot Kl=cot KS+cot KD. (c) Conventional 2-port analysis for discontinuity parameters.

and the result interpreted as an equivalent single length l_i of short circuited line by the relationship

$$\cot \kappa_i l_i = \cot \kappa_i S + \cot \kappa_i D, \qquad i = 1, 2, \cdots, N, \quad (2)$$

where κ_i is the propagation constant for the ith mode.

B. Two-Mode Shunt Discontinuities.

1) The Resonance Relation: We now consider in greater detail the special case of a two-mode shunt discontinuity, which will concern us henceforth. A two-mode discontinuity is defined as one which couples two propagating modes to each other but to none of the remaining propagating modes which may exist in a multimode waveguide. Its equivalent circuit consists of two disjoint portions as illustrated in Fig. 1(b) (solid lines). For thin transverse discontinuities in a uniform waveguide, the two-mode coupling network may be represented as shown in Fig. 3(a), *i.e.*, a two-port connected in shunt at the discontinuity plane across the two modal transmission lines representing the coupled modes of interest.

Equivalent short circuit data for the two-port in the discontinuity plane may be computed from the observed resonant plunger positions as described in Section II-A, 3). The equivalent single line lengths, defined in (2), are designated in Fig. 3(c) by $l_1 \equiv \Sigma$ and $l_2 \equiv \Delta$ and determined by the relationships

$$\cot \kappa_1 \Sigma = \cot \kappa_1 S + \cot \kappa_1 D,$$
$$\cot \kappa_2 \Delta = \cot \kappa_2 S + \cot \kappa_2 D. \quad (3)$$

These corresponding lengths Δ and Σ constitute a set of data equivalent to that which would be obtained if the

two-port network in the discontinuity plane were measured directly by a variable short circuit technique. This conventional two-port data is most directly interpretable if the network in the discontinuity plane is represented by the transformer type circuit in Fig. 3(c). Then the resonance condition (1) evaluated at the left transformer terminals, yields the tangent relation between Δ and Σ,

$$\tan \kappa_2(\Delta - \Delta_0) - \gamma \tan \kappa_1(\Sigma - \Sigma_0) = 0, \qquad (4)$$

where

$$-\gamma = n^2(Z_1/Z_2).$$

The parameters Δ_0, Σ_0 and γ of the equivalent circuit are readily obtained from a graph of (4) plotted from the measured sets of resonant Δ, Σ values.[8]

It may be noted that Σ and Δ can be eliminated between (3) and (4) to yield an analytical expression for the resonance curves on the two-mode resonance diagram. This is a rather involved transcendental relation between D and S; generally, the curves possess no simple periodicity in either D or S. A resonance diagram was computed for a simple network (see Section II-B, 4) in order to anticipate the type of curves to be obtained from an actual measurement; an experimentally determined diagram is presented in Fig. 11 in the last section.

2) Fixed Points of the D, S Resonance Diagram: The curves of a resonance diagram for any shunt discontinuity will always pass through certain "fixed points" of the D, S plane. These points correspond to resonant field distributions in which the transverse electric field at the discontinuity plane in either mode vanishes. The coordinates of the fixed points, indicated by the circles drawn on the grid of Fig. 2, are

$$D = m\frac{\lambda_{gi}}{2}, \qquad S = n\frac{\lambda_{gi}}{2}, \qquad i = 1, 2, \qquad (5)$$

where the λ_g's are the guide wavelengths of the relevant modes and m and n are integers. Considered as data, such points yield no new information.

3) Resonance Curves for Special Structures: Resonance curves for the special class of two-mode shunt discontinuities whose network representation in the discontinuity plane is such that a short circuit is seen at one port when the second port is short circuited, pass, in addition, through the points designated by crosses in Fig. 2, the coordinates of which are

$$D = m\frac{\lambda_{g1}}{2}, \qquad S = n\frac{\lambda_{g2}}{2}. \qquad (6)$$

This special class of networks is representable by a shunt susceptance plus a transformer in the discontinuity plane. The field distribution associated with this resonance is somewhat peculiar: finite fields exist only in one mode to the left of the discontinuity plane and only in the other mode to the right of that plane.

One particular group of resonance curves obtainable under special conditions deserves some attention mainly to point out that these curves, or others nearly equivalent to them, should be avoided in experiment since little information concerning the network in the discontinuity plane can be abstracted from them. The conditions referred to are: a) that the two modes have commensurable wavelengths, and b) that the network in the discontinuity plane be represented by a two-port for which an open circuit is seen at one port when the second port is open-circuited. This implies that the network comprises a series reactance plus a transformer. In the absence of any discontinuity, condition a) permits separate resonances in the two modes to exist simultaneously when

$$D + S = m\frac{\lambda_{g1}}{2} = n\frac{\lambda_{g2}}{2}, \qquad (7)$$

where

$$\frac{\lambda_{g}^2}{\lambda_{g1}} = \frac{m}{n}, \qquad m, n = \text{integers}.$$

A discontinuity introduced into the cavity and described by condition b) will not disturb these resonant plunger positions and the corresponding curves on the resonance diagram for the discontinuity will appear in unperturbed form (straight lines). The special cases mentioned are illustrative, and the discussion is not intended to be exhaustive.

4) Sample Calculations of Resonance Data: To illustrate the nature of the resonance curves to be obtained from the proposed cavity measurement, a set of D, S resonance data was computed for the following assumed simple network: a transformer directly coupling the two transmission lines [Fig. 4(a)]. The resulting curves, together with relevant numerical values, are shown in Fig. 4(b) and serve to exemplify some of the remarks made earlier in this section. The curves are nonperiodic and pass through the fixed points defined by (5) and (6). The modal guide wavelengths chosen for the computations have a ratio of nearly 3:2, and since the transformer coupling network is included in the class discussed above some of the resonance curves are approximately straight lines. In particular, the fourth curve of Fig. 4(b) satisfies approximately the condition that $D+S=\lambda_{g1}=(3/2)\lambda_{g2}$.

III. Measurement Procedure in Circular Waveguide

A. E_{01}-H_{01} Mode Discontinuities.

The measurement technique described above has been applied to the measurement of two-mode discontinuities coupling the E_{01} and H_{01} modes in circular waveguide. For reference, the field configurations of the E_{01} and H_{01} modes are reproduced in Fig. 5. Most important, both modes possess complete rotational symmetry about the guide axis. The cutoff wavelengths λ_c of the first ten (first seventeen, counting orthogonal

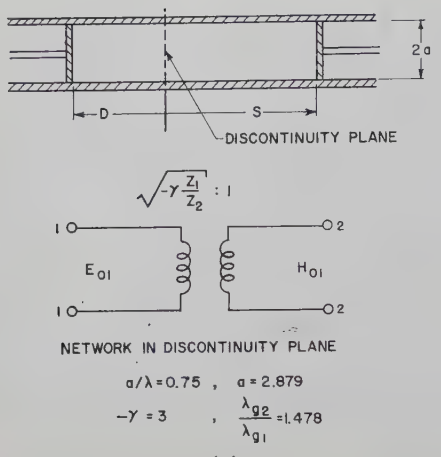

(a)

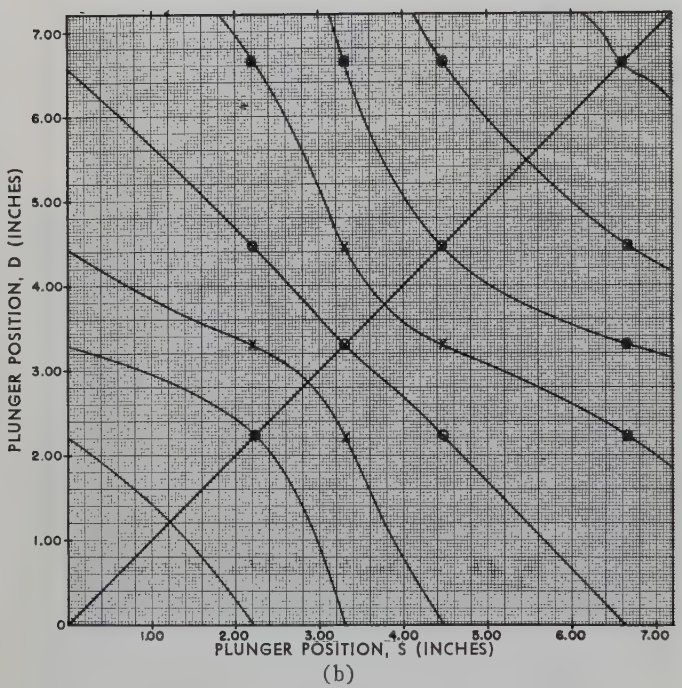

(b)

Fig. 4—Sample calculation of resonance data.

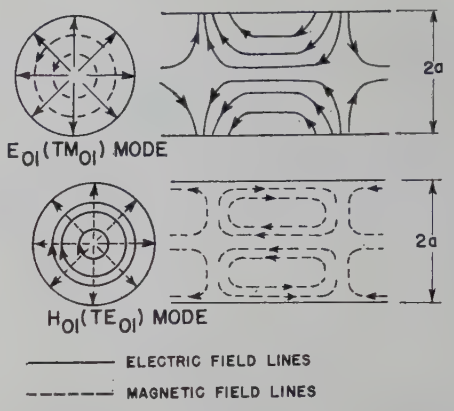

Fig. 5—Field patterns of the E_{01} and H_{01} modes of circular waveguide.

TABLE I

Mode	λ_c/a*
H_{11}	3.412
E_{01}	2.613
H_{21}	2.057
H_{01}, E_{11}	1.640
H_{31}	1.496
E_{21}	1.223
H_{41}	1.182
H_{12}	1.178
E_{02}	1.138

* λ_c is the cutoff wavelength and a is the guide radius.

polarizations) modes of circular waveguide are given in Table I.

Discontinuities which may couple the E_{01} and H_{01} modes to each other but to no other propagating mode in the waveguide may be obtained from the following considerations of symmetry. If the guide axis is an R-fold rotation axis for the discontinuity then, in view of the symmetry of an incident H_{01} or E_{01} mode, the scattered modes (E_{mn}, H_{mn}) must have azimuthal mode indexes such that

$$m = kR, \qquad k = 0, 1, 2, \cdots. \tag{8}$$

It is desired that the discontinuity scatter into only two propagating modes, *i.e.*, the E_{01} and H_{01} modes. On inspection of Table I, it is seen that it is sufficient to take $R \geq 5$ and to restrict the guide radius-to-wavelength ratio such that the E_{02} mode is cut off. In order to couple the E_{01} and H_{01} modes to each other, the discontinuity structures must not possess reflection symmetry with respect to any plane containing the waveguide axis. Typical shunt, *i.e.*, thin transverse, E_{01}-H_{01} discontinuities are illustrated in the upper right hand corner of the photograph, Fig. 6.

B. Description of Measuring Equipment.

Measurements of two-mode discontinuities coupling the E_{01} and H_{01} modes have been carried out at the S band of frequencies in 5.758″ ID (Nominal 6″) circular waveguide. A photograph and block diagram of the resonance measuring system are shown in Figs. 6 and 7. The system comprises three main assemblies: the microwave source assembly, the frequency monitoring assembly, and the measuring cavity assembly. Only the cavity assembly will be described in any detail since the other units are composed of standard commercial components.

The measuring cavity assembly consists of the cavity to be brought to resonance, a number of probes for sampling the electromagnetic fields in the cavity, and an amplifier system for the sampled signal. The measuring cavity, constructed in two half-sections, is based on a similar design by Sheingold.[11] One half-section, shown

[11] L. S. Sheingold, An Experimental Investigation of the Transmission Properties of the Dominant Circular—Electric Mode, Cruft Lab., Harvard Univ., Cambridge, Mass., Tech. Rep. No. 167; September 1, 1953.

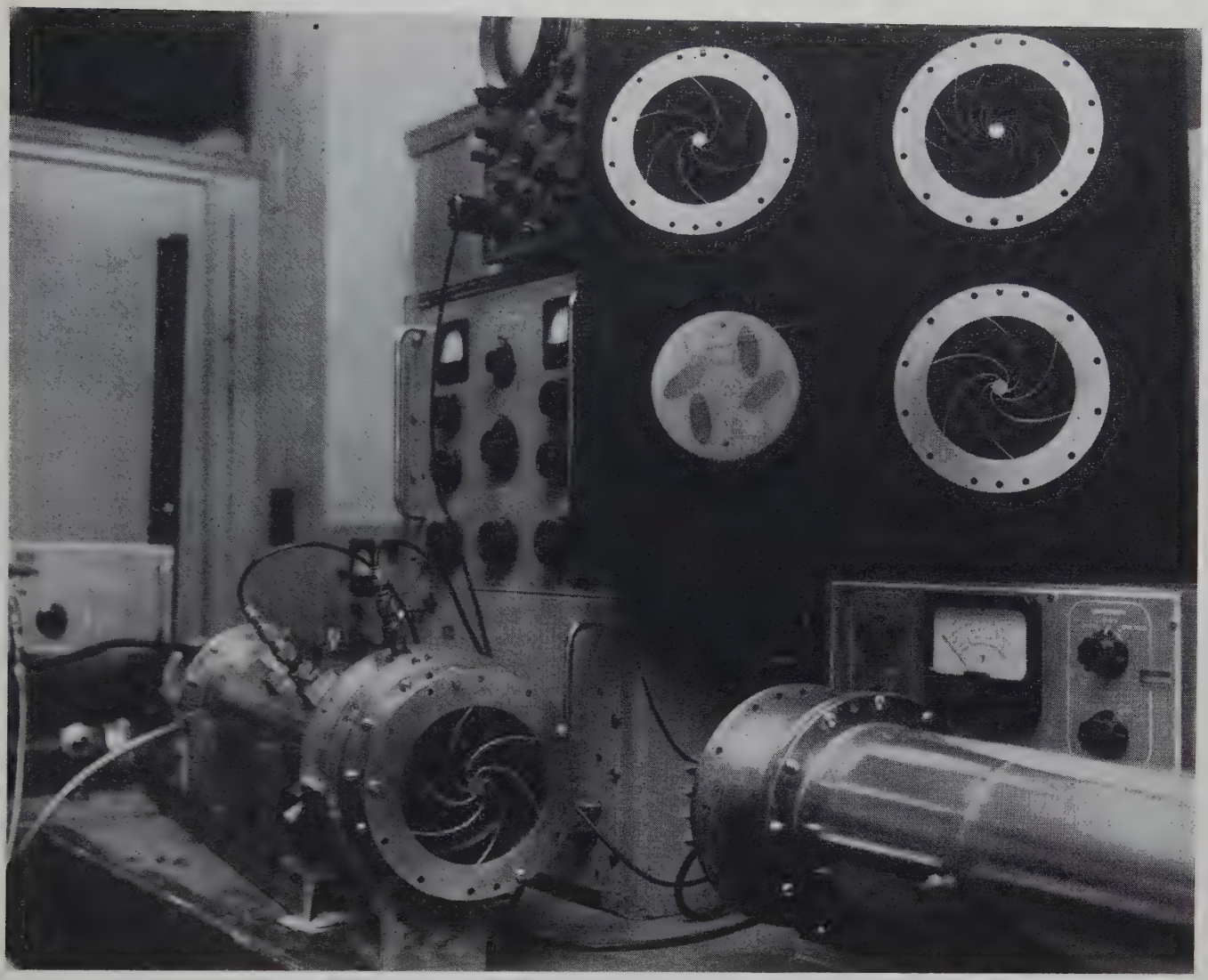

Fig. 6—Measuring cavity and typical E_{01}-H_{01} shunt discontinuities.

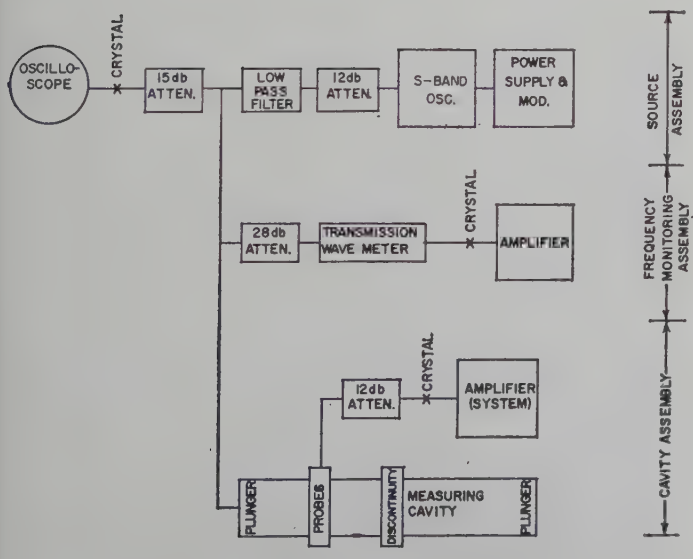

Fig. 7—Block diagram of the resonance measuring system.

in Fig. 8, consists of a length of brass pipe closed at one end by a contacting plunger, provided with a flange at the other end, and equipped with measuring and exciting probes; the other half-section differs only in that it has no provision for probes. Discontinuities to be measured are inserted at the flange between the two halves of the cavity. The short circuiting plungers make contact with the guide walls by means of compressed wire gaskets woven on Monel alloy. Good contact is required to join the radial currents induced by the E_{01} mode on the plunger face with the longitudinal currents induced on the guide walls. A hemispherical brass boss is centered on each plunger face to accentuate the difference between the susceptances presented by the plunger to the E_{11} and H_{01} modes, which have the same cutoff wavelength (Table I). The difference in plunger susceptance is the only feature causing the empty cavity to become resonant in these two modes at distinct

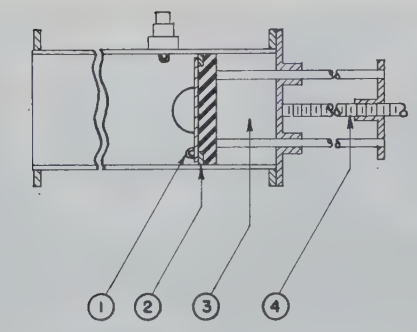

① EXCITATION LOOP
② MONEL GASKET
③ DISSIPATIVE MATERIAL
④ PRECISION DRIVE SCREW

Fig. 8—Cross-section of the measuring cavity.

plunger positions. In the range of interest (frequencies lying between the H_{01} mode and the E_{02} mode cutoff frequencies), the symmetrical boss does not couple the E_{01} and H_{01} modes to each other or to any other propagating mode. The plungers are positioned by a precision drive screw with pitch 0.050″/revolution; an automatic revolution counter and vernier are attached.

The probes employed are shielded magnetic loops; a mechanically interchangeable electric probe was also constructed. The probe mounted in one plunger face is connected to the source, and the plane of all loop probes can be rotated in position. A separate sub-assembly carrying a probe which, in addition, can be moved azimuthally through a 90 degree sector is also incorporated.

C. Identification of Modes at Resonance.

The measuring cavity may be brought to a resonance involving one or more of the propagating modes by an adjustment of either the frequency or the plungers. Resonance is indicated experimentally by maximum transmission from the source to a detector probe through the cavity. In the process of obtaining the E_{01}-H_{01} resonance diagram, the pertinent resonances are easily identified by rotational symmetry of the combined modal fields. However, in the location of modal reference planes as described in the next section, it is necessary to distinguish between the E_{01} and H_{01} modes, themselves. The azimuthally movable probe provides the most direct way of identifying the circularly symmetrical modes. The probe is responsive to the tangential magnetic field at the guide wall, and the absence or presence of any variation with azimuthal position is indicative of resonance in a symmetrical or nonsymmetrical mode, respectively. In order to distinguish E_{01} and H_{01} resonances in the empty cavity, one may rotate the plane of the magnetic loop. A response for transverse orientation of the plane of the loop distinguishes an H mode.

Alternatively, the nondegenerate uncoupled modes in the empty cavity may be distinguished by the change in the position of a cavity plunger necessary to restore the cavity to resonance for a small change $\delta\lambda$ in source wavelength. The required fractional change $\delta(L/\lambda_g)$ in the resonant plunger position is given, in view of the relations.

$$\frac{d\lambda_g}{d\lambda} = \left(\frac{\lambda_g}{\lambda}\right)^3 \quad \text{and} \quad \frac{2L}{\lambda_g} = n, \quad n = 1, 2, \cdots, \tag{9}$$

by

$$\frac{\delta\left(\frac{L}{\lambda_g}\right)}{\delta\lambda} = \frac{n}{2\lambda_g}\left(\frac{\lambda_g}{\lambda}\right), \tag{10}$$

where L is the length of the cavity at resonance. Comparison of a measured ratio $\delta(L/\lambda_g)/\delta\lambda$ with the right hand side of (10) computed for the various possible modes leads to the identification of the resonant mode.

D. Calibration of Cavity for Effective Modal Short Circuit Positions.

The data required for the analysis of the discontinuity are the electrical distances at resonance from the discontinuity plane to the generally not coincident modal short circuits in the E_{01} and H_{01} modes. The usual experimental procedure for the location of the appropriate reference plane combines an approximate mechanical with a precise electrical measurement. A flat short circuiting plate is attached to the flange of that section of the empty cavity containing the source probe. At the desired frequency, the plunger is moved until the cavity section is brought to resonance in the mode for which the effective short circuit position is to be determined, and the dial indication [designated by $\tilde{D}_R$ in (11) below] corresponding to the cavity plunger position is noted. The precise distance from the short circuiting plate to the effective modal short circuit is then $n\lambda_g/2$, where λ_g is the corresponding guide wavelength. The integer n is determined from an approximate mechanical measurement of the cavity section length, or from (10). For the location of the analogous reference plane $\tilde{S}_R$ in the second half of the cavity, one connects the second half to the first half, sets the plunger in the latter at position $\tilde{D}_R$ and varies the plunger in the former until resonance is achieved. The reference plane locations $\tilde{D}_R$ and $\tilde{S}_R$ are required at every operating frequency and cannot be predicted from a single frequency measurement since the variation of the equivalent reactance of the plunger is not known.

If $\tilde{D}$ and $\tilde{S}$ denote the indicator readings for the resonant plunger positions taken during a measurement, the

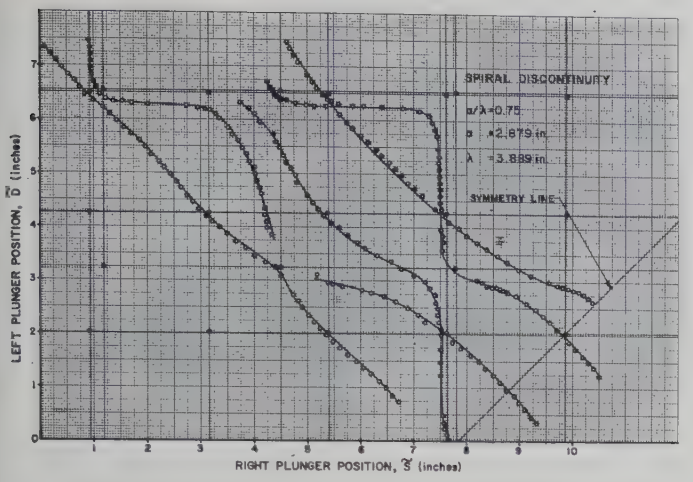

Fig. 9—Experimental resonance diagram, spiral discontinuity.

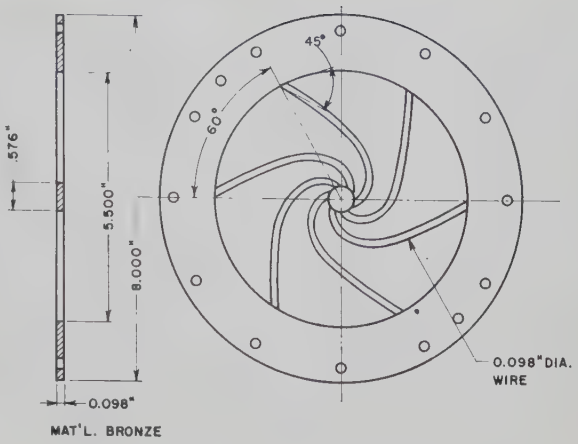

Fig. 10—Spiral E_{01}-H_{01} mode discontinuity.

desired electrical distances $\kappa_{1,2}D$ and $\kappa_{1,2}S$ in (3) are then replaced as follows:

$$\kappa_{1,2}D = \kappa_{1,2}(\tilde{D} - \tilde{D}_{R_{1,2}}), \qquad \kappa_{1,2}S = \kappa_{1,2}(\tilde{S} - \tilde{S}_{R_{1,2}}), \quad (11)$$

where the subscripts $_{1,2}$ distinguish the two modes in question.

E. Special Techniques and Experimental Results.

Methods for recognizing when the cavity is resonant in the coupled (E_{01}, H_{01}) modes, and the calibration procedure linking observed plunger positions $\tilde{D}$, $\tilde{S}$ with the D, S values required in the computation of the discontinuity have been presented; it remains to describe any special techniques and experimental difficulties related to obtaining a set of $\tilde{D}$, $\tilde{S}$ values and to exhibit typical experimental results.

Although only three resonance measurements are needed, in principle, for the determination of the three parameters Σ_0, Δ_0, γ specifying the E_{01}-H_{01} mode coupling network, a precise evaluation employing an averaging scheme requires a larger number of data points. In practice, it is tedious to identify a given resonance as a desired one in the E_{01}-H_{01} modes, as distinct from a spurious resonance arising from other propagating modes. A simpler procedure is to start from a known E_{01}-H_{01} resonance, as, for example, from one occurring at a fixed point $\tilde{D}_R \pm n\lambda_g/2$, $\tilde{S}_R \pm n\lambda_g/2$ [see (5)], and to track that resonance as $\tilde{D}$ changes slightly, with a corresponding compensation in $\tilde{S}$. It was found extremely helpful to record data points $\tilde{D}$, $\tilde{S}$ graphically as illustrated in Fig. 9 in the progress of measurement.

When spurious mode resonances occur at nearly the same plunger positions as desired ones, the appreciable spurious mode amplitudes may influence the measurement in two ways: a) they may obscure desired resonances, and b) they may tune any small coupling due to asymmetries or other imperfections existing between network sections of Fig. 1(b), and thus appreciably affect the desired mode fields. Overlap of desired and

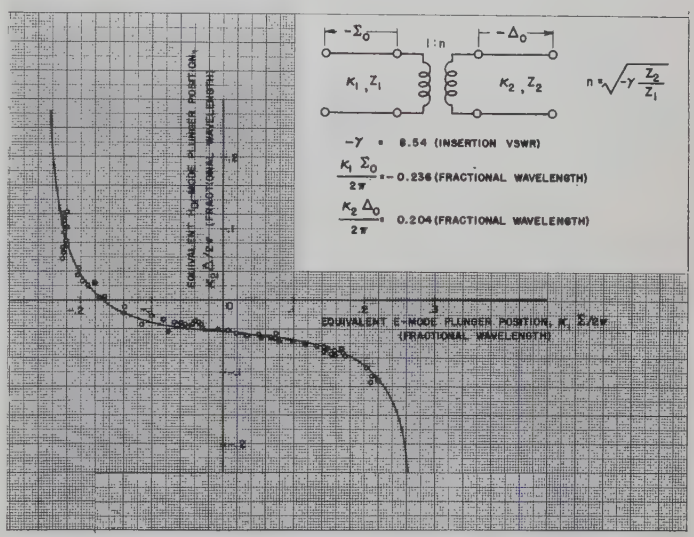

Fig. 11—Tangent curve for two-port in the discontinuity plane, (spiral discontinuity).

spurious mode resonances is minimized by the high (loaded) Q of the measuring cavity. Plotting the observed data in the progress of the measurement aids in circumventing a).

The experimental resonance diagram in Fig. 9 was obtained for the spiral E_{01}-H_{01} mode discontinuity. This spiral discontinuity structure, shown in Fig. 10, consists of six symmetrically disposed logarithmic spirals which are defined by the requirement that, at every point, the spiral makes an angle of 45 degrees with a guide radius drawn through the point. This type of spiral was suggested by the fact that a small elliptical obstacle couples the E_{01} and H_{01} modes most strongly if placed with its major axis at 45 degrees to the unperturbed E_{01} and H_{01} mode transverse electric fields. The measurements were carried out at 3.075 KMc corresponding to a guide radius-to-wavelength ratio, $a/\lambda = 0.75$. This resonance diagram illustrates the nature of the resonance curves and actually contains considerab'y more extensive data than that required for the deter-

mination of the discontinuity parameters. It may be observed that the resonance curves pass close to, rather than through, the "fixed points" computed from calibration measurements. This may be attributed to the finite thickness of the discontinuity.

From each point $\tilde{D}$, $\tilde{S}$ on the resonance diagram, a point Σ, Δ on the tangent curve for the network in the discontinuity plane may be computed via (3) and (11). Fig. 11 shows this result for points chosen from all the curves of Fig. 9; only data from the immediate neighborhood of the "fixed points" have been excluded because of the thickness effect noted previously. The final test of the internal consistency of the two-mode data was a precision analysis of the tangent curve,[7] which will be described briefly. Values Δ' corresponding to measured values of Σ were computed from the tangent relation employing the parameters Σ_0, Δ_0, γ listed on Fig. 11. The differences $(\Delta'-\Delta)$ between the measured and computed values are a measure of the accuracy with which the parameters Σ_0, Δ_0, γ represent the experimental data or the internal consistency. For the data presented, the measure of accuracy, $|\Delta'-\Delta|/\lambda_{g2} < 0.005$, is comparable to values attained in single mode precision measurements.

Mode Couplers and Multimode Measurement Techniques*

D. J. LEWIS†

Summary—**The measurement of harmonic and spurious signals in waveguide systems is complicated by the fact that one must usually deal with a multimodal measurement. Since the energy may propagate in any mode consistent with the frequency and waveguide geometry, the measurement system used must discriminate between these different modes.**

A simple and direct approach to this problem is through the use of "mode couplers" which couple selectively to any desired mode. Theoretical and practical details for mode couplers for the first five modes in rectangular waveguide are presented, as well as the application and limitations of this measurement technique.

Introduction

THE measurement of spurious and harmonic signals in waveguide systems is usually complicated by the fact that one must work with a multimode system. The energy one wishes to measure can be propagated in every mode consistent with the frequency and waveguide geometry. For example, a 6000-mc signal in a standard S-band waveguide ($3\times1\frac{1}{2}$ inches) can travel in the TE_{10}, TE_{20}, TE_{01}, TE_{11}, and TM_{11} modes. The distribution of power among these modes will, of course, depend on how the guide is excited.

To specify more exactly the nature of the problem, assume that the total power carried in an n-mode system is to be measured. To solve this problem n couplers are required, the output of each coupler being a linear function of the amplitude of each mode. Thus:

$$E = k_1M_1 + k_2M_2 + \cdots k_nM_n. \tag{1}$$

A series of n amplitude and phase measurements using these couplers will therefore yield the following set of equations:

$$\begin{aligned}
E_1 &= k_{11}M_1 + k_{12}M_2 + \cdots k_{1j}M_j + \cdots k_{1n}M_n \\
E_2 &= k_{21}M_1 + k_{22}M_2 + \cdots \\
&\cdots \\
E_r &= k_{r1}M_1 \quad \cdots \quad k_{rj}M_j \\
&\cdots \\
E_n &= k_{n1}M_1 \quad \cdots \quad k_{nn}M_n.
\end{aligned} \tag{2}$$

Theoretically it should be possible to solve for the strength of the different modes from these equations but clearly, where more than two or three modes are involved, the solution of such a set of complex equations will be a tedious task. An alternative is to reduce the value of the cross-coupling terms k_{rj} to a value so low that the output of each coupler is essentially dependent on only one mode. This approach also greatly simplifies the measurement technique since the need for phase measurements is eliminated.

Mode Couplers

The basic mode coupler is shown in Fig. 1. It consists of two parallel waveguides mutually coupled through two small apertures. The signal to be measured is traveling from left to right in the lower or primary waveguide. The upper or secondary waveguide con-

* Manuscript received by the PGMTT, May 13, 1958; revised manuscript received, July 28, 1958.

† Inst. for Cooperative Res., The Moore School of Electrical Engineering, University of Pennsylvania, Philadelphia, Pa.

tains a probe to extract the coupled power and a termination to eliminate reflections. The dimensions of the secondary waveguide are such that at the signal frequency only the TE_{10} mode can propagate.

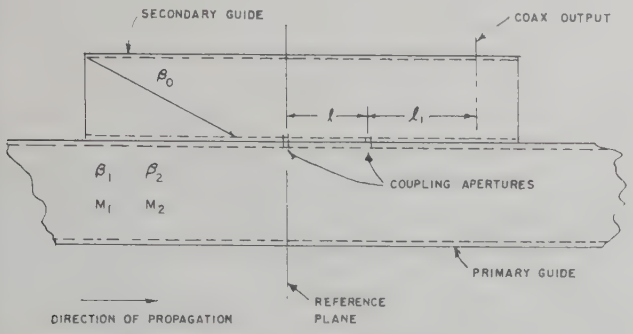

Fig. 1—Basic mode coupler.

For the sake of simplicity the discussion will be restricted to the case of two modes of propagation having field strengths M_1 and M_2 and phase constants β_1 and β_2, respectively. The phase constant of the TE_{10} mode in the secondary guide is β_0. The coupling apertures are identical and have field coupling coefficients k_1 for the M_1 and k_2 for the M_2 mode. The aperture spacing is l.

To develop the coupling equations, we assume a reference plane at the first aperture. Omitting the phase shift in the apertures, the forward coupled wave measured at the probe which results from M_1 is then given by:

$$E_{f1} = k_1 M_1 [e^{-i\beta_1 l} + e^{-i\beta_0 l}] e^{-i\beta_0 l_1} \tag{3}$$

or

$$|E_{f1}| = 2k_1 M_1 \cos \frac{(\beta_1 - \beta_0)l}{2}. \tag{4}$$

Similarly E_{f2} the forward wave coupled from M_2 is:

$$E_{f2} = k_2 M_2 [e^{-i\beta_2 l} + e^{-i\beta_0 l}] e^{-i\beta_0 l_1} \tag{5}$$

and

$$|E_{f2}| = 2k_2 M_2 \cos \frac{(\beta_2 - \beta_0)l}{2}. \tag{6}$$

Our objective is to design the system so that the probe output will be a measure of the strength of either M_1 or M_2 with a minimum of interference from the other. If we wish to sample M_1, the difference between the coupled waves is maximized by establishing the conditions:

$$E_{f1} = 2k_1 M_1 \tag{7a}$$

$$E_{f2} = 0. \tag{7b}$$

This requires that:

$$(\beta_1 - \beta_0)l = 2n\pi \tag{8a}$$

$$(\beta_2 - \beta_0)l = (2k + 1)\pi \tag{8b}$$

$$n = 0, 1, 2, 3 \cdots$$

$$k = 0, 1, 2, 3 \cdots.$$

Eq. (8a) and (8b) must be satisfied simultaneously to meet the imposed conditions. Taking the ratio of these two equations, one can develop the necessary relations between the phase constants of the two modes in question and the phase constant β_0 of the secondary waveguide as follows:

$$\frac{(\beta_1 - \beta_0)}{(\beta_2 - \beta_0)} = \frac{2n}{2k + 1} \tag{9}$$

$$n = 0, 1, 2, 3 \cdots$$

$$k = 0, 1, 2, 3 \cdots.$$

The behavior of this ratio can be readily visualized with the aid of the normalized phase constant plots given in Fig. 2. It can be seen that for a given f_0, to obtain the correct ratio for (9) one must pick the appropriate value of f_{c0} (the cutoff frequency of the TE_{10} mode in the secondary guide). If l is then selected to satisfy either (8a) or (8b) (the other of course is automatically satisfied) the coupler will have the desired characteristic of rejecting M_2 while giving maximum response to M_1.

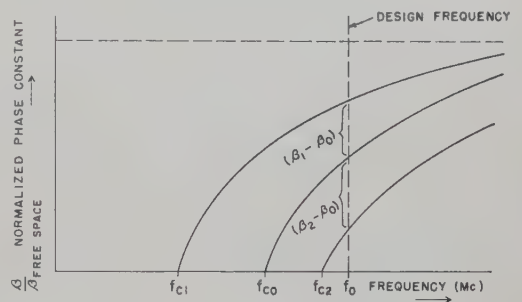

Fig. 2—Normalized plots of phase constant as a function of frequency for three modes having cutoff frequencies f_{c0}, f_{c1}, and f_{c2}.

The values selected for n and k in (9) are quite arbitrary. However, large values of n and k lead to greater aperture spacing. Since this results in smaller bandwidths as well as greater physical dimensions, it is advantageous to pick small numbers. A ratio of **2/3** in (9) was found satisfactory experimentally.

If β_0 is made equal to β_1, then from (4) the coupling to M_1 will depend only on k. In this case, l is simply dimensioned to satisfy (8b). This would not be a practical design for the TE_{10} mode, however, since the secondary guide would have the same dimensions as the primary guide. The secondary guide itself would then be capable of supporting each of the higher order modes associated with the primary guide.

It is evident from Fig. 2 that (8a) and (8b) can be satisfied only at the design frequency, f_0. The variation of coupling with frequency is easy to picture, however, since the arguments of the cosine functions in the coupling equations [(4) and (6)] are proportional to the differences between the curves in Fig. 2. These differences are plotted in Fig. 3 while the coupling corresponding to these curves is shown in Fig. 4.

The mode selectivity can be defined as the difference in coupling between the desired and undesired modes.

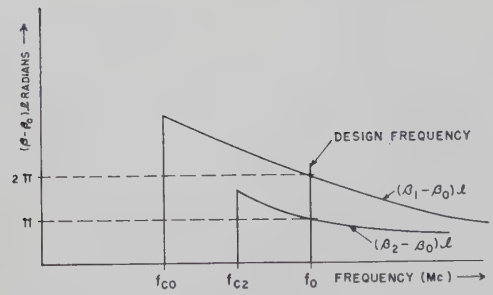

Fig. 3—Variation of $(\beta_1-\beta_0)l$ and $(\beta_2-\beta_0)l$ with frequency.

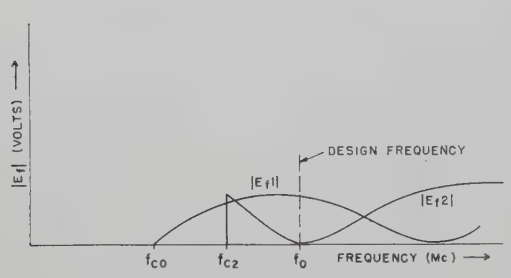

Fig. 4—Output as a function of frequency for the two modes, M_1 and M_2.

Therefore:

$$S = 20 \log \frac{\dfrac{|E_{f1}|}{M_1}}{\dfrac{|E_{f2}|}{M_2}}. \tag{10}$$

Substituting from (4) and (6):

$$S = 20 \log \left[\frac{\cos \dfrac{(\beta_1 - \beta_0)l}{2}}{\cos \dfrac{(\beta_2 - \beta_0)l}{2}} \right] + 20 \log \left(\frac{k_1}{k_2} \right). \tag{11}$$

Typical curves of S are shown in Fig. 5.

The second term in (11) is the contribution to the mode selectivity which arises from the difference in coupling of two different modes to a given aperture. For example, a narrow slot will couple strongly to any mode which has a magnetic field component parallel to the slot and weakly to modes whose H fields are perpendicular to the slot. This approach has been investigated by Judy and Angelakos [3] in connection with the development of mode selective directional couplers. Their results were used extensively in the design of the coupling aperture of the mode couplers.

The total mode selectivity, then, is a function of two different mechanisms, one depending on the field configuration of the mode, and the other on the phase constant or velocity with which the mode propagates. By choosing the correct combination of aperture geometry, aperture spacing, and secondary waveguide dimensions, one may achieve a considerable degree of mode selectivity.

For example, suppose a pair of longitudinal slots in

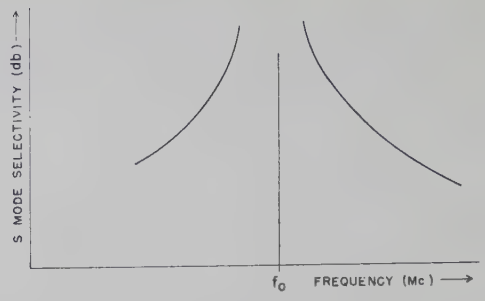

Fig. 5—Mode selectivity as a function of frequency.

the center of the broad face of the waveguide are used as the coupling apertures. Because of their location at a point of minimum longitudinal magnetic field, the slots will not couple to TE_{10}, TM_{11}, or TE_{11} waves. They will couple to TE_{20} and TE_{01} modes. One may then choose the slot separation l and the secondary guide phase constant β_0 to reject either the TE_{01} or TE_{20} mode. The coupler will then couple to only one mode out of the five possible in the primary guide. Unfortunately, there is no guarantee that one will be able to eliminate all the undesired modes in any given case. It may also be noted that the couplers may produce mode conversions in the primary waveguide. In the example above the longitudinal slots will couple TE_{01} into TE_{20} or TE_{20} into TE_{01} in the primary guide as well as coupling either of these modes into TE_{10} in the secondary guide. However, this mode conversion will be a minor effect as long as the total power coupled from each mode is small.

Multihole Couplers

Following standard coupler theory [6] it can be shown that if the coupler has n coupling apertures whose coupling coefficients have a binomial distribution, then (4) can be written as:

$$|E_{f1}| = 2k_1 M_1 \cos^{(n-1)} \frac{(\beta_1 - \beta_0)l}{2} \tag{12}$$

$$|E_{f2}| = 2k_2 M_2 \cos^{(n-1)} \frac{(\beta_2 - \beta_0)l}{2}. \tag{13}$$

Substituting into (10), the equation for mode selectivity:

$$S = 20\,(n-1) \log \left[\frac{\cos \dfrac{(\beta_1 - \beta_0)l}{2}}{\cos \dfrac{(\beta_2 - \beta_0)l}{2}} \right] + 20 \log \frac{k_1}{k_2}. \tag{14}$$

It can be seen that the mode selectivity can be increased by using multihole couplers.

Negatively Traveling Waves

The coupling equations, (4) and (6), were derived on the assumption that the signal was traveling to the right. A wave traveling to the left will result in an output:

$$E_{f1}' = k_1 M_1' e^{-j\beta_0 l_1} [1 + e^{-j(\beta_0+\beta_1)l}] \tag{15}$$

for M_1 or

$$|E_{f1}'| = k_1 M_1' \cos \frac{(\beta_0 + \beta_1)l}{2} \tag{16}$$

and

$$|E_{f2}| = k_2 M_2' \cos \frac{(\beta_0 + \beta_2)l}{2} \tag{17}$$

for M_2'. It is apparent that in general both of the backward traveling waves will appear at the output terminal. Since this will seriously interfere with the measurement of the forward wave, reflections from the load must be held to a minimum.

Error Considerations

In using the couplers one may simply ignore the effects of the cross-coupling when making a set of measurements. Since the mode selectivities cannot be infinite, this procedure will result in some error. A relationship between the mode selectivity and this error is of considerable interest.

To develop the error equation we start with (2). The first equation is divided by k_{11}, the second by k_{22}, and so on, giving:

$$\begin{aligned}
\frac{E_1}{k_{11}} &= M_1 + \frac{k_{12}M_2}{k_{11}} + \cdots \frac{k_{1j}}{k_{11}} + \cdots \frac{k_{1n}}{k_{11}} M_n \\
\frac{E_2}{k_{22}} &= \frac{k_{21}}{k_{22}} M_1 + M_2 + \cdots \\
&\vdots \\
\frac{E_r}{k_{rr}} &= \frac{k_{r1}}{k_{rr}} M_1 + \cdots \frac{k_{rj}}{k_{rr}} M_j \cdots \frac{k_{rn}}{k_{rr}} M_n \\
&\vdots \\
\frac{E_n}{k_{nn}} &= \frac{k_{n1}}{k_{nn}} M_1 + \cdots M_n.
\end{aligned} \tag{18}$$

Now E_r/k_{rr} is the apparent value of M_r obtained with the rth coupler when the cross-coupling is neglected. For a 5-mode system, the error in the over-all power measurement which will result when the interference is neglected will be:

$$\delta \text{ db} = 10 \log_{10} \frac{\sum_{r=1}^{5} \left| \frac{E_r}{k_{rr}} \right|^2}{\sum_{j=1}^{5} |M_j|^2}. \tag{19}$$

This states that the error δ is 10 times the log of the ratio of the apparent power to the true power. Substituting from (18) this becomes:

$$\delta = 10 \log_{10} \frac{\sum_{r=1}^{5} \left[\sum_{j=1}^{5} M_j \frac{k_{rj}}{k_{rr}} \right]^2}{\sum_{j=1}^{5} |M_j|^2}. \tag{20}$$

The maximum error will occur when the coupling coefficients k_{rr} have the same value for all r, when the cross-coupling coefficients k_{rj} have the same value for all r and j, and when the modes are of equal amplitude. Eq. (20) then reduces to:

$$\delta \text{ db} = 20 \log_{10} \left[1 + 4 \left| \frac{k_{rj}}{k_{rr}} \right| \underline{/\psi} \right] \tag{21}$$

or, setting $\left| k_{rj}/k_{rr} \right| \underline{/\psi} = S$,

$$\delta \text{ db} = 20 \log (1 + 4s). \tag{22}$$

Since s is complex, the maximum value of δ will be obtained when s is a negative real number.

$$\delta \max = 20 \log (1 - 4|s|). \tag{23}$$

If the s values and M's are different instead of being equal, the situation is more complicated, but it can be shown that the maximum total error will always be less than δ max [assuming of course that the maximum value of s is equal to the value of s in (22)].

A more realistic case is obtained by assuming that for each coupler only one mode causes serious interference, and further that each mode causes interference only once during a set of measurements. If all the s's are again equal, then:

$$\delta \max = 20 \log (1 - s). \tag{24}$$

These two curves of maximum error are plotted in Fig. 6 as a function of S, the mode selectivity where:

$$S = 20 \log s. \tag{25}$$

The needed mode selectivity for any desired degree of accuracy can be obtained directly from these curves. In practice, the error will usually be much less than indicated by Fig. 6, since this represents the worst possible case.

The error curves of Fig. 6 can be used to specify the return loss required of the load. Eqs. (16) and (17) show that in the worst possible case the reflected waves will be coupled exactly as strongly as the desired incident mode. If the return loss for a given mode is 20 db, then the effective mode selectivity for that mode will be 20 db. Therefore, one may relabel the S axis of Fig. 6 as return loss and obtain a direct relation between the quality of the load and the worst error it can introduce.

If the amplitudes of the individual modes are to be found, the mode selectivity requirements become more severe. Reference to (18) shows that the error depends on the relative strength of each mode as well as the mode selectivity of each coupler. Fortunately, the largest error is always made in connection with the

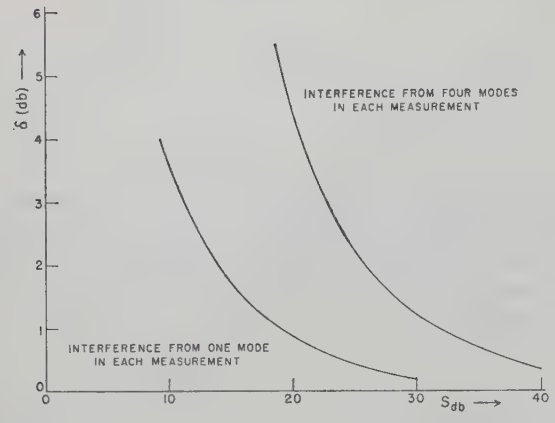

Fig. 6—The maximum error in the measurement of total power when the mode interference is ignored.

measurement of the weakest and therefore least significant mode.

Experimental Models

Three typical mode couplers are shown in Figs. 7 through 15. In each case the primary guide was a length of standard *S*-band waveguide. The secondary guide is fabricated from sheet brass. Note that because the secondary guide is operated much closer to cutoff than normal, special attention must be given to the design of the probes, terminations, and bends used in this guide. The coupling aperture used in the couplers is a slot 0.75 inch long by 0.1 inch wide.

The curves of coupling and mode selectivity show rather good agreement with the theoretical predictions. Mode selectivities ranging from 15 db to greater than 30 db were obtainable over a 200-mc bandwidth. The frequency of maximum selectivity for the couplers was within 1 per cent (or about 50 mc) of the design frequency in every case.

Application of the Couplers

It has been pointed out that for second harmonic measurements five couplers, one for each mode, will be required. For third harmonic measurements one would evidently require 11 couplers, and so on, with the required number of couplers increasing rapidly with the order of the harmonic. Clearly a point is very quickly reached where the complexity and expense of such a system would make practical application out of the question. Furthermore, with the techniques outlined thus far, there is no way of rejecting an arbitrarily large number of modes. The problem is further complicated by the existence of degenerate modes. These modes can only be separated by means of aperture selectivity, since mode selectivity based on differences in phase constants obviously cannot be obtained.

Fortunately, the number of modes which actually propagate is often considerably less than the number theoretically possible. As an example, an idea symmetrical coax to waveguide adaptor (consisting of a waveguide with a perpendicular probe in the center of

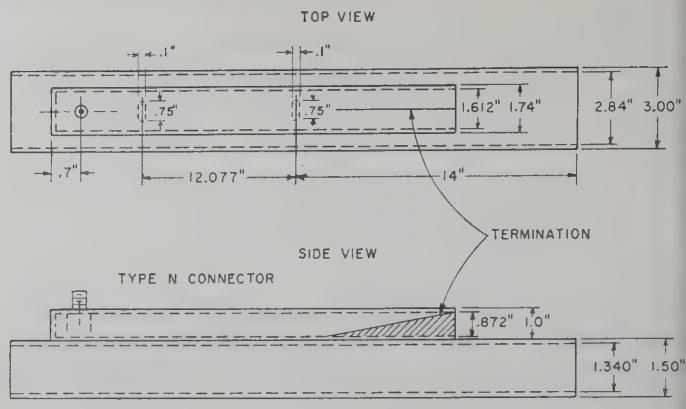

Fig. 7—TE_{10} coupler.

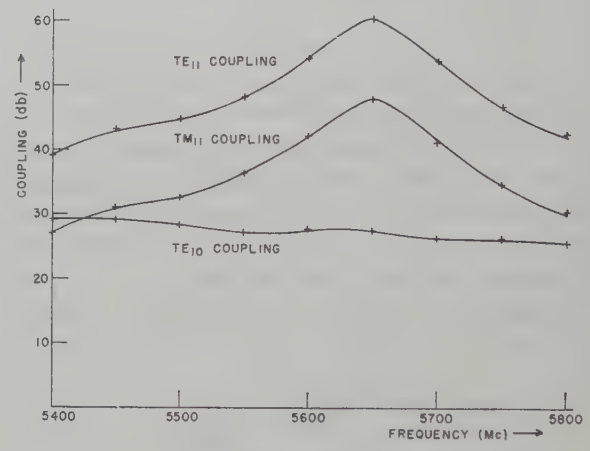

Fig. 8—TE_{10} coupler. Experimental curves of coupling as a function of frequency for the TE_{10}, TE_{11}, and TM_{11} modes. Coupling to the TE_{01} and the TE_{20} modes was less than 70 db.

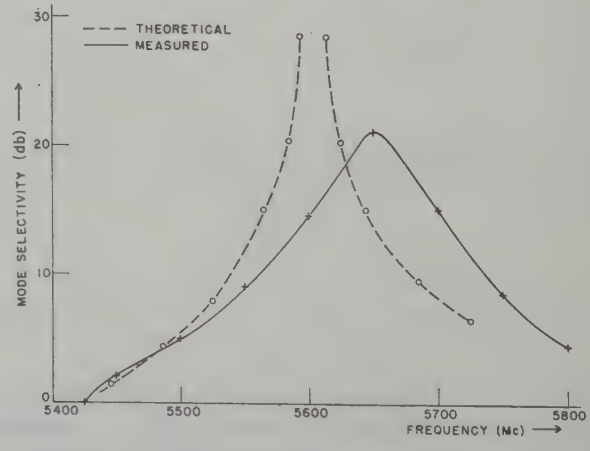

Fig. 9—TE_{10} coupler. Mode selectivity as a function of frequency for the TM_{11} mode.

the broad face) when operating at a second harmonic frequency excites TE_{11}, TM_{11}, and TE_{10}, but does not excite TE_{20} and TE_{01} although both of these latter modes could propagate. This is due to the mechanical symmetry of the device. Only three couplers will be required to measure the second harmonic modes excited by such a probe. Since this type of adaptor is common in microwave circuits, these three couplers will handle a wide variety of such specific problems as the

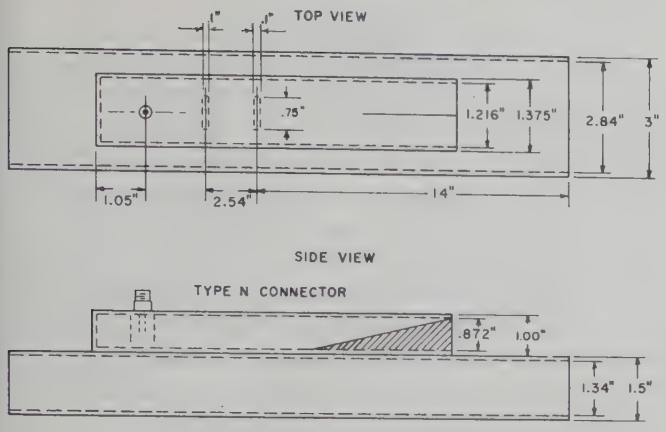

Fig. 10—TM_{11} coupler.

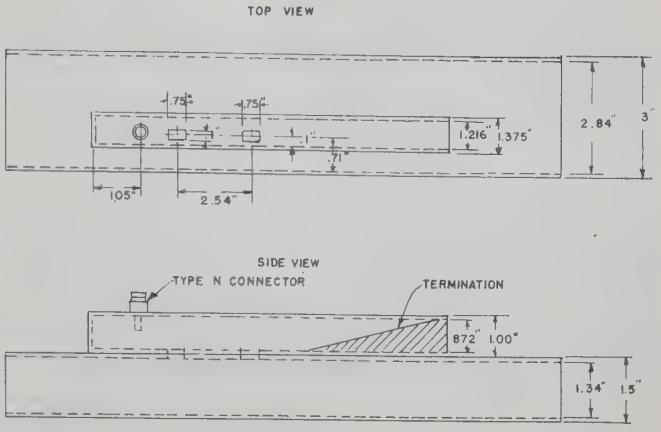

Fig. 13—TE_{11} coupler.

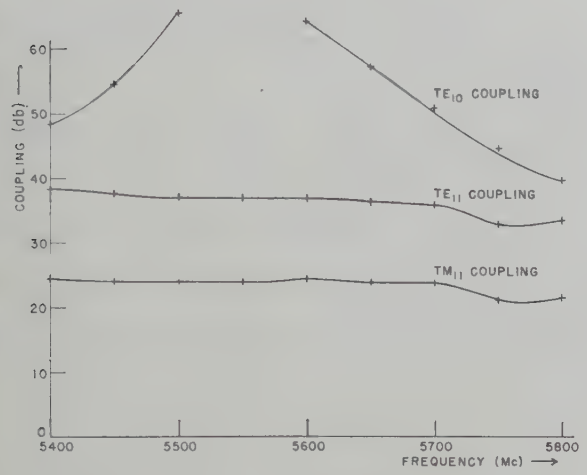

Fig. 11—TM_{11} coupler. Experimental curves of coupling as a function of frequency for the TM_{11}, TE_{11}, and TE_{10} modes. Coupling to the TE_{01} and TE_{20} modes was less than 70 db.

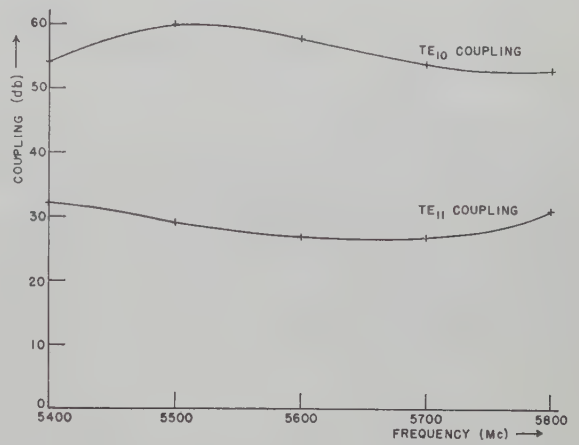

Fig. 14—TE_{11} coupler. Experimental curves of coupling as a function of frequency for the TE_{11} and TE_{10} modes. Coupling to the TM_{11} and TE_{20} modes was less than 70 db. Coupling to the TE_{01} mode was approximately constant at 30 db.

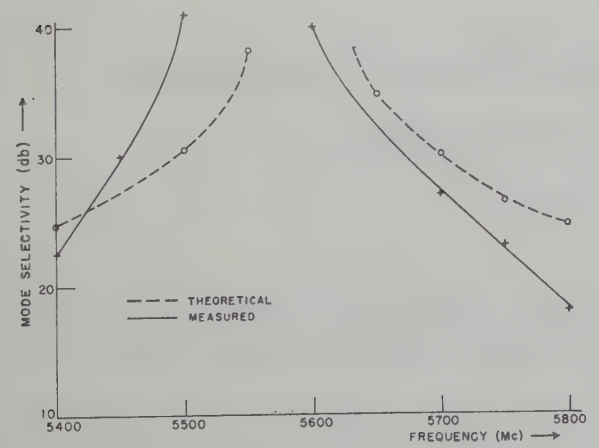

Fig. 12—TM_{11} coupler. Mode selectivity as a function of frequency for the TE_{10} modes.

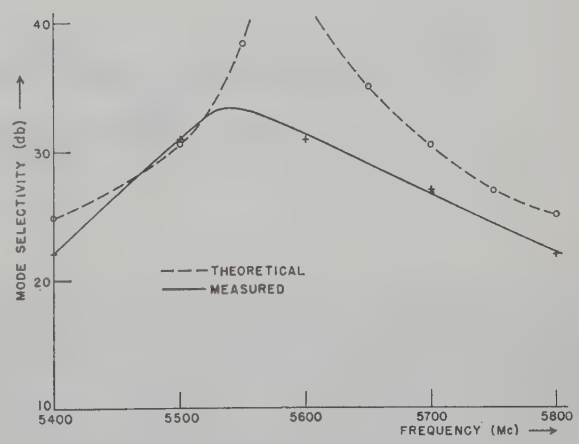

Fig. 15—TE_{11} coupler. Mode selectivity as a function of frequency for the TE_{10} mode.

measurement of the second harmonic output of magnetrons. The three couplers of Figs. 7 through 15 were designed for this application.

The results of a series of second harmonic measurements on an RK5586 magnetron with a set of five couplers are shown in Fig. 16. These curves were obtained by measuring the power in each mode as the magnetron supply voltage was varied. The magnetron was operated at 2800 mc at a pulse repetition rate of 1000 PPS with a 1-μsec pulse length. The termination used was a standard *S*-band dummy load which had a VSWR ranging from less than 1.05 for the TE_{10} mode to a maximum of 1.1 for the TE_{11} mode. The measurements were made directly at the output of the coax to waveguide trans-

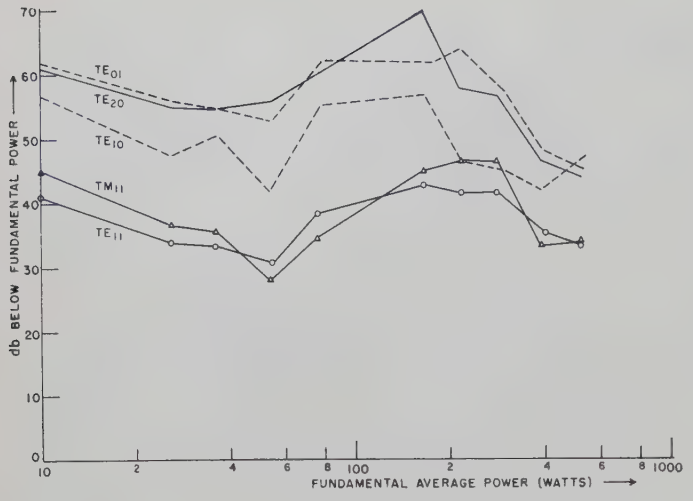

Fig. 16—Second harmonic average power content in the TE_{10}, TE_{20}, TE_{01}, TE_{11}, and TM_{11} modes.

ducer used with the 5586 magnetron. Evidently the concentration of power in the TE_{11}, TM_{11}, and TE_{10} modes is due to the symmetry of this transducer.

The couplers used to obtain the curves of Fig. 16 were adapted for use in a pressurized system. However, at the power levels involved (500 kw) arcing was not a problem and pressurization was not used. These measurements were made by Dr. Pietro Lombardini [7].

Conclusions

Experimental models of the mode couplers indicate that mode selectivities of the order of 30 db or greater over bandwidths of 200 mc or greater are obtainable in simple two-hole couplers. Degenerate modes pose a special problem and may result in substantially lower selectivities. As many as four modes can be simultaneously rejected while coupling strongly to a fifth. The application of these couplers seems limited to systems in which the number of propagating modes is small, but within this limitation they provide a quick and covenient power measurement technique.

Bibliography

[1] H. A. Bethe, "Lumped Constants for Small Holes," M.I.T. Rad. Lab., Cambridge, Mass., Rep. No. 194; March 24, 1943.
[2] S. B. Cohn, "Determination of aperture parameters by electrolytic tank measurements," Proc. IRE, vol. 39, pp. 1416–1421; November, 1951.
[3] H. A. Judy and D. J. Angelakos, "Mode Selective Directional Couplers," Inst. of Eng. Res., University of California, Berkeley, Calif., Rep. No. 31, Contract N70HR 29529, ser. 60, issue no. 119; September 15, 1954.
[4] S. E. Miller, "Coupled wave theory and waveguide applications," *Bell Sys. Tech. J.*, vol. 33, p. 661; May, 1954.
[5] C. G. Montgomery, "Technique of Microwave Measurements," M.I.T. Rad. Lab. Ser., McGraw-Hill Book Co., Inc., New York, N. Y., no. 8; 1949.
[6] W. W. Mumford, "Directional couplers," Proc. IRE, vol. 35, pp. 160–165; February, 1947.
[7] P. Lombardini, "Final Report Task 1, Interference Studies," University of Pennsylvania, Philadelphia, Pa., no. ES-27-030-05; April 15, 1958.

Measurement of Harmonic Power Generated by Microwave Transmitters*

VERNON G. PRICE†

Summary—**A measurement technique is described that can be used to determine quantitatively the power levels of the higher order modes propagating in a straight, lossless, rectangular waveguide. The technique employs a number of small calibrated electric probes which are fixed on the broad and narrow walls of the waveguide measurement section to sample the electric fields within. The method used to calibrate these probes is briefly discussed, and information on accuracy and limitations of the probe technique is presented. Some measurement results on the power levels in the modes of the second and third harmonic frequencies in the outputs of high power *S*-band magnetrons and klystrons are presented.**

The multiple-probe technique has reduced the time required to take measurements at a given frequency to about one-half hour. An automatic computer has been programmed to perform all of the required mathematical operations and has reduced the computation time to less than one-half hour for each measurement frequency.

* Manuscript received by the PGMTT, July 3, 1958; revised manuscript received, September 5, 1958. The work reported here was supported by the Rome Air Development Center under Contract No. AF 30(602)-1670.

† General Electric Microwave Lab., Palo Alto, Calif.

Introduction

In recent years several workers have advanced methods of measurement of the harmonic frequency power in the output of microwave tubes. Interest in these measurements has been stimulated to a large extent by the acute problems of radio interference between microwave systems which can result from unwanted radiation of harmonic frequency energy. However, measurement of this power is complicated by the fact that harmonics in waveguide lines may propagate in many different modes which are convertible one to another by the presence of obstacles or ports. This paper

presents one of the possible techniques for measurement of the powers in higher order modes at harmonic frequencies in waveguides. To accomplish this measurement, a number of small, fixed electric probes are located on the walls of a waveguide measurement section to sample the electric field within. From each of these probes a measurement of relative phase angle and absolute power output is made with a frequency selective microwave receiver tuned to the particular harmonic (or spurious nonharmonic) frequency of interest. It is necessary, of course, that each probe and its associated cabling be calibrated so that a measured power output level will correspond to a calculable value of electric field within the waveguide. From this measurement of probe output power and relative phase angle, one can compute the power level in each of the modes which are above cutoff at the measurement frequency.

The mathematical analysis underlying the present technique is identical with that presented by Forrer and Tomiyasu,[1,2] although the laboratory procedures are different. For example, they used a sliding electric probe on the broad wall of a section of waveguide which they positioned in both the transverse and longitudinal dimensions to sample the electric fields within. The sliding probe, while electrically simple, is cumbersome to employ, and avoidance of voltage breakdown under high power was difficult. To avoid arcing, they found it necessary, in fact, to turn off the high power source each time the sliding probe was moved to a new position. This procedure not only was time consuming, but it also gave rise to possible inaccuracies, because it was not certain that the source when turned on again at each new probe position would be operating as it was during the previous position.

In the technique used by Lewis,[3] a direct measurement of the power in higher order modes is possible by the use of a set of calibrated mode selective couplers. With this method, Lewis was able to measure the power of five higher order modes at the second harmonic of an *S*-band signal. It probably would be difficult, however, to design a set of mode couplers which could be used for measurements in which dozens of higher order modes are propagating. In the use of the multiple probe technique, on the other hand, it has been possible to measure the power in eleven modes at a third harmonic frequency of an *S*-band signal with good accuracy. Measurements at a frequency in which twenty-five modes propagate can be made with reduced accuracy. In addition, it is possible to measure all of the quantities necessary to determine the modal powers in only a few minutes at any one frequency as contrasted with several hours required in the sliding probe method.

[1] M. P. Forrer and K. Tomiyasu, "Effects and measurement of harmonics in high power waveguide systems," 1957 IRE National Convention Record, pt. 1, pp. 263–269.

[2] M. P. Forrer and K. Tomiyasu, "Determination of higher order propagating modes in waveguide systems," *J. Appl. Phys.*, vol. 29, pp. 1040–1045; July, 1958.

[3] D. J. Lewis, "Mode couplers and multimode measurement techniques," this issue, p. 110.

In the following paragraphs, a brief outline is presented of the measurement method used. The technique employed in calibration of the probes is discussed, and the results of some high power tests are presented with an estimate of the measurement accuracy.

Outline of Measurement Technique

The electric probe method is based on the fact that one can determine the maximum number of modes in which a signal might propagate in a waveguide at each frequency of interest. A chart of the cutoff frequencies for two waveguide sizes is given in Fig. 1. For example,

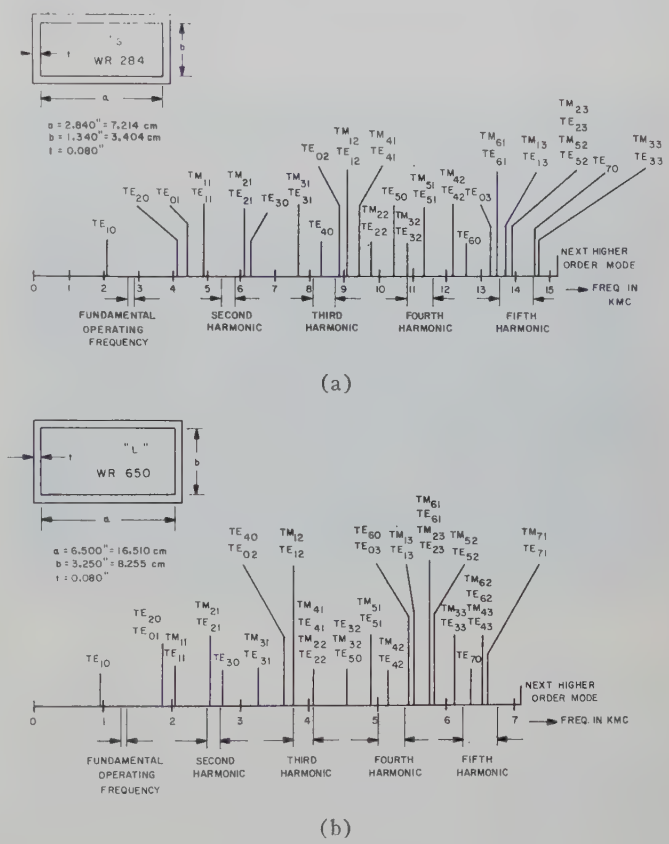

Fig. 1—Chart of mode cutoff frequencies for (a) *S*-band and (b) *L*-band waveguides.

in WR-284 waveguide, a signal at 5 kmc could propagate in the TE_{10}, TE_{20}, TE_{01}, TM_{11}, and TE_{11} modes but no others. With this knowledge, one can make an analysis. The analysis requires that depending on the modal complexity, measurements must be made at a number of prescribed locations on the waveguide walls. An illustration of a WR-650 waveguide section with its probes in position is shown in Fig. 2. In general, the minimum number of probes required is slightly more than the number of modes which can propagate at a given frequency. For example, the number of probes required at each broad-wall cross section is equal to the highest *m*-index to occur for a propagating mode. Similarly, the number of probes required at a cross section on the narrow wall is equal to the highest *n*-index to occur for a propagating mode. Thus, to measure the TE_{71} and TM_{43}

modes, one needs at least seven equally spaced broad-wall probes and three equally spaced narrow wall probes. The number of measurement cross sections required is determined by the following relationships:

$$\text{Number of broad-wall cross sections} = 1 + n_{\max}(1)$$
$$\text{Number of narrow wall cross sections} = 1 + m_{\max}(1)$$

where $n_{\max}(1)$ is the maximum n-index to occur in a propagating mode whose m-index is unity and $m_{\max}(1)$ is the maximum m-index to occur in a propagating mode whose n-index is unity. Thus, if the TE_{71} mode were propagating, probe measurements would need to be made at eight narrow wall cross sections. Also, if the TE_{13} mode were propagating, probe measurements would need to be made at four broad-wall cross sections.

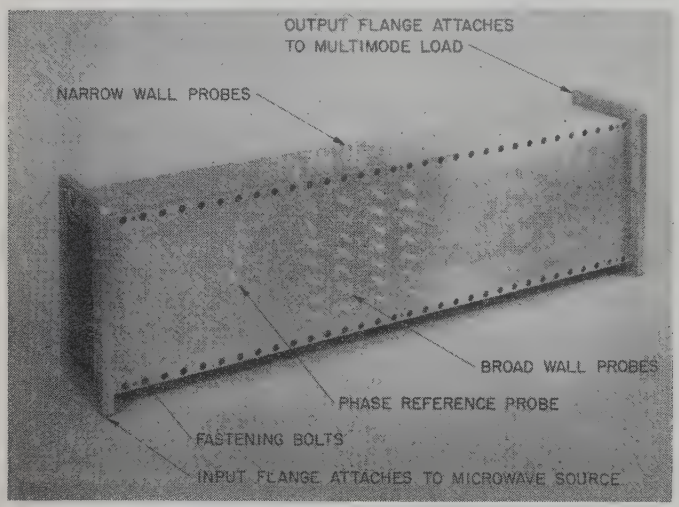

Fig. 2—Illustration of a probe section fabricated in WR-650 waveguide.

The probes at each cross section protrude only a few mils into the waveguide for minimum perturbation of the fields; hence, one can assume that the electric field amplitude of each mode will vary as a sine function over the cross-sectional dimension of the waveguide. Under this assumption, one can use the principle of numerical Fourier analysis to determine the values of the electric field phasors at each probe position. If these phasors are separated into their real and imaginary parts and referred to one cross section, one can write a set of linear equations, the solution of which gives the desired values of electric field intensities for each of the modes of interest. The power in the modes may then be computed readily by integrating Poynting's vector over the waveguide cross section.

This mathematical computation is quite time consuming even for just a few modes. To reduce the computation time, a program has been written for the IBM 650 and 704 computers to perform all of the required steps once the experimental data is obtained. It has been found possible to compute the power in 44 modes at the fifth harmonic of an L-band source in less than twenty minutes, including punching the input data cards and the solution print-out.

A block diagram of the apparatus used to measure the absolute power and relative phase angle at each probe is shown in Fig. 3. Coaxial switches are used to connect the probes to the measurement set.

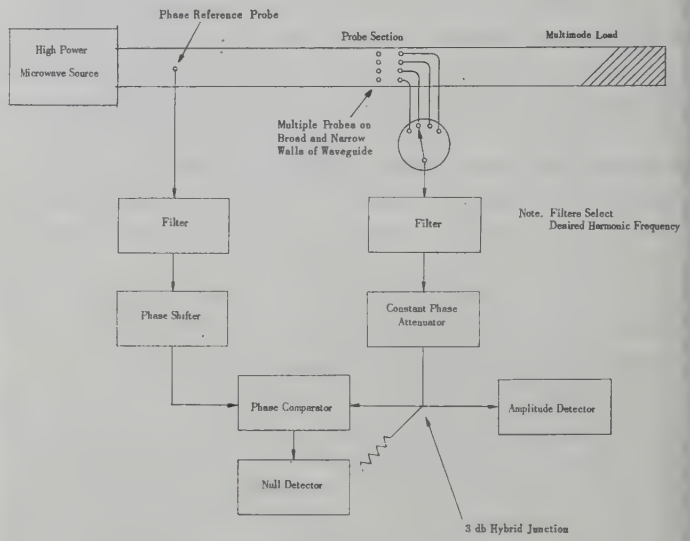

Fig. 3—Simplified block diagram of phase and amplitude measurement equipment.

Probe Calibration Procedure

The function of the probes is to sample the electric field at various prescribed locations on the waveguide wall. The magnitudes and relative phases of the electric fields at the probes are quantities from which the power levels of the several propagating modes of interest may be computed. However, since the magnitude of the electric field at a probe is determined by a measurement of the power output at the end of its connecting cable, it is necessary to find the relationship between the electric field E_i at the ith probe and this power output, P_i. The relationship may be expressed by the equation

$$|E_i|^2 = \frac{P_i}{C_i} \tag{1}$$

where C_i is the probe coupling coefficient which is unique to the ith probe.

To evaluate C_i experimentally, a measurement of P_i is made for each probe with a known value of $|E_i|$ due to a single mode propagating in the probe section. In order to establish a known value of $|E_i|$, a single mode at the desired harmonic frequency is launched into the probe section and, to insure only forward propagating modes, a suitable multimode load is used. To calibrate the broad-wall probes, the TE_{10} mode is used and is launched by means of a very gradual waveguide transition. The power in this mode flowing in the z-direction is given by

$$W_z^{TE_{10}} = G^{TE_{10}} \left| E_{\max}^{TE_{10}} \right|^2 \tag{2}$$

where $\left|E_{\max}^{TE_{10}}\right|$ is the maximum amplitude of the electric field of the TE_{10} mode and $G^{TE_{10}}$ is a calculable

quantity defined in the following equation:

$$G^{TE_{10}} = \frac{a^3 b \epsilon_0 f_c^2}{2c} \sqrt{1 - \left(\frac{f_c}{f}\right)^2} \tag{3}$$

where

a = broad-wall dimension of waveguide,
b = narrow wall dimension of waveguide,
ϵ_0 = free space dielectric constant,
c = velocity of light,
f_c = cutoff frequency for TE_{10} mode,
f = operating frequency.

In the mathematical analysis, it is assumed that the broad-wall probes at each cross section are spaced at p equal intervals across the waveguide walls. Therefore, the power output of the ith probe due to the calibrating mode is given by

$$P_i^{TE_{10}} = C_i \left| E_{max}^{TE_{10}} \right|^2 \sin^2 \frac{i\pi}{p} . \tag{4}$$

Solving (2) and (4) for $\left|E_{max}^{TE_{10}}\right|$ and equating yields

$$C_i = \frac{G^{TE_{10}}}{L_i \sin^2\left(\frac{i\pi}{p}\right)} \tag{5}$$

where $L_i = W_g^{TE_{10}}/P_i^{TE_{10}}$ is the insertion power ratio of the ith probe. This ratio is determined for each broad-wall probe by using an RF substitution technique.

The value of C_i, given by (5), may now be inserted into (1) to get an expression for the electric field $|E_i|$ at a probe:

$$|E_i|^2 = \left[\frac{L_i \sin^2\left(\frac{i\pi}{p}\right)}{G^{TE_{10}}}\right] P_i. \tag{6}$$

Eq. (6) is used for the measurement of the electric fields on the broad wall, and a similar equation is used for the narrow wall probes. In the latter case, a single TE_{01} mode is launched into the probe section with suitable termination to provide the desired calibration information.

The mathematical analysis requires that measurements be made of the probe power outputs as well as the relative phase angles from one probe to another. Therefore, it is necessary, as part of the calibration procedure, to measure the relative phase angles of the probes and their attached cables and switches when a single TE_{10} or TE_{01} mode is launched into the probe section. During fabrication of the probe section, every attempt is made to make the length of the cables attached to each probe the same. However, it is not practical to make the electrical lengths of these equal to $n\pi$ with tolerances closer than about ± 10 degrees. Hence, during the phase calibration procedure, the exact electrical length of the lines to each probe (to within ± 0.5 degree) is measured and recorded.

Measurement Results

The harmonic output powers of two types of S-band tubes were measured. These types were a 4.7-megawatt S-band magnetron and a 1.3-megawatt S-band klystron. In these tests the tubes were operated at the electrode voltage ratings and drive conditions recommended by their manufacturers. If the tubes are measured when operating at lower or higher values than those recommended, it has been observed that the harmonic content can change by a large amount. Table I is a tabulation of the harmonic power output of an S-band klystron and magnetron. In the tubes tested, no directed efforts were made to reduce the harmonic frequency outputs of the tubes.

TABLE I
Harmonic Power Output

	S-Band Magnetron	S-Band Klystron
Fundamental TE_{10}	4.7 Megawatts (0-db reference)	1.3 Megawatts (0-db reference)
2nd Harmonic		
TE_{10}	105 watts	23 watts
TE_{20}	—	6
TE_{01}	—	6
TE_{11}	—	13
TM_{11}	25	60
Total 2nd harmonic power	130 watts (−45.5 db)	108 watts (−41 db)
3rd Harmonic		
TE_{10}	4356 watts	4 watts
TE_{20}	24	—
TE_{30}	6036	—
TE_{40}	22	—
TE_{01}	1	5
TE_{11}	7	1
TE_{21}	2	—
TE_{31}	10	1
TM_{11}	6	1
TM_{21}	6	—
TM_{31}	15	—
Total 3rd harmonic power	10,485 watts (−26.5 db)	12 watts (−50.4 db)

Limitations and Accuracy

While the multiple probe technique allows one to determine the power levels of a large number of modes in a waveguide, it does have some limitations. As the modal order increases, so does the order of the determinant that must be solved; therefore, the number of modes one can measure is limited both by the storage capacity of the computer available and by the large errors that can occur in the solution of high-order determinants even for small errors in the probe readings which supply the experimental data for the determinants. The order of the determinants to be solved is related to the mode indices by the following:

Order of determinant for broad wall $= 2[1 + n_{max}(1)]$

Order of determinant for narrow wall $= 2[1 + m_{max}(1)]$.

Or, the order of determinants is twice as great as the number of cross sections required to evaluate the modes

at any frequency. Thus, to evaluate the modes which may propagate at 8500 mc in WR-284 waveguide, determinants of order as high as eight must be solved for the narrow wall probes and determinants of order as high as four must be solved for the broad-wall probes. If one wished to measure the power in the modes at 7000 mc in WR-650 waveguide, however, determinants of order as high as sixteen would need to be solved, and it is with determinants of this size that large errors can occur in the computed modal power for slight inaccuracies in measurement of probe outputs. It is not likely that this is a basic limitation of the electric probe technique, but rather of the particular computer program written to carry out the mathematical operations. The inclusion of redundant experimental data having finite accuracy into a computer program designed to accommodate it might make possible accurate measurement of a large number of higher order modes.

It is of importance to consider the accuracy, repeatability, and resolution of the apparatus needed to make the measurements with the probe technique. A determination of the accuracy of the results has been made by launching a TE_{20} mode with good single mode purity and known power level into the probe measurement section and its multimode load. The outputs from each probe were measured and the data were reduced with an automatic computer. The measured power input was 201 milliwatts, while the power as indicated in the computer results was 196 milliwatts in the TE_{20} mode, 1.5 milliwatts in the TE_{10} mode, and a few microwatts in other propagating modes.

Experience with measurements of the harmonic output of a number of high power tubes has shown that, if the environmental conditions are unchanged, the power levels measured at each probe are repeatable within ± 1 db, while the phase angles recorded at each probe are repeatable within $\pm 2°$. This repeatability is possible even though the high power tubes are operated under pulsed conditions. An analysis was made of the change in reported modal power in the computer results if the data input to the computer were altered in random manners with changes in both probe powers and probe phase angles. As a result of a series of tests with random variations in the data, the probable modal power levels reported for the magnetron and klystron are within ± 10 per cent of their true values. Under the ideal conditions obtained during calibration operations, the measurement apparatus itself is capable of resolving changes of ± 0.1 db and ± 0.5 degree of phase angle.

Conclusions

A method of measurement of the harmonic power in rectangular waveguide has been presented which has some advantages over other techniques for higher order mode measurement. The use of multiple probes on the waveguide walls, as contrasted with the sliding probe of Forrer and Tomiyasu, has proved to be mechanically superior and has reduced the time required to obtain the experimental data to less than a half hour at each frequency. It is probable that more modes could be measured with the multiple probe technique than with the method of Lewis. The procedure used to calibrate the probes with known signals was discussed and comparison was made of the power levels in the harmonics of high power *S*-band magnetrons and klystrons. Some of the limitations and an estimate of the accuracy are included.

Acknowledgment

The author wishes to express his gratitude to his coworkers, W. Barnett, M. Forrer, C. Milazzo, J. Rooney, and K. Tomiyasu.

Tunable Passive Multicouplers Employing Minimum-Loss Filters*

J. F. CLINE† AND B. M. SCHIFFMAN‡

Summary—Several multicoupler techniques are described for operating twenty or more UHF transmitters and receivers simultaneously with a single localized antenna system. The types of multicouplers considered include the simple parallel-connected filter type and several distributed-line types, in which the individual branches are separately tuned. The filters used are of the symmetrical, narrow-band, direct-coupled resonator type, designed to obtain minimum center-frequency insertion loss for a given insertion loss in the adjacent channels. Design formulas are given for these filters, and characteristic response shapes are presented. The extra-channel susceptance, which is the principal factor limiting the number of channels obtainable in a single multicoupler, is discussed in terms of the input coupling coefficient, the resonator parameters, and the lengths of the connecting lines.

Introduction

THE NUMBER of antennas that can be accommodated in a given air, sea or ground-based installation is limited by considerations of space restrictions, mutual disturbance of radiation patterns, and intercoupling of signals. In certain complex electronic systems now in existence and in others being planned, the large number of individual transmitters and receivers makes it impossible to satisfy the system requirements by a multiplicity of antennas alone, and, therefore, special multicoupler networks involving filters and other components are necessary to permit the sharing of antennas by groups of receivers and transmitters.

This paper has evolved from a study program covering several aspects of multicoupler design. The multicouplers considered here consist of minimum-loss narrow-band filters connected together in different ways. The basic assumptions are that the number of branches is large, *i.e.*, twenty or more, while the pass band of each branch is small in comparison with the minimum channel separation. A typical application is found in the 225 to 400 mc band, with a minimum channel spacing of 2 mc, an adjacent channel isolation of 60 db, a channel-center loss of 1 db or less, and a pass bandwidth sufficient for typical AM, SSB, or NBFM speech modulated signals.

The problems considered here include the design of the minimum-loss filters, the manner of their interconnection, and their effects upon each other from the standpoint of the impedance matching problem. Since these mutual effects involve both the interconnection scheme and the filter design, these two topics must be considered simultaneously. Fixed-tuned, complementary-filter multicouplers are not considered here; instead, the emphasis is on the type of multicoupler in which separate narrow-band channels are independently tunable. Since it may be necessary to change the center frequencies of the individual channels frequently, the preferable method for avoiding excessive impedance mismatch in the multicoupler is to design each branch in such a way as to introduce a minimum of mismatch, rather than to use a matching scheme that involves mutual adjustments of two or more channels at once.

Multicoupler Network Connections

In all of the figures, the letters A, LS, R, and T are used to represent antennas, line-stretchers, receivers, and transmitters, respectively. Most of the diagrams are drawn under the assumption that the transmission line sections are of the coaxial or strip-line variety and that the resonant or anti-resonant devices, including those within the filters, are coaxial resonators. However, the waveguide or wire-circuit counterparts may be considered in situations where those techniques are applicable. The results of the filter analysis given in the following section apply equally well to the RF and the microwave regions, since they are expressed in terms of such basic quantities as the loaded and unloaded value of Q, the coupling coefficient, the normalized frequency displacement, and the insertion loss.

Fig. 1 shows two possible multicoupler arrangements. The symbol S represents a two-position switch. Symbols having the same subscript represent parts operating on a common frequency. In the circuit at the left, the isolation between the channels is provided entirely by the filters in the multicoupler, on a frequency difference basis. In the circuit at the right, additional isolation is provided by the two-port antenna system, on the basis of either phase cancellation or field orientation. In general, an antenna system having any number of ports greater than unity can be used in this application. An example of a three-port microwave antenna system of this type is described by Honey and Jones.[1]

* Manuscript received by the PGMTT, June 13, 1958; revised manuscript received, August 29, 1958. The work on which this paper is based was conducted at the Stanford Res. Inst., Menlo Park, Calif., under the sponsorship of AF Cambridge Res. Center, under Contract AF 19(604)-2247. The measurements illustrated in Figs. 12 and 13 were conducted under the sponsorship of the U. S. Navy Dept., Bureau of Ships, under Contract NObsr-72765.

† Stanford Res. Inst., Menlo Park, Calif.
‡ Varian Associates, Inc., Palo Alto, Calif.

[1] R. C. Honey and E. M. T. Jones, "A versatile multi-port biconical antenna," 1957 IRE National Convention Record, pt. 1, pp. 129–137.

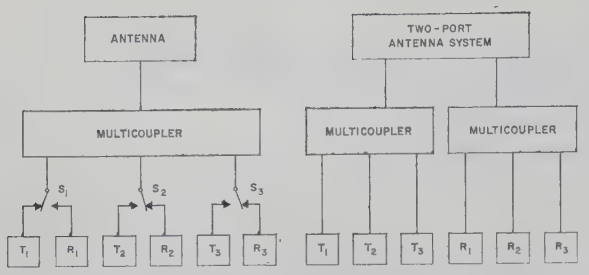

Fig. 1—Two possible antenna-multicoupler systems.

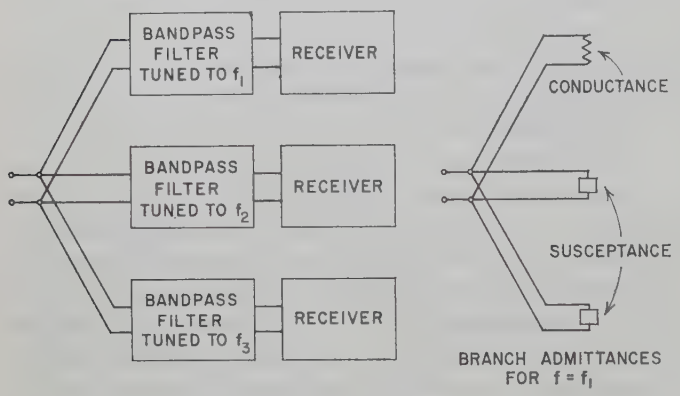

Fig. 2—Parallel-connected multicoupler.

Fig. 2 illustrates a common-junction parallel-connected multicoupler. The admittance, looking from the left into the common junction, is measured at the frequency f_1, which is the center frequency of the upper branch. The input admittance of the upper filter at this frequency is a conductance approximately equal to the characteristic admittance of the connecting lines. The other filters appear as small susceptances, the values of which, in general, are increased considerably by the effects of the short connecting lines between the junction and the filters. The sum of these extra-channel susceptances appearing at the common junction produces an admittance mismatch at this point. This mismatch is the principal factor limiting the number of permissible branches in the multicoupler. It can be reduced by shortening the connecting lines, improving the junction design, and by applying the usual compensation techniques, but it cannot be eliminated entirely over a whole band of frequencies.

Figs. 3 through 6 show several ways of connecting filters in a distributed fashion along a transmission line. In Fig. 3, LS_N is adjusted so that the admittance looking toward the right from the Nth junction is as near zero as possible at the operating frequency of R_N and T_N. At the same frequency each of the other filters looks like a small capacitance, which can be compensated locally. Once LS_N has been adjusted, LS_{N-1} is then adjusted so that the admittance looking toward the right from the $N-1$ junction is as near zero as possible at the operating frequency of R_{N-1} and T_{N-1}, etc.

A possible circuit-packaging arrangement for the different sections in Fig. 3 is suggested in Fig. 4, where

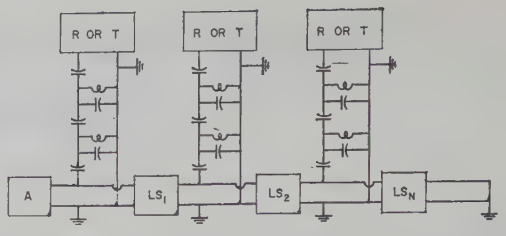

Fig. 3—Distributively-connected multicoupler.

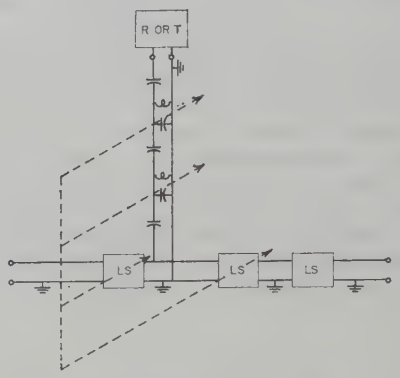

Fig. 4—Single multicoupler section.

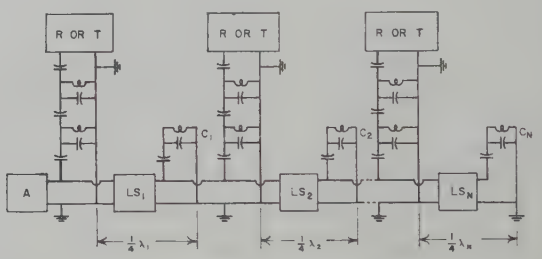

Fig. 5—Line-stretcher and isolation-resonator connections.

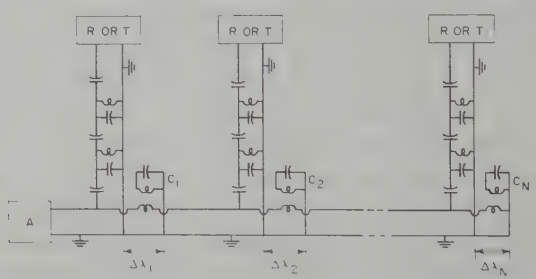

Fig. 6—Circuit employing isolation resonators only.

the entire diagram represents a single section of Fig. 3. Three line stretchers are used instead of one, and two of the line stretchers are gang-tuned together with the band-pass filter. This makes each section nearly independent of the others as far as tuning is concerned. The third line stretcher is adjusted separately, depending upon where the particular section in question is placed in the network chain. Once set, it ordinarily is not reset during tuning operations.[2]

[2] The idea of connecting and ganging filters and line stretchers in a separate package was suggested verbally by L. E. Friedman, formerly with Balco Research Laboratories of Newark, N. J.

If it is permissible to restrict the tuning range of each section in Fig. 3 so that the center frequencies always increase monotonically with section number, the line stretchers can be eliminated and their function can be performed by means of a mechanical arrangement in which the filter ports slide along the transmission line. Even if such a restriction is not permissible, the line stretchers still can be eliminated if a means can be devised for sliding the filter ports past each other or plugging them in at different points along the line. Another method is to use a line that is long enough so that each sliding filter port has a freedom of motion of at least a half wavelength at its lowest frequency of operation.

The circuit of Fig. 5 avoids the interdependence effects of the adjacent line stretchers by the interposition of resonators coupled to the line. For example, the resonator C_1 is adjusted to place, in effect, a short circuit in parallel with the line at the frequency of operation of R_1 and T_1. The line stretcher LS_1 then is adjusted to separate the cavity and the filter by a quarter wavelength, so that the filter port is, in effect, in parallel with an open circuit. The new problems in Fig. 5 are associated with the design of these added resonators and their coupling to the line, with the object of producing an isolating effect in the pass band while producing as little effect as possible in adjacent channels.

Fig. 6 illustrates a scheme for avoiding the use of either sliding ports or line stretchers. The coupled resonators C_1, C_2, etc., act as open circuits at their center frequencies, and they are placed as close as possible to the filter junctions; that is, the distances $\Delta\lambda$ in the diagram are made as small as possible.

Other applicable types of multicouplers have been described by Carlin,[3] by Cohn and Coale,[4] and by Lewis and Tillotson.[5] Carlin's multicoupler has the practical disadvantage that each section operates on the principle of a balanced bridge, in which the antenna impedance is one arm of the bridge, so that a careful balance must be maintained in order to provide the required isolation. The other two multicouplers employ directional filters that are constant-resistance networks and are best suited for use in fixed-tuned multicouplers where the pass bands are more nearly contiguous. They are more complex than is necessary in the present application, where the pass bands are narrow in comparison with the channel separations. Multicouplers employing resistance-terminated lines also have been used, especially for receiver application in strong signal areas where the added losses can be tolerated, but the additional loss makes their use undesirable in cases where a more satisfactory solution can be found.

[3] H. J. Carlin, "UHF multiplexer uses selective couplers," *Electronics*, vol. 28, pp. 152–155; November, 1955.
[4] S. B. Cohn and F. S. Coale, "Directional channel-separation filters," Proc. IRE, vol. 44, pp. 1018–1024; August, 1956.
[5] W. D. Lewis and L. C. Tillotson, "A non-reflecting branching filter for microwaves," *Bell Sys. Tech. J.*, vol. 27, pp. 83–95; January, 1948.

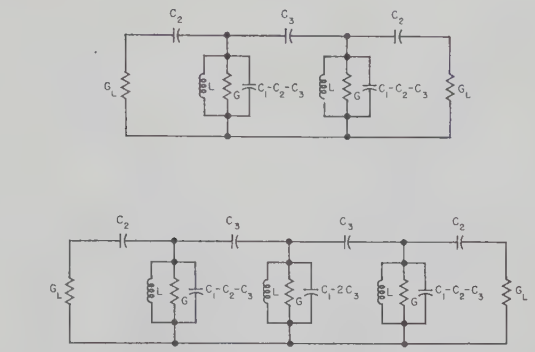

Fig. 7—Equivalent circuits of direct-coupled cavity-resonator filters near resonance.

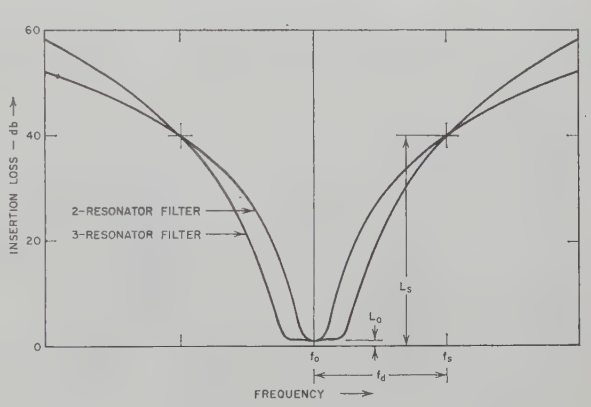

Fig. 8—Notation for filter response curves.

Filter Designs

Design Basis

The narrow-band filters considered here are of the symmetrical, direct-coupled resonator type. Primary attention has been given to two and three-resonator capacitively coupled filters, equivalent circuits for which appear in Fig. 7. The terminal load conductances are denoted as G_L, the terminal coupling capacitances are denoted as C_2, and the internal coupling capacitances are denoted as C_3. The resonators each are represented as a parallel combination of inductance L, conductance G, and a capacitance of which the major part is denoted as C_1. All resonators in any one filter are identical and have a value of unloaded Q that is denoted as Q_U. It may be noted that the total of all capacitances connected to the upper terminal of each resonator is exactly equal to C_1. The value C_1 is a resonator design parameter which is not set by the filter response specifications, but may be fixed at any arbitrary value within the limits imposed by the resonator geometry. Terminal and internal coupling coefficients are defined as $k_T = C_2/C_1$ and $k = C_3/C_1$, respectively.

Fig. 8 shows typical response curves for the two types of filters and introduces certain symbols needed for their description. The center frequency is denoted as f_0 and the insertion loss in decibels at that frequency is denoted as L_0. A design frequency f_S is defined at a point in the filter stop band where the insertion loss in decibels is

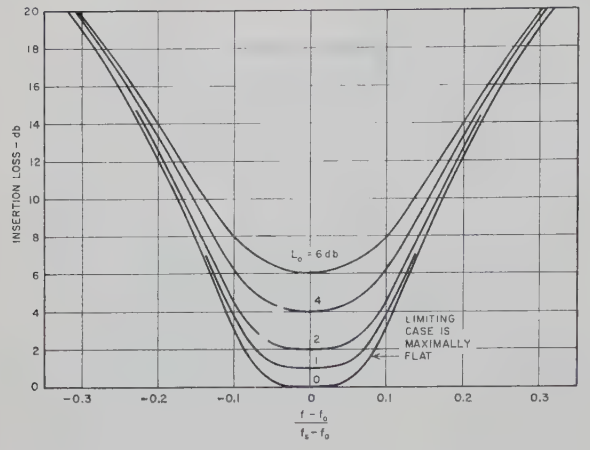

Fig. 9—Two-resonator minimum-loss response curves for $L_s = 40$ db.

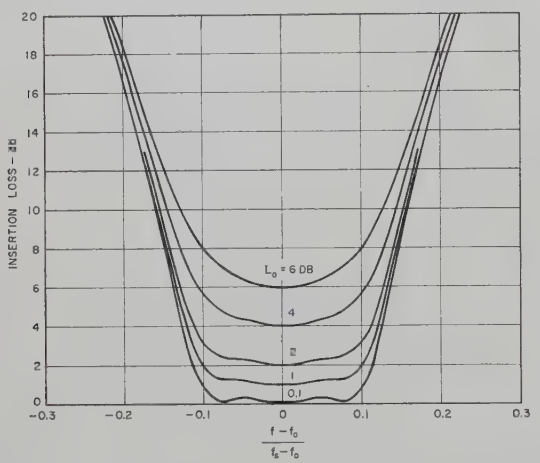

Fig. 10—Three-resonator minimum-loss response curves for $L_s = 60$ db

made equal to a design value L_S. The difference between f_s and f_0 is denoted as f_d. The symbol ω, appearing with various subscripts at other points in this paper, is used in the usual way to represent 2π times the value of f carrying the same subscript. The symbols f and ω without subscripts represent the general frequency variable.

The filters described here are symmetrical filters designed on a *minimum loss* basis, *i.e.*, the values of f_0, f_d, and L_S are specified and k_T and k are then adjusted to produce the smallest value of L_0 for a given value of Q_U. Whatever response shapes result from following this design procedure are then accepted if they are adequate for the particular application. Some typical response curves are shown in Figs. 9 and 10.

Two-Resonator Filters

The general expression for insertion loss, in decibels, as derived by Cohn and Shimizu,[6] is

$$L_I = 10 \log_{10} \left\{ \left[\frac{(1 + Q_T/Q_U)^2}{2kQ_T} + \frac{kQ_T}{2} \right]^2 + 2 \left[\frac{(1 + Q_T/Q_U)^2}{k^2} - Q_T^2 \right] u^2 + \frac{4Q_T^2}{k^2} u^4 \right\} \quad (1)$$

where the normalized frequency variable is defined by $u = (f - f_0)/f_0$ and Q_T is the Q of each cavity due to terminal loading only.

The first term of (1) determines the midband loss and is a number that is generally less than 10. The second term, which is significant only for filters with large degrees of overcoupling or undercoupling, has a coefficient which is the difference between two approxinately equal quantities and is, therefore, small. The third term, however, increases as the fourth power of u and is therefore the only significant term in the stop band. Hence the insertion loss in decibels at frequency f_s is given quite accurately by

$$L_s = 10 \log_{10} \left(\frac{4Q_T^2}{k^2} u_s^4 \right) \quad (2)$$

where u_s is the value of u for $f = f_s$, *i.e.*, $u_s = (f_s - f_0)/f_0$. It can now be seen that the ratio Q_T/k must be held constant in the process of finding a minimum-midband loss design for specified values of L_s and u_s.

First, u is set equal to zero in (1). Then the equation is rearranged to give the band-center loss, in decibels, as

$$L_0 = 20 \log_{10} \left[\frac{1}{2} \left(\frac{Q_T}{k} \right) \left(\frac{Q_T + Q_U}{Q_T Q_U} \right)^2 + \frac{Q_T^2}{2} \left(\frac{k}{Q_T} \right) \right]. \quad (3)$$

The argument of the above equation is differentiated with respect to Q_T while holding Q_U and (Q_T/k) invariant. The derivative is then set equal to zero, and after simplifying the result with the aid of (2), the condition for minimizing L_0 is found to be

$$Q_U u_s = \frac{10^{L_s/40} \sqrt[4]{1 + Q_T/Q_U}}{\sqrt{2} Q_T/Q_U}. \quad (4)$$

When (2) and (4) are substituted in (3) we obtain the following expression for the minimum center-frequency loss of a symmetrical two-resonator filter, in decibels:

$$L_0 = 10 \log_{10} \left[\frac{1}{4} \left(\frac{Q_T}{Q_U} + 1 \right) \left(\frac{Q_T}{Q_U} + 2 \right)^2 \right]. \quad (5)$$

In practice, the value of Q_T/Q_U which satisfies (5) can be found either by a graphical method, by an iterative process, or by solving the cubic equation. This value of Q_T/Q_U inserted in (4) gives a simple relation between the minimum value of Q_U, the stop band insertion loss L_S, and the normalized frequency variable u_s which will yield that insertion loss.

Finally, the value of the internal coupling coefficient k is obtained by rearranging (2) as follows:

$$k = 2Q_T u_s^2 / 10^{L_s/20}. \quad (6)$$

[6] S. B. Cohn and J. Shimizu, "Strip Transmission Lines and Components," Stanford Res. Inst., Menlo Park, Calif., Project No. 1114, Quart. Prog. Rep. 2, Contract No. DA 36-039SC-63232, pp. 4–6; May, 1955.

Thus the electrical design of the two-resonator filter has been completely specified by (4) through (6) for given values of Q_U, L_s, and u_s.

Three-Resonator Filter

A similar procedure is followed for the three-resonator filter. From expressions derived by Taub and Bogner,[7] the midband insertion loss in decibels is given by

$$L_0 = 20 \log_{10} \frac{1/Q_L^2 Q_U + 2k^2/Q_L}{2k^2/Q_T} \tag{7}$$

where Q_L is defined by $1/Q_L = 1/Q_T + 1/Q_U$. Eq. (7) applies to a symmetrical filter, and our notation, not that of Taub and Bogner, is used. In the case of the optimum three-resonator filter it is impossible to achieve a perfect maximally-flat or Tchebycheff response in a symmetrical filter having internal losses, as pointed out by Dishal and Sellers[8] and by Taub and Bogner.[7] By way of comparison, however, the symmetrical design derived below has the following advantages over the exact response shape design:

1) A better pass-band match is possible.

2) Midband loss is lower for the same values of f_s, L_s, and Q_U. As derived by Taub and Bogner from expressions given by M. Dishal[9] the loss, in decibels, is

$$L_I = L_0 + 10 \log_{10} \left\{ 1 + \left[\frac{b^2 - ca}{c^2} \right] (2u)^2 + \left[\frac{a^2 - 2b}{c^2} \right] (2u)^4 + \frac{(2u)^6}{c^2} \right\} \tag{8}$$

where

$$a = \frac{2}{Q_L} + \frac{1}{Q_U}, \qquad b = 2k^2 + \frac{2}{Q_L Q_U} + \frac{1}{Q_L^2},$$

and

$$c = \frac{2k^2}{Q_L} + \frac{1}{Q_L^2 Q_U}.$$

The insertion loss at the normalized frequency u_s (corresponding to f_s in Fig. 10) as determined from (7) and (8), is given to an excellent approximation by

$$L_s = 20 \log_{10} \left(\frac{4Q_T}{k^2} u_s^3 \right). \tag{9}$$

It is apparent from the above that Q_T/k^2 is the quantity that must be held constant in order to determine the minimum midband loss of a three-resonator filter for a constant value of L_s. The analysis then proceeds in a manner similar to that of the two-resonator case.

The design relation for this case is thus found to be

$$Q_U u_s = \frac{10^{L_s/60} \sqrt[3]{1 + Q_T/Q_U}}{\sqrt[3]{4 Q_T/Q_U}}. \tag{10}$$

By combining (7), (9) and (1) we then obtain an explicit formula for Q_T/Q_U

$$\frac{Q_T}{Q_U} = \frac{3}{2} \left(\sqrt{1 + \frac{8}{9} (10^{L_0/20} - 1)} - 1 \right). \tag{11}$$

The value of the internal coupling coefficient k is obtained by rearranging (9) as follows:

$$k = \frac{2\sqrt{Q_T u_s^3}}{10^{L_s/40}}. \tag{12}$$

Thus the electrical design of a symmetrical three-resonator filter having minimum insertion loss is completely specified by (10) through (12).

Approximate Design Formulas

Certain approximations, accurate to within 5 per cent for values of L_0 less than 1 db, can be obtained for the quantities $Q_U u_s$ and Q_T/Q_U in (4), (5), (10), and (11). Design formulas for the two-resonator filter, based on these approximations, can be written as

$$k \approx 1.41 \frac{\omega_d}{10^{L_s/40} \omega_0} \tag{13}$$

$$k_T \approx 1.19 \frac{\sqrt{G_L \omega_d L}}{10^{L_s/80}} \tag{14}$$

$$Q_U \approx 6.15 \frac{10^{L_s/40} \omega_0}{L_0 \omega_d} \tag{15}$$

while corresponding formulas for the three-resonator filter are

$$k \approx 1.57 \frac{\omega_d}{10^{L_s/60} \omega_0} \tag{16}$$

$$k_T \approx 1.31 \frac{\sqrt{G_L \omega_d L}}{10^{L_s/120}} \tag{17}$$

$$Q_U \approx 8.21 \frac{10^{L_s/60} \omega_0}{L_0 \omega_d}. \tag{18}$$

The value L in (14) and (17) is the value of the resonator equivalent inductance shown in Fig. 7.

Factors Limiting the Number of Branches

Each multicoupler branch in Figs. 2 through 6, at band center, presents to the junction an input admittance approximately equal to G_L. Outside its pass band, each branch presents an input admittance which is essentially a susceptance, described here by the term *extra-channel susceptance.*

[7] J. J. Taub and B. F. Bogner, "Design of three-resonator band pass filters having minimum insertion loss," Proc. IRE, vol. 45, pp. 681–686; May, 1957.

[8] M. Dishal and B. Sellers, "Design of three-resonator dissipative band-pass filters having minimum insertion loss," Proc. IRE, vol. 46, p. 498; February, 1958.

[9] M. Dishal, "Design of dissipative band-pass filters producing desired exact amplitude-frequency characteristics," Proc. IRE, vol. 37, pp. 1050–1069; September, 1949.

The multicoupler is set up in such a way that the center frequency of each branch is different from that of any other branch. In general, the extra-channel susceptance of each branch, measured or calculated at the center frequency of another branch, is small in comparison with G_L. However, the total effect of all of these small extra-channel susceptances is the principal factor limiting the permissible number of branches. Consequently, it is important to make the extra-channel susceptance of each branch as small as possible. Each of these extra-channel susceptances is equal to the extra-channel susceptance of its filter, transformed through the short length of conductor connecting the filter port to the junction or branch point. In the usual case, this is approximately equal to the sum of the extra-channel susceptance of the filter alone plus the lumped capacitance of the short conductor to ground. At VHF and higher frequencies, the magnitudes of the various quantities are such that the capacitance of this short conductor is the larger of these two components unless the conductor is less than a small fraction of an inch in length. This makes it important to design the junction in such a way as to minimize this effect as much as possible.

In the parallel-junction multicoupler shown in Fig. 2, the extra-channel susceptances add directly at the junction. If it is assumed, for simplicity, that each susceptance consists entirely of the lumped susceptance of the short line between the junction and the filter port, the total susceptance in, for example, a 20-channel multicoupler is 20 times the average lumped susceptance of one branch line. The largest total susceptance that can be compensated by practical means over a two-to-one frequency band is probably about equal to G_L. If the characteristic impedance of the lines is also equal to G_L, and if the average frequency is taken as 300 mc, for example, the lines can average no more than about 0.2 inch in length. When the added effects of the filters are considered, this length must be reduced even further. Consequently, the distributed type of multicoupler shown in Fig. 3 seems to offer more promise when there are more than five or ten branches, since the extra-channel susceptance is not concentrated at one point. It appears quite possible to design the distribution line so that the branch susceptances in effect become part of the distributed shunt susceptance of the distribution line itself. In this case, the connecting line effects become less important, and attention can be turned to the extra-channel susceptances of the filters themselves.

It is easily shown that in either the two or the three-resonator filter, the extra-channel susceptance is essentially unchanged when the second resonator is short-circuited. The value of the extra-channel susceptance then is given approximately by

$$B_{xc} \approx \omega k_T C_1 + \omega k_T{}^2 C_1 \frac{\omega_0{}^2}{\omega_0{}^2 - \omega^2} \qquad (19)$$

where ω is 2π times the frequency of measurement or calculation and ω_0 is 2π times the center frequency of the filter in question. The value of k_T is given by either (14) or (17) for the minimum-loss filter designs described in this paper. The minimum-loss filter is well suited to multicoupler applications because of its small value of k_T. For the parameters of other filter designs having any number of resonators, the reader is referred to a recent article by Cohn.[10]

The last term in (19) represents a series combination of inductance and capacitance that is resonant at $\omega = \omega_0$. This series combination, in parallel with C_2, as indicated by the first term, forms the extra-channel equivalent circuit for the filter. This is shown schematically in the upper part of Fig. 11, which represents a group of seven filters tuned to relative frequencies of $\omega_0/\omega = 0.985$, 0.99, etc., as indicated. In the case where $\omega_0/\omega = 1$, the approximation upon which (19) is based is not valid, and the input admittance is approximately equal to G_L. The bar charts below the equivalent circuits illustrate qualitatively the way in which the two branch susceptances values vary with ω_0. The value of ω is the same in all cases. The left hand branch susceptance, ωC_2, increases with decreasing ω_0 because k_T, and hence C_2 also, increases as ω_0 decreases. For values of ω_0 far removed from ω, the susceptance of the right hand branch, represented by the last term in (19), becomes negligible. Also, its sign changes when ω_0 passes through ω. Consequently, when there are a large number of channels spread over a wide frequency range, it may be possible in some cases to neglect the last term in (19) from the standpoint of its average effect, and the average extra-channel susceptance of a filter then reduces to that of C_2 alone.

Although this paper, as stated in the Introduction, has evolved from a study program in which the multicouplers under consideration operate in the 225 to 400 mc band with twenty or more branches, some of the first experimental measurements on equipment designed from the above formulas were made in connection with another multicoupler study program[11] conducted in the HF range and involving only four branches. Figs. 12 and 13 show the measured insertion loss and admittance of a four-branch, parallel-connected multicoupler, in which each branch consists of a minimum-loss filter containing three resonant circuits. In these measurements, the center frequencies were set at 17, 18, 19, and 20 mc. The admittance was measured at the common junction of the four filter ports and the heavy segments of the curve define bandwidths of 0.2 mc. The shunt susceptance of the junction connections at 20 mc, normalized with respect to the characteristic admittance, was measured separately and found to be 0.29.

[10] S. B. Cohn, "Direct-coupled resonator filters," PROC. IRE, vol. 45, pp. 187–196; February, 1957.

[11] Sponsored by U. S. Navy Dept., Bureau of Ships, under contract NObsr-72765.

Fig. 11—Multicoupler branch susceptance values.

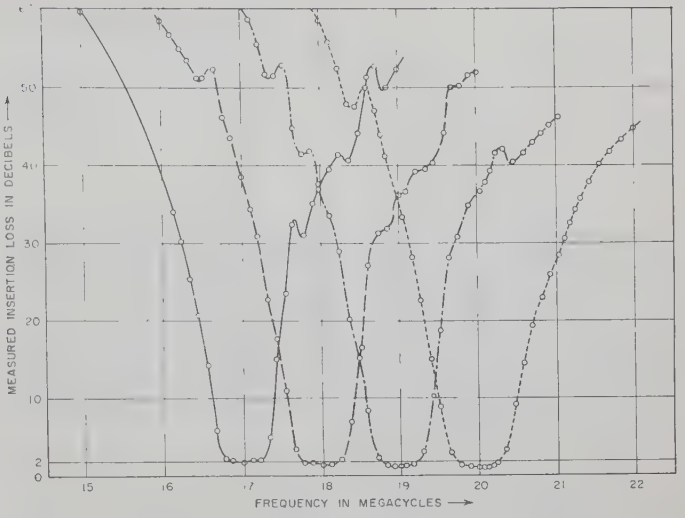

Fig. 12—Measured insertion loss in a four-branch multicoupler.

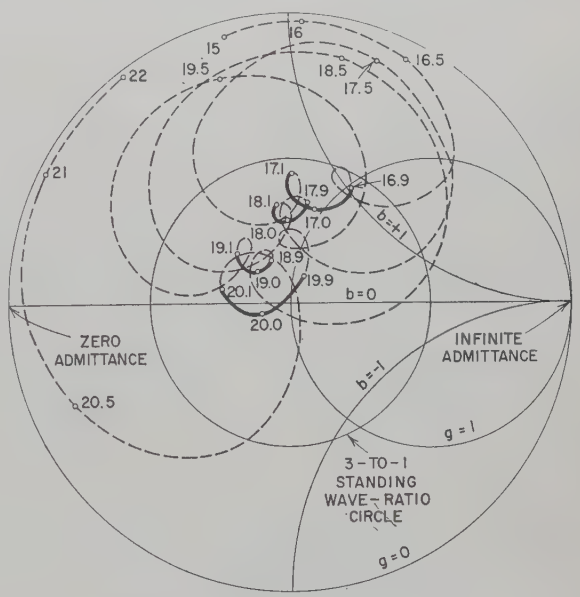

Fig. 13—Measured admittance in a four-branch multicoupler.

The filter centered at 20 mc, tested alone, had values of $L_0=1$ db, $L_s=30$ db, and $\omega_d/\omega_0=0.05$. The filter centered at 17 mc had values of $L_0=1.2$ db, $L_s=37$ db and $\omega_d/\omega_0=0.059$. The resulting values of Q_U given by (18) are 500 and 480, respectively, which agree reasonably well with a value of 530 obtained in separate measurements on the coils alone. The higher loss of about 1.9 db at 17 mc in Fig. 12 is due to the fact that a mismatch exists at that frequency, as shown in Fig. 13. The ripples in the stop band of each branch in Fig. 12 occur in or near the frequencies of the pass bands of the other branches. They can be explained in terms of the shunting action at the junction produced by each filter in and near its pass band. Generally speaking, this is not detrimental to the operation of the multicoupler.

Conclusions

When the pass band of each channel is much narrower than the minimum channel separation, an effective multicoupler may be formed by connecting together several narrow-band filters, either in parallel at a common junction or distributed along a transmission line. The distributed connection is superior to the parallel connection when the number of branches in the multicoupler becomes larger than about five or ten. The directional filter approach to multicoupler design is more complicated than necessary in the present case and is best suited to contiguous pass band applications, which are not considered here.

The narrow-band filters can be designed to produce a minimum center-frequency insertion loss for given values of channel spacing, adjacent-channel insertion loss, and unloaded resonator Q. Symmetrical two and three-resonator filters designed on this basis have response functions that are suitable for many applications, including the present one. In the case of the three-resonator filter, the center-frequency insertion loss is smaller than that obtained in the maximally-flat, unsymmetrical three-resonator filter.

Acknowledgment

The authors wish to acknowledge the helpful suggestions and constructive criticism of Dr. Seymour B. Cohn.

A Wide-Band Strip-Line Balun*

E. M. T. JONES† AND J. K. SHIMIZU†

Summary—A new wide-band strip-line balun that uses a pair of dual coupled-strip-line band-pass filters is described. It can operate over bandwidths up to about 8:1 in the frequency range of about 100 to 10,000 mc. Design data and theoretical performance curves for typical wide-band baluns of this type are presented. The measured performance of an experimental balun operating over a 3:1 frequency range centered at 3000 mc is compared with the theoretical performance, and the effects of discontinuities and dissymmetries in the experimental balun are discussed.

Introduction

A STRIP-LINE balun is used to connect an unbalanced structure, such as a single-conductor strip transmission line, to a balanced structure, such as a two-conductor strip transmission line or a balanced printed circuit antenna. Recently, several strip-line baluns[1] have been constructed that operate over a limited frequency band. The baluns described here can easily be designed to operate over several octaves.

One form of the wide-band strip-line balun is shown in Fig. 1(a). The balanced signal is obtained from the unbalanced signal by first dividing the signal into two parts, and then passing the divided signal through two equal-length coupled-strip-line band-pass filters.[2] These dual filters are one-quarter wavelength long at band center and have the property that the image phase shift of the upper filter (with the pair of shorted strips) is always 180 degrees greater than that of the lower filter (with the pair of open-circuited strips). At the frequencies where the normalized image impedances of the coupled-strip-line filters are equal to unity, the input VSWR of the balun is also unity and the ratio of balanced to unbalanced voltage at the output ports is infinite.

The other form of balun to be considered is shown in Fig. 1(b). It is similar to that of Fig. 1(a) except that one of the band-pass filters has been staggered with respect to the other one by a distance, l, equal to any odd multiple of a quarter wavelength at midband. This device has a ratio of balanced to unbalanced voltage of infinity at the output both when the distance l is equal to a quarter wavelength and when the image impedances of the two filters are equal. The input VSWR of this balun is unity, however, only when the image impedances of the filters are equal. Comparing the two forms of baluns of Fig. 1(a) and 1(b), the latter has the better balance-to-unbalance ratio, while the former has the better input match.

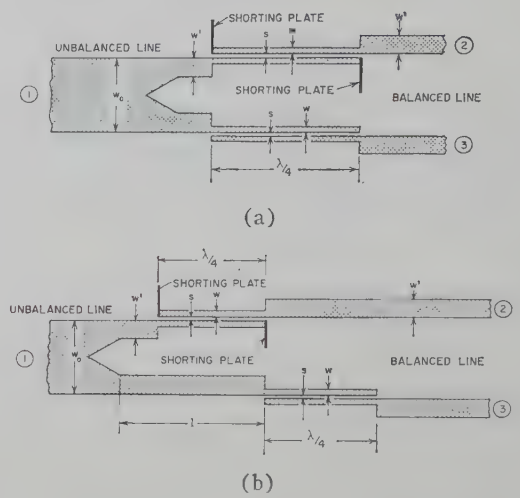

Fig. 1—Plan views of two wide-band strip-line baluns.

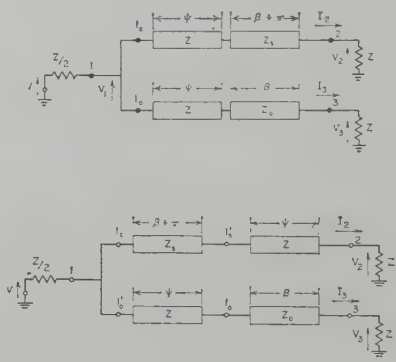

Fig. 2—Equivalent circuits of two wide-band baluns.

General Analysis

The equivalent circuit of the balun of Fig. 1(a) is shown in Fig. 2(a). The equivalent circuit of the balun in Fig. 1(b) with the staggered band-pass filters is shown in Fig. 2(b). The notation used is as follows.

$$Z_s = \frac{2Z_{oe}Z_{oo}\sin\theta}{[(Z_{oe}-Z_{oo})^2-(Z_{oe}+Z_{oo})^2\cos^2\theta]^{1/2}}$$

= image impedance of the band-pass filter with the pair of short-circuited strips.

$$Z_o = \frac{Z_{oe}Z_{oo}}{Z_s} = \text{image impedance of the band-pass filter with the pair of open-circuited strips.}$$

* Manuscript received by the PGMTT, June 13, 1958; revised manuscript received, August 7, 1958. The work reported in this paper was sponsored by the AFCRC under Contract AF 19(604)-1571. More detailed information about this balun is contained in a report by the authors, "A Wide-Band Strip-Line Balun," Stanford Res. Inst., Menlo Park, Calif., Sci. Rep. No. 3; June, 1958.

† Stanford Res. Inst., Menlo Park, Calif.

[1] E. G. Fubini, "Stripline radiators," IRE TRANS. ON MICROWAVE THEORY AND TECHNIQUES, vol. MTT-3, pp. 149–156; March, 1955.

[2] E. M. T. Jones and J. T. Bolljahn, "Coupled-strip-transmission-line filters and directional couplers," IRE TRANS. ON MICROWAVE THEORY AND TECHNIQUES, vol. MTT-4, pp. 77–81; April, 1956.

Z_{oe} = characteristic impedance of one coupled strip, measured with respect to ground, with equal currents flowing in the same direction.

Z_{oo} = characteristic impedance of one coupled strip, measured with respect to ground, with equal currents flowing in opposite directions.

θ = electrical length of each band-pass filter.

$$\beta = \cos^{-1}\left[\left(\frac{Z_{oe}+Z_{oo}}{Z_{oe}-Z_{oo}}\right)\cos\theta\right]$$

= image phase shift of the filter with the pair of open-circuited strips.

$\beta+180°$ = image phase shift of the filter with the pair of short-circuited strips.

ψ = electrical length of the transmission line of characteristic impedance, Z.

In each of these baluns the input impedances measured to the right at Ports 1_s and 1_o are duals, since the image impedances, Z_s and Z_o are chosen to satisfy

$$Z_s Z_o = Z^2. \tag{1}$$

The ratio of balanced to unbalanced voltage at Port 2 or Port 3 of either balun is

$$\frac{V_b}{V_u} = \left|\frac{1-\dfrac{V_3}{V_2}}{1+\dfrac{V_3}{V_2}}\right|. \tag{2}$$

The normalized impedance Z_{1s}/Z measured to the right at Port 1_s and the normalized impedance Z_{1o}/Z measured to the right at Port 1_o are related to V_3/V_2 as

$$\frac{V_3}{V_2} = -\frac{Z_{1s}}{Z} = -\frac{Z}{Z_{1o}}. \tag{4}$$

The VSWR of the balun measured at Port 1 is

$$\text{VSWR} = \frac{1+|r_{1s}|^2}{1-|r_{1s}|^2} = \frac{1+|r_{1o}|^2}{1-|r_{1o}|^2} \tag{5}$$

where r_{1o}, the reflection coefficient at Port 1_o, is the negative of r_{1s}, the reflection coefficient at Port 1_s. Thus, the input VSWR of this balun with the unstaggered filters is a function only of the magnitude of the input reflection coefficient of either of its balanced branches. If the ratio of balanced to unbalanced voltage at the output ports is expressed in terms of the reflection coefficients, it is found that

$$\left|\frac{V_b}{V_u}\right| = \frac{1}{|r_{1s}|} = \frac{1}{|r_{1o}|}. \tag{6}$$

Eq. (6) shows that the ratio of balanced to unbalanced voltage of the balun with the unstaggered filters is also only a function of the magnitude of the reflection coefficient of either of its balanced branches. Note too that the balun performance is independent of the electrical length, ψ, of the transmission lines connecting to the two band-pass filters.

Returning now to the balun with the staggered filters shown in Fig. 1(b) it is found that the ratio V_3/V_2 may be expressed as

$$\frac{V_3}{V_2} = -\frac{\cos\psi\left(\cos\beta + j\left(\frac{Z_s}{Z}\right)\sin\beta\right) + j\sin\psi\left(\cos\beta + j\left(\frac{Z_s}{Z}\right)\sin\beta\right)}{\cos\psi\left(\cos\beta + j\left(\frac{Z}{Z_s}\right)\sin\beta\right) + j\sin\psi\left(\cos\beta + j\left(\frac{Z_s}{Z}\right)\sin\beta\right)}. \tag{7}$$

For the balun of Fig. 1(a) the ratio V_3/V_2 may be expressed as

$$\frac{V_3}{V_2} = -\frac{\cos\beta + j\left(\frac{Z_s}{Z}\right)\sin\beta}{\cos\beta + j\left(\frac{Z}{Z_s}\right)\sin\beta}. \tag{3}$$

It is seen that $V_3/V_2 = -1$ corresponding to $V_b/V_u = \infty$ when $Z_s/Z = 1$ or when $\cos\psi = 0$.

The input impedance of the upper branch of the balun at Port 1_s is

$$\frac{Z_{1s}}{Z} = \frac{\cos\beta + j\dfrac{Z_s}{Z}\sin\beta}{\cos\beta + j\dfrac{Z}{Z_s}\sin\beta} \tag{8}$$

while that of the lower branch at Port $1_o'$ is

$$\frac{Z_{1o}'}{Z} = -\frac{\cos\psi\left(\cos\beta + j\left(\frac{Z}{Z_s}\right)\sin\beta\right) + j\sin\psi\left(\cos\beta + j\left(\frac{Z_s}{Z}\right)\sin\beta\right)}{\cos\psi\left(\cos\beta + j\left(\frac{Z_s}{Z}\right)\sin\beta\right) + j\sin\psi\left(\cos\beta + j\left(\frac{Z}{Z_s}\right)\sin\beta\right)}. \tag{9}$$

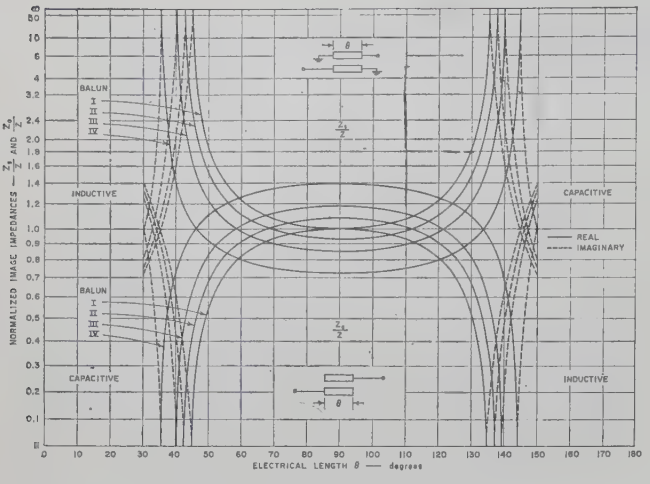

Fig. 3—Image impedance of the band-pass filters used in Baluns I, II, III, and IV.

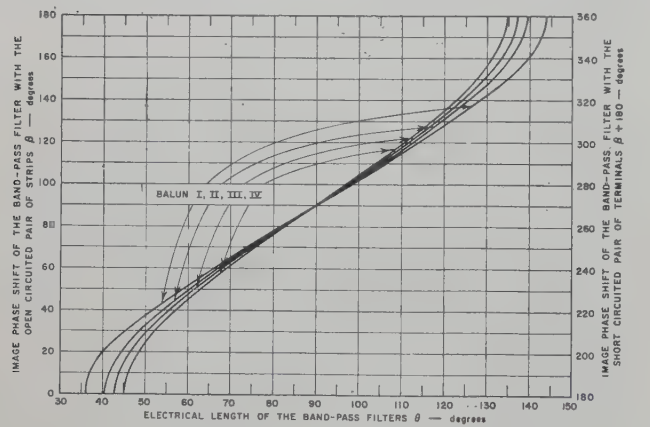

Fig. 4—Image phase shift of the band-pass filters used in Baluns I, II, III, and IV.

The input impedance at Port 1 normalized to the impedance $Z/2$ of the input line is

$$2Z_1/Z = \frac{2}{Z/Z_{1s} + Z/Z'_{1o}} \tag{10}$$

and the input VSWR in terms of the input impedance at Port 1 is

$$\text{VSWR} = \frac{|1 + 2Z_1/Z| + |1 - 2Z_1/Z|}{|1 + 2Z_1/Z| - |1 - 2Z_1/Z|}. \tag{11}$$

The VSWR is unity only when $Z_s/Z = 1$.

The Theoretical Performance of Wide-Band Baluns

Baluns with Two Unstaggered Band-Pass Filters of Equal Conductor Size

The frequency variation of the normalized image impedances, Z_s/Z and Z_o/Z, of the filters incorporated in these baluns is plotted in Fig. 3, and the frequency variation of the image phase shift of the filters is plotted in Fig. 4. The frequency variation of the input VSWR and the ratio of output balanced to unbalanced voltage, V_b/V_u, of four baluns with unstaggered band-pass filters

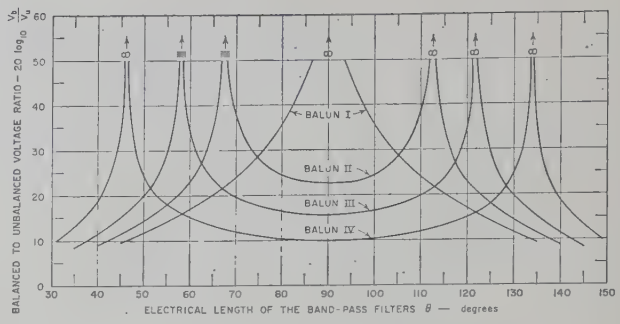

(a)

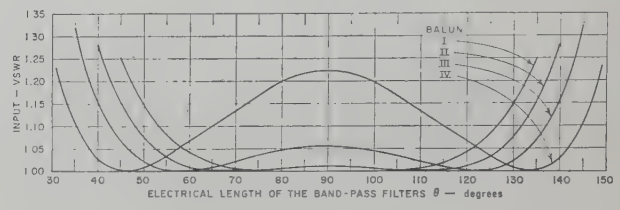

(b)

Fig. 5—Theoretical performance of Baluns I, II, III, and IV.

TABLE I

Summary of Electrical Parameters of Four Wide-Band Strip-Line Baluns, Each Having Two Unstaggered Band-Pass Filters of Equal Conductor Size

Parameter	Balun			
	I	II	III	IV
Z_{oe}/Z_{oo}	5.828	6.500	7.420	9.600
Z_{oe}/Z	2.415	2.250	2.730	3.200
Z_{oo}/Z	0.415	0.393	0.368	0.334
Z_s/Z (midband)	1.000	0.925	0.849	0.721
Z_o/Z (midband)	1.000	1.081	1.179	1.387
Design θ for perfect operation (degrees)	90 ± 0	90 ± 22.5	90 ± 32	90 ± 44

is shown in Fig. 5. Table I summarizes their pertinent electrical parameters. It is seen that Balun I, which has $Z_s = Z_o = Z$ at midband, has unity VSWR and $V_b/V_u = \infty$ at midband.

The frequency response of the VSWR has a maximally flat characteristic and is less than 1.018 over a 1.77:1 frequency range. The ratio of V_b/V_u over this frequency range is always greater than 20 db. Stated another way, the power in the unwanted unbalanced mode is always less than 1 per cent over this frequency range.

Baluns II, III, and IV are designed so that at midband $Z_o > Z$ and $Z_s < Z$, while maintaining the condition that $Z_s Z_o = Z^2$ at all frequencies. Inspection of the curves in Fig. 5 shows that increasing the ratio of Z_o/Z_s at midband increases the midband VSWR, decreases the midband ratio of V_b/V_u, and increases the separation of the frequencies of perfect balun operation. Balun IV, with a VSWR of 1.22 at midband, has a ratio of V_b/V_u of 3.16 at midband, corresponding to 10 per cent of the power in the unbalanced mode. Over a 4.76:1 frequency range, the performance of this balun is at least as good as at midband.

Between the output conductors of the balun there is a plane of symmetry characterized by the fact that electric field lines of the balanced mode are perpendicular to it while electric field lines of the unbalanced mode are parallel to it. In critical balun applications the unbalanced mode may be suppressed by inserting a resistance card along this plane. As an example, if the unbalanced mode is completely suppressed, Balun IV still has a power transfer efficiency of 90 per cent or better over a 4.76:1 frequency range.

Baluns with Two Band-Pass Filters of Different Conductor Size

General: When these baluns are constructed using two dual coupled-strip-line band-pass filters having different cross-sectional dimensions, it is found that for a given ratio of balanced to unbalanced impedance they possess much wider bandwidths than if the filters have conductors of the same dimensions. This behavior holds true whether or not the band-pass filters are staggered. In order for the filters with unequal conductor sizes to be duals (*i.e.*, $Z_sZ_o=Z^2$ at all frequencies) it is only necessary that ${}^sZ_{oe}/{}^sZ_{oo}={}^oZ_{oe}/{}^oZ_{oo}$.[3]

Baluns with Two Unstaggered Band-Pass Filters of Different Conductor Size Having ${}^sZ_{oe}/{}^sZ_{oo}=5.828$:[4] The frequency variation of the input VSWR and the ratio of the output balanced to unbalanced voltage V_b/V_u of four baluns, each having two unstaggered band-pass filters of different conductor size and ${}^sZ_{oe}/{}^sZ_{oo}=5.828$, are shown in Fig. 6. Because the ${}^sZ_{oe}/{}^sZ_{oo}$ ratio for these baluns is the same as the Z_{oe}/Z_{oo} ratio of Balun I, the frequency variation of the normalized image impedances Z_s/Z and Z_o/Z is the same as that of Balun I. However, because the ${}^sZ_{oe}$ values for these baluns are smaller than Z_{oe} for Balun I, the Z_s/Z curves for these baluns are displaced downward from the Z_s/Z curve of Balun I, while the Z_o/Z curves are displaced upward. The frequency variation of the image phase shift for these filters is identical to that for Balun I and is shown in Fig. 4. Table II lists their pertinent electrical parameters.

Balun IIa is designed to have the same midband performance as Balun II; Balun IIIa to have the same midband performance as Balun III; and Balun IVa to have the same midband performance as Balun IV.

A comparison of the theoretical performance of Balun I of Fig. 5 to that of Baluns IIa and IIIa and IVa of Fig. 6 shows the improvement in balun bandwidth obtained by designing the two band-pass filters to have different conductor sizes while maintaining the ratio of even to odd characteristic impedance of the filters at 5.828. Here the bandwidth is defined as the frequency band over which the VSWR at the edges of the band equals that at the center. A comparison of the performance of Baluns II and IIa, III and IIIa, and IV and IVa shows that in each case the former balun has a slightly wider bandwidth. This increase in bandwidth, however, is achieved at the expense of using filters with higher ratios of even to odd characteristic impedance that are much harder to construct. Hence, it is believed that in most applications it is preferable to construct baluns containing filters with unequal conductor dimensions.

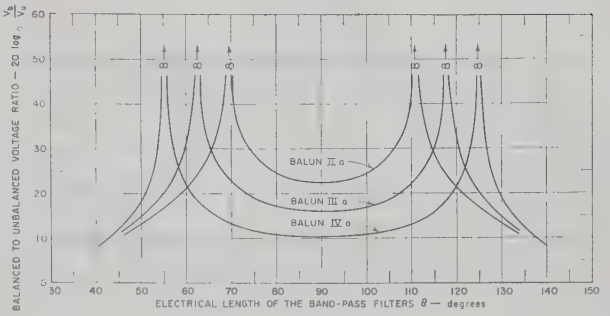

(a)

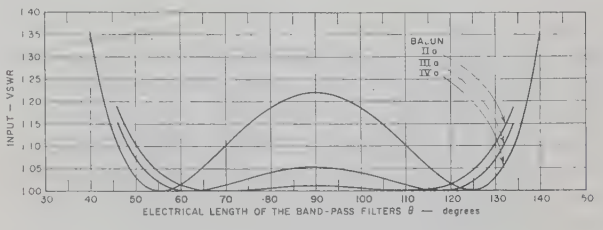

(b)

Fig. 6—Theoretical performance of Baluns IIa, IIIa, and IVa.

TABLE II

SUMMARY OF ELECTRICAL PARAMETERS OF THREE WIDE-BAND STRIP-LINE BALUNS EACH HAVING TWO UNSTAGGERED BAND-PASS FILTERS OF UNEQUAL CONDUCTOR SIZE

Parameter	Balun		
	IIa	IIIa	IVa
${}^sZ_{oe}/{}^sZ_{oo}={}^oZ_{oe}/{}^oZ_{oo}$	5.828	5.828	5.828
${}^sZ_{oe}/Z$	2.233	2.049	1.740
${}^sZ_{oo}/Z$	0.383	0.351	0.298
${}^oZ_{oe}/Z$	2.609	2.846	3.348
${}^oZ_{oo}/Z$	0.447	0.488	0.574
Z_s/Z (midband)	0.925	0.849	0.721
Z_o/Z (midband)	1.081	1.179	1.387
Design θ for perfect operation (degrees)	90 ± 21	90 ± 28	90 ± 35

Baluns With Two Unstaggered Band-Pass Filters Having ${}^sZ_{oe}/{}^sZ_{oo}=17.399$:[5] The bandwidth of extremely-wide-band baluns is approximately proportional to the logarithm of the ratio of ground-plane spacing to conductor cross-section dimensions in the band-pass filters. Hence the maximum practical bandwidth of extremely wide-band baluns which have very small center conductor dimensions is determined by mechanical con-

[3] Superscripts *s* and *o* denote band-pass filters with short and open-circuited parts, respectively.

[4] A directional coupler of the type described by Jones and Bolljahn, *op. cit.*, with $Z_{oe}/Z_{oo}=5.828$ would have a midband coupling of −3 db.

[5] A directional coupler of the type described by Jones and Bolljahn, *op. cit.*, with $Z_{oe}/Z_{oo}=17.399$ would have a midband coupling of −1 db.

TABLE III

SUMMARY OF ELECTRICAL PARAMETERS OF FOUR WIDE-BAND STRIP-LINE BALUNS EACH HAVING TWO UNSTAGGERED BAND-PASS FILTERS OF UNEQUAL CONDUCTOR SIZE

Parameter	Balun V	Balun VI	Balun VII	Balun VIII
$\frac{{}^{s}Z_{oe}}{{}^{o}Z_{oo}} = \frac{{}^{o}Z_{oe}}{{}^{o}Z_{oo}}$	17.399	17.399	17.399	17.399
${}^{s}Z_{oe}/Z$	8.117	7.944	7.413	5.911
${}^{s}Z_{oo}/Z$	0.466	0.456	0.426	0.339
${}^{o}Z_{oe}/Z$	2.143	2.189	2.346	2.943
${}^{o}Z_{oo}/Z$	0.123	0.125	0.135	0.169
Z_s/Z (midband)	0.990	0.968	0.904	0.721
Z_o/Z (midband)	1.010	1.032	1.106	1.387
Design θ for perfect operation (degrees)	90± 15.47	90± 25.96	90± 39.97	90± 53.73

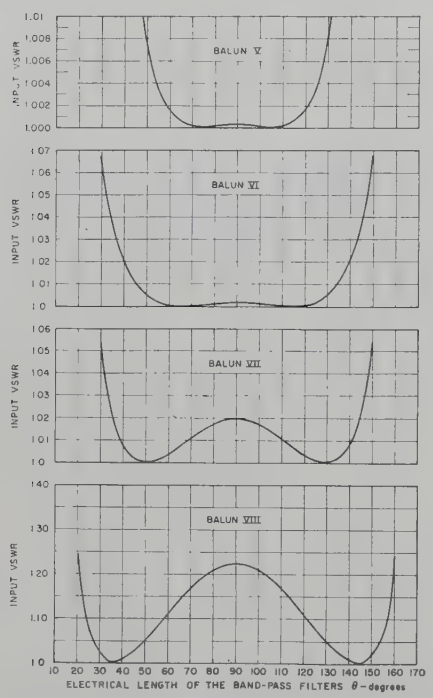

Fig. 7—Theoretical input VSWR of Baluns V, VI, VII, and VIII.

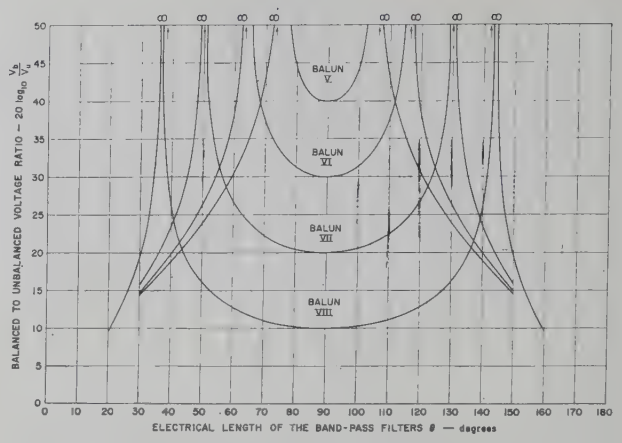

Fig. 8—Theoretical balanced to unbalanced voltage ratio, V_b/V_u, of Baluns V, VI, VII, and VIII.

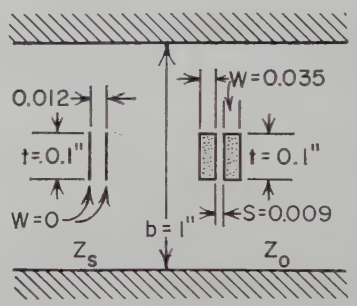

Fig. 9—Cross section of a coupled strip-line region of Balun VIII.

struction tolerances. Baluns V, VI, VII, and VIII have been selected for consideration here because their band-pass filters have conductors whose cross-section dimensions are about as small as can be constructed conveniently.

Table III summarizes the pertinent electrical parameters of these baluns. The frequency variation of the input VSWR of these baluns is shown in Fig. 7, and the ratio of the output balanced to unbalanced voltage, V_b/V_u, is shown in Fig. 8. Inspection of the curves in Figs. 7 and 8 shows that increasing the ratio of Z_o/Z_s at midband increases the midband VSWR, decreases the midband ratio of V_b/V_u, and increases the separation of the frequencies of perfect balun operation.

Fig. 7 shows that Baluns V, VI, VII, and VIII have maximum VSWR of 1.0002, 1.002, 1.020, and 1.220, respectively, over the corresponding bandwidth of 1.65, 2.34, 4.00, and 7.74:1. In Fig. 8, the curves of V_b/V_u indicate that for these baluns the corresponding minimum percentage power transfer efficiency over the operating frequency band is 99.99, 99.90, 99.00, and 90.00. Comparison between Baluns IV and VIII, where both baluns have a VSWR of 1.22 and a ratio V_b/V_u of 3.16 at midband, shows that the performance of Balun VIII is at least as good as at midband over 1.626 times the frequency range that can be obtained with Balun IV.

Fig. 9 illustrates the approximate cross-section dimensions of the coupled strips of the two band-pass filters of Balun VIII when the impedance Z is 100 ohms, and the cross section is air filled. If the cross section were filled with dielectric to support the conductors their dimensions would be even smaller. Nevertheless, it is believed that with care this balun could be constructed with either an air-filled or dielectric-filled cross section with sufficient precision that its measured performance would be close to the theoretical performance.

Baluns With Two Staggered Band-Pass Filters of Different Conductor Size:[6] This section describes the frequency variation of the input VSWR and output bal-

[6] The staggering technique can also be applied to baluns that have filters with equal cross-section dimensions.

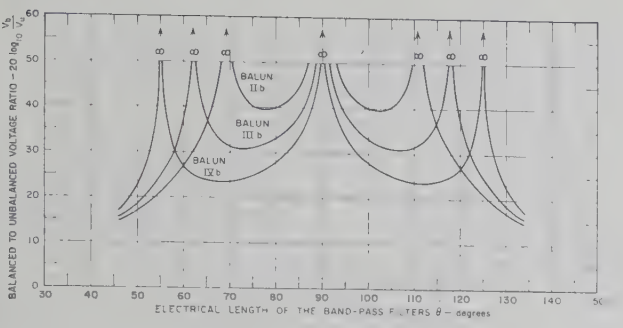

(a)

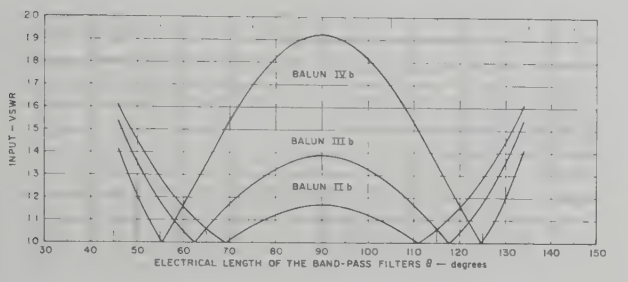

(b)

Fig. 10—Theoretical performance of Baluns IIb, IIIb, and IVb.

anced to unbalanced voltage ratio of three baluns having staggered band-pass filters. Each of these baluns utilizes two staggered coupled-strip-line band-pass filters having dual input impedances but different cross-sectional dimensions. The electrical parameters of Baluns IIb, IIIb, and IVb are the same as those of Baluns IIa, IIIa, and IVa with the single important difference that one of the band-pass filters in each of Baluns IIb, IIIb, and IVb is staggered with respect to the other by a distance l equal to one-quarter wavelength at midband.

The ratio of balanced to unbalanced output voltage of these baluns is plotted in Fig. 10(a), while the input VSWR is shown in Fig. 10(b). It is seen by comparing Fig. 10(a) to Fig. 6(b) that this quarter-wavelength staggering greatly increases the ratio of balanced to unbalanced voltage over the band, while a comparison between Fig. 10(b) and Fig. 6(b) shows that the staggering also increases the average input VSWR.

Experimental Model of Balun I

Construction

An experimental model of Balun I was constructed which had the electrical parameters given in Table I, and a center frequency of 3 kmc. Its dimensions are listed in Table IV. A photograph of this balun is shown in Fig. 11. For convenience in measuring the performance of this balun with standard measuring equipment (normally at a 50-ohm level), the output terminal impedance was transformed from 100 ohms to 50 ohms in five steps. This transformer was designed to have an "equal-ripple" VSWR response, with a maximum

TABLE IV
Dimensions of Experimental Model of Balun I

	Dimension (fractions of an inch)
Ground-plane spacing b	0.500
Thickness t of all strips	0.062
Width w' of strip having Z of 100 ohms	0.147
Width w_0 of strip having $Z/2$ of 50 ohms	0.555
Width w of strips in band-pass filters	0.033
Spacing s between strips in band-pass filters	0.0166
Length l of band-pass filters	0.984

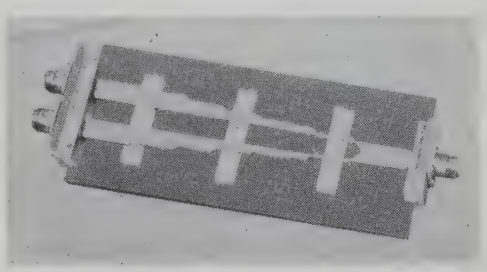

Fig. 11—Photograph showing the internal construction of experimental strip-line Balun I.

VSWR of 1.065 over the frequency band of 3.5:1.[7] The length of each transformer is 0.984 inch, while the width of the strips in the stepped transformer is 0.485, 0.372, 0.262, and 0.187 inch. In order to reduce discontinuity effects in the balun at places where there are sudden changes in strip cross section, tapers were provided at each transformer step and a V-shaped notch was placed at the power divider. In Fig. 11, the strips are shown supported with polyfoam blocks and with small polystyrene spacers inserted between the strips at four places to maintain the coupling spacing uniform.

Experimental Results

The balanced to unbalanced voltage ratio, V_b/V_u, of the balun was computed by means of (2), using the measured values of the magnitude and phase of V_3/V_2 at the output terminals.

The measured VSWR and V_b/V_u ratio compared with the theoretical values are plotted in Fig. 12. It is seen that the measured values deviate from the theoretical values; nevertheless, the experimental balun has good performance since the V_b/V_u ratio is greater than 11.4 db over a 3:1 frequency range. It is believed that the deviation between the theoretical and experimental values of V_b/V_u is caused by discontinuities and physical dissymmetries of the arms of the balun containing the band-pass filters. The relatively high VSWR of the input line is undoubtedly caused by a symmetrically located discontinuity at the power divider. Some idea of the magnitude of this latter discontinuity can be in-

[7] S. B. Cohn, "Optimum design of stepped transmission-line transformers," IRE Trans. on Microwave Theory and Techniques, vol. MTT-3, pp. 16–21; April, 1955.

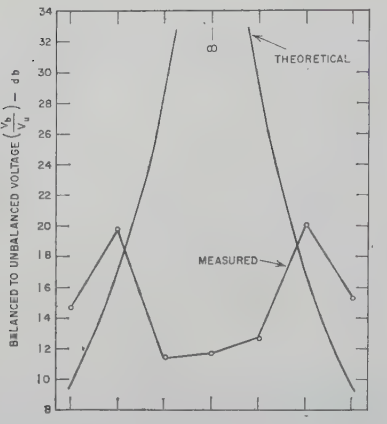

(a)

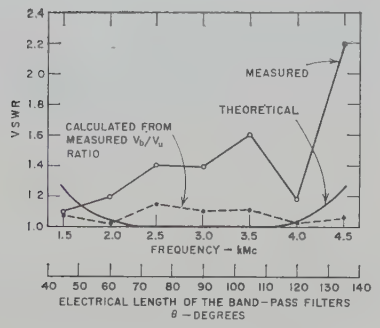

(b)

Fig. 12—Experimental performance of strip-line Balun I.

ferred by comparing the measured VSWR in Fig. 12 with the VSWR calculated from the measured V_b/V_u ratio by means of (5) and (6).

Conclusions

The theoretical analysis of these baluns has shown that they have good wide-band performance. The baluns using unstaggered band-pass filters have a very low VSWR over their operating frequency range; in comparison, the baluns using staggered band-pass filters have a higher input VSWR, but a better balance of the output voltage over the same bandwidth. However, in either type of balun the balanced to unbalanced voltage ratio may be greatly increased by inserting a suitably oriented resistance card between the strips connecting to the output ports.

The measured performance of the experimental balun is good over a 3:1 frequency range, although the experimental performance agrees only approximately with theory, because of discontinuity effects. It is believed that, by reducing junction discontinuities, the balun performance can be made to conform closely to the theoretical results.

Acknowledgment

The authors wish to acknowledge the suggestions and help of Dr. S. B. Cohn.

Periodic Structures in Trough Waveguide*

A. A. OLINER† and W. ROTMAN‡

Summary—The center fin in trough waveguide can be modified in a periodic fashion to alter the propagation characteristics of the guide. Two such periodic modifications, one an array of circular holes and the second a periodic array of teeth, have been measured fairly extensively and analyzed theoretically. These configurations are useful in connection with antenna scanning or waveguide filter applications.

The array of holes produces only a mild slowing of the propagating wave, but the toothed structure, which may alternatively be described as a series of flat strips extending beyond the edge of the fin, can cause the propagating wave to vary from a very slow to a very fast wave. The periodic structures are theoretically treated by two methods, a transverse resonance procedure and a periodic cell approach. These theoretical results agree very well with each other and with the measured data.

* Manuscript received by the PGMTT, July 14, 1958; revised manuscript received, September 12, 1958. Part of this study was supported by the Air Force Cambridge Research Center under Contract No. AF 19(604)-2031.

† Microwave Res. Inst., Polytechnic Inst. of Brooklyn, Brooklyn, N. Y.

‡ Air Force Cambridge Res. Ctr., Bedford, Mass.

I. Introduction

TROUGH waveguide is a relatively new waveguide type possessing a number of interesting properties. The geometry of the guide is shown in Fig. 1. It is derived from symmetrical strip transmission line by placing a short circuit at the midplane of the latter;[1] for this reason, the dominant mode in trough waveguide is identical with the first higher mode in the strip transmission line. The electric field distribution is indicated in Fig. 1 as being oppositely directed in the top and bottom portions; hence, if the plate spacing in the region beyond the edge of the center fin is less than a half wavelength, the field is of the below cutoff type in this outer region when viewed in the transverse direction. Thus, by virtue of symmetry, one of the guide walls is reactive and the structure is non-radiating.

[1] Airborne Instruments Lab., advertisement on trough waveguide, Proc. IRE, vol. 44, p. 2A; August, 1956.

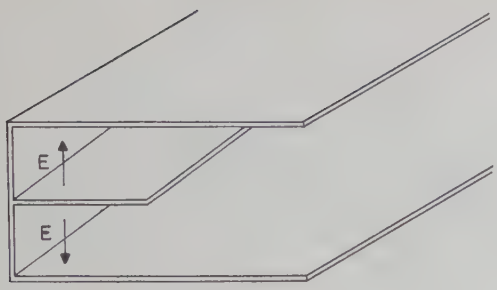

Fig. 1—The trough waveguide.

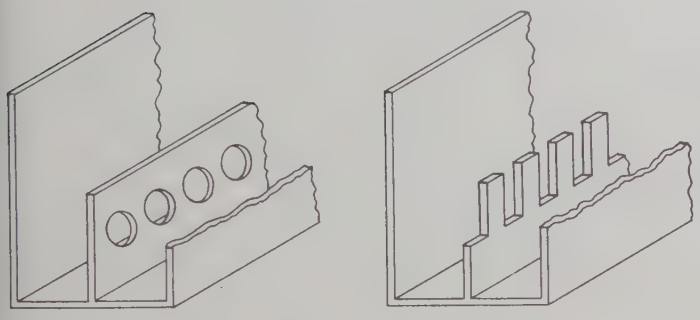

Fig. 2—Two types of periodic structures in trough waveguide. (a) Array of holes. (b) Array of teeth.

The dominant mode in trough waveguide is an H, or TE, mode, with a transverse wavenumber which is independent of frequency. Expressions for the transverse wavenumber, or alternatively the cutoff wavelength, as a function of guide geometry are available both for center fins of zero thickness and for fins of finite thickness.[2]

Trough waveguide possesses three properties of particular interest. First, it can be coupled very smoothly to coaxial line; second, the dominant mode possesses a nominal bandwidth of approximately 3:1, in contrast to the approximately 2:1 value for normal rectangular waveguide; and third, it is an open structure, so that any asymmetry produces radiation. Those features concerned with the large bandwidth and excellent match to coaxial line are useful for a variety of component applications. The open nature of the line lends itself to the design of novel types of line source antennas.[2,3]

Since the variation with frequency of the trough waveguide propagation characteristics is similar to that of an ordinary waveguide, a considerable measure of added versatility is obtained by periodically loading the waveguide. By properly choosing the loading, the wave, which is ordinarily a fast wave, can be made into a slow wave or into an even faster wave, pass and stop bands can be obtained, or rapid variations of propagation constant with frequency can be produced. While periodic loading can produce these effects in many types of waveguiding structures, this loading in trough waveguide can be achieved readily by modifications in the center fin only. In fact, these modifications may be produced, if desired, by photo-etching or stamping techniques. For example, periodic structures in trough waveguide have been employed in antenna rapid scan applications by the Air Force Cambridge Research Center, and in filter applications by the Airborne Instruments Laboratory.

A study of two types of periodic structures in trough waveguide is described in this paper. These two types, which are shown in Fig. 2, are an array of circular holes in the center fin, and a series of flat strips extending beyond the edge of the center fin. For convenience, the second structure will be referred to as an array of teeth. Both types of structures were examined experimentally and analyzed theoretically.

An array of circular holes never produces a heavy loading, and its effect on the trough waveguide is to cause a mild slowing of the wave. The propagation characteristics of the toothed array, on the other hand, are significantly different from those of the unloaded trough waveguide. By proper choice of dimensions, the width and location in frequency of the pass bands may be selected as desired, and the wave may be made fast or slow.

The trough waveguide periodic structures were analyzed theoretically by two methods: a periodic cell approach, and a transverse resonance procedure. In the case of the array of holes, the results of both methods agreed very well with each other and with the measured values. In the case of the array of teeth, the periodic cell approach yields accurate values only when the teeth are far apart, because of the strong mutual coupling between neighboring teeth. For this reason, only the transverse resonance analysis of the array of teeth is included in this paper.[4] This analysis agrees very well with the measured data over a wide range of parameter values.

The theoretical expressions for the propagation characteristics of these periodic arrays are not only accurate but are also in simple and practical form. Numerical values can be readily obtained from them.

In the transverse resonance analysis of the array of teeth, it was necessary, as an intermediate step, to derive an expression for the characteristic impedance of multistrip transmission line. The geometry of this line is indicated in Fig. 11(a) of the appendix, where a simple approximate expression for the characteristic impedance is derived. This simple expression is compared there with a cumbersome rigorous conformal mapping result; the approximate form shows remarkable accuracy over a wide range of dimensions. This intermediate result may also be of value in itself.

[2] W. Rotman and A. A. Oliner, "Asymmetrical Trough Waveguide Antennas," IRE Trans. on Antennas and Propagation, to be published.

[3] W. Rotman and N. Karas, "Some new microwave antenna designs based on the trough waveguide," IRE Convention Rec., part I, pp. 230–235; 1956.

[4] The periodic cell analysis for the toothed array is included in a forthcoming Air Force Cambridge Res. Ctr. Rep. by W. Rotman and N. Karas, "Trough Waveguide Radiators with Periodic Posts."

II. Array of Circular Holes

A. *Periodic Cell Analysis*

The first of the two methods employed for determining the propagation characteristics of trough waveguide loaded by an array of round holes in the center fin is the periodic cell approach. This approach is most suitable for geometries in which the holes are not too closely spaced to each other. However, since the mutual coupling between circular holes is known to be quite small, results obtained with the periodic cell approach should be valid even when the holes are fairly close to each other.

The geometry of the array of holes is indicated in Fig. 3, together with the notation to be employed. As seen, the array need not be centered in the fin.

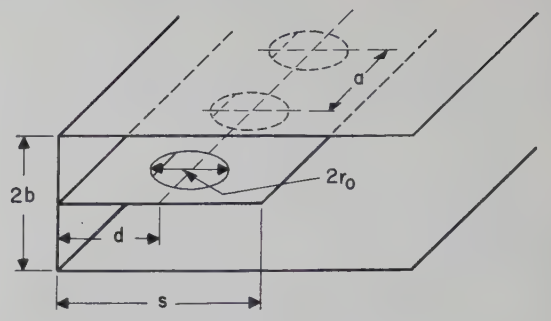

Fig. 3—Geometry of array of circular holes in center fin of trough waveguide.

A view of the center fin alone is shown in Fig. 4(a). The periodic cell approach first requires the choice of a unit cell, which is shown in Fig. 4(a) to lie between reference planes T_1 and T_2. The second step, that of deducing an equivalent network for the unit cell, is indicated in Fig. 4(b). This network is seen to consist of two lengths of unloaded trough waveguide, each equal to one-half the length of the unit cell, and coupled together at the midplane of the unit cell by an equivalent circuit for the circular hole by itself. The third step in the procedure is indicated by Fig. 4(c); it consists of obtaining a smooth transmission line equivalent to the original periodically loaded line. This equivalence is valid only at the accessible reference planes T_1 and T_2, of course. The unloaded trough waveguide and the equivalent smooth line are characterized, respectively, by propagation wavenumbers $\kappa_0 (= 2\pi/\lambda_{go})$ and $\hat{\kappa}$, and characteristic admittances Y_o and $\hat{Y}$. The quantity of final interest is the equivalent macroscopic guide wavelength λ_g of the periodically loaded trough waveguide, and this quantity is, of course, related to $\hat{\kappa}$ by

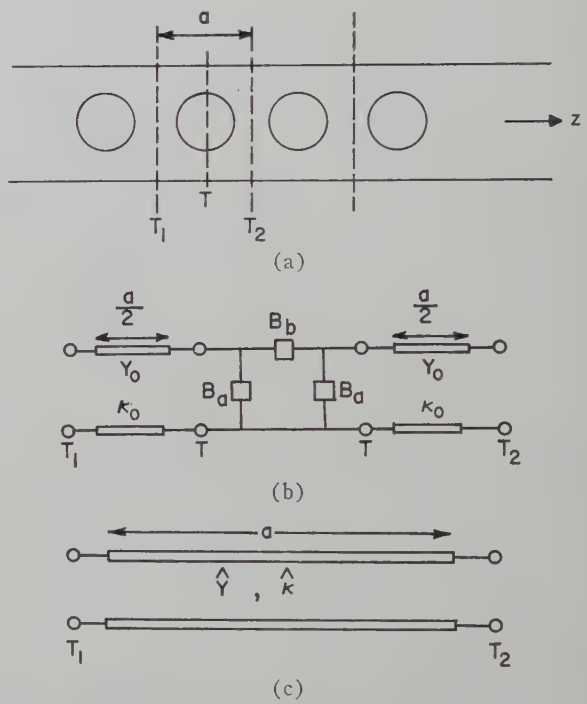

Fig. 4—Development of periodic cell analysis for array of holes. (a) View of center fin. (b) Equivalent network of unit cell. (c) Equivalent smooth transmission line.

$$\lambda_g = 2\pi/\hat{\kappa}. \tag{1}$$

One method of obtaining equivalence at reference planes T_1 and T_2 between the composite equivalent network of Fig. 4(b) and the equivalent smooth transmission line of Fig. 4(c) is by the use of bisection theorems, taking advantage of the symmetry of the networks. Each of the two networks is bisected and short circuit and open circuit terminations are placed successively at the midplanes. The corresponding input admittances to each network are then equated; the following relation is obtained as a result:

$$\cos \hat{\kappa} a = \left[\frac{B_a' + B_b'}{B_b'}\right] \cos \kappa_0 a + \frac{1}{2B_b'}\left[1 - B_a'(B_a' + 2B_b')\right] \sin \kappa_0 a, \tag{2}$$

where B_a' and B_b' are the pi network parameters at centerline reference plane T of a single round hole in trough waveguide, normalized to the characteristic admittance Y_o of the unloaded guide. From (2) and (1) one readily calculates the guide wavelength λ_g of ultimate interest.

Before numerical results can be computed, however, expressions are needed for B_a' and B_b'. Such expressions were derived from general small aperture relations for a symmetrical longitudinal aperture,[5] the latter being obtained by a generalization of well-known results for transverse apertures. The resulting expressions are

$$B_b' = -\frac{3b\lambda_{go}}{k_{co}(4r_o)^3 \sin^2 k_{co}d} \tag{3}$$

$$B_a' = \frac{\lambda_{go}(2k_{co}r_o)^3 \cos^2 k_{co}d}{3\pi^2 b} \cdot \left[1 - \frac{1}{2}\left(\frac{k}{k_{co}}\right)^2 \tan^2 k_{co}d\right], \tag{4}$$

[5] A. A. Oliner, "Equivalent Circuit for Round Hole in Trough Waveguide," Memorandum No. 38, R-645-58, PIB-573, Microwave Res. Inst., Polytechnic Institute of Brooklyn, Brooklyn, N. Y.; February, 1958.

where most of the symbols are indicated in Fig. 3. Lengths r_o, d, and $2b$ are seen to be the hole radius, the distance from the center of the hole to the side wall of the guide, and the spacing between the top and bottom plates, respectively. Quantity k $(=2\pi/\lambda)$ is the free space wavenumber, λ_{go} is the guide wavelength of the unloaded trough waveguide, and k_{co} $(=2\pi/\lambda_{co})$ is the cutoff wavenumber of the unloaded guide, and is related to κ_o in (2) by

$$\kappa_0 = \sqrt{k^2 - k_{co}^2}. \tag{5}$$

The cutoff wavelength λ_{co} for a zero-thickness center fin may be obtained either from a curve[2] or from the following transcendental relation:

$$\frac{\lambda_{co}}{4b} = \frac{s}{b} + \frac{2}{\pi}\ln 2 + \frac{\lambda_{co}}{2\pi b} S_1\left(\frac{4b}{\lambda_{co}}\right) - \frac{\lambda_{co}}{\pi b} S_1\left(\frac{2b}{\lambda_{co}}\right), \tag{6}$$

where S_1 is the rapidly convergent arcsine sum

$$S_1(x) = \sum_{n=1}^{\infty}\left(\sin^{-1}\frac{x}{n} - \frac{x}{n}\right). \tag{7}$$

The contributions from the arcsine sums are relatively small, although they are not negligible. For the range $s/b > 1$, the arcsine sums contribute less than 3 per cent to the value of λ_{co}/b.

With the knowledge of λ_{co}, κ_o can be found readily from (5), and B_b' and B_a' from (3) and (4). The substitution of these quantities into (2) then permits the determination, via (1), of the guide wavelength λ_g of the periodically loaded structure.

B. *Transverse Resonance Procedure*

The second method used for analyzing the array of holes is the transverse resonance procedure. The limitation in the applicability of the transverse resonance procedure is that the holes must not come too near to the edge of the fin or to the wall contacting the other side of the fin.

The transverse transmission direction, along which the resonance is performed, is taken in the guide cross section along the plane of the center fin. This direction is indicated in Fig. 5(a) as the x direction. As a simplification in the form of the transverse equivalent network, the fringing field at the edge of the fin is replaced in a rigorous manner by an extension l of the center fin and by a magnetic wall termination. The resulting transverse equivalent network, which parallels the structure of Fig. 5(a), is shown in Fig. 5(b). The lengths of line in Fig. 5(b) are characterized by the transverse wavenumber k_t and characteristic admittance Y_t, while the pi equivalent circuit parameters B_a and B_b represent the influence of the array of holes on the transversely propagating wave. This transversely propagating wave consists of two TEM waves, one in the upper and one in the lower parallel plate region, with oppositely directed electric fields and incident at an arbitrary "angle" on

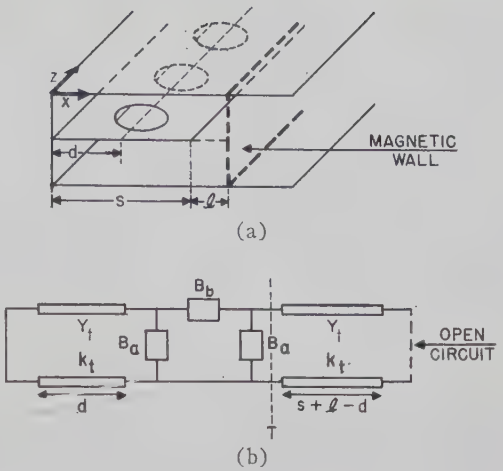

Fig. 5—Transverse resonance analysis of array of holes. (a) Array of holes. (b) Transverse equivalent network.

the array of holes. This angle is a means by which k_t is specified (it is given by $k_t = k\cos\theta$, if θ is the angle of incidence). The equivalent circuit that represents such a wave incident on the array of circular holes has been determined by means of small aperture relations to be:

$$B_b' = -\frac{1}{k_t}\left(\frac{3ab}{8r_o^3}\right) \tag{8}$$

$$B_a' = \left(\frac{2r_o^3}{3ab}\right)\left(\frac{k^2}{k_t} - 2k_t\right), \tag{9}$$

where the parameters are normalized to the characteristic admittance Y_t. The geometrical quantities r_o, a and b are indicated in Fig. 3, and $k(=2\pi/\lambda)$ is the free space wavenumber.

The transverse resonance relation is obtained by equating to zero the sum of the input admittances seen looking in both directions away from some reference plane, chosen as T for convenience, in the equivalent network of Fig. 5(b). One finds as a result the transcendental equation

$$\tan k_t(s - d + l) + B_a' + B_b'\left[\frac{B_a' - \cot k_t d}{B_b' + B_a' - \cot k_t d}\right] = 0, \tag{10}$$

where

$$l = \frac{2b}{\pi}\ln 2 + \frac{1}{k_t} S_1\left(\frac{2k_t b}{\pi}\right) - \frac{2}{k_t} S_1\left(\frac{k_t b}{\pi}\right), \tag{11}$$

and S_1 has been defined in (7). When one substitutes for B_b' and B_a' from (8) and (9), expression (10) becomes rather involved. Since the influence of the array of holes is small, however, it is appropriate to employ a perturbation procedure, by perturbing about the solution for the unloaded guide. The transverse wavenumber k_{co} for the unloaded guide depends only on the guide geometry, as seen from relation (6); for the loaded guide,

the transverse wavenumber k_t is seen to depend on wavelength also, in view of the dependence of B_a' on k in (9).

For the perturbation procedure, one writes

$$k_t = k_{co} + \Delta k_t, \tag{12}$$

and approximates l by l_o, which can be done with negligible error. In addition, use is made of the resonance relation for the unloaded trough waveguide, which may be written as

$$s + l_0 = \frac{\pi}{2k_{co}} \tag{13}$$

for the lowest mode. Relations (12), (8) and (9) are then substituted into (10), and (13) is employed to simplify the resulting form. After some algebra, one finds

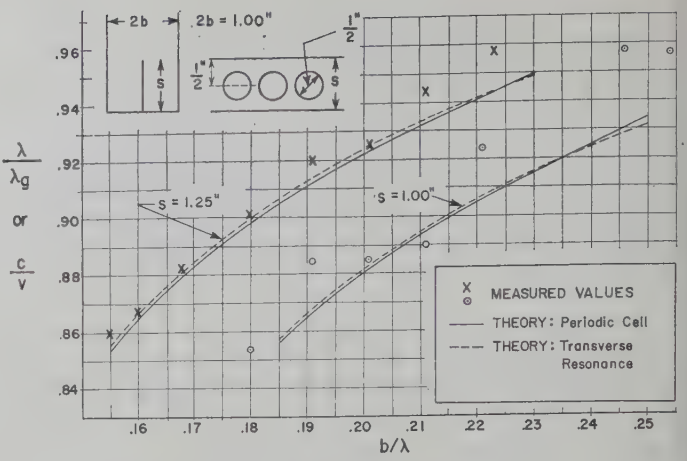

Fig. 6—Propagation characteristics of trough waveguide with an array of circular holes in the center fin.

$$\frac{\Delta k_t}{k} = \frac{1 - \frac{1}{2}\left(\frac{k}{k_{co}}\right)^2 - \cot^2 k_{co}d}{\frac{\pi k}{2k_{co}^2}\csc^2 k_{co}d\left[\frac{3ab}{8r_0^3} - \frac{2r_0^3}{3ab}(k^2 - 2k_{co}^2)\right] - \left(\frac{k}{k_{co}}\right)^3 + \cot k_{co}d \csc^2 k_{co}d\left(\frac{\pi k}{2k_{co}} - 2kd\right)}. \tag{14}$$

In order to relate Δk_t to the guide wavelength λ_g of the periodically loaded guide, one first recognizes that

$$\frac{\lambda}{\lambda_g} = \sqrt{1 - \left(\frac{k_t}{k}\right)^2}. \tag{15}$$

Relation (12) is then substituted into (15); after simplification one finds

$$\frac{\lambda}{\lambda_g} = \frac{\lambda}{\lambda_{go}} - \frac{\lambda_{go}}{\lambda_{co}}\frac{\Delta k_t}{k}, \tag{16}$$

where $\Delta k_t/k$ is given by (14), λ_{co} by (6), and λ_{go} $(=2\pi/\kappa_o)$ by (5).

C. *Comparison with Measurement*

Measurements were taken of the guide wavelengths as a function of frequency for two different trough waveguides, each loaded with a periodic array of circular holes. These measurements are compared in Fig. 6 with theoretical values obtained from both the periodic cell and transverse resonance approaches discussed in Sections A and B. The measured values are indicated as individual points; a certain scatter appears in the data but it should be noted that the ordinate scale is greatly expanded. It is also seen that the theoretical values obtained from the two different approaches agree extremely well with each other. The agreement with the measured values is also good. The close agreement found between the two sets of theoretical values occurs because the measured structures still lie within the approximations inherent in both theoretical approaches; the range of applicable dimensions is increased because circular holes do not couple strongly to their environment.

It is recognized that

$$\frac{\lambda}{\lambda_g} = \frac{c}{v}, \tag{17}$$

where v is the phase velocity of the wave in the loaded guide while c is the velocity in free space. The curves were plotted in the form λ/λ_g to indicate that in this range the waves are still fast waves.

III. Array of Teeth

As indicated in the introduction, only the transverse resonance analysis will be presented for this structure because of the strong mutual coupling between neighboring teeth.

A. *Transverse Resonance Analysis*

The geometry of the array of teeth located on the center fin of trough waveguide is shown in Fig. 7(a). The transverse transmission direction, along which the transverse resonance is performed, is again in the direction shown as x in Fig. 7(a), as in the case of the array of holes. The form of the transverse equivalent network is not as straightforward in this case, however. The form shown in Fig. 7(b) is an approximate one, but one which is capable of high accuracy, nevertheless.

The transversely propagating wave is different in character in the two regions, one of width s and the other of width h. In the former region, the wave is similar to that for the case of the array of holes; it consists of two component TEM waves, one in the upper and one in the lower parallel plate region, with oppositely directed electric fields and traveling together at an

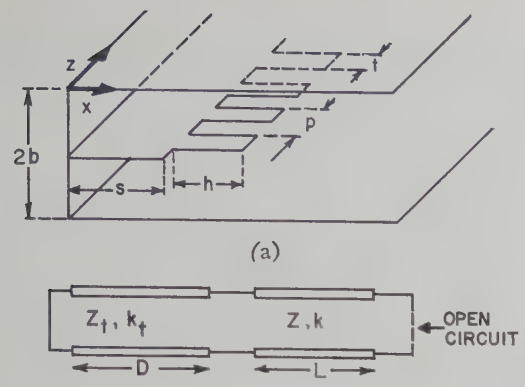

(a)

$D = s + \delta_1$

$L = h - \delta_1 + \delta_2$

(b)

Fig. 7—Transverse resonance analysis of array of teeth. (a) Array of teeth. (b) Transverse equivalent network.

arbitrary angle with respect to the x direction. This angle is alternatively represented by the fact that the wavenumber k_t is different from k. The second region, whose cross-section is shown in Fig. 11(a) of the appendix, can be designated as a multistrip transmission line region. In this region, the transversely propagating wave is constrained to travel in the x direction, so that the wavenumber becomes equal to k. The resonance of the transverse equivalent network yields the resultant value of k_t.

The approximation in the network of Fig. 7(b) occurs in the representation of the junction between the line characterized by Z_t and k_t and that by Z and k. This junction is very difficult to analyze theoretically, and one rigorous representation for it specifies the locations of the input and output reference planes and includes an ideal transformer between them. The approximation employed here sets the transformer turns ratio equal to unity and places the input and output reference planes at the same location; these planes are not located at the physical junction plane, as would occur if the junction effect were negligible, but rather are both shifted a distance δ_1 into the multistrip region. This choice of approximation was motivated by the fact that this form is actually rigorously correct for a certain junction which is a simplification of the structure obtained by taking the Babinet dual of the actual junction. The ultimate justification for the approximation lies in the ability of the network to agree with the measured data; as will be seen below, this postulated simple form is quite accurate.

As indicated by the network of Fig. 7(b), compensation for the fringing field at the edge of the multistrip region is made by extending the strips a distance δ_2 and terminating them by a magnetic wall. The same type of compensation for the fringing field was performed for the edge of the fin in the case of the array of holes. However, since the structures are different the amounts of shift are different, and for the multistrip line the value is not known.

The resonance relation is obtained readily from the network of Fig. 7(b) by choosing a convenient reference plane and equating to zero the sum of the input impedances seen looking in both directions away from the reference plane. One finds for the resonance relation

$$\tan k_t D = \frac{Z}{Z_t} \cot kL, \tag{18}$$

where the symbols are defined in Fig. 7(b). The ratio of characteristic impedances occurring in (18) is evaluated in the appendix; substitution of this result into (18) yields

$$\tan k_t D = \frac{k_t}{k}\left[1 + \frac{p}{\pi b} \ln \csc \frac{\pi t}{2p}\right] \cot kL, \tag{19}$$

where the new symbols are defined in Fig. 7(a). Eq. (19) is seen to be a simple transcendental equation for k_t. When the resultant wave propagating along the loaded trough waveguide is a fast wave, k_t is real. When this wave is a slow wave, however, k_t is imaginary and (19) takes the form

$$\tanh |k_t| D = \frac{|k_t|}{k}\left[1 + \frac{p}{\pi b} \ln \csc \frac{\pi t}{2p}\right] \cot kL. \tag{20}$$

The guide wavelength λ_g of the resulting wave propagating along the loaded trough waveguide (in the z direction) is then obtained from (15).

Before numerical values can be obtained from (19) or (20), the values of δ_1 and δ_2 occurring in D and L must be specified. Since the theoretical determination of these quantities seems a formidable task, an empirical procedure was used for their evaluation. It is first recognized that for a very slow wave the propagation characteristics are essentially independent of the value of D, as seen from (20). Hence, by comparing the theoretical and experimental values of λ/λ_g for a very slow wave situation, the value of $\delta_2 - \delta_1$ can be determined. Once this is known, δ_1 is found by proceeding similarly for a wave which is very fast, using (19) rather than (20). The actual experimental points to which comparison was made are the two extreme points on the $s/b = 1.25$ curve of Fig. 8. The values of δ_1 and δ_2 obtained from these two points are $\delta_1 = .26$, $\delta_2 = .22$. All of the theoretical curves of Figs. 8, 9, and 10 were computed using these two values.

B. *Comparison with Measurement*

Measurements of the propagation characteristics of trough waveguide loaded by an array of teeth attached to the center fin were made over a rather wide range of dimensional values and frequencies. The results of these measurements are plotted as individual points on Figs.

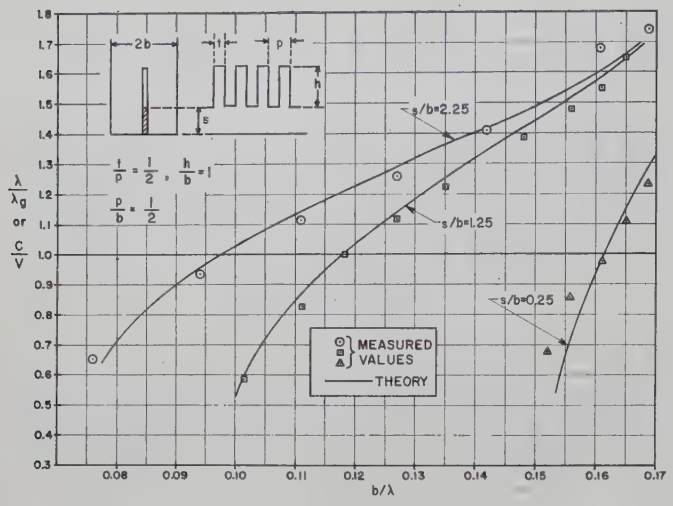

Fig. 8—Effect of center fin width on guide wavelength of periodically toothed trough waveguide.

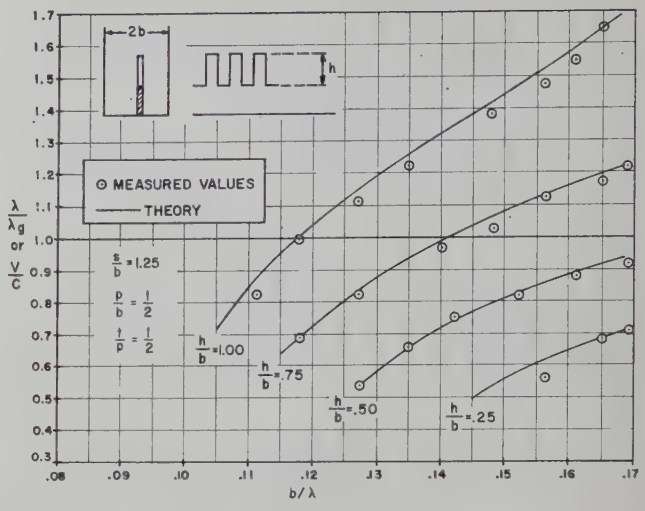

Fig. 9—Effect of tooth height on guide wavelength of periodically toothed trough waveguide.

8, 9, and 10. Although the abscissa scale is labeled b/λ, b was maintained constant throughout the series of measurements.

The corresponding theoretical values appear on these figures as solid lines. These values are computed from (19) or (20) together with (15), and in all cases the values of δ_1 and δ_2 discussed above were employed. Very good agreement can be noted between the measured and theoretical values for all cases. This order of agreement over such a wide range of parameter values testifies to the correctness of the postulated simple form for the transverse equivalent network of Fig. 7(b). It should also be noted that this simple form permits a rapid calculation of the propagation characteristics.

Since the λ/λ_g or c/v values in Figs. 8, 9, and 10 range both above and below unity, the wave can be either slow or fast. Furthermore, as seen in Fig. 8, the slope of the curve can be varied considerably, yielding a narrow pass band, if desired. The versatility exhibited in Fig. 8 is obtained by changing only the width s of the supporting fin; a smaller center fin yields a narrower pass band. From Fig. 9, one notes that large variations in performance follow from changes in the lengths h of the teeth. In Fig. 10 it is seen that changes in the periodicity of the teeth tend to lift the whole curve up or down. The lowest curve of Fig. 10 corresponds to the case for which the teeth are absent; the effect of the teeth is seen to be quite significant.

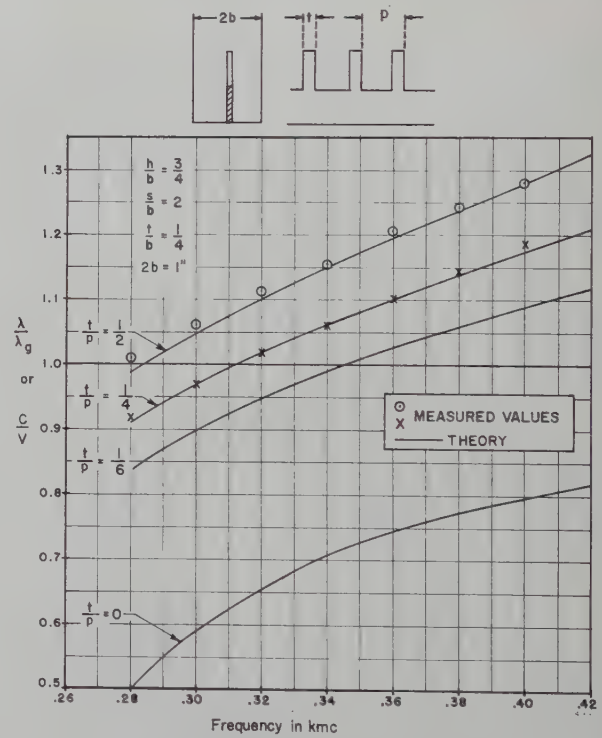

Fig. 10—Effect of tooth spacing on guide wavelength of periodically toothed trough waveguide.

Appendix

Characteristic Impedance of Multistrip Transmission Line

The toothed region of the trough waveguide loaded by the periodic array of teeth when viewed in the transverse direction has been designated as a multistrip transmission line. In the derivation of the transverse resonance relation for this structure it is necessary to have available a simple analytical expression for the characteristic impedance of this multistrip line. A rigorous conformal mapping result can be obtained but it is too cumbersome for use in the transverse resonance relation. However, a simple but highly accurate expression is derived in the manner described below.

A cross section of the multistrip line is shown in Fig. 11(a), together with typical electric field lines and a unit cell to indicate the periodic nature of the structure. In Fig. 11(b), this unit cell is shown bisected, enlarged, and placed on its side. From symmetry, the unit cell is bounded by magnetic walls as shown; the distribution of magnetic field lines in the cell is also indicated in the figure. The bisected unit cell can be represented by the equivalent network in Fig. 11(c), in which the distortion

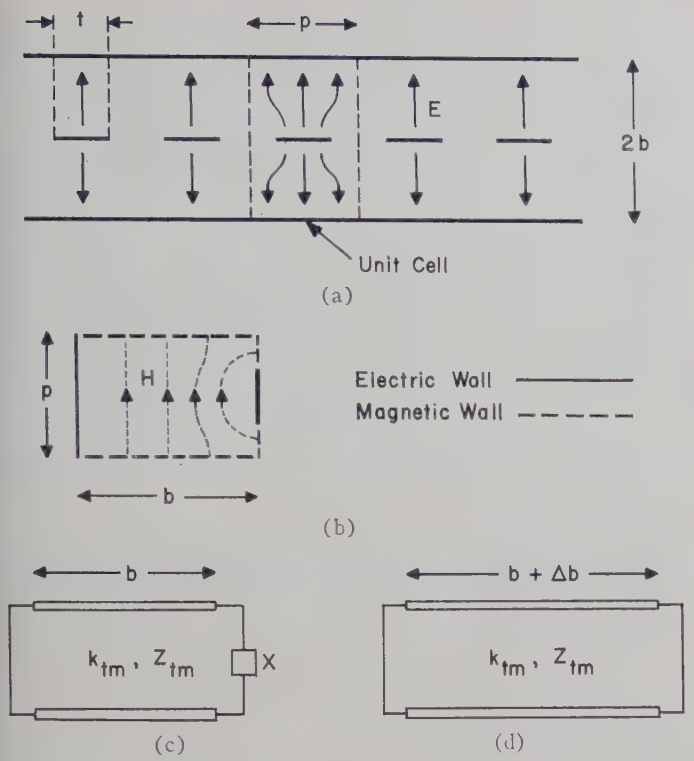

Fig. 11—Development of network representation for unit cell of multistrip transmission line. (a) Cross section, showing unit cell and electric field lines. (b) Bisected unit cell placed on its side, showing magnetic field lines. (c) Equivalent network representing bisected unit cell. (d) Simplified equivalent network with modified length of line.

of the field lines is accounted for by the reactance X. Since the reactance is equivalent to a short-circuited length of line, this equivalent network can be replaced by the simplified one of Fig. 11(d), which involves a modification in the line length. The additional length Δb of line is then related to the normalized reactance X' by

$$\tan k_{tm}\Delta b = X', \tag{21}$$

where k_{tm} represents the transverse wavenumber of the multistrip line.

The reactance X' can be evaluated by employing a Babinet equivalence. The original structure, taken from the unit cell, is shown in Fig. 12(a), while its Babinet dual structure is given in Fig. 12(b). It is noted that in the duality process the magnetic and electric walls are interchanged, and the magnetic field lines of the original structure become the electric field lines of the dual structure. The dual structure is readily seen to be a bisected capacitive slit whose normalized susceptance B' is given by[6]

$$B' = \frac{k_{tm}p}{\pi} \ln \csc \frac{\pi t}{2p}, \tag{22}$$

since the guide wavelength of the wave "incident" on the slit is $\lambda_{tm}(=2\pi/k_{tm})$. But, by the Babinet equivalence,

[6] N. Marcuvitz, "Waveguide Handbook," Rad. Lab. Ser., vol. 10, McGraw-Hill Book Company, Inc., New York, N. Y., p. 218, eq. 2(a); 1951. Only the static contribution of 2(a) is used.

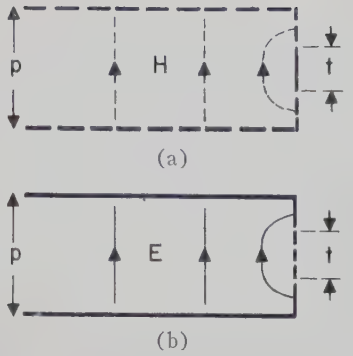

Fig. 12—Reactance structure and its Babinet dual. (a) Reactance structure. (b) Babinet dual structure.

the normalized reactance X' of the original structure is equal to B' of (22). Furthermore, since k_{tm} is the transverse wavenumber of a TEM mode (along the multistrip line), $k_{tm}=0$. Thus, in relation (21), the tan can be replaced by its argument, the k_t values cancel when (22) is employed for X', and one obtains

$$\Delta b = \frac{p}{\pi} \ln \csc \frac{\pi t}{2p}. \tag{23}$$

The characteristic impedance of the bisected unit cell represented by the network of Fig. 11(d) is

$$Z_b = 120\pi \frac{b + \Delta b}{p}. \tag{24}$$

From Fig. 11(a) it is seen that the unbisected unit cell consists of two bisected cells in parallel, so that the characteristic impedance Z of the complete unit cell is

$$Z = 30\pi \left[\frac{2b}{p} + \frac{2}{\pi} \ln \csc \frac{\pi t}{2p} \right], \tag{25}$$

after substitution is made for Δb from (23).

The application to the transverse resonance relation (18) requires not Z alone, but its ratio to Z_t, the characteristic impedance of the structure obtained when the array of center strips of Fig. 11(a) is replaced by a continuous conducting sheet, but for a wave traveling in the direction of the strips with wavenumber k_t rather than k. The value of Z_t, normalized to the same unit cell, is given by

$$Z_t = 30\pi \frac{2b}{p} \frac{k}{k_t}, \tag{26}$$

since the propagating mode is an H mode. From (25) and (26) one obtains finally

$$\frac{Z}{Z_t} = \frac{k_t}{k} \left[1 + \frac{p}{\pi b} \ln \csc \frac{\pi t}{2p} \right]. \tag{27}$$

Relation (27) was the form employed for Z/Z_t in the step from (18) to (19).

The variation of the bracketed quantity in (27) with $2b/p$ is shown in Fig. 13, with t/p as a parameter. For

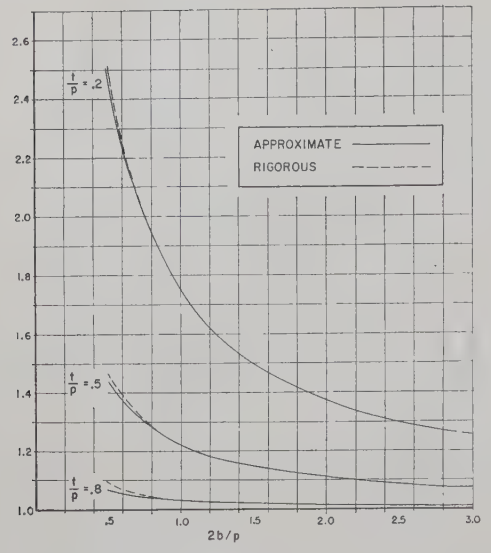

Fig. 13—Theoretical values for the characteristic impedance of multistrip line.

wide strips this quantity is nearly unity. Also included in Fig. 13 is the corresponding result obtained from a rigorous conformal mapping.[7] The rigorous result is too cumbersome in form to be useful in the transverse resonance procedure, but one sees from the comparison in Fig. 13 that the approximate result (27) is extremely accurate over a wide range of parameter values. It is also interesting that in the range in which the two results begin to disagree, the accuracy of the tables required for the rigorous result becomes poor, so that asymptotic expressions must be employed for the functions involved and the rigorous result becomes more difficult to compute from. However, in this range the geometric proportions of the multistrip line are such that other approximations become suitable.

[7] C. A. Hachemeister, "The Impedance and Fields of Some TEM Mode Transmission Lines," Rep. R-623–57, PIB-551, Microwave Res. Inst., Polytechnic Institute of Brooklyn, N. Y.; April 16, 1958.

A Study of a Serrated Ridge Waveguide*

H. S. KIRSCHBAUM† AND R. TSU‡

Summary—**The serrated, or periodically slotted ridge produces a periodic loading which retards the phase velocity of the wave in a waveguide. Such structures may be used to provide a variable index of refraction for microwave lenses and as elements in microwave filters. Two approaches are presented in this paper giving the frequency dependence of the index of refraction. One is based on equivalent circuit representations which are qualitatively valid for the effect of the loading. Circuit parameters which determine the shape of the index of refraction curve are calculated from the experimental data. The other approach providing a purely analytic expression of the index of refraction is derived by a field matching method. Calculations show good agreement with test data.**

Introduction

A SERRATED ridge waveguide is a ridge waveguide with slots cut periodically in the ridge, the slots being transverse to the direction of propagation. The periodicity of the slotting is very small compared to the width of the waveguide, being about 12 per cent of the guide width for those cases studied experimentally.

The purpose of slotting the ridge is to add reactive loading in the guide in order to decrease the phase velocity of the wave. The degree of reduction in phase-velocity depends upon the degree of loading. Such a structure can be used as a means of obtaining a large range of refractive index for use in microwave lenses.[1,2] It may also be used in microwave filter circuitry.

This paper presents a description of two approaches to the evaluation of the index of refraction from the significant dimensions of the guide and its ridge. The first of these is a heuristic approach which seeks to explain the behavior of the guide on the basis of physical reasoning. This leads to two possible transmission line equivalences for the serrated ridge guide, from which the index of refraction can be calculated. This is essentially a semiempirical approach. It enables one to extend the range of knowledge about this structure through the performance of a few judiciously chosen experiments. The second approach involves an attempt to solve the wave equation for the propagation constant in the axial direction of the guide, through the expedient of field

* Manuscript received by the PGMTT, May 23, 1958; revised manuscript received, August 4, 1958. The work described was done, in part, under contract between The Ohio State Univ. Res. Found. and the Sperry Gyroscope Co., Div. of Sperry Rand Corp., Great Neck, L. I., N. Y.

† Battelle Memorial Inst., Columbus, Ohio. Formerly The Ohio State University, Columbus, Ohio.

‡ The Ohio State University, Columbus, Ohio.

[1] R. L. Smedes, "High efficiency microwave lens," *Sperry Eng. Rev.*, vol. 9, pp. 1–10; May–June, 1956.

[2] E. K. Proctor, "Methods of reducing chromatic aberration in metal plate microwave lenses," IRE TRANS. ON ANTENNAS AND PROPAGATION, vol. AP-6, pp. 231–239; July, 1958.

matching at certain selected boundaries in the guide. The method is based in part in the selection of an assumed set of hybrid fields to be used in the matching procedure. The method is by no means rigorous and can only be justified by results.

In the case of the first approach, the serrated ridge waveguide is viewed as a ridge waveguide having a short ridge, upon which posts are placed periodically. Since the periodicity is small, it is assumed that the structure is infinitesimally distributed with series LC loading across the waveguide. With this assumption an equation for the index of refraction is calculated which contains the static capacitive loading of the posts and the upper cutoff frequency as two parameters. These parameters are found from experimental data. The second transmission line equivalence[3] is viewed as a transmission line corresponding to a ridge waveguide with a full height ridge which is series loaded periodically with short-circuited stubs. The index of refraction calculated from also fits experimental data fairly closely.

In the second approach, two major assumptions are made with regard to the wave numbers in the directions transverse to the guide axis. These are as follows (see Fig. 1):

a) The wave number k_x associated with a pure ridged-guide for the dominant TE mode remains unaltered by the introduction of the slots periodically; and,

b) At frequencies near cutoff, the structure acts as if the slots were not present. In other words it is assumed that the wave number k_x is the same as for the pure ridge case and that k_y is zero at cutoff, taking on values only above cutoff.

In addition a major assumption is made with regard to the nature of the fields in the guide. It is assumed that the transverse field components parallel to the top and bottom faces of the guide are negligible.

Good agreement with experimental data seems to justify these assumptions, and the results so obtained can be put into forms similar to those obtained by the semiempirical approach.

Analysis

Shunt LC Loading

A rectangular waveguide or a ridged waveguide can be represented by an equivalent transmission line insofar as the dominant mode is concerned. The serrated ridge loading structure of Fig. 2 may be looked at in either of two ways. In the first of these, it can be thought of as a ridged guide having a ridge height equal to $(h-d)$. Set upon this ridge are closely spaced posts of height d. A single post partially crossing a waveguide looks very much like a series LC structure in the equivalent transmission line representation. Although there is undoubtedly coupling between adjacent posts, this series LC circuit was added to the equivalent transmission line of the ridged guide in an attempt to see how closely such a loading element approximates the true situation.

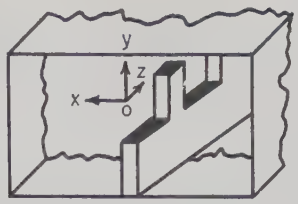

Fig. 1—A section of a serrated ridged waveguide.

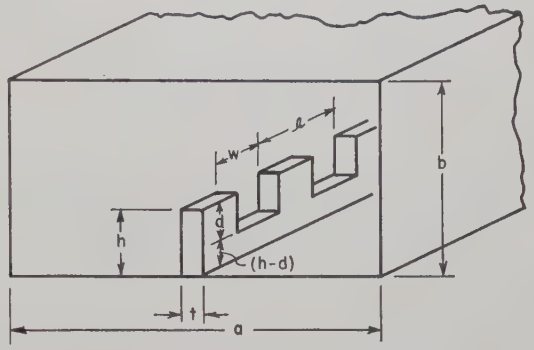

Fig. 2—Serrated ridged waveguide with parameters.

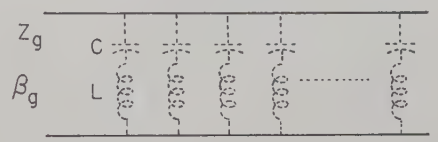

Fig. 3—Equivalent shunt loading due to posts on ridge of height $(h-d)$.

In this representation the loading consists of closely-spaced posts on a ridge of height $(h-d)$. This loading is represented in Fig. 3 as uniformly distributed LC sections. In this figure C is the capacitance per unit of axial length between the posts and the upper surface of the guide. The inductance L per unit length is such that its resonance with C accounts for the upper cutoff frequency characteristic of the index of refraction vs frequency curve. The series impedance and shunt admittance per unit length of the equivalent transmission line of the basic ridged guide are

$$Z_{se} = \beta_g Z_g = \frac{2\pi\eta}{\lambda} \tag{1}$$

$$Y_{sh} = \beta_g / Z_g = \frac{2\pi}{\lambda\eta}\left[1 - \left(\frac{\lambda}{\lambda_c}\right)^2\right] \tag{2}$$

where

λ is the free-space wavelength
η is the intrinsic impedance of free space and is μ_0/ϵ_0
λ_c is the cutoff wavelength of the ridged guide of ridge height $(h-d)$.

The shunt loading elements have a shunt admittance per unit length given by

$$Y_{sh}' = \frac{\omega C}{1 - \omega^2 LC} = \frac{2\pi}{\lambda\eta} \cdot \frac{C/\epsilon_0}{1 - (f/f_r)^2} \tag{3}$$

[3] J. R. Pierce, "Travelling Wave Tubes," D. Van Nostrand Co., Inc., New York, N. Y., ch. IV; 1950.

where f_r is the series resonant frequency of the LC loading element. The shunt-loaded guide phase constant is then

$$\beta_g' = \frac{2\pi}{\lambda_g'} = \sqrt{Z_{se}(Y_{sh} + Y_{sh}')}$$

$$= \frac{2\pi}{\lambda}\sqrt{1 - \left(\frac{\lambda}{\lambda_c}\right)^2 + \frac{C/\epsilon_0}{1 - (f/f_r)^2}}. \quad (4)$$

From this the index of refraction is

$$n = \sqrt{1 - \left(\frac{\lambda}{\lambda_c}\right)^2 + \frac{C/\epsilon_0}{1 - (f/f_r)^2}}. \quad (5)$$

In this expression λ_c is the cutoff wavelength of a basic ridged guide of height $(h-d)$ and f_r is the upper cutoff frequency of the loaded ridged guide. Application of this expression to a particular example is shown shortly.

Series Stub Loading

A second way of looking at the loading structure is to view it as a ridge of full height h. Periodically this ridge is series-loaded with short-circuited stubs of length d. The equivalent circuit would be that of the transmission line series loaded with shorted stubs. Again there is probably coupling between stubs, but the simple stub is used to see how closely such a loading element can approximate the true situation.

The stub is characterized by two parameters, the characteristic impedance Z_s of the stub, and the phase constant β_s of wave propagation down and back on the stub. The impedance Z_s is in ohms per unit of length in the axial direction in the guide. Hence if mutual coupling between stubs were negligible, this would be the impedance looking into one stub divided by the distance between stubs.

Eqs. (1) and (2) are applicable to this representation provided the cutoff wavelength corresponding to a ridge height h is substituted for λ_c in (2). To distinguish this cutoff wavelength from that (λ_c) for a ridge height of $(h-d)$, the cutoff wavelength for a ridge height h will be denoted λ_c'. Hence for this case, the stubs have a series impedance per unit of length given by

$$Z_{se}' = Z_s \tan \beta_s d \quad (6)$$

where β_s is the phase constant for propagation down the slot, and Z_s is the characteristic impedance of the slot per unit of length in the axial direction of the main guide. Thus the index of refraction is

$$n = \frac{\beta_g}{2\pi/\lambda} = \frac{\sqrt{(Z_{se} + Z_{se}')Y_{sh}}}{2\pi/\lambda}$$

$$= \frac{\sqrt{\left(\frac{2\pi\eta}{\lambda} + Z_s \tan \beta_s d\right)Y_{sh}}}{2\pi/\lambda}$$

$$= \sqrt{\left[1 - \left(\frac{\lambda}{\lambda_c'}\right)^2\right]\left[1 + \frac{\lambda Z_s}{2\pi\eta}\tan \beta_s d\right]}. \quad (7)$$

This expression has the characteristic that for all values of d it gives the same lower cutoff frequency, as contrasted to (5). This difference may be superficial, since at the present time the parameters c, f_r, Z_s, and β_s are obtained by getting the best fit with experimental data.

Example

Both of the above representations were fitted to the case $d/h = 0.700$.[4] The dimensions of the waveguide are listed in Fig. 5. The curves of Figs. 5 and 6 are plotted against frequency normalized to 2.72 kmc. This frequency is the experimentally obtained lower cutoff frequency. This frequency should correspond very closely to the value obtained from λ_c'.

In Fig. 4 there is plotted the experimentally obtained

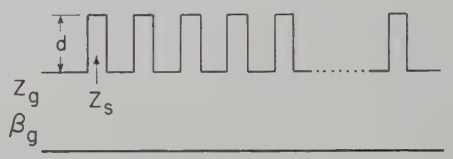

Fig. 4—Equivalent series loading due to stubs in ridge of height h.

function $1/n^2 - 1 + (\lambda/\lambda_c)^2$ against the normalized frequency $(f/f_c')^2$. If (5) is a good representation, this function should be a straight line. As Fig. 5 shows, the representation of a shunt LC loading on a basic ridged guide of ridge height $(h-d)$ is a very good one. The intercepts of this line with the coordinate axes give $\epsilon_0/c = 1.0$ and $(f_r/f_c')^2 = 7.5$. The LC resonant frequency calculated from this is 7.47 kmc, which corresponds to a wavelength of 4.02 cm. The depth of the slot is 0.89 cm, hence the slot is close to being $\lambda/4$ wavelengths long at the upper cutoff frequency.

The "goodness of fit" of the series stub loading cannot be determined as easily as for the shunt LC loading. Here a $\beta_s d'$ was used which made $\beta_s d'$ equal to $\pi/2$ at the upper cutoff frequency. This can be done by using $\beta_s = 2\pi/\lambda$ and $d' = (d + \text{a correction for end effects})$, or $d' = d$ and β_s is somewhat greater than $2\pi/\lambda$. In this particular case for $\beta_s = 2\pi/\lambda$, $d' = 1.13\ d$. The value of Z_s cannot be found as easily as the parameters in the case of the first representation.

Fig. 6 shows a plot of n vs (f/f_c') with $Z_s/\eta = 1.2$. This does not necessarily represent the best possible fit. Several values of Z_s should be tried and the best fit chosen perhaps on the basis of minimizing the mean square of the deviation between the calculated curve and the experimental curve.

Both of these representations were tested for a wide variety of ridge and slot dimensions. Over most of the range of dimensional variation these representations gave very good results. However, when the top of the

[4] Experimental data are based on unpublished data (Sperry Reference 7220, 4559; 5440 Series) taken by the Microwave Electronics Div., Sperry Gyroscope Co., Div. of Sperry Rand Corp.

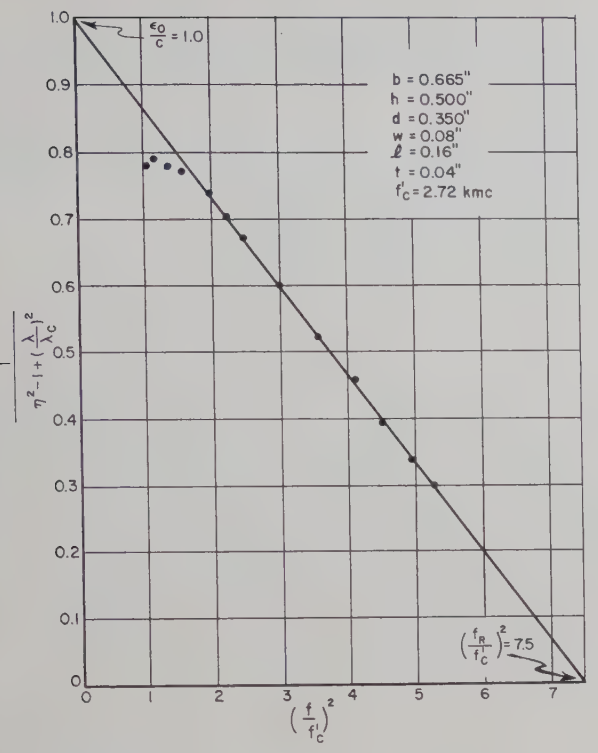

Fig. 5—Variation of

$$\frac{1}{n^2 - 1 + \left(\frac{\lambda}{\lambda_c}\right)^2}$$

with normalized frequency squared.

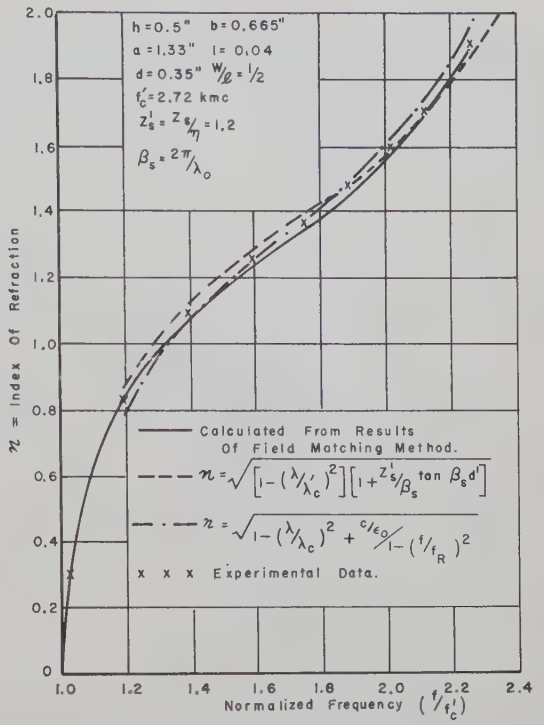

Fig. 6—Comparison of test data with result of calculations.

ridge approach too closely to the top of the guide, the simple equivalent circuits fail. This occurred for h/b greater than about 0.9. Both representations are of doubtful value near the upper cutoff frequency for d/h less than about 0.2, since the upper cutoff frequencies can no longer be accurately determined by extrapolating the shunt LC loading equivalent circuit.

Field Matching Method

The problem of calculating n from the guide dimension, is a boundary value problem with periodic boundary conditions. A rigorous method for this type of problem that leads to an exact and useful solution has not yet been developed.

This section develops a rather simple expression for the propagation constant of the dominant wave based on an assumed approximate set of fields matched over the mutual boundaries of different regions. The method in general is by no means rigorous, and the assumption made can only be justified by results.

Let k_x, k_y and k_z be the wave numbers associated with a solution of the wave equation in the rectangular coordinates with directions respectively as shown in Fig. 1, then

$$k_x^2 + k_y^2 + k_z^2 = k^2 \tag{8}$$

where k is the free space wave number. The two major assumptions are as follows:

a) The wave number k_x associated with a pure ridge guide for the dominant TE mode remains unaltered by the introduction of slots periodically.

b) At cutoff the wave number k_y is zero and takes on values only above cutoff. Good agreement with experimental data seems to have justified the validity of these assumptions.

In order to seek a set of fields that will satisfy the two assumptions, E_x is assumed to be negligible. Due to the periodicity of the boundary, higher order periodic modes are excited[5,6] and the excited waves are periodic in the form of Floquet's solution,

$$F(x, y, z) = \sum_{n=-\infty}^{\infty} A_n F(x, y) e^{j(\omega t - \beta g_n z)} \tag{9}$$

$$\beta g_n = \beta g_0 + \frac{2\pi n}{l}. \tag{10}$$

where βg_0 is the propagation constant of the dominant mode, l is the period of serration, and n is any integer.

Let the entire waveguide in one period be divided into four regions as shown in Fig. 7. Instead of solving the wave equation

$$\frac{\partial^2 E_z}{\partial x^2} + \frac{\partial^2 E_z}{\partial y^2} = (\beta g_n^2 - k^2) E_z$$

[5] L. Brillouin, "Waveguides for slow waves," *J. Appl. Phys.*, vol. 19, pp. 1023–1041; November, 1948.
[6] L. Brillouin, "Wave Propagation in Periodic Structures," Dover Publications, Inc., New York, N. Y.; 1953.

for an E_z that satisfies all the boundary conditions, an approximate set of fields are chosen which satisfy the wall boundaries and which leave the mutual boundaries open for matching. In the following equations, the left hand subscripts denote the region under consideration.

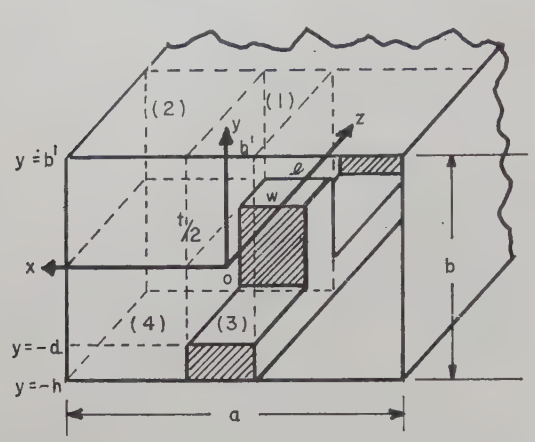

Fig. 7—Showing regions into which guide is divided.

Region (1): $\begin{cases} -t/2 < x < t/2 \\ 0 < y < b \end{cases}$
Region (2): Outside of (1) and (3), above $y=0$
Region (3): $\begin{cases} -t/2 < x < t/2 \\ -d < y < 0 \\ 0 < z < W \end{cases}$
Region (4): Outside of (1) and (3), below $y=0$.

In region (1), consistent with the assumptions, the fields are

$$ {}_1E_z = \sum_{n=-\infty}^{\infty} A_n \sinh k_{y_n}(b' - y) \cos k_x x e^{-j\beta g_n z} $$

$$ {}_1H_y = \sum_{n=-\infty}^{\infty} \frac{-k_x}{j\omega\mu} A_n \sinh k_{y_n}(b' - y) \sin k_x x e^{-j\beta g_n z} $$

$$ {}_1H_z = \sum_{n=-\infty}^{\infty} \frac{-k_x}{\omega\mu} \frac{\beta g_n}{k_{y_n}} A_n \cosh k_{y_n}(b' - y) \sin k_x x e^{-j\beta g_n z} \quad (11) $$

$$ {}_1H_x = \sum_{n=-\infty}^{\infty} \frac{-K^2}{j\omega\mu} \frac{A_n}{k_{y_n}} \cosh k_{y_n}(b' - y) \cos k_x x e^{-j\beta g_n z} $$

$$ {}_1E_y = \sum_{n=-\infty}^{\infty} \frac{-j\beta g_n}{k_{y_n}} A_n \cosh k_{y_n}(b' - y) \cos k_x x e^{-j\beta g_n z} $$

$$ \beta g_n{}^2 = k^2 - k_x{}^2 + k_{y_n}{}^2 $$

$$ K^2 = k^2 \left[1 - \left(\frac{k_x}{k} \right)^2 \right]. \quad (12) $$

In (11), the hyperbolic function for the y variation is due to the choice of sign of $k_{y_n}{}^2$ in (12). The fields in region (2) and (4) can be derived similar to the fields in region (1). Due to the assumption that $k_{y_0}=0$ at cutoff, it can be shown[7] that these fields will lead to a cutoff condition in accordance with that of a pure ridge guide of ridge height h derived by Cohn[8] or Hopfer.[9] In other words the wave number k_x is equal to the cutoff wave number $k_c' = 2\pi/\lambda_c'$.

If a standing wave due to reflection at $Y=-d$, together with higher order attenuated modes, is assumed for the fields in region (3), then

$$ {}_3H_z = C_0 \cos k_x x \sin K(y + d) + \sum_{m=1}^{\infty} C_m \cos \frac{m\pi z}{W} \cos k_x x e^{\gamma_m y} $$

$$ {}_3H_x = -\frac{C_0 K}{j\omega\mu} \cos k_x x \cos K(y + d) + \sum_{m=1}^{\infty} \frac{K}{j\omega\mu} \frac{C_m}{\gamma_m} \frac{m\pi z}{W} \cos k_x x e^{\gamma_m y} $$

$$ {}_3H_y = -\frac{k_x}{j\omega\mu} \sin k_x x \sin K(y + d) + \sum_{m=1}^{\infty} -\frac{k_x}{j\omega\mu} C_m \cos \frac{m\pi z}{W} \sin k_x x e^{\gamma_m y} $$

$$ {}_3H_z = \sum_{m=1}^{\infty} \frac{k_x}{j\omega\mu} \frac{m\pi/W}{\gamma_m} C_m \sin \frac{m\pi z}{W} \sin k_x x e^{\gamma_m y} $$

$$ {}_3E_y = \sum_{m=1}^{\infty} \frac{m\pi/W}{\gamma_m} C_m \sin \frac{m\pi z}{W} \cos k_x x e^{\gamma_m y} \quad (13) $$

where

$$ \gamma_m{}^2 = k_x{}^2 + \left(\frac{m\pi}{W} \right)^2 - k^2. $$

For $m>0$, if the period is much smaller than the wavelength, γ_m becomes real and is approximately $m\pi/W$. This means the higher order modes are attenuated rapidly, as they travel down into the slot and is the reason reflection at $y=-d$ is not required for $m>0$ in (13).

Going back to the guide constant βg_n, for $n \neq 0$, $\beta g_n \approx 2\pi n/l$. These rapidly phase changing modes are essential in order to satisfy the periodic boundary condition.

To match the fields in region (1) with the slot wave, a variational technique is used. The fields ${}_1E_z$ and ${}_3E_z$ must be equal to a field E defined over the common boundary from 0 to W, and ${}_1H_x$ must be equal to ${}_3H_x$ over the slot opening. Together with (11) through (13), there results

[7] R. Tsu, "Analysis of a Serrated Ridged Waveguide," Antenna Lab., The Ohio State Univ. Res. Found., Rep. 744-4; December 31, 1957.

[8] S. B. Cohn, "Properties of ridge waveguide," PROC. IRE, vol. 35, pp. 783–788; August, 1947.

[9] S. Hopfer, "The design of ridged waveguides," IRE TRANS. ON MICROWAVE THEORY AND TECHNIQUES, vol. MTT-3, pp. 20–29; October, 1955.

$$\frac{\coth k_{y_0}b'}{k_{y_0}} = \frac{\frac{l}{W}\left\{\frac{\cot Kd}{K}\int_0^W E dz \int_0^W E^* dz - \sum_{m=1}^{\infty}\frac{2}{\gamma_m}\int_0^W E\cos\frac{m\pi z}{W}dz\int_0^W E^*\cos\frac{m\pi z}{W}dz\right\}}{\int_0^W E^{j\beta_{g_0}z}dz\int_0^W E^* e^{-j\beta_{g_0}z}dz}$$

$$-\frac{\sum_{n=-\infty}^{\infty}{}' \frac{\coth k_{y_n}b'}{k_{y_n}}\int_0^W E e^{j\beta_{g_n}z}dz\int_0^W E^* e^{-j\beta_{g_n}z}dz}{\int_0^W E e^{j\beta_{g_0}z}dz\int_0^W E^* e^{-j\beta_{g_0}z}dz}. \quad (14)$$

Eq. (14) is in the variational form such that $\coth k_{y_0}b'/k_{y_0}$ is stationary with respect to small variation of E from its corrected value.[10] $\sum_{n=-\infty}^{\infty}{}'$ denotes summation from $-\infty$ to ∞ without the term $n=0$. Similarly another variational form in terms of the H field can be formulated, however, results will be obtained from (14).

A very simple expression results if the trial field is taken to be unity, or $E=1$. In this case (14) gives

$$\frac{l}{W}\frac{\cot Kd}{K} - \sum_{n=1}^{\infty}\frac{l^3\coth\frac{2\pi nb'}{l}}{2\pi^3n^3W^2}\left(1-\cos\frac{2\pi nW}{l}\right) - \frac{\coth k_{y_0}b'}{k_{y_0}} = 0. \quad (15)$$

$\beta g_n \approx 2\pi n/l$ for $n\neq 0$ is used to obtain (15).

To identify the meaning of each term in (15), it is interesting to note that the first term is the normalized admittance of the slot, the last term is the normalized admittance due to the fields above the teeth, and the middle term can be regarded as a discontinuity admittance y_1 due to a step in the y-direction as shown in Fig. 8(a). Eq. (15) does not give satisfactory results since the trial field of unity drops out the term involving summation over m. According to Fig. 8(b), we can identify this missing term as being the step discontinuity admittance y_2 due to a step in z-direction. Fig. 8(c) represents a step discontinuity admittance y_3 due to a step in x-direction if the field E_x were not assumed to be zero. Hence if the rest of the discontinuity admittances be added to (15), there results

$$\frac{l}{W}\frac{\cot Kd}{K} - \sum_{n=1}^{\infty} l\left(\frac{l}{W}\right)^2\frac{\coth\frac{2\pi nb'}{l}}{2\pi^3n^3}\cdot\left(1-\cos\frac{2\pi nW}{l}\right) - y_2 - y_3 = \frac{\coth k_{y_0}b'}{k_{y_0}}. \quad (16)$$

To find y_2, the discontinuity capacitance per unit length for a symmetrical step in z is $C_2=(\epsilon_0/\pi)\ln\csc(\pi W/2l)$. Thus the admittance y_2 normalized with respect to $-j\omega\mu l/K^2W$ is

[10] L. Lewin, "Advanced Theory of Waveguides," Iliffe & Sons Ltd., London, Eng.; 1951.

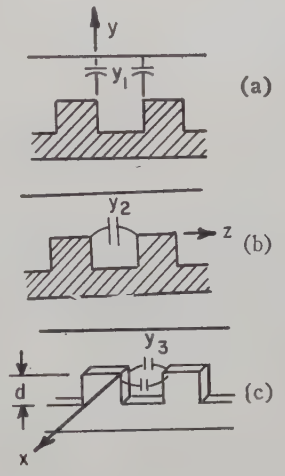

Fig. 8—Discontinuity capacitances y_1, y_2 and y_3.

$$(j\omega C_2 l)\left(\frac{-j\omega\mu}{K^2}\right)\frac{l}{W}.$$

The factor l/W appears for all the quantities referring to the slot [see (16)]. Similarly, for the case shown in Fig. 8(c), the discontinuity capacitance per unit length $C_3=C_2$, and the admittance y_3 normalized with respect to

$$\left(\frac{l}{W}\right)\frac{-j\omega\mu}{K^2},$$

is given by

$$\left(\frac{l}{W}\right)\left(\frac{-j\omega\mu}{K^2}\right)j\omega(2C_3l)kd.$$

The factor two in front of C_3 is due to two step discontinuities at $x=\pm t/2$ in shunt, and the factor kd takes into account the slot depth because the total step discontinuity consists of all such elements in shunt from $y=0$ to $y=-d$. These normalizations are required because of the form of the admittances appearing in (16). Therefore

$$y_2+y_3 = \frac{l}{W}\frac{(C_2/\epsilon_0)l}{1-\left(\frac{k_x}{k}\right)^2} + \frac{l}{W}\frac{(2C_3/\epsilon_0)lkd}{1-\left(\frac{k_x}{k}\right)^2} \quad (17)$$

where $C_2=C_3=(\epsilon_0/\pi)\ln\csc(\pi W/2l)$ farads/meters. Rearranging (16), there results

$$k_{y_0} \tanh k_{y_0} b' = \frac{W}{l} K \tan Kd \frac{1}{1 - \left[\sum_{n=1}^{\infty} l\left(\frac{l}{W}\right) \frac{\coth \frac{2\pi n b'}{l}}{2\pi^3 n^3} \left(1 - \cos \frac{2\pi n W}{l}\right) + \frac{\frac{C_2}{\epsilon_0} l}{1 - \left(\frac{k_x}{k}\right)^2} + \frac{2\frac{C_2}{\epsilon_0} lkd}{1 - \left(\frac{k_x}{k}\right)^2} \right] K \tan Kd} \tag{18}$$

where

$$K = k\sqrt{1 - \left(\frac{k_x}{k}\right)^2}$$

$$\beta g_0 = k\sqrt{1 - \left(\frac{k_x}{k}\right)^2 + \left(\frac{k_{y_0}}{k}\right)^2}$$

$$k_x = k_c = 2\pi f_c' \sqrt{\mu_0 \epsilon_0}.$$

From (18), the propagation constant of the dominant mode can be calculated. Note that the term in the braces can easily be calculated for each given k, and a simple graph can be used to determine k_{y_0}. It is interesting to note that the index of refraction

$$n \equiv \frac{\beta g_0}{k} = \sqrt{1 - \left(\frac{k_x}{k}\right)^2 + \left(\frac{k_{y_0}}{k}\right)^2} \tag{19}$$

is of the same form as the shunt LC loading formula, and with a little rearranging, (19) becomes

$$n = \sqrt{1 - \left(\frac{k_x}{k}\right)^2 + \left(\frac{k_{y_0}}{k}\right)^2}$$

$$= \sqrt{\left\{-1\left(\frac{k_x}{k}\right)^2\right\}\left\{1 + \frac{k_{y_0}^2}{k^2\left[1 - \left(\frac{k_x}{k}\right)^2\right]}\right\}}$$

$$= \sqrt{\left[1 - \left(\frac{k_x}{k}\right)^2\right]\left[1 - \left(\frac{k_{y_0}}{K}\right)^2\right]}$$

which is identical in form to (7) derived from series stub loading consideration. The index of refraction calculated from (18) for the example given previously is also plotted in Fig. 6.

Conclusions

The equivalent circuit representations give a good physical picture for the effect of the loading although they are only qualitatively correct. Effort to correlate the loading parameters with the dimensions of the structure was made; however,[11] no simple relation seems to exist. On the other hand, the field matching results give the desired accuracy. It is worth noting that a better trial field for the variational expression, for example, a field that symmetrically goes to infinity at the extremities of each slot, may be used. Further improvements, if desired, have to be made with a better set of hybrid fields without neglecting the field E_x [see discussions prior to (16)].

[11] H. Kirschbaum and R. Tsu, "A Study of a Serrated Ridged Waveguide," Antenna Lab., The Ohio State Univ. Res. Found., Rep. 744-2; July 31, 1957.

Design Considerations for High-Power Microwave Filters*

SEYMOUR B. COHN†

Summary—**The need for high-power filters is reviewed briefly, and various design approaches are discussed. The major portion of the paper treats the power-handling capacity of multiple-resonator filters using inductive windows or posts as coupling elements. A formula is derived that gives the relative power capacity of a waveguide filter of this type in terms of the bandwidth and cavity dimensions, and the element values of the low-pass prototype filter. By means of this formula it is shown quantitatively how high-power ratings may be achieved through the use of enlarged cavities. Methods for eliminating spurious filter responses and of reducing the reflected energy are discussed.**

I. Introduction

In the microwave range, equipments often interfere with each other even when operating at different frequencies. This interchannel interference can arise from the generation and radiation of large amounts of RF energy outside of the operating bandwidth of a transmitter, or it can be the result of inadequate RF selectivity in a receiver. For example, magnetrons are known to produce strong harmonics, and are also likely to emit spurious "moding" energy at frequencies that are not harmonically related to the fundamental frequency. Some of these unwanted components may be at a level only 20 db below the fundamental, and hence are capable of causing serious interference to receivers in other systems. Fortunately, interchannel interference can be eliminated through the use of RF filters. High-power filters may be used between a generator and an antenna to prevent the radiation of signals outside the operating bandwidth, and low-power filters may be used at the input of a receiver to prevent the entrance of strong signals of undesired frequency. A discussion of filters in the high-power class is given in this paper. Low-power filters represent less of a problem, and considerable design information may be found in the literature.

In the design of filters intended for high-power applications, one must prevent electric field strengths approaching the breakdown point. Sharp edges in high-field-strength regions must therefore be avoided, and resonant buildup of the field must be limited to a safe value. One approach to the high-power filter problem has been made by Vogelman,[1] who has proposed a varying-impedance waveguide structure in which the changes of height are tapered rather than abrupt. Vogelman has shown how to compute the pass-band and spurious responses of this filter and has verified experimentally its frequency response and high-power capability. A second approach has been used by Wheeler and Bachman[2] in which resonant irises and resonant posts are quarter-wave coupled in a waveguide to synthesize an m-derived band-pass filter. Breakdown is avoided by evacuating the filter, which greatly increases the breakdown field strength. A third approach proposed by Torgow[3] uses a circuit of hybrid junctions, loads, and waveguides of different cutoff frequencies to create pass bands and absorbing bands. Since resonant elements are avoided, the power-handling capacity can be very high. A fourth approach is to use the multiple-cavity type of band-pass filter, in which inductive windows or posts are used for coupling the waveguide resonators. The power-handling capacity of this configuration has been studied recently by the author of this paper, and it is shown here that this filter can have virtually as large a power rating as desired, up to the full rating of the terminating waveguide.

II. Power-Handling Formulas for Multiple-Resonator Filters

A multiple-resonator band-pass filter can be designed[4] to have the response function of a lumped-constant low-pass prototype filter, where, through an appropriate transformation, zero frequency for the latter corresponds to the center of the pass band for the former (see Fig. 1). Thus, with the proper choice of coupling-element values and cavity lengths, the waveguide filter and prototype filter of Fig. 2 are equivalent. In this figure, $g_1, g_2, \cdots, g_i, \cdots, g_n$ are element values of the prototype filter (in farads for i odd and henries for i even), b_T is the height of the terminating guides, $b_1, b_2, \cdots, b_i, \cdots, b_n$ are cavity heights, $m_1, m_2, \cdots, m_i, \cdots, m_n$ are integers equal to the cavity lengths in half guide wavelengths, E_T is the maximum electric field strength in the matched output waveguide, and $E_1, E_2, \cdots, E_i, \cdots, E_n$ are the maximum electric field strengths in the cavities. In terms of these quantities, the cavity field strengths at the center of the pass band are given

* Manuscript received by the PGMTT, August 1, 1958; revised manuscript received, August 28, 1958. The work described in this paper was supported by the U. S. Army Signal Eng. Labs. under Contract DA 36-039 SC-74862.

† Stanford Res. Inst., Menlo Park, Calif.

[1] J. H. Vogelman, "High-power microwave filters," 1958 IRE National Convention Record, pt. 1, pp. 84–90. Also, "High-power filters using higher-order-mode resonance," presented at PGMTT Natl. Symp., Stanford, Calif., May 7, 1958.

[2] H. A. Wheeler and H. L. Bachman, "Evacuated waveguide filter for suppressing spurious transmission from high-power S-band radar," this issue, p. 154.

[3] E. N. Torgow, "Hybrid junction-cutoff waveguide filters," this issue, p. 163.

[4] S. B. Cohn, "Direct-coupled-resonator filters," Proc. IRE, vol. 45, pp. 187–196; February, 1957.

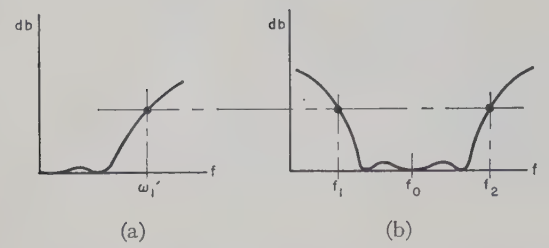

(a) (b)

Fig. 1—Correspondence between (a) low-pass prototype response and (b) equivalent band-pass response.

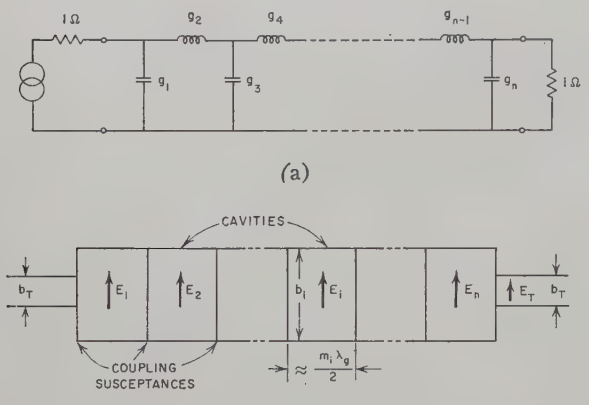

Fig. 2—Low-pass prototype filter and equivalent waveguide-cavity filter.

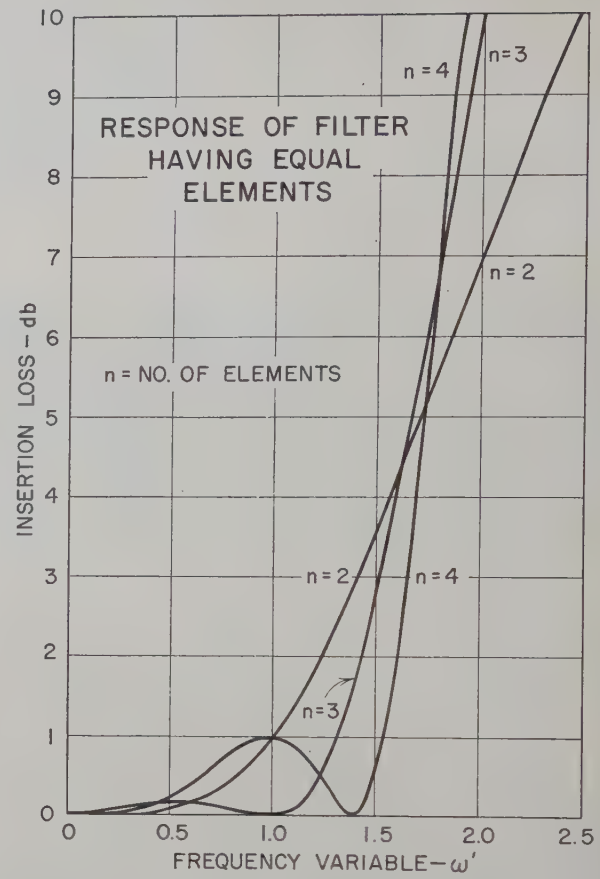

Fig. 3—Insertion-loss vs frequency response of multiple-cavity filter with $g_i = 1$.

by the following formula, which is derived in Section V:[5]

$$E_i = E_T \frac{\lambda_0}{\lambda_{g0}} \sqrt{\frac{2 g_i \omega_1' b_T}{m_i \pi w b_i}} \qquad (1)$$

where $w = (f_2 - f_1)/f_0$, and where $\omega_1' = 2\pi f_1'$ for the prototype filter and f_1 and f_2 for the band-pass filter are corresponding points of equal insertion loss (see Fig. 1). Note that ω_1', f_1, and f_2 may be taken as desired either at the edges of the pass band or at any insertion-loss level in the stop band. In this formula it is assumed that the waveguide width and guide wavelength are the same throughout. [See (14) for generalization of (1).]

It is desirable in a high-power multiple-cavity filter to have equal electric field strengths in the cavities, since this condition maximizes the power-handling capacity for a given degree of selectivity. Examination of (1) shows that for cavities of equal size, the condition for equal electric field strength at the pass-band center is that $g_1, g_2, \cdots, g_n$ all be the same. The response function of the prototype low-pass filter for this special case is shown in Fig. 3 for various numbers of elements and with all values of g_i set equal to unity.[6] It is seen that only the central portion of the pass band of the equivalent band-pass filter can be used if the insertion loss (due to reflection) is to be low.

Fig. 4 shows how the electric field strengths vary with frequency for the case of $g_i = 1$ in the prototype filter. These curves were computed from the prototype filter, recognizing that the voltages across the capacitances and the currents through the inductances are proportional to the field strengths in the respective cavities. It is seen in Fig. 4 that the field strengths are equal only at $\omega' = 0$, that is, at the center of the pass band of the equivalent band-pass filter. The power rating at any frequency with respect to the power capacity at band center is equal to the square of the reciprocal of the largest relative electric field strength at that frequency. Thus, for example, in the case of a four-cavity filter having $g_i = 1$, the power capacity at $\omega' = 0.4$ is 80 per cent of that at $\omega' = 0$, and at $\omega' = 1$ it is 50 per cent.

The power-handling capacity of the filter is defined best as a percentage of the power rating of the terminating waveguide. Thus, if the filter and terminating waveguide are under equal air pressure, the relative power capacity is as follows:

$$\text{relative power capacity} = \left(\frac{E_T}{E_i}\right)^2 \cdot 100 \text{ per cent}, \qquad (2)$$

where E_i is the largest of the cavity field-strength values in the filter at the frequency in question. Hence,

[5] The portion of (1) under the square-root sign is actually dimensionless, since the units of $g_i \omega_1'$ are canceled by the prototype-filter load resistance that would appear in the expression if it had not been set equal to one ohm.

[6] G. L. Ragan, "Microwave Transmission Circuits," M.I.T. Rad. Lab. Ser., vol. 9, ch. 10, by A. W. Lawson and R. M. Fano, p. 681; McGraw-Hill Book Co., Inc., New York, N. Y.; 1948.

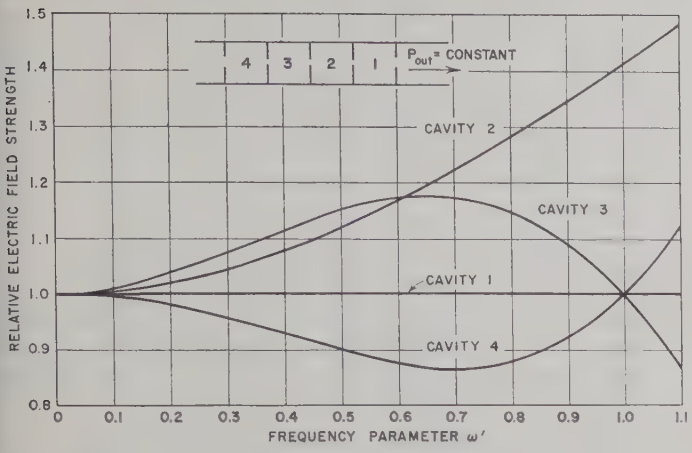

Fig. 4—Effect of frequency on electric field strengths in multiple-cavity filter with $g_i=1$.

relative power capacity

$$= \frac{m_i \pi w b_i}{2 g_i \omega_1' b_T} \left(\frac{\lambda_{g0}}{\lambda_0}\right)^2 \cdot 100 \text{ per cent.} \quad (3)$$

The subscript i to be used in (3) is the number between 1 and n that minimizes this expression for a given n-resonator filter.

Examination of (1) shows that the cavity field strengths may be made equal even with unequal g_i values, if m_i and b_i are also made variable in the filter. Thus the superior maximally flat or equal-ripple response functions may be utilized without impairing the power rating of the filter, if the different cavities are properly proportioned. The larger cavities, of course, will have an increased number of undesired resonances, but the smaller cavities will tend to suppress these in the overall response.

III. Calculated Examples

A few examples will now be given of the relative power capacity of typical filters. As a first example, assuming $g_i=1$, $\omega_1'=1$, $w=0.2$, $\lambda_0/\lambda_{g0}=0.8$, $m=2$, and $b_i=b_T$, (3) shows that at the center of the pass band the filter can be rated at 99 per cent of the power rating of the terminating waveguide. As a second example, assume that 40 db of insertion loss is required at the edges of a 20 per cent frequency band. For a four-cavity filter and $g_i=1$, calculation shows that $\omega_1'=3.89$ at the 40-db point of the prototype filter, and therefore $\omega_1'=3.89$ and $w=0.2$ are corresponding values. Now if we assume $\lambda_0/\lambda_{g0}=0.8$, $m_i=2$, and $b_i=2b_T$, then the power rating at band center is 50.5 per cent of the power capacity of the terminating waveguide.

As a comparison to the last example, consider the power rating of a four-cavity filter whose g_i values are designed to yield a maximally flat response, with the 40-db points still at the edges of a 20 per cent frequency band. (The necessary formulas can be found in the literature.)[4] Calculation shows that $g_1=g_4=0.765$, $g_2=g_3=1.848$, and that the 40-db point occurs at $\omega_1'=3.16$. In this case, the largest field strength occurs in the middle cavities, and, assuming the same values of λ_0/λ_{g0}, m_i, w, and b_i/b_T as in the last example, the filter rating at band center is equal to 33.5 per cent of the power rating of the terminating waveguide. This should be compared with 50.5 per cent in the preceding example.

Another interesting question is how the power rating of a multiple-resonator filter changes with the number of resonators when the stop-band bandwidth is held constant. The pass band bandwidth will increase with the number of resonators, approaching the stop-band bandwidth in the limit, and it is therefore clear that the power rating will also increase. A calculation has been carried out for the case of equal elements and the parameters of the second example with the following results:

Number of Resonators	ω_1' at 40-db Point	Relative Power Capacity (per cent)
1	200	1.0
2	14.16	13.9
3	5.86	33.5
4	3.89	50.5
5	3.10	63.3
6	2.70	72.7
100	2.00	98.1

The advantage of using a large number of resonators is clearly evident. However, considerations of size, adjustment difficulty, and dissipation loss will place a limit of, perhaps, six to ten resonators in a practical filter.

IV. System Considerations for High-Power Filters

It is evident from the preceding discussion that high-power filters are likely to have numerous undesired spurious responses. Fig. 5 shows how several filters in cascade may be used to eliminate spurious responses out to very high frequencies. The filter of smallest bandwidth, Filter 1, must have larger cavities than the others in order to carry the required power. As a result it will almost inevitably have a number of spurious responses in the range of interest. These spurious responses can be suppressed by one or more filters of greater bandwidth and more widely spaced spurious responses, as shown in the figure.

The high-power band-pass filter considered above provides stop-band insertion loss through reflection of the incident energy. In some instances, this reflection may have an adverse effect on the power source, and the energy should be dissipated rather than reflected. As shown by the examples in Fig. 6, this may be done by means of a broad-band ferrite isolator, or by a circuit of hybrid junctions and a pair of identical band-pass filters so arranged as to divert the energy reflected from the filters into an auxiliary resistive load. Equivalent performance can be achieved by directional filters, which have the combined properties of directional couplers and of filters.[7] Directional filters would be particularly useful

[7] S. B. Cohn and F. S. Coale, "Directional channel-separation filters," Proc. IRE, vol. 44, pp. 1018–1024; August, 1956.

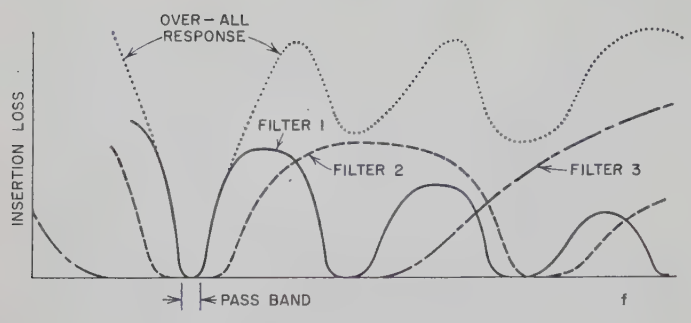

Fig. 5—Connection of filters in cascade to eliminate spurious responses.

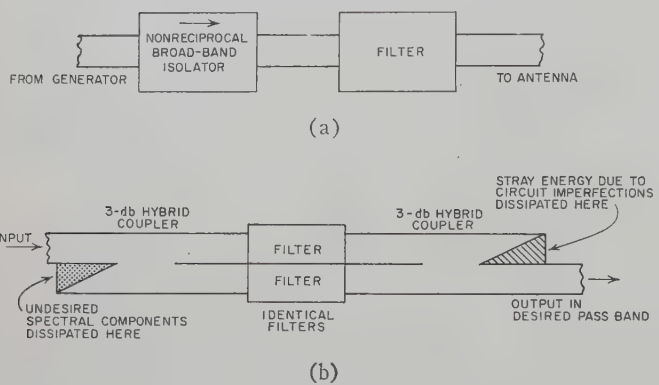

Fig. 6—Suggested means for dissipating energy reflected from filter. Network in (a) utilizes a broad-band nonreciprocal isolator; network in (b) utilizes a pair of identical filters and hybrid junctions.

for removing discrete spurious frequencies and dissipating their energy into a load.

It is believed that wide-bandwidth high-power filters can also be achieved by leaky-wall structures like that of Fig. 7. Near the desired operating frequency the holes would be waveguides below cutoff, and very little energy would leak through them. Above the cutoff frequency of the holes, the energy would pass through the holes and be absorbed in the surrounding lossy material. By having a sufficient number of holes on all four walls of the waveguide, it should be possible to obtain a stop band free of spurious responses in any waveguide mode up to a very high frequency. Of course the edges of the holes in the broad walls should be rounded to maximize the power capacity.

V. Derivation of Field-Strength Formula for Multiple-Resonator Filter

The following derivation is based on a previous analysis of multiple-resonator filters.[4] In that analysis, the low-pass prototype filter of Fig. 2(a) was related to the waveguide filter of Fig. 2(b) by means of the intermediary transmission-line circuit of Fig. 8. The equivalence of Fig. 8 to the waveguide filter is a direct one, with the lines of characteristic impedance Z_0 and electrical length 180 degrees representing the cavity resonators at resonance, and the lines of characteristic impedance $K_{i,i+1}$ and electrical length 90 degrees representing the coupling susceptances at the proper reference planes. It

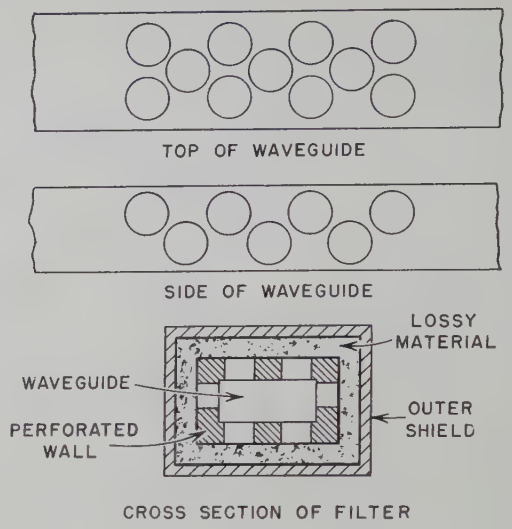

Fig. 7—Leaky-waveguide technique for dissipating unwanted energy above the desired signal frequency.

has been shown[4] that the latter length is independent of frequency to the first order, and therefore the lines of characteristic impedance $K_{i,i+1}$ act as impedance inverting transformers over a wide band of frequencies. The equivalence of Fig. 8 to the low-pass prototype filter depends upon the change in frequency variable shown in Fig. 1.

For convenience in the analysis, the cavities and terminating lines are assumed to have equal characteristic impedance Z_0, and the cavity electrical lengths at resonance are assumed to be 180 degrees. At a later point in the analysis these quantities will be generalized. Also, for convenience the various elements are numbered from the load end of the filter.

Fig. 9 shows how the voltages and currents in the filter may be computed at the center frequency in terms of the voltage, V_T, across the load resistance. The phases of the various quantities are unimportant in this problem, and therefore only magnitudes of the voltages and currents are shown. The following simple relations between these magnitudes were used in the computation: for a 90-degree line of characteristic impedance Z_c,

$$V_{\text{in}} = Z_c I_{\text{out}} \quad \text{and} \quad I_{\text{in}} = \frac{V_{\text{out}}}{Z_c}; \tag{4}$$

and for a 180-degree line

$$V_{\text{in}} = V_{\text{out}} \quad \text{and} \quad I_{\text{in}} = I_{\text{out}}. \tag{5}$$

Starting at the load end and proceeding back through the filter, one can verify the expressions in Fig. 9, and show that the voltages at the centers of the resonators are of the following form:

$$V_1 = \frac{Z_0 V_T}{K_{01}} \qquad V_2 = \frac{K_{01} V_T}{K_{12}}$$

$$V_3 = \frac{Z_0 K_{12} V_T}{K_{01} K_{23}} \qquad V_4 = \frac{K_{01} K_{23} V_T}{K_{12} K_{34}} \text{ etc.} \tag{6}$$

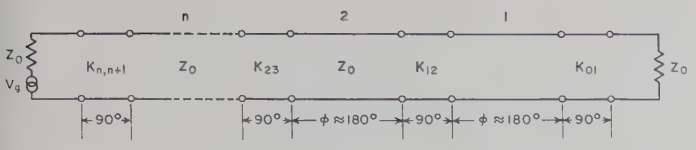

Fig. 8—Equivalent circuit of a multiple-resonator filter.

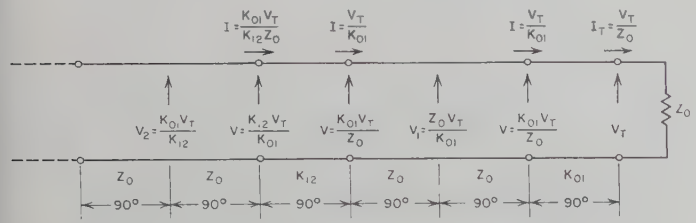

Fig. 9—Voltage and current magnitudes in the equivalent multiple-resonator filter.

In a waveguide filter the characteristic impedances $K_{i,i+1}$ are less than Z_0 and it is easily verified that the voltages V_i correspond to the maximum voltages in the various cavities.

The characteristic impedances $K_{i,i+1}$ have been shown[4] to be related to the element values g_i of the prototype filter by

$$\frac{K_{i,i+1}}{Z_0} = \frac{L}{\sqrt{g_i g_{i+1}}}, \qquad i = 1 \text{ to } n-1, \tag{7}$$

and

$$\frac{K_{01}}{Z_0} = \sqrt{\frac{L}{g_1}}. \tag{8}$$

The formula for $K_{n,n+1}$ is not as simple in general, but in the usual case of a symmetrical waveguide filter $K_{n,n+1}=K_{01}$. (If an unsymmetrical waveguide filter is of interest, Ref. 4 should be consulted for the correct expression for $K_{n,n+1}$.) Subject to the assumption of half-wavelength cavities of height and width equal to that of the terminating waveguide, the parameter L is given by

$$L = \frac{\pi w}{2\omega_i}\left(\frac{\lambda_{g0}}{\lambda_0}\right)^2 \tag{9}$$

where w is the relative bandwidth $(f_2-f_1)/f_0$, and f_0, f_1, f_2, and ω_1' are defined in Fig. 1. λ_{g0} and λ_0 are the guide wavelength and free-space wavelength at the center frequency. (A more accurate form of (9) has been given,[4] but (9) is sufficiently accurate for power-capacity calculations.) At this point the limitation on cavity length and height may be removed. A study of the original derivation of (9) shows that

$$L_i = \frac{m_i \pi w b_i}{2\omega_1' b_T}\left(\frac{\lambda_{g0}}{\lambda_0}\right)^2 \tag{10}$$

where m_i is the length of the ith cavity in half guide wavelengths, b_i is the height of the cavity, and b_T is the height of the terminating waveguide. Combination of the above formulas results in

$$V_i = V_T\sqrt{\frac{g_i}{L}} = V_T\frac{\lambda_{g0}}{\lambda_0}\sqrt{\frac{2\omega_1' g_i b_i}{m_i \pi w b_T}}, \quad i = 1 \text{ to } n. \tag{11}$$

The voltages are related to the field strengths by

$$V_i = E_i b_i \quad \text{and} \quad V_T = E_T b_T, \tag{12}$$

and hence

$$E_i = E_T\frac{\lambda_0}{\lambda_{g0}}\sqrt{\frac{2g_i\omega_1' b_T}{m_i \pi w b_i}} \tag{13}$$

where E_T is the maximum electric field strength in the output waveguide, and E_i is the maximum electric field strength in the ith cavity.

Eq. (13) assumes that the cavity widths and terminating-waveguide widths are all equal. If this restriction is removed, one can show that (13) becomes

$$E_i = E_T\left[\frac{2g_i\omega_i' a_T b_T}{m_i \pi w a_i b_i}\right]^{1/2}\left[1-\left(\frac{\lambda_0}{2a_T}\right)^2\right]^{1/4}\left[1-\left(\frac{\lambda_0}{2a_i}\right)^2\right]^{1/4} \tag{14}$$

where a_i is the width of the ith cavity and a_T the width of the terminating waveguide.

VI. Conclusions

The coupled-resonator filters described in this paper are suited for use with high-power microwave tubes to suppress harmonics and spurious "moding" energy. The design techniques are believed to be sufficiently rigorous for practical structures, but are as yet unsupported by experimental verification. Further study of spurious pass bands and their elimination is desirable, and coupling configurations having optimum power capacity should be investigated. It is hoped that, despite their preliminary nature, the findings in this paper will prove of value to the engineer working in this relatively new field of high-power filtering.

Evacuated Waveguide Filter for Suppressing Spurious Transmission from High-Power *S*-Band Radar*

H. A. WHEELER† AND H. L. BACHMAN†

Summary—A one-megawatt magnetron, used in a search radar, tunes over the *S* band of 3.1 to 3.5 kmc, and simultaneously causes interference in the band of 3.7 to 4.0 kmc by occasional oscillation in spurious modes. For insertion in the antenna line of this radar, a band-pass filter has been designed to provide over 120 db attenuation in the interference band. It is a wave filter with *M*-derived terminations for impedance matching and with three sections including traps resonant in the stop band, for high attenuation, all made of nine resonant irises spaced ¼ wavelength in a waveguide. Each filter is sealed by pressure windows and evacuated to handle the high-power pulses. Two such filters are connected in parallel between 3-db directional couplers to make a nonreflecting assembly.

Introduction

THE FILTER to be described has been developed to meet some unusual requirements, by means of an advanced design in waveguide, together with special provisions to handle high-power pulses. The M-33 Fire Control System contains a search radar which was found to cause interference with microwave relay links operating in a slightly higher frequency band. It was determined that the *S*-band magnetron, which is intended to oscillate in the 8-mode (or pi-mode), transmits also some spurious high-power pulses on a higher frequency corresponding to the 7-mode. Therefore, a filter was needed to suppress the spurious pulses while passing the normal pulses.

The most severe requirement of this filter is the transmission of high-power (one-megawatt) pulses through the resonant circuits that form the filter. This dictated the use of a waveguide structure with special provisions for handling the high electric gradients (such as a vacuum). The required amount of attenuation is obtained in the waveguide environment by structural elements simulating a carefully computed lumped circuit. The further requirement of avoiding substantial reflection is met by assembling a pair of such filters between two directional-coupler hybrid junctions. This arrangement is patterned after the well-known balanced duplexer, which behaves as a nonreflecting filter below the power level of breakdown within the filter structure. Here the interior will be evacuated to an unusually high degree to preclude breakdown in the dielectric space.

This paper presents a general description of the nonreflecting filter assembly, a complete description of the wave filter with design formulas, a procedure for realizing such a filter in a waveguide structure, and the results obtained in a practical design. A particular feature is the evaluation of the reactance arms of the filter in a form normalized for resonators in a waveguide, and suited for testing the realization of these arms.

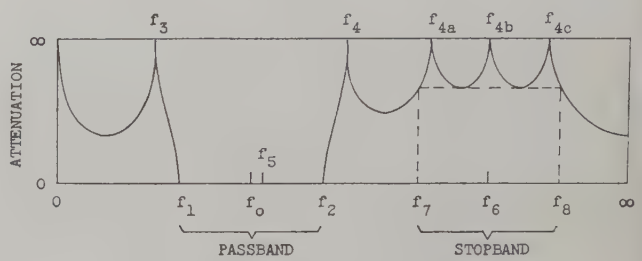

Fig. 1—Attenuation over frequency range.

Fig. 1 is a frequency diagram showing the basis for specifying and realizing the required attenuation. The principal frequency bands are the pass band in which no attenuation is desired and the stop band in which high attenuation is desired.

The frequency band of the radar is 3.1–3.5 kmc. A nominal pass band was chosen, 1.25 times as wide, between cutoff frequencies of 3.05 and 3.55 kmc. The interference band or stop band was designated as 3.7–4.0 kmc which covers the overlap between the 7-mode band (3.50–3.95 approx) and the TD-2 relay band (3.70–4.20). The objective of high attenuation over the interference band was satisfied with a computed attenuation greater than 120 db.

After a list of symbols, there will be a general description of the complete filter arrangement and its capabilities, followed by the formulas for the filter sections and the computations for the present purpose.

Symbols

R = mid-series image resistance at midband
G = mid-shunt image conductance at midband
jG = impedance inverter based on G
L = inductance in arm of half-section
C = capacitance in arm of half-section
C_0, L_0 = elements of series arm of constant-K half-section
X = reactance of series arm of half-section
B = susceptance of shunt arm of half-section
$b = B/G$ = susceptance ratio (normalized susceptance)

* Manuscript received by the PGMTT, May 14, 1958; revised manuscript received, July 28, 1958. More comprehensive formulas and rules are available from the authors on request.
† Wheeler Labs., Great Neck, N. Y.

av $|b|$ = average magnitude of b at f_1 and f_2
$Q = \omega L/R$ of series resonance
$Q = \omega C/G$ of shunt resonance
$\omega = 2\pi f$ = radian frequency
f = cycle frequency
f_c = cutoff frequency of low-pass analog
f_∞ = trap frequency of low-pass analog
$f_0 = \sqrt{f_1 f_2}$ = midfrequency of pass band
$f_8 = \sqrt{f_7 f_8}$ = midfrequency of stop band
λ_0 = wavelength in waveguide at f_0
m = parameter of M-derived half-section (VI type)
m_5 = parameter of derived half-section (V type)
α = attenuation of half-section (on image basis) (napiers)
exp $-\alpha$ = response ratio of symmetric section
= output/input ratio of voltage or current
sub-0 = midband
sub-1, 2 = cutoff frequency at edge of nominal pass band
sub-3, 4 = trap frequency (VI type)
sub-7, 8 = edge of stop band (V type)
sub-4, 4*a*, 4*b*, 4*c* = trap frequency (V type)
sub-5, *a*, *b*, *c* = series arm of derived half-section (V type)
sub-*oa*, *ab*, *bc*, *oc* = full-shunt arm made of the two mid-shunt arms at junction of two different half-sections
Type IV = constant-K band-pass filter (no trap frequencies)
Type VI = M-derived band-pass filter (symmetrical trap frequencies)
Type V = band-pass filter with single trap frequency above the band.

The Nonreflecting Assembly

A wave filter attenuates by reflection. It happens that a magnetron will emit even more spurious pulses if the load presents too much reflection in the frequency range of these pulses. Therefore, the solution of the present problem requires a nonreflecting filter assembly. This result is achieved by using a matched pair of wave filters in a certain environment based on well-known principles.

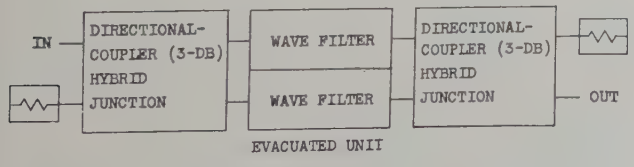

Fig. 2—Diagram of nonreflecting filter assembly.

Fig. 2 shows the essentials of the nonreflecting filter assembly, patterned after the balanced duplexer. Two identical wave filters are connected between input and output terminal junctions, each being a four-port with one of its ports connected to a dummy load.

Each terminal junction is essentially a hybrid junction supplemented by a phase difference of 90° between one pair of ports and the other pair. These properties are combined in the well-known 3-db directional coupler, so this component is utilized.

The resulting assembly retains the transmission and attenuation properties of the wave filters because the pair of filters are essentially connected in parallel between the indicated input and output ports. However, the reflections from the two filters at either end are canceled out, as seen from the input or output port, and the reflected power is diverted to the dummy load at the corresponding end. In this way, the complete assembly becomes a nonreflecting filter.

The entire nonreflecting filter in its operating environment is shown in a more recent presentation by R. D. Campbell, dealing with the operational situation that requires this filter [19].

The Wave Filter

The wave filter is essentially a band-pass filter designed on the basis of image parameters. It comprises a number of sections chosen to meet the requirements with economy in the number of parts. It is embodied in a waveguide structure by means of several specialized irises with proper spacing.

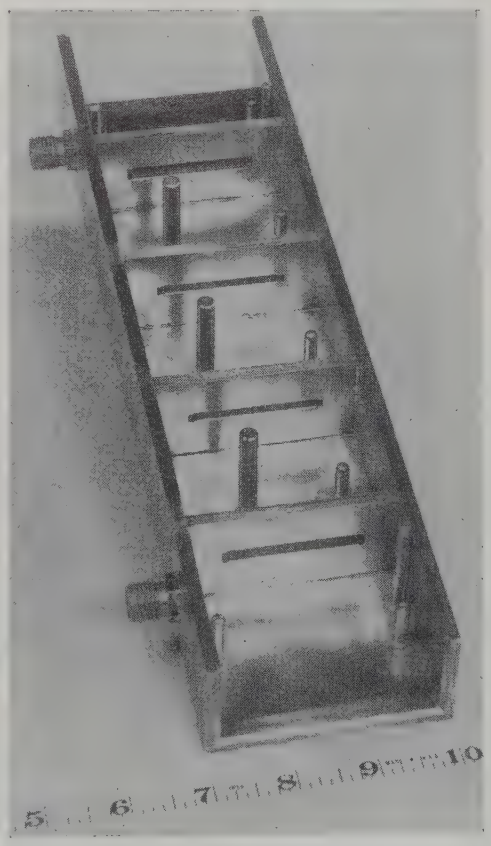

Fig. 3—Photo of wave filter (top removed).

Fig. 3 shows the type of construction used for each wave filter. As will be explained further on, the filter is to be evacuated to prevent breakdown in the dielectric space, so it is constructed in a waveguide section suitable for sealing with pressure windows at the ends. The

internal pieces comprise the irises which make the filter. (This particular structure is a preliminary model which differs from the final design in minor details, especially in having thicker internal partitions.)

Fig. 4 shows the equivalent lumped networks which form the basis for the waveguide structure. In a waveguide, shunt arms are easy to make because they can be inserted while the walls remain intact, while series arms are very difficult, requiring breaks in the walls and the addition of external parts. Fig. 4(a) shows how the complete filter is made of shunt arms in a waveguide, while 4(b) shows the equivalent ladder network of shunt and series arms.

The waveguide form in Fig. 4(a) obtains the effect of shunt and series arms by using shunt arms spaced $\frac{1}{4}$ wavelength in the guide. This is a well-known principle, exemplified in evacuated TR tubes that formed the background of the present development.

Each of the arms of the filter is resonant in the pass band. Alternate arms are also antiresonant at one or two trap frequencies just outside the pass band. In the end arms, the trap frequencies are used for image-impedance matching over the useful part of the pass band. In the intermediate arms, the trap frequencies are used for high attenuation in the stop band.

Next there will be presented in some detail the design of the wave filter.

Image-Parameter Design

The time-honored image-parameter viewpoint of Campbell and Zobel, as summarized by Shea, offers the only practical method for designing a filter of this degree of complexity [1, 2]. There are 25 lumped constants to be computed. There is no symmetry about the pass band, so we cannot use a low-pass analog to reduce to one-half the number of constants to be evaluated. The pass band and stop band are of such width and proximity that no simplifying assumptions are valid. The large number of elements makes it necessary to compute each one within close tolerances. The method of image parameters enables straightforward computations with reasonable simplicity.

Fig. 4 shows the complete filter arrangement to be computed, while Fig. 1 shows the attenuation pattern to be obtained. The kind of sections and the number of sections have been chosen to meet the requirements of this development, considering various factors that will be mentioned.

The filter is shown as a succession of shunt arms (9 as required for 8 contiguous half-sections) separated by quarter-wave sections or inverters. This is common practice in waveguides. Two types of sections are used. Most of the attenuation is provided by 3 sections of V type, a double-tuned section with a trap frequency above the pass band. At each end, impedance matching is provided by a half-section of the well-known M-derived VI type [1, 2]. These type designations are the customary ones based on the number of elements in one

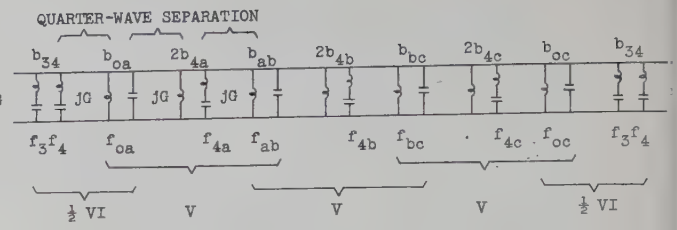

(a) Complete filter with inverters.

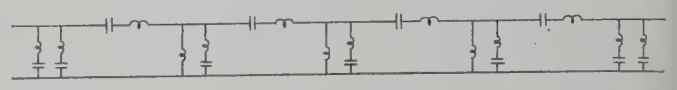

(b) Equivalent filter in ladder form.

Fig. 4—Complete band-pass wave filter of eight half-sections.

half-section (5 and 6 in these cases).

The attenuation pattern shows the nominal pass band (between cutoff frequencies) and the basis for defining the stop band (including 3 trap frequencies). In the present case, these bands are specified as mentioned above and in the example computed below. The two trap frequencies just above and below the pass band are determined by the impedance-matching requirement in the end half-sections.

The immediate purpose is to give the formulas for computing the lumped reactance arms in this filter. They will be evaluated in terms of shunt susceptance, this being suitable for realization and testing in shunt arms in a waveguide. This is the most direct way of specifying the required properties of the reactance arms which make up the filter.

Referring to the problem of voltage breakdown, the voltage at all the shunt arms, except the end arms, increases near the cutoff frequencies. This is a result of the increasing image resistance at these junctions. By using only 0.8 of the nominal pass band, the ratio of excess voltage, relative to midband, is held down to about 1.3, for the same pulse power.

In the pass band, the principal problem is impedance matching, which means avoiding reflections in the "confluent" wave filter. Dissipative attenuation is less important, except near the cutoff frequencies. In general, it is proportional to the phase slope and to the average dissipation factor of all the reactance elements. These factors combine to make such attenuation negligible over the utilized fraction of the pass band, so it is ignored in the design procedure.

The VI type is selected for the end half-sections because it is the simplest that can give, over 0.8 of the pass band, an image resistance that approximately matches a constant resistance. In this design, the image resistance at the ends of the filter is theoretically between the midband value and another value lower by 0.04 of the midband value. In order to obtain this property, the trap frequencies must be separated by 1.25 times the nominal bandwidth, so their values cannot be chosen for greatest benefit in attenuation.

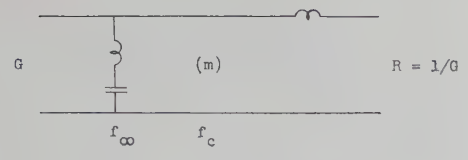

(a) Low-pass M-derived half-section (for reference).

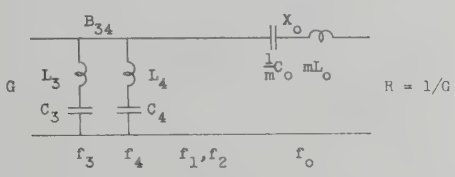

(b) VI-type M-derived half-section.

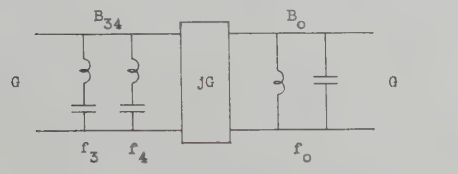

(c) VI-type half-section with inverter.

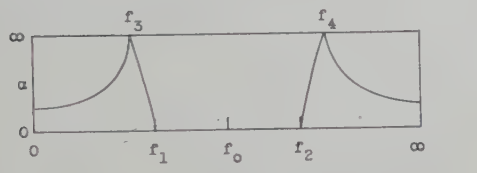

(d) Attenuation over frequency range.

Fig. 5—VI-type filter half-section.

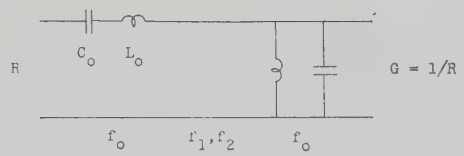

(a) IV-type constant-R half-section (for reference).

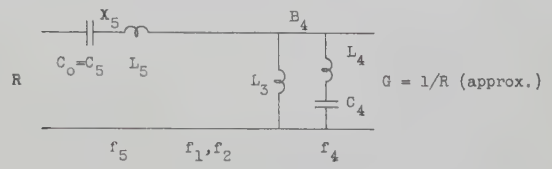

(b) V-type half-section.

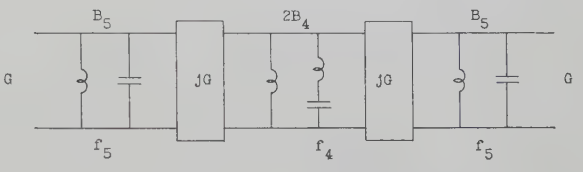

(c) V-type whole section with inverters.

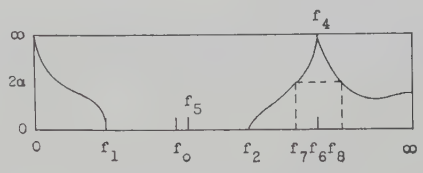

(d) Attenuation over frequency range.

Fig. 6—V-type filter section.

The V type is chosen for the repeating whole sections because it is the type of section that gives the greatest attenuation over a stop band just above the pass band. It was estimated that three such sections would give more than sufficient attenuation.

The actual attenuation or insertion loss outside the pass band is that obtained when the filter is connected between generator and load of equal values of constant resistance. This condition is approximated in practice. The actual attenuation always exceeds the image attenuation, so the latter is safely assumed as a basis for estimating the required number of sections

The inverter or quarter-wave section is a part of this design [4], [6], [7], [9], [10]. It enables a ladder network of series and shunt arms to be simulated by a sequence of shunt arms, the kind best suited for a waveguide structure. Theoretically, the inverter is a section of waveguide having a length of one-quarter wave at all frequencies. It is so called because any impedance, seen through the inverter, appears to have its value inverted about the wave resistance of the inverter. Since G is the wave conductance at midband, the symbol for the inverter is jG; this is chosen because the equivalent pi or T network has three arms of values $\pm jG$. In practice, the effective length of the quarter-wave section varies somewhat over the pass band, and these variations are taken into account in the design of the adjacent shunt arms. There is one inverter per half-section; this determines the total length in waveguide.

Having given a general description of the filter, there follows a more specific description of each of the two types of sections (Shea, [1], [2]).

Fig. 5 shows the VI-type half-section. Since its properties have ratio symmetry about the midfrequency (meaning, the same properties at equal frequency ratios above and below the midfrequency), this type has a low-pass analog [Fig. 5(a)] which is a helpful reference in formulating the band-pass filter. The low-pass cutoff frequency (f_c) is half the bandwidth of the band-pass filter ($f_2 - f_1$). The low-pass trap frequency (f_∞) is similarly related to the band-pass trap frequencies (f_3, f_4).

The band-pass half-section [Fig. 5(b)] is shown in conventional ladder form. The series arm is evaluated in terms of the corresponding constant-K (IV type) series arm (C_0, L_0) and the constant (m) of this M-derived type. The inverter form [Fig. 5(c)] has two shunt arms (instead of one shunt and one series) separated by the inverter (jG). Each shunt arm contains the indicated susceptance (B_{34}, B_0). The attenuation diagram [Fig. 5(d)] shows the variation of the attenuation (α) outside the pass band.

Fig. 6 shows the V-type section. Since its properties do not have symmetry about the pass band, there is no low-pass analog. A helpful reference is the IV-type band-pass half-section [Fig. 6(a)]. Its series and shunt arms are resonant at the midfrequency (f_0). The V-type half-section [Fig. 6(b)] has a series arm resonant at a frequency (f_5) within the pass band but above midband. The shunt arm as a whole is resonant at the same fre-

TABLE I

FORMULAS FOR VI TYPE

$$m = 0.6 \tag{1}$$

$$f_c = \frac{f_2 - f_1}{2} \tag{2}$$

$$f_\infty = \frac{f_4 - f_3}{2} = \frac{f_c}{\sqrt{1 - m^2}} = 1.25 f_c \tag{3}$$

$$f_0 = \sqrt{f_1 f_2} = \sqrt{f_3 f_4} \tag{4}$$

$$f_4, f_3 = \sqrt{f_0^2 + f_\infty^2} \pm f_\infty \tag{5}$$

$$Q_0 = \frac{m L_0 \omega_0}{R} = \frac{m f_0}{f_2 - f_1}. \tag{6}$$

At f_1 and f_2:

$$|b_0|_1 = |b_0|_2 = m = 3/5 \tag{7}$$

$$|b_{34}|_1 = |b_{34}|_2 = 1/m = 5/3. \tag{8}$$

At $f = 0$ or ∞:

$$\sinh \alpha = \frac{m}{\sqrt{1 - m^2}} = 3/4; \alpha = 0.693 = 6.02 \text{ db}. \tag{9}$$

Note: 1 napier = 8.686 db.

Note: Over 4/5 of nominal pass band, this value of m holds the reflection coefficient less than 0.020 at each M-derived termination; for two terminations, SWR < 0.7 db.

TABLE II

FORMULAS FOR V TYPE

For $\cosh \alpha_7 = \sinh \alpha_8$;

$\alpha_7 \doteq \alpha_8$ if $\exp -2\alpha_7 \ll 1$:

$$f_4^2 = f_7^2 + \frac{f_8^2 - f_7^2}{1 + \frac{f_7^2}{f_8^2}\left(\frac{f_8^2 - f_5^2}{f_7^2 - f_5^2}\right)^2}. \tag{10}$$

Before f_5 is known, substitute f_0 as approximation in preceding formula.

$$m_5 = \frac{1 - \left(\frac{f_2 - f_1}{\sqrt{f_4^2 - f_1^2} + \sqrt{f_4^2 - f_2^2}}\right)^2}{1 + \left(\frac{f_2 - f_1}{\sqrt{f_4^2 - f_1^2} + \sqrt{f_4^2 - f_2^2}}\right)^2} \tag{11}$$

$$f_5 = f_0/\sqrt{m_5} = \sqrt{f_1 f_2/m_5} \tag{12}$$

$$f_6 = \sqrt{f_7 f_8} \tag{13}$$

$$Q_5 = \frac{L_5 \omega_5}{R} = \sqrt{m_5}\,\frac{f_0}{f_2 - f_1} \tag{14}$$

At f_1: $|b_5|_1 = |1/b_4|_1 = 1 + (1 - m_5)\dfrac{f_1}{f_2 - f_1}$ (15)

At f_2: $|b_5|_2 = |1/b_4|_2 = 1 - (1 - m_5)\dfrac{f_2}{f_2 - f_1}$ (16)

$$\text{av}\,|b_5| = \text{av}\,|1/b_4| = \frac{1 + m_5}{2} \tag{17}$$

$$\cosh \alpha_7 = \frac{f_2(f_7^2 - f_5^2)}{f_7(f_2^2 - f_5^2)} \sqrt{\frac{f_4^2 - f_2^2}{f_4^2 - f_7^2}} \tag{18}$$

$$\sinh \alpha_8 = \frac{f_2(f_8^2 - f_5^2)}{f_8(f_2^2 - f_5^2)} \sqrt{\frac{f_4^2 - f_2^2}{f_8^2 - f_4^2}}. \tag{19}$$

$$\text{At } f = \infty\text{: } \sinh \alpha = \frac{f_2\sqrt{f_4^2 - f_5^2}}{f_2^2 - f_5^2}. \tag{20}$$

If $f_4/f_5 < \sqrt{2}$, there is a minimum attenuation at

$$f = \frac{f_4}{\sqrt{2 - (f_4/f_5)^2}}\text{: } \sinh \alpha = \frac{2 f_2 f_5 \sqrt{(f_4^2 - f_2^2)(f_4^2 - f_5^2)}}{f_4^2(f_2^2 - f_5^2)}. \tag{21}$$

Extra attenuation by staggering n sections:

$$\Delta\alpha = (n - 1)6 \text{ db}. \tag{22}$$

Note: To distinguish from sub-4 in VI type, substitute sub-4*a*, 4*b*, 4*c* in successive sections of V type. For sub-5, substitute sub-*a*, *b*, *c* (shortened from sub-5*a*, 5*b*, 5*c*).

quency, and one branch (C_4L_4) is resonant at the trap frequency (f_4).

It is noted that the V-type half-section is a combination of two simpler types (Shea, III_2 and IV_1 [1], [2]) with an intervening ideal transformer. There are some advantages in deriving the formulas for these parts separately and then combining them to form the V type, which was done for the present purpose. (The IV and VI types can likewise be subdivided, but this offers no advantage in the case of frequency patterns having ratio symmetry.)

The inverter form of whole section [Fig. 6(c)] contains two inverters and the shunt arms of two half-sections (B_5, $2B_{34}$, B_5). The attenuation diagram [Fig. 6(d)] shows the variations of the attenuation (2α of two half-sections) outside the pass band.

The first objective in the V type is the selection of a trap frequency (f_4) which will give equal attenuation at the two edges of the stop band (f_7, f_8). This is nearly the optimum for several like sections of V type between the VI-type half-sections, because the latter contribute much less attenuation in the stop band. There will be given some formulas for approximately computing the best trap frequency.

In several sections of V type, there is a set of unequal trap frequencies (f_{4a}, etc.) that will give greatest attenuation over the stop band. For the present case of three sections, such a set is indicated in Fig. 1. There has been derived for this development a simple and explicit procedure for approximately evaluating such a set of trap frequencies, but this procedure is beyond the present scope [16]. The principles are familiar.

There has been found a simple rule for the advantage to be gained by staggering the trap frequencies in this manner rather than repeating the same value. The minimum attenuation over the stop band is thereby increased by $(n-1)6$ db for n sections. Staggering the trap frequencies for three sections gives 12 db more attenuation.

The formulas to be given are based on the theoretical lumped constants of the ladder form, leading to the corresponding shunt arms of the inverter form. Some significant ratios are formulated, such as the susceptance ratio ($b = B/G$) and the resonance ratio (Q). In most cases, the formulas are given in such forms that the narrow-band approximations are simple and perhaps apparent. Ratios are expressed in terms of the cycle frequencies (f) but the radian frequencies (ω) may be substituted.

Table I gives the formulas for the VI type of Fig. 5. The specified value of the derivation constant ($m = 0.6$) gives a favorable pattern of image conductance at the

TABLE III
PRESENT DESIGN VALUES

Pass:	$f_1 = 3.05, f_2 = 3.55$ kmc.
Stop:	$f_7 = 3.70, f_8 = 4.00$.
(1)	$m = 0.6$
(2)	$f_c = 0.25$
(3)	$f_\infty = 0.3125$
(4)	$f_0 = 3.290$
(5)	$f_3 = 2.992, f_4 = 3.617$
(10)	$f_4 = 3.78$
(11)	$m_5 = 0.961$
(12)	$f_5 = 3.358$
(13)	$f_6 = 3.847$
Changing subscripts from 5 to a, b, c; and from 4 to $4a$, $4b$, $4c$:	
	$f_{4a} = 3.708$, $f_{4b} = 3.780$, $f_{4c} = 3.953$
(11)	$m_a = 0.951$, $m_b = 0.961$, $m_c = 0.973$,
(12)	$f_a = 3.378$, $f_b = 3.358$, $f_c = 3.337$
(9)	2 half-sections (VI), $2\alpha > 12.04$ db
(18)	$\alpha_7 = 1.75$ nap $= 15.2$ db
(19)	$\alpha_8 = 1.87$ nap $= 16.2$ db
Average:	$\alpha_{78} = 1.81$ nap $= 15.7$ db
(21)	min $\alpha = 1.77$ nap $= 15.4$ db
Total:	Stopband, min. attenuation:
	2 half-sections (VI) > 12.0 db
	6 half-sections (V) 94.2 db
	Stagger 3 sections 12 db
	>118.2 db

Note: See Fig. 7 for pattern of all frequencies.

termination whose midshunt arm includes the pair of trap resonators (f_3, f_4). Over the middle 0.8 of a narrow pass band, the image conductance departs from its midband value (G) by less than -0 and $+0.04$ of this value.

The formulas are simplified by starting with the low-pass analog and converting to the band-pass frequency scale with ratio symmetry.

Outside the trap frequencies, the image attenuation approaches but always exceeds the limiting value given by (9), which is 6 db per half-section. Therefore each of the end half-sections may be relied on for this much attenuation.

Table II gives the formulas for the V type of Fig. 6. The derivation of the V type involves a constant (m_5) which is slightly less than unity; it is expressed in a form to bring out its small difference from unity.

One problem in computation is the interrelation of the formulas for f_4 (10) and f_5 or m_5 (11, 12). The value of f_4 need be evaluated only approximately, because it is required only for optimizing the stop band attenuation and not for validity of the filter design. For this approximation, it is here sufficient to substitute f_0 for f_5 in (10) for computing f_4. As mentioned above, the staggering of f_4 in several sections is not formulated here although it is employed in the example to be described [16].

At the junction of two different half-sections in a common shunt arm, their susceptance ratios are merely added to get the composite value.

In each shunt arm, it is sufficient to specify the one or two trap frequencies and the susceptance ratios at the two cutoff frequencies. All lumped constants are then determined. This specification is considered to be the best basis for testing the simulation in a waveguide iris, because the trap frequencies are most easily measured and the susceptance is most critical near cutoff.

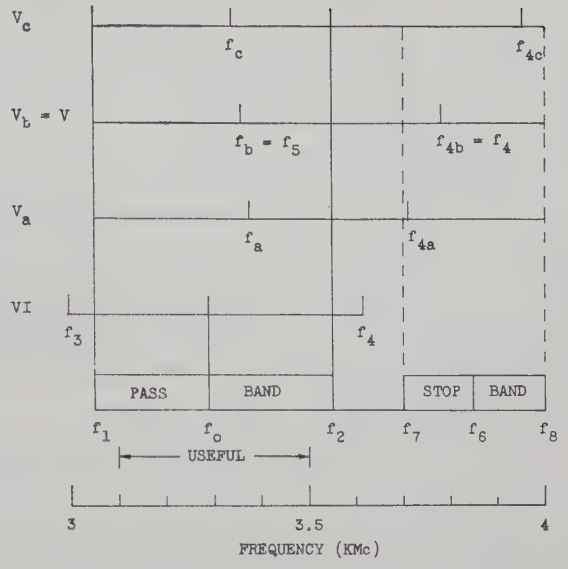

Fig. 7—Diagram of design frequencies.

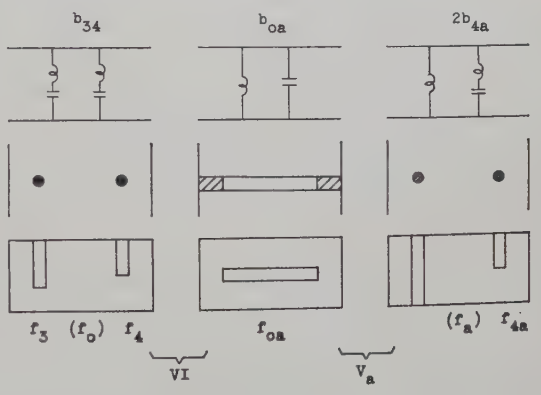

Fig. 8—Iris shunt arms in waveguide.

Table III gives the critical frequencies and attenuation computed for the present design. Fig. 7 is a diagram of these frequencies. The susceptance ratios are easily computed from the critical frequencies, to complete the specifications for the shunt arms.

SPECIFYING AND TESTING DISTRIBUTED ARMS

An iris in a waveguide is a distributed circuit complex that can be used to simulate a set of lumped constants, not exactly but to a close approximation. The approximation is best if the specifications are based on the most critical properties, and on those that can be tested most accurately. Naturally, any test must be based on a valid definition of the property to be simulated.

Fig. 8 shows the types of shunt arms that are to be simulated, and the iris structures to be used for this purpose. These are based on familiar principles. Each iris is resonant (zero susceptance) at a frequency in the pass band (f_0, f_{0a}, f_a). Two types have antiresonance (infinite susceptance) provided by posts resonant at the frequen-

cies noted. In general, all parts of one iris are interdependent. (The interaction between successive irises is ignored in computation but may require a small correction by experiment.)

For defining the objective of each shunt arm or iris, reference is made to the composite filter, as shown in Fig. 4. In the ladder form, one arm is isolated by properly removing the two adjacent arms. A shunt arm is isolated by an open-circuit in each adjacent series arm. Carrying this reasoning over to the inverter form, one shunt arm is isolated by a short-circuit on each adjacent shunt arm; through the inverter, this appears to be an open-circuit, as required.

This viewpoint is powerful because it gives a definition which may be interpreted to include the imperfections of the inverters, to a first approximation. Each shunt arm may utilize the small susceptance of the quarter-wave section, that remains at frequencies differing from its design frequency (presumably midband). Therefore, the susceptance of the arm at each end includes that of one quarter-wave section, while the susceptance of each intermediate arm includes twice that amount.

Fig. 9 shows how this principle may be applied in measuring the susceptance of one shunt arm in a waveguide. There are different procedures for an end arm or an intermediate arm, to be described with reference to Fig. 9(a).

In the case of an end arm, its susceptance is measured with a fixed short-circuit $\frac{1}{4}$ wavelength behind, so its susceptance is included as part of the shunt arm.

In the case of an intermediate arm, it is not so simple, because one side must be left accessible for the measurement. Measurements of the susceptance are made with a fixed short-circuit, first at $\frac{1}{4}$ and then at $\frac{3}{4}$ wavelength behind. The average of these two is the desired susceptance, which includes twice the susceptance of a quarter-wave section. Fig. 9(b) shows how these tests would appear on the rim of the reflection chart.

Since the iris has some thickness, however small, there is some question as to where the reference plane is. It can be determined by applying some insight in any particular case, if that degree of precision is needed [18].

The trap frequencies are most easily measured by the deep minimum in a transmission test. This is substantially independent of generator, load, and adjacent quarter-wave lines. A susceptance test should place this point on a pole of the reflection chart, such as f_4 in Fig. 9(b). (This fact may be used to locate the proper reference plane [18].)

By these techniques, an iris may be adjusted by trial to simulate a computed shunt arm in a waveguide. The entire filter is assembled from the 9 irises adjusted according to these formulas and rules.

Low-Power Tests

The low-power performance comprises frequency characteristics without regard for pulse-power capability, so there is no appreciable difference between air and vacuum. (Presumably, there is a slight difference caused by mechanical deformation under differential pressure.) The dimensions of essential contours were specified on the basis of tests in air, then transferred to the final design for evacuation.

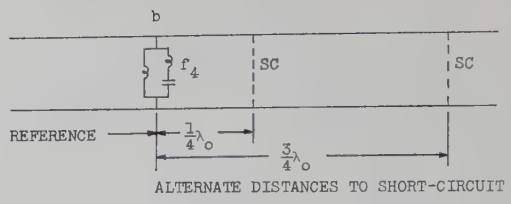

(a) Arrangement of iris in measuring line.

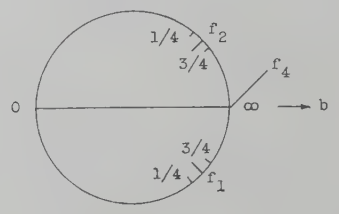

(b) Plot of observations on reflection chart.

Fig. 9—Test for susceptance of shunt arm in waveguide.

The tests to be presented were made on a single filter, between nonreflecting input and output waveguides, before installing the pressure windows. The performance in the pass band is plotted in Fig. 10 for the experimental model, all dimensions having been determined by separate tests of the irises. The performance is described in terms of reflection and attenuation.

The experimental model was found to have the pass band located about 1 per cent higher than intended, in frequency. Presumably this was caused by interaction between the irises, which were assumed independent, though separated only by a distance comparable with their height. By way of compensation, all dimensions were then specified 1 per cent larger than the model in order to center the actual pass band on the desired pass band. The curves in Fig. 10 are shifted, relative to the observed curves, 1 per cent lower in frequency, to show what would be expected after this change in dimensions.

In Fig. 10(a), the reflection is plotted in terms of standing-wave ratio (SWR) over the pass band. The upper curve (dotted line) was observed when first assembled after designing the irises individually, and represents the cumulative errors of the many dimensions and some approximations in the assumptions for equivalence to the lumped network. The lower curve (solid line) was observed after corrective elements (inductive posts) had been inserted in the quarter-wave section at each end. Before this correction, the reflection was within 6.5 db SWR over the useful band; afterward, it was within 4 db SWR.

In Fig. 10(b), the insertion loss is plotted from tests on the experimental model, after insertion of the corrective elements. It is the sum of two parts respectively caused by reflection and dissipation. The reflection loss

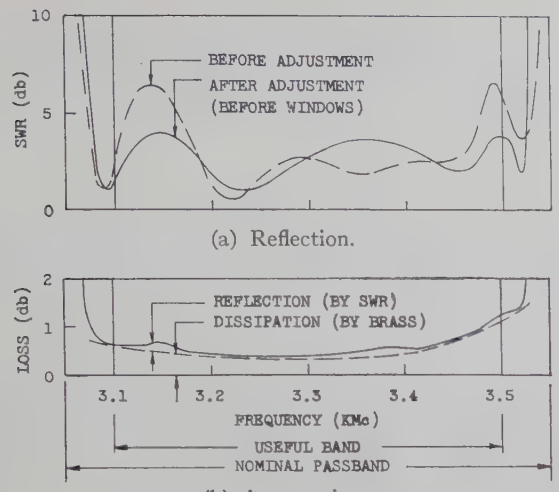

(a) Reflection.

(b) Attenuation.

Fig. 10—Reflection and attenuation in pass band.

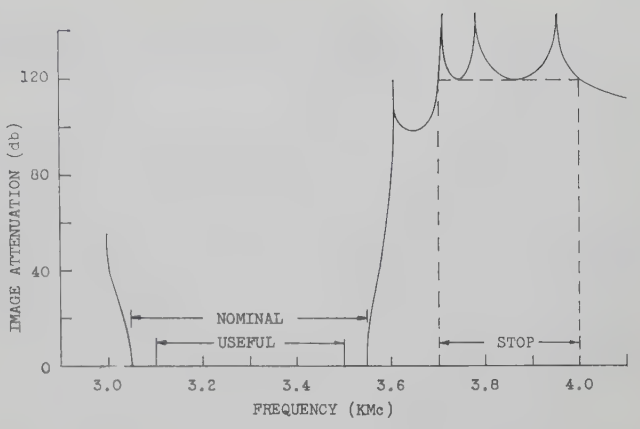

Fig. 11—Attenuation above pass band.

by about 0.2 db. The sum of these effects hold the dissipation loss. The reflection loss is related to the SWR plotted in Fig. 10(a). The remaining loss is caused by skin dissipation in the metal walls. The latter is proportional to phase slope over the pass band; it has a minimum value (about 0.3 db) at mid-band and increases at the edges of the useful band. The total insertion loss is within 1.2 db over the useful band, averaging about 0.6 db.

The properties of the experimental model are modified slightly by two differences in the final design, as follows:

	Experimental	*Final*
Metal walls	Brass	Copper
Pressure windows	Omitted	Included

The change from brass to copper reduces the skin dissipation by a factor of $\frac{1}{2}$. The addition of the glass windows for pressure sealing increases the dissipation loss within a lower limit, but leaves the average about the same. The windows slightly increase the reflection. The result is reflection within 6 db SWR and total insertion loss within 1.0 db over the useful band, averaging about 0.7 db.

In Fig. 11 is plotted the attenuation above the pass-band, computed on an image basis. It is over 120 db in the specified stop band. Tests of the experimental model over the stop band have verified that the attenuation exceeds 70 db, the limit of the equipment used. Interpretation of this information requires consideration of the modes in the waveguide.

As a general rule, when operating between input and output circuits of matched pure resistance, a lumped network provides an amount of insertion loss greater than the image attenuation. This rule would apply to the present case if we could consider only the propagating mode in the waveguide and ignore the higher modes. In the reduced size of waveguide chosen for the filter structure, the higher modes are propagated only above 4.3 kmc, which is well above the specified stop band. However, there remains some doubt whether the higher modes are negligible in the stop band. Another factor, probably of less importance, is the distributed nature of the iris shunt arms, which are assumed to simulate closely the lumped equivalents. In view of these considerations, it is uncertain whether the actual attenuation is greater or less than the computed image attenuation.

The nonreflecting assembly converts the wave filter (which attenuates only by reflection) into a selective attenuator. The attenuation in the stop band is substantially the same as the insertion loss caused by a single filter between nonreflecting input and output waveguides.

In the pass band, the reflection from the assembly is that of the hybrid junctions plus the uncanceled difference of the reflections from the pair of filters (since they will not be exactly alike). The difference of the transmission through the pair of filters causes a slight loss in recombination, which is added to the dissipation loss.

The discussion of Figs. 10 and 11 indicates the low-power performance to be expected of this design, and the extent to which this performance has been verified by tests.

High-Power Considerations

The nonreflecting assembly is intended to carry one-megawatt pulses of about one microsecond duration with some safety factor for moderate reflection from the load (say 3 db SWR). This means that each filter should be able to carry pulses of 0.5 megawatt into the reflecting load or 0.7 megawatt into a matched load, with some margin.

As is usually the case in pulse transmission, the power limitation is imposed by voltage breakdown in the dielectric, not by heating. This amount of pulse power is easily handled by air in ordinary waveguide and accessories, but the insertion of the resonators in the present filter tends to cause much higher gradients.

Such resonance can be obtained in a spacious cavity, such as a half-wave section of guide, without excessive gradient. However, this kind of resonator presents several difficulties. For the present purpose, the principal fault would be the failure of attenuation at frequencies somewhat higher than the pass band, where most at-

tenuation is required. Other handicaps are the greater size and the greater difficulty of choosing and simulating a suitable lumped network.

It was desired to realize the required resonance in the most compact form that could be readily predicted and constructed. The so-called "wide-band" TR tubes had a background of theory and structural experience, including evacuation and pressure sealing, so it was decided to use the same principles and general arrangement for the present filter. This decision was based on the idea of complete evacuation to prevent voltage breakdown, so fairly small gaps would stand the voltage.

In accordance with the practice in TR tubes, the partition for the simple resonant iris was made of fairly thin sheet ($\frac{1}{16}$ inch) for ease of construction. This required a slot of width comparable with the thickness (minimum about $\frac{1}{16}$ inch). The resulting small gap and the open ends of the resonant posts experience the highest gradient.

The voltage across the slot exceeds 20 kv rms and the maximum gradient reaches about 20 kv/mm rms, which is about 10 times that of air. Comparable gradients are experienced in the magnetron for which the present filter is designed. However, it has been found difficult to maintain in a cold structure the degree of evacuation and surface purity required to withstand this gradient without some kind of discharge.

Some samples have been made which carried pulse power through a pair of filters into a matched load, up to about 1 megawatt, the maximum used in the tests. Further improvements are in progress, particularly in the techniques of evacuation.

Conclusion

For suppressing spurious transmission from a certain *S*-band radar, there has been designed a nonreflecting filter assembly in which the principal feature is the pair of wave filters built in waveguide and evacuated to carry high-power pulses.

Each of these wave filters is made of 25 reactors or their equivalent in 9 reactance arms suitable for waveguide shunt arms. These involve 5 trap frequencies outside the pass band and some reasonance frequencies near midband. The image-parameter method of design, based on the wave-filter concept, has enabled all computations in explicit form. Among the features are *M*-derived terminations for impedance matching over the pass band, another type of section giving greatest attenuation above the pass band, and the staggering of the trap frequencies in several sections of this type for maximum attenuation over the stop band. This is the only method of design known to the writers that would yield comparable performance with a reasonable amount of effort.

The specifications for all reactance arms are presented in a form suitable for testing simulation in shunt arms made of irises in a waveguide. The recommended set of essential quantities includes only the trap frequencies and the susceptance ratios at the cutoff frequencies. The application of these formulas has yielded a practical design reasonably fulfilling the expectations based on the computations.

Acknowledgments

The writers wish to express their appreciation of the contributions and assistance of their associates, particularly I. Koffman, who performed most of the experimental work.

Bibliography

[1] T. E. Shea, "Transmission Networks and Wave Filters," D. Van Nostrand Co., Inc., New York, N. Y.; 1929. (Band-pass filters, pp. 315–318.)

[2] F. E. Terman, "Radio Engineers' Handbook," McGraw-Hill Book Co., Inc., New York, N. Y.; 1943. (Band-pass filters, pp. 230–231.)

[3] W. D. Lewis and L. C. Tillotson, "A non-reflecting branching filter for microwaves," *Bell. Sys. Tech. J.*, vol. 27, pp. 83–95; January, 1948. (Branching filter using hybrid junctions and quarter-wave path difference for band selection without causing reflection in input and output lines.)

[4] H. A. Wheeler, "Transmission lines and equivalent networks," *Wheeler Monographs*, vol. 1, no. 1; April, 1948. (Concept of inverter, references.)

[5] C. G. Montgomery, R. H. Dicke, and E. M. Purcell, "Principles of Microwave Circuits," *M.I.T. Rad. Lab. Ser.*, McGraw-Hill Book Co., Inc., New York, N. Y., vol. 8; 1948. (Resonant irises in waveguide, hybrid junctions, directional couplers.)

[6] A. W. Lawson and R. M. Fano, "The Design of Microwave Filters," M.I.T. Rad. Lab. Ser., McGraw-Hill Book Co., Inc., New York, N. Y., vol. 9, ch. 10, pp. 613–716; 1948. (Includes resonant irises spaced $\frac{1}{4}$ wavelength in waveguide, many references.)

[7] W. C. Caldwell, "Bandpass TR Tubes," M.I.T. Rad. Lab. Ser., McGraw-Hill Book Co., Inc., New York, N. Y., vol. 14, ch. 3, pp. 67–114; 1948. (Filters made of resonant irises spaced $\frac{1}{4}$ wavelength in waveguide, pressure windows, references.)

[8] C. W. Zabel, "Balanced Duplexers," M.I.T. Rad. Lab. Ser., McGraw-Hill Book Co., Inc., New York, N. Y., vol. 14, ch. 8, pp. 350–375; 1948. (Nonreflecting filter, properties of hybrid junctions.)

[9] H. A. Wheeler, "Generalized transformer concepts for feedback amplifiers and filter networks," *Wheeler Monographs*, vol. 1, no. 5; August, 1948. (Inverter concept between shunt arms, references.)

[10] W. W. Mumford, "Maximally-flat filters in waveguide," *Bell Sys. Tech. J.*, vol. 27, pp. 684–713; October, 1948. (Concept of inverter and shunt arms; references.)

[11] N. Marcuvitz, "Waveguide Handbook," M.I.T. Rad. Lab. Ser., McGraw-Hill Book Co., Inc., New York, N. Y., vol. 10; 1951. (Simulation of lumped circuits in waveguide structures.)

[12] H. J. Riblet, "The short-slot hybrid junction," Proc. IRE, vol. 40, pp. 180–184; February, 1952. (Properties of 3-db side-wall directional coupler, application to nonreflecting filter used as balanced duplexer, many references.)

[13] E. Hadge, "Compact top-wall hybrid junction," IRE Trans. on Microwave Theory and Techniques, vol. MTT-1, pp. 29–30; March, 1953. (Pair of parallel slots in common wide face of parallel waveguides.)

[14] H. Heins, "Radar duplexer uses dual TR tubes," *Electronics*, vol. 27, pp. 149–151; August, 1954. (Nonreflecting filters, simple explanation.)

[15] C. W. Jones, "Broad-band balanced duplexers," IRE Trans. on Microwave Theory and Techniques, vol. MTT-5, pp. 4–12; January, 1957. (Nonreflecting filter, side-wall and top-wall short-slot 3-db directional couplers as hybrid junctions.)

[16] H. A. Wheeler, "Image-Parameter Design of *S*-Band Waveguide Filter," Wheeler Labs., Great Neck, N. Y., Rep. 765; November 15, 1957. (The present topic, complete design formulas.)

[17] H. L. Bachman, "A Waveguide Filter for Suppressing the Spurious Transmission of a High-Power *S*-Band Radar," Wheeler Labs., Great Neck, N. Y., Rep. 764; 1958. (In preparation.) (Main report on this project, list of other reports, pp. 765–769.)

[18] H. L. Bachman, "Specifying and testing distributed elements in *S*-band waveguide filter," Wheeler Labs., Great Neck, N. Y., Rep. 766; April 16, 1958.

[19] R. D. Campbell, "Radar interference to microwave communication services," *AIEE Trans.*, Paper No. 58-817, preprinted and presented before AIEE; June, 1958. (The operational situation requiring the *S*-band filter described in present paper.)

Hybrid Junction—Cutoff Waveguide Filters*

EUGENE N. TORGOW†

Summary—Low-pass and band-pass filter characteristics can be obtained in waveguide by the use of an arrangement of a waveguide hybrid junction and lengths of cutoff waveguide. Low-pass filters are obtained by terminating a conjugate pair of ports of the hybrid in identical cutoff waveguide sections through short lengths of phase correcting lines. Band-pass characteristics can be realized by introducing a third cutoff waveguide having a lower cutoff frequency at the input port of the hybrid.

These filters have a matched input at all frequencies above the lower end of the pass band and are characterized by low-pass band insertion loss, steep skirt selectivity, and moderate rejection band attenuation. The power handling capabilities of the structure exceed those possible with conventional microwave filter circuits, and the design is particularly well suited for use at frequencies above 10 kmc. Simple techniques are available for constructing filters of this type having variable cutoff frequencies and variable bandwidths.

Introduction

THE waveguide filter design techniques most commonly used today are based upon the approximate equivalence of lumped networks to such structures as iris loaded waveguide, corrugated waveguides, and coupled cavity structures.[1–3] Recently a class of directional filters has been described which makes use of frequency selective couplers to extract a desired narrow band of frequencies from one port of a multiport structure.[4,5] These filters present a matched input impedance at all frequencies as signals in the rejection band are extracted from a third port of the filter rather than reflected back to the input. The filter to be described in this paper is related to the directional filter class in that it too delivers one band of frequencies to one port and the remaining frequencies to the other ports, and presents a matched input impedance in the rejection band as well as in the pass band. This filter makes use of a hybrid junction and relies upon the frequency selective reflections from cutoff waveguides rather than frequency selective coupling. Relatively wide band filters can be obtained by this technique. Another type of filter employing Tee junctions and cutoff waveguides has been described[6] which utilizes short-circuited lengths of cutoff guides as reactive elements to obtain low-pass and band rejection filters. The principle of operation and the performance of these filters are quite different from those of the filter to be described here.[7]

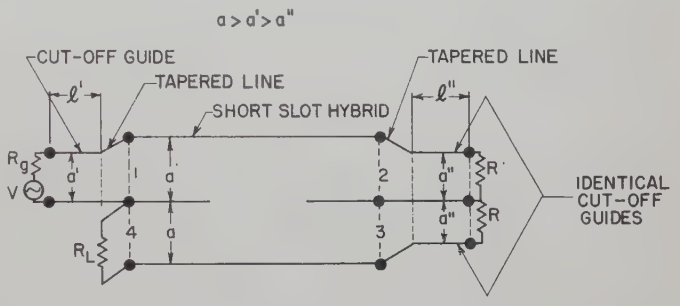

Fig. 1—Short slot hybrid band-pass filter.

Theory of Operation

A band-pass filter employing a short slot hybrid junction is illustrated in Fig. 1. Two conjugate arms of the hybrid (labelled ports 2 and 3) are connected to identical sections of cutoff waveguide through linear tapers. The cutoff sections are in turn terminated in matched resistive loads. The input to the hybrid (port 1) is connected through linear tapers to a waveguide having a lower cutoff frequency than that of the guides at ports 2 and 3. The output is taken from port 4. When a signal is applied to the input of the filter, only those frequencies above the cutoff of the input guide will enter the hybrid at port 1. In the ideal case, the power into the hybrid divides equally and appears at ports 2 and 3 with the signals at these ports 90 degrees out of phase. If the signal frequency is below the cutoff of the guides terminating these ports, the signal power undergoes complete reflection. Due to the 90 degrees difference in phase between the two signals reflected from ports 2 and 3, and the additional phase displacement each reflected signal experiences in traversing the coupler, the signals arrive in phase at port 4 and in phase opposition at port 1. Therefore, signals applied to the input port at frequencies between the cutoff frequency of the input guide and the cutoff frequency of

* Manuscript received by the PGMTT, June 23, 1958; revised manuscript received, September 2, 1958. The work described here was sponsored by the Rome Air Dev. Center under Contract No. AF-30(602)-1650.

† Microwave Res. Inst., Polytechnic Inst. of Brooklyn, Brooklyn, N. Y.

[1] W. W. Mumford, "Maximally flat filters in waveguide," *Bell Sys. Tech. J.*, vol. 27, p. 684 ff.; October, 1948.

[2] S. B. Cohn, "Analysis of a wide-band waveguide filter," PROC. IRE, vol. 37, pp. 651–656; June, 1949.

[3] J. R. Whinnery, "Design of microwave filters," Proc. of the Symposium on Modern Network Synthesis, Polytechnic Inst. of Brooklyn, Brooklyn, N. Y.; April, 1952. This article presents a complete summary of the art of microwave filter design and has an extensive bibliography.

[4] F. S. Coale, "A traveling wave directional filter," IRE TRANS. ON MICROWAVE THEORY AND TECHNIQUES, vol. MTT-4, pp. 256–260; October, 1956.

[5] S. B. Cohn and F. S. Coale, "Directional channel-separation filters," 1956 IRE CONVENTION RECORD, pt. 5, pp. 106–112.

[6] Rizzi, P. A., "Microwave filters utilizing the cutoff effect," IRE TRANS. ON MICROWAVE THEORY AND TECHNIQUES, vol. MTT-4, pp. 36–40; January, 1956.

[7] The author has recently learned that a similar approach employing hybrid junctions and band rejection filters has been described by W. D. Lewis of the Bell Telephone Labs. (U.S. Pat. No. 2,531,447.) However, Lewis did not consider the use of cutoff waveguide sections and the advantages gained by their use.

the two lines connected to ports 2 and 3 will arrive at port 4 and will suffer no attenuation in the ideal case. Signals at frequencies above the upper cutoff frequency will arrive at ports 2 and 3, be transmitted through the two guide sections and be absorbed by the resistive terminations to these two guides. Thus these signals will not appear at port 4 and band-pass characteristics are obtained between port 1 and port 4.

Fig. 2 shows a similar filter employing a magic-Tee junction in place of the short slot hybrid. The basic principle of operation in this case differs from the previous case in that there is no phase difference between the signals arriving at the conjugate arms 2 and 3. In order to cause signals reflected from these ports to emerge from port 4, it is necessary to reverse the phase of one of these reflected waves re-entering the Tee. This is accomplished by the introduction of a length of line l_1, whose electrical length is 90 degrees, between the terminals of port 2 (or port 3) and the cutoff terminating section. This length of line has no effect on the performance of the filter in its rejection band, although the presence of this length of line will affect the performance of cascaded filters of this type. While the assumption was made that the electrical length of the inserted line section was 90 degrees at all frequencies in order to explain the operation of the filter, it will be shown that when an actual line is used which has an electrical length of 90 degrees at the mid-frequency of the pass band, relatively wide pass bands can still be obtained. Low-pass filters can be obtained by omitting the cutoff waveguide section at the input to port 1.

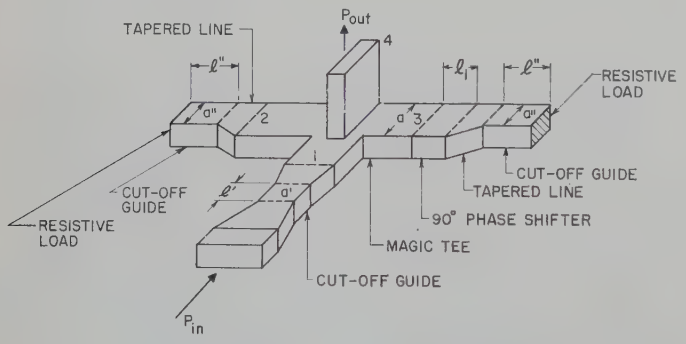

Fig. 2—Magic-Tee band-pass filter.

Linear tapers were used between the cutoff lines and the full width waveguide to improve the rejection band response of the filters. Their use does not affect the pass band performance of the filters as long as the two tapers at the outputs of ports 2 and 3 are identical, for they only serve to change the phase of the reflections from the cutoff guides by the same amount. In the rejection band, however, they serve to reduce the reflections from these guides, thereby insuring that the rejection band attenuation remains high. A step discontinuity, at this point, could introduce significant reflections, and this reflected energy would appear at port 4.

The performance of the hybrid junction-cutoff waveguide filters can be described by the following set of equations for the circuit illustrated in Fig. 3:

$$V_{r_1} = V_{i_1}(S_2S_{12}^2 + S_3S_{13}^2) \tag{1}$$

$$V_{r_4} = V_{i_1}S_{12}S_{13}(S_3 \pm S_2) \tag{2}$$

where

$$S_2 = \frac{V_{i_2}}{V_{r_2}} \quad \text{and} \quad S_3 = \frac{V_{i_3}}{V_{r_3}}.$$

Therefore,

$$\text{insertion loss} = 20 \log \left| S_{12}S_{13}(S_3 \pm S_2) \right| \tag{3}$$

$$\text{input reflection factor} = (S_2S_{12}^2 + S_3S_{13}^2). \tag{4}$$

These expressions were derived by making use of the symmetries in the scattering matrix of an ideal, lossless reciprocal hybrid, namely:

$$S_{ii} = 0 \qquad S_{12} = S_{34}$$

$$S_{14} = S_{23} = 0$$

$$S_{ij} = S_{ji} \qquad S_{13} = \pm S_{24}$$

where the positive sign applies to the short slot hybrid and the negative sign applies to the magic-Tee. The reflection factors of the terminations S_2 and S_3 are defined in Fig. 3 in terms of the incident and reflected voltages as defined for the four-port. It will be recognized that the voltage incident upon the port of the hybrid is the voltage reflected from the termination, and vice versa.

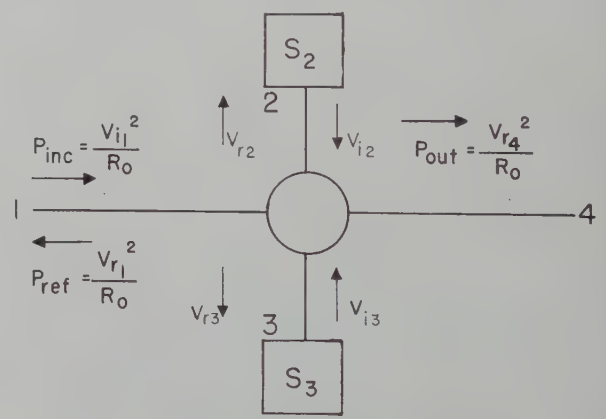

Fig. 3—Schematic diagram of a low-pass filter.

While these expressions are based upon the assumption that the hybrid junction exhibits ideal characteristics, they have been used to analyze the behavior of filters with imperfect hybrids. This was done by ascribing certain of the hybrid characteristics to the terminations S_2 and S_3. For small deviations from ideal hybrid performance, good agreement was obtained between calculated and measured results.

Filter Characteristics

Several factors affect the electrical performance of low-pass hybrid junction-cutoff waveguide filters. In those frequency bands where good hybrid junctions are

available, it is simple to design waveguide sections having the required cutoff frequencies. These sections are cut off and will reflect almost all of the energy incident upon them in the pass band of the filter. For filters using short slot hybrids, there should be no relative phase difference between the reflections from the lines terminating a conjugate pair of arms. When a magic-Tee is used, however, one such termination must provide for a phase reversal of the reflected wave in order to obtain maximum output from the filter. The use of a quarter wavelength of line as a phase shifter will therefore affect the bandwidth of the filter, as such lines can have an electrical length of 90 degrees only at a single frequency. When the line length is not 90 degrees, some of the energy incident upon the filter will be reflected from the input port and the insertion loss of the filter will increase. Eqs. (3) and (4) have been used to determine the insertion loss of the filter over its pass band. When the phase difference between S_2 and S_3 is allowed to deviate from 180 degrees by ± 60 degrees, the insertion loss reaches a maximum of 2.5 db. As this deviation allows for a bandwidth of about 2:1, it is probable that the useful bandwidth of these filters will be limited by the bandwidths of the hybrid junctions rather than by the phase shifter. For a bandwidth corresponding to 180 degrees ± 10 degrees, a maximum VSWR of 1.2 and an insertion loss of only 0.06 db will be obtained as a result of the phase shifter. This analysis also serves to indicate the degree to which the two cutoff waveguides terminating the conjugate arms of a hybrid must be identical in order to insure a low-pass band insertion loss.

Two factors limit the isolation between the input and the output ports of the filter in the rejection band. One is the directivity of the hybrid junction, and the other is the reflections from the terminations to the conjugate hybrid arms which were assumed to be matched in the rejection band of the filter. As the directivity of a good hybrid rarely exceeds 30 db over an appreciable frequency band, this figure represents an upper limit on the rejection band attenuation. The filter attenuation will be further reduced if there are reflections at ports 2 and 3. In order to minimize such reflections, linear tapers were employed between all cutoff sections of waveguide and the full width waveguides. These proved to be adequate in the rejection region, although the match in the region close to cutoff could be improved.

The characteristics of both the low-pass and the band-pass filters in the regions near the cutoff frequencies of the filter are of particular interest. It is desirable to obtain filters exhibiting a low insertion loss in the pass band up to the cutoff frequency and a sharply rising attenuation above this frequency. The filter behavior near a cutoff frequency is dependent upon the particular cutoff waveguide section which begins to propagate at that frequency. Just above its cutoff frequency, a waveguide is operating in a region where the wall losses are high and the impedance of the guide is quite different from the impedance of the full width waveguides feeding this section. The input cutoff section which provides for the lower cutoff of the band-pass filter therefore increases the pass band insertion loss due to both reflection and dissipation of the input signal. This effect may prevent the application of this technique to very narrow band filters. The dissipation in the guides terminating the conjugate ports 2 and 3, which control the upper cutoff frequency, does not affect the performance of the filter, as these sections lead to matched absorbing loads, in the upper rejection band. However, the reflections due to the mismatch presented by these guides will have the proper phase so as to appear at the output of the filter, thereby lowering the rejection band insertion loss. While linear tapers, which were employed in the experimental models of these filters, provide for adequate matching well above cutoff, more sophisticated matching techniques may be required in order to obtain a rapid increase in attenuation above the upper cutoff frequency.

The sharpness of the slope of the attenuation curve at both ends of the pass band depends to a considerable degree upon the lengths of the cutoff waveguide sections. This is obvious in the case of the input guide section, as its attenuation at any frequency below cutoff is a direct function of its length. In the case of the upper cutoff frequency of the filter, the insertion loss of the filter is a function of the power reflected from the inputs to the pair of cutoff waveguides at ports 2 and 3. For lossless lines of finite length terminated in a resistive load, the input reflection factor is a function of the length of line. When such lines are below cutoff, the line has an imaginary characteristic impedance and attenuates rather than propagates the signal. The input impedance is given by

$$Z_{\text{in}} = Z_0 \frac{Z_t + Z_0 \tanh \alpha l}{Z_0 + Z_t \tanh \alpha l} \tag{5}$$

where

Z_0 = characteristic impedance of line
Z_1 = terminating impedance
α = attenuation factor of line
l = length of line.

For a line below cutoff, as Z_0 is imaginary and Z_t is real, Z_{in} is complex and approaches Z_t for small α or small l and approaches Z_0 for large α or large l. Thus, at frequencies just below cutoff the input impedance will have a large resistive component, while at frequencies far below cutoff this impedance will be largely reactive. The rate at which the impedance becomes reactive, and therefore has a high reflection factor, is a function of the length of line. Wall losses in the cutoff guide section will appear as a resistive component, and will therefore tend to reduce the rate at which the insertion loss rises near cutoff.

For most filter applications, it is sufficient to choose the lengths of the cutoff waveguide sections on the basis of the attenuation factor of a lossless line below cutoff.

General Considerations

Hybrid junction-cutoff waveguide filters are particularly well suited for use at frequencies above 10 kmc. Conventional filter design techniques generally lead to complex structures containing discontinuities which require fairly close mechanical tolerances in order to obtain the specified filter characteristics. The presence of these discontinuities also tends to lower the peak power handling capacity of the guide. Above X band these problems become more critical as the smaller sized waveguides used at these frequencies have limited power handling capacities. In addition, the dimensions required for the filter elements are smaller and therefore require closer tolerances. Fabrication of these smaller filters is also more difficult. Most of these difficulties can be minimized in the case of the hybrid junction-cutoff waveguide filters.

By making use of existing hybrid junction designs, a comparatively simple design procedure is required to adapt these junctions to filters. As the cutoff characteristics are determined by the widths of the waveguides terminating the various ports of the junction, and as this is the largest dimension associated with the guide cross section, the largest possible mechanical tolerance is obtained for a given tolerance on the cutoff frequency. As full height waveguide is employed throughout, and as there are no discontinuities in the filter structure outside of the hybrid junction itself, the power handling capacity of the hybrid junction can be approached. The fact that the power capacity of a waveguide decreases as its cutoff frequency is approached is, to a great extent, offset in the case of the filter by the fact that these guides become badly mismatched near cutoff and therefore reflect power. In order to insure proper behavior of the filter, it is necessary that the two cutoff sections terminating the conjugate arms of the hybrid be identical. Where machining of these parts to the desired tolerance becomes difficult, electroforming techniques can be employed to obtain the desired uniformity of construction.

These filters can be readily used in frequency band separating filter arrays. If ports 2 and 3 are fed into a second hybrid as shown in Fig. 4, rather than into matched loads, signals in the frequency band above the upper cutoff frequency will appear at one port of the second hybrid. Successive sections of similar filters can then be used in this manner to separate out any specified number of channels, provided that the over-all bandwidth of the array is no greater than the useful bandwidth of the input hybrid junction. Fig. 4 also shows how a tunable filter can be obtained by the use of sections of waveguide having variable cutoff frequencies.

When lengths of cutoff guides and hybrids are used to make a filter, the over-all length of the structure can be fairly large. This is admittedly not too advantageous in the waveguide sizes for L, S, C and X band. However, at the higher frequencies the smaller size of waveguide and the shorter wavelengths make it possible to obtain fairly compact filters. This technique of filter design may also prove to be useful at lower frequencies by making use of the space saving features of strip line. Hybrid rings and other types of hybrid junctions have been realized in strip line[8] and these can be combined with trough line[9] sections which have low frequency cutoffs and which can be readily fed from strip line structures.

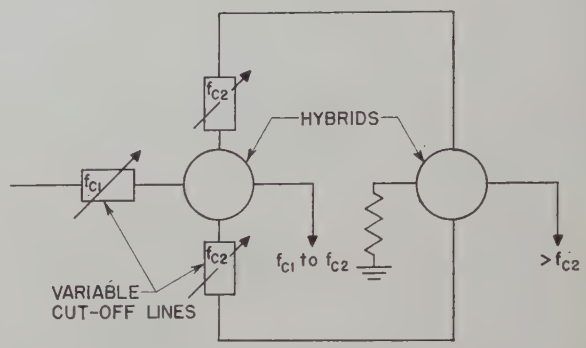

Fig. 4—Tunable filters and filter arrays.

Experimental Results

A number of filters using different types of hybrid junctions were constructed and tested. The experimental work was done at X band primarily because of the fact that hybrid junctions in X-band waveguide were readily available in the laboratory. Fig. 5 shows the insertion loss characteristics of a filter designed for a 600-mc pass band centered at 9200 mc. The hybrid junction used in this filter was a commercially available magic-Tee junction and the cutoff waveguides were machined from copper tubing. The cutoff sections were 5 cm long and had 10.2 cm long linear tapers at each end. The input section of cutoff waveguide was designed for a cutoff frequency of 8.9 kmc and the pair of guides terminating ports 2 and 3 were designed to cut off at 9.5 kmc. While the pass band insertion loss of this filter was fairly low, the use of electroformed cutoff sections was seen to lead to an improved performance, particularly near the upper cutoff frequency. This is shown in Fig. 6. This particular filter was assembled using a standard X band folded magic-Tee whose characteristics were found experimentally to be identical to the characteristics of the magic-Tee used with the first filter over the same frequency band. The cutoff guides were designed to have upper and lower cutoff frequencies at 9.0 kmc and 9.5 kmc, respectively. The higher losses which one would expect with narrow band filters is illustrated in Fig. 7, which shows the characteristics of a filter with a 200-mc bandwidth at 8950 mc. While

[8] J. K. Shimizu, "Strip line 3-db directional couplers," 1957 IRE WESCON Convention Record, pt. 1, pp. 4–15.

[9] H. S. Keen, "Scientific Report on Study of Strip Transmission Lines," Airborne Instruments Lab. Rep. No. 2830–2; December, 1955.

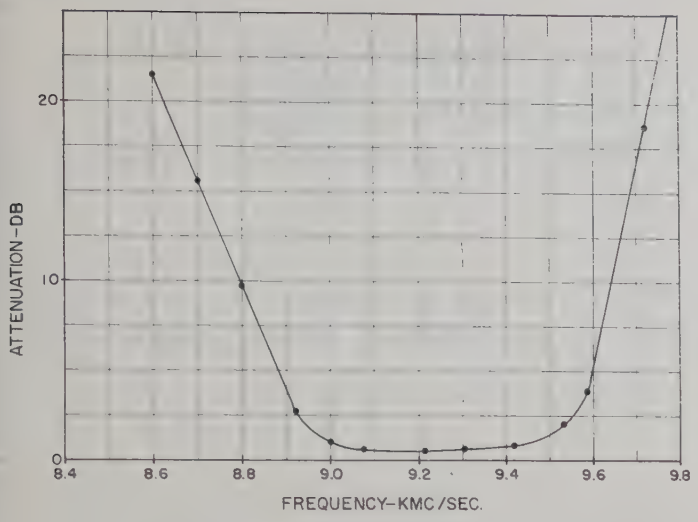

Fig. 5—Magic-Tee cutoff waveguide filter, $f_0 = 9.2$ kmc and bandwidth = 600 mc.

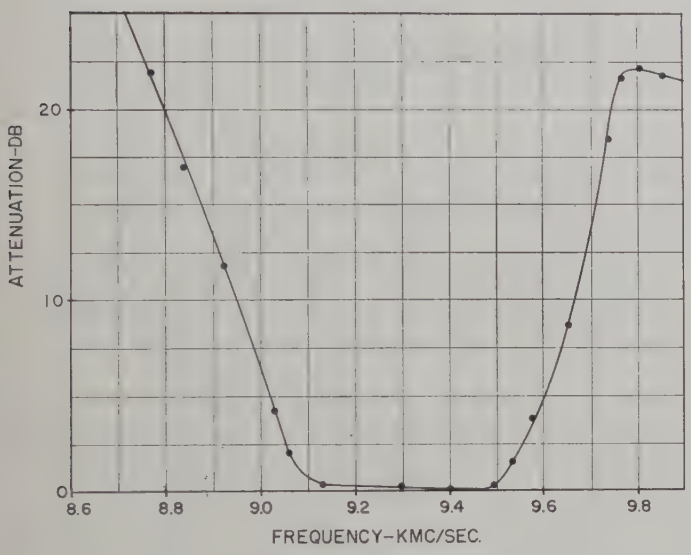

Fig. 6—Folded-Tee cutoff waveguide filter, $f_0 = 9.3$ kmc and bandwidth = 500 mc. Electroformed pair of cutoff waveguides.

the pass band insertion loss was somewhat higher for this filter than for the wider band filters, the midband loss was still only 0.5 db.

Due to the nature of the device, the input VSWR rises below the lower cutoff frequency of the filter. However, the filter presents a fairly well matched input impedance at all frequencies above this cutoff, including the range above the upper cutoff frequency of the filter. The measured input VSWR of the 200-mc bandwidth filter was less than 1.25 over the pass band and was 1.15

Fig. 7—Folded-Tee cutoff waveguide filter, $f_0 = 8.95$ kmc and bandwidth = 200 mc. Electroformed pair of cutoff waveguides.

at midband. The VSWR was less than 1.5 over the entire upper rejection band. Similar results were obtained for the other filters.

Conclusions

The hybrid junction-cutoff waveguide filters offer several advantages over conventional types of waveguide filters. Where the moderate rejection band attenuation does not present a handicap, filters which are simple to design and easy to construct can be obtained. These filters can make use of existing hybrid junctions and will have a power handling capacity which approaches that of the hybrid junction. Not only are the mechanical tolerances required by the cutoff sections not as critical as the tolerances required for irises and other elements of the more conventional filter types, but also simple tuning procedures, such as those which can be introduced to obtain variable pass band filters, can be employed to adjust the waveguide sections to the desired cutoff frequency. The technique described here can be readily adapted for multichannel filter arrays as well as to tunable filters. Above the lower cutoff frequency in the case of band-pass filters, and at all frequencies in the case of low-pass filters, these devices exhibit the matched input impedance associated with directional filters. The general technique can be extended to all frequency bands and to all types of transmission lines where hybrid junctions can be designed and where cutoff characteristics can be obtained.

Practical Design of Strip-Transmission-Line Half-Wavelength Resonator Directional Filters*

R. D. WANSELOW† AND L. P. TUTTLE, JR.†

Summary—Strip-transmission-line directional filters have been found extremely useful since they serve as a combination multiplexer and filter assembly. A step by step procedure has been developed for the quarter-wave coupled filter design having a prescribed bandwidth, skirt selectivity, and passband ripple tolerance for narrow band multiplexing applications.

An experimental study of the strip-transmission-line resonator as an integral part of the directional filter utilizing direct and quarter-wave coupling between the half-wave resonants has been carried out; and an efficient method of tuning a filter is described. This study has included not only problems of insertion loss caused by dissipation but also effects on filter characteristics caused by variations in environmental temperature.

Introduction

DIRECTIONAL filters are circuits commonly used in multiplexing signals of different frequencies. In a previous paper[1] several unique strip-transmission-line directional filter circuits were described, including the half-wavelength resonator directional filter. The purpose of this paper is to present one design procedure for the development of this type of filter, having a prescribed bandwidth, skirt selectivity, and pass-band ripple tolerance with no undesirable spurious responses over a two to one band of frequencies for narrow band multiplexing applications in the frequency spectrum where strip-transmission-line techniques are useful.

The basic half-wavelength resonator directional filter is shown in Fig. 1(a). The input and output lines shown are reversible since the network is a symmetrical passive network. A study of the phase relationships shows that a wave at the center frequency of the filter entering arm 1 will couple to arm 4. Arm 3 is always isolated from the input. The input line is nonreflecting when the other arms are connected to their characteristic impedances. Representative response characteristics of a maximally flat filter are shown in Fig. 2. By direct or quarter-wave coupling the resonators in cascade, as shown in Fig. 1(b) and 1(c) respectively, greater selectivity is achieved. The filters shown in Fig. 1 will not produce very low midband insertion loss due to the relatively large initial input gap widths that are required in narrow band filters. It was observed that a relatively high mismatch existed in the line 1–2 when the first resonator of a narrow band filter was directly coupled to this line. By inserting a very short length of line in the input and output coupling regions, as shown in Fig. 3, the coupling of power to the filter is improved as a result of less than a 2 to 1 VSWR in the through line and the midband insertion loss is greatly reduced to an acceptable value of less than 2 db.

A number of strip-transmission-line directional filters using direct and quarter-wave coupling were tested. As a result of these tests, it was found experimentally that to obtain a bandwidth tolerance of ± 2 per cent or less, low Q filters ($Q_0 \lesssim 40$) may utilize either direct or quarter-wave coupling of the half-wave resonants. Filters with a higher Q ($Q_0 \gtrsim 40$) should employ quarter-wave coupling only, since direct coupling requires relatively large coupling reactances (wide gaps), which in turn present spurious transmission effects when the strip-transmission-line gaps are greater than approximately $\lambda/10$. Since the design of direct coupled strip-transmission-line filters is given quite adequately by Cohn,[2] this paper will be devoted almost entirely to the design and development of quarter-wave coupled strip-transmission-line directional filters. The theory of quarter-wavelength coupling is described by Ragan.[3] As the Q of a given microwave filter is increased, the fabrication and adjustment of the resonant cavities or strips (as in this case) utilizing direct coupled resonators becomes increasingly more difficult. Thus by employing quarter-wave coupling between the filter resonators, the tolerances on the dimensions of the coupling elements are eased which in turn meet bandwidth tolerance specifications more readily. Tuning of the half-wavelength resonator strips with screws centered above and below the strips was necessary to obtain an acceptable symmetrical band-pass characteristic. Representative tuning screws for each half-wavelength strip are sketched in Fig. 4.

Experimental strip-transmission-line half-wavelength resonator directional filters having one to five per cent bandwidths at S band have been developed with less than 2 db mid-band insertion loss. A three-section Tchebycheff filter with two per cent bandwidth, having a rejection greater than 25 db at frequencies two per cent from the center frequency, had a midband insertion loss of 1 db with no spurious responses over a two to one band of frequencies. The air-strip-transmission-line

* Manuscript received by the PGMTT, May 2, 1958; revised manuscript received, August 15, 1958. The work for this paper was sponsored by North American Aviation under Purchase Order No. H662-X-600010.

† Antenna Lab., Melpar, Inc., Falls Church, Va.

[1] S. B. Cohn and F. S. Coale, "Directional channel-separation filters," PROC. IRE, vol. 44, pp. 1018–1024; August, 1956.

[2] S. B. Cohn, "Direct-coupler-resonator filters," PROC. IRE, vol. 45, pp. 191–192; February, 1957.

[3] G. L. Ragan, "Microwave Transmission Circuits," M.I.T. Rad. Labs. Ser., vol. 9, McGraw-Hill Book Company, Inc., New York, N. Y., pp. 677–706; 1948.

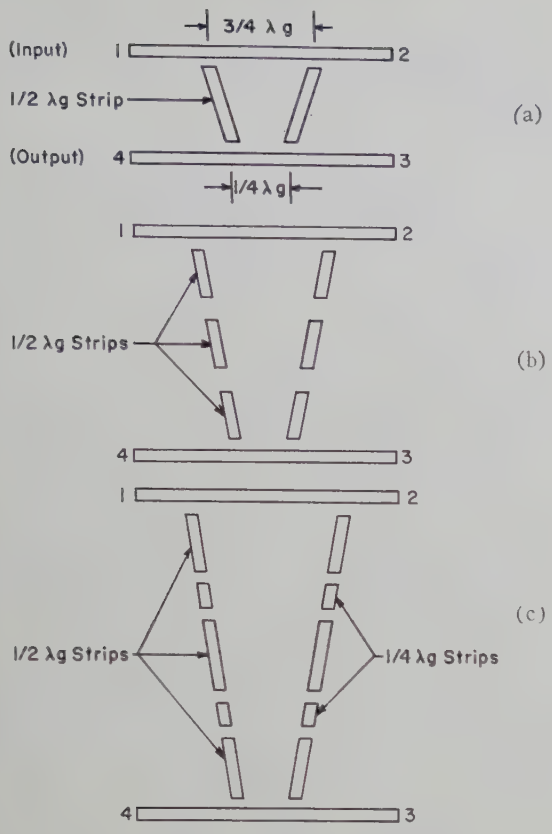

Fig. 1—Half-wavelength resonator directional filter configurations. (a) Basic half-wavelength resonator directional filter. (b) Three section direct coupled directional filter. (c) Three section quarter-wave coupled directional filter.

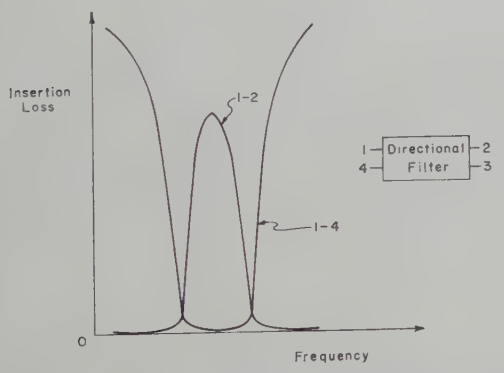

Fig. 2—Insertion loss response characteristics of a directional filter.

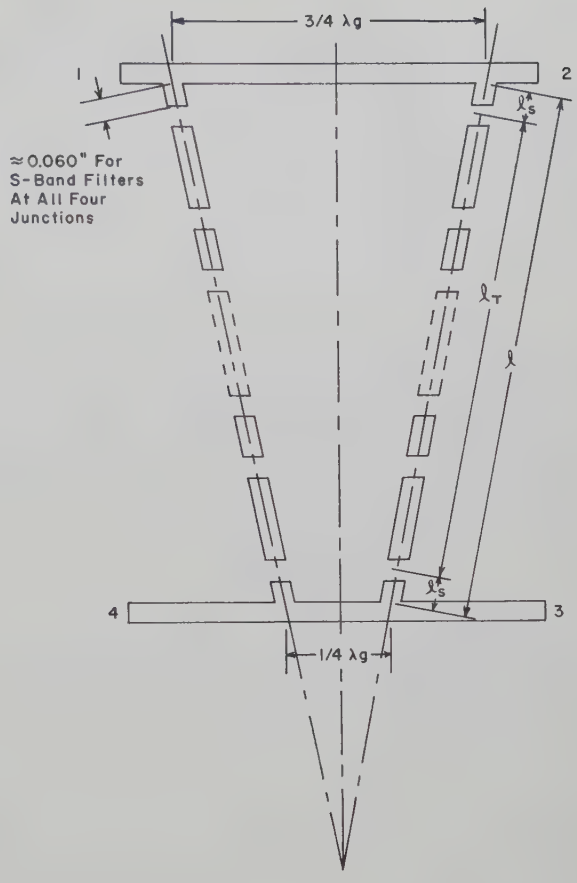

Fig. 3—n-section quarter-wave coupled half-wavelength resonator directional filter.

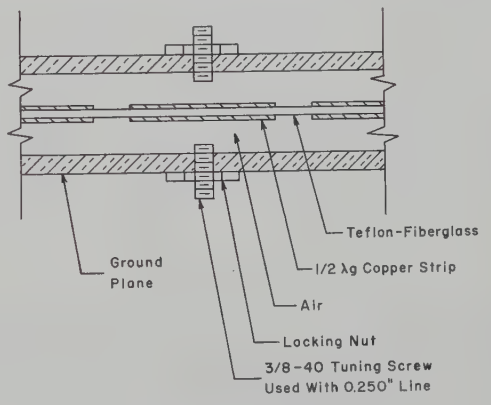

Fig. 4—Tuning screws for one resonant strip in a balanced air strip-transmission-line.

filters were fabricated from copper clad Teflon-fiberglass sheets by using engraving techniques. The design techniques discussed in this paper are general and thus are not confined to the above-stated filter characteristics.

Design Procedure

This design procedure is for quarter-wave coupled directional filters. The major portion of the development of this type of filter lies in the design of the band-pass filter which contains the half-wavelength resonators between the input and output transmission lines of the filter. The first step in the synthesis of such filters is the selection of the transmission coefficient corresponding to a network having the desired rejection-band characteristics. In multiplexing signals of closely spaced frequencies, the skirt selectivity specification of each filter in the multiplexer is very important as well as utilizing a minimum of space as most present-day applications require. Therefore, for given band rejection characteristics or skirt selectivity, fewer elements are required when the synthesis is based on a Tchebycheff distribution of the first kind with small tolerable ripple rather than a Butterworth distribution. Following the selection of the transmission coefficient, the corresponding low-pass prototype filter can be synthesized from

which a low-pass to band-pass transformation is to be made. From the low-pass prototype the normalized reactive parameters can be obtained for use in the following procedure.

Assuming a narrow bandwidth and infinite unloaded Q, the loaded Q, Q_0, of the filter may be stated as follows:

$$Q_0 = \frac{f_0}{\Delta f} \tag{1}$$

where f_0 is the center frequency and Δf is the filter bandwidth of the band-pass filter. In practice, (1) is very accurate even though the unloaded Q is far from infinite. The loaded Q, Q_{Ln}, of each nth half-wavelength element is determined by the prototype normalized reactive element values, C_n, from the equation:

$$Q_{Ln} = \tfrac{1}{2} C_n Q_0. \tag{2}$$

Since the end discontinuity is the same at both ends of a resonant strip of a quarter-wavelength coupled filter when the filter is loaded at each end by equal resistances, the normalized coupling reactance, $|\bar{X}_n|$, of these end gaps for each nth half-wavelength resonant element is specified[4]

$$|\bar{X}_n| = \sqrt{\frac{4}{\pi} Q_{Ln}}. \tag{3}$$

This condition exists in the subject filter due to the fact that the input and output tabs will present equal resistances at the terminals of the conventional filters which are utilized to construct the V arms of the directional filter.

For filters with 10 per cent or less bandwidth, (3) is accurate enough for most applications. Thus by substituting (2) into (3) a very useful relation is found:

$$|\bar{X}_n| = \sqrt{\frac{2}{\pi} C_n Q_0}. \tag{4}$$

By synthesizing the desired transmission coefficient or utilizing Weinberg's tables,[5] the low-pass prototype normalized element values, C_n, are obtained which determine each normalized gap reactance, $|\bar{X}_n|$. By utilizing a reference table of normalized capacitive reactance, $|\bar{X}|$, vs gap spacing, g, in inches, the gap distance between strips can be determined. For narrow band filters at S band such a graph is shown in Fig. 5. This data was obtained by utilizing Bradley's method[6] of one stage strip-transmission-line filters having different gap spacings at a specified frequency.

From Cohn[7] the separation of gap reactances, l_n, for each nth resonant element when the two end gap discontinuities for each nth resonant strip are equal may be stated

$$l_n = \frac{\lambda_{g0}}{2}\left[\frac{\pi - \tan^{-1}\left(\dfrac{2}{|\bar{X}_n|}\right)}{\pi}\right], \tag{5}$$

where

$$\lambda_{g0} = \frac{\lambda_0}{\sqrt{\epsilon_r}} \tag{6}$$

λ_{g0} = strip-transmission-line wavelength at center frequency of filter

λ_0 = electrical wavelength at center frequency of filter in air

ϵ_r = relative dielectric constant of transmission medium.

A band-pass filter layout with designated dimensions is shown in Fig. 6. The quarter-wavelength coupling dimensions, $S_{n-1,n}$ between the $n-1$ and nth resonant elements are set simply by

$$S_{n-1,n} = \frac{l_{n-1} + l_n}{2} - \frac{\lambda_{g0}}{4}. \tag{7}$$

By inserting one of these band-pass filters into each of the two V arms of the directional filter, the resultant configuration is as shown in Fig. 3. In Fig. 3 the distance, l_T, corresponds to that in Fig. 6.

For the filter to present a high impedance to the main transmission line (arm 1–2 in Fig. 3) in the stop bands of the band-pass filter, the length, l_s, in Fig. 3 must necessarily be a small part of a wavelength. It was found experimentally that the filter will have a low acceptable mid-band insertion loss when l_s satisfies the following equation:

$$l_s = 0.060'' + \frac{g_1}{2} \tag{8}$$

where g_1 is the width of the first and last gap of the filter in inches.

Experimental Results

By utilizing the design procedure for quarter-wave coupled directional filters, filters with band-pass response characteristics of the Butterworth or Tchebycheff type can be designed and fabricated with a midband insertion loss of less than 2 db. When utilizing either type of coupling technique, especially direct coupling, close electrical tolerances on the pass-band characteristics require extreme mechanical fabrication tolerances. Since all the filters to be discussed were fabricated by engraving methods, copper residue fibers within the coupling gaps, which normally remained after the en-

[4] E. H. Bradley, "Design and development of strip-line filters," IRE Trans. on Microwave Theory and Techniques, vol. MTT-4, pp. 86–93; April, 1956.

[5] L. Weinberg, "Modern synthesis network design from tables I–IV," *Electronic Design*, vol. 4, pp. 22–25; September 15, 1956, pp. 22–25; October 1, 1956, pp. 46–47; October 15, 1956, pp. 34–37; November 1, 1956.

[6] E. H. Bradley, *op. cit.*, p. 89.

[7] S. B. Cohn, *op. cit.*, p. 192.

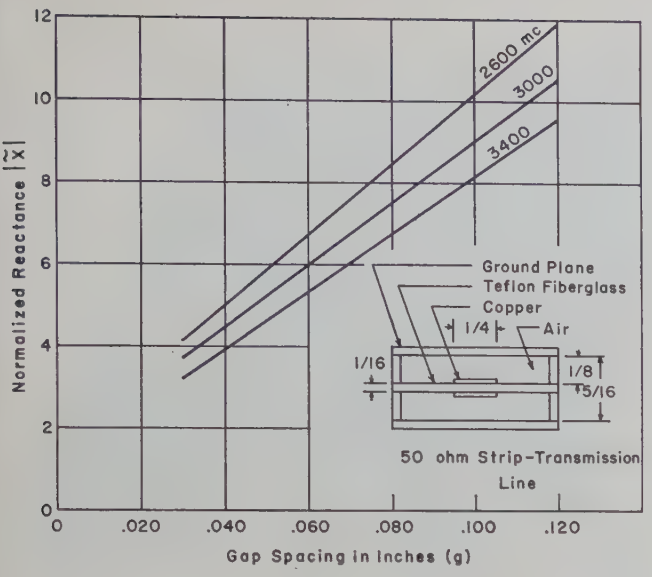

Fig. 5—Reference data of normalized reactance vs gap spacing for strip-transmission-line *S*-band filters.

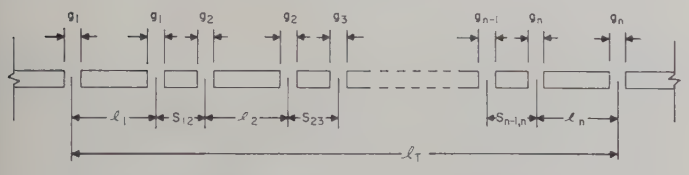

Fig. 6—*n*-section quarter-wave coupled filter.

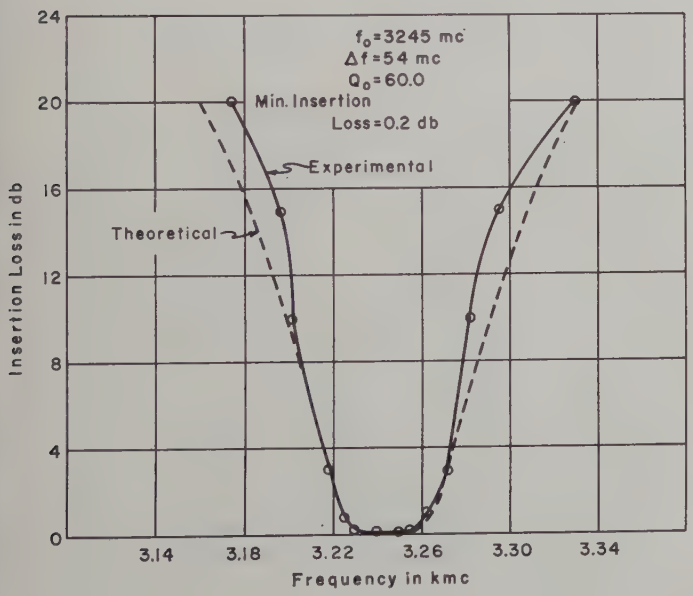

Fig. 7—Butterworth response characteristics of a two section quarter-wave coupled directional filter.

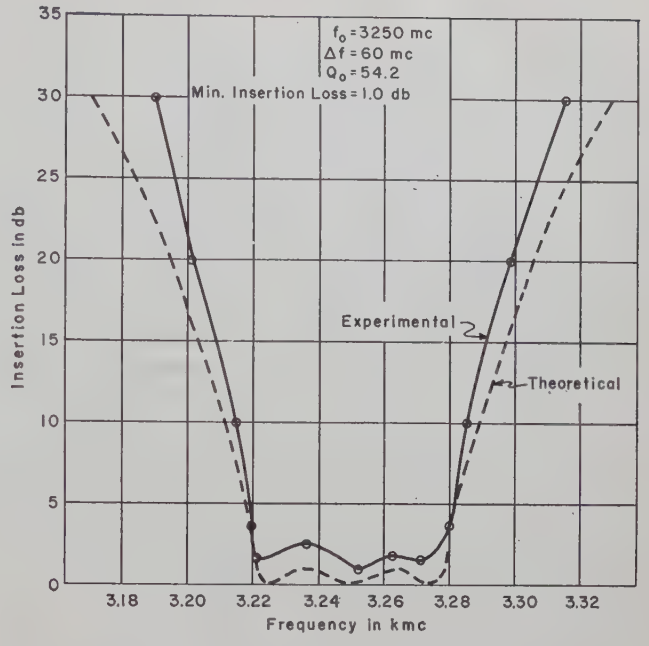

Fig. 8—Tchebycheff response characteristics of a three section quarter-wave coupled directional filter.

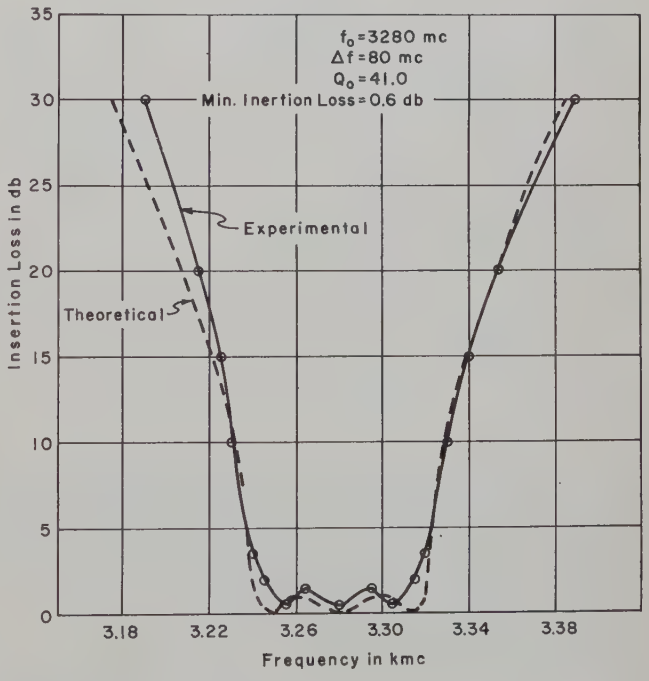

Fig. 9—Tchebycheff response characteristics of a three section direct coupled directional filter.

graving process was completed, were removed by cleaning with ferric chloride and subsequent washing with methyl alcohol. Thus, by cleaning the coupling gaps a more reproducible band-pass characteristic can be obtained.

Figs. 7 and 8 show insertion loss response characteristics of quarter-wave coupled Butterworth and Tchebycheff filters respectively. It should be noted in these two filters, each with a loaded Q of the same order of magnitude, that the Butterworth filter has a midband insertion loss of 0.2 db as compared to the Tchebycheff filter with a 1.0 db loss. The Tchebycheff design of Fig. 8 has the desirable feature of possessing more than 25 db selectivity at frequencies two per cent from the center frequency. The response characteristic of a direct coupled Tchebycheff filter is shown in Fig. 9. Both Tchebycheff filters of Figs. 8 and 9 were designed to have a 1 db ripple in the pass band.

In many applications, filters of the type described in this paper must have a large insertion loss over a wide frequency spectrum outside of their fundamental pass bands. Spurious responses were observed at approximately integer multiples of the fundamental but were less pronounced as the frequency increased. Spurious responses of this type can be removed with a low-pass filter having a cutoff frequency somewhat less than that of the first spurious response.

By properly placing an adjustable short in arm 3 of the directional filter, any mismatch which may be due to improperly tuned filter elements or the crystal output detector in arm 4 may be partially tuned out. The results of such a test are plotted in Fig. 10. It is seen that the adjustable short improves the midband insertion loss as well as decreasing pass-band ripple. As the bandwidth becomes relatively wider, the short is less effective since it is a frequency-sensitive device. This situation was made possible since the directivity of arm 3 was far from infinite.

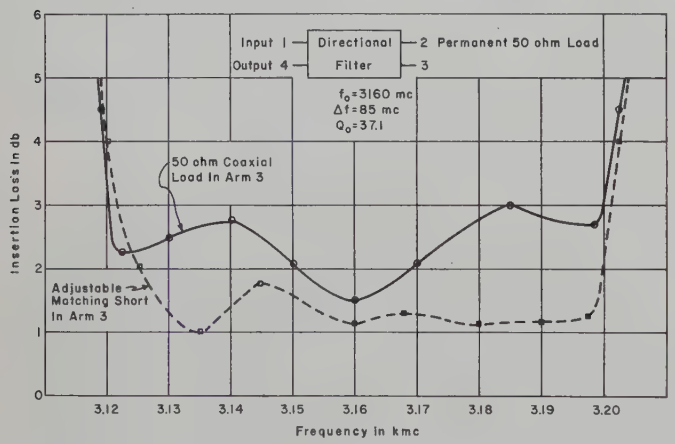

Fig. 10—Directional filter Tchebycheff response characteristics with different loading of the directivity arm number 3.

In an effort to further improve the midband insertion loss of narrow band directional filters, the copper clad Teflon-fiberglass was silver-plated several times the thickness of the skin depth at *S*-band frequencies, after which the filter was engraved. Although it was felt that this would increase the unloaded Q of the strip-transmission-line structure, no improvement of the midband insertion loss over the standard copper clad dielectric was observed. The most noted improvement of insertion loss was obtained using a Butterworth design rather than a Tchebycheff of the same loaded Q. Experimentally the improvement varied from 0.2 to 0.8 db, depending on the loaded Q and the selectivity desired.

Three of these directional filters engraved on one copper clad Teflon-fiberglass card as shown in Fig. 11 had a multiplexed insertion loss characteristic as shown in Fig. 12. The bandwidth of each filter is 60 mc and the center frequencies were spaced 60 mc apart. From the insertion loss and VSWR plots of these filters, it is seen

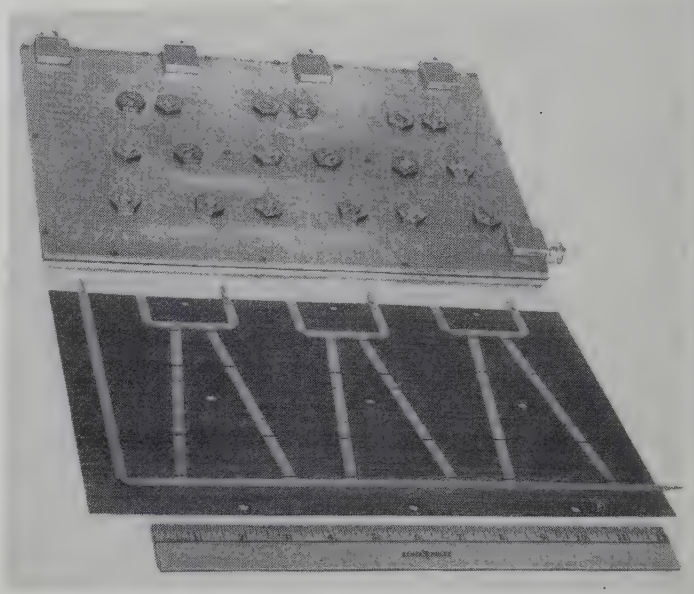

Fig. 11—Three multiplex directional filters: assembled unit and center conductor.

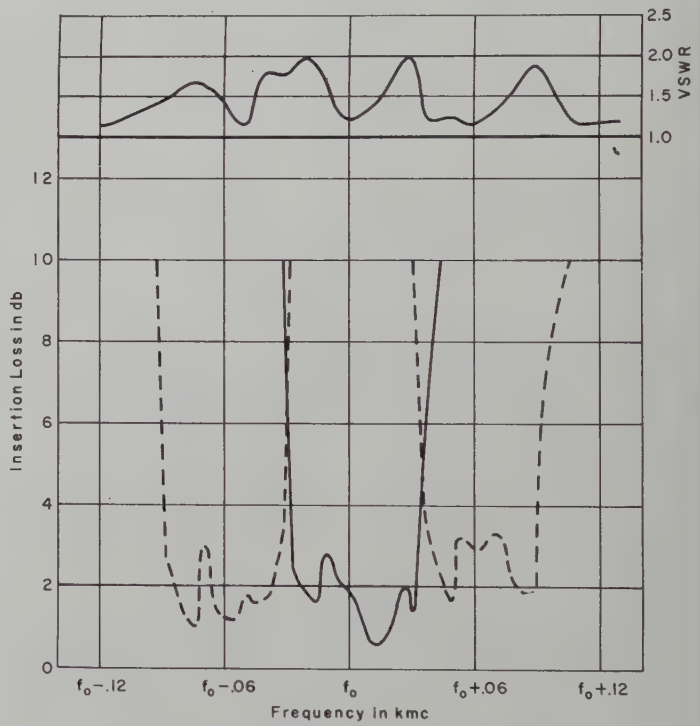

Fig. 12—Insertion loss and VSWR characterissics of three *S*-band multiplexed directional filtter.

that the theory of the directional filter proves to be excellent in practice.

A multiplexed filter array consisting of a number of filters operated very well under extreme environmental temperature. The center frequency of the *S*-band filters shifted approximately one mc at a temperature of 125°C as compared to room temperature.

The tuning procedure developed for these directional filters is an easy and rapid technique of tuning and will be discussed in the next section. It was found experimentally that the center frequency of these narrow band

directional filters could be shifted approximately ±2 per cent about the designed center frequency without noting any deleterious effects on the band-pass characteristics.

Tuning Procedure

The tuning procedure for direct or quarter-wave coupled filters involves a method of quarter-wave shifting the VSWR nulls on the input transmission line to the filter. The procedure to follow will refer to the circuit layout in Fig. 13. Adjustment of any tuning screws for a meter deflection must carefully be made for the maximum possible meter deflection while keeping each pair of tuning screws equidistant from the resonant balanced strip-transmission-line.

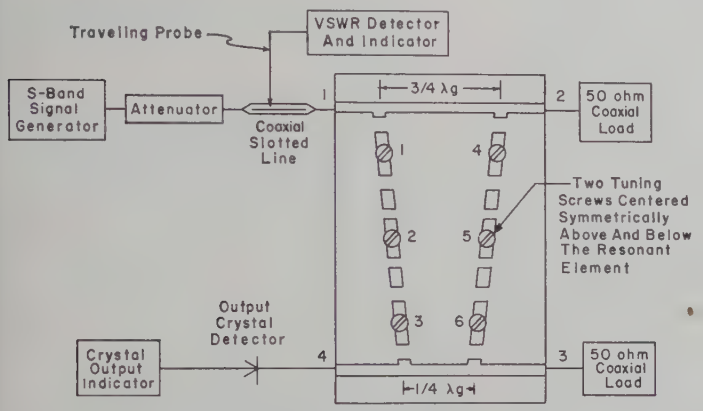

Fig. 13—Circuit for tuning a directional filter.

Procedure:

1) With the signal generator calibrated to the filter center frequency and all tuning screws shorted to the resonant strips, place a 50 ohm coaxial load in arms 2 and 3 and a crystal detector in arm 4.

2) Adjust the second resonant section (containing screws 4, 5, and 6) by turning the screws out from the strips until they are flush with the ground plane. Then adjust these three screws one at a time for a rough minimum insertion loss as measured with the crystal output detector.

3) Remove the 50 ohm load in arm 2 and replace with a variable short. Carefully adjust this short until minimum insertion loss is measured with the output crystal detector. This short reflects an open circuit to the input junction of this second resonant section.

4) Re-short all the tuning screws (4, 5, and 6) and with the slotted line locate two nulls in the standing wave pattern. Interpolate the position of these nulls to locate the maximum point between the nulls and place the slotted line probe at this maximum.

5) Tune the pair of tuning screws (4) nearest the input line of the second resonant section until maximum VSWR is obtained and lock in place.

6) Move the slotted-line probe one-quarter wavelength in either direction to one of the original nulls (now a maximum). Tune the middle pair of tuning screws (5) for a maximum and lock in place.

7) Tune the last pair of tuning screws (6) for minimum insertion loss as measured with the output crystal detector (the VSWR will become a minimum) and lock in place.

8) Readjust the variable short in arm 2 for a maximum VSWR. The short will now reflect a short circuit at the input junction to the second tuned resonant section and an open circuit to the input junction of the first untuned resonant section due to the $\frac{3}{4}\lambda_g$ coupling distance between junctions.

9) Tune screws 1, 2, and 3 in the first resonant section respectively the same as screws 4, 5, and 6 in the second resonant section according to the steps 5, 6, and 7 of this procedure.

10) Replace the variable short in arm 2 with a 50 ohm coaxial load and insert a variable short in place of the load in arm 3. Adjust this short for an optimum band-pass characteristic. This short in arm 3 when positioned properly will partially tune out any small mismatched reactances in the output line (3–4) which may be present due to the filter, crystal detector, or both.

11) If more than one directional filter is connected to line 1–2, screws 1 and 4 of all untuned filters should be shorted to the strip-transmission-line while one filter is being tuned. Once a filter is tuned properly it should have no effect on adjacent filters while they are being tuned.

Conclusion

The design formulas presented here provide the engineer with a practical design procedure for the development of narrow band half-wavelength resonator directional filters having a specified bandwidth and skirt selectivity in a strip-transmission-line structure. Since the tuning of this filter is relatively simple, the authors feel that this type of filter will prove desirable for some multiplexing applications.

Acknowledgment

The authors wish to thank E. O. Houseman for many helpful discussions.

Correspondence

A High Average Power Broad-Band Ferrite Load Isolator for *S* Band*

A broad-band high average power *S*-band load isolator has been developed by using a dielectric loaded waveguide and a composite ferrite. A partial height dielectric was centrally mounted on the broadwall of a vertically constricted *S*-band waveguide, Fig. 1. The cross section dimensions of the dielectric were chosen to increase the operating bandwidth of the isolator. Adjacent to either side of the dielectric 2 thin flat slabs of ferrite were positioned. A large ratio of ferrite width to thickness was chosen to achieve maximum heat dissipation. The ferrite element was composed of 2 ferrite types. Towards the source end of the isolator a long length of a narrow resonance linewidth and low dielectric loss ferrite was mounted. This portion of the ferrite element provided the majority of the isolation loss. However, since this ferrite possessed only a moderate Curie temperature the average effective power handling capacity of the isolator composed of this ferrite alone was limited to less than 1600 watts. To maintain a large value of the isolation loss in the presence of an appreciable load mismatch a second ferrite piece of a higher Curie temperature ferrite was employed. A small length of the higher Curie temperature ferrite was mounted adjacent to the first ferrite and towards the load end of the isolator. The length of the second ferrite was chosen to provide 3 to 4 db isolation loss.

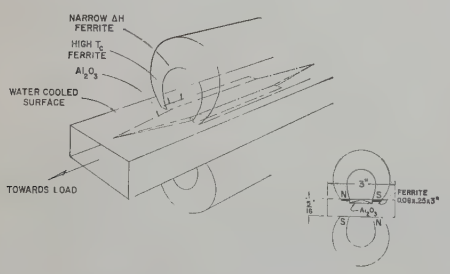

Fig. 1—Basic elements of the high-power *S*-band isolator.

A skew transverse magnetizing field was employed which assisted in increasing the bandwidth of the isolator. Magnetic field skewing was produced by magnetizing the upper and lower permanent magnets unequally. A reduction of magnet size was accomplished by employing a vertically constricted waveguide at some sacrifice of the peak power handling capacity.

High average power performance was measured with a nominal 600–800-watt CW magnetron tunable over the 2.5 to 3.7-kmc band. Isolation loss was checked at low and high powers. Measurements of insertion loss were made in detail at low power and checked at selected frequency points at high power. This simplification in measurement was permissible since it was found that insertion loss decreased very slightly at the higher average powers.

In addition to isolation and insertion loss the power absorbed by the ferrite was determined with the isolator operating at high average power in the reverse direction. This technique enables the simulation of high average power operation with moderate power sources. From a knowledge of these quantities it is possible to compute the effective average power capacity, P_{eff}, of the isolator when operating into a given load mismatch as follows:

$$P_{eff}(1 - T_F) + \Gamma T_F P_{eff}(1 - T_R) = P_{abs}$$

$$P_{eff} = \frac{P_{abs}}{1 + T_F\Gamma\left(1 - T_R - \frac{1}{\Gamma}\right)}$$

where P_{abs} is the average power absorbed by the ferrite in the reverse direction.

Γ is the power reflection coefficient of the load.
T_F is the isolator power transmission coefficient in the insertion loss direction.
T_R is the power transmission coefficient in the isolation loss direction.

The computed effective power capacity yields a value which is less than the actual power capacity. This discrepancy occurs because the present measurement of the absorbed power is made under conditions wherein the heat absorbed is concentrated in a limited portion of the ferrite length. In practice a large proportion of the dissipated power would be more uniformly distributed throughout the sample as a result of the insertion loss absorption.

For the ferrites and ferrite geometry employed in these studies, high-power nonlinear phenomena were not evident. In experimental circumstances, where ferrites of lower resonance line width or higher saturation magnetizations are employed, or where higher RF powers and ferrite geometries more susceptible to spin wave instabilities are utilized, direct measurement of isolator performance at the rated power levels must be made to evaluate the nonlinear effects.

Fig. 2 presents performance data taken for a water cooled isolator operating at 2 effective power levels; milliwatt and greater than 1650 watts CW (2:1 load mismatch). The ferrite element consisted of a combination of magnesium manganese and nickel ferrite slabs positioned as shown in Fig. 1. The isolation to insertion loss db ratio manifested while the unit was absorbing 400 watts CW in the reverse direction was found to be in excess of 20/1 over greater than 15 per cent bandwidth.

Fig. 3 presents performance data for an isolator constructed from a single type of

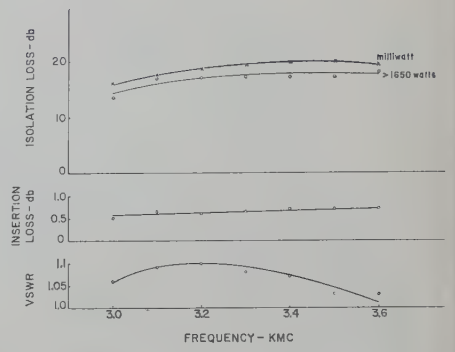

Fig. 2—Performance data for a high-power load isolator using magnesium manganese R-1 and nickel ferrite 106.

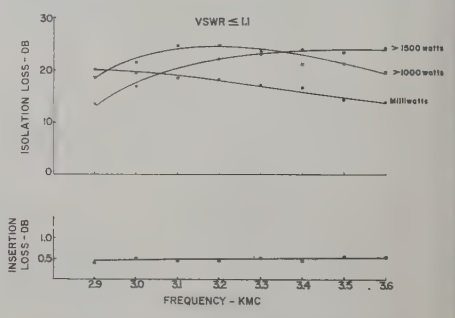

Fig. 3—Performance data for a high-power load isolator using $Ni_{0.7}Cu_{0.3}Mb_{0.02}Fe_{1.9}O_4$ ferrite.

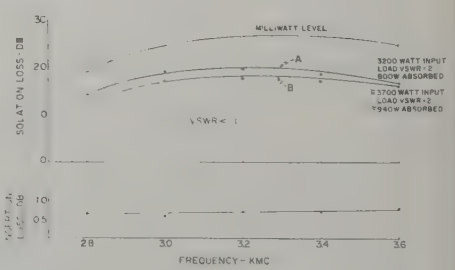

Fig. 4—Performance data for a high-power load isolator using $Ni_{0.7}Cu_{0.3}Mn_{0.02}Fe_{1.9}O_4$ and nickel ferrite, ferroxcube 106.

nickel ferrite of composition $Ni_{0.7}Cu_{0.3}Mn_{0.02}Fe_{1.9}O_4$. A noticeable frequency shift of the peak isolation occurs as the power is raised. The shift of the resonance peak toward the higher frequencies arises from the decrease of saturation magnetization of the ferrite that accompanies ferrite heating.

Fig. 4 shows performance data of an isolator constructed with the nickel ferrite used in Fig. 3 plus a portion of a higher Curie temperature nickel ferrite. Ferroxcube 106, positioned on the load end of the unit. The effective power capacity when operating into a 2/1 load mismatch exceeded 3000 watts CW for 14 db or greater isolation and 0.6 db or less insertion loss throughout the 2.8 to greater than 3.6 kmc band (>25 per cent bandwidth). A greater than 3700-watt effective average power capacity is shown

* Received by the PGMTT, August 4, 1958.

for curve B. A comparison of the data of Figs. 3 and 4 reveals the improvement in average power handling capacity obtained by using a high Curie temperature tip of ferrite positioned on the load end. The trend of decreasing isolation loss at the low end of the band as the effective power is raised is markedly reduced in Fig. 4, where, for the composite ferrite isolator, isolation loss at 2.9 kmc is greater than 15 db for an effective average input power of 3200 watts. Without the high Curie temperature ferrite the isolator of Fig. 3 displays a reverse loss of <13 db at 2.9 kmc for an effective average input of only 1500 watts.

E. N. Skomal
Sylvania Microwave Phys. Lab.
Mountain View, Calif.

Reflection Coefficient of E-Plane Tapered Waveguides*

In a paper by Matsumaru,[1] formulas of the input reflection coefficients of the linearly and sinusoidally E-plane tapered waveguides are given. Excellent agreements between the theoretical and experimental results have been found in both cases. In this note we wish to add some analytical remarks.

The analysis given in the above paper is different from the rigorous one given by Walker and Wax.[2] The latter led to a nonlinear differential equation

$$\frac{dR}{dx} - 2\gamma R + \frac{1-R^2}{2}\frac{d}{dx}\ln[Z(x)] = 0 \quad (1)$$

where R is the reflection coefficient, $Z(x)$ is the surge impedance of the tapered line, and $\gamma=\alpha+j\beta$ is the wave propagation constant. If the tapered line is loss-free, then we have $\gamma=j\beta$. On the assumption that the phase constant, β is independent of x, and that $R^2\ll 1$, Bolinder[3] obtained an approximate expression of the input reflection coefficient

$$R = \frac{1}{2}\int_0^l \frac{d}{dx}[\ln Z(x)]\cdot e^{-j2\beta z}dx \quad (2)$$

for a finite tapered line of length l, terminated by $Z(0)=Z_1$ and $Z(l)=Z_2$ at each end.

It may be shown that Mr. Matsumaru's equations (4) and (12) are equivalent to (2) in this communication. On substitution of the surge impedance of a sinusoidal taper

$$Z(x) = \frac{Z_1+Z_2}{2} - \frac{Z_1-Z_2}{2}\cos\left(\frac{\pi x}{l}\right) \quad (3)$$

into our (2), we obtain his (12). Substituting the surge impedance of a linear taper

$$Z(x) = Z_1 + (Z_2 - Z_1)x/l \quad (4)$$

into our (2), and letting $x=y+l/2$, we obtain his (4), with its independent variable x being replaced by y. Therefore, it appears that Bolinder's assumption of $R^2\ll 1$ should also apply to Mr. Matsumaru's analytical results. This is not, however, stated explicitly in his paper.

For a linearly tapered line defined by (4), (2) may be integrated exactly in terms of Ci and Si, the cosine and sine integrals. The input reflection coefficient is

$$R = \tfrac{1}{2}e^{ju_2}\{[Ci(u_2) - Ci(u_1)] - j[Si(u_2) - Si(u_1)]\} \quad (5)$$

where $u_1=2\beta l/(k-1)$, $u_2=2\beta lk/(k-1)$ and $k=Z_2/Z_1$. This expression appears to be somewhat simpler than Mr. Matsumaru's (8), and his (7), a binomial-expansion approximation, is not necessary in this case. If a change of variable, $u=2\beta(q^{-1}+x)$, is made, his (5) leads directly to the above result—our (5).

In the treatment of a sinusoidally tapered line, noting that $r=(Z_1-Z_2)/(Z_2+Z_1)$ tends to zero first, and letting l tend to zero next, Mr. Matsumara showed how his (15) becomes

$$R = (Z_2 - Z_1)/(Z_2 + Z_1),$$

the reflection coefficient of two directly connected waveguides. It is felt that this statement, although correct, might mislead one to think that Matsumaru's (12) is exact. To clarify this point, we let l in his (15) tend to zero first and retain the higher order terms; (15) then becomes

$$\lim_{l\to 0} R = \left(\frac{Z_2-Z_1}{Z_2+Z_1}\right) + \frac{1}{3}\left(\frac{Z_2-Z_1}{Z_2+Z_1}\right)^3 + \cdots = \frac{1}{2}\ln\frac{Z_2}{Z_1}.$$

It is seen that as l tends to zero, R tends to $\frac{1}{2}\ln(Z_2/Z_1)$ rather than to $(Z_2-Z_1)/(Z_2+Z_1)$. This limiting case indicates somewhat the approximate nature of Matsumaru's (12), from which his (15) is derived. It might be said that the approximation becomes increasingly good as r tends to zero; then

$$\lim_{l\to 0} R = \frac{1}{2}\ln\frac{Z_2}{Z_1} \cong \frac{Z_2-Z_1}{Z_2+Z_1}.$$

It is also noted that our (5) also becomes $\frac{1}{2}\ln(Z_2/Z_1)$ as l tends to zero. As long as we use our (2) or its equivalent—Mr. Matsumaru's equations (4) and (12)—this is true, regardless of the nature of $Z(x)$ or type of taper. This can be seen directly from our (2), in which the phase factor tends to unity as l tends to zero. Direct integration gives the proof.

Eq. (2) in this demonstration may be considered as the first approximation of the solution to our differential equation (1), which—together with higher order approximations—has been discussed elsewhere.[4] In general it may be said that if the length of taper is longer than half of a guide-wavelength, the second order approximation has no significant effect.

Richard F. H. Yang
Andrew Corporation
Chicago, Illinois

Author's Comment[5]

I am grateful to Mr. Yang for his remarks regarding my paper; his detailed remarks strengthen some of the weak points in it.

First, his analysis of his (4) is known to me, and I have no further comments to make on it. Next, his formula (5) is probably quite useful in calculating the reflection coefficient of linear tapers. In the latter part of his communication, he has made some remarks on the limiting cases of R. Although I had previously considered these analytical studies, I did not discuss them fully since they seemed to be too detailed for my paper.

As I mentioned in my paper, the main purpose was to present practical design data rather than detailed analyses. I would like to take this opportunity to add some comments on the experimental data described in my paper. Figs. 1 and 2, plotted in the K-plane,

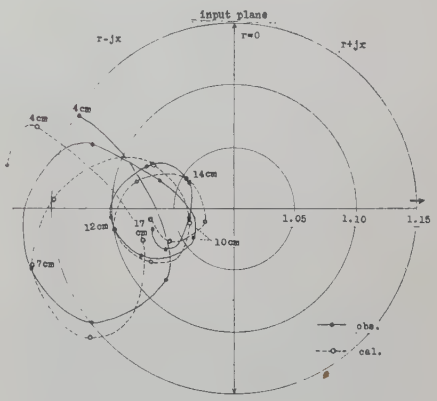

Fig. 1—Results of experiments, part I ($Z_2/Z_1=2.0$). Data are shown for linear-taper lengths from 4 to 17 cm.

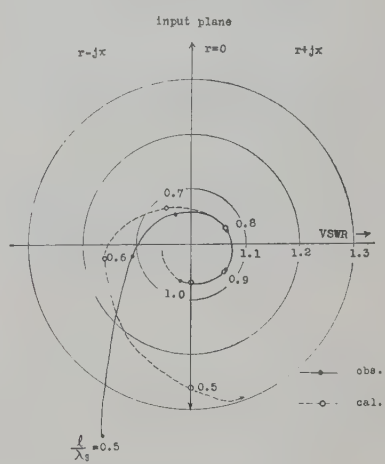

Fig. 2—Results of experiments, part III ($Z_1/Z_2=2.4$). The normalized sinusoidal-taper length l/λ_g was varied from 0.5 to 1.0.

show the reflection coefficients of the data obtained from experiments, parts I and III, respectively. The conically looped circular loci of R of the linear tapers in Fig. 1 show the typical behavior for the cases of $Z_2>Z_1$. It should be mentioned that the position of R follows almost the course of one conical cycle every half-wavelength (4.9 cm). For

Received by the PGMTT, August 4, 1958

* Received by the PGMTT, June 30, 1958.

[1] K. Matsumaru, "Reflection coefficient of E-plane tapered waveguides," IRE Trans. on Microwave Theory and Techniques, vol. MTT-6, pp. 143–149; April, 1958.

[2] L. R. Walker and N. Wax, "Non-uniform transmission lines and reflection coefficients," *J. Appl. Phys.*, vol. 17, pp. 1043–1045; December, 1946.

[3] F. Bolinder, "Fourier transforms in the theory of inhomogeneous transmission lines," Proc. IRE, vol. 38, p. 1354; November, 1950.

[4] L. Solymar, "On higher order approximations to the solution of nonuniform transmission lines," Proc. IRE, vol. 45, pp. 1547–1548; November, 1957.

the cases of $Z_1 > Z_2$, (experiments, part II), the loci of R are like open eccentric spirals about the center. The loci of sinusoidal tapers in Fig. 2 appear similar to a reduced concentric spiral about the center; these are typical for the cases of $Z_1 > Z_2$. The position of R also sweeps almost one cycle every half-wavelength. The locations in the K-plane and the forms of these loci are almost identical for several surge impedance ratios; hence these two figures depict typical characteristics for the general cases. Moreover, regarding the limiting cases of $l=0$ for linear tapers, I have obtained reasonable data for the behavior of R.

K. MATSUMARU
Elec. Comm. Lab.
Kichijoji, Tokyo, Japan

The Permeability Matrix for a Ferrite Medium Magnetized at an Arbitrary Direction and Its Eigenvalues*

In analysis of propagation through magnetized ferrites it is usually assumed that the applied magnetostatic field is along one of the axes of the microwave carrier. It may be of interest to analyze the more general case; one in which the applied magnetostatic field is at an angle arbitrary to the axes of the microwave carrier.

If the geometry of Fig. 1, where H_0 stands for the applied magnetostatic field and the carrier axes are x, y and z, is assumed, then, using the equation for the motion of the magnetization[1]

$$\frac{\partial M}{\partial t} = \gamma M \times H \tag{1}$$

the following relation between the vector B and H results:

$$\begin{vmatrix} B_x \\ B_y \\ B_z \end{vmatrix} = \begin{vmatrix} \mu+(\mu_0-\mu)\sin^2\theta\cos^2\phi & \frac{\mu_0-\mu}{2}\sin^2\theta\sin 2\phi+j\kappa\cos\theta & \frac{\mu_0-\mu}{2}\sin 2\theta\cos\phi-j\kappa\sin\theta\sin\phi \\ \frac{\mu_0-\mu}{2}\sin^2\theta\sin 2\phi-j\kappa\cos\theta & \mu+(\mu_0-\mu)\sin^2\theta\sin^2\phi & \frac{\mu_0-\mu}{2}\sin 2\theta\sin\phi+j\kappa\sin\theta\cos\phi \\ \frac{\mu_0-\mu}{2}\sin 2\theta\cos\phi+j\kappa\sin\theta\sin\phi & \frac{\mu_0-\mu}{2}\sin 2\theta\sin\phi-j\kappa\sin\theta\cos\phi & \mu_0-(\mu_0-\mu)\sin^2\theta \end{vmatrix} \begin{vmatrix} H_x \\ H_y \\ H_z \end{vmatrix} \tag{2}$$

or, in short notation,

$$B = MH \tag{3}$$

where the usual approximations of small signal theory[1] have been used. One may observe that this completely general permeability matrix still preserves Hermitian character as long as losses are neglected; and, of course, it reduces to simple well-known forms in cases when H_0 is along any of the axes of the microwave carrier.

It may be sometimes desirable to express the relation between the vectors B and H in a canonical form. This can be accomplished by finding the principal axes of the medium —or, to put it differently—by finding a coordinate system in which there exists a relation of the form

$$(B_\alpha') = (\lambda_{\alpha\alpha})(H_\alpha') \tag{4}$$

where B_α' and H_α' are the components of the magnetic induction and magnetic intensity along the axes of the new coordinate system, and $(\lambda_{\alpha\alpha})$ is a diagonal matrix composed of the eigenvalues of the permeability matrix of (2). The procedure of finding the components of the matrix $(\lambda_{\alpha\alpha})$ is usually referred to as an eigenvalue problem.[2] In our case it amounts to finding an unitary matrix P such that

$$PMP^{-1} = (\lambda_{\alpha\alpha})$$
$$P^{-1} = \tilde{P}^*. \tag{5}$$

The transformation of the components of the magnetic induction and the magnetic intensity from the original to the new coordinate system are

$$B' = PB$$
$$H' = PH. \tag{6}$$

To find the matrix P we solve the eigenvalue equation

$$(M - I\lambda)U = 0 \tag{7}$$

where U is a matrix composed of three row vectors from which the matrix P can be constructed by means of an orthonormalization process.[3] Eq. (7) has a unique solution only if the determinant

$$|M - I\lambda| = 0, \tag{8}$$

which yields the results

$$\lambda_{1,2} = \mu \pm \kappa$$
$$\lambda_3 = \mu_0. \tag{9}$$

The eigenvalues of (9) are exactly the same as they would be if the applied magnetostatic field were along any one of the coordinate axes of Fig. 1. This fact may be somewhat surprising.

The amount of algebra involved in finding the matrix P corresponding to the permeability matrix of (2) is prohibitive. We shall try a simpler but still general enough case in which the applied magnetostatic field is in the $x-y$ plane, *i.e.*, $\theta=\pi/2$ in Fig. 1. In such a case the permeability matrix becomes

$$M = \begin{vmatrix} \mu+(\mu_0+\mu)\cos^2\phi & \frac{\mu_0-\mu}{2}\sin 2\phi & -j\kappa\sin\phi \\ \frac{\mu_0-\mu}{2}\sin 2\phi & (\mu+(\mu_0-\mu)\sin^2\phi & j\kappa\cos\phi \\ j\kappa\sin\phi & -j\kappa\cos\phi & \mu \end{vmatrix}. \tag{10}$$

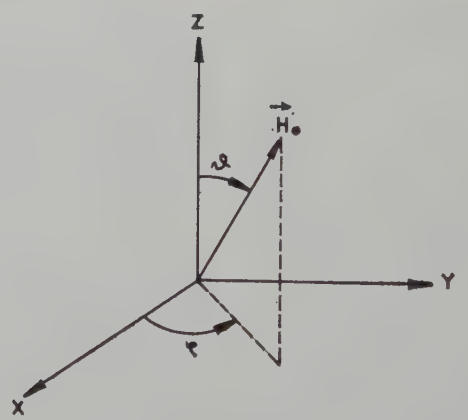

Fig. 1.

The corresponding unitary matrix P can be found to be

* Received by the PGMTT, September 12, 1958.

[1] D. Polder, "On the theory of electromagnetic resonance," *Phil. Mag.*, vol. 40, pp. 99–115; 1949.

[2] See, *e.g.*, H. Goldstein, "Classical Mechanics," Addison-Weseley Publishing Co., Inc., p. 119, 1956.

[3] H. Goldstein, *ibid.*, p. 328.

TABLE I

Original coordinate system	New coordinate system
$\nabla \times E = -\frac{\partial B}{\partial t}$	$\nabla' \times E' = -\frac{\partial B'}{\partial t}$.
$\nabla \times H = j + \frac{\partial D}{\partial t}$	$\nabla' \times H'^* = j' + \frac{\partial D'}{\partial t}$.
$\nabla \cdot B = 0$	$\nabla' \cdot B' = 0$
$\nabla \cdot D = \rho$	$\nabla' \cdot D' = \rho'$
$[B = MH$	$B' = (\lambda_{\alpha\alpha})H'$
$D = \epsilon E$	$D' = \epsilon E'^*$

Transformation equations

$$B' = PB$$
$$H' = PH$$
$$E' = -jP^* E$$
$$D' = jPD$$
$$j' = jPj$$
$$\nabla' = P^* \nabla$$
$$\rho' = -j\rho$$

$$P = \begin{bmatrix} j\frac{\sin\phi}{\sqrt{2}} & -j\frac{\cos\phi}{\sqrt{2}} & \frac{1}{\sqrt{2}} \\ -j\frac{\sin\phi}{\sqrt{2}} & j\frac{\cos\phi}{\sqrt{2}} & \frac{1}{\sqrt{2}} \\ \cos\phi & \sin\phi & 0 \end{bmatrix} . \quad (11)$$

We can now transform the entire set of Maxwell's equations to the new coordinate system which, we hope, will be simpler to work with. Table I shows the results.

It is indeed the case that the Maxwell equations—including the relations between the magnetic induction and magnetic intensity, and electric displacement and electric intensity—are much simpler in the primed than in the unprimed form. It may be an advantage in a particular problem involving arbitrary angle of magnetization of a ferrite to work in the primed system as far as possible before switching back to the original one.

George Tyras
Boeing Airplane Co.
Pilotless Aircraft Div.
Seattle, Wash.

Resistive-Film Calorimeters for Microwave Power Measurement*

Two papers[1,2] published recently in these Transactions have described calorimetric techniques for the measurement of microwave power at the milliwatt level which are free from the limitations inherent in existing methods using resistance-type milliwattmeters.

As the authors point out, the development of improved techniques is especially important at frequencies of the order of 10^4 mc and above. Somewhat similar work has recently been carried out in the United Kingdom at the Radio Research Station, Slough, and this note summarizes the essential features of the techniques used.

A 3-cm band calorimeter[3] in the form of a differential air thermometer has been developed for the power range 10–100 mw. This consists of two identical tapered resistive films located inside thin glass cells which are connected by a capillary tube containing a movable liquid index. One film absorbs the input microwave power and the other serves as a control against variations in ambient temperature. A measurement is made in terms of the equivalent dc power by a null technique. The input voltage standing-wave ratio (VSWR) is less than 1.15 over the band 8800–10,000 mc.

Comparison experiments have shown that the error limit is not more than ± 2 per cent. The instrument is extremely compact, and could be adapted for use at other frequencies.

Sucher and Carlin suggest that the substitution error in their calorimeters would be reduced to a minimum by using a transverse film as the absorbing load. This technique has in fact been used by the author for the measurement of power flow in rectangular waveguides, preliminary details being published in 1956.[4] A thin mica strip sputtered with platinum is located in the transverse plane, and with the optimum value of film resistivity an input VSWR of 1.1 or less can be obtained over the band 8500–10,000 mc, if the film is followed by a movable plunger. The input power can be determined in a dc calibration by utilizing the change of resistance produced in the platinum film, or, more conveniently, by observations of the temperature rise indicated by a thermocouple attached to the film. The wires of the thermocouple are parallel to the broad face of the waveguide. A detailed comparison[5] at 9200 mc, against reference standards operating at higher power levels has already confirmed that the technique affords a simple yet accurate method of power measurement in the range 1–100 mw.

Recent experiments (details of which are shortly to be published) have shown that this type of film bolometer can still be used at frequencies as low as 3000 mc. Furthermore, if a stable multirange dc amplifier is connected to the thermojunction, powers in range 100 μw–100 mw can be measured in a single instrument. Using this arrangement, the time constant of the 3-cm band model is not more than 5 seconds, compared with 2.6 minutes for the calorimeter described by James and Sweet.[2] The error limit is approximately ± 2 per cent at 100 mw and ± 5 per cent at 100 μw. Measurements at the latter level are at present limited in their accuracy as a result of random fluctuations in ambient temperature and amplifier gain. At a frequency of 10,000 mc, these fluctuations result in output variations equivalent to a power of about 3 μw. This "noise level" could probably be reduced by isolating the absorbing load in the manner described by James and Sweet.[2]

This note is published by permission of the Director of Radio Research of the Department of Scientific and Industrial Research, England.

J. A. Lane
Dept. Sci. Indust. Res., Radio Res. Station
Ditton Park, Slough, Bucks, England

* Received by the PGMTT, September 22, 1958.

[1] M. Sucher and H. J. Carlin, "Broad-band calorimeters for the measurement of low and medium level microwave power. I. Analysis and design," IRE Trans. on Microwave Theory and Techniques, vol. MTT-6, pp. 188–194; April, 1958.

[2] A. V. James and L. O. Sweet, "Broad-band calorimeters for the measurement of low and medium level microwave power. II. Construction and performance," IRE Trans. on Microwave Theory and Techniques, vol. MTT-6, pp. 195–202; April, 1958.

[3] A. C. Gordon-Smith, "A milliwattmeter for centimetre wavelengths," *Proc. IEE*, vol. 102, pp. 685–686; September, 1955.

[4] J. A. Lane, "A film radiometer for centimetre wavelengths," *Nature*, vol. 177, p. 392; February, 1956.

[5] J. A. Lane, "Transverse film bolometers for the measurement of power in rectangular waveguides," *Proc. IEE*, vol. 105, pp. 77–80; January, 1958.

PGMTT News

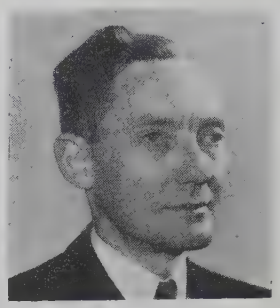

Welcoming addresses were given at the 1958 PGMTT National Symposium by A. L. Aden (*left*), Symposium Chairman, Professor H. H. Skilling (*center*), Stanford University, and W. L. Pritchard, Chairman of the PGMTT Administrative Committee.

1958 National Symposium

Stanford University was the location of the 1958 PGMTT National Symposium, held on May 5–7. Four hundred and thirty-seven registrants attended the six technical sessions held in Cubberley Auditorium.

Thirty-nine papers were given, six of which had been invited. Highlighting the technical sessions were papers on new ferrite devices, solid-state microwave amplifiers, and high-power filters.

Dr. Frederick E. Terman, Provost and Dean of Engineering, Stanford University, gave the keynote address," Basic Research in Industry and Education," at the Annual Banquet held on May 6th. W. L. Pritchard, Chairman of the Administrative Committee, presented the Microwave Prize certificate to Dr. Harold Seidel of Bell Telephone Laboratories. The Group's annual prize was announced in the October issue of these TRANSACTIONS.

The technical papers presented during the three-day Symposium are featured in this issue.

Members of the Program Committee are (*left to right*): G. J. Wheeler, Sylvania Microwave Physics Lab.; S. B. Cohn, Stanford Research Institute; H. J. Shaw, Stanford University; P. H. Vartanian, Jr., Microwave Engineering Labs.; P. D. Lacy, Hewlett-Packard Co.; E. M. T. Jones, Stanford Research Institute; K. Tomiyasu, General Electric Microwave Lab.; A. L. Aden, Sylvania Microwave Physics Lab.

Plans for the National Symposium were coordinated by the Steering Committee (*left to right*): W. A. Edson, General Electric Microwave Lab.; J. L. Melchor, Microwave Engineering Labs.; T. Moreno, *Finance*, Varian Associates; S. B. Cohn, Stanford Research Institute; W. H. Thon, Sylvania Microwave Tube Lab.; K. Tomiyasu, *Technical Program*, General Electric Microwave Lab.; A. L. Aden, *Symposium Chairman*, Sylvania Microwave Physics Lab.; J. R. Whinnery, University of California; G. H. Keitel, *Publicity*, General Electric Microwave Lab.; H. Schroeder, *Local Arrangements*, Sylvania Microwave Physics Lab.; T. N. Anderson, Airtron, Inc.; H. Heffner, Stanford University; and P. D. Lacy, Hewlett-Packard Co.

Dr. Frederick E. Terman delivering the keynote address at the Annual PGMTT Banquet.

Dr. Harold Seidel receiving the Microwave Prize certificate from W. L. Pritchard.

Seated at the dais table are (*left to right*): Professor and Mrs. H. H. Skilling, W. L. Pritchard, Mrs. F. E. Terman, Dr. F. E. Terman, Mrs. M. Leifer, M. Leifer, *Toastmaster*, A. L. Aden, Mrs. A. L. Aden, H. Seidel, Mrs. K. Tomiyasu, and K. Tomiyasu.

Intermission during the 1958 PGMTT National Symposium. Left photo (*left to right*), W. W. Mumford, T. S. Saad and A. C. Beck; center photo, H. N. Chait, K. J. Button, and L. Swern; right photo, S. Weisbaum, J. H. Rowen, and W. D. Hershberger.

CALL FOR PAPERS FOR 1959 PGMTT NATIONAL SYMPOSIUM

On June 1–3, at Harvard University, Cambridge, Mass., the IRE Professional Group on Microwave Theory and Techniques will hold the 1959 PGMTT National Symposium in cooperation with the Division of Applied Physics, Harvard University.

Prospective authors are requested to submit papers in the areas related to:

Microwave Components
Microwave Physics
Microwave Systems.

One-hundred word abstracts in triplicate and 500-word summaries in triplicate should be sent before February 15, 1959 to:

Dr. Henry J. Riblet, Chairman
Technical Program Committee
1959 PGMTT National Symposium
92 Broad Street
Wellesley, Massachusetts

Foreign papers are to be submitted in English. The Technical Program Committee should be advised if any paper will have been presented elsewhere or published prior to the Symposium.

The Symposium Committee Chairmen are:

Chairman, W. L. Pritchard, Raytheon Manufacturing Co.
Assistant Chairman, H. Scharfman, Raytheon Manufacturing Co.
Technical Program, H. J. Riblet, Microwave Development Laboratories
Publicity, R. A. Rivers, Aircom, Inc.
Local Arrangements, T. S. Saad, Sage Laboratories.

Contributors

Wesley P. Ayres, for a photograph and biography, please see page 268 of the October, 1957, issue of these TRANSACTIONS.

❖

Henry L. Bachman (S'51–A'52) was born in Brooklyn, N. Y., on April 29, 1930. He received the B.E.E. degree in 1951 and M.E.E. degree in 1954 from the Polytechnic Institute of Brooklyn.

H. L. BACHMAN

Mr. Bachman has been employed since 1951 as an engineer by the Wheeler Laboratories, Great Neck, N. Y., where he has specialized in microwave antennas and transmission lines.

He is a member of Eta Kappa Nu and Tau Beta Pi, and an associate member of Sigma Xi.

❖

Richard C. Becker (S'53–M'56) was born on March 1, 1931, in Chicago, Ill. He received the B.S. degree in electrical engineering from Fournier Institute of Technology in 1953. In 1954 he was awarded the M.S. degree in electrical engineering, and in 1956 the M.S. degree in mathematics at the University of Illinois, where he is now completing the requirements for the Ph.D. degree in electrical engineering.

R. C. BECKER

During the summer of 1952, Mr. Becker was employed by the Illinois Bell Telephone Company and participated in the engineering planning and design of a light-route microwave radio relay system. The following summer was spent at the Advanced Antenna Laboratory of the Andrew Corporation.

In 1954 he was engaged in research on microstrip transmission lines and components at the University of Illinois, and from September, 1954, to November, 1956, was employed there as research assistant in the Antenna Laboratory. His present position is that of research assistant in the Ultramicrowave Laboratory at the University of Illinois, where he is working on the problem of submillimeter wave generation, and is a part-time member of the instructional staff of the Electrical Engineering Department.

Mr. Becker is a member of Eta Kappa Nu and Tau Beta Pi.

W. Earl Bell was born on April 2, 1921, in Winnipeg, Man., Canada. He attended the University of Alberta, Edmonton, Alta., and the University of London in England.

W. E. BELL

From 1940 to 1945, he served as an electrical engineer with the Royal Canadian Navy. He then joined the National Research Council of Canada at the Chalk River Laboratories, Ont., Canada, working on atomic physics and cosmic rays.

He became affiliated with Newmont Exploration Ltd., Jerome, Ariz., in 1950, and was engaged in exploration geophysics and instrument research and development. At Varian Associates, Palo Alto, Calif., where he has been since 1954, he is concerned with atomic physics and geophysical research.

He has held an appointment as research associate in geophysics at Stanford University, Stanford, Calif., since 1957. He holds a U. S. patent, and has eight more pending.

Mr. Bell is a member of the American Physical Society, American Geophysical Union, Peninsula Geological Society, and the Society of Exploration Geophysicists.

❖

A. Bloom was born in Chicago, Ill., on March 7, 1923. After attending the University of California in Berkeley for one year, he served with the U. S. Signal Corps from 1943–1946, including duty in China.

A. BLOOM

Returning to the University, he received the B.A. degree with honors in physics in 1947 and the Ph.D. degree in 1951. His dissertation concerned "Experiments on Scattering of 190-MEV Deuterons by Protons."

He was a research assistant at the Westinghouse Electric Company's Research Laboratories during the summer of 1947, and from 1948 to 1951 he was a teaching assistant at the University of California.

He has been employed by Varian Associates, Palo Alto, Calif., since 1951.

Dr. Bloom is a member of Phi Beta Kappa, Sigma Xi, the American Physical Society, and the American Association for the Advancement of Science.

Sanborn C. Brown was born in Beirut, Lebanon, on January 19, 1913. He received the B.A. and M.A. degrees from Dartmouth College, Hanover, N. H., in 1935 and 1937, respectively, and the Ph.D. degree in physics from the Massachusetts Institute of Technology, Cambridge, in 1944.

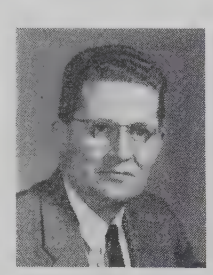

S. C. BROWN

From 1935–1937, he was an assistant in physics at Dartmouth. He was a teaching fellow at M.I.T. from 1938 to 1941, when he became an instructor. He was an assistant professor from 1945 to 1949. He then was appointed to his present position as associate professor of physics.

In 1941 he worked as a civilian with the Office of Scientific Research and Development.

Dr. Brown is a Fellow of the American Physical Society, and served as chairman of its Division of Electron Physics from 1951–1952, a Fellow of the AAAS, and treasurer of the American Association of Physics Teachers. He also served as secretary of the Gaseous Electronics Conference Committee, 1956–1957, and as a member of the AIEE Subcommittee on Electrical Properties of Gases during 1952–1955.

❖

Herman N. Chait (A'55) was born in Boston, Mass., on February 15, 1924. He attended Northeastern University in Boston and transferred to Tufts College, Medford, Mass., where he obtained the B.S.E.E. degree in 1945. He has since done graduate work at the University of Maryland.

H. N. CHAIT

After serving for three years as an electronics technician in the U. S. Navy, Mr. Chait joined the Naval Research Laboratory, Washington, D. C., where he has done research and development work in the microwave region. He has also worked on the design of signal generators and test equipment. At present he is a member of the Microwave Antennas and Components Branch at NRL, doing research on antennas and microwave applications of ferrites.

Mr. Chait is a member of RESA and co-holder of the first Microwave Prize of the PGMTT.

J. F. Cline (A'43–SM'47) was born on June 19, 1917, in Cadillac, Mich. He received the B.S.E., M.S., and Ph.D. degrees in electrical engineering from the University of Michigan, Ann Arbor, in 1938, 1941, and 1950, respectively, and was employed in both the Engineering Research Institute and the Department of Electrical Engineering of that university from 1942 to 1957.

J. F. Cline

He was appointed assistant professor in 1950. During the summer of 1952 he was employed as research engineer in the Physical Research Unit of Boeing Airplane Company. While on leave from the university for the academic year 1953–1954, he was employed as design specialist in the antenna laboratory of the Long Beach plant of the Douglas Aircraft Company. During the summer of 1956, he was employed as research physicist at Hughes Research and Development Laboratories. Since February, 1957, he has been employed as senior research engineer in the Electromagnetics Laboratory of Stanford Research Institute, Menlo Park, Calif.

Dr. Cline is a member of AIEE, Eta Kappa Nu, and Sigma Xi.

❖

S. B. Cohn, for photograph and biography, please see page 242 of the April, 1958, issue of these Transactions.

❖

Paul D. Coleman (A'46–M'56) was born in Stoystown, Pa., on June 4, 1918. He received the B.A. degree from Susquehanna University, Selinsgrove, Pa., in January, 1940, the M.S. degree in physics from Pennsylvania State University in 1942, and the Ph.D. degree in physics from Massachusetts Institute of Technology in 1951.

P. D. Colem an

Mr. Coleman was employed as a physicist with the Signal Corps, later Air Corps WADC, Dayton, Ohio, from May, 1942, to September, 1946. During this period he was engaged in work on electromagnetic theory, and received the Air Force Meritorious Civilian Award in 1946 for his contribution to aircraft antenna theory.

From 1946 to 1951, he was concurrently a physicist with the Air Force Cambridge Research Center and a research associate in physics in the Research Laboratory of Electronics at M.I.T., where he was concerned with the generation of submillimeter waves.

In 1951 Mr. Coleman became an associate professor in electrical engineering at the University of Illinois, where he established the Ultramicrowave Group in the Electrical Engineering Research Laboratory. He is presently a Professor on the Graduate Electrical Engineering staff, directing research on submillimeter wave generation.

He is a member of the American Physical Society, Sigma Xi, and Pi Mu Epsilon.

❖

L. B. Felsen was born in Munich, Germany, on May 7, 1924. He entered the United States in 1940, and during World War II was concerned with work on electronic ballistic calibration devices in the U. S. Army. He received the B.E.E., M.E.E., and D.E.E. degrees from the Polytechnic Institute of Brooklyn, N. Y., in 1948, 1949, and 1952, respectively.

L. B. Felsen

Since 1948, he has been employed at the Microwave Research Institute of the Polytechnic Institute of Brooklyn and presently holds the position of research associate professor. His work has been concerned chiefly with electromagnetic diffraction problems and microwave circuit and measurement techniques.

Dr. Felsen is a member of Eta Kappa Nu, Tau Beta Pi, Sigma Xi, and USA Commission 6 of URSI.

❖

Dominic A. Fleri was born in Brooklyn, N. Y., on November 8, 1931. He received the B.S. degree in physics from the Polytechnic Institute of Brooklyn, Brooklyn, N. Y. in 1953, and the M.S. degree in physics from New York University in June, 1958. He joined the Sperry Gyroscope Company in Great Neck, N. Y., in June, 1953 but was called to active duty with the U. S. Army Signal Corps in February, 1954. During his two-year military service he was assigned primarily as an electronics instructor at the Signal School, Fort Monmouth, N. J.

D. A. Fleri

He returned to Sperry in January, 1956, and since then he has been engaged in microwave applications in the Microwave Circuits Section of the Microwave Electronics Department, Great Neck, N. Y.

Gerard L. Hanley was born in Brooklyn, N. Y., on August 9, 1930. He received the B.S. degree in electrical engineering from the University of Notre Dame, South Bend, Ind., in 1952. From 1952 to 1954 he was employed by the Sperry Gyroscope Company in the Microwave Antenna and Component Development Department in Great Neck, N. Y. After two years of service in the U. S. Army, he returned to Sperry to work with the same group. In June, 1957, Polytechnic Institute of Brooklyn, Brooklyn, N. Y. awarded him the M.E.E. degree.

G. L. Hanley

❖

Hubert Heffner (S'49–A'52–SM'56) was born in Lincolnton, N. C., on December 26, 1924. He received the B.S. degree in physics in 1947 and the M.S. and Ph.D. degrees in electrical engineering in 1949 and 1952, respectively, from Stanford University, Stanford, Calif. From 1949 to 1951, he was a predoctoral fellow of the Atomic Energy Commission.

H. Heffner

During World War II he served in the U. S. Army Signal Corps, and was in charge of several microwave relay stations in Germany. From 1952–1954, Dr. Heffner was on the technical staff of Bell Telephone Laboratories, where he was engaged in vacuum-tube research. Since 1954, he has been on the faculty of Stanford University, and is now associate professor of electrical engineering.

Dr. Heffner is a member of Phi Beta Kappa, Sigma Xi, and the American Physical Society.

❖

Robert M. Hill was born on September 20, 1926, in New York, N. Y. He received the B.A. degree in physics from Cornell University, Ithaca, N. Y., in 1949, and the Ph.D. degree in 1953 from Duke University, Durham, N.C., where he was successively a teaching assistant, research fellow, and research associate.

R. M. Hill

He served with the U. S. Army as a radio technician from

1943 to 1945. He joined Sylvania Electric Products, Inc., in 1953, and is presently head of the Research Department at the Microwave Physics Laboratory, Mountain View, Calif.

Dr. Hill is a member of Sigma Pi Sigma, Sigma Xi, and the American Physical Society.

❖

Charles M. Johnson was born in Nashville, Tenn., on May 31, 1923. He received the B.E. degree in civil engineering from Vanderbilt University in Nashville in 1944, and was employed as a structural engineer until 1948, when he returned to graduate school at Duke University in Durham, N. C. He received the Ph.D. degree in physics in 1951 for microwave spectroscopy research in the millimeter region.

C. M. Johnson

From July, 1951, until October, 1956, he was a staff member of the Radiation Laboratory of The Johns Hopkins University, Baltimore, Md., as research associate until 1953 and research scientist until 1956. Since then he has been research manager of the microwave and infrared sections of Electronic Communications, Inc., Timonium, Md.

Dr. Johnson is a member of the American Physical Society and Sigma Xi.

❖

E. M. T. Jones, for photograph and biography, please see p. 458 of the October, 1958, issue of these Transactions.

❖

Walter K. Kahn (S'50–A'51–M'56) was born on March 24, 1929, in Mannheim, Germany, and came to the United States in 1938. He completed his undergraduate studies at the Cooper Union School of Engineering, New York, N. Y., receiving the bachelor's degree in electrical engineering in 1951.

W. K. Kahn

Upon graduation, Mr. Kahn was employed at the Wheeler Laboratories, New York, where he worked on microwave radar system development. Concurrently he engaged in graduate study at the Polytechnic Institute of Brooklyn, N. Y., receiving the master's degree in electrical engineering in 1954.

At that time he joined the staff of the Microwave Research Institute of the Polytechnic Institute of Brooklyn, where he is presently studying general diffraction theory and propagation in multimode waveguides.

Mr. Kahn is a member of Sigma Xi.

❖

R. H. Kingston (S'48–A'52—SM'58) was born in Somerville, Mass., on February 13, 1928. He received the B.S. and M.S. degrees in electrical engineering from the Massachusetts Institute of Technology, Cambridge, in 1948. Under the co-operative plan in electrical engineering during the years 1945 to 1948, he worked at the Philco Corporation on component testing, radar system design, and frequency modulation and circuit theory. In June, 1951 he received the Ph.D. degree in physics from M.I.T., where his major field was the physics of solids.

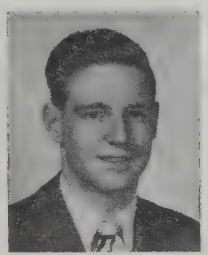

R. H. Kingston

He joined the staff of the Lincoln Laboratory at M.I.T. at this time, where he has been engaged in solid-state device research and development. From September, 1951 to September, 1952, on leave of absence from the Lincoln Laboratory, he was a member of the technical staff at Bell Telephone Laboratories in Murray Hill, N. J. He edited the book, "Semiconductor Surface Physics."

Dr. Kingston is a member of Tau Beta Pi and Sigma Xi, and a Fellow of the American Physical Society.

❖

Herbert Kirschbaum (A'55) was born in Cleveland, Ohio, on February 6, 1920. He received the B.S. degree in 1942 from Cooper Union, New York, N. Y., thereafter entering the employ of the Westinghouse Electric Corporation. He received the M.S. degree from the University of Pittsburgh, Pennsylvania, under the Pitt-Westinghouse cooperative plan, in 1946. In the same year he joined the staff of The Ohio State University to teach and do research on pulse transformers.

H. Kirschbaum

During 1952–1953, he took a leave of absence from The Ohio State University to complete requirements for the Ph.D. degree at the Carnegie Institute of Technology, Pittsburgh, Pa. Upon returning to The Ohio State University, in addition to teaching, he was affiliated with the Antenna Laboratory of The University. He left Ohio State in September, 1957, to join the Systems Engineering Division of Battelle Memorial Institute, Columbus, Ohio, where he is currently engaged in research on servo systems.

Dr. Kirschbaum is a member of Eta Kappa Nu and Sigma Xi.

❖

Lawrence Levey (S'52–M'56) was born in Brooklyn, N. Y., on March 23, 1930. He received the B.E.E. degree in 1952 and the M.E.E. degree in 1953 from the Polytechnic Institute of Brooklyn, N. Y., where he currently is continuing his graduate studies.

L. Levey

In 1952–1953 Mr. Levey held a research fellowship at the Microwave Research Institute of the Polytechnic Institute of Brooklyn. Since then he has been employed at the Institute presently in the capacity of research associate.

His work has been concerned chiefly with the development of microwave power standards, multimode measurement techniques, and ferrite components.

Mr. Levey is a member of Eta Kappa Nu and Sigma Xi.

❖

David J. Lewis was born in Denver Colo., on March 16, 1930. He received the B.S. degree in electrical engineering from Massachusetts Institute of Technology, Cambridge, Mass., in 1955 and the M.S. degree from the University of Pennsylvania, Philadelphia, Pa., in 1957. Mr. Lewis has been employed as a research assistant and instructor by the University of Pennsylvania since 1955. He is currently engaged in radar interference problems.

D. J. Lewis

Richard S. Mangiaracina was born on August 31, 1931, in Brooklyn, N. Y. He received the B.S. degree in physics from the Polytechnic Institute of Brooklyn in 1953. He worked for the Sylvania Electric Products Company and then served two years with the U. S. Army as an instructor in electronics.

R. Mangiaracina

In 1956, he became affiliated with the Sperry Gyroscope Company's Microwave Electronics Division in Great Neck, N. Y. In August, 1958, he became a research assistant in physics at the University of Buffalo.

❖

Jack L. Melchor (SM'56) was born on July 6, 1925, in Mooresville, N. C. He received the B.S. and M.S. degrees in physics from the University of North Carolina in Chapel Hill. His undergraduate studies were interrupted by military service in the U. S. Navy. In 1949 he worked as a civilian physicist with the U. S. Navy Mine Countermeasures Station.

J. L. Melchor

While attending the University of Notre Dame, South Bend, Ind., in 1950 he was a U. S. Rubber Company Fellow in high polymer physics. In 1952 and 1953 he worked with the Missile Division of Bendix Aviation Corporation, and received the Ph.D. degree from Notre Dame in 1953. He then joined the Electronic Defense Laboratory of Sylvania Electric Products, Inc., Mountain View, Calif., where he was engaged in ferrite research at microwave frequencies.

In 1956 Dr. Melchor left Sylvania to form Microwave Engineering Laboratories, Inc., Palo Alto, Calif. He is president of the organization and does research and development on microwave components and systems. He is a member of Sigma Xi and RESA.

❖

F. R. Morgenthaler, for a photograph and biography, please see page 243 of the April, 1958, issue of these Transactions.

❖

Francis J. O'Hara (A'55) was born on April 9, 1930, in Cambridge, Mass. He received the B.S. degree in physics in 1951 from Boston College, Newton, Mass. He subsequently studied at Harvard University, Cambridge, Mass., and at Northeastern University, Boston, Mass., and was awarded the M.S. degree in communications by the latter university in 1958.

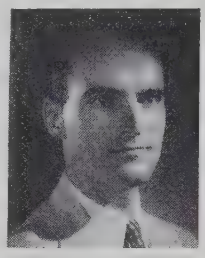

F. J. O'Hara

In 1953, he joined the engineering staff of Microwave Associates, Inc., where he performed product development work on TR tubes. Since 1955 he has been a member of a development group for microwave ferrite devices at the Raytheon Manufacturing Company, Waltham, Mass.

❖

Arthur A. Oliner (M'47–SM'52) was born in Shanghai, China, on March 5, 1921. He received the B.A. degree from Brooklyn College, N. Y., in 1941 and the Ph.D. degree in physics from Cornell University, Ithaca, N. Y., in 1946. From 1941 to 1944 he was a graduate teaching assistant in the physics department. He participated in an Office of Scientific Research and Development project at Cornell University from 1944 to 1945.

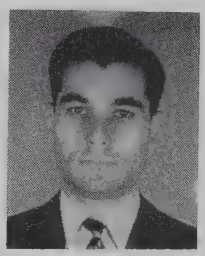

A. A. Oliner

Since 1946 Dr. Oliner has been with the Microwave Research Institute of the Polytechnic Institute of Brooklyn, N. Y., where he has been engaged in research on a variety of topics in the microwave field. While on a leave of absence he spent the summer of 1952 at the Microwave Laboratory of Hughes Aircraft Company, Culver City, Calif. He has also taught graduate courses in physics and electrical engineering, and is a research associate professor at Brooklyn Polytechnic.

He is a member of the American Physical Society and Sigma Xi. He is also a member of the IRE Committee on Antennas and Waveguides, and the Administrative Committee of the PGMTT.

❖

Vernon G. Price (S'48–M'52) was born in Salt Lake City, Utah, on October 15, 1924. He received the B.S. and M.S. degrees in electrical engineering in 1948 and 1949, respectively, from the University of Utah.

V. G. Price

After being employed for one year by the Utah State Engineering Experiment Station on a Navy project studying high voltage breakdown in piezoelectric crystals, he then joined the underwater sound staff at the Navy Electronics Laboratory. In 1955 Mr. Price joined the General Electric Microwave Laboratory, where he has been working on measurement and control of harmonic and spurious microwave energy.

❖

Walter Rotman (A'49–M'53) was born in St. Louis, Mo., on August 24, 1922. He received the B.S. and M.S. degrees from Massachusetts Institute of Technology in 1947 and 1948. From 1942 to 1945, he served in the Air Force, working on radar equipment. During his student career he worked as a research assistant in the Research Laboratory of Electronics at M.I.T.

W. Rotman

In 1948, Mr. Rotman joined the Airborne Antenna Group of the Air Force Cambridge Research Center, where he is now engaged in antenna research. His fields of interest include progressive wave antennas, microwave optical systems, and missile antennas.

Mr. Rotman is a member of RESA and Sigma Xi.

❖

Nicholas G. Sakiotis (S'48–A'50–M'55) was born in Lakeland, Fla., on March 5, 1928. He received the B.E.E. degree from the College of the City of New York in 1950.

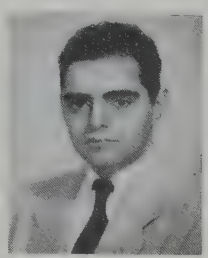

N. G. Sakiotis

After working with the Glenn L. Martin Company and the Marine Radar Design Branch of the Bureau of Ships, Mr. Sakiotis joined the Antenna Research Branch of the Naval Research Laboratory, Washington, D. C., in 1951. While with the Laboratory, he has investigated figure-of-revolution scanners and is at present engaged in making a study of the microwave properties of the ferrite materials.

He is a co-holder of the first Microwave Prize of the PGMTT.

❖

Howard Scharfman (S'47–A'50–M'55) was born in New York, N. Y., on December 27, 1924. He served with the U. S. Signal Corps, working on radar and pulse modulation equipment, from 1943–1946. He received the B.S.E.E. degree in 1947 from New York University and the M.S.E.E. degree

in 1948 from Northwestern University.

After working at the Kew Gardens, N. Y., plant of the Sylvania Electric Company during the summer of 1948, he taught undergraduate electrical engineering and continued his graduate studies at the Polytechnic Institute of Brooklyn until 1950. He then joined the Antenna Section of the Seattle, Wash., division of the Boeing Airplane Company, where he did research and development on receivers, antenna pattern ranges, and aircraft antennas.

H. Scharfman

From 1951–1954, he was at the Radiation Laboratory of The Johns Hopkins University, Institute for Cooperative Research, where he worked on VHF and UHF circuits and microwave scattering problems while completing graduate studies for the D.S.E.E. degree in electrical engineering.

In 1954 he became affiliated with the Missile and Radar Division of the Raytheon Manufacturing Company, Waltham, Mass., as head of the microwave ferrite section. Since January, 1957, he has been manager of the Special Microwave Device Group, which is engaged in research, development, and production of ferrite materials and devices for commercial sale.

Dr. Scharfman is a member of Eta Kappa Nu and Sigma Xi.

❖

B. M. Schiffman, for a photograph and biography, please see page 244 of the April, 1958, issue of these Transactions.

❖

J. K. Shimizu, for photograph and biography, please see page 459 of the October, 1958, issue of these Transactions.

❖

Ernest Stern (S'55–M'56) was born on June 5, 1928, in Wetter, Germany. He served as an electronics technician with the U. S. Navy during 1946 and 1947. He received the B.S. degree in engineering from Columbia University, New York, N. Y., in 1953 and completed studies for the M.S. degree at Cornell University, Ithaca, N. Y., in 1955. From 1953 to 1955 he was a research assistant in the Radio Astronomy Laboratory at Cornell University.

E. Stern

In 1955 he joined the engineering staff of the Sperry Gyroscope Company, Great Neck, N. Y., where he performed experimental studies on the nonlinear microwave properties of ferrites at high microwave power levels. His current activities involve the evaluation and design of solid-state microwave amplifiers.

❖

Sidney J. Tetenbaum (S'47–A'53) was born on August 30, 1922, in the Bronx, N. Y. He received the B.S. degree in mathematics from the City College of New York in 1943, the master's degree in electrical engineering from New York University in 1948, and the Ph.D. degree in physics from Yale University, New Haven, Conn., in 1952.

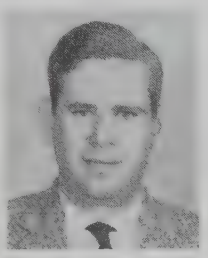

S. J. Tetenbaum

He served with the U. S. Army Signal Corps from 1943 to 1946. From 1946 to 1948 he was employed as a scientific investigator on the Panel on Electron Tubes of the Research and Development Board. He was a research engineer with Varian Associates, Palo Alto, Calif., during 1952 to 1954.

He then joined Sylvania Electric Products, Inc., and is presently a project leader at the Microwave Physics Laboratory, Mountain View, Calif.

Dr. Tetenbaum is a member of Phi Beta Kappa, Sigma Xi, and the American Physical Society.

❖

Eugene N. Torgow (S'48–A'49–SM'54) was born on November 26, 1925 in New York, N. Y. He received the B.E.E. degree from the Cooper Union School of Engineering, New York, N. Y., in 1946, and the M.E.E. degree at the Polytechnic Institute of Brooklyn, Brooklyn, N. Y., in 1949.

E. N. Torgow

During 1946–47, he served with the U. S. Army Air Force, doing radar repair and maintenance in the Pacific Theater. In 1948, he joined the staff of the Microwave Research Institute of the Polytechnic Institute of Brooklyn, where he worked on research and development of microwave attenuators and power measuring devices. From 1951 to 1953, he established and supervised a microwave laboratory at the Allen B. DuMont Laboratories, East Paterson, N. J.

In 1953, Mr. Torgow returned to the Microwave Research Institute and since then has been engaged in strip line and waveguide filter development. He became leader of the Component Research Section in 1957.

Mr. Torgow is a member of Sigma Xi and AIEE.

❖

Raphael Tsu was born on December 27, 1932, in Shanghai, China. He received the B.E.E. degree from the University of Dayton, Ohio, in 1956, and the M.S. degree from The Ohio State University in Columbus in 1957.

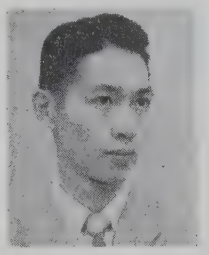

R. Tsu

He came to this country in January, 1953. From then until January, 1956, he did research on electronic tubes at the University of Dayton. While still a candidate for the B.E.E. degree he instructed laboratory courses at the University. From February, 1956 to September, 1956, he was a research assistant at the Nuclear Research Center of Carnegie Institute of Technology, Pittsburgh, Pa., where he was a graduate student in physics. Since 1956 he has been employed by the Antenna Laboratory at The Ohio State University, and is currently working toward the Ph.D. degree.

Mr. Tsu is a member of Sigma Xi and Pi Mu Epsilon.

❖

Lauren P. Tuttle, Jr. (S'56) was born in Bloomfield, N. J., on June 21, 1931. He attended the University of Chattanooga, Tenn., and received the B.S. degree in electrical engineering at the University of Florida in Gainesville in 1957. While in college, Mr. Tuttle worked two years as student assistant at the Severe Weather Radar Laboratory of the University of Florida; there he engaged in the radar tracking of hurricanes and unusually severe weather.

L. P. Tuttle

During the Korean conflict he served as leading division petty officer on the *USS Boxer* in charge of shipboard electronics systems.

Since graduation he has been in the Antenna Laboratory of Melpar, Inc., Falls Church, Va., working on the development of strip-transmission-line circuits.

Mr. Tuttle was a student member of the AIEE.

George S. Uebele (M'56) was born on January 28, 1930, in San Francisco, Calif. In 1952, he received the B.S. degree in engineering from the University of California at Berkeley. He joined the technical staff at Hughes Aircraft Company and was awarded a Hughes Aircraft scholarship to the University of Southern California, where he received the M.S. degree in engineering in 1954.

G. S. UEBELE

Since 1952, he has been concerned with the development of microwave components, especially ferrite devices. He is now head of the component development group, circuits section, Microwave Engineering Department, Microwave Laboratory.

Mr. Uebele is a member of Tau Beta Pi and Eta Kappa Nu.

❖

Perry H. Vartanian, Jr. (S'52–M'56–SM'56), for a photograph and biography, please see pages 244–245 of the April, 1958, issue of these TRANSACTIONS.

❖

Robert D. Wanselow (S'52–M'55) was born on June 21, 1930, in Mineola, N. Y. He received the B.A. and B.S.E.E. degrees in 1953 and the M.S.E.E. degree in 1955, all from Columbia University, New York, N. Y., and was a graduate assistant there in the engineering school while working for his advanced degree.

R. D. WANSELOW

In 1955, Mr. Wanselow joined the Hughes Aircraft Company, Culver City, Calif. As a research engineer he instructed engineers on Hughes' latest fire control systems and performed evaluation and maintenance studies on a surveillance radar system.

Since 1957, when he joined Melpar, Inc., Falls Church, Va., as a senior engineer, he has been engaged in research and development work on electronic countermeasures systems. At present he is working on the design and development of antennas and microwave components in the Melpar Antenna Laboratory.

Mr. Wanselow was a student member of the AIEE.

Harold A. Wheeler (A'27–M'28–F'35) was born in St. Paul, Minn., on May 10, 1903. He received the B.S. degree in physics from George Washington University, Washington, D. C., in 1925 and did postgraduate studies in physics at The Johns Hopkins University, Baltimore, Md., until 1928.

H. A. WHEELER

He was employed by the Hazeltine Corporation from 1924 to 1945, advancing to vice-president and chief consulting engineer. Since 1946, he has engaged in independent work as a consulting radio physicist, and since 1947, his principal occupation has been as President of Wheeler Laboratories, Inc. In this capacity, he is directing the Great Neck and Smithtown laboratories, specializing in microwaves and antennas.

His specialization in frequency-selective networks dates back to a college thesis on "wave filter determinants," published in 1928. Subsequent work on wideband amplifiers for television was presented in IRE papers, which were recognized by the Morris N. Liebman Memorial Prize in 1940. "Wheeler Monographs," Vol. I, is a collection of postwar papers dealing mostly with special topics in network theory.

Mr. Wheeler has served the IRE in such positions as Director (1934, 1940–1945), chairman of the Standards Committee, and chairman of the Long Island Section. He is a Fellow of the AIEE and Radio Club of America, Associate Member of IEE, and member of Sigma Xi and Tau Beta Pi.

❖

Robert G. Williams, Captain, USMC, (S'52–A'53–M'58) was born on June 30, 1931, in Brooklyn, N. Y. He received the B.S.E.E. degree in 1953 from the University of Colorado in Boulder. He then was commissioned a second lieutenant in the U. S. Marine Corps.

R. G. WILLIAMS

After attending Basic School and the Communication Officer's School, Quantico, Va., he served with the Communication Company, Third Marine Division, in Japan until July, 1955.

Following his overseas duty, he entered the U. S. Naval Postgraduate School, Monterey, Calif., and received the M.S. degree in electronic engineering in 1958. Presently, he is assistant project officer, Marine Aviation Detachment, at the Naval Air Missile Test Center, Point Mugu, Calif.

Capt. Williams is a member of Eta Kappa Nu and Sigma Tau.

James C. Wiltse (S'48—A'53) was born on March 16, 1926, in Tannersville, N. Y. He received the B.E.E. degree in 1946 from Rensselaer Polytechnic Institute, Troy, N. Y. After one year of shipboard duty as an electronics officer in the U. S. Navy he was employed by the General Electric Company for about a year. From 1948 to 1951 he taught in the department of electrical engineering at Rensselaer. Mr. Wiltse also continued his graduate studies there and completed the requirements for the M.E.E. degree in 1951.

J. C. WILTSE

From then until 1958 he was associated with The Johns Hopkins University, most recently as a member of the staff of the Radiation Laboratory. He concurrently completed studying for the Doctor of Engineering degree at Johns Hopkins. At the present time he is employed by Electronic Communications, Inc., of Timonium, Md.

He is a member of Sigma Xi, Tau Beta Pi, and Eta Kappa Nu.

❖

Leo Young (M'54–SM'57) was born in Vienna, Austria, on August 18, 1926. After winning a scholarship from St. John's College, Cambridge, England, he obtained the B.A. degree with honors in mathematics in 1945 and the B.A. degree in physics with honors in 1947. He received the M.A. degree from Cambridge University in 1950.

L. YOUNG

He was an engineer with A. C. Cossor, Ltd., London, from 1948 to 1951. From then until 1953 he was associated with Decca Radar, Ltd., as head of the Microwave and Antenna Laboratory.

He came to the United States in 1953 and joined the Westinghouse Electric Corporation, Baltimore, Md., where he is presently a fellow engineer in the Electronics Division.

He was awarded the M.S. degree in electrical engineering by The Johns Hopkins University in 1956. He won the Westinghouse Corporation's B. G. Lamme Scholarship for 1958, and is using it for one year of graduate studies at Johns Hopkins before returning to Westinghouse.

Mr. Young, a registered professional engineer in Maryland, is a member of Sigma Xi and the American Institute of Electrical Engineers, and an associate member of the Institution of Electrical Engineers.

140 KMC

ULTRAMICROWAVE* EQUIPMENT BY

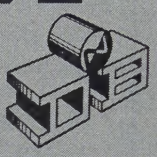

–it works–it's accurate–it's available

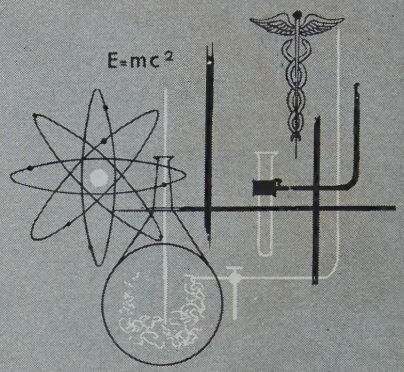

These millimeter wave units can greatly enlarge your scope of microwave activity. Research previously considered impractical at 140 KMC can now be carried on successfully.

De Mornay-Bonardi manufactures cavity wavemeters, crystal multipliers, crystal mounts, E-H tuners, and standing wave detectors specifically for use at 140 KMC. They work—we've been using these units effectively in our own laboratories for developing other items. These instruments are accurate—functionally as accurate as De Mornay-Bonardi equipment used at 90 KMC. You can order these units now—we're currently filling orders on 140 KMC instruments.

Write for complete data

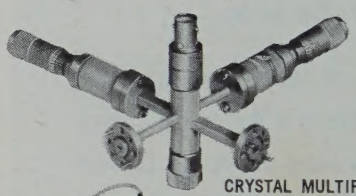
CRYSTAL MULTIPLIERS

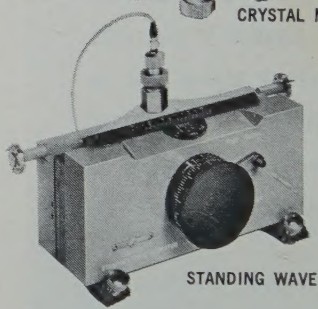
STANDING WAVE DETECTORS

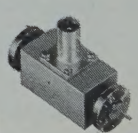
CRYSTAL MOUNTS

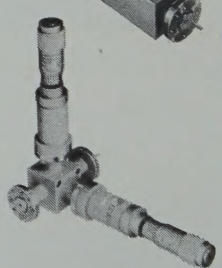
E-H TUNERS

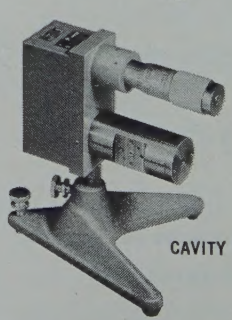
CAVITY WAVEMETERS

DE MORNAY-BONARDI®

DE MORNAY-BONARDI

780 SOUTH ARROYO PARKWAY • PASADENA, CALIF.

*TRADE MARK DE MORNAY-BONARDI

INSTITUTIONAL LISTINGS

The IRE Professional Group on Microwave Theory and Techniques is grateful for the assistance given by the firms listed below, and invites application for Institutional Listing from other firms interested in the Microwave field.

AIRTRON, INC., 1101 W. Elizabeth Ave., Linden, N. J.
Designers and Producers of Complete Line of Microwave, Electronic and Aircraft Components

COLLINS RADIO CO., Cedar Rapids, Iowa
Complete Industrial Microwave, Communication, Navigation and Flight Control Systems

MICROWAVE DEVELOPMENT LABS., INC., 92 Broad St., Babson Park 57, Mass.
Designers, Developers and Producers of Microwave Components and Assemblies, 400 mc to 70 kmc

SAGE LABORATORIES, INC., 159 Linden St., Wellesley 81, Mass.
Microwave Engineering Specialists

WEINSCHEL ENGINEERING CO., INC., Kensington, Md.
Attenuation Standards, Coaxial Attenuators and Insertion Loss Test Sets

WHEELER LABORATORIES, INC., 122 Cutter Mill Road, Great Neck, N. Y.
Consulting Services, Research & Development, Microwave Antennas & Waveguide Components

The charge for an Institutional Listing is $50.00 per issue or $140.00 for four consecutive issues. Applications for Institutional Listings and checks (made out to the Institute of Radio Engineers) should be sent to Tore N. Anderson, PGMTT Advertising Editor, 1539 Deer Path, Mountainside, N.J.

FXR

New... UNIVERSAL RATIOMETER

Model **B811A**

NOW IN ONE COMPACT PACKAGE TWO INSTRUMENTS

FXR's — B811A Universal Ratiometer combines, at less cost, the many features of a separate ratiometer and standing wave amplifier.

- COMPACT PACKAGE — PRINTED WIRING CONSTRUCTION
- INCREASED SENSITIVITY FOR MORE ACCURATE REFLECTOMETER MEASUREMENTS
- TWO CYCLE PRECISION LOG METER — VSWR REFLECTOMETER READINGS OF 1.02 TO ∞ ON ONLY TWO SCALES
- VSWR, DB AND Γ SCALES ELIMINATE CONVERSION TABLES
- BUILT-IN INPUT TRANSFORMERS — NO ACCESSORIES REQUIRED
- EXPANDED VSWR SCALES AND FULL 70 DB STANDING WAVE AMPLIFIER OPERATION
- CRYSTAL AND BOLOMETER OPERATION

Accessories for reflectometer measurements also available . . . Write for details.

FXR, Inc. formerly F-R MACHINE WORKS, Inc.

DESIGN • DEVELOPMENT • MANUFACTURE

26-12 BOROUGH PLACE, WOODSIDE 77, N. Y.

TELEPHONE: AStoria 8-2800

FXR

PRECISION MICROWAVE EQUIPMENT

•

HIGH POWER MODULATORS

•

RADAR COMPONENTS

•

ELECTRONIC TEST EQUIPMENT